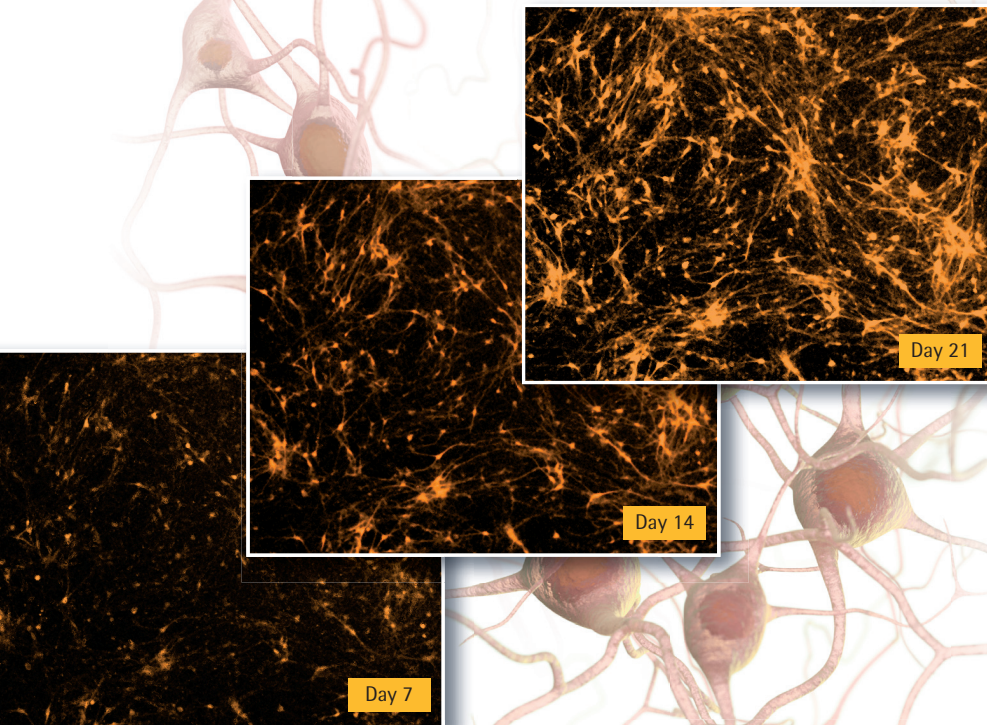




sartorius

Monitor and analyze hiPSC-derived neurons



Human induced pluripotent stem cell-derived neurons provide a new approach aimed at modeling neurological diseases and are critical for the characterization and evaluation of these novel model systems.

Reveal the dynamic nature of hiPSC-derived neurons in mono or co-culture conditions using the IncuCyte® S3 System for real-time, long-term quantitative analysis.

Essenbio.com/neuroscience

- Optimize culture conditions for (hiPSC)-derived neurons.
- Visualize and quantify neurite dynamics using phase (monoculture) or fluorescent (co-culture) IncuCyte® NeuroTrack software.
- Monitor neuronal cell health (e.g. apoptosis) and validate mechanisms.



turning science **into solutions**

IncuCyte®
by SARTORIUS

Cell Press Selections

Reprint supplement

The Dynamic Neuron

Functions and Processes in Neuronal Cell Biology

CellPress

www.cell.com

CELLSDYNAMICPNS

IncuCyte[®]

by SARTORIUS



turning science **into solutions**



sartorius

No matter the time of day or night,
see exactly what happened
to your cells and when.

Biological processes are dynamic, and a single snapshot in time may not capture rare or transient events, causing you to miss a relevant response. With the IncuCyte® S3 live-cell analysis system and reagents, automatically follow the sequence of biological events continuously, then 'rewind and replay' the experiment to see what really happened to your cells while you were away.

The IncuCyte S3 combines image-based measurements, a physiologically relevant environment, and microplate throughput to enable researchers to visualize and analyze cell behaviors at a scale and in ways that were previously not possible—all without ever removing cells from the incubator.

Visit www.essenbio.com/IncuCyte to learn about the next-generation IncuCyte S3 System and the benefits of real-time, automated live-cell analysis.



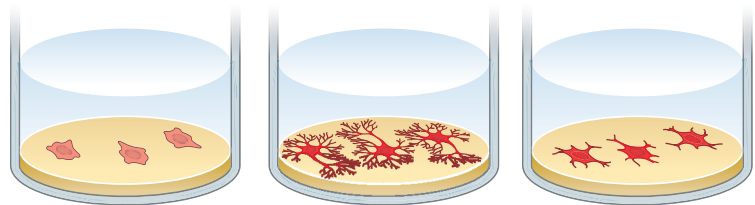
IncuCyte®
by SARTORIUS



sartorius

Confidently measure and assess neurite dynamics and cell viability in real-time

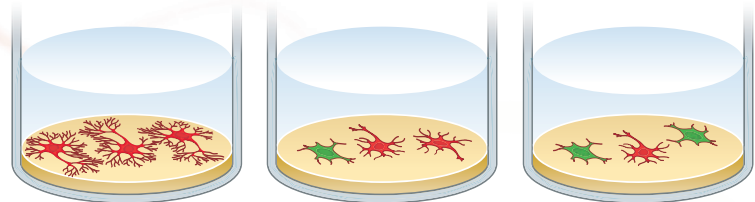
Neurite outgrowth, network stability and disruption of mature neural networks



Neurite outgrowth

Disruption

Cytotoxicity and apoptosis in neuronal cultures



Neuronal network

Monitoring neuronal cell health

Automatically acquire images and analyze sensitive neuronal cultures for days or weeks—*inside your incubator.*



Essenbio.com/neuroscience

turning science **into solutions**

IncuCyte[®]
by SARTORIUS

Foreword

From the smallest vesicle to the behavior of entire cells, the dynamics of neurons are key to the insight into their function and dysfunction. Since the advent of tools sensitive enough to observe neurons, scientists have been studying and trying to understand the flurry of activity that goes on within them. The reviews and research featured in this edition of *Cell Press Selections* provide insight into the progress current neuroscientists are making on how these vastly complicated, lively cells work.

Covering the scope of early developing neurites to degenerating axons and local synaptic vesicle movements to transport across a neuron and expanding from dividing neuronal stem cells into migrating neurons, the reviews and articles in this collection highlight the diversity of ways in which cell biology is influencing neuroscience. The insights gained from these areas of research will not only impact basic neurobiology but also have implications for developmental disorders, nervous system injury, and a host of other human disorders—the mechanisms of which are being discovered piece by piece in this vibrant area of science.

These articles represent only a small portion of the exciting research Cell Press has published and will continue to publish on neuronal cell biology. We hope you will visit www.cell.com on a regular basis to keep up with this fast-moving field.

Finally, we are grateful for the support of Essen BioScience (now part of Sartorius), who helped to make the publication of this collection possible.

Emily Niederst

Scientific Editor, *Neuron*



sartorius

Continually monitor and analyze neurite dynamics

Insights into neurite outgrowth, network stability and the disruption of mature neural networks can remain hidden if non-image based end-point analysis are used.

The IncuCyte® Live-cell Analysis System enables both visual examination and real-time analysis of human iPSC-derived neurons, primary neurons, immortalized and neuronal-like cells in mono-cultures and co-cultures.

Essenbio.com/neuroscience



turning science **into solutions**

IncuCyte®
by SARTORIUS

The Dynamic Neuron

Functions and Processes in Neuronal Cell Biology

Reviews

Axon Self-Destruction: New Links among SARM1, MAPKs, and NAD⁺ Metabolism

Josiah Gerdts, Daniel W. Summers, Jeffrey Milbrandt, and Aaron DiAntonio

Moonlighting Motors: Kinesin, Dynein, and Cell Polarity

Wen Lu and Vladimir I. Gelfand

The Interplay of Axonal Energy Homeostasis and Mitochondrial Trafficking and Anchoring

Zu-Hang Sheng

Articles

An Intrinsic Epigenetic Barrier for Functional Axon Regeneration

Yi-Lan Weng, Ran An, Jessica Cassin, Jessica Joseph, Ruifa Mi, Chen Wang, Chun Zhong, Seung-Gi Jin, Gerd P. Pfeifer, Alfonso Bellacosa, Xinzhong Dong, Ahmet Hoke, Zhigang He, Hongjun Song, and Guo-li Ming

Golgi-Resident Gαo Promotes Protrusive Membrane Dynamics

Gonzalo P. Solis, Oleksii Bilousov, Alexey Koval, Anne-Marie Lüchtenborg, Chen Lin, and Vladimir L. Katanaev

RNA Docking and Local Translation Regulate Site-Specific Axon Remodeling In Vivo

Hovy Ho-Wai Wong, Julie Qiaojin Lin, Florian Ströhl, Cláudio Gouveia Roque, Jean-Michel Cioni, Roberta Cagnetta, Benita Turner-Bridger, Romain F. Laine, William A. Harris, Clemens F. Kaminski, and Christine E. Holt

Regulation of Cerebral Cortex Folding by Controlling Neuronal Migration via FLRT Adhesion Molecules

Daniel del Toro, Tobias Ruff, Erik Cederfjäll, Ana Villalba, Gönül Seyit-Bremer, Víctor Borrell, and Rüdiger Klein

Nucleolin-Mediated RNA Localization Regulates Neuron Growth and Cycling Cell Size

Rotem Ben-Tov Perry, Ida Rishal, Ella Doron-Mandel, Ashley L. Kalinski, Katalin F. Medzihradzsky, Marco Terenzio, Stefanie Alber, Sandip Koley, Albina Lin, Meir Rozenbaum, Dmitry Yudin, Pabitra K. Sahoo, Cynthia Gomes, Vera Shinder, Wasim Geraisy, Eric A. Huebner, Clifford J. Woolf, Avraham Yaron, Alma L. Burlingame, Jeffery L. Twiss, and Mike Fainzilber

Human iPSC-Derived Cerebral Organoids Model Cellular Features of Lissencephaly and Reveal Prolonged Mitosis of Outer Radial Glia

Marina Bershteyn, Tomasz J. Nowakowski, Alex A. Pollen, Elizabeth Di Lullo, Aishwarya Nene, Anthony Wynshaw-Boris, and Arnold R. Kriegstein

Retrogradely Transported TrkA Endosomes Signal Locally within Dendrites to Maintain Sympathetic Neuron Synapses

Kathryn M. Lehigh, Katherine M. West, and David D. Ginty

(continued)

**Ligl1 Connects Cell Polarity with Cell-Cell Adhesion
in Embryonic Neural Stem Cells**

*Yves Jossin, Minhui Lee, Olga Klezovitch, Elif Kon,
Alexia Cossard, Wen-Hui Lien, Tania E. Fernandez,
Jonathan A. Cooper, and Valera Vasioukhin*

**Synaptic Vesicle Endocytosis Occurs on
Multiple Timescales and Is Mediated by
Formin-Dependent Actin Assembly**

*Tolga Soykan, Natalie Kaempf, Takeshi Sakaba,
Dennis Vollweiter, Felix Goerdeler, Dmytro Puchkov,
Natalia L. Kononenko, and Volker Haucke*

Axon Self-Destruction: New Links among SARM1, MAPKs, and NAD⁺ Metabolism

Josiah Gerdts,¹ Daniel W. Summers,^{1,2} Jeffrey Milbrandt,^{1,3} and Aaron DiAntonio^{2,3,*}

¹Department of Genetics

²Department of Developmental Biology

³Hope Center for Neurological Disorders

Washington University School of Medicine in St. Louis, 660 Euclid Avenue, St. Louis, MO 63110, USA

*Correspondence: diantonio@wustl.edu

<http://dx.doi.org/10.1016/j.neuron.2015.12.023>

Wallerian axon degeneration is a form of programmed subcellular death that promotes axon breakdown in disease and injury. Active degeneration requires SARM1 and MAP kinases, including DLK, while the NAD⁺ synthetic enzyme NMNAT2 prevents degeneration. New studies reveal that these pathways cooperate in a locally mediated axon destruction program, with NAD⁺ metabolism playing a central role. Here, we review the biology of Wallerian-type axon degeneration and discuss the most recent findings, with special emphasis on critical signaling events and their potential as therapeutic targets for axonopathy.

Injury-induced axonal degeneration is a genetically encoded program of subcellular self-destruction. Recent genetic studies have identified essential molecular components of this axon degeneration program. In this review, we focus on three key players: (1) the axonal maintenance factor NMNAT2, whose regulation helps explain the potent axoprotective activity of the “Wallerian degeneration slow” protein; (2) dual leucine zipper kinase (DLK) and associated MAP kinase components, which promote both axon degeneration and axon regeneration; and (3) SARM1, which has emerged as the central executioner in the axonal degeneration program. Recent exciting work is uncovering mechanistic links among these proteins, suggesting that this field is on the cusp of a unified model for the mechanism of axonal degeneration. In this review, we summarize the current understanding of axon degeneration, with particular emphasis on the integration of these components into a single pathway, highlighting biochemical and metabolic steps within the degeneration program that represent therapeutic targets to block axon loss in disease.

Axons can extend to great lengths of more than 1 m in humans, making them uniquely susceptible to damage that often results in irreversible disability. Axon loss is a prominent feature of many important neurological disorders, including neuropathies, traumatic injury, and multiple neurodegenerative disorders. Peripheral neuropathy is the most common condition in which axon dysfunction and degeneration are the central abnormalities, and it may be either acquired or hereditary. Acquired neuropathies include diabetic and chemotherapy-induced neuropathy (Albers and Pop-Busui, 2014; Cashman and Höke, 2015; Grisold et al., 2012), which are increasingly common because of the growing prevalence of diabetes and improving rates of cancer survivorship. Traumatic brain injury also involves prominent axon damage, resulting in diffuse axonal injury in the brain and spinal cord that directly impairs neuronal function and accelerates neurodegeneration (Johnson et al., 2013). The full contribution of axon degeneration to human morbidity is difficult to estimate because no pharmacologic tools currently exist that

slow or halt axon degeneration; however, histologic studies have revealed early and prominent axon loss in Alzheimer’s disease, Parkinson’s disease, multiple sclerosis, amyotrophic lateral sclerosis, and others (Benarroch, 2015; Burke and O’Malley, 2013; Coleman, 2005), suggesting an important role for axon degeneration in these diseases. Thus, halting axon destruction offers hope for therapeutic benefit in a wide range of neurologic diseases.

Degeneration of damaged nerves was observed more than 160 years ago by Augustus Waller (Waller, 1850) and was long believed to be a passive phenomenon. Lunn et al. (1989) challenged this notion by discovering a naturally occurring mouse strain with profoundly delayed Wallerian degeneration. When mice bearing the autosomal dominant “Wallerian degeneration slow” (*Wlds*) allele underwent sciatic nerve transection, the distal axons remained structurally and metabolically intact for up to 2 weeks without physical connection to a cell body, whereas axons from wild-type mice degenerated in less than 2 days (Lunn et al., 1989; Tsao et al., 1994). The *Wlds* mouse transformed our understanding of axon degeneration, leading to the modern view that axons, like cell bodies, possess a genetically encoded capacity for active self-destruction. Moreover, the *Wlds* gene protects axons in a variety of disease models other than axotomy, including models of glaucoma, peripheral neuropathy, and motor neuron disease (Beirowski et al., 2008; Ferri et al., 2003; Hasbani and O’Malley, 2006; Mi et al., 2005; Sajadi et al., 2004; Wang et al., 2002), suggesting that the mechanism of Wallerian-type axon degeneration is engaged in many neurological disorders involving axon loss.

Throughout this review we use the term “axon degeneration” to refer exclusively to the Wallerian axon destruction pathway that promotes pathologic axon degeneration in the settings of injury, transport failure, and poisoning with chemotherapeutic agents. There is a distinct caspase- and BAX-dependent pathway that promotes degeneration in the setting of developmental axon pruning and growth factor deprivation (Nikolaev et al., 2009; Pease and Segal, 2014; Schoenmann et al., 2010;

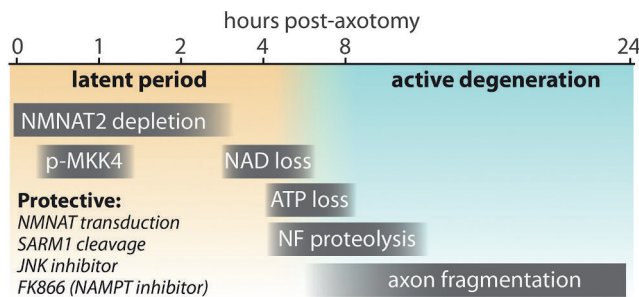


Figure 1. Time Course of Events in Axon Degeneration in Cultured DRG Neurons

The “latent period” (from injury to ~4–6 hr) precedes morphological changes and is characterized by NMNAT2 depletion (Di Stefano et al., 2015) and transient phosphorylation of MKK4 at S257/T261 (Yang et al., 2015). During this window, axon degeneration can be halted by several protective manipulations, including NMNAT protein transduction (Sasaki and Milbrandt, 2010), SARM1 cleavage (Gerdts et al., 2015), and addition of FK866 (Sasaki et al., 2009b; Di Stefano et al., 2015) or JNK inhibitors (Miller et al., 2009). As NAD⁺ declines from 3–6 hr (Wang et al., 2005), ATP levels also decline (Yang et al., 2015), and an active and irreversible phase of axon degeneration begins with neurofilament (NF) proteolysis (Yang et al., 2013) stimulated by calcium influx and finally frank morphologic fragmentation of the axons. These events also occur *in vivo*, albeit over a slower time course.

Vohra et al., 2010). In this review, we focus solely on the Wallerian degeneration pathway and do not address developmental axon loss or the phagocytic clearance of damaged axons, which have been reviewed elsewhere (Luo and O’Leary, 2005; Schuldiner and Yaron, 2015). However, there is some molecular commonality between injury-induced and developmental axon loss (Gerdts et al., 2013; Schoenmann et al., 2010; Vohra et al., 2010), so processes described below may also play a currently unappreciated role in the development and plasticity of neural circuits.

Basic Features of Axon Degeneration

Axon degeneration signaling is intrinsic to the axon. After injury, pro-destructive signaling takes place within the distal axon segment independent of *de novo* transcription or translation or external cues. The temporal progression of axon destruction following axotomy involves an early “latent” period lasting ~4–6 hr *in vitro* (Figure 1) and ~36 hr in adult nerves *in vivo*. During this phase the distal axon remains physically and metabolically intact (Coleman, 2005). Critical steps in axon degeneration signaling take place early during the latent period, long before axon degeneration is morphologically evident. This early latent phase thus appears to be an ideal window for therapeutic intervention. In contrast, late steps in axon degeneration, such as energetic failure, influx of calcium and resultant calpain-mediated proteolysis of neurofilaments and other structural proteins, axon fragmentation, and engulfment by phagocytic cells (Kurant, 2011; Wang et al., 2012; Yang et al., 2013), may be beyond the point of no return from a therapeutic perspective.

Axon destruction is unique among cellular destruction programs because it is spatially restricted. With classic Wallerian degeneration of a peripheral nerve, the axon segment distal to a point of injury undergoes selective breakdown, while the proximal axon segment and cell soma remain intact. Hence, axon destruction signaling must distinguish between the portions of

axon to be destroyed and those to be spared. Two potential mechanisms could explain the differential sensitivity of proximal and distal axons to injury-induced destruction. The loss of communication with the cell body could deprive the distal axon of an axonal maintenance factor required for axon survival. Alternatively, a pro-degenerative signal could be selectively activated in the distal axon following injury. As we shall see, both mechanisms are at play following axon injury and likely work together to trigger axon loss. The coordinated activity of both positive and negative axon stability mechanisms, exemplified by NMNAT2 and SARM1, may help ensure that in healthy axons, degeneration signaling is tightly maintained in an “off” state in order to prevent spurious axon degeneration.

The Nicotinamide Adenine Dinucleotide Biosynthetic Enzyme NMNAT Protects Axons

A strong yet mysterious link between axon degeneration and nicotinamide adenine dinucleotide (NAD⁺) metabolism emerged from studies of the *Wlds* mouse. Cloning of the *Wlds* gene revealed it to encode a chimeric fusion protein comprised of the NAD biosynthetic enzyme nicotinamide mononucleotide adenylyltransferase (NMNAT1), which forms NAD⁺ from nicotinamide mononucleotide (NMN) and ATP (Figure 2), and a fragment of the ubiquitination factor UBE4B (Conforti et al., 2000). Although there was initially controversy as to the functional domains of the *Wlds* protein, it is now clear that NMNAT1 is the axoprotective component (Araki et al., 2004). The *Wlds* fusion protein confers aberrant localization of the nuclear enzyme NMNAT1 to the axon, where it functions autonomously. Accordingly, manipulations that increase axonal localization of NMNAT1 confer *Wlds*-like axon protection (Babetto et al., 2010; Sasaki et al., 2009a). Direct transduction of NMNAT1 protein into severed axons *in vitro* within 4 hr after axon transection (see Figure 1) is sufficient to prevent later fragmentation of the axons (Sasaki and Milbrandt, 2010), definitively demonstrating that NMNAT1 exerts its protective effect locally within the axonal compartment. Moreover, *Wlds*-expressing axons rapidly degenerate when *Wlds* is depleted after injury by protein destabilization, demonstrating a continuous local requirement for NMNAT activity in isolated axons (Wang et al., 2015).

This axon protective activity is not a specific property of NMNAT1 but is shared with divergent NMNAT proteins, including the three mammalian NMNAT paralogs (1–3) and structurally dissimilar enzymes from archaeobacteria (Sasaki et al., 2009b; Yahata et al., 2009; Yan et al., 2010). Moreover, mutation in the active site abolishes axonal protection from NMNAT1 or the *Wlds* protein (Araki et al., 2004; Sasaki et al., 2009b), confirming that enzymatic activity is required. Not only does NMNAT1 expression protect mammalian axons, but it also profoundly delays axonal degeneration in *Drosophila* (Hoopfer et al., 2006; MacDonald et al., 2006). NMNAT enzymatic activity is also necessary for axon protection in *Drosophila* (Avery et al., 2009), although not in some models of cell death (Zhai et al., 2008). Hence, the axoprotective mechanism of NMNAT enzymes is evolutionarily conserved.

Although NMNAT1 is the active moiety of the *Wlds* protein, axonal mis-localization of this nuclear protein is an unnatural consequence of mutation, and endogenous NMNAT1 is not believed to have a role in axon destruction or maintenance in

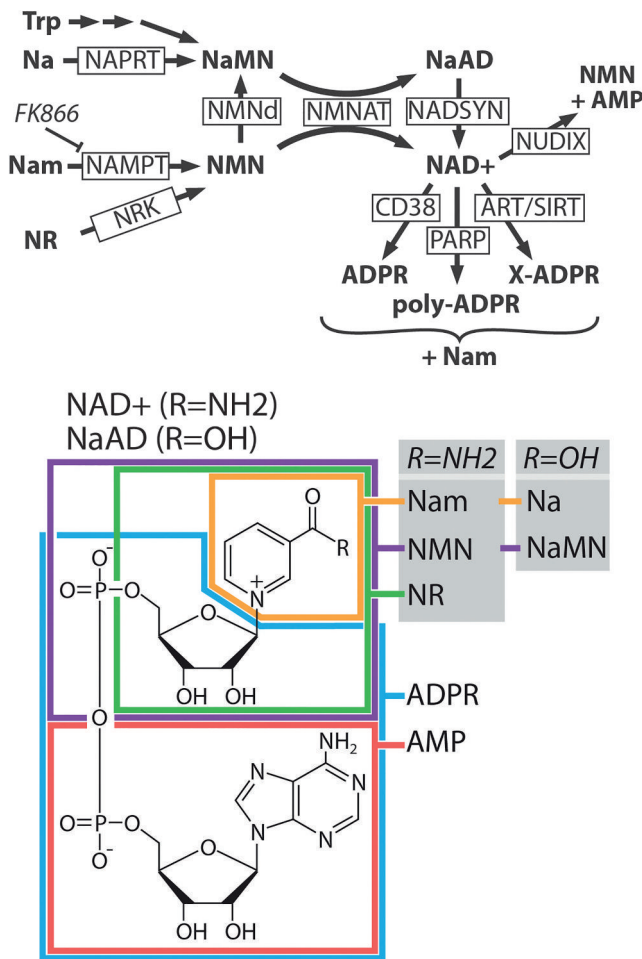


Figure 2. Pathways of NAD⁺ Synthesis and Breakdown

Top: NAD⁺ is synthesized from nicotinamide (Nam), nicotinic acid (Na), nicotinamide riboside (NR), or tryptophan (Trp). All synthetic pathways require NMNAT. NaMN can be synthesized from NMN in some bacteria by the enzyme NMN deaminase (NMNd), which has no mammalian ortholog. NAD⁺ is broken down by multiple classes of enzymes, including the glycohydrolase CD38 (Aksoy et al., 2006), PARPs, NUDIX phosphohydrolases (McLennan, 2006), ARTs, and sirtuins (SIRTs). PARPs create polymers of ADPR that are often attached to a protein substrate. ARTs transfer ADPR from NAD⁺ to an acceptor molecule (X) such as a protein. SIRTs transfer an O-acetyl group from a protein substrate to the ADPR moiety of NAD⁺ to yield O-acetyl-ADPR and Nam. NaAD, nicotinic acid adenine dinucleotide; NADSYN, NAD synthetase; NAPRT, nicotinic acid phosphoribosyltransferase; NRK, nicotinamide riboside kinase; NUDIX, nucleoside diphosphate moiety linked X. Bottom: structure of NAD⁺ with substrate moieties approximately outlined. For a more detailed overview of this pathway, see Belenky et al. (2007) and Chiarugi et al. (2012).

wild-type animals. Instead, it is likely that NMNAT1 protects axons by substituting for its axonal paralog, NMNAT2. Gilley and colleagues demonstrated that NMNAT2 is trafficked anterogradely in the axoplasm, and unlike NMNAT1 and NMNAT3, NMNAT2 is labile because of constitutive proteasomal degradation. NMNAT2 turnover in the setting of disrupted axon transport thus leads to depletion of axonal NMNAT2. NMNAT2 may represent a “survival factor” whose depletion can trigger the axon destruction cascade, as knockdown of NMNAT2 in cultured neurons is sufficient to cause axon degeneration in the absence of

injury (Gilley and Coleman, 2010); however, this model has yet to be tested in *in vivo* injury models. Thus, it is likely that NMNAT2 loss following axon injury is an initiating event in the axon destruction pathway, and axon protection by other NMNAT proteins, including NMNAT1 and Wlds, occurs because they provide continuous NMNAT activity within the axon. Although at one level this explains why Wlds and NMNAT1 are axoprotective—they substitute for the labile NMNAT2—at a more mechanistic level it leaves open the question of how NMNAT activity blocks axon degeneration. Indeed, despite the discovery of axon protection by NMNAT more than a decade ago, the role of its product NAD⁺ in axon protection and destruction remains unclear.

NAD⁺ is a ubiquitous metabolite with critical roles in energy metabolism and cell signaling (Belenky et al., 2007; Chiarugi et al., 2012). Surprisingly, a series of results suggest that increased axonal NAD⁺ levels alone cannot account for the protective activity of NMNAT. First, NAD⁺ steady-state levels are unchanged by NMNAT1 overexpression (Mack et al., 2001), likely because the rate-limiting step in NAD⁺ synthesis is the upstream conversion of nicotinamide (Nam) to NMN that is catalyzed by the enzyme nicotinamide phosphoribosyltransferase (NAMPT) (Figure 2). Second, increasing NAD⁺ levels via metabolite supplementation, overexpression of other enzymes in the pathway, or mutations in NAD⁺-consuming enzymes that lead to a doubling of NAD⁺ levels in the axon provide modest or no axon protection (Sasaki et al., 2006, 2009b; Wang et al., 2005). Although it cannot be excluded that NMNAT expression increases NAD⁺ abundance in a subcellular compartment that is not detected by whole-cell or whole-axon measurements, these findings suggest that increased steady-state NAD⁺ does not explain NMNAT protection.

An alternative model to explain axon protection by NAD⁺ synthesis is replenishment of NAD⁺ in the setting of rapid loss. Loss of NAD⁺ leads to failure of metabolic processes including glycolysis and leads to cell death in some settings (Alano et al., 2010; Fu et al., 2013). Wang et al. (2005) demonstrated that following axon injury, NAD⁺ levels rapidly decline in the distal axon segment prior to morphologic disruption. NMNAT expression delayed both NAD⁺ loss and axon degeneration, consistent with an upstream role for NAD⁺ synthesis in axonal preservation; however, it was unclear whether NAD⁺ depletion was a cause or consequence of the degenerative process. As discussed in the section on SARM1 below, recent findings demonstrate that activation of this axodestructive molecule triggers the rapid consumption of NAD⁺, supporting the model that NMNAT protects axons at least in part by countering SARM1-dependent NAD⁺ loss.

DLK/JNK MAP Kinase Signaling Promotes Axon Degeneration

Overexpression of Wlds and NMNAT1 demonstrate that genetic manipulations can regulate axon degeneration; however, these are gain-of-function manipulations and so do not prove whether or not an endogenous pro-degenerative program exists. If gene products function to promote axon degeneration, then loss of function mutations in these components should delay or block axon degeneration. In recent years, a series of genetic screens in both flies and mice have identified a number of genes that

are required for axonal degeneration (Bhattacharya et al., 2012; Osterloh et al., 2012; Rudhard et al., 2015; Wakatsuki et al., 2011; Wishart et al., 2012). The first gene identified with this phenotype was DLK (DLK/MAP3K12) (Miller et al., 2009), a mitogen-activated protein kinase (MAPK) kinase kinase with a previously described role in regulating synaptic development (Collins et al., 2006; Nakata et al., 2005).

Injury studies in mice and flies demonstrate a role for DLK in axon degeneration. When mutant mice lacking DLK undergo sciatic nerve transection, degeneration of the distal axons is significantly delayed compared to wild-type animals. DLK works through the downstream MAPK JNK (*c-jun* n-terminal kinase), as pharmacological inhibitors of the JNK, but not P38 MAPKs, lead to axon preservation comparable with DLK ablation (Miller et al., 2009). Inhibition of this pathway also delays axon fragmentation in response to the neurotoxic chemotherapeutic vincristine (Miller et al., 2009; Yang et al., 2015), which causes chemotherapy-induced peripheral neuropathy, an important clinical problem involving axon loss. The role of DLK/JNK in promoting degeneration in response to both axotomy and a neurotoxin suggests that this MAPK pathway functions in a core degeneration program downstream of diverse insults. Moreover, this function is conserved in *Drosophila* as mutation of the DLK ortholog Walenda leads to similar axon preservation after both traumatic and neurotoxic injury (Bhattacharya et al., 2012; Miller et al., 2009).

Although loss of DLK is axoprotective, the duration of axon protection is significantly less than with overexpression of NMNAT/Wlds. This indicates that DLK ablation leads to partial blockade of the axon degeneration cascade. Yang et al. (2015) recently demonstrated that this is due to functional redundancy with related kinases, identifying two additional members of the MAPKKK family, MEKK4 (MAP3K4) and MLK2 (MAP3K10), which promote axon degeneration. Knockdown of each leads to short-term axon protection similar to DLK, but combined genetic disruption of the three MAPKKKs leads to long-lasting protection in both cultured neurons and retinal ganglion cell axons in vivo, demonstrating that MAPKKK activity constitutes a major node in axon destruction signaling (Yang et al., 2015).

These three MAPKKKs activate the MAPKKs MKK4 and MKK7 that in turn converge on the JNK family of MAPKs (JNK1–3) (Yang et al., 2015). The double MKK4/MKK7 knockout (KO) leads to improved axon protection compared with either mutant alone, although MKK4 appears to play the more important role. Similarly, simultaneous genetic disruption of all three JNK proteins (JNK1–3) affords stronger axon protection than knockdown of any individual JNK paralog. Thus, there is redundancy throughout the MAP kinase cascade. One unexplained mystery is why pharmacological inhibitors of JNK are much less effective than genetic manipulation of JNK1–3, even when given at doses that should block all three isoforms (Bennett et al., 2001; Miller et al., 2009; Yang et al., 2015).

Surprisingly, activation of the JNK axis is detected remarkably early after axon injury; MKK4 phosphorylation at activating residues S257/T261 is detected in distal optic nerve segments within 5–15 min of nerve crush, and this signal dissipates within 30–60 min (Yang et al., 2015). MKK4 activation thus precedes morphologic axon fragmentation by an extended period of hours (in vitro) to days (in vivo), during which time downstream pathway

components continue to promote axon dismantling. In this regard, axon-protective JNK inhibitors are effective only when applied to axons within 3 hr after injury in vitro (Miller et al., 2009), confirming that the MAPK pathway performs a pro-destructive function as the axon commits to degenerate and before the active breakdown phase of axon loss (Figure 1).

Once JNKs are activated, how do they promote axon degeneration? JNK kinases have diverse biological functions in stress responses, apoptosis, and cellular proliferation (Leppä and Bohmann, 1999). Although the canonical target of JNKs is the transcription factor AP-1, axon degeneration is local and does not involve transcriptional regulation. Thus efforts are focused on identifying axonal JNK targets. One identified target is SCG10 (stathmin 2), a member of the stathmin family of microtubule binding proteins. SCG10 is a direct JNK target that undergoes rapid phosphorylation-dependent proteasomal degradation after axon injury (Shin et al., 2012a, 2014). SCG10 loss is likely in part responsible for JNK-mediated axon dismantling because SCG10 knockdown accelerates injury-induced degeneration, whereas expression of JNK-insensitive SCG10 modestly delays degeneration. It is likely that additional unidentified JNK targets mediate the metabolic failure and protease activation that characterize the later stages of axon degeneration.

In addition to identifying downstream targets of JNK, a second major area of investigation is to define the mechanism by which axon injury activates the MAPK pathway. One important clue comes from the study of DLK, which plays a dual role in the axon injury response, promoting both destruction of the distal axon and regrowth of the proximal axon (Hammarlund et al., 2009; Shin et al., 2012b; Xiong et al., 2010; Yan et al., 2009). This suggests that DLK is a sensor of axon injury, coordinating the degenerative and regenerative responses. What aspect of axon injury activates DLK? One intriguing candidate is cytoskeletal disruption. In worms, flies, and mice, genetic and/or pharmacological manipulations that impair normal cytoskeletal function activate DLK (Bounoutas et al., 2011; Marcette et al., 2014; Valakh et al., 2013, 2015). Cytoskeletal disruption occurs in traumatic axon injury and in response to neurotoxic chemotherapeutics such as vincristine and paclitaxel that cause neuropathy and so is well positioned to serve as an injury signal. In addition, other mechanisms can regulate DLK, including calcium influx (Yan and Jin, 2012), degradation by ubiquitin ligases (Collins et al., 2006; Nakata et al., 2005), and feedback phosphorylation loops (Huntwork-Rodriguez et al., 2013). However, most of these mechanisms have been studied in the context of development or regeneration, and less is known about their role in DLK activation in the degenerating distal axon. Recently, Yang et al. made a major breakthrough in our understanding of MAPK activation following axon injury, demonstrating that the pro-degeneration molecule SARM1 promotes and the axo-protective molecule NMNAT inhibits MAPK activation. These exciting findings are described below in a section on SARM1 and MAPK activation.

SARM1 Is the Executioner of Axonal Degeneration

SARM1 is an essential component of the axon degeneration mechanism, and we suggest that it is the defining molecule in this program, whose activation triggers an irreversible

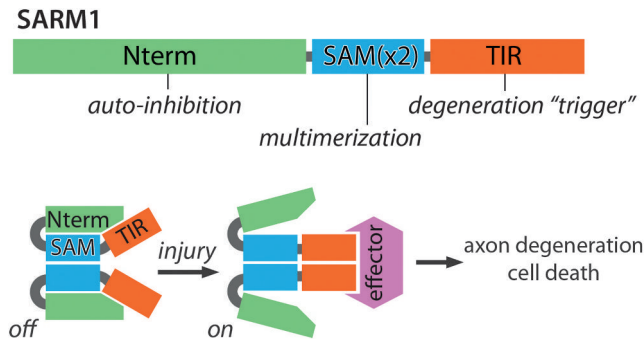


Figure 3. A Working Model of SARM1 Auto-inhibition and Activation upon Injury

Top: SARM1 is made up of three regions: (1) an auto-inhibitory N terminus (Nterm) comprised of multiple ARMs, (2) tandem SAM domains that mediate SARM1-SARM1 binding (SAMx2), and (3) a TIR domain that triggers axon degeneration upon multimerization. Bottom: SARM1 multimers are inactive (auto-inhibited) in uninjured axons. Injury leads to SARM1 activation, perhaps through release of inhibition, exposing TIR domain multimers that transmit a pro-destructive signal to unknown effector molecule(s).

commitment to axon destruction. A role for SARM1 in axon degeneration was first identified in a large-scale genetic screen in *Drosophila*. In an elegant and arduous mosaic loss-of-function screen, Osterloh et al. (2012) demonstrated that mutations in *dSarm* (also called *ect4*) led to a profound delay in the degeneration of olfactory receptor neuron axons after axotomy. SARM1 was also identified in a genome-wide RNAi screen in primary mouse neurons, in which knockdown of SARM1 led to long-lasting protection of sensory neurons against injury-induced axon degeneration (Gerdtts et al., 2013). In vivo, SARM1 KO mice show marked preservation of axons for up to 14 days after nerve transection, which is comparable with the protection afforded by overexpression of axon-targeted NMNAT (Gerdtts et al., 2013; Osterloh et al., 2012). As with DLK, SARM1 is also required for axon degeneration in response to vincristine in cellular models of chemotherapy-induced peripheral neuropathy. Finally, one study showed that SARM1 mediates rapid axon loss in cultured DRG neurons following trophic factor withdrawal, in parallel with a transcription-dependent pathway (Gerdtts et al., 2013); however, another study showed that *SARM1*^{-/-} DRG explant cultures degenerate normally in response to trophic withdrawal (Osterloh et al., 2012). Altogether, these findings demonstrate that SARM1 is an essential component of an evolutionarily conserved axon degeneration program that responds to disparate insults.

Although SARM1 was recently linked to axon degeneration, prior studies in other contexts provide insights into the SARM1 mechanism of action. SARM1 is an intracellular protein that is predominantly associated with the outer mitochondrial membrane (Panneerselvam et al., 2012), although this mitochondrial location is not necessary for its role in axon destruction (Gerdtts et al., 2013). SARM1 is also present at synapses and associated with microtubules (Chen et al., 2011; Kim et al., 2007). SARM1 contains a C-terminal Toll-interleukin receptor (TIR) domain, suggesting that it might function like the other four known cytosolic TIR-containing proteins as a scaffold for Toll-like receptor (TLR) signaling. However, SARM1 is unique among these proteins in that loss of SARM1 does not impair TLR signaling (Kim et al.,

2007), and SARM1 overexpression paradoxically inhibits TLR signaling (Carty et al., 2006). Moreover, the SARM1 TIR domain evolutionarily predates TIR-containing receptors and appears to be the ancestral mammalian TIR domain because of its similarity to TIR domains found in bacterial proteins (Zhang et al., 2011). Hence, SARM1 is likely not a canonical TLR adaptor, although SARM1 does function in cellular stress responses. Mammalian SARM1 is most highly expressed in the nervous system and promotes neuronal death under hypoxic conditions (Kim et al., 2007) and in response to viral infection (Mukherjee et al., 2013). The role of SARM1 in regulating neuronal cell death is described in more detail below. In *C. elegans* and *Drosophila*, the SARM1 orthologs *tir-1* and *dSARM* (*ect-4*) function in innate immunity (Akhouayri et al., 2011; Couillault et al., 2004; Liberati et al., 2004), and in *C. elegans*, *tir-1* also regulates non-apoptotic programmed cell death and some cell fate decisions (Blum et al., 2012; Chuang and Bargmann, 2005). It is not known whether SARM1 uses the same or distinct mechanisms to drive adaptive responses such as induction of host defense genes as it does to promote degenerative responses in the axon.

What is the molecular function of SARM1? SARM1 has no known enzymatic activity, but it has multiple protein interaction domains that appear to have distinct roles in SARM1 regulation and activity. In addition to the C-terminal (TIR) domain, SARM1 contains two tandem sterile alpha motif (SAM) domains and an N-terminal region with multiple armadillo repeat motifs (ARMs). Typically, SAM domains mediate homo- and/or heteromultimerization (Qiao and Bowie, 2005), while ARM domains participate in diverse protein interactions. As an initial step toward understanding this domain architecture in relation to axon degeneration, a structure-function study was performed by expressing SARM1 mutant proteins in DRG neurons undergoing axon injury. This analysis generated a straightforward model of SARM1 action (Gerdtts et al., 2013) (Figure 3).

First, the N-terminal domain of SARM1 is auto-inhibitory, restraining the pro-degenerative activity of the protein. Although overexpression of full-length SARM1 does not cause or accelerate axon degeneration, SARM1 lacking the N-terminal domain elicits highly penetrant axon degeneration and cell death in both mammalian and *Drosophila* neurons in the absence of injury. Interestingly, the N-terminal region of the *C. elegans* SARM1 ortholog *tir-1* similarly exerts an auto-inhibitory function in the control of odorant receptor gene expression (Chuang and Bargmann, 2005), demonstrating commonality in mechanism despite the very different cellular outcome. Whether or how an upstream signal relieves SARM1 auto-inhibition is unknown, but one attractive model is that injury leads to a conformation change that exposes, or allows the formation of, a TIR domain dimer (see below).

Second, the SAM and TIR domains of SARM1 have cooperative pro-destructive roles. The SAM domains mediate SARM1-SARM1 binding, and this is essential for SARM1 function. The TIR domain is the critical effector, and functional SARM1 complexes require multiple TIR domains to promote axon degeneration. These roles are illustrated by the dominant-negative activity of TIR-less SARM1 mutants, which form non-functional complexes with full-length SARM1 (Gerdtts et al., 2013). Thus, SARM1 undergoes SAM-mediated multimerization that brings

multiple TIR domains into proximity. The associated TIR domains are the active portion of the SARM1 complex, initiating downstream signaling. Therefore, forced dimerization of TIR domains using pharmacologically controlled dimerization domains is sufficient to trigger rapid axon degeneration (Gerdtts et al., 2015; Yang et al., 2015) (Figure 3). It is presumed that the TIR multimer serves as a scaffold that associates with and activates a downstream effector (Figure 3), much like the TIR domains of TLR proteins (Kang and Lee, 2011).

The insights gleaned from these structure-function studies have enabled the development of novel experimental tools to study critical aspects of SARM1 function. For instance, does SARM1 participate directly in the degeneration process after injury, or does it instead function prior to injury to regulate the capacity of the neuron to respond to a subsequent injury? The temporal requirement for SARM1 after injury was examined using a fully functional protease-sensitized SARM1 mutant molecule that could be inactivated by addition of a drug. Expression of this SARM1 mutant in *SARM1*^{-/-} neurons promoted injury-induced axon degeneration similar to wild-type neurons; however, SARM1 inactivation blocked degeneration, even if the drug was added 2 hr after injury. Thus, in this system, SARM1 activity was required after axon severing, indicating that SARM1 functions within the injured axon to promote destruction. Moreover, local activation of SARM1 signaling within axons is sufficient to cause local destruction: when TIR dimerization is elicited in axons grown in compartment chambers, the treated axons degenerate, leaving untreated proximal axon and soma intact (Gerdtts et al., 2015). Taken together, SARM1 functions locally within the axon after injury, where its activation is sufficient to cause destruction, and this raises the question of what destructive process lies downstream of SARM1.

SARM1 Activation Triggers NAD⁺ Depletion

Recent work has linked SARM1 to NAD⁺, the metabolic product of NMNAT enzymes. Following axotomy, NAD⁺ levels decline in the axon (Wang et al., 2005). This loss of NAD⁺ is markedly suppressed in *SARM1*^{-/-} axons both in vitro and in vivo, placing NAD⁺ loss downstream of SARM1 (Gerdtts et al., 2015). To evaluate whether NAD⁺ loss is a consequence of SARM1 activation, NAD⁺ levels were measured following SARM1 activation via chemically induced TIR dimerization. Remarkably, upon TIR dimerization, neuronal NAD⁺ was depleted within minutes, followed quickly by ATP loss and later by morphological destruction of the axon. This SARM1-induced NAD⁺ depletion occurs via chemical breakdown of NAD⁺ rather than synthetic blockade or efflux. In heterologous cells, TIR dimerization led to cleavage of exogenous NAD⁺, yielding nicotinamide (Gerdtts et al., 2015), and so SARM1-induced NAD⁺ depletion in neurons is also likely due to NAD⁺ cleavage. NAD⁺ depletion may be the essential function of SARM1, as alternative methods to induce NAD⁺ loss can bypass the requirement for SARM1 in axon degeneration. SARM1-independent NAD⁺ breakdown in *SARM1*^{-/-} cells induced by a pharmacologically controlled poly ADP-ribose polymerase (PARP) enzyme causes axon degeneration, demonstrating that NAD⁺ loss is sufficient to trigger degeneration. Interestingly, SARM1-induced axon destruction was fully blocked by concurrent increased NAD⁺ synthesis, either by expression of

the NAD⁺ synthetic enzymes NAMPT and NMNAT or by supplementation with the NAD⁺ precursor NR (see Figure 2) (Gerdtts et al., 2015). Together, these findings unify previous observations regarding Wlds/NMNAT axon protection with the recent discovery that SARM1 loss prevents axon degeneration, providing a framework for understanding the axon destructive pathway.

Assuming that SARM1 functions to trigger rapid NAD⁺ breakdown in axons, as seems likely, the question becomes, by what mechanism does SARM1 degrade NAD⁺? There are two potential models. First, the SARM1 TIR domain may have intrinsic enzymatic NADase activity. This would be a novel and surprising finding, as the best studied TIR domains serve as scaffolds. However the SARM1 TIR domain may have additional properties, as it is the ancestral TIR domain and is more similar to bacterial TIR domains than to other metazoan TIR domains (Zhang et al., 2011). The second possibility is that SARM1 TIR can activate an NAD⁺-consuming enzyme. NAD⁺ can be consumed by a variety of enzymes, including PARPs, ADP ribosyltransferases (ARTs), and sirtuin proteins, that yield nicotinamide and an ADP-ribosylated product (Figure 2). SARM1 activation still depletes NAD⁺ in cells mutant for the NAD⁺-consuming enzymes PARP1 and CD38, so these cannot be the relevant enzymes (Gerdtts et al., 2015). Identification of the relevant enzyme may require an understanding of the underlying chemical reaction, which is currently not known. Nicotinamide is formed from NAD⁺ upon SARM1 activation, but whether it is produced in a single step is unclear. Moreover, the fate of the ADP ribose (ADPR) moiety of NAD⁺ after SARM1 activation is still unknown, as it is not detected in poly ADP-ribose or in ADP-ribosylated protein targets. Identification of the NAD⁺-consuming enzyme and the reaction it catalyzes is quite important, as it is an additional novel therapeutic candidate for blocking axon loss.

Mechanistic Links between Axodestructive SARM1 and Axoprotective NMNAT2

Although there are strong data that NAD⁺ depletion is downstream of SARM1 activation, additional compelling data indicate that the relationship among NAD⁺ metabolism, SARM1, and axon degeneration is more complex. As described above, NMNAT2 is an endogenous axon survival factor that synthesizes NAD⁺ from NMN and ATP. Genetic KO of NMNAT2 is embryonic lethal, and the embryos have dramatic defects in axon extension (Gilley et al., 2013, 2015). Remarkably, the embryonic lethality and axon defects in NMNAT2 KO mice are rescued by loss of SARM1 as NMNAT2/SARM1 double-KO animals are healthy into adulthood (Gilley et al., 2015). This epistatic relationship is consistent with the model that NMNAT2 functions to inhibit SARM1 activity: NMNAT2 inhibition of SARM1 is not necessary if SARM1 is missing. This model is also consistent with data from transected axons. NMNAT2 is a labile protein that is lost within 2 to 3 hr after axotomy, and loss of NMNAT2 is sufficient to trigger axon degeneration. Moreover, SARM1 appears to function at roughly the same time after axotomy (Gerdtts et al., 2015). Hence, loss of NMNAT2 may be the trigger that activates SARM1. How might NMNAT2 loss activate SARM1? An obvious candidate is NAD⁺ loss. NMNAT2 synthesizes NAD⁺, so loss of NMNAT2 should lead to a decline in NAD⁺ levels. If lower NAD⁺

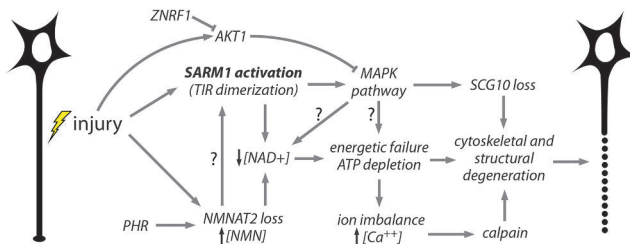


Figure 4. Working Model of an Integrated Axon Degeneration Signaling Cascade

Injury leads to SARM1 activation (Osterloh et al., 2012) and NMNAT2 depletion (Gilley and Coleman, 2010). PHR1 promotes NMNAT2 turnover, leading to faster depletion (Babetto et al., 2013; Xiong et al., 2012). Activated SARM1 promotes NAD⁺ depletion (Gerdts et al., 2015), and NMNAT2 loss prevents NAD⁺ synthesis and causes an increased ratio of NMN to ATP+ADP+AMP, which may activate SARM1 (Gilley et al., 2015). NAD⁺ loss leads to glycolytic failure and ATP depletion. SARM1 also activates MAPK pathway signaling (Yang et al., 2015), which promotes SCG10 proteolysis (Shin et al., 2012a) and contributes to ATP depletion, perhaps via NAD⁺ depletion. MAPK activation is counteracted by injury-stimulated AKT1 activity (Yang et al., 2015), and AKT is in turn destabilized by ZNRF1 (Wakatsuki et al., 2011). Energetic failure promotes ionic imbalance including intra-axonal calcium accumulation, leading to calpain activation and proteolysis of intermediate filaments in the axonal cytoskeleton (Yang et al., 2013). Cumulative structural damage leads to irreversible fragmentation of the damaged axon (Wang et al., 2012). Arrows with question marks reflect postulated interactions.

levels activate SARM1, then this would induce SARM1-dependent NAD⁺ cleavage and result in a feedforward mechanism triggering catastrophic NAD⁺ loss in the axon. Axonal NMNAT1/Wlds would protect axons at two levels, substituting for NMNAT2 to reduce SARM1 activation and promoting NAD⁺ synthesis to counter SARM1-dependent NAD⁺ depletion.

Recently, Coleman, Conforti, and colleagues proposed an alternative model, the NMN hypothesis (Di Stefano et al., 2015). Not only does NMNAT2 synthesize NAD⁺, but it also consumes NMN as a substrate to synthesize NAD⁺. In this model, NMN levels rise with the loss of NMNAT2, and this is the trigger for axon degeneration. There are functional data that support a role for NMN in promoting axon degeneration. For example, the enzyme NAMPT that synthesizes NMN from nicotinamide and phosphoribosyl pyrophosphate is inhibited by FK866. Treatment with FK866 leads to a short-lived delay in axon degeneration (Sasaki et al., 2009b; Di Stefano et al., 2015), although the degree of protection is much less than that afforded by expression of NMNAT1/Wlds or by loss of SARM1. Perhaps the most intriguing evidence supporting the NMN hypothesis is that expression of a bacterial NMN deamidase enzyme that converts NMN to NaMN (nicotinic acid mononucleotide) provides robust axon preservation that is comparable with NMNAT/Wlds (Di Stefano et al., 2015). The observation that both NMNAT and NMN deamidase consume NMN, and both lead to long-lasting axonal protection, is most simply explained by the NMN hypothesis.

If NMNAT protects axons by consumption of NMN, this would appear to contradict the model that NAD⁺ synthesis by NMNAT protects axons by counteracting NAD⁺ depletion by SARM1 (Gerdtts et al., 2015). However, these models are not necessarily contradictory or even mutually exclusive. NAD⁺ breakdown induced by SARM1 activation leads to

increased nicotinamide, which is converted to NMN by NAMPT. If NMN accumulation actually promotes SARM1 activation, then its accumulation through this salvage pathway provides a plausible mechanism for a feedforward process. NMNAT activity could thus counteract axon destruction by preventing NMN accumulation upstream of SARM1 activation and restoring NAD⁺ levels downstream (Figure 4). This model may explain why the NAMPT inhibitor FK866 delays axon degeneration after injury (Sasaki et al., 2009b; Di Stefano et al., 2015) but accelerates it after direct SARM1 activation (Gerdtts et al., 2015).

The NMN hypothesis successfully explains a number of findings, yet some observations are inconsistent with this model. For example, the axon degeneration program is evolutionarily conserved in *Drosophila*, yet NMN is not an intermediate in the NAD⁺ biosynthesis pathway in the fly and so is unlikely to accumulate in injured axons (Gossmann et al., 2012). Other findings are also difficult to reconcile with the NMN hypothesis. First, NMN is postulated to trigger axon degeneration, yet exogenous addition of NMN can delay injury-induced degeneration (Wang et al., 2015). Second, overexpression of NAMPT, which synthesizes NMN, leads to short-lived axonal protection following injury (Sasaki et al., 2006), although the NMN hypothesis would predict this to accelerate or induce axon degeneration. Taken together, these findings do not lead to a single, simple model. Although it is clear that altering NMN and NAD⁺ homeostasis profoundly affects axonal survival, additional studies are required to determine the relevant mechanisms.

SARM1 Activation Triggers MAPK Activation

Forced dimerization of the SARM1 TIR domains triggers NAD⁺ depletion (Gerdtts et al., 2015) and activates MAPK signaling (Yang et al., 2015). These results tie SARM1 and NAD⁺ to pro-degenerative MAPK signaling in the axon. Work in *C. elegans* provided the first evidence that SARM1 activates MAPK signaling. The *C. elegans* SARM1 ortholog *tir-1* acts upstream of the MAPKKK *nsy-1* both in innate immunity signaling and in the control of odorant receptor expression (Chuang and Bargmann, 2005; Liberati et al., 2004). Mammalian SARM1 also signals through a MAPK pathway, regulating mammalian dendrite morphogenesis (Chen et al., 2011). Yang et al. (2015) tested this relationship in injured mammalian axons, finding that axotomy induces a SARM1-dependent MKK4 phosphorylation in optic nerves. In addition, MAPK pathway activation is downstream of an NMNAT-sensitive step, as injury-induced MKK4 phosphorylation in optic nerves was absent in mice overexpressing NMNAT1. In conjunction with the functional data described above showing that MAPK signaling is required for axon degeneration, this work leads to the model that SARM1 induces and NMNAT1 inhibits axon injury-induced MAPK activation, and MAPK activation triggers axonal degeneration (Yang et al., 2015).

Several questions about MAPK signaling in axon destruction remain unanswered. First, how does SARM1 trigger MAPK activation? Although the biochemical steps are unknown, SARM1 can bind to JNK3 (Kim et al., 2007), consistent with a direct activation mechanism. Second, how does JNK activity in the distal

axon drive degeneration while proximal JNK activity promotes axon regrowth? Third, what is the relationship between SARM1-induced MAPK activation and NAD⁺ depletion? Do they function in a linear pathway, and if so, which is a downstream consequence of the other? Fourth, how can SARM1-dependent MAPK activation peak within minutes of injury (Yang et al., 2015) while SARM1 and NMNAT appear to function hours after injury? NMNAT protein can be transduced into severed axons up to 4 hr after injury and still exert potent protection (Sasaki and Milbrandt, 2010), and cleavage of protease-sensitized SARM1 up to 2 hr after injury is similarly protective (Gerdtts et al., 2015). These protein transduction and overexpression studies may not reflect the true kinetics of endogenous NMNAT2 loss or SARM1 activation, but they suggest that any destructive signaling downstream of SARM1 and NMNAT would be activated hours, not minutes, after injury. This inconsistency suggests that MAPKs may not only be active immediately after injury but also may function at other stages to promote degeneration.

Additional Pathways Modulate the Core Axon Degeneration Program

The studies described above suggest that loss of NMNAT2 and activation of SARM1 and the MAPK cascade are central elements of a core axon degeneration process. Identification of these key nodes in the program provides a framework for understanding the mechanism of additional genes and drugs that modulate axon degeneration. Multiple investigators are identifying factors that can affect the degeneration program, and at least a subset is likely to impinge on the NMNAT2/SARM1/MAPK program (Barrientos et al., 2011; Bhattacharya et al., 2012; Brace et al., 2014; Mishra et al., 2013; Wakatsuki et al., 2011). Two exciting recent examples are the identification of the PHR ubiquitin ligase as an important regulator of NMNAT2 levels and of the kinase AKT as a negative regulator of MKK4.

The PHR ligase functions as an E3 ubiquitin ligase with well-described roles in the regulation of synaptic development (Collins et al., 2006; Nakata et al., 2005). Recently, work in *Drosophila* and mouse demonstrates that this protein also promotes Wallerian degeneration (Babetto et al., 2013; Xiong et al., 2012). Loss of the *Drosophila* PHR ortholog *highwire* leads to profound protection of injured axons that is comparable with that elicited by overexpression of Wlds/NMNAT1. Xiong et al. (2012) demonstrated that Highwire ubiquitinates and promotes the degradation of the endogenous *Drosophila* NMNAT protein. In the absence of Highwire, NMNAT levels are high prior to injury and remain elevated after injury, leading to axonal protection (Xiong et al., 2012). Loss of the mouse PHR ortholog *Phr1* boosts the levels of NMNAT2 and leads to axonal protection, although after injury, NMNAT2 levels still decline, indicating that additional mechanisms promote NMNAT2 loss after injury in the mouse (Babetto et al., 2013). As additional genes are identified that regulate axonal degeneration, it will be important to assess their role in regulating NMNAT2 levels. Indeed, a recent study demonstrated that SkpA is a component of the Highwire ligase complex that functions with Highwire to promote axonal degeneration via regulation of NMNAT (Brace et al., 2014). In addition to ubiquitination, NMNAT2 is also regulated by palmitoylation, which con-

trols NMNAT2 localization and function (Milde et al., 2013). Hence, molecular pathways that control expression, stability, and/or localization of NMNAT2 are likely to be key factors controlling the stability of axons. More broadly, mechanisms that boost NAD⁺ synthesis may promote axon maintenance. Indeed, the neuroprotective molecule P7C3, which is protective in animal models of neurodegenerative diseases and axon loss, has been proposed to work by activating NAMPT, the rate-limiting enzyme in the NAD⁺ biosynthesis pathway (Wang et al., 2014).

Positive and negative regulation of the pro-degenerative MAPK pathway is another candidate mechanism for modifying the axon degeneration program. The kinase AKT is such a negative regulator, directly phosphorylating MKK4 at Ser78 within minutes of axon injury. This phosphorylation favors axon preservation as AKT inhibition or expression of MKK4-Ser78Ala, which is AKT resistant, both accelerate injury-induced axon degeneration (Yang et al., 2015). Interestingly, AKT is also regulated by injury: it is targeted for proteasomal degradation by the action of the E3 ligase ZNRF1, leading to a decline in AKT protein levels following axon injury (Wakatsuki et al., 2011). This decline in AKT may accelerate axon degeneration by removing a negative regulator of MAPK signaling. Although the protective effect of AKT in the setting of axon transection is somewhat modest, regulation of MKK4 by AKT may be important in the setting of reversible axon damage and highlights the potential for identifying modulatory mechanisms that impinge on the core degeneration program. Finally, factors that block the activation or function of SARM1 are predicted to potentially block axon degeneration and to be therapeutic candidates for preservation of axons following injury and disease; however, to date no such factors have been identified.

Sarmoptosis: A Destructive Role for SARM1 beyond the Axon

SARM1 induces degeneration by triggering a metabolic catastrophe that can be compartmentalized within the cell, allowing selective loss of the axon while preserving the neuron. However, when SARM1 is active in the cell body, this metabolic crisis is highly effective in triggering cell death. Engineered SARM1 fragments induce cell death in primary neurons as well as immortalized cell lines (Gerdtts et al., 2013, 2015), with the site of activation within the cell determining whether this leads to selective axon loss or cell death. Moreover, endogenous SARM1 promotes neuronal cell death in response to various insults, including mitochondrial poisons, oxygen-glucose deprivation, and neurotropic viruses (Kim et al., 2007; Mukherjee et al., 2013; Summers et al., 2014). This function is conserved in *C. elegans*: the SARM1 ortholog *tir-1* promotes non-apoptotic developmental cell death, death triggered by anoxia, and motor neuron degeneration in an ALS model (Blum et al., 2012; Hayakawa et al., 2011; Vérièpe et al., 2015). Hence, SARM1 is a flexible executioner, able to trigger local axon loss or global neuron death.

Sarmoptosis, or SARM1-dependent death, is distinct from the well-characterized death programs of apoptosis, necroptosis, and parthanatos (Summers et al., 2014). These programmed self-destruction pathways are defined predominantly by their reliance on specific executioner factors (e.g., caspases) and via morphological criteria (Kroemer et al., 2009). The classic

pathway for programmed cell death is apoptosis. Several lines of evidence demonstrate that SARM1-dependent death is distinct from apoptosis. Pan-caspase inhibitors, BclXI overexpression, and transcriptional inhibitors, which are standard inhibitors of apoptosis, do not block SARM1-dependent death of sensory neurons during mitochondrial dysfunction. Moreover, loss of SARM1 does not inhibit neuronal cell death after expression of pro-apoptotic proteins or trophic factor withdrawal (Gerdtts et al., 2013; Osterloh et al., 2012), a classic model of caspase-dependent apoptosis (Yuan and Yankner, 2000). Studies with activated SARM1 fragments also support this distinction. Cell death induced by SARM1 lacking the auto-inhibitory N-terminal domain occurs without caspase activation and is transcription-independent. There appear to be cell-type-specific SARM1 actions as it triggers caspase-3 activation and cell death in immune cells (Panneerselvam et al., 2013).

Sarmoptosis shares some features with non-apoptotic cell destruction programs such as necroptosis (RIPK dependent) and parthanatos (Parp1 dependent), two death pathways that promote neurodegeneration (Vanden Berghe et al., 2014). In models of sarmoptosis, cell death is preceded by large swellings of the plasma membrane, a prominent feature of energetic crisis that is observed during necroptosis. However, RIPK inhibitors, which block necroptosis, do not inhibit SARM1-dependent neuronal cell death. SARM1 activation stimulates rapid NAD⁺ depletion, which also occurs when Parp1 is activated during parthanatos to generate poly ADP-ribose (Andrabi et al., 2008). However, pharmacological inhibition of Parp1 does not affect activated SARM1-mediated cell death nor death of sensory neurons upon mitochondrial dysfunction (Summers et al., 2014), and activated SARM1 potently induces neuronal cell death in Parp1 mutant neurons (Gerdtts et al., 2015). Finally, SARM1-dependent NAD⁺ depletion does not generate PolyADP-ribose or detectable protein PARylation (Gerdtts et al., 2015), which distinguishes SARM1-mediated cell death from parthanatos. Taken together, these studies define sarmoptosis as a distinct and novel programmed cell destruction pathway that contributes to neurodegeneration.

Although the cell death programs described above can act in isolation, neuronal cell death in response to traumatic injury is highly complex. For example, both apoptotic and non-apoptotic pathways are implicated in neuronal death after cerebellar ischemia (Yuan, 2009). There is likely crosstalk among sarmoptosis and other programmed death pathways in pathological models of neuronal death. Indeed, SARM1 and Parp1 are both activated in response to oxidative stress and both trigger NAD⁺ depletion (Berger, 1985; Summers et al., 2014), suggesting that combinatorial inhibition of SARM1 and Parp1 might be beneficial. Understanding the interplay among death networks will be essential for designing the most effective therapeutics for neurodegeneration.

Future Directions

More than 160 years after Waller's seminal discovery, the field of axonal degeneration is rapidly progressing. We now understand that axon degeneration is an active and regulated process, and the key molecular players are being identified and their functions elucidated. Although there is much left to discover about the

fundamental mechanisms underlying axon degeneration, the next generation of questions are already clear. The most pressing challenge is to leverage these new mechanistic insights to develop therapeutic agents that can preserve axons and maintain neuronal function in the injured and diseased nervous system. Here the demands are 2-fold. First, we must identify those conditions that would benefit from blocking Sarm1-dependent degeneration. This may be limited to axonopathies such as peripheral neuropathy, but it may also include neurodegenerative diseases in which axon loss is an early event or in which sarmoptosis contributes to neuronal cell death. With clinical targets defined, the second goal is to identify pharmacological agents that block the pathway. Although the development of such therapies remains on the horizon, recent progress in defining the axon degeneration pathway provides obvious candidate targets. These include agents to (1) promote NAD⁺ biosynthesis, including preservation of NMNAT2 activity; (2) block the activation or function of SARM1; and (3) inhibit the activity of the MAPK pathway. Pharmaceutical companies are developing selective inhibitors of relevant kinases (Patel et al., 2015); however, similar progress in identifying agents to manipulate NMNAT2 turnover and SARM1 function will require a much more detailed understanding of the biochemical events underlying the core axon degeneration program.

Moving forward, it will be interesting to link the roles of MAPK signaling, NAD⁺ metabolism, and SARM1 biology in axonal degeneration to broader questions in neuronal physiology and pathophysiology. For MAPK signal a central mystery is how the consequence of MAPK signaling is selectively regulated. Here we discussed the role of the MAPK pathway in axonal degeneration, yet the same molecules promote axonal regeneration or apoptosis in other situations. What are the key determinants choosing among these outcomes, and might manipulating these specificity mechanisms provide novel therapeutic approaches for neuronal protection or repair? NAD⁺ metabolism is an area that has been underexplored in the nervous system. As animals age, NAD⁺ levels drop, and advanced age is a significant risk factor for many neurodegenerative diseases. What mechanisms lead to this decline in NAD⁺, and might maintenance of a youthful NAD⁺ concentration promote neuronal health? Finally, what are the links between the role of SARM1 for axon degeneration and in other pathways, including innate immunity and developmental signaling? Is the fundamental molecular mechanism of SARM1 action conserved? In the axon, SARM1 triggers a metabolic crisis due to a rapid depletion of NAD⁺, yet in other systems, SARM1 participates in conventional signaling pathways. Might there be an unappreciated role for SARM1-dependent modulation of NAD⁺ levels in innate immunity or developmental signaling? Finally, the power of SARM1 to sculpt the axon locally may not be limited to degenerative events. SARM1 is well positioned to mediate structural synaptic plasticity via the selective elimination of axon branches. Indeed, the emerging appreciation of the potential implications of the SARM1 axon degeneration program is reminiscent of early work in the area of apoptosis. The identification of a new degenerative program that is both active and regulable may have profound implications for our understanding of neuronal development, homeostatic function, and disease.

ACKNOWLEDGMENTS

This work was supported by NIH grant NS087632 to J.M. and A.D. and grants DA020812 and NS065053 to A.D. We thank members of the DiAntonio and Milbrandt laboratories for fruitful discussion.

REFERENCES

- Akhouryri, I., Turc, C., Royet, J., and Charroux, B. (2011). Toll-8/Tollo negatively regulates antimicrobial response in the *Drosophila* respiratory epithelium. *PLoS Pathog.* 7, e1002319.
- Aksoy, P., White, T.A., Thompson, M., and Chini, E.N. (2006). Regulation of intracellular levels of NAD: a novel role for CD38. *Biochem. Biophys. Res. Commun.* 345, 1386–1392.
- Alano, C.C., Garnier, P., Ying, W., Higashi, Y., Kauppinen, T.M., and Swanson, R.A. (2010). NAD⁺ depletion is necessary and sufficient for poly(ADP-ribose) polymerase-1-mediated neuronal death. *J. Neurosci.* 30, 2967–2978.
- Albers, J.W., and Pop-Busui, R. (2014). Diabetic neuropathy: mechanisms, emerging treatments, and subtypes. *Curr. Neurol. Neurosci. Rep.* 14, 473.
- Andrabi, S.A., Dawson, T.M., and Dawson, V.L. (2008). Mitochondrial and nuclear cross talk in cell death: parthanatos. *Ann. N Y Acad. Sci.* 1147, 233–241.
- Araki, T., Sasaki, Y., and Milbrandt, J. (2004). Increased nuclear NAD biosynthesis and SIRT1 activation prevent axonal degeneration. *Science* 305, 1010–1013.
- Avery, M.A., Sheehan, A.E., Kerr, K.S., Wang, J., and Freeman, M.R. (2009). Wld S requires Nmnat1 enzymatic activity and N16-VCP interactions to suppress Wallerian degeneration. *J. Cell Biol.* 184, 501–513.
- Babetto, E., Beirowski, B., Janeckova, L., Brown, R., Gilley, J., Thomson, D., Ribchester, R.R., and Coleman, M.P. (2010). Targeting NMNAT1 to axons and synapses transforms its neuroprotective potency in vivo. *J. Neurosci.* 30, 13291–13304.
- Babetto, E., Beirowski, B., Russler, E.V., Milbrandt, J., and DiAntonio, A. (2013). The Phr1 ubiquitin ligase promotes injury-induced axon self-destruction. *Cell Rep.* 3, 1422–1429.
- Barrientos, S.A., Martinez, N.W., Yoo, S., Jara, J.S., Zamorano, S., Hetz, C., Twiss, J.L., Alvarez, J., and Court, F.A. (2011). Axonal degeneration is mediated by the mitochondrial permeability transition pore. *J. Neurosci.* 31, 966–978.
- Beirowski, B., Babetto, E., Coleman, M.P., and Martin, K.R. (2008). The *Wld^S* gene delays axonal but not somatic degeneration in a rat glaucoma model. *Eur. J. Neurosci.* 28, 1166–1179.
- Belenky, P., Bogan, K.L., and Brenner, C. (2007). NAD⁺ metabolism in health and disease. *Trends Biochem. Sci.* 32, 12–19.
- Benarroch, E.E. (2015). Acquired axonal degeneration and regeneration: Recent insights and clinical correlations. *Neurology* 84, 2076–2085.
- Bennett, B.L., Sasaki, D.T., Murray, B.W., O'Leary, E.C., Sakata, S.T., Xu, W., Leisten, J.C., Motiwala, A., Pierce, S., Satoh, Y., et al. (2001). SP600125, an anthrapyrazolone inhibitor of Jun N-terminal kinase. *Proc. Natl. Acad. Sci. U S A* 98, 13681–13686.
- Berger, N.A. (1985). Poly(ADP-ribose) in the cellular response to DNA damage. *Radiat. Res.* 101, 4–15.
- Bhattacharya, M.R.C., Gerdts, J., Naylor, S.A., Royse, E.X., Ebstein, S.Y., Sasaki, Y., Milbrandt, J., and DiAntonio, A. (2012). A model of toxic neuropathy in *Drosophila* reveals a role for MORN4 in promoting axonal degeneration. *J. Neurosci.* 32, 5054–5061.
- Blum, E.S., Abraham, M.C., Yoshimura, S., Lu, Y., and Shaham, S. (2012). Control of nonapoptotic developmental cell death in *Caenorhabditis elegans* by a polyglutamine-repeat protein. *Science* 335, 970–973.
- Bounoutas, A., Kratz, J., Emtage, L., Ma, C., Nguyen, K.C., and Chalfie, M. (2011). Microtubule depolymerization in *Caenorhabditis elegans* touch receptor neurons reduces gene expression through a p38 MAPK pathway. *Proc. Natl. Acad. Sci. U S A* 108, 3982–3987.
- Brace, E.J., Wu, C., Valakh, V., and DiAntonio, A. (2014). SkpA restrains synaptic terminal growth during development and promotes axonal degeneration following injury. *J. Neurosci.* 34, 8398–8410.
- Burke, R.E., and O'Malley, K. (2013). Axon degeneration in Parkinson's disease. *Exp. Neurol.* 246, 72–83.
- Carty, M., Goodbody, R., Schröder, M., Stack, J., Moynagh, P.N., and Bowie, A.G. (2006). The human adaptor SARM negatively regulates adaptor protein TRIF-dependent Toll-like receptor signaling. *Nat. Immunol.* 7, 1074–1081.
- Cashman, C.R., and Höke, A. (2015). Mechanisms of distal axonal degeneration in peripheral neuropathies. *Neurosci. Lett.* 596, 33–50.
- Chen, C.-Y., Lin, C.-W., Chang, C.-Y., Jiang, S.-T., and Hsueh, Y.-P. (2011). Sarm1, a negative regulator of innate immunity, interacts with syndecan-2 and regulates neuronal morphology. *J. Cell Biol.* 193, 769–784.
- Chiarugi, A., Dölle, C., Felici, R., and Ziegler, M. (2012). The NAD metabolome—a key determinant of cancer cell biology. *Nat. Rev. Cancer* 12, 741–752.
- Chuang, C.F., and Bargmann, C.I. (2005). A Toll-interleukin 1 repeat protein at the synapse specifies asymmetric odorant receptor expression via ASK1 MAPKKK signaling. *Genes Dev.* 19, 270–281.
- Coleman, M. (2005). Axon degeneration mechanisms: commonality amid diversity. *Nat. Rev. Neurosci.* 6, 889–898.
- Collins, C.A., Wairkar, Y.P., Johnson, S.L., and DiAntonio, A. (2006). Highwire restrains synaptic growth by attenuating a MAP kinase signal. *Neuron* 51, 57–69.
- Conforti, L., Tarlton, A., Mack, T.G., Mi, W., Buckmaster, E.A., Wagner, D., Perry, V.H., and Coleman, M.P. (2000). A Ufd2/D4Cole1e chimeric protein and overexpression of Rbp7 in the slow Wallerian degeneration (*WldS*) mouse. *Proc. Natl. Acad. Sci. U S A* 97, 11377–11382.
- Couillault, C., Pujol, N., Reboul, J., Sabatier, L., Guichou, J.-F., Kohara, Y., and Ewbank, J.J. (2004). TLR-independent control of innate immunity in *Caenorhabditis elegans* by the TIR domain adaptor protein TIR-1, an ortholog of human SARM. *Nat. Immunol.* 5, 488–494.
- Di Stefano, M., Nascimento-Ferreira, I., Orsomando, G., Mori, V., Gilley, J., Brown, R., Janeckova, L., Vargas, M.E., Worrell, L.A., Loreto, A., et al. (2015). A rise in NAD precursor nicotinamide mononucleotide (NMN) after injury promotes axon degeneration. *Cell Death Differ.* 22, 731–742.
- Ferri, A., Sanes, J.R., Coleman, M.P., Cunningham, J.M., and Kato, A.C. (2003). Inhibiting axon degeneration and synapse loss attenuates apoptosis and disease progression in a mouse model of motoneuron disease. *Curr. Biol.* 13, 669–673.
- Fu, D., Jordan, J.J., and Samson, L.D. (2013). Human ALKBH7 is required for alkylation and oxidation-induced programmed necrosis. *Genes Dev.* 27, 1089–1100.
- Gerdts, J., Summers, D.W., Sasaki, Y., DiAntonio, A., and Milbrandt, J. (2013). Sarm1-mediated axon degeneration requires both SAM and TIR interactions. *J. Neurosci.* 33, 13569–13580.
- Gerdts, J., Brace, E.J., Sasaki, Y., DiAntonio, A., and Milbrandt, J. (2015). SARM1 activation triggers axon degeneration locally via NAD⁺ destruction. *Science* 348, 453–457.
- Gilley, J., and Coleman, M.P. (2010). Endogenous Nmnat2 is an essential survival factor for maintenance of healthy axons. *PLoS Biol.* 8, e1000300.
- Gilley, J., Adalbert, R., Yu, G., and Coleman, M.P. (2013). Rescue of peripheral and CNS axon defects in mice lacking NMNAT2. *J. Neurosci.* 33, 13410–13424.
- Gilley, J., Orsomando, G., Nascimento-Ferreira, I., and Coleman, M.P. (2015). Absence of SARM1 rescues development and survival of NMNAT2-deficient axons. *Cell Rep.* 10, 1974–1981.
- Gossmann, T.I., Ziegler, M., Puntervoll, P., de Figueiredo, L.F., Schuster, S., and Heiland, I. (2012). NAD(+) biosynthesis and salvage—a phylogenetic perspective. *FEBS J.* 279, 3355–3363.
- Grisold, W., Cavaletti, G., and Windebank, A.J. (2012). Peripheral neuropathies from chemotherapeutics and targeted agents: diagnosis, treatment, and prevention. *Neuro-oncol.* 14 (Suppl 4), iv45–iv54.

- Hammarlund, M., Nix, P., Hauth, L., Jorgensen, E.M., and Bastiani, M. (2009). Axon regeneration requires a conserved MAP kinase pathway. *Science* 323, 802–806.
- Hasbani, D.M., and O'Malley, K.L. (2006). Wld(S) mice are protected against the Parkinsonian mimetic MPTP. *Exp. Neurol.* 202, 93–99.
- Hayakawa, T., Kato, K., Hayakawa, R., Hisamoto, N., Matsumoto, K., Takeda, K., and Ichijo, H. (2011). Regulation of anoxic death in *Caenorhabditis elegans* by mammalian apoptosis signal-regulating kinase (ASK) family proteins. *Genetics* 187, 785–792.
- Hoopfer, E.D., McLaughlin, T., Watts, R.J., Schuldiner, O., O'Leary, D.D.M., and Luo, L. (2006). Wlds protection distinguishes axon degeneration following injury from naturally occurring developmental pruning. *Neuron* 50, 883–895.
- Huntwork-Rodriguez, S., Wang, B., Watkins, T., Ghosh, A.S., Pozniak, C.D., Bustos, D., Newton, K., Kirkpatrick, D.S., and Lewcock, J.W. (2013). JNK-mediated phosphorylation of DLK suppresses its ubiquitination to promote neuronal apoptosis. *J. Cell Biol.* 202, 747–763.
- Johnson, V.E., Stewart, W., and Smith, D.H. (2013). Axonal pathology in traumatic brain injury. *Exp. Neurol.* 246, 35–43.
- Kang, J.Y., and Lee, J.-O. (2011). Structural biology of the Toll-like receptor family. *Annu. Rev. Biochem.* 80, 917–941.
- Kim, Y., Zhou, P., Qian, L., Chuang, J.-Z., Lee, J., Li, C., Iadecola, C., Nathan, C., and Ding, A. (2007). MyD88-5 links mitochondria, microtubules, and JNK3 in neurons and regulates neuronal survival. *J. Exp. Med.* 204, 2063–2074.
- Kroemer, G., Galluzzi, L., Vandenabeele, P., Abrams, J., Alnemri, E.S., Baehrecke, E.H., Blagosklonny, M.V., El-Deiry, W.S., Golstein, P., Green, D.R., et al.; Nomenclature Committee on Cell Death 2009 (2009). Classification of cell death: recommendations of the Nomenclature Committee on Cell Death 2009. *Cell Death Differ.* 16, 3–11.
- Kurant, E. (2011). Keeping the CNS clear: glial phagocytic functions in *Drosophila*. *Glia* 59, 1304–1311.
- Leppä, S., and Bohmann, D. (1999). Diverse functions of JNK signaling and c-Jun in stress response and apoptosis. *Oncogene* 18, 6158–6162.
- Liberati, N.T., Fitzgerald, K.A., Kim, D.H., Feinbaum, R., Golenbock, D.T., and Ausubel, F.M. (2004). Requirement for a conserved Toll/interleukin-1 resistance domain protein in the *Caenorhabditis elegans* immune response. *Proc. Natl. Acad. Sci. U S A* 101, 6593–6598.
- Lunn, E.R., Perry, V.H., Brown, M.C., Rosen, H., and Gordon, S. (1989). Absence of Wallerian Degeneration does not Hinder Regeneration in Peripheral Nerve. *Eur. J. Neurosci.* 1, 27–33.
- Luo, L., and O'Leary, D.D.M. (2005). Axon retraction and degeneration in development and disease. *Annu. Rev. Neurosci.* 28, 127–156.
- MacDonald, J.M., Beach, M.G., Porpiglia, E., Sheehan, A.E., Watts, R.J., and Freeman, M.R. (2006). The *Drosophila* cell corpse engulfment receptor Draper mediates glial clearance of severed axons. *Neuron* 50, 869–881.
- Mack, T.G., Reiner, M., Beirowski, B., Mi, W., Emanuelli, M., Wagner, D., Thomson, D., Gillingwater, T., Court, F., Conforti, L., et al. (2001). Wallerian degeneration of injured axons and synapses is delayed by a Ube4b/Nmnat chimeric gene. *Nat. Neurosci.* 4, 1199–1206.
- Marcette, J.D., Chen, J.J., and Nonet, M.L. (2014). The *Caenorhabditis elegans* microtubule minus-end binding homolog PTRN-1 stabilizes synapses and neurites. *eLife* 3, e01637.
- McLennan, A.G. (2006). The Nudix hydrolase superfamily. *Cell. Mol. Life Sci.* 63, 123–143.
- Mi, W., Beirowski, B., Gillingwater, T.H., Adalbert, R., Wagner, D., Grumme, D., Osaka, H., Conforti, L., Arnhold, S., Addicks, K., et al. (2005). The slow Wallerian degeneration gene, WldS, inhibits axonal spheroid pathology in gracile axonal dystrophy mice. *Brain* 128, 405–416.
- Milde, S., Gilley, J., and Coleman, M.P. (2013). Axonal trafficking of NMNAT2 and its roles in axon growth and survival in vivo. *BioArchitecture* 3, 133–140.
- Miller, B.R., Press, C., Daniels, R.W., Sasaki, Y., Milbrandt, J., and DiAntonio, A. (2009). A dual leucine kinase-dependent axon self-destruction program promotes Wallerian degeneration. *Nat. Neurosci.* 12, 387–389.
- Mishra, B., Carson, R., Hume, R.I., and Collins, C.A. (2013). Sodium and potassium currents influence Wallerian degeneration of injured *Drosophila* axons. *J. Neurosci.* 33, 18728–18739.
- Mukherjee, P., Woods, T.A., Moore, R.A., and Peterson, K.E. (2013). Activation of the innate signaling molecule MAVS by bunyavirus infection upregulates the adaptor protein SARM1, leading to neuronal death. *Immunity* 38, 705–716.
- Nakata, K., Abrams, B., Grill, B., Goncharov, A., Huang, X., Chisholm, A.D., and Jin, Y. (2005). Regulation of a DLK-1 and p38 MAP kinase pathway by the ubiquitin ligase RPM-1 is required for presynaptic development. *Cell* 120, 407–420.
- Nikolaev, A., McLaughlin, T., O'Leary, D.D.M., and Tessier-Lavigne, M. (2009). APP binds DR6 to trigger axon pruning and neuron death via distinct caspases. *Nature* 457, 981–989.
- Osterloh, J.M., Yang, J., Rooney, T.M., Fox, A.N., Adalbert, R., Powell, E.H., Sheehan, A.E., Avery, M.A., Hackett, R., Logan, M.A., et al. (2012). dSarm/Sarm1 is required for activation of an injury-induced axon death pathway. *Science* 337, 481–484.
- Panneerselvam, P., Singh, L.P., Ho, B., Chen, J., and Ding, J.L. (2012). Targeting of pro-apoptotic TLR adaptor SARM to mitochondria: definition of the critical region and residues in the signal sequence. *Biochem. J.* 442, 263–271.
- Panneerselvam, P., Singh, L.P., Selvarajan, V., Chng, W.J., Ng, S.B., Tan, N.S., Ho, B., Chen, J., and Ding, J.L. (2013). T-cell death following immune activation is mediated by mitochondria-localized SARM. *Cell Death Differ.* 20, 478–489.
- Patel, S., Cohen, F., Dean, B.J., De La Torre, K., Deshmukh, G., Estrada, A.A., Ghosh, A.S., Gibbons, P., Gustafson, A., Huestis, M.P., et al. (2015). Discovery of dual leucine zipper kinase (DLK, MAP3K12) inhibitors with activity in neurodegeneration models. *J. Med. Chem.* 58, 401–418.
- Pease, S.E., and Segal, R.A. (2014). Preserve and protect: maintaining axons within functional circuits. *Trends Neurosci.* 37, 572–582.
- Qiao, F., and Bowie, J.U. (2005). The many faces of SAM. *Sci. STKE* 2005, re7.
- Rudhard, Y., Sengupta Ghosh, A., Lippert, B., Böcker, A., Pedaran, M., Krämer, J., Ngu, H., Foreman, O., Liu, Y., and Lewcock, J.W. (2015). Identification of 12/15-lipoxygenase as a regulator of axon degeneration through high-content screening. *J. Neurosci.* 35, 2927–2941.
- Sajadi, A., Schneider, B.L., and Aebischer, P. (2004). Wlds-mediated protection of dopaminergic fibers in an animal model of Parkinson disease. *Curr. Biol.* 14, 326–330.
- Sasaki, Y., and Milbrandt, J. (2010). Axonal degeneration is blocked by nicotinamide mononucleotide adenyltransferase (Nmnat) protein transduction into transected axons. *J. Biol. Chem.* 285, 41211–41215.
- Sasaki, Y., Araki, T., and Milbrandt, J. (2006). Stimulation of nicotinamide adenine dinucleotide biosynthetic pathways delays axonal degeneration after axotomy. *J. Neurosci.* 26, 8484–8491.
- Sasaki, Y., Vohra, B.P.S., Baloh, R.H., and Milbrandt, J. (2009a). Transgenic mice expressing the Nmnat1 protein manifest robust delay in axonal degeneration in vivo. *J. Neurosci.* 29, 6526–6534.
- Sasaki, Y., Vohra, B.P.S., Lund, F.E., and Milbrandt, J. (2009b). Nicotinamide mononucleotide adenyl transferase-mediated axonal protection requires enzymatic activity but not increased levels of neuronal nicotinamide adenine dinucleotide. *J. Neurosci.* 29, 5525–5535.
- Schoenmann, Z., Assa-Kunik, E., Tiomny, S., Minis, A., Haklai-Topper, L., Arama, E., and Yaron, A. (2010). Axonal degeneration is regulated by the apoptotic machinery or a NAD⁺-sensitive pathway in insects and mammals. *J. Neurosci.* 30, 6375–6386.
- Schuldiner, O., and Yaron, A. (2015). Mechanisms of developmental neurite pruning. *Cell. Mol. Life Sci.* 72, 101–119.
- Shin, J.E., Miller, B.R., Babetto, E., Cho, Y., Sasaki, Y., Qayum, S., Russler, E.V., Cavalli, V., Milbrandt, J., and DiAntonio, A. (2012a). SCG10 is a JNK target in the axonal degeneration pathway. *Proc. Natl. Acad. Sci. U S A* 109, E3696–E3705.

- Shin, J.E., Cho, Y., Beirowski, B., Milbrandt, J., Cavalli, V., and DiAntonio, A. (2012b). Dual leucine zipper kinase is required for retrograde injury signaling and axonal regeneration. *Neuron* **74**, 1015–1022.
- Shin, J.E., Geisler, S., and DiAntonio, A. (2014). Dynamic regulation of SCG10 in regenerating axons after injury. *Exp. Neurol.* **252**, 1–11.
- Summers, D.W., DiAntonio, A., and Milbrandt, J. (2014). Mitochondrial dysfunction induces Sarm1-dependent cell death in sensory neurons. *J. Neurosci.* **34**, 9338–9350.
- Tsao, J.W., Brown, M.C., Carden, M.J., McLean, W.G., and Perry, V.H. (1994). Loss of the compound action potential: an electrophysiological, biochemical and morphological study of early events in axonal degeneration in the C57BL/Ola mouse. *Eur. J. Neurosci.* **6**, 516–524.
- Valakh, V., Walker, L.J., Skeath, J.B., and DiAntonio, A. (2013). Loss of the spectraplakins short stop activates the DLK injury response pathway in *Drosophila*. *J. Neurosci.* **33**, 17863–17873.
- Valakh, V., Frey, E., Babetto, E., Walker, L.J., and DiAntonio, A. (2015). Cytoskeletal disruption activates the DLK/JNK pathway, which promotes axonal regeneration and mimics a preconditioning injury. *Neurobiol. Dis.* **77**, 13–25.
- Vanden Berghe, T., Linkermann, A., Jouan-Lanhouet, S., Walczak, H., and Vandenabeele, P. (2014). Regulated necrosis: the expanding network of non-apoptotic cell death pathways. *Nat. Rev. Mol. Cell Biol.* **15**, 135–147.
- Vérièpe, J., Fossouo, L., and Parker, J.A. (2015). Neurodegeneration in *C. elegans* models of ALS requires TIR-1/Sarm1 immune pathway activation in neurons. *Nat. Commun.* **6**, 7319.
- Vohra, B.P.S., Sasaki, Y., Miller, B.R., Chang, J., DiAntonio, A., and Milbrandt, J. (2010). Amyloid precursor protein cleavage-dependent and -independent axonal degeneration programs share a common nicotinamide mononucleotide adenylyltransferase 1-sensitive pathway. *J. Neurosci.* **30**, 13729–13738.
- Wakatsuki, S., Saitoh, F., and Araki, T. (2011). ZNRF1 promotes Wallerian degeneration by degrading AKT to induce GSK3B-dependent CRMP2 phosphorylation. *Nat. Cell Biol.* **13**, 1415–1423.
- Waller, A. (1850). Experiments on the Section of the glossopharyngeal and hypoglossal nerves of the frog, and observations of the alterations produced thereby in the structure of their primitive fibres. *Philos. Trans. R. Soc. Lond.* **140**, 423–429.
- Wang, M.S., Davis, A.A., Culver, D.G., and Glass, J.D. (2002). WldS mice are resistant to paclitaxel (taxol) neuropathy. *Ann. Neurol.* **52**, 442–447.
- Wang, J., Zhai, Q., Chen, Y., Lin, E., Gu, W., McBurney, M.W., and He, Z. (2005). A local mechanism mediates NAD-dependent protection of axon degeneration. *J. Cell Biol.* **170**, 349–355.
- Wang, J.T., Medress, Z.A., and Barres, B.A. (2012). Axon degeneration: molecular mechanisms of a self-destruction pathway. *J. Cell Biol.* **196**, 7–18.
- Wang, G., Han, T., Nijhawan, D., Theodoropoulos, P., Naidoo, J., Yadavalli, S., Mirzaei, H., Pieper, A.A., Ready, J.M., and McKnight, S.L. (2014). P7C3 neuroprotective chemicals function by activating the rate-limiting enzyme in NAD salvage. *Cell* **158**, 1324–1334.
- Wang, J.T., Medress, Z.A., Vargas, M.E., and Barres, B.A. (2015). Local axonal protection by WldS as revealed by conditional regulation of protein stability. *Proc. Natl. Acad. Sci. U S A* **112**, 10093–10100.
- Wishart, T.M., Rooney, T.M., Lamont, D.J., Wright, A.K., Morton, A.J., Jackson, M., Freeman, M.R., and Gillingwater, T.H. (2012). Combining comparative proteomics and molecular genetics uncovers regulators of synaptic and axonal stability and degeneration in vivo. *PLoS Genet.* **8**, e1002936.
- Xiong, X., Wang, X., Ewanek, R., Bhat, P., DiAntonio, A., and Collins, C.A. (2010). Protein turnover of the Wallenda/DLK kinase regulates a retrograde response to axonal injury. *J. Cell Biol.* **191**, 211–223.
- Xiong, X., Hao, Y., Sun, K., Li, J., Li, X., Mishra, B., Soppina, P., Wu, C., Hume, R.I., and Collins, C.A. (2012). The Highwire ubiquitin ligase promotes axonal degeneration by tuning levels of Nmnat protein. *PLoS Biol.* **10**, e1001440.
- Yahata, N., Yuasa, S., and Araki, T. (2009). Nicotinamide mononucleotide adenylyltransferase expression in mitochondrial matrix delays Wallerian degeneration. *J. Neurosci.* **29**, 6276–6284.
- Yan, D., and Jin, Y. (2012). Regulation of DLK-1 kinase activity by calcium-mediated dissociation from an inhibitory isoform. *Neuron* **76**, 534–548.
- Yan, D., Wu, Z., Chisholm, A.D., and Jin, Y. (2009). The DLK-1 kinase promotes mRNA stability and local translation in *C. elegans* synapses and axon regeneration. *Cell* **138**, 1005–1018.
- Yan, T., Feng, Y., Zheng, J., Ge, X., Zhang, Y., Wu, D., Zhao, J., and Zhai, Q. (2010). Nmnat2 delays axon degeneration in superior cervical ganglia dependent on its NAD synthesis activity. *Neurochem. Int.* **56**, 101–106.
- Yang, J., Weimer, R.M., Kallop, D., Olsen, O., Wu, Z., Renier, N., Uryu, K., and Tessier-Lavigne, M. (2013). Regulation of axon degeneration after injury and in development by the endogenous calpain inhibitor calpastatin. *Neuron* **80**, 1175–1189.
- Yang, J., Wu, Z., Renier, N., Simon, D.J., Uryu, K., Park, D.S., Greer, P.A., Tournier, C., Davis, R.J., and Tessier-Lavigne, M. (2015). Pathological axonal death through a MAPK cascade that triggers a local energy deficit. *Cell* **160**, 161–176.
- Yuan, J. (2009). Neuroprotective strategies targeting apoptotic and necrotic cell death for stroke. *Apoptosis* **14**, 469–477.
- Yuan, J., and Yankner, B.A. (2000). Apoptosis in the nervous system. *Nature* **407**, 802–809.
- Zhai, R.G., Zhang, F., Hiesinger, P.R., Cao, Y., Haueter, C.M., and Bellen, H.J. (2008). NAD synthase NMNAT acts as a chaperone to protect against neurodegeneration. *Nature* **452**, 887–891.
- Zhang, Q., Zmasek, C.M., Cai, X., and Godzik, A. (2011). TIR domain-containing adaptor SARM is a late addition to the ongoing microbe-host dialog. *Dev. Comp. Immunol.* **35**, 461–468.

Review

Moonlighting Motors: Kinesin, Dynein, and Cell Polarity

Wen Lu¹ and Vladimir I. Gelfand^{1,*}

In addition to their well-known role in transporting cargoes in the cytoplasm, microtubule motors organize their own tracks – the microtubules. While this function is mostly studied in the context of cell division, it is essential for microtubule organization and generation of cell polarity in interphase cells. Kinesin-1, the most abundant microtubule motor, plays a role in the initial formation of neurites. This review describes the mechanism of kinesin-1-driven microtubule sliding and discusses its biological significance in neurons. Recent studies describing the interplay between kinesin-1 and cytoplasmic dynein in the translocation of microtubules are discussed. In addition, we evaluate recent work exploring the developmental regulation of microtubule sliding during axonal outgrowth and regeneration. Collectively, the discussed works suggest that sliding of interphase microtubules by motors is a novel force-generating mechanism that reorganizes the cytoskeleton and drives shape change and polarization.

Kinesin-1-Driven Microtubule Sliding in Neurons and Non-Neuronal Cells

The standard and well-studied function of conventional kinesin (also known as kinesin-1 or KIF5) is to transport cargoes along microtubules towards plus-ends. Recently, several studies, including the work of our group, have uncovered a novel ‘unconventional’ function of kinesin-1 in sliding cytoplasmic microtubules against each other. Biochemical studies demonstrated that, in addition to the well-characterized N-terminal motor domain [1,2], kinesin-1 has another microtubule-binding site at the C terminus of the heavy chain (kinesin-1 heavy chain, KHC) [3,4]. This C-terminal microtubule-binding site contains multiple basic amino acids that are highly conserved across many species (Figure 1). This site can bind to an acidic E-hook at the tubulin C terminus through complementary electrostatic interactions [3,4], and, unlike the N-terminal motor domain, is ATP-independent. Using the N-terminal motor domain and the C-terminal binding site, kinesin-1 can cross-bridge two microtubules and move them against each other (microtubule sliding, Figure 1). In this case, the microtubule that is bound to the C terminus of the heavy chain becomes a ‘cargo’ for kinesin-1, while the other microtubule serves as a track (Figure 1). When kinesin-1 motor walks on one microtubule (track), it moves another microtubule (cargo) relative to the track microtubule (Figure 1). Experiments overexpressing the kinesin-1 C-terminal tail in tissue culture cells showed that the C-terminal tail decorates microtubules uniformly [5,6], indicating that all microtubules are identical in their ability to bind to the kinesin-1 C-terminal tail. Thus kinesin-1 probably binds to two microtubules in a random orientation (statistically 50% upright and 50% upside-down, simplified as two opposite kinesin-1 motors in Figure 2). Therefore, it is likely that every microtubule serves both as a cargo and as a track at the same time. In this scenario, kinesin-1 only slides antiparallel microtubules against each other (Figure 2A). If it cross-bridges parallel microtubules, the forces of kinesins in opposite orientations are subtracted, and no movement can be produced (Figure 2B).

Trends

Contrary to the textbook view, cytoplasmic microtubules in interphase cells are not static; they robustly slide in the cytoplasm moved by microtubule motors.

Two motors contribute to microtubule sliding: kinesin-1 that slides microtubules against each other, and cytoplasmic dynein that drives microtubule movement relative to the cell cortex.

Sliding microtubules can drive cell shape change by pushing against the plasma membrane.

Plus-end motor kinesin-1 and minus-end motor dynein cooperate to achieve the correct microtubule organization in the axons.

Microtubule sliding activity is developmentally regulated independently of the global regulation of the motor activity.

F-actin in the growth cone of growing neurites antagonizes the neurite outgrowth by preventing sliding microtubules from penetrating into the growth cone.

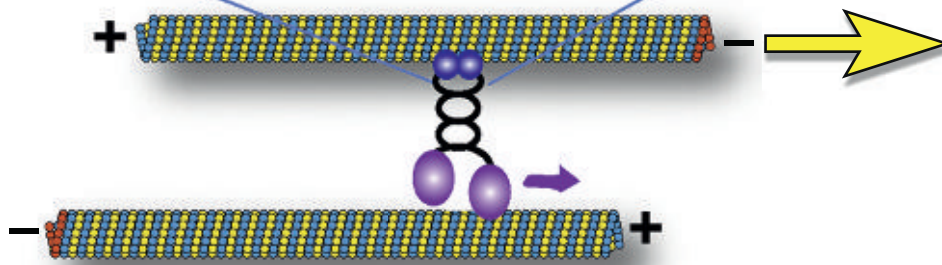
Cargoes can be transported by hitchhiking on moving microtubules.

¹Department of Cell and Molecular Biology, Feinberg School of Medicine, Northwestern University, 303 East Chicago Avenue, Ward 11-100, Chicago, IL 60611, USA

*Correspondence: vgelfand@northwestern.edu (V.I. Gelfand).

ATP-independent microtubule binding domain

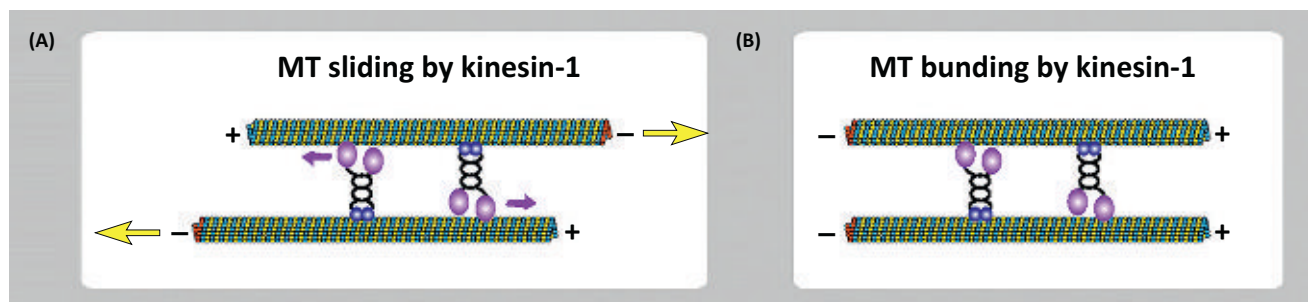
DSKQRSQAE	R	K	K	Y	Q	Q	E	V	R	I	K	E	A	V	R	Q	R	N	M	R	R	M	<i>C. elegans</i>	
EAKEGAMRD	R	K	R	Y	Q	Y	E	V	D	R	I	K	E	A	V	R	Q	K	H	L	G	R	R	<i>Drosophila</i>
EAKEGAMRD	R	K	R	Y	Q	M	E	V	D	R	I	K	E	A	V	R	Q	R	N	L	A	R	R	<i>Aplysia</i>
DAKEGAMRD	R	K	R	Y	Q	H	E	V	D	R	I	K	E	A	V	R	Q	K	N	L	A	R	R	Squid
ETKEGAMRD	R	K	R	Y	Q	Q	E	V	D	R	I	K	E	A	V	R	Q	R	N	F	A	K	R	Sea urchin
EAKESAMRD	R	K	K	Y	Q	Q	E	V	D	R	I	K	E	V	I	R	A	K	N	Q	S	R	R	Zebrafish
EAKENASRD	R	K	R	Y	Q	Q	E	V	D	R	I	K	E	A	V	R	S	K	N	M	A	R	R	<i>Xenopus</i>
EAKENAMRD	R	K	R	Y	Q	Q	E	V	D	R	I	K	E	A	V	R	A	K	N	M	A	R	R	Chicken
EAKENASRD	R	K	R	Y	Q	Q	E	V	D	R	I	K	E	A	V	R	S	K	N	M	A	R	R	Rat
EAKENASRD	R	K	R	Y	Q	Q	E	V	D	R	I	K	E	A	V	R	S	K	N	M	A	R	R	Mouse
EAKEGAMKD	R	K	R	Y	Q	Q	E	V	D	R	I	K	E	A	V	R	Y	K	S	G	K	R	R	Human KIF5A
EAKENASRD	R	K	R	Y	Q	Q	E	V	D	R	I	K	E	A	V	R	S	K	N	M	A	R	R	Human KIF5B
EAKENAMRD	R	K	R	Y	Q	Q	E	V	D	R	I	K	E	A	V	R	A	K	N	M	A	R	R	Human KIF5C



Trends in Cell Biology

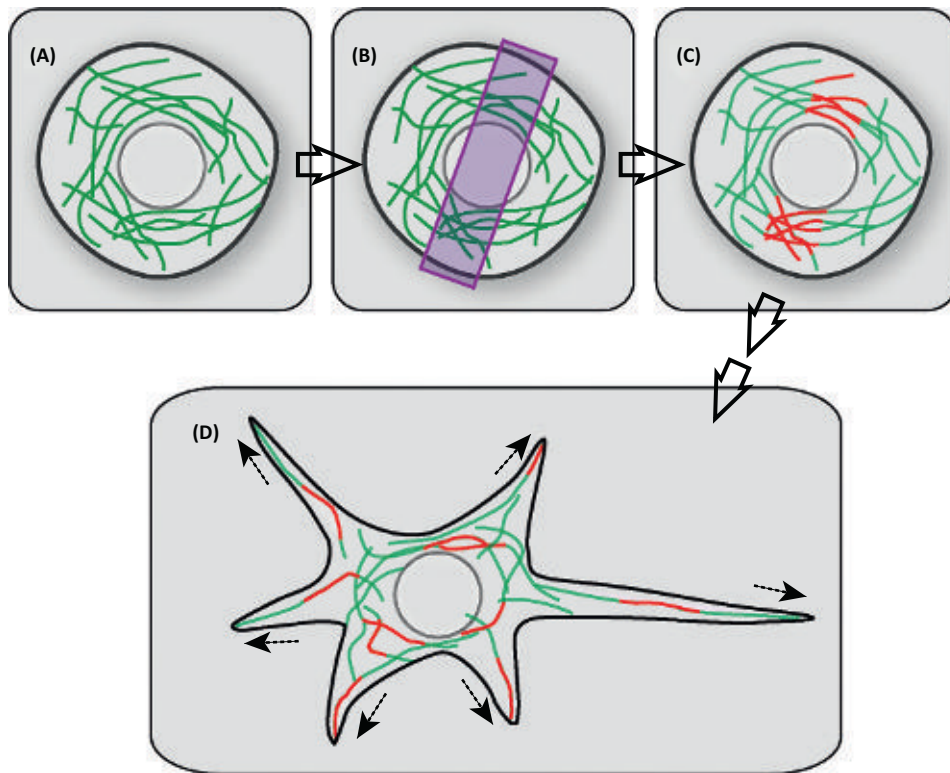
Figure 1. Highly Conserved C-Terminal Microtubule Binding Site of Kinesin-1 Heavy Chain. Amino acids of kinesin-1 heavy chain C-terminal region from 11 species are aligned in Clustal Omega (www.ebi.ac.uk/Tools/msa/clustalo) using the following kinesin heavy chain protein sequences: *Caenorhabditis elegans* (roundworm); *Drosophila melanogaster* (fruit fly), *Aplysia californica* (California sea hare), *Doryteuthis pealeii* (longfin inshore squid), *Strongylocentrotus purpuratus* (purple sea urchin), *Danio rerio* (zebrafish), *Xenopus tropicalis* (western clawed frog), *Gallus gallus domesticus* (chicken), *Rattus norvegicus* (brown rat), *Mus musculus* (house mouse), and *Homo sapiens* (KIF5A, KIF5B, and KIF5C). The ATP-independent microtubule binding site is highlighted in the light blue box, and all basic residues in the microtubule binding site are labeled in red.

Microtubule sliding by kinesin-1 was first proposed based on *in vivo* observations in a study of the fungus *Ustilago maydis*. Straube and colleagues demonstrated that kinesin-1 causes microtubule bending and bundling [7]. To directly visualize microtubule sliding, our group fused a photoconvertible protein tag to tubulin and imaged microtubule movement in



Trends in Cell Biology

Figure 2. Microtubule Sliding by Kinesin-1 Requires Antiparallel Orientation. Kinesin-1 binding to two microtubules using its motor domain and C-terminal microtubule binding site leads to sliding of antiparallel microtubules (A) and bundling of parallel microtubules (B).



Trends in Cell Biology

Figure 3. Visualization of Microtubule Sliding in *Drosophila* Neurons Using Photoconvertible Tubulin. (A) A spherical-shaped young neuron expressing photoconvertible Eos-tagged α -tubulin. (B) 400 nm light is applied to a restricted area to photoconvert a subset of microtubules in the young neurons. (C) A subset of microtubules is photoconverted from green to red. (D) Red microtubule fragments are scattered throughout the cell body and in the newly formed neurites by microtubule-microtubule sliding, revealed by time-lapse movies.

interphase cells. Local photoconversion of this probe can be used to apply fiduciary marks on microtubules. Following these marks (photoconverted microtubule segments) allows visualization of microtubule movements in live cells (Figure 3). We documented robust microtubule sliding in many types of tissue culture cells, including *Drosophila* S2 cells, *Xenopus* fibroblasts, and rat kangaroo epithelial Ptk2 cells [8,9]. Table 1 provides an overview of different approaches to visualizing microtubule sliding.

Experiments in *Drosophila* S2 cells demonstrated that depolymerization of actin cytoskeleton with latrunculin B, or its fragmentation by cytochalasin D before plating, results in formation of multiple radial processes filled with microtubules [8,10–14]. We further demonstrated that this dramatic process formation is driven by kinesin-powered microtubule sliding [8].

We later detected microtubule sliding by kinesin-1 in cultured *Drosophila* primary neurons, including embryonic neurons [15] and larval motor neurons [16], as well as in sensory neurons *in vivo* [6]. Furthermore, not only do microtubules slide in differentiating neurons, but, remarkably, their sliding drives initial extension of neurites in cultured neurons by pushing against the plasma membrane at the tips of the neurites [15–17], consistent with the data that destabilization of actin filaments induces fast axon outgrowth [18]. These data demonstrate that, at least at the initial stages of neurite outgrowth, microtubule sliding by kinesin-1 provides the driving forces for neurite extension [15]. These data are consistent with the previous work in cultured rat

Table 1. Summary of Visualization of Microtubule Sliding and Related Motors

Species	Cell type	Visualization method	Motors involved	Refs
<i>Ustilago maydis</i>	Single cell	GFP- α -tubulin	Kinesin-1 and dynein	Straube <i>et al.</i> 2006 [7]
<i>Drosophila melanogaster</i>	S2 cells (tissue culture)	mCherry-tubulin and Dendra2- α -tubulin (photoconversion);	Kinesin-1	Jolly <i>et al.</i> 2010 [8]
<i>Xenopus</i>	Fibroblast (tissue culture)	Dendra2- <i>Xenopus</i> α -tubulin (photoconversion)	Kinesin-1	Jolly <i>et al.</i> 2010 [8]
Rat	Kangaroo epithelial Ptk2 cells (tissue culture)	GFP-tubulin	Kinesin-1	Jolly <i>et al.</i> 2010 [8]
<i>Drosophila melanogaster</i>	Embryonic neurons (primary culture)	tdEos2- α -tubulin (photoconversion)	Kinesin-1	Lu <i>et al.</i> 2013 [15]
<i>Drosophila melanogaster</i>	Larval motor neurons (primary culture)	tdEos2- α -tubulin (photoconversion)	Kinesin-1	Lu <i>et al.</i> 2015 [16]
<i>Drosophila melanogaster</i>	Sensory neurons underneath the pupal bristles <i>in vivo</i>	tdMaple3- α -tubulin (photoconversion)	Kinesin-1	Winding <i>et al.</i> 2016 [6]
<i>Caenorhabditis elegans</i>	Motor neurons <i>in vivo</i>	EBP-2-GFP (plus-end microtubule marker)	Kinesin-1	Yan <i>et al.</i> 2013 [21]
Mouse	Myoblast C2C12 (tissue culture)	mEos2-tubulin (photoconversion)	Kinesin-1 and dynein	Mogessie <i>et al.</i> 2015 [39]
Amoeba <i>Reticulomyxa</i>	Single cell	Differential interference contrast (DIC) microscopy movie	Dynein	Koonce <i>et al.</i> 1987 [65]; Euteneuer <i>et al.</i> 1989 [66]
Rat	Sympathetic neurons (primary culture)	EGFP-tubulin and photobleaching	Dynein	He <i>et al.</i> 2005 [25]
Mouse/monkey	Neuro-2a and Cos7 (tissue culture)	GFP-tagged and mCherry-tagged microtubule-associated protein MAP2c (fluorescence speckle and total internal reflection fluorescence, TIRF, microscopy)	Dynein	Dehmelt <i>et al.</i> 2006 [28]; Mazel <i>et al.</i> 2014 [29]
Chicken	Dorsal root ganglion neurons (primary culture)	EGFP- α -tubulin	Dynein	Grabham <i>et al.</i> 2007 [30]
Chicken	Dorsal root ganglion neurons (primary culture)	Docked mitochondria as fiducial markers for bulk cytoskeleton movements	Dynein	Roossien <i>et al.</i> 2014 [31]
<i>Drosophila melanogaster</i>	Larval brain neurons (primary culture) and S2 cells (tissue culture)	GFP-CAMSAP (minus-end microtubule marker) and EB1-GFP (plus-end microtubule marker)	Dynein	Del Castillo <i>et al.</i> 2015 [14]

hippocampal neurons describing shorter axons after kinesin-1 knockdown [19]. Furthermore, kinesin-dependent microtubule sliding is also required for neurite membrane extension during axon regeneration after injury in culture [16]. In a recently published study from our group, we were able to detect kinesin-dependent microtubule sliding in the growing sensory neurons underneath pupal bristles *in vivo* [6], further indicating that microtubule sliding is important for neuronal development.

Interestingly, another motor that can slide microtubules, cytoplasmic dynein, is dispensable for neurite outgrowth and axonal regeneration [8,14–16,20] (see more on the role of dynein in the section of 'Interplay between kinesin-1 and dynein in microtubule organization'). To experimentally test the kinesin-driven microtubule sliding mechanism presented in Figure 1, we generated a mutant form of kinesin that decreases its microtubule-sliding ability without affecting its cargo-transporting function. We mutated four highly conserved amino residues at the C-terminal microtubule binding site (914-RKRYQ-918 to 914-AAAYA-918) based on a human kinesin-1 (KIF5B) tail mutant that showed a 20-fold decrease in microtubule binding *in vitro* [4], creating Khc^{mutA}. Khc^{mutA} significantly reduced kinesin-1 tail microtubule binding and thus kinesin-driven microtubule sliding in *Drosophila* S2 cells, while conventional kinesin-driven

cargo transport was unaffected [6]. This sliding-deficient mutant allows us to experimentally dissociate the defects caused by impaired microtubule sliding from the defects caused by the reduced cargo transport. Based on the S2 work, we generated a genomic knock-in *Drosophila* line carrying this tail mutant, *Khc^{mutA}* [6]. Remarkably, *Khc^{mutA}* displayed reduced in kinesin-driven microtubule sliding in cultured neurons and neurons *in vivo*. Furthermore, *Khc^{mutA}* flies showed major defects of neurite outgrowth in culture, and of axonal and dendritic patterning *in vivo* [6]. These defects in the nervous system lead to decreased locomotion and increased lethality, which indicates that kinesin-driven microtubule sliding is an essential developmental process in addition to the well-recognized kinesin-driven cargo transport.

A similar tail mutant in the C-terminal microtubule binding site was generated in *C. elegans* by the group of Shen [21] who showed that microtubule polarity in dendrites, but not kinesin-driven mitochondria transport, is affected in this mutant. Shen and colleagues proposed that kinesin-1 slides plus-ends out microtubules out of the dendrites (consistent with the model presented in Figure 2A).

Both the motor domain and the ATP-independent microtubule binding site at the C terminus of the heavy chain are highly evolutionary conserved [5,6,22] (Figure 1). Therefore, we propose that microtubule sliding can serve as a universal and essential mechanism driving reorganization of the microtubule networks. In agreement with this idea, we have observed microtubule sliding in mammalian cells [8]; furthermore, human kinesin-1 heavy chain (KIF5B) fully rescues microtubule sliding in *Drosophila* S2 cells [6]. Because neurons are the most polarized cell type in animals, microtubule sliding is essential for neurons by providing the mechanical force for cell shape changes during neuronal differentiation and regeneration.

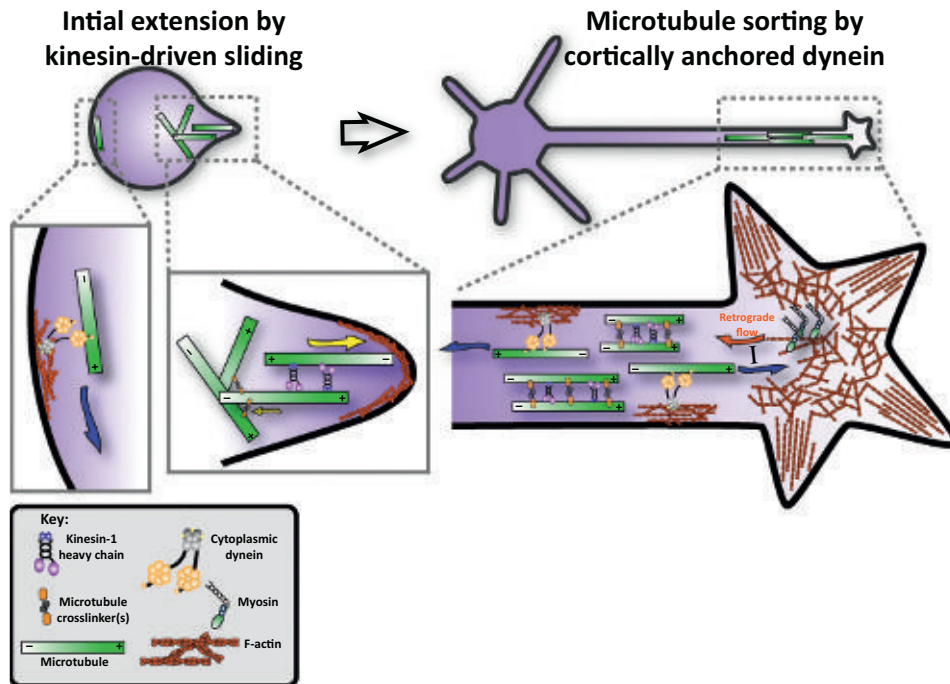
Interplay Between Kinesin-1 and Dynein in Microtubule Organization

In addition to the plus-end motor kinesin-1, minus-end motor cytoplasmic dynein has also been implicated as a motor for microtubule movement in neurons and tissue culture cells.

Using cultured rat sympathetic neurons, the Baas and colleagues have shown that dynein is important for the transport of microtubule fragments released from centrosomes, and for the anterograde transport of microtubules in axons [23–27]. Dehmelt and colleagues demonstrated that dynein pushes bundled microtubules outwards in Neuro2A neuroblastoma cell and primary hippocampal neurons, and that this movement is important for neurite initiation [28]. Directional movement and bending of microtubules is associated with and dependent on cortical dynein in COS7 cells and Neuro2A cells [29]. The group of Vallee showed that dynein is required for microtubule advance into the growth cone during axonal outgrowth in both chicken DRG neurons and rat hippocampal neurons [30]. This is further supported by a study from Miller and colleagues showing that *en masse* microtubule anterograde translocation was abolished upon dynein inhibition in chicken DRG neurons [31].

The popular model of dynein-driven microtubule movement is that the dynein complex binds to an immobilized stable scaffold, such as cortical F-actin, and pushes microtubules in the cytoplasm [28,31,32] (Figure 4). Alternatively, dynein can potentially bind to two microtubules simultaneously, using its two motor domains, and slide them apart. Such a possibility was demonstrated *in vitro* [33], although it is unclear whether this takes place in cells.

Interestingly, kinesin-driven and dynein-driven sliding models are not mutually exclusive. A recent study from our group showed that kinesin-1 and dynein activities are coordinated and function at different developmental stages to ensure normal neurite outgrowth and correct organization of microtubules in the axons of *Drosophila* larval brain neurons [34]. In this study we showed that, at early stages of initial neurite outgrowth, kinesin-1-driven microtubule sliding



Trends in Cell Biology

Figure 4. A Model of Microtubule Motors Driving Microtubule Sliding at Different Stages. Kinesin-1 drives the sliding apart of antiparallel microtubules in early-stage neurons, inducing the formation of initial neurites in spherical-shaped young neurons (left panel). At later stages, cytoplasmic dynein anchors at cell cortex by interacting with F-actin, and sorts out microtubules in the wrong orientation (minus-ends out), and slides microtubules of right orientation (plus-ends out) towards the growth cone to counteract actin retrograde flow driven by myosins (right panel). Both kinesin-driven and dynein-driven microtubule sliding can be regulated by microtubule crosslinker(s).

breaks the spherical symmetry of undifferentiated neurons, and drives initial neurite extensions, with minus-ends of microtubules pushing out the plasma membrane at the tips of the processes. This sliding can be favored in the anterograde direction because microtubules tangled or crosslinked in the cell body restrict retrograde sliding and provide the mechanical support for initial neurite extension (Figure 4, left panel). Later, cytoplasmic dynein becomes essential for microtubule sorting, establishing the uniform (plus-ends out) orientation of microtubules in the axons by sliding ‘minus-end-out’ microtubules towards the cell body (Figure 4, right panel). It can potentially also participate in outgrowth by moving plus-end out microtubules towards the tips, as demonstrated by other laboratories [23–26,30,31]. Dynein sorting function requires its recruitment to actin cortex because depolymerization of F-actin phenocopied dynein inhibition, while artificial recruitment of dynein to the plasma membrane bypassed the requirement for F-actin [34]. This is consistent with a recent report from the group of Hoogenraad showing that initially the neurites of rat hippocampal and cortical neurons contain microtubules of mixed polarity; in later stages the mixed orientation in axons changes to the uniform (plus-ends-out), while the mixed orientation in dendrites is preserved [35]. This suggests that during polarization the sorting machinery removes minus-end-out microtubules only from axons. In addition to its function of sorting minus-ends-out microtubules, dynein may mediate the forward movement of plus-ends-out microtubules, antagonizing myosin-mediated actin retrograde flow and neurite retraction [26,30,31] (Figure 4, right panel).

What triggers this transition from kinesin-driven to dynein-driven sliding is not unknown. The easiest explanation is that the transition is simply triggered by the changing geometry of the

developing neuron. Cortical dynein alone in a spherical cell cannot initiate process formation because by definition it would only move microtubules parallel to the cell surface, while kinesin-1 slides microtubules to form initial neurite extension by pushing against the plasma membrane (Figure 4, left panel). After the initial process is formed, dynein tethered to the cortex of the process started to drive both outgrowth, by pushing the plus-ends-out microtubules forward, and sorting by removing the minus-ends-out microtubules because the force produced by cortical dynein in the process will be directed parallel to the axis of the axon. At the same time, the ability of kinesin-1 to slide microtubules would be constrained because kinesin-1 cannot slide parallel microtubules in the axons, and instead bundles them (Figure 2B and Figure 4, right panel). Thus, simple geometry can explain the shift from kinesin-driven to dynein-driven neurite extension. In addition to cell geometry, biochemical regulation can also contribute to the switch between kinesin-1 and dynein sliding activity (see below).

Developmental Regulation of Microtubule Sliding

Because microtubule sliding is essential for axon elongation and regeneration, it is not surprising that sliding is developmentally regulated. Microtubule sliding is only active in young growing neurons, and becomes undetectable as they mature [15,16]. Downregulation of microtubule sliding is not caused by inhibition of kinesin-1 because kinesin-1-dependent organelle transport is still active in mature neurons [9,15,16,36]. We demonstrated that a 'mitotic' kinesin, Pavarotti (a kinesin-6 family member known in other organisms as MKLP1, CHO1, or KIF20A), is a potent negative regulator of kinesin-1-driven sliding of cytoplasmic microtubules [17], most likely by crosslinking antiparallel microtubules in neurons. Because Pavarotti contains multiple nuclear localization signals (NLS) at its C-terminal tail, and is mainly localized in the nucleus in interphase cells [37,38], it is likely that translocation of Pavarotti from the nucleus to the cytoplasm causes inhibition of microtubule sliding. This speculation is supported by the fact that ectopic expression of NLS-mutated Pavarotti resulted in dramatic inhibition of microtubule sliding and axon growth [17].

Microtubule sliding is downregulated in fully grown mature neurons; however, sliding can be reactivated by axonal injury. Reactivation depends on the formation of antiparallel microtubules near the injury site, and is essential for driving initial axonal regeneration [16]. It will be interesting to see whether suppression of kinesin-6 could stimulate axonal regeneration and, if so, whether it can be potentially used for treatment of neurodegenerative diseases as well as spinal cord and brain injuries.

Another example of developmental regulation of microtubule sliding is observed during mouse myogenesis. Microtubule movement has been demonstrated in mouse myoblast C2C12 cells during myogenesis and differentiation [39]. Straube and colleagues demonstrated that a novel isoform of microtubule-associated protein MAP4, oMAP4, functions as a microtubule crosslinker that inhibits microtubule sliding during myogenic differentiation [39]. The ability of oMAP4 to inhibit sliding is mostly regulated by its expression level: expression is upregulated during myogenic differentiation, when microtubule sliding is greatly reduced [39]. Thus, although microtubule crosslinking could serve as a general braking mechanism, the regulators themselves could be cell type-specific (oMAP4 during myogenic differentiation versus kinesin-6 in neurons).

Moreover, developmental downregulation of microtubule sliding observed in neurons [15–17] may help to resolve the longstanding debate about whether tubulin is transported as a polymer or as subunits in the axons [40,41]. Microtubule movement along the axons has been reported in *Xenopus* embryonic neurons [42,43] and rat sympathetic neurons [23,44], but no microtubule movement could be detected in rat neuron-like PC-12 cells [45], chicken DRG neurons [46], or mouse sensory neuron [47]. It is interesting to note that neurons in which microtubule

movement was reported are characterized by fast neurite outgrowth ($>25 \mu\text{m/h}$) [15,42,48–50]. As we reported, microtubule movement rate is highly correlated with neurite growth rate [15,17]. Therefore, the discrepancies in the previous studies are likely explained by different neurite outgrowth rates at different development stages: the high level of microtubule sliding is only detected during fast outgrowth, whereas during slow neurite outgrowth microtubule sliding becomes undetectable and/or easily obscured by microtubule dynamics.

The Role of F-actin in the Growth Cone

Despite the fact that F-actin is at the extreme periphery of the leading edge of the growth cone, numerous studies have shown that it is dispensable for neurite outgrowth; instead, disruption of F-actin leads to faster neurite outgrowth, probably by allowing microtubules penetrate into the growth cone to drive the extension [18,51–57]. Consistent with these findings, we showed that both fragmentation of F-actin by cytochalasin D and its total depolymerization by latrunculin B stimulate neurite outgrowth in *Drosophila* embryonic neurons. In the absence of F-actin at the neurite tip, sliding microtubules push directly against the cell membrane to make membrane protrusions [15,17]. In addition, it has been shown that local disruption of F-actin (cytochalasin D and latrunculin B) in rat hippocampal neurons favors axonal specification, and global disruption of F-actin leads to the formation of multiple long axons [18]. Disruption of F-actin also caused defects in axon targeting and branching [54,55]. Thus, F-actin in the growth cone plays an important role in outgrowth control and growth cone steering by allowing microtubule penetration in part of the growth cone towards local guidance cues [58,59]. Uncoupling of microtubules and F-actin in the growth cone, such as in mutants of the microtubule and actin crosslinker, spectraplakin/short stop, led to mistargeting of axons *in vivo* [60,61].

Intriguingly, a recent paper from the laboratory of Svitkina [62] questioned these studies, and claimed that F-actin polymerization drives neurite extension. We cannot exclude the possibility that, at particular stages of slow axonal outgrowth, actin filaments do provide some driving force for axonal and/or dendritic outgrowth or steering. However, Chia *et al.* [62] did not directly show that actin polymerization indeed drives neurite extension. Instead, they showed that after treatment with cytochalasin D or latrunculin B some F-actin remains as a cluster ('actin bulb') at the collapsed growth cone of some growing neurites. They argued that actin polymerization is required for neurite extension. In fact, cytochalasin D binds to growing ends of F-actin and prevent the addition of actin monomers (G-actin) [63], while latrunculin B binds to G-actin and prevents F-actin assembly [64], which means that both drugs effectively inhibit actin dynamics. The remnants of actin staining at the neurite tip after drug treatment suggested that these actin filaments are stable, which, together with the bulk of other published data [15,17,18,51–57], argues against their conclusion that actin polymerization drives neurite extension. Furthermore, their interpretation failed to explain why actin-specific inhibitors increase rather than decrease the rate of axon outgrowth.

Cargo Riding on Moving Microtubules: Another Form of Hitchhiking

Cargo transport and microtubule sliding are two main and conserved functions of kinesin-1. It is possible that some cargoes can simply ride on sliding microtubules and be transported within the cells along microtubules. This hypothesis was first proposed based on the observations of organelles moving with sliding microtubules in the amoeba *Reticulomyxa* [65–67]. More recently, an observation of concerted movement of peroxisomes in *Drosophila* S2 cells led to the speculation that they are attached to a moving microtubule [12]. Our recent study of *Drosophila* ooplasmic streaming revisited this hitchhiking hypothesis. We showed that kinesin-driven microtubule sliding is required for cytoplasmic streaming in *Drosophila* oocytes [22]. Unlike sliding in neurons, microtubule sliding in oocytes occurs between the cortex-anchored and free microtubules. This sliding generates unidirectional movement of cytoplasm. Inhibition of sliding by a kinesin mutation (*Khc^{mutA}*, see section 'Kinesin-1-driven microtubule sliding in

neurons and non-neuronal cells') resulted in a more diffuse pattern of posterior determinants in the oocyte. We propose that cytoplasmic streaming refines the posterior determination by bringing determinants that are attached to moving microtubules to the posterior pole for proper anchorage [22]. This is consistent with previous studies suggesting that streaming transports polarity determinants in the oocytes [68–70]. This 'ride-on-microtubules' mode of transport can serve as a quick and efficient way of redistributing organelles and mRNAs/proteins in parallel with microtubule reorganization, especially in big cells such as oocytes. More validation and future studies in other cell types and higher organisms are needed to further test this hypothesis.

Concluding Remarks and Future Perspectives

With the recent studies from multiple groups, interphase microtubule sliding emerges as a novel driving force for neurite outgrowth and microtubule reorganization. Kinesin-1 and cytoplasmic dynein both play important roles in driving microtubule movements, and in defining cell shape and microtubule organization/orientation. Furthermore, new studies reveal that motor-driven microtubule sliding is tightly controlled by developmental mechanisms. The new studies provide insights into the mechanism and regulation of this microtubule movement in neurons and other cells, and generate many more interesting questions: how do kinesin-1 and dynein switch their activities between microtubule sliding and cargo transport? How is dynein anchored to the cortex to slide microtubules in the axons? Is the activity of dynein-sorting mechanism differently regulated in axons versus dendrites? What regulates the activity of crosslinkers that inhibit microtubule sliding in neurons and other cell types? More studies will be necessary to address these important issues (see Outstanding Questions).

References

- Hirokawa, N. *et al.* (2009) Kinesin superfamily motor proteins and intracellular transport. *Nat. Rev. Mol. Cell Biol.* 10, 682–696
- Rice, S. *et al.* (1999) A structural change in the kinesin motor protein that drives motility. *Nature* 402, 778–784
- Hackney, D.D. and Stock, M.F. (2000) Kinesin's IAK tail domain inhibits initial microtubule-stimulated ADP release. *Nat. Cell Biol.* 2, 257–260
- Seeger, M.A. and Rice, S.E. (2010) Microtubule-associated protein-like binding of the kinesin-1 tail to microtubules. *J. Biol. Chem.* 285, 8155–8162
- Navone, F. *et al.* (1992) Cloning and expression of a human kinesin heavy chain gene: interaction of the COOH-terminal domain with cytoplasmic microtubules in transfected CV-1 cells. *J. Cell Biol.* 117, 1263–1275
- Winding, M. *et al.* (2016) Role of kinesin-1-based microtubule sliding in *Drosophila* nervous system development. *Proc. Natl. Acad. Sci. U. S. A.* 113, E4985–4994
- Straube, A. *et al.* (2006) Conventional kinesin mediates microtubule–microtubule interactions in vivo. *Mol. Biol. Cell* 17, 907–916
- Jolly, A.L. *et al.* (2010) Kinesin-1 heavy chain mediates microtubule sliding to drive changes in cell shape. *Proc. Natl. Acad. Sci. U. S. A.* 107, 12151–12156
- Barlan, K. *et al.* (2013) The microtubule-binding protein enscosin is an essential cofactor of kinesin-1. *Curr. Biol.* 23, 317–322
- Ling, S.C. *et al.* (2004) Transport of *Drosophila* fragile X mental retardation protein-containing ribonucleoprotein granules by kinesin-1 and cytoplasmic dynein. *Proc. Natl. Acad. Sci. U. S. A.* 101, 17428–17433
- Kim, H. *et al.* (2007) Microtubule binding by dynactin is required for microtubule organization but not cargo transport. *J. Cell Biol.* 176, 641–651
- Kulic, I.M. *et al.* (2008) The role of microtubule movement in bidirectional organelle transport. *Proc. Natl. Acad. Sci. U. S. A.* 105, 10011–10016
- Ally, S. *et al.* (2009) Opposite-polarity motors activate one another to trigger cargo transport in live cells. *J. Cell Biol.* 187, 1071–1082
- Del Castillo, U. *et al.* (2015) Interplay between kinesin-1 and cortical dynein during axonal outgrowth and microtubule organization in *Drosophila* neurons. *eLife* 4, e10140
- Lu, W. *et al.* (2013) Initial neurite outgrowth in *Drosophila* neurons is driven by kinesin-powered microtubule sliding. *Curr. Biol.* 23, 1018–1023
- Lu, W. *et al.* (2015) Kinesin-1-powered microtubule sliding initiates axonal regeneration in *Drosophila* cultured neurons. *Mol. Biol. Cell* 26, 1296–1307
- del Castillo, U. *et al.* (2015) Pavarotti/MKLP1 regulates microtubule sliding and neurite outgrowth in *Drosophila* neurons. *Curr. Biol.* 25, 200–205
- Bradke, F. and Dotti, C.G. (1999) The role of local actin instability in axon formation. *Science* 283, 1931–1934
- Ferreira, A. *et al.* (1992) Suppression of kinesin expression in cultured hippocampal neurons using antisense oligonucleotides. *J. Cell Biol.* 117, 595–606
- Beaven, R. *et al.* (2015) *Drosophila* CLIP-190 and mammalian CLIP-170 display reduced microtubule plus end association in the nervous system. *Mol. Biol. Cell* 26, 1491–1508
- Yan, J. *et al.* (2013) Kinesin-1 regulates dendrite microtubule polarity in *Caenorhabditis elegans*. *eLife* 2, e00133
- Lu, W. *et al.* (2016) Microtubule-microtubule sliding by kinesin-1 is essential for normal cytoplasmic streaming in *Drosophila* oocytes. *Proc. Natl. Acad. Sci. U. S. A.* 113, E4995–5004
- Ahmad, F.J. and Baas, P.W. (1995) Microtubules released from the neuronal centrosome are transported into the axon. *J. Cell Sci.* 108, 2761–2769
- Ahmad, F.J. *et al.* (1998) Cytoplasmic dynein and dynactin are required for the transport of microtubules into the axon. *J. Cell Biol.* 140, 391–401
- He, Y. *et al.* (2005) Role of cytoplasmic dynein in the axonal transport of microtubules and neurofilaments. *J. Cell Biol.* 168, 697–703
- Ahmad, F.J. *et al.* (2000) Motor proteins regulate force interactions between microtubules and microfilaments in the axon. *Nat. Cell Biol.* 2, 276–280

Outstanding Questions

Is there a specific mechanism that switches motors from the cargo-transporting to a microtubule-transporting mode?

How are actin dynamics at the growth cone coupled to microtubule sliding?

How is dynein anchored to the cortex of neurites?

Does differential regulation and/or anchoring of dynein contribute to differentiation of axons and dendrites?

Is microtubule hitchhiking a major mode of cargo transport in any cell type? What types of cargoes are translocated by this mechanism?

Research on microtubule organization by motor proteins in our laboratory is supported by the National Institute of General Medical Science under award number R01GM052111.

27. Rao, A.N. *et al.* (2016) Sliding of centrosome-unattached microtubules defines key features of neuronal phenotype. *J. Cell Biol.* 213, 329–341
28. Dehmelt, L. *et al.* (2006) A microtubule-based, dynein-dependent force induces local cell protrusions: implications for neurite initiation. *Brain Cell Biol.* 35, 39–56
29. Mazel, T. *et al.* (2014) Direct observation of microtubule pushing by cortical dynein in living cells. *Mol. Biol. Cell* 25, 95–106
30. Grabham, P.W. *et al.* (2007) Cytoplasmic dynein and LIS1 are required for microtubule advance during growth cone remodeling and fast axonal outgrowth. *J. Neurosci.* 27, 5823–5834
31. Roossien, D.H. *et al.* (2014) Cytoplasmic dynein pushes the cytoskeletal meshwork forward during axonal elongation. *J. Cell Sci.* 127, 3593–3602
32. Muresan, V. and Muresan, Z. (2012) Unconventional functions of microtubule motors. *Arch. Biochem. Biophys.* 520, 17–29
33. Tanenbaum, M.E. *et al.* (2013) Cytoplasmic dynein crosslinks and slides anti-parallel microtubules using its two motor domains. *eLife* 2, e00943
34. Del Castillo, U. *et al.* (2015) Interplay between kinesin-1 and cortical dynein during axonal outgrowth and microtubule organization in neurons. *eLife* 4
35. Yau, K.W. *et al.* (2016) Dendrites in vitro and in vivo contain microtubules of opposite polarity and axon formation correlates with uniform plus-end-out microtubule orientation. *J. Neurosci.* 36, 1071–1085
36. Lu, W. *et al.* (2013) Organelle transport in cultured *Drosophila* cells: s2 cell line and primary neurons. *J. Visualized Exp.* 50838
37. Ministrini, G. *et al.* (2002) Domains of the Pavarotti kinesin-like protein that direct its subcellular distribution: effects of mislocalisation on the tubulin and actin cytoskeleton during *Drosophila* oogenesis. *J. Cell Sci.* 115, 725–736
38. Ministrini, G. *et al.* (2003) Localization of Pavarotti-KLP in living *Drosophila* embryos suggests roles in reorganizing the cortical cytoskeleton during the mitotic cycle. *Mol. Biol. Cell* 14, 4028–4038
39. Mogessie, B. *et al.* (2015) A novel isoform of MAP4 organises the paraxial microtubule array required for muscle cell differentiation. *eLife* 4, e05697
40. Baas, P.W. and Brown, A. (1997) Slow axonal transport: the polymer transport model. *Trends Cell Biol.* 7, 380–384
41. Hirokawa, N. *et al.* (1997) Slow axonal transport: the subunit transport model. *Trends Cell Biol.* 7, 384–388
42. Reinsch, S.S. *et al.* (1991) Microtubule polymer assembly and transport during axonal elongation. *J. Cell Biol.* 115, 365–379
43. Tanaka, E.M. and Kirschner, M.W. (1991) Microtubule behavior in the growth cones of living neurons during axon elongation. *J. Cell Biol.* 115, 345–363
44. Wang, L. and Brown, A. (2002) Rapid movement of microtubules in axons. *Curr. Biol.* 12, 1496–1501
45. Lim, S.S. *et al.* (1989) Progressive and spatially differentiated stability of microtubules in developing neuronal cells. *J. Cell Biol.* 109, 253–263
46. Lim, S.S. *et al.* (1990) A test of microtubule translocation during neurite elongation. *J. Cell Biol.* 111, 123–130
47. Okabe, S. and Hirokawa, N. (1992) Differential behavior of photo-activated microtubules in growing axons of mouse and frog neurons. *J. Cell Biol.* 117, 105–120
48. Slaughter, T. *et al.* (1997) Microtubule transport from the cell body into the axons of growing neurons. *J. Neurosci.* 17, 5807–5819
49. Yu, W.Q. and Baas, P.W. (1995) The growth of the axon is not dependent upon net microtubule assembly at its distal tip. *J. Neurosci.* 15, 6827–6833
50. Yu, W. *et al.* (1996) Microtubule transport and assembly during axon growth. *J. Cell Biol.* 133, 151–157
51. Marsh, L. and Letourneau, P.C. (1984) Growth of neurites without filopodial or lamellipodial activity in the presence of cytochalasin-B. *J. Cell Biol.* 99, 2041–2047
52. Forscher, P. and Smith, S.J. (1988) Actions of cytochalasins on the organization of actin filaments and microtubules in a neuronal growth cone. *J. Cell Biol.* 107, 1505–1516
53. Joshi, H.C. *et al.* (1985) Tension and compression in the cytoskeleton of PC 12 neurites. *J. Cell Biol.* 101, 697–705
54. Bentley, D. and Toroian-Raymond, A. (1986) Disoriented path-finding by pioneer neurone growth cones deprived of filopodia by cytochalasin treatment. *Nature* 323, 712–715
55. Dent, E.W. and Kalil, K. (2001) Axon branching requires interactions between dynamic microtubules and actin filaments. *J. Neurosci.* 21, 9757–9769
56. Ruthel, G. and Hollenbeck, P.J. (2000) Growth cones are not required for initial establishment of polarity or differential axon branch growth in cultured hippocampal neurons. *J. Neurosci.* 20, 2266–2274
57. Flynn, K.C. *et al.* (2012) ADF/cofilin-mediated actin retrograde flow directs neurite formation in the developing brain. *Neuron* 76, 1091–1107
58. Geraldo, S. and Gordon-Weeks, P.R. (2009) Cytoskeletal dynamics in growth-cone steering. *J. Cell Sci.* 122, 3595–3604
59. Kahn, O.I. and Baas, P.W. (2016) Microtubules and growth cones: motors drive the turn. *Trends Neurosci.* 39, 433–440
60. Lee, S. *et al.* (2000) *short stop* is allelic to *kakapo*, and encodes rod-like cytoskeletal-associated proteins required for axon extension. *J. Neurosci.* 20, 1096–1108
61. Lee, S. and Kolodziej, P.A. (2002) Short Stop provides an essential link between F-actin and microtubules during axon extension. *Development* 129, 1195–1204
62. Chia, J.X. *et al.* (2016) Neurite outgrowth is driven by actin polymerization even in the presence of actin polymerization inhibitors. *Mol. Biol. Cell* 27, 3695–3704
63. Casella, J.F. *et al.* (1981) Cytochalasin D inhibits actin polymerization and induces depolymerization of actin filaments formed during platelet shape change. *Nature* 293, 302–305
64. Spector, I. *et al.* (1989) Latrunculins – novel marine macrolides that disrupt microfilament organization and affect cell-growth. 1. Comparison with cytochalasin-D. *Cell Motil. Cytoskeleton* 13, 127–144
65. Koonce, M.P. *et al.* (1987) Active sliding between cytoplasmic microtubules. *Nature* 328, 737–739
66. Euteneuer, U. *et al.* (1989) Microtubule bundles of *Reticulomyxa* networks are of uniform polarity. *Eur. J. Cell Biol.* 49, 373–376
67. Orokos, D.D. *et al.* (2000) Organelles are transported on sliding microtubules in *Reticulomyxa*. *Cell Motil. Cytoskeleton* 47, 296–306
68. Glotzer, J.B. *et al.* (1997) Cytoplasmic flows localize injected oskar RNA in *Drosophila* oocytes. *Curr. Biol.* 7, 326–337
69. Forrest, K.M. and Gavis, E.R. (2003) Live imaging of endogenous RNA reveals a diffusion and entrapment mechanism for nanos mRNA localization in *Drosophila*. *Curr. Biol.* 13, 1159–1168
70. Mische, S. *et al.* (2007) Direct observation of regulated ribonucleoprotein transport across the nurse cell/oocyte boundary. *Mol. Biol. Cell* 18, 2254–2263

Special Series: Mitochondria

Feature Review

The Interplay of Axonal Energy Homeostasis and Mitochondrial Trafficking and Anchoring

Zu-Hang Sheng^{1,*}

Mitochondria are key cellular power plants essential for neuronal growth, survival, function, and regeneration after injury. Given their unique morphological features, neurons face exceptional challenges in maintaining energy homeostasis at distal synapses and growth cones where energy is in high demand. Efficient regulation of mitochondrial trafficking and anchoring is critical for neurons to meet altered energy requirements. Mitochondrial dysfunction and impaired transport have been implicated in several major neurological disorders. Thus, research into energy-mediated regulation of mitochondrial recruitment and redistribution is an important emerging frontier. In this review, I discuss new insights into the mechanisms regulating mitochondrial trafficking and anchoring, and provide an updated overview of how mitochondrial motility maintains energy homeostasis in axons, thus contributing to neuronal growth, regeneration, and synaptic function.

Neurons Face Unique Challenges in Maintaining Energy Homeostasis

Mitochondria are the main cellular energy powerhouses that convert glucose and pyruvate into ATP through the electron transport chain and oxidative phosphorylation [1]. Mitochondria provide most of the ATP required in the brain to power various neuronal functions [2]. Thus, a constant ATP supply is essential for nerve cell growth, survival, and function [3]. In the brain, synapses are the primary sites of ATP consumption; here, mitochondria supply ~93% of the ATP, while glycolysis generates only ~7% of the ATP [4]. Due to their high-energy demand and unique polarized structures, neurons require specialized mechanisms to maintain energy homeostasis throughout the cell, particularly at distal synapses and in axons that can extend several centimeters long or even up to a meter in some peripheral nerves [5,6]. Given that ATP has a limited diffusion capacity in the long axonal process [7,8], a fundamental question remains: do energy deficits or bioenergetic failure occur early in distal axons under physiological and pathological stress conditions? This is a particularly important question that is relevant to a range of neurodegenerative diseases that associate with degeneration of synaptic terminals during the early disease stages and with energy deficits [9,10].

Mitochondria in axons and at synapses maintain energy homeostasis that is essential for synaptic functions [4], including synapse assembly [11], generation of action and synaptic potentials [12], and synaptic vesicle (SV) trafficking and recycling [8,13]. In addition, mitochondria efficiently buffer transient Ca^{2+} by sequestering Ca^{2+} influx [14–17]. While less than 50% of

Trends

Mitochondria are the main cellular power plants that supply energy essential for neuronal growth, survival, and function.

Neurons face exceptional challenges in maintaining energy homeostasis, especially at distal synapses and growth cones, where energy is in high demand.

Anchored mitochondria ideally serve as local energy sources.

The energy-dependent regulation of mitochondrial trafficking to, and anchoring at, distal axons and synapses is essential to ensure that these metabolically active areas are adequately supplied with ATP during the growth of developing neurons, the regeneration of injured mature neurons, and the maintenance of synaptic activity.

SNPH is one intriguing anchoring protein that is specific for axonal mitochondria and, thus, serves as an attractive target for future investigations of mechanisms that recruit mitochondria into activated synapses and injured axons.

¹Synaptic Function Section, The Porter Neuroscience Research Center, National Institute of Neurological Disorders and Stroke, National Institutes of Health, Room 2B-215, 35 Convent Drive, Bethesda, MD 20892-3706, USA

*Correspondence: shengz@ninds.nih.gov (Z.-H. Sheng).

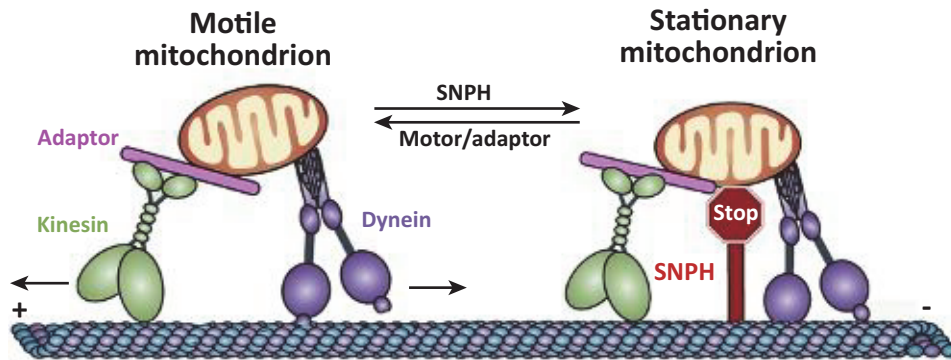
presynaptic terminals in hippocampal regions have mitochondria [18], most synapses may have motile mitochondria passing by. Depleting mitochondria from axon terminals impairs synaptic transmission [8,13,19]. Defective mitochondrial transport combined with energy deficits is implicated in the failed axonal regeneration after injury and the pathogenesis of several major neurological disorders, including Alzheimer's and Parkinson's diseases [20–22]. Mitochondria also alter their motility under certain stress conditions or when their integrity is impaired [23–26]. Therefore, efficient regulation of mitochondrial motility is critical for neurons to meet altered energy requirements and to remove damaged mitochondria or replenish healthy ones, thus maintaining energy homeostasis in distal axons and at synapses.

Thus, research into the mechanisms regulating mitochondrial motility and distribution in response to changes in energy consumption and homeostasis is an important emerging frontier. Recent advances provide exciting lines of evidence as to how mitochondrial trafficking and anchoring are coordinated to sense and respond to altered energy requirements under physiological and pathological stress conditions. Here, I provide a brief overview of the mechanisms regulating axonal mitochondrial trafficking and anchoring and discuss recent findings on how: (i) mitochondrial transport influences energy homeostasis in distal axons and at synapses, thus regulating axonal growth and regeneration, and synaptic function; and (ii) mitochondrial recruitment is regulated in response to changes in bioenergetic status. Additional insights from different perspectives can be found in other outstanding reviews [5,6,10,21,27–32].

The Mechanisms of Mitochondrial Trafficking and Anchoring

Long-distance mitochondrial transport is driven by microtubule (MT)-based and ATP-dependent molecular motors: the plus end-directed kinesin and the minus end-directed dynein [33]. Axonal MTs are uniformly arranged so that their plus-end is directed distally and the minus-end is toward the soma; thus, kinesin motors move in an anterograde direction toward distal axons, while dynein motors mediate retrograde transport toward the soma. Kinesin-1 family members, also known as KIF5A, KIF5B, and KIF5C, are the main motors driving mitochondrial transport in neurons [34,35]. Kinesin-1 motor proteins contain two heavy chains (KHC) and two light chains (KLC). The motor domain of KHC has ATPase activity and binds directly to MTs, whereas its C-terminal domain associates with a KLC or interacts with cargoes. The monomeric kinesin-3 motor family member KIF1B α has also been demonstrated to mediate the anterograde transport of mitochondria in neurons [33]. Motor proteins are recruited to mitochondria through their cargo adaptors, thus ensuring targeted trafficking and regulation of mitochondrial transport [21] (Figure 1, Box 1).

In axons of the central nervous system (CNS) *in vitro*, most mitochondria remain stationary, while approximately 20–30% are motile [8]. Those motile mitochondria can become stationary and stationary ones can be remobilized in response to changes in bioenergetic status and synaptic activity. Thus, axonal mitochondria deploy an anchoring mechanism in addition to motor-driven transport. This model was recently validated by a study demonstrating that syntaphilin (SNPH) acts as a 'static anchor' specific for axonal mitochondria [36,37]. SNPH selectively targets to the outer membrane of axonal mitochondria through its C-terminal mitochondria-targeting domain and axon-sorting sequence. SNPH arrests axonal mitochondrial transport by anchoring them to MTs. Overexpressing SNPH abolished axonal mitochondrial transport, whereas deleting *snph* robustly enhanced axonal mitochondrial motility to 78% in 2-week-old cultured hippocampal neurons and to 71% in *ex vivo* axonal bundles of sciatic nerves from 2-month-old mice [22,36,37]. These data indicate that SNPH acts as an anchoring protein that restricts axonal mitochondrial transport. Thus, *snph*-knockout (KO) mice serve as an ideal genetic model for investigating how enhanced transport of axonal mitochondria influences synaptic function, axonal growth, and regenerative capacity in response to altered energy requirements.



Trends in Cell Biology

Figure 1. Motors and/or Adaptors and Anchoring Proteins Have Opposite Roles in Regulating Axonal Mitochondrial Motility. Long-distance axonal mitochondrial transport is driven by microtubule (MT)-based molecular motors: the plus end-directed kinesin and the minus end-directed dynein. Axonal MTs are uniformly arranged so that their plus-end is directed distally and the minus-end is toward the soma; thus, most kinesin motors move toward distal axons, while dynein motors mediate retrograde transport toward the soma. The kinesin-1 family proteins (KIF5A, KIF5B, and KIF5C) are the main motors driving mitochondrial transport in neurons. Kinesin-1 motors interact with mitochondria through adaptor proteins. Axonal mitochondria also deploy an anchoring mechanism in addition to motor-driven transport. Syntaphilin (SNPH) acts as a 'static anchor' specific for axonal mitochondria. SNPH arrests mitochondrial transport by anchoring them to MTs. In central nervous system (CNS) axons, most mitochondria remain stationary, while approximately 20–30% are motile. Motile mitochondria can become stationary and stationary ones can be remobilized. The balance of motile versus stationary axonal mitochondria depends on the relative action of the motor and/or adaptor and SNPH.

Energy-Demanding Synaptic Activity Regulates Mitochondrial Transport

Synaptic function is driven by ATP [4], which supports synapse assembly [11], powers action potentials [12], and fuels SV trafficking and recycling [8,13,38,39]. Due to the high energy demand at synapses, the constant and local ATP supply is critical to maintaining ionic gradients and supporting neurotransmission. Dysfunction or loss of synaptic mitochondria leads to synaptic deficits, which are associated with the neuropathologies found in several major neurodegenerative diseases [21]. Elevated intracellular Ca^{2+} , through activation of voltage-dependent calcium channels or NMDA receptors, recruits mitochondria to activated synapses [40–42]. The mechanisms underlying such activity-dependent mitochondrial recruitment were not known until the identification of Miro as a Ca^{2+} sensor [35,43,44]. Miro is a mitochondrial outer membrane protein with Ca^{2+} -binding EF hands [45]. By sensing cytosolic Ca^{2+} , Miro arrests mitochondria at activated synapses through the inactivation of the transport machineries. A Miro- Ca^{2+} sensing model was proposed whereby, when a trafficking mitochondrion passes through an active synapse, elevated Ca^{2+} binds to Miro and induces its conformational changes, thus disrupting the motor–adaptor complexes of KIF5-Trak-Miro (in mammals) or KIF5-Milton-Miro (in *Drosophila*) [35,44]. By this mechanism, mitochondria are immobilized at activated synapses (Figure 2A,B). However, this model has been disputed because it is unclear whether the KIF5 motor remains associated with arrested mitochondria or is released from the organelle upon immobilization. It is also unclear how this sensing pathway inactivates dynein-mediated retrograde transport. A genetic mouse study using a neuronal *miro1* deletion showed that Miro1 loss did not prevent Ca^{2+} -dependent inhibition of mitochondria motility [46]. A second study consistently showed that mitochondrial trafficking in *miro1* deletion neurons remained sensitive to neuronal activation [47]. These two mouse genetic studies raise questions as to whether Miro1 is essential for the Ca^{2+} -mediated inhibition of mitochondrial transport and whether the remaining Miro2 in these *miro1* mutant neurons or other mechanisms in place can immobilize mitochondria by sensing Ca^{2+} . These studies also suggest that mitochondrial immobilization requires a static anchoring mechanism.

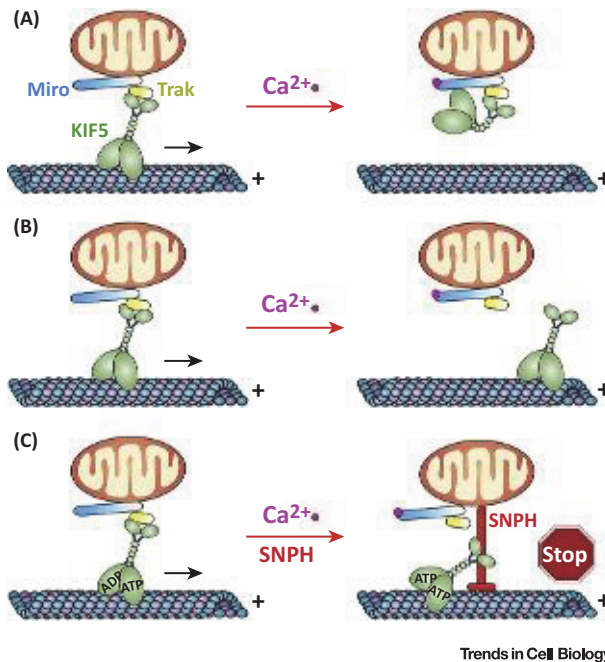
Box 1. Motors and Adaptors in Mitochondrial Transport

The *Drosophila* protein Milton and its mammal orthologs Trak1 and Trak2 function as adaptors linking the C-terminal domain of KIF5 motors to mitochondria through Miro1 or Miro2, Rho-GTPases present in the mitochondrial outer membrane [45,80,81]. Miro contains EF hand Ca^{2+} -binding motifs and GTPase domains, thus allowing mitochondrial transport to be regulated in response to Ca^{2+} signaling. KIF5, Milton/Trak, and Miro1/2 constitute the motor–adaptor complexes driving anterograde mitochondrial transport. Mutation of the *milton* or *miro* genes in *Drosophila* depletes mitochondria at synaptic terminals [29,81]. In mouse hippocampal neurons, the Miro1/Trak2 complex is a key regulator of mitochondrial transport [35]. Expressing Miro1 facilitates the recruitment of Trak2 to mitochondria, while depleting Trak1 impairs mitochondrial transport in axons [82,83]. The role of Miro was further confirmed in two recent studies with *miro1* deletion mouse models. The first study showed that neuron-specific loss of Miro1 caused the depletion of mitochondria from corticospinal tract axons, resulting in progressive neurological deficits [46]. However, the second study demonstrated that Miro1, but not Miro2, is the primary regulator of mitochondrial transport in both axons and dendrites. Miro1 deletion caused a depletion of mitochondria from distal dendrites accompanied by a marked reduction in dendritic complexity [47]. Syntabulin is an alternative KIF5 adaptor for driving mitochondrial transport. It attaches to the outer mitochondrial membrane via its C-terminal domain and recruits KIF5 motors to mitochondria [34]. Depleting syntabulin or blocking its coupling to KIF5 impaired mitochondrial transport from the soma to distal axons. The presence of several motor adaptors for mitochondria highlights the complex regulation of their motility in response to various physiological signals. Dynein motors mediate retrograde mitochondrial movement in axons. Cytoplasmic dynein comprises two dynein heavy chains (DHCs) and several intermediate (DICs), light intermediate (DLICs), and light chains (DLCs). DHCs function as motors and the association of the dynein motor with cargoes and the regulation of its motility involve other polypeptides. Dynein associates with *Drosophila* mitochondria and mutations in DHC alter the velocities and run lengths of mitochondrial retrograde transport in axons [84]. Compared with Trak-Miro as the KIF5 adaptor complex, adaptors that recruit dynein motors to mitochondria are less well known. Recent studies suggest that KIF5 and dynein motors share the same set of mitochondrial adaptor complexes. The loss of *dmiro* impaired both kinesin- and dynein-driven mitochondrial transport, while overexpressing dMiro altered bi-directional mitochondrial transport [82,85]. Trak1 and Trak2 contain separate binding domains for KIF5 and dynein/dynactin, thus allowing their coupling with both KIF5 and dynein [51]. Mitochondria move bi-directionally and frequently change direction, suggesting a model in which the relative activity of opposite-moving motors is regulated through their interactions with the adaptor complexes.

This possibility was tested in a recent study showing that activating the Miro- Ca^{2+} sensing pathway failed to arrest axonal mitochondria in *snph* KO hippocampal neurons [37]. Deleting the *snph* gene abolished the activity-dependent immobilization of mitochondria in axons, but not in dendrites, consistent with SNPH expression that is specific to axonal mitochondria. It was further revealed that SNPH competes with Trak2 to bind with KIF5 motors and inhibits motor ATPase activity. Thus, synaptic activity favors the KIF5-SNPH anchoring interaction and SNPH coordinates with the Miro- Ca^{2+} sensing mechanism for arresting axonal mitochondrial trafficking. These findings suggest a new ‘engine-switch and brake’ model, whereby, when a motile mitochondrion passes by an activated synapse, SNPH responds to elevated Ca^{2+} levels (stop sign) to switch off the engine (motor) and places a brake on the mitochondrion, thereby arresting the mitochondrion on the MT track. When the Ca^{2+} signal is removed, the cargo-loaded motor-adaptor complexes can be quickly reactivated (Figure 2C). This ‘engine-switch and brake’ model represents an interplay between the KIF5-Trak-Miro complex and the anchoring protein SNPH, thus effectively turning on/off trafficking and the anchoring mechanism in response to changes in energy-demanding synaptic activity.

Mitochondrial Motility Influences Energy Homeostasis and Presynaptic Strength

A quantitative analysis of presynaptic ATP levels showed that electrical activity imposes large bioenergetic demands that are met via local ATP synthesis in presynaptic boutons, in which SV recycling consumes most of the presynaptic ATP [38]. A brief interruption of local ATP synthesis severely impairs presynaptic function. Consistently, Pathak *et al.* [39] showed that SV endocytosis requires higher ATP consumption compared with SV exocytosis and reacidification. While both these studies suggest that presynaptic ATP supply is required to maintain sustained synaptic transmission, they also raise the question of whether defects in mitochondrial anchoring at presynaptic boutons cause local energy deficits, thus impairing the maintenance of SV release and recycling. Previous studies provided evidence that the loss of mitochondria from



Trends in Cell Biology

Figure 2. Synaptic Activity Regulates Mitochondrial Transport. (A,B) Miro- Ca^{2+} sensing models. Miro is a mitochondrial outer membrane protein with two Ca^{2+} -binding EF hands. By sensing cytosolic Ca^{2+} levels, Miro arrests mitochondria at activated synapses by inactivating KIF5 transport machineries. When a trafficking mitochondrion passes through an active synapse, elevated Ca^{2+} binds to Miro and induces its conformational changes, thus disrupting the KIF5–Trak–Mito complex [35,44]. Through this mechanism, mitochondria are immobilized at activated synapses. Two alternative models were proposed depending on whether (A) the KIF5 motor remains associated with arrested mitochondria or (B) is disconnected with the organelle upon immobilization. Two recent genetic studies showed that the loss of Miro1 in neurons did not inhibit the Ca^{2+} -dependent arrest of remaining mitochondria [46,47], thus raising the possibility that activity-dependent mitochondrial immobilization requires a static anchoring mechanism. (C) Engine-switch and brake model. When a motile mitochondrion passes by an activated synapse, the anchoring protein syntaphilin (SNPH) responds to elevated Ca^{2+} (stop sign), switches off the engine (motor), and places a brake on mitochondrion, thereby arresting mitochondria on the microtubule (MT) track. When the Ca^{2+} signal is removed, the cargo-loaded motor–adaptor complexes can be quickly reactivated to drive the mitochondrion to new active synapses. This engine switch and brake model suggests an interplay between the motor–adaptor transport complex and the anchoring protein SNPH [37]. Through this mechanism, neurons effectively regulate axonal mitochondrial distribution in response to changes in energy-demanding synaptic activity.

axonal terminals inhibits synaptic transmission due to insufficient ATP supply. For example, expressing mutant Milton in *Drosophila* photoreceptors impaired synaptic transmission by reducing synaptic mitochondria [29]. Expressing a loss-of-function mutant of syntabulin, a mitochondrial KIF5 motor adaptor [34], reduced mitochondrial trafficking to axonal terminals, accelerated synaptic depression, and slowed recovery during high-frequency firing [19]. Mutation in the mitochondrial fission protein Drp1 in *Drosophila* reduced synaptic localization of mitochondria and impaired SV mobilization from the reserve pool, thus depleting SVs much faster than in wildtype neurons during prolonged trains of stimulation, a phenotype partially rescued by adding ATP to the synapses [13]. Consistently, a conditional *drp1* KO mouse line with a postnatal deletion in CA1 hippocampal neurons failed to maintain mitochondrial-derived ATP levels at presynaptic terminals during neuronal activity, thus impairing SV recycling and memory in the mutant mice [48].

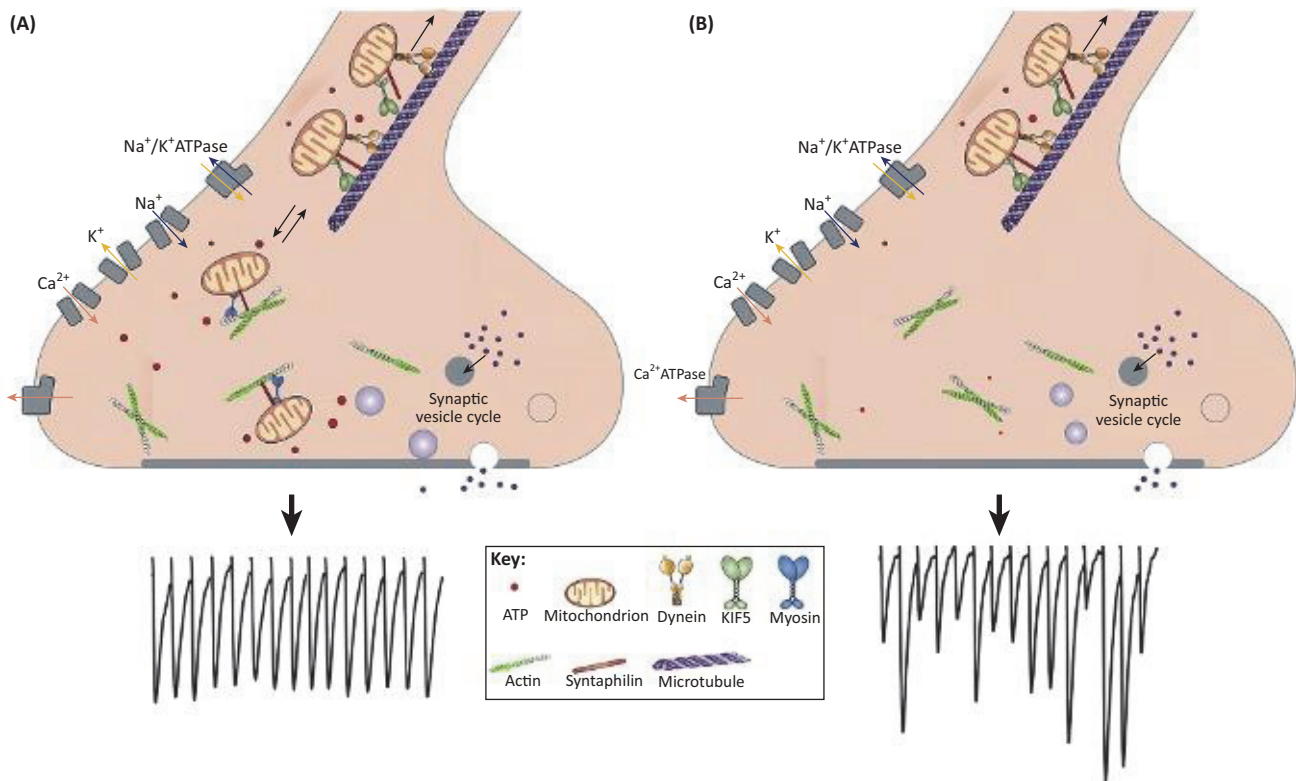
In cultured mature neurons, approximately 20–30% of axonal mitochondria move bi-directionally, some of which pass through or pause at presynaptic terminals [5,6]. By imaging both axonal and presynaptic mitochondria in live hippocampal neurons, five patterns of mitochondrial motility and distribution were recently characterized in axons: nonsynaptic stationary

($54.07 \pm 2.53\%$) and synaptic stationary mitochondria ($16.29 \pm 1.66\%$), and motile mitochondria passing through synapses ($14.77 \pm 1.58\%$), pausing at synapses briefly ($7.01 \pm 1.29\%$) or for more than 200 s ($8.30 \pm 1.52\%$) [8]. These patterns are consistent with a previous study in cortical neurons [42] and further supported by a recent *in vivo* 3D electron microscopy analysis of perfusion-fixed hippocampi, where 33% of total synapses contained presynaptic mitochondria, 31% of synapses were located less than 3 μm from the nearest axonal mitochondrion, and 36% of synapses were more than 3 μm from the nearest axonal mitochondrion [49].

The balance between these motile and synaptic pools of mitochondria responds quickly to changes in synaptic activity and likely the status of energy homeostasis. Thus, a proposed model is one in which a stationary mitochondrion retained within presynaptic boutons constantly supplies ATP to support ATP-dependent presynaptic functions. Conversely, for a presynaptic terminal lacking an anchored mitochondrion, ATP is mainly supplied through diffusion from mitochondria outside the synapse. When mitochondria move closer, more ATP is supplied to the synapse, and vice versa. Therefore, a motile mitochondrion passing through this presynaptic bouton dynamically alters local ATP homeostasis, influencing ATP-dependent synaptic functions (Figure 3).

This model was recently tested by combining live neuron imaging and electrophysiological analysis in a *snph* mutant mouse model in which axonal mitochondrial motility was robustly increased (78%) [8]. First, using cultured hippocampal neurons and hippocampal slices from age-matched wildtype and *snph*^{-/-} mice, it was shown that enhanced axonal mitochondrial motility significantly increased the variability of pulse-to-pulse amplitudes of excitatory postsynaptic currents (EPSCs). Overexpressing SNPH reduced the variability found in wildtype neurons by abolishing mitochondria motility. Second, using dual-channel imaging of mitochondrial motility and synapto-pHluorin at single-bouton levels, it was further shown that mitochondrial movement either into or out of presynaptic boutons influenced SV cycling due to the large fluctuations of synaptic ATP levels. In the absence of an anchored mitochondrion, presynaptic boutons lack a constant on-site ATP supply under intensive synaptic activity. A motile mitochondrion passing through could spatially and temporally supply ATP, thus changing presynaptic energy levels when a mitochondrion moves in or out of synapses and consequently influencing ATP-dependent synaptic activities (Figure 3). Therefore, fluctuations of presynaptic ATP levels contribute to the variability in presynaptic strength. Thus, the study discussed above reveals that axonal mitochondrial motility is one of the primary mechanisms underlying the plasticity and reliability of presynaptic strength in the CNS.

In neurons, glycolysis also produces ATP, a process independent of mitochondria. Thus, increased glycolysis could supply ATP in boutons that lack mitochondria. By measuring presynaptic ATP levels, the Ryan group demonstrated that glycolysis supports the maintenance of ATP levels at resting presynaptic boutons [38]. Blockage of the ATP synthesis pathways by application of either the glycolysis inhibitor 2-deoxyglucose or mitochondrial ATPase inhibitor oligomycin alone reduced presynaptic ATP levels during synaptic activity. Their study suggests that ATP supply from both glycolysis and mitochondria is required to sustain activity-dependent ATP consumption. It was also reported that mitochondria-derived ATP is dispersed in axons and diffused to non-mitochondria-containing presynaptic boutons. Thus, the capacity for SV recycling is similar in the presynaptic boutons with or without a mitochondrion [39]. These findings raise a question as to whether presynaptic mitochondria could provide more ATP sources to sustain increased synaptic efficacy. By 3D electron microscopy, the Harris group recently demonstrated that sustained synaptic activity is specific to mitochondria-containing presynaptic boutons during long-term potentiation [49]. Presynaptic boutons with mitochondria have more docked SVs than those without mitochondria in the hippocampal CA1 area. This is largely attributed to the fact that efficient SV mobilization is



Trends in Cell Biology

Figure 3. Mitochondrial Motility Influences Energy Homeostasis and Presynaptic Strength. (A) A stationary mitochondrion retained within a presynaptic bouton constantly supplies ATP to support various presynaptic functions, including establishing the proton gradient necessary for neurotransmitter loading; removing Ca^{2+} from nerve terminals; powering synaptic vesicle (SV) transport from reserve pools to release sites; and driving SV exo- and endocytotic recycling, thus maintaining presynaptic strength. (B) For a presynaptic terminal lacking an anchored mitochondrion, ATP is mainly supplied through diffusion from mitochondria outside the synapses. When a mitochondrion moves closer, more ATP supplies the synapse and vice versa. Thus, a motile mitochondrion passing through this presynaptic bouton dynamically alters local ATP levels and influences ATP-dependent synaptic functions, leading to wide pulse-to-pulse variability of synaptic strength, particularly under increased energy demand during sustained synaptic activity.

restricted to presynaptic boutons with or near mitochondria. This study further supports a previous study that ATP production from presynaptic mitochondria is the main local energy source driving SV mobilization from the reserve pool to sustain the lasting synaptic efficacy [13].

While MT-based kinesin and dynein motors drive mitochondrial transport along long-range MT tracks, actin-based myosin motors mediate short-range movement at presynaptic terminals, where actin filaments form the major cytoskeletal architecture. It was reported that actin anchors mitochondria at nerve growth factor stimulation sites, although underlying mechanisms remain unclear [50], thus raising an interesting question as to whether motile mitochondria are recruited to, and captured at, presynaptic terminals via MT–actin crosstalk.

Regulation of Mitochondrial Motility by Energy Metabolism and Growth Status

Mitochondrial trafficking and distribution in polarized neurons is the central issue concerning the maintenance of energy homeostasis throughout cells. Proper mitochondrial transport into growth cones and branches in developing neurons ensures an adequate ATP supply in these metabolically active regions. Recent studies established a correlation between polarized mitochondrial transport and axonal and dendritic morphology. For example, a recent study reported the differential functions of the motor adaptors Trak1 and Trak2 in driving polarized

mitochondrial transport and, thus, axonal and dendritic growth [51]. While Trak1 is required for axonal mitochondria transport through binding to both kinesin-1 and dynein motors, Trak2 predominantly mediates mitochondrial transport into dendrites by interacting with the dynein motors. Consistently, depleting Trak1 inhibited axonal outgrowth, while disrupting Trak2-mediated mitochondrial trafficking impaired dendrite morphology. A genetic mouse study provided further evidence showing the differential roles of Miro1 and Miro2 in mitochondrial trafficking and neuronal morphogenesis [47]. Miro1, but not Miro2, is the main regulator of mitochondrial trafficking. Deleting Miro1 *in vivo* during mouse development disrupted neuronal morphogenesis, while Miro1 disruption in mature neurons led to a loss of distal dendritic complexity.

Emerging evidence suggests that neurons have a special mechanism that activates mitochondrial biogenesis and delivers mitochondria to distal axons by sensing energy requirements. Neuronal growth requires a considerable amount of energy to drive the synthesis of raw building materials and the delivery of these materials to new growing tips. Mitochondrial biogenesis and a local mitochondria-derived ATP supply are required for axonal growth during development [52]. AMP-activated protein kinase (AMPK) is a master regulator of cellular energy homeostasis and is activated upon stresses that deplete cellular ATP supplies. Earlier activation of mitochondrial biogenesis through the AMPK–PGC-1 α –NRF1 axis accelerates the generation of new mitochondria and increases mitochondrial density and the ATP:ADP ratio in axonal terminals, thereby ensuring an energy production capability that is sufficient for axonal growth.

It is assumed that stationary mitochondria ideally serve as local energy stations that constantly supply ATP and, thus, maintain local ATP homeostasis. This issue was recently examined in a study using cortical neurons that found a solid causal correlation of mitochondrial distribution patterns with the ATP:ADP ratio in axonal terminals [22]. Overexpressing SNPH restricted axonal mitochondria within the proximal axons due to reduced flux to distal axons, which correlated with a reduced ATP:ADP ratio in the most distal axon segment and smaller-sized growth cones. Conversely, overexpressing Miro1 increased the mitochondrial density in distal axons and the average size of growth cones. These results suggest that proper mitochondrial density in distal axons is required to maintain growth capacity. High ADP levels are thought to suppress mitochondrial motility [53]. Using a motor-assisted transport model combined with probability simulations, Mironov reported that [ADP] gradients in the proximity of active synapses and growth cones slowed down mitochondrial motility and, thus, targeted mitochondria to ‘hot spots’ with high energy consumption.

Recent studies support the notion that the balance between motile and stationary mitochondria responds to changes in axonal growth status via AMPK. One study highlighted a critical role for SNPH in mediating mitochondrial anchoring through the AMPK pathway [54]. Activation of AMPK increases anterograde flux of mitochondria into distal axons and induces axonal branching. As a cellular energy sensor, AMPK activation may replenish the ATP supply in distal axons by recruiting mitochondria and anchoring them through signaling pathways that have not yet been revealed. Intriguingly, depleting SNPH reduces the stationary pool size of axonal mitochondria accompanied by decreased axon branching, thus establishing a causal relation between SNPH-mediated anchoring and AMPK-induced axonal branching. However, an important mechanistic question remains: do SNPH and/or motor complexes act as a downstream effector of the AMPK pathways in recruiting mitochondria by sensing metabolic signals? The KIF5 motor might be a potential target because its light chain is phosphorylated by AMPK [55]. It would be interesting to investigate the mechanisms by which axonal mitochondria are immobilized or remobilized to sense changes in the local ATP:ADP ratio or metabolic signals.

Tao *et al.* [56] provided further evidence showing that AMPA activation is required for axonal branch formation in an ATP-dependent manner by balancing mitochondrial trafficking and anchoring. Activation of AMPK increases the anterograde transport of mitochondria toward axonal terminals and accumulates mitochondrial docking in regions preceding the emergence of new axonal branches. The formation of axonal branches is blocked by the mitochondrial uncoupler FCCP, thus providing a link between mitochondria-derived ATP and the formation and/or maintenance of axonal branches. A third study revealed an intriguing mechanism underlying the role of mitochondria in determining axon branching sites [57]. Anchored mitochondria in local hot spots promote the maturation of axonal filopodia into axon branching through ATP generation that powers local intra-axonal mRNA translation and protein synthesis. Blocking mitochondrial respiration or inhibiting protein synthesis impaired the maturation of axonal branches, despite mitochondria having been anchored at these hot spots. These studies support the notion that the balance between motile and stationary mitochondria in axons responds to changes in axonal growth status via AMPK. Thus, regulating mitochondrial trafficking and anchoring is critical to maintaining the local ATP supply necessary for energy-demanding axonal growth and branching.

Glucose is the main carbon source for mitochondria-derived ATP production. In particular, neurons rely heavily on a continuous supply of glucose to maintain mitochondrial energy metabolism. A recent study revealed that glucose levels can also regulate mitochondrial motility in neurons [58]. Extracellular glucose arrests mitochondrial transport through the enzyme OGT, a putative metabolic sensor. Post-translational modification of Milton by OGT-dependent O-GlcNAcylation is required for regulating mitochondrial distribution. Through this mechanism, neurons may accumulate axonal mitochondria in areas where cytosolic glucose is elevated, thus ensuring rapid ATP production by sensing changes in the glucose supply.

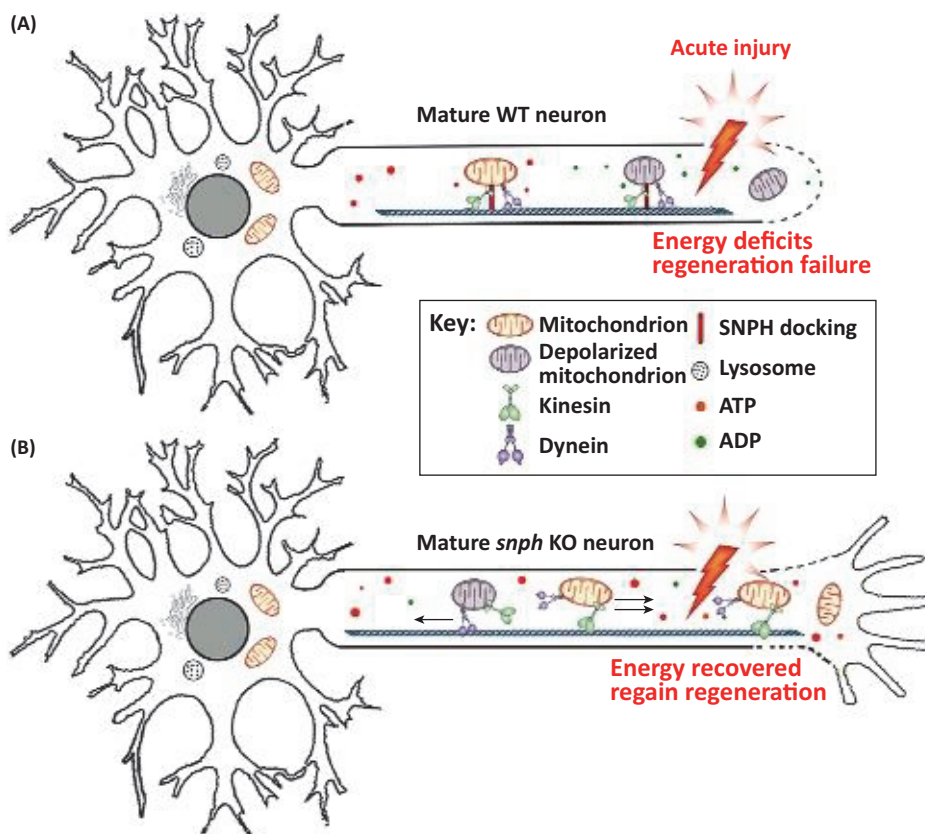
Mitochondrial Transport Facilitates Axon Regeneration by Rescuing Energy Deficits

While young neurons during early developmental stages have robust axon growth capacity, mature neurons typically fail to regenerate after spinal cord injury or traumatic brain injury, leading to permanent neurological impairments. It was suggested that mature neurons lose their growth capacity due to an intrinsic decline of permissive conditions for regeneration [59]. Thus, it is critical to understanding which intrinsic mechanisms account for the mature neuron-associated decline of regrowth capacity. Injury to mature neurons usually leads to an inability to reform an active growth cone, where damaged membranes are resealed, cytoskeletal structures are rearranged, and regrowth programs are activated, including the synthesis of raw building materials, their transport, and the assembly of axonal components. All of these regrowth events require high levels of energy consumption [60]. Mitochondria-derived ATP production provides most of the axonal energy. Given the limited diffusion capacity of intracellular ATP through extremely long axons, axonal mitochondria are the main source of the ATP necessary to assemble a new growth cone and support axon regeneration. Axonal injury is a strong stress condition that induces mitochondrial depolarization [61,62]. Dysfunctional mitochondria not only supply less ATP, causing local energy deficits, but also release toxic reactive oxygen species (ROS) and apoptotic factors that further trigger axonal pathology and degeneration [63]. Therefore, enhancing mitochondrial transport not only removes those damaged mitochondria, but also delivers healthy ones into injured axons to meet increased energy requirements during regeneration. To test the above hypothesis, one would first need to address two fundamental questions: (i) Do mature neurons maintain an effective capacity to recruit healthy mitochondria to injured axons? and (ii) If this capacity declines with neuron maturation, does enhancing mitochondrial transport enable mature neurons to regain axon regenerative capacity?

These issues were recently examined using live imaging of mitochondrial transport, mitochondrial integrity, and dynamic ATP levels in injured axons within a microfluidic chamber system combined with an *in vivo* mouse model [22]. Examination of the relative SNPH expression and axonal mitochondrial transport throughout neuronal developmental stages revealed that the mature neuron-associated decline of regrowth capacity correlated well with progressively increased levels of SNPH expression. In cultured cortical neurons, SNPH becomes detectable after DIV9, and peaks at DIV22. Axonal mitochondrial motility at DIV7 is 47%, twice as high as that at DIV18. This *in vitro* SNPH expression pattern is consistent with a robust increase in SNPH expression in mature neurons of rat brains. These results suggest that mature neuron-associated increase in SNPH expression and decline in mitochondrial transport is one of the intrinsic mechanisms diminishing axonal regenerative capacity. This study showing a progressive decline in axonal mitochondrial transport over neuronal maturation is also consistent with three recent *in vitro* and *in vivo* studies [64–66]. In ganglion cell dendrites in the intact retina, mitochondria are highly motile (30%) during developmental stages; as dendrites mature, mitochondria reach stable positions, such as synapses and branch points [64]. Another study evaluated axonal regrowth 6 days after injury following the manipulation of axonal mitochondrial transport in mature cortical neurons by overexpressing SNPH or Miro1 transgenes [22]. Expressing SNPH arrested all mitochondrial transport and abolished axons regrowth after injury. By contrast, expressing Miro1 enhanced mitochondrial transport and robustly increased axonal regrowth capacity. This study indicates that mature neurons can regain their regrowth capacity by enhancing mitochondrial transport. By monitoring mitochondrial membrane potentials and the ATP:ADP ratio, it was also shown that axonal injury is an acute stress condition that damages local mitochondria and reduces ATP supply, thus triggering energy deficits in the injury sites [22]. Furthermore, by crushing sciatic nerves *in vivo* in adult *snph* KO mice, it was found that enhanced mitochondrial transport in *snph* KO sciatic nerves facilitated *in vivo* axonal regeneration [22].

The findings that mitochondrial transport influences axonal regenerative capacity in mouse models are supported by several previous reports. In the *Caenorhabditis elegans* mutant *ric-7*, which has impaired mitochondrial transport to distal axons, injured axons degenerate rapidly; such degeneration can be suppressed by forcing mitochondria into the axons [67]. When mitochondria were eliminated from fly axons by depleting Milton, upregulation of Nmnat, which is known to suppress axon degeneration [68], failed to suppress axon degeneration [69], suggesting that mitochondrial trafficking to axons is critical to suppressing axonal degeneration. Using both *Drosophila* and mouse models, Avery *et al.* [70] identified axonal mitochondria as a key target for *Wld^S*, an effective protein that protects axon from Wallerian degeneration after injury [71]. *Wld^S* enhances mitochondrial flux into axons, which is essential for maximal axonal protection after injury [70]. A peripheral injury of CNS axons induces a global increase in the axonal transport of organelles, including mitochondria, lysosomes, and other axonal building blocks, thus supporting axon regeneration [72]. Recently, two other studies provided *in vivo* evidence in worms and mice that mitochondrial transport has a critical role in enhancing neuronal regenerative capacity after injury. In *C. elegans*, axotomy triggered an energy stress in injured axons and recruited and increased axonal mitochondrial density to supply ATP for sustained axonal regeneration [73]. This injury-induced response occurred via the activation of the dual leucine zipper kinase 1 (DLK-1), a conserved regulator of axon regeneration. Using adult mouse retinal ganglion cells as an *in vivo* injury model, Cartoni *et al.* [74] reported that expression of the mitochondrial protein *Armcx1* enhanced mitochondrial transport by recruiting stationary mitochondria. Such enhanced transport is critical to protecting axotomized neurons from cell death and promoting axon regeneration. Although the mechanisms enhancing axonal mitochondrial transport by DLK-1 and *Armcx1* have not yet been elucidated, these studies reveal new molecular players in the regulation of neuronal injury responses.

Energy deficit is defined as an insufficient ATP supply when mitochondria are damaged and/or an increased energy consumption, such as during axonal regeneration. Mitochondrial damage by axonal injury, mature neuron-associated decline of mitochondrial transport, and enhanced energy consumption collectively contribute to energy deficits in injured axons. Enhanced mitochondrial transport rescues energy deficits by replenishing healthy mitochondria to injured axons (Figure 4). Thus, activating an intrinsic 'growth program' requires the recovery of energy supply through enhanced mitochondrial transport. Such coordinated regulation may represent a valid therapeutic strategy to facilitate nerve regeneration and recovery after injury and diseases. The future development of safe and effective small-molecule compounds will be an attractive strategy to selectively increase mitochondrial motility and rescue the local energy deficits within injured axons [75].



Trends in Cell Biology

Figure 4. Illustration of Enhanced Mitochondrial Transport Critical for Mature Neurons to Regain Axonal Regenerative Capacity. (A) An energy deficit is defined as an insufficient ATP supply when mitochondria are damaged and/or there is increased energy consumption during regeneration. Mitochondrial damage by axonal injury and mature neuron-associated decline of mitochondrial transport collectively contribute to local energy deficits in injured axons, thus leading to regeneration failure. Energy deficits may reflect the intrinsic restriction of mature neurons to regenerate following injury. (B) Enhanced mitochondrial transport by deleting syntaphilin (SNPH) not only helps remove those dysfunctional mitochondria, but also replenishes healthy ones to the injured axons, thus recovering mitochondrial integrity and rescuing energy deficits. An enhanced local ATP supply is critical to meeting the metabolic requirements of axon regeneration. Thus, activating an intrinsic 'growth program' requires the recovery of energy supply by enhancing mitochondrial transport. Such coordinated regulation may represent a valid therapeutic strategy to facilitate nerve regeneration and functional recovery after injury and in disease. Abbreviations: KO, knockout; WT, wildtype.

Concluding Remarks

Mitochondria are the main cellular power plants that produce energy essential for neuronal growth, survival, and function. Neurons face exceptional challenges in maintaining energy homeostasis, especially at distal synapses and growth cones, where energy is in high demand. Anchored mitochondria ideally serve as local energy sources. The energy-dependent regulation of mitochondrial trafficking and anchoring ensures that these metabolically active areas are adequately supplied with ATP during the growth of developing neurons, the regeneration of injured mature neurons, and the maintenance of synaptic activity.

It is well documented that mitochondrial dysfunction and impaired mitochondrial transport are involved in major neurodegenerative diseases and neurological disorders [20,21,76]. Damaged mitochondria fail to produce ATP and associate with an altered redox status. Bioenergetic deficits and chronic oxidative stress trigger axonal pathology and synaptic dysfunction, thus contributing to the pathogenesis of neurodegenerative diseases [30]. Indeed, energy failure or an impaired bioenergetic metabolism emerges as a common problem during the early stages of aging-associated neurodegenerative diseases, including Alzheimer's and Parkinson's diseases [10,77–79].

SNPH is an intriguing anchoring protein that is specific for axonal mitochondria and, thus, serves as an attractive target for future investigations of the mechanisms that recruit mitochondria into activated synapses and injured axons. Studies have demonstrated that the relative SNPH enrichment on axonal mitochondria controls mitochondrial motility and the mature neuron-associated decline of mitochondrial transport correlates with progressively increased SNPH expression [22,36]. Declined axonal mitochondrial transport in mature neurons is also supported by three recent *in vitro* and *in vivo* studies [64–66]. Elevated SNPH expression and, thus, mitochondrial anchoring in mature neurons is necessary to maintain synaptic function. However, when mature neurons are injured and diseased, SNPH-mediated mitochondrial anchoring restricts axonal regrowth and regenerative capacity. These findings can be used to propose the hypothesis that mature neuron-associated SNPH expression is an intrinsic mechanism that restricts the removal of dysfunctional mitochondria from axons, thus leading to energy deficits at distal synapses under pathological conditions. The selective removal of SNPH from those damaged mitochondria would enhance their transport, allowing for efficient repair or elimination in the somatodendritic regions where mature lysosomes are relatively enriched. Thus, spatially and temporally removing SNPH from axonal mitochondria may be an attractive pathway to replenish healthy mitochondria at distal terminals to rescue energy deficits and, thus, support neuron regeneration after injury and maintain synaptic transmission in disease. Therefore, the development of new optogenetic tools to test this hypothesis will help advance our understanding of how mitochondrial trafficking and anchoring in axons and at synapses are regulated through the sensing and integration of changes in local metabolic status under various physiological and pathological stresses. Future studies should be directly relevant to the challenge that mature neurons face in maintaining an energy supply in health and, similarly, recovering energy deficits in neurological disorders and regeneration after injury and diseases (see Outstanding Questions).

Acknowledgments

The author apologizes to those colleagues whose work could not be cited owing to space limitations and journal guidelines to cite the most recent literature. The author thanks his lab members B. Zhou, T. Sun, and M-Y. Lin for their research contributions and constructive discussions; X-T. Cheng for illustration and reference editing; and S. Cuddy and D. Schoenberg for critical reading. The work was supported by the Intramural Research Program of NINDS, NIH ZIA NS003029 and ZIA NS002946 (Z-H. Sheng).

Outstanding Questions

How are mitochondrial trafficking and anchoring regulated through the sensing and integration of changes in the local bioenergetics status under various physiological stresses?

Does the anchoring protein SNPH act as a downstream effector of AMPK pathways in recruiting mitochondria by sensing the metabolic signals?

Are mobile mitochondria captured at active presynaptic terminals through the MT-actin track switch and crossstalk?

Do energy deficits occur in distal axons and at synapses during the early stages of certain pathological conditions?

Is an energy deficit associated with a range of neurodegenerative diseases? If this is the case, does the recovery of energy supply slow down the pathogenesis?

How is SNPH removed from axonal mitochondria in mature neurons to spatially and temporally enhance axonal mitochondrial transport and rescue energy deficits, and, thus, support neuron regeneration after injury and disease?

References

- Mattson, M.P. *et al.* (2008) Mitochondria in neuroplasticity and neurological disorders. *Neuron* 60, 748–766
- Zhu, X.H. *et al.* (2012) Quantitative imaging of energy expenditure in human brain. *Neuroimage* 60, 2107–2117
- Nicholls, D.G. and Budd, S.L. (2000) Mitochondria and neuronal survival. *Physiol. Rev.* 80, 315–360
- Harris, J.J. *et al.* (2012) Synaptic energy use and supply. *Neuron* 75, 762–777
- Saxton, W.M. and Hollenbeck, P.J. (2012) The axonal transport of mitochondria. *J. Cell Sci.* 125, 2095–2104
- Sheng, Z.H. (2014) Mitochondrial trafficking and anchoring in neurons: new insight and implications. *J. Cell Biol.* 204, 1087–1098
- Hubley, M.J. *et al.* (1996) The effects of temperature, pH, and magnesium on the diffusion coefficient of ATP in solutions of physiological ionic strength. *Biochim. Biophys. Acta* 1291, 115–121
- Sun, T. *et al.* (2013) Motile axonal mitochondria contribute to the variability of presynaptic strength. *Cell Rep.* 4, 413–419
- Cheng, H.C. *et al.* (2010) Clinical progression in Parkinson disease and the neurobiology of axons. *Ann. Neurol.* 67, 715–725
- Pathak, D. *et al.* (2013) Energy failure: does it contribute to neurodegeneration? *Ann. Neurol.* 74, 506–516
- Lee, C.W. and Peng, H.B. (2008) The function of mitochondria in presynaptic development at the neuromuscular junction. *Mol. Biol. Cell* 19, 150–158
- Attwell, D. and Laughlin, S.B. (2001) An energy budget for signaling in the grey matter of the brain. *J. Cereb. Blood Flow Metab.* 21, 1133–1145
- Verstreken, P. *et al.* (2005) Synaptic mitochondria are critical for mobilization of reserve pool vesicles at *Drosophila* neuromuscular junctions. *Neuron* 47, 365–378
- Medler, K. and Gleason, E.L. (2002) Mitochondrial Ca²⁺ buffering regulates synaptic transmission between retinal amacrine cells. *J. Neurophysiol.* 87, 1426–1439
- David, G. and Barrett, E.F. (2003) Mitochondrial Ca²⁺ uptake prevents desynchronization of quantal release and minimizes depletion during repetitive stimulation of mouse motor nerve terminals. *J. Physiol.* 548, 425–438
- Talbot, J.D. *et al.* (2003) Inhibition of mitochondrial Ca²⁺ uptake affects phasic release from motor terminals differently depending on external [Ca²⁺]. *J. Neurophysiol.* 90, 491–502
- Billups, B. and Forsythe, I.D. (2002) Presynaptic mitochondrial calcium sequestration influences transmission at mammalian central synapses. *J. Neurosci.* 22, 5840–5847
- Shepherd, G.M.G. and Harris, K.M. (1998) Three-dimensional structure and composition of CA3-CA1 axons in rat hippocampal slices: Implications for presynaptic connectivity and compartmentalization. *J. Neurosci.* 18, 8300–8310
- Ma, H. *et al.* (2009) KIF5B motor adaptor syntabulin maintains synaptic transmission in sympathetic neurons. *J. Neurosci.* 29, 13019–13029
- Chen, H. and Chan, D.C. (2009) Mitochondrial dynamics—fusion, fission, movement, and mitophagy—in neurodegenerative diseases. *Hum. Mol. Genet.* 18, R169–R176
- Sheng, Z.H. and Cai, Q. (2012) Mitochondrial transport in neurons: impact on synaptic homeostasis and neurodegeneration. *Nat. Rev. Neurosci.* 13, 77–93
- Zhou, B. *et al.* (2016) Facilitation of axon regeneration by enhancing mitochondrial transport and rescuing energy deficits. *J. Cell Biol.* 214, 103–119
- Cai, Q. *et al.* (2012) Spatial parkin translocation and degradation of damaged mitochondria via mitophagy in live cortical neurons. *Curr. Biol.* 22, 545–552
- Mironov, S.L. (2009) Complexity of mitochondrial dynamics in neurons and its control by ADP produced during synaptic activity. *Int. J. Biochem. Cell Biol.* 41, 2005–2014
- Miller, K.E. and Sheetz, M.P. (2004) Axonal mitochondrial transport and potential are correlated. *J. Cell Sci.* 117, 2791–2804
- Chang, D.T. and Reynolds, I.J. (2006) Mitochondrial trafficking and morphology in healthy and injured neurons. *Prog. Neurobiol.* 80, 241–268
- MacAskill, A.F. and Kittler, J.T. (2010) Control of mitochondrial transport and localization in neurons. *Trends Cell Biol.* 20, 102–112
- Birsa, N. *et al.* (2013) Mitochondrial trafficking in neurons and the role of the Miro family of GTPase proteins. *Biochem. Soc. Trans.* 41, 1525–1531
- Schwarz, T.L. (2013) Mitochondrial trafficking in neurons. *Cold Spring Harb. Perspect. Biol.* 5, a011304
- Mishra, P. and Chan, D.C. (2016) Metabolic regulation of mitochondrial dynamics. *J. Cell Biol.* 212, 379–387
- Frederick, R.L. and Shaw, J.M. (2007) Moving mitochondria: establishing distribution of an essential organelle. *Traffic* 8, 1668–1675
- Belanger, M. *et al.* (2011) Brain energy metabolism: focus on astrocyte-neuron metabolic cooperation. *Cell Metab.* 14, 724–738
- Hirokawa, N. *et al.* (2010) Molecular motors in neurons: transport mechanisms and roles in brain function, development, and disease. *Neuron* 68, 610–638
- Cai, Q. *et al.* (2005) Syntabulin-mediated anterograde transport of mitochondria along neuronal processes. *J. Cell Biol.* 170, 959–969
- Macaskill, A.F. *et al.* (2009) Miro1 is a calcium sensor for glutamate receptor-dependent localization of mitochondria at synapses. *Neuron* 61, 541–555
- Kang, J.S. *et al.* (2008) Docking of axonal mitochondria by syntaphilin controls their mobility and affects short-term facilitation. *Cell* 132, 137–148
- Chen, Y. and Sheng, Z.H. (2013) Kinesin-1-syntaphilin coupling mediates activity-dependent regulation of axonal mitochondrial transport. *J. Cell Biol.* 202, 351–364
- Rangaraju, V. *et al.* (2014) Activity-driven local ATP synthesis is required for synaptic function. *Cell* 156, 825–835
- Pathak, D. *et al.* (2015) The role of mitochondrially derived ATP in synaptic vesicle recycling. *J. Biol. Chem.* 290, 22325–22336
- Rintoul, G.L. *et al.* (2003) Glutamate decreases mitochondrial size and movement in primary forebrain neurons. *J. Neurosci.* 23, 7881–7888
- Yi, M.Q. *et al.* (2004) Control of mitochondrial motility and distribution by the calcium signal: a homeostatic circuit. *J. Cell Biol.* 167, 661–672
- Chang, D.T. *et al.* (2006) Mitochondrial trafficking to synapses in cultured primary cortical neurons. *J. Neurosci.* 26, 7035–7045
- Saotome, M. *et al.* (2008) Bidirectional Ca²⁺-dependent control of mitochondrial dynamics by the Miro GTPase. *Proc. Natl. Acad. Sci. U. S. A.* 105, 20728–20733
- Wang, X. and Schwarz, T.L. (2009) The mechanism of Ca²⁺-dependent regulation of kinesin-mediated mitochondrial motility. *Cell* 136, 163–174
- Fransson, A. *et al.* (2003) Atypical Rho GTPases have roles in mitochondrial homeostasis and apoptosis. *J. Biol. Chem.* 278, 6495–6502
- Nguyen, T.T. *et al.* (2014) Loss of Miro1-directed mitochondrial movement results in a novel murine model for neuron disease. *Proc. Natl. Acad. Sci. U. S. A.* 111, E3631–E3640
- Lopez-Domenech, G. (2016) Loss of dendritic complexity precedes neurodegeneration in a mouse model with disrupted mitochondrial distribution in mature dendrites. *Cell Rep.* 17, 317–327
- Shields, L.Y. *et al.* (2015) Dynamin-related protein 1 is required for normal mitochondrial bioenergetic and synaptic function in CA1 hippocampal neurons. *Cell Death Dis.* 6, e1725

49. Smith, H.L. *et al.* (2016) Mitochondrial support of persistent presynaptic vesicle mobilization with age-dependent synaptic growth after LTP. *Elife* 5, e15275
50. Chada, S.R. and Hollenbeck, P.J. (2004) Nerve growth factor signaling regulates motility and docking of axonal mitochondria. *Curr. Biol.* 14, 1272–1276
51. van Spronsen, M. *et al.* (2013) TRAK/Milton motor-adaptor proteins steer mitochondrial trafficking to axons and dendrites. *Neuron* 77, 485–502
52. Vaarmann, A. *et al.* (2016) Mitochondrial biogenesis is required for axonal growth. *Development* 143, 1981–1992
53. Mironov, S.L. (2007) ADP regulates movements of mitochondria in neurons. *Biophys. J.* 92, 2944–2952
54. Courchet, J. *et al.* (2013) Terminal axon branching is regulated by the LKB1-NUAK1 kinase pathway via presynaptic mitochondrial capture. *Cell* 153, 1510–1025
55. Amato, S. *et al.* (2011) AMP-activated protein kinase regulates neuronal polarization by interfering with PI 3-kinase localization. *Science* 332, 247–251
56. Tao, K. *et al.* (2014) AMP-activated protein kinase mediates activity-dependent axon branching by recruiting mitochondria to axon. *Dev. Neurobiol.* 74, 557–573
57. Spillane, M. *et al.* (2013) Mitochondria coordinate sites of axon branching through localized intra-axonal protein synthesis. *Cell Rep.* 5, 1564–1575
58. Pekkmaz, G. *et al.* (2014) Glucose regulates mitochondrial motility via Milton modification by O-GlcNAc transferase. *Cell* 158, 54–68
59. Liu, K. *et al.* (2011) Neuronal intrinsic mechanisms of axon regeneration. *Annu. Rev. Neurosci.* 34, 131–152
60. Bradke, F. *et al.* (2012) Assembly of a new growth cone after axotomy: the precursor to axon regeneration. *Nat. Rev. Neurosci.* 13, 183–193
61. O'Donnell, K.C. *et al.* (2013) WldS and PGC-1 α regulate mitochondrial transport and oxidation state after axonal injury. *J. Neurosci.* 33, 14778–14790
62. Cavallucci, V. *et al.* (2014) Acute focal brain damage alters mitochondrial dynamics and autophagy in axotomized neurons. *Cell Death Dis.* 5, e1545
63. Alvarez, S. *et al.* (2008) Acute energy restriction triggers Wallerian degeneration in mouse. *Exp. Neurol.* 212, 166–178
64. Faits, M.C. *et al.* (2016) Dendritic mitochondria reach stable positions during circuit development. *Elife* 5, e11583
65. Smit-Rigter, L. *et al.* (2016) Mitochondrial dynamics in visual cortex are limited *in vivo* and not affected by axonal structural plasticity. *Curr. Biol.* 26, 2609–2616
66. Lewis, T.L., Jr *et al.* (2016) Progressive decrease of mitochondrial motility during maturation of cortical axons *in vitro* and *in vivo*. *Curr. Biol.* 26, 2602–2608
67. Rawson, R.L. *et al.* (2014) Axons degenerate in the absence of mitochondria in *C. elegans*. *Curr. Biol.* 24, 760–765
68. Gilley, J. and Coleman, M.P. (2010) Endogenous Nmnat2 is an essential survival factor for maintenance of healthy axons. *PLoS Biol.* 8, e1000300
69. Fang, Y. *et al.* (2012) A novel *Drosophila* model of nerve injury reveals an essential role of Nmnat in maintaining axonal integrity. *Curr. Biol.* 22, 590–595
70. Avery, M.A. *et al.* (2012) Wld(S) prevents axon degeneration through increased mitochondrial flux and enhanced mitochondrial Ca²⁺ buffering. *Curr. Biol.* 22, 596–600
71. Conforti, L. *et al.* (2014) Wallerian degeneration: an emerging axon death pathway linking injury and disease. *Nat. Rev. Neurosci.* 15, 394–409
72. Mar, F.M. *et al.* (2014) CNS axons globally increase axonal transport after peripheral conditioning. *J. Neurosci.* 34, 5965–5970
73. Han, S.M. *et al.* (2016) Mitochondria localize to injured axons to support regeneration. *Neuron* 92, 1308–1323
74. Cartoni, R. *et al.* (2016) The mammalian-specific protein Armcx1 regulates mitochondrial transport during axon regeneration. *Neuron* 92, 1294–1307
75. Kaasik, A. (2016) Mitochondrial mobility and neuronal recovery. *N. Engl. J. Med.* 375, 1295–1296
76. Schon, E.A. and Przedborski, S. (2011) Mitochondria: the next (neurode)generation. *Neuron* 70, 1033–1053
77. Zheng, B. *et al.* (2010) PGC-1 α , a potential therapeutic target for early intervention in Parkinson's disease. *Sci. Transl. Med.* 2, 52ra73
78. Parihar, M.S. and Brewer, G.J. (2007) Mitochondrial failure in Alzheimer disease. *Am. J. Physiol. Cell Physiol.* 292, C8–C23
79. Kapogiannis, D. and Mattson, M.P. (2011) Disrupted energy metabolism and neuronal circuit dysfunction in cognitive impairment and Alzheimer's disease. *Lancet Neurol* 10, 187–198
80. Frederick, R.L. *et al.* (2004) Yeast Miro GTPase, Gem1p, regulates mitochondrial morphology via a novel pathway. *J. Cell Biol.* 167, 87–98
81. Smith, M.J. *et al.* (2006) Mapping the GRIF-1 binding domain of the kinesin, KIF5C, substantiates a role for GRIF-1 as an adaptor protein in the anterograde trafficking of cargoes. *J. Biol. Chem.* 281, 27216–27228
82. Guo, X. *et al.* (2005) The GTPase dMiro is required for axonal transport of mitochondria to *Drosophila* synapses. *Neuron* 47, 379–393
83. Brickley, K. and Stephenson, F.A. (2011) Trafficking kinesin protein (TRAK)-mediated transport of mitochondria in axons of hippocampal neurons. *J. Biol. Chem.* 286, 18079–18092
84. Pilling, A.D. *et al.* (2006) Kinesin-1 and Dynein are the primary motors for fast transport of mitochondria in *Drosophila* motor axons. *Mol. Biol. Cell* 17, 2057–2068
85. Russo, G.J. *et al.* (2009) *Drosophila* Miro is required for both anterograde and retrograde axonal mitochondrial transport. *J. Neurosci.* 29, 5443–5455

An Intrinsic Epigenetic Barrier for Functional Axon Regeneration

Yi-Lan Weng,^{1,2,12} Ran An,^{1,2,3,12} Jessica Cassin,^{1,4,12} Jessica Joseph,^{1,5} Ruifa Mi,² Chen Wang,⁶ Chun Zhong,^{1,2} Seung-Gi Jin,⁷ Gerd P. Pfeifer,⁷ Alfonso Bellacosa,⁸ Xinzhong Dong,⁹ Ahmet Hoke,² Zhigang He,⁶ Hongjun Song,^{1,2,4,5,9,10,13,14,*} and Guo-li Ming^{1,2,5,9,10,11,13}

¹Institute for Cell Engineering

²Department of Neurology

Johns Hopkins University School of Medicine, Baltimore, MD 21205, USA

³Department of Neurology, Huashan Hospital, State Key Laboratory of Medical Neurobiology, Fudan University, Shanghai 200040, China

⁴Pre-doctoral Human Genetics Training Program

⁵Graduate Program in Cellular and Molecular Medicine

Johns Hopkins University School of Medicine, Baltimore, MD 21205, USA

⁶F.M. Kirby Neurobiology Center and Department of Neurology, Boston Children's Hospital, 300 Longwood Avenue, Boston, MA 02115, USA

⁷Center for Epigenetics, Van Andel Research Institute, Grand Rapids, MI 49503, USA

⁸Cancer Epigenetics and Cancer Biology Programs, Fox Chase Cancer Center, Philadelphia, PA 19111, USA

⁹The Solomon H. Snyder Department of Neuroscience, Johns Hopkins University School of Medicine, Baltimore, MD 21205, USA

¹⁰Department of Neuroscience, Mahoney Institute for Neurosciences, Perelman School for Medicine, University of Pennsylvania, Philadelphia, PA 19104, USA

¹¹Department of Psychiatry and Behavioral Sciences, Johns Hopkins University School of Medicine, Baltimore, MD 21205, USA

¹²These authors contributed equally

¹³Senior author

¹⁴Lead Contact

*Correspondence: shongjun@mail.med.upenn.edu

<http://dx.doi.org/10.1016/j.neuron.2017.03.034>

SUMMARY

Mature neurons in the adult peripheral nervous system can effectively switch from a dormant state with little axonal growth to robust axon regeneration upon injury. The mechanisms by which injury unlocks mature neurons' intrinsic axonal growth competence are not well understood. Here, we show that peripheral sciatic nerve lesion in adult mice leads to elevated levels of Tet3 and 5-hydroxymethylcytosine in dorsal root ganglion (DRG) neurons. Functionally, Tet3 is required for robust axon regeneration of DRG neurons and behavioral recovery. Mechanistically, peripheral nerve injury induces DNA demethylation and upregulation of multiple regeneration-associated genes in a Tet3- and thymine DNA glycosylase-dependent fashion in DRG neurons. In addition, Pten deletion-induced axon regeneration of retinal ganglion neurons in the adult CNS is attenuated upon Tet1 knockdown. Together, our study suggests an epigenetic barrier that can be removed by active DNA demethylation to permit axon regeneration in the adult mammalian nervous system.

INTRODUCTION

Epigenetic DNA methylation marks are established during development and function as a basic mechanism to maintain stable

cellular states via the silencing of gene expression upon terminal differentiation (Jaenisch and Bird, 2003; Ma et al., 2010). Unlike developing neurons with robust growth capacity, mature mammalian neurons enter into a dormant growth state and maintain an intrinsic barrier to extensive axonal growth in the adult peripheral nervous system (PNS) and central nervous system (CNS) (Goldberg et al., 2002; He and Jin, 2016; Liu et al., 2011; Rossi et al., 2007; Zhou and Snider, 2006). Interestingly, peripheral axon injuries switch adult dorsal root ganglion (DRG) neurons to a pro-regenerative state via de novo gene transcription (Costigan et al., 2002; Moore and Goldberg, 2011; Smith and Skene, 1997). In the adult CNS, axon regeneration can also be induced, for example by deletion of PTEN in retinal ganglion neurons and corticospinal neurons (Liu et al., 2010; Park et al., 2008). Previous studies have mostly focused on cytoplasmic signaling and transcription factor-based mechanisms to promote intrinsic axon growth capacity, mostly with manipulations of one or two genes at a time (Hammarlund and Jin, 2014; Liu et al., 2011; Moore and Goldberg, 2011; Tedeschi and Bradke, 2017). Given that global and sustained gene induction is necessary for regenerative axonal growth to occur in injured neurons, epigenetic mechanisms could play a pivotal role in providing transcription factors access to developmentally silenced genomic loci and in orchestrating transcriptional reactivation of a large repertoire of regeneration-associated genes (RAGs) (Cho and Cavalli, 2014; Trakhtenberg and Goldberg, 2012; Weng et al., 2016; Wong and Zou, 2014). Indeed, histone modifications, which are essential for the maintenance of barriers between transcriptionally active euchromatin and transcriptionally silent heterochromatin, have previously been implicated in PNS axon regeneration (Cho et al., 2013; Finelli et al., 2013; Gaub et al., 2011; Puttagunta et al., 2014). Notably, regulation of histone acetylation

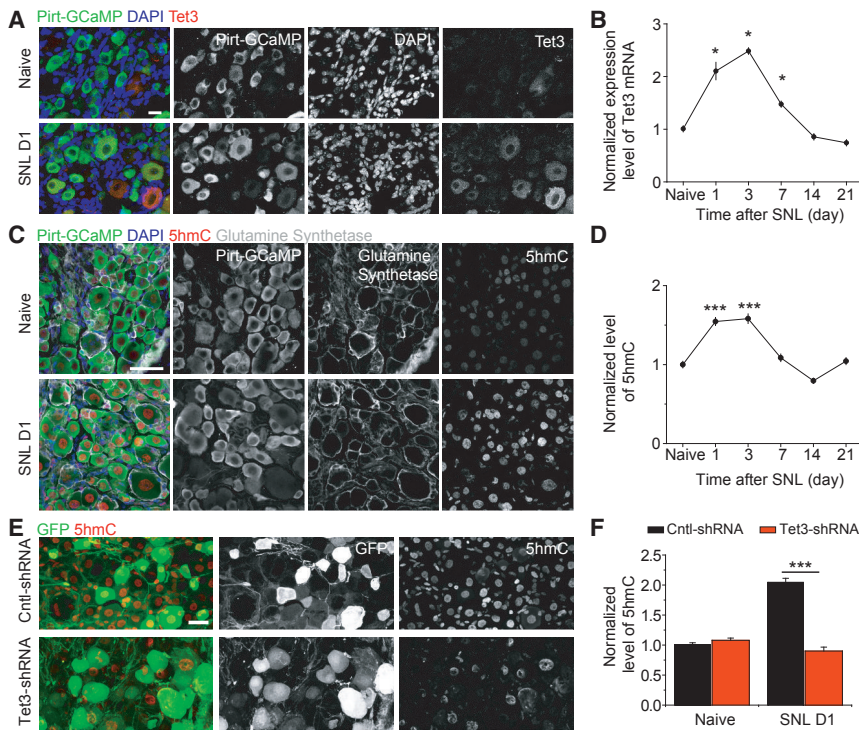


Figure 1. SNL Upregulates Tet3 and 5hmC Levels in Adult DRG Neurons In Vivo

(A) Sample confocal images of Tet3 in situ, GFP immunostaining, and DAPI of L4 DRGs in adult Pirt-GCaMP3 neuronal reporter mice under naive conditions and at 1 day upon sciatic nerve lesion (SNL). Scale bar, 20 μ m.

(B) Time course of Tet3 induction in axotomized DRGs by qPCR analysis. Values represent mean \pm SEM ($n = 3$ for each group; * $p < 0.05$; two-way ANOVA).

(C) Sample confocal image of immunostaining for GFP, 5hmC, glutamine synthetase, a marker for glia, and DAPI in DRGs of adult Pirt-GCaMP3 neuronal reporter mice under naive conditions and at SNL D1. Scale bar, 50 μ m.

(D) Quantification of 5hmC levels at different time points after SNL. The signal intensity in NeuN⁺ neuronal nuclei of naive L4 DRGs was set as 1.0 and 100–180 neuronal nuclei from each condition in three independent experiments were quantified. Values represent mean \pm SEM ($n = 3$ for each group; *** $p < 0.001$; two-way ANOVA).

(E and F) Immunohistochemical analysis of 5hmC levels in Ctrl and Tet3 KD DRG neurons under naive conditions and at SNL D1. Shown are sample images (E) (scale bar, 20 μ m) and quantification (F). Similar to (D). Values represent mean \pm SEM ($n = 3$ for each group; *** $p < 0.001$; two-way ANOVA).

via HDAC is essential for axon regeneration in the adult PNS but is not sufficient to activate the expression of several well-established RAGs, such as ATF3 and Smad1, therefore suggesting additional barriers (Finelli et al., 2013).

Originally thought to be largely irreversible in fully differentiated cells, DNA methylation in neurons has recently been shown to be dynamically regulated during development and in response to physiological stimuli (Gräff et al., 2011; Guo et al., 2011a; Lister et al., 2013; Shin et al., 2014b; Yao et al., 2016). The reconfiguration of the neuronal methylome results from the orchestration of both DNA methylation and demethylation processes (Guo et al., 2011a). Ten-eleven translocation methylcytosine dioxygenases (Tets) have been found to iteratively oxidize 5-methylcytosine (5mC) to 5-hydroxymethylcytosine (5hmC), 5-formylcytosine (5fC) and 5-carboxycytosine (5caC), allowing cell-cycle-independent removal of DNA methylation (He et al., 2011; Ito et al., 2011; Tahiliani et al., 2009). Subsequent studies have shown that Tet-initiated DNA oxidation is followed by the thymine DNA glycosylase (TDG)-mediated base excision pathway to complete the demethylation process (Bellacosa and Drohat, 2015; Guo et al., 2011c; He et al., 2011; Ito et al., 2011). Tet family members have been shown to be important for many biological processes including activity-regulated neuronal gene expression, synaptic transmission, and scaling, as well as memory formation and extinction (Feng et al., 2015; Kaas et al., 2013; Rudenko et al., 2013; Yu et al., 2015). One very recent study showed increased 5hmC levels upon axotomy of adult DRG neurons (Loh et al., 2017). However, little is known about the function of DNA methylation in axon regeneration (Iskandar et al., 2010; Puttagunta et al., 2014). The identification of active DNA demethylation machinery provides an entry point to test

the hypothesis that DNA demethylation serves as a fundamental mechanism to globally reprogram the cellular state of mature mammalian neurons to permit axonal regeneration.

RESULTS

Peripheral Axon Injury of Adult DRG Neurons Induces Elevation of 5hmC Levels

To screen for epigenetic factors that exhibit responsiveness to axonal injury, we first performed qPCR analysis of known DNA demethylation mediators, including Tet1–3, Apobec1–3, Gadd45a, Gadd45b, Gadd45g, and Tdg (Guo et al., 2011b), in adult DRGs of naive mice and upon sciatic nerve lesion (SNL). Consistent with a previous report (Befort et al., 2003), SNL robustly elevated the expression of Gadd45a, a regulator of active DNA demethylation (Ma et al., 2009) on day 1 (D1) (Figure S1A). Interestingly, Tet3 expression, but not Tet1 and Tet2, was also induced (Figure S1A). In situ analysis showed little Tet1 or Tet2 expression in the adult DRG (Figure S1B). Analysis using a mouse reporter line, which expresses GCaMP3 from the endogenous *Pirt* locus and labels 95% of neurons (but not glia) in the adult DRG (Kim et al., 2016), showed Tet3 induction by SNL to be neuron-specific (Figure 1A). We confirmed Tet3 upregulation at the protein level by western blot (Figure S1C). Time course analysis by qPCR showed that Tet3 expression reached its peak at SNL D3 and returned to basal levels by D14 (Figure 1C). Pharmacological experiments revealed that Tet3 induction in the DRG was attenuated by the Ca²⁺ chelator BAPTA-AM and KN93, an inhibitor of CaMKII, but not KN92, an inactive analog (Figure S1D). It is known that Ca²⁺ is propagated from injured axons back to DRG neuronal nuclei (Cho et al., 2013; Rishal

and Fainzilber, 2014), therefore our results suggest a model wherein Tet3 expression is induced by retrograde Ca^{2+} signaling from injured axons.

Consistent with a role of Tet proteins in oxidizing 5mC to its derivatives, 5hmC levels were increased in Pirt-GCaMP3⁺ DRG neurons at SNL D1 (Figure 1C). Quantitative dot-blot analysis of semi-purified DRG neurons confirmed the global increase of 5hmC levels, suggesting large-scale epigenetic changes after SNL (Figure S1E). Time course analysis showed that 5hmC levels gradually increased until SNL D3 and returned to basal levels by D21 (Figures 1D and S1F).

To investigate the molecular mechanism underlying injury-induced elevation of 5hmC levels, we infected DRGs via targeted intrathecal AAV2/9-GFP injection, which labeled over 70% of all neurons in L4/5 DRGs and their sciatic nerve axons (Figures S1G and S1H). Using previously characterized small hairpin RNA (shRNA) (Yu et al., 2015), we found that induction of 5hmC levels in GFP⁺ DRG neurons at SNL D1 was abolished upon Tet3 knockdown (KD) (Figures 1E and 1F), suggesting that Tet3 is responsible for the increased 5hmC levels upon SNL.

Tet3 Is Required for Functional Axon Regeneration of Adult DRG Neurons

To examine the potential functional role of Tet3 in injury-induced axonal regeneration, we first used an in vitro neurite outgrowth assay with primary neurons from adult mouse DRGs. Cultures were infected with AAV2/9 to co-express GFP and shRNA against Tet1, Tet2, or Tet3, followed by re-plating to mimic axotomy (Figures S2A and S2B). We found that Tet3 KD, but not Tet1 or Tet2 KD, reduced the number and the total neurite length of neurite-bearing neurons (Figures S2C–S2E).

We next assessed the in vivo role of Tet3 in functional axon regeneration of adult DRG neurons after SNL via intrathecal AAV2/9 injection-mediated expression of GFP and shRNA (Figures S1G and S1H). Regenerating sensory axons were identified by SCG10 immunostaining (Shin et al., 2014c) (Figure 2A). We found that the extension of SCG10⁺ axons was significantly decreased upon Tet3 KD compared to control animals at SNL D3 (Figure 2B). To validate these results, we directly examined regeneration of GFP⁺ axons at SNL D7 when pre-existing lesioned axons were fully degenerated (Di Maio et al., 2011; Shin et al., 2012). We quantified the number of regenerating GFP⁺ axons in coronal sections at incremental distances from the lesion site (Figure S2F). We did not detect any differences in axonal morphology or numbers upon Tet3 KD in the absence of SNL (Figures S2G and S2H). In contrast, there was a significant reduction of axonal growth in Tet3 KD animals at SNL D7 compared to animals injected with control shRNA (Ctrl; Figures 2C and 2D). Notably, over 45% of Tet3 KD neurons failed to extend axons 1 mm or more beyond the lesion site compared to only 17% of Ctrl neurons (Figure 2E). Conversely, over 62% of Ctrl neurons extended axons over 6 mm from the lesion site compared to only 33% of Tet3 KD neurons (Figure 2E). There were few cleaved caspase3⁺ neurons in the DRG under all conditions (Figure S2I), ruling out the potential contribution of cell death to observed deficits in axon regeneration.

Regenerating axons of sciatic nerves extend to the epidermis and start to re-innervate the skin of the hind paw ~2–3 weeks af-

ter injury. Analysis of skin biopsies showed no GFP⁺ sensory axon innervation to the epidermis of the hind paw at SNL D7, indicating effective degeneration of preexisting mature axons of both Ctrl and Tet3 KD neurons (Figures S2J and S2K). At SNL D21, innervation to all three epidermal zones by GFP⁺ regenerating axons of Tet3 KD neurons was significantly reduced, but no difference was observed in naive neurons with or without Tet3 KD (Figures 2F and 2G). These results suggest that Tet3 is required for regenerative axonal growth and re-innervation of target areas of the sciatic nerve.

To assess the functional outcome, we performed behavioral tests to quantify the latency of heat-evoked hind paw withdrawal (Wright et al., 2014). Both Ctrl and Tet3 KD animals exhibited similar response latencies to radiant thermal stimulus at SNL D1 and D7 (Figure 2H). Starting from SNL D14, the withdrawal latency gradually recovered in the Ctrl group, but only minimally in Tet3 KD animals (Figure 2H). Together, these results establish that injury-induced Tet3 upregulation plays an essential role in functional sensory axon regeneration of adult DRG neurons.

Tet3 Regulates Expression of Regeneration-Associated Genes

To investigate the molecular mechanism underlying Tet3-dependent axon regeneration, we assessed whether Tet3 regulates the expression of known RAGs. qPCR analysis of DRGs at SNL D1 showed that induction of a subset of RAGs was significantly attenuated by Tet3 KD, including ATF3, Smad1, STAT3, and c-Myc (Costigan et al., 2002; Moore and Goldberg, 2011; Smith and Skene, 1997) (Figure 3A). Interestingly, Tet3 KD also led to decreased expression of some RAGs in naive DRG neurons, including Smad1 and STAT3 (Figure 3A). Thus, Tet3 regulates expression of multiple RAGs both under basal conditions and upon injury.

ATF3 is one of the most robustly induced genes by SNL and has been shown to enhance peripheral nerve regeneration by increasing the intrinsic growth competence of adult DRG neurons (Fagoie et al., 2015; Seiffers et al., 2007). We therefore focused on ATF3 for in-depth analyses. Consistent with a previous finding (Seiffers et al., 2007), ATF3 protein was barely detectable in naive DRGs, but was robustly upregulated at SNL D1 in Pirt-GCaMP3⁺ DRG neurons and not in glutamine synthetase-expressing glial cells (Figures 3B). Importantly, this induction was greatly attenuated by Tet3 KD (Figures 3C and 3D). The impairment was not due to a delay of ATF3 induction, as the defect persisted through SNL D7 (Figure 3D). Quantitative immunohistological analysis revealed similar levels of phospho-c-Jun in Ctrl and Tet3 KD neurons at SNL D7 (Figures S3A and S3B), suggesting an intact retrograde axonal injury signaling that triggers accumulation of nuclear phospho-c-Jun via the JNK pathway (Rishal and Fainzilber, 2014).

Tet3 Function Is Required for DNA Demethylation of RAGs

To understand how Tet3 regulates the expression of RAGs, we first asked whether SNL induces demethylation of RAGs in adult DRG neurons in vivo. Because the whole DRG contains many times more glial cells than neurons (Delree et al., 1989; Thakur et al., 2014), we enriched neuronal nuclei using a

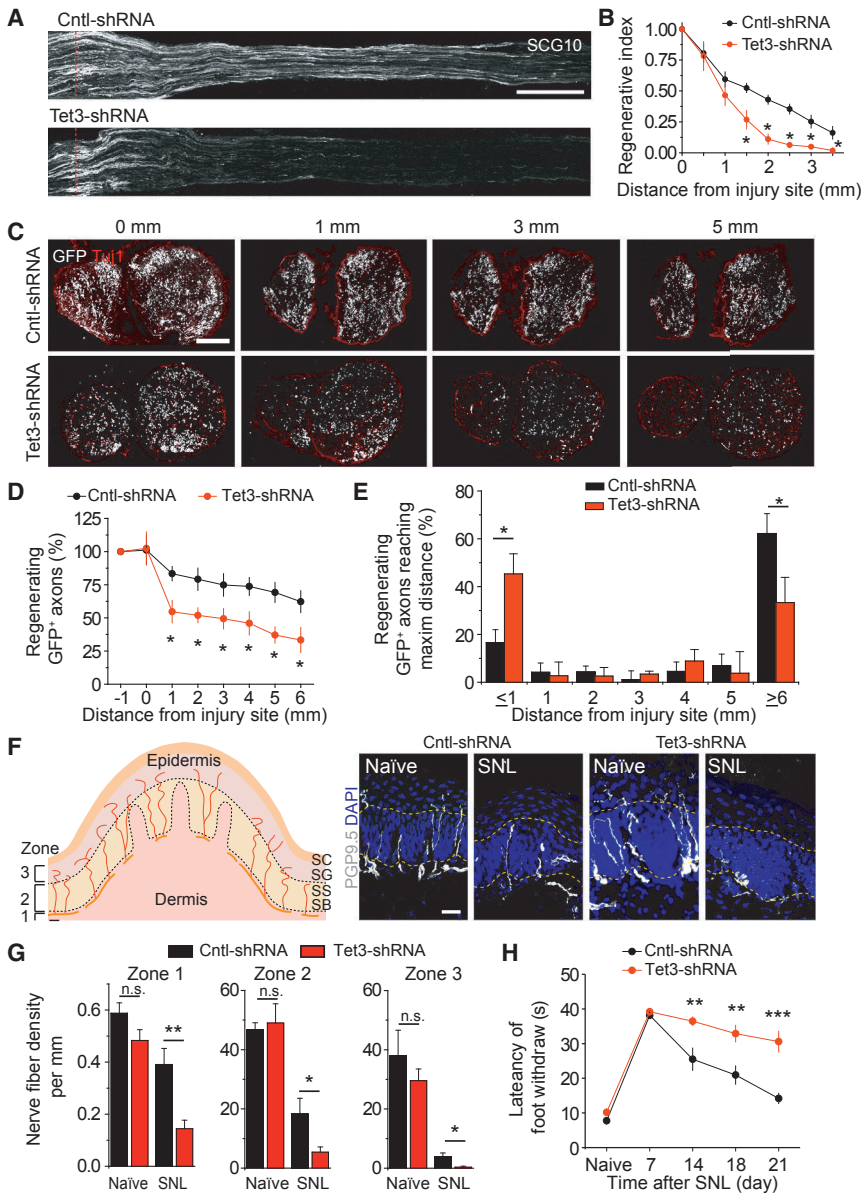


Figure 2. Tet3 Is Required for Functional Axon Regeneration of Adult DRG Neurons upon SNL In Vivo

(A and B) Analysis of regeneration of sensory axons by SCG10 immunostaining at SNL D3. Shown are sample images of regenerating sensory axons identified by SCG10 (A) (scale bar, 500 μ m) and quantification (B). SCG10 immunofluorescence intensity was measured at different distal distances and normalized to that at the lesion site as the regenerative index. Values represent mean \pm SEM (n = 5 for each group; *p < 0.05; two-way ANOVA). (C–E) Analysis of regenerating axons visualized by GFP labeling at SNL D7. Cross-sections of sciatic nerves at –1 to 6 mm distal to the lesion site from AAV-Ctrl and AAV-Tet3 KD treated animals were analyzed. Shown are sample images of GFP and Tuj1 (C) (scale bar, 300 μ m) and quantification (D and E). Values represent mean \pm SEM (n = 3–4 for each group; *p < 0.05; two-way ANOVA).

(F and G) Assay of re-innervation of epidermal area of the hindpaw by regenerating sensory axons. Shown in (F) are the schematic diagram and sample images of cross sections of hindpaw glabrous skin of Ctrl and Tet3 KD mice immunostained with the pan neuronal marker PGP9.5. The dotted line indicates the border between dermis and epidermis. Scale bar, 20 μ m. Also shown are quantifications of the number of intraepidermal nerve fibers in a 1 mm segment of different epidermal areas (G). Values represent mean \pm SEM (n = 4 for each group; **p < 0.01; *p < 0.05; n.s. p > 0.1; two-way ANOVA).

(H) Assessment of thermal sensory recovery after SNL in AAV-Ctrl and AAV-Tet3 KD treated animals. Values represent mean \pm SEM (n = 9–12 animals per group; **p < 0.01; ***p < 0.001; two-way ANOVA).

sucrose cushion method (Kozlenkov et al., 2014). We initially used methylation-sensitive restriction enzyme cutting coupled with qPCR to screen CC^mGG sites and quantify their methylation levels (Guo et al., 2011a). While the *ATF3* promoter was not methylated, multiple CC^mGG sites in the gene body and distal enhancer regions (DE1–DE4) were hypermethylated and exhibited a significant decrease in methylation levels upon SNL at D1 (Figure S3C). One recent study showed that injuries upregulate c-Myc expression in DRGs but not in retinal ganglion cells (RGCs), and forced c-Myc expression promotes axon regeneration of RGCs after optic nerve injury (Belin et al., 2015). Interestingly, significant DNA demethylation was also observed at putative c-Myc distal enhancer sites (Figure S3D). To ensure that DNA demethylation indeed occurred in neurons, we performed bisulfite-sequencing from NeuN⁺ nuclei purified by fluorescence-activated cell sorting (FACS). We found a sig-

nificant decrease in methylation levels at multiple CpG sites within DE1–DE2 regions of *ATF3* at SNL D1 (Figure S3E). In contrast, we did not observe any demethylation within the *GAP43* loci from the same neuronal samples (Figure S3F). Therefore, injury-induced DNA demethylation in adult DRG neurons appears to be region-specific.

To determine the specific role of Tet3 in injury-induced DNA demethylation, we engineered AAV to co-express H2B-GFP and shRNA in adult DRGs in vivo and FACS-purified eight groups of NeuN⁺ nuclei: GFP[–] uninfected neurons or GFP⁺ neurons expressing either Ctrl-shRNA or Tet3-shRNA, under either naive or SNL D1 conditions (Figure 3E). Due to the limited material for bisulfite-sequencing analysis, we focused on the *ATF3* DE1 region. Quantitative analysis from three independent experiments showed that SNL induced significant DNA demethylation in both GFP⁺ and GFP[–] neurons following injection of AAV expressing Ctrl-shRNA and GFP (Figures 3E and 3F). In contrast, upon injection of AAV expressing Tet3-shRNA and GFP, GFP⁺ neurons showed minimal changes in methylation levels, whereas GFP[–] neurons still exhibited SNL-induced demethylation at these CpG sites from the

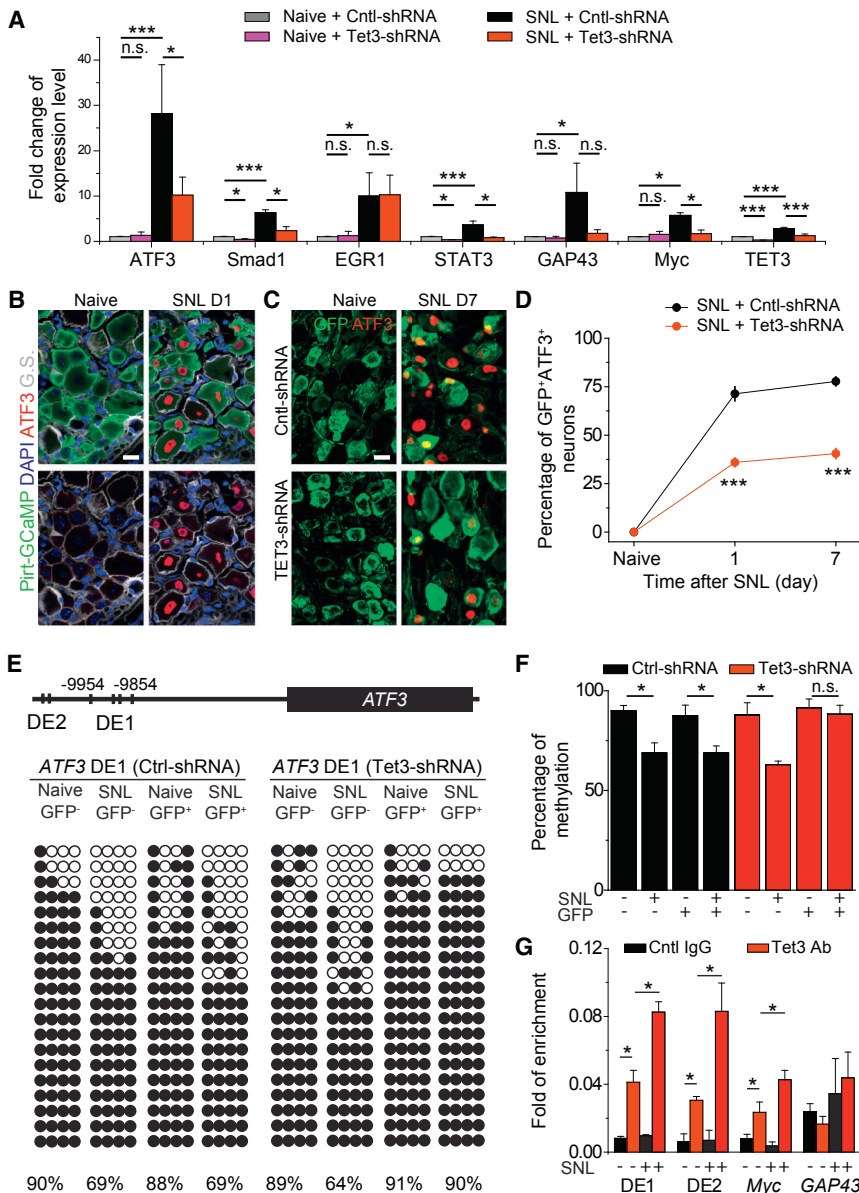


Figure 3. Tet3 Regulates the Expression of Multiple Injury-Induced RAGs and Mediates Active DNA Demethylation of *ATF3* Genomic Regions

(A) Analysis of expression of some known RAGs. The mRNA expression was assessed by qPCR at SNL D1 and compared to the Ctrl naive group. Values represent mean \pm SEM ($n = 3$ for each group; *** $p < 0.001$; * $p < 0.05$; n.s. $p > 0.1$; two-way ANOVA).

(B–D) Assessment of ATF3 induction in Tet3 KD DRGs at SNL D1 and D7. Shown are sample images of immunostaining for GFP, ATF3, and glutamine synthetase (G.S.) in Pirt-GCaMP3 neuronal reporter mice (B) and for ATF3 and GFP in normal mice (C) and quantifications (D). Scale bars, 20 μ m. Values represent mean \pm SEM ($n = 4$ for each group; *** $p < 0.001$; two-way ANOVA).

(E and F) Methylation status of the *ATF3* distal enhancer region 1 (DE1) in Ctrl and Tet3 KD DRG neurons. AAV transduced (GFP⁺) and non-transduced (GFP⁻) NeuN⁺ neurons from L4 and L5 DRGs at SNL D1 were isolated by FACS and subjected to bisulfite sequencing analysis. (E) Sample reads of individual alleles. Open circles indicate unmethylated cytosines and closed circles indicate methylated cytosines. (F) Summary from three independent biological replicates with at least 20 alleles each. Values represent mean \pm SEM ($n = 3$ for each group; * $p < 0.05$; two-way ANOVA).

(G) ChIP-qPCR analysis of Tet3 binding to different genomic regions that were also examined for DNA methylation levels (as shown in Figure S3C). Values represent mean \pm SEM ($n = 3$ for each group; * $p < 0.05$; two-way ANOVA).

same DRGs (Figures 3E and 3F). Furthermore, chromatin immunoprecipitation (ChIP) analysis using anti-Tet3 antibodies (Jin et al., 2016) showed enriched Tet3 binding at the DE1 and DE2 regions of the *ATF3* gene, which was further enhanced upon SNL (Figure 3G). We also observed similar binding properties of Tet3 to the *c-Myc* locus but not to the *GAP43* locus (Figure 3G). Together, these results suggest a model wherein peripheral nerve injury leads to enhanced recruitment of Tet3 to methylated CpG sites of enhancers of RAGs followed by demethylation of these CpG sites, resulting in upregulated gene expression.

TDG Coordinates with Tet3 to Regulate RAG Expression and Axon Regeneration

Tet family proteins have been shown to exert functions independent of DNA demethylation activity (Chen et al., 2013; Williams et al., 2011). In addition, 5hmC has been proposed as a signaling

mechanism itself via its binding partners (Iurlaro et al., 2013; Mellén et al., 2012; Spruijt et al., 2013). Transient elevation of 5hmC upon injury is consistent with its role as an intermediate of active DNA demethylation (Figure 1D). We further examined the role of TDG, a critical downstream mediator of active DNA demethylation (Bellacosa and Drohat, 2015; Wu and Zhang, 2014; Cortellino et al., 2011) (Figure S4A), in SNL-induced intrinsic axon regeneration competence. Upon TDG KD (Figure S4B), axonal regeneration was significantly reduced at SNL D7 (Figures 4A and 4B). We confirmed our results via AAV-mediated co-expression of GFP and Cre in DRGs of adult *Tdg*^{f/f} mice (Figures 4C and 4D).

To investigate further whether Tet3 and TDG share the same molecular mechanisms in regulating axon regeneration, we evaluated the expression of known RAGs in TDG KD samples. SNL-induced ATF3 expression was attenuated in TDG KD neurons at both SNL D1 and D7, similar to the effect of Tet3 KD (Figures 4E and 4F). qPCR analysis of DRGs at SNL D1 showed that TDG KD attenuated the induction of a similar subset of RAGs as Tet3 KD (Figure 4G). Tet proteins generate 5hmC, 5fC, and 5caC through iterative oxidation of 5mC, whereas TDG excises 5fC and 5caC to initiate base-excision repair to complete the DNA

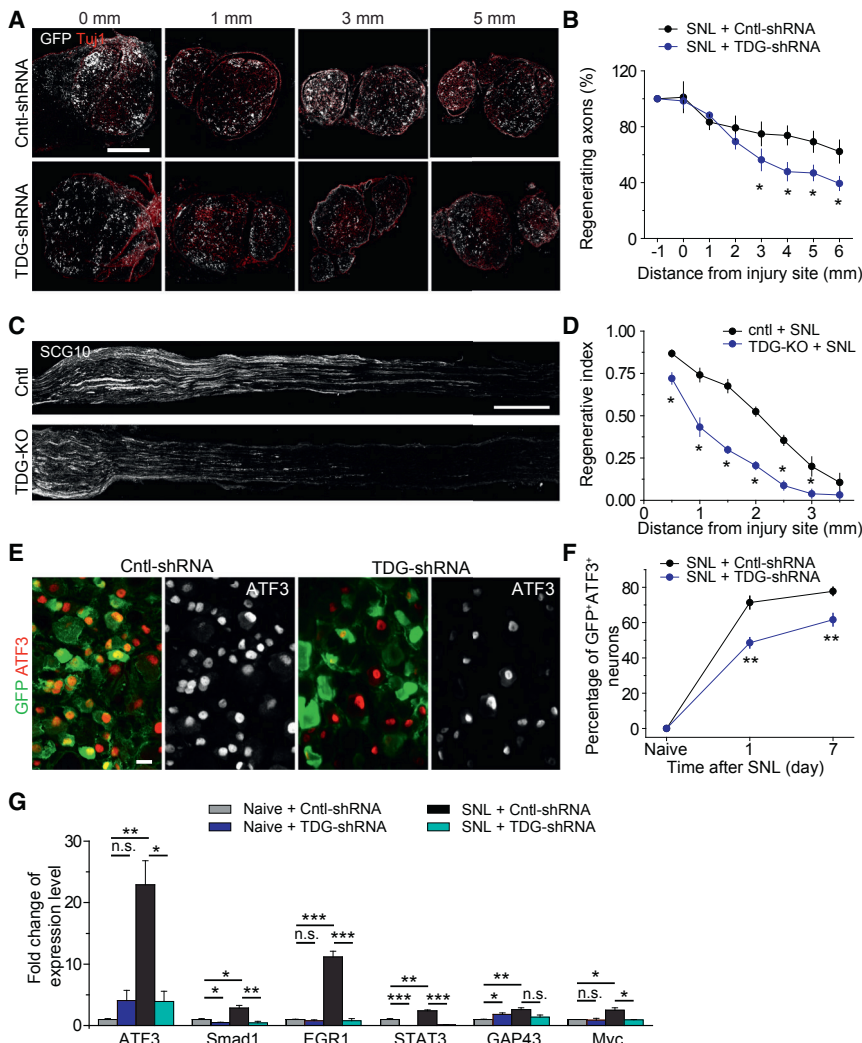


Figure 4. TDG Is Required for SNL-Induced Axon Regeneration and ATF3 Expression in Adult DRG Neurons

(A–D) In vivo axon regeneration assay. Similar to Figures 2C and 2D, shown are sample images (A) (scale bar, 300 μ m) and quantification (B) at SNL D7 with expression of control-shRNA or TDG-shRNA. The same data from Ctrl-shRNA in Figure 2C is replotted for comparison. Similar to Figures 2A and 2B, also shown are sample images of regenerating sensory axons identified by SCG10 (C) (scale bar, 500 μ m) in *TDG^{fl/fl}* mice expressing GFP (Ctrl), or GFP and Cre (TDG-KO) and quantifications (D). Values represent mean \pm SEM (n = 4 for each group; *p < 0.05; two-way ANOVA).

(E and F) Assessment of ATF3 induction in TDG KD DRGs. Similar to Figure 3B, shown are sample images (E) (scale bar, 20 μ m) and quantifications (F). Values represent mean \pm SEM (n = 4 for each group; **p < 0.01; two-way ANOVA).

(G) TDG-dependent expression of multiple SNL-induced RAGs. The mRNA expression was assessed by qPCR at SNL D1 and compared to the Ctrl naive group. Values represent mean \pm SEM (n = 3 for each group; ***p < 0.001; **p < 0.01; *p < 0.05; n.s. p > 0.1; two-way ANOVA).

DISCUSSION

In addition to the extrinsic barrier imposed by the inhibitory environment (He and Koprivica, 2004; Silver et al., 2014), poor intrinsic growth capacity of mature CNS neurons is a major contributing factor to regeneration failure (Liu et al., 2011). Therefore, defining how injured mature PNS neurons switch to a pro-regenerative state may not only reveal the basic biology

of mature mammalian neurons, but may also suggest novel therapeutic strategies for promoting axon regeneration within both the PNS and CNS. Our results support a model wherein peripheral nerve injury, via retrograde Ca^{2+} signaling, upregulates Tet3 expression and the active DNA demethylation pathway, which in turn removes an intrinsic barrier to the expression of an ensemble of RAGs and to functional axon regeneration of mature PNS neurons in vivo (Figure S5). Our initial study also suggests a similar intrinsic epigenetic barrier of DNA methylation for induced axon regeneration in the adult CNS.

Large-scale and long-lasting changes in the expression of RAGs after injury have been associated with the regenerative capacity of mature PNS neurons. Epigenetic mechanisms, such as DNA demethylation, are well-suited to orchestrate transcriptional re-activation of a large repertoire of RAGs over an extended period of time. Many RAGs, including ATF3 and c-Myc, exhibit developmentally regulated expression patterns and diminished expression in mature neurons (Figure 3A), which might be maintained via DNA methylation. Indeed, we found that at putative enhancer regions of both *ATF3* and *c-Myc*, multiple loci are hypermethylated in mature DRG neurons under basal

demethylation process (Figure S4A). While Tet3 KD blocked SNL-induced 5hmC level increases (Figure 1F), TDG KD led to a further increase of 5hmC levels at SNL D7 (Figures S4C and S4D). These results suggest that the complete DNA demethylation process, not SNL-induced 5hmC increase alone, primarily mediates the induction of RAGs and unlocks the axonal growth capacity of mature DRG neurons.

Tet1 Is Involved in PTEN Deletion-Induced Retinal Ganglion Neuron Axon Regeneration

To assess whether active DNA demethylation is also required for axon regeneration in the adult CNS, we employed the model of PTEN deletion-induced axon regeneration of RGCs in adult mice (Park et al., 2008). We co-expressed Cre and shRNA for Tet1, Tet2, or Tet3, in adult RGCs, followed by axotomy and axonal labeling (Park et al., 2008). Interestingly, expression of shRNA-Tet1, but not shRNA-Tet2 or shRNA-Tet3, attenuated axonal regeneration of RGCs in comparison to the shRNA-control (Figure 5). Therefore, Tet signaling is also required for induced axon regeneration in the adult CNS with the specific involvement of Tet1.

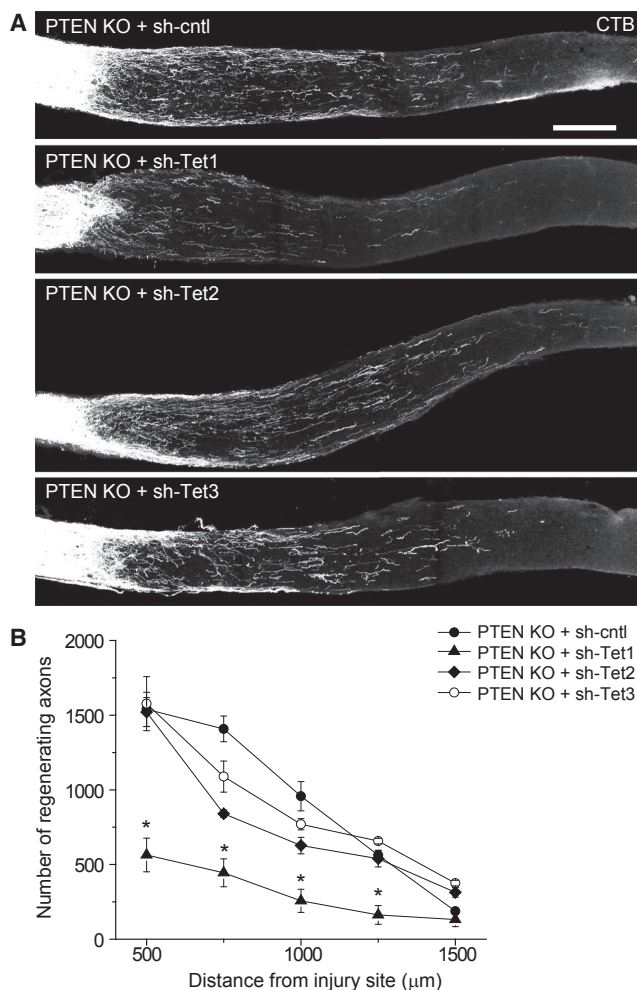


Figure 5. Tet1 Is Required for Pten Deletion-Induced Axon Regeneration of Retinal Ganglion Neurons in the Adult Mouse

Adult *Pten*^{fl/fl} mice were injected with AAVs to co-express GFP, Cre, and control shRNA, or shRNA against Tet1, Tet2, or Tet3 in the eye, followed by optic nerve crush 2 weeks later. RGC axons were anterogradely labeled by cholera toxin β subunit 12 days after injury. Shown are sample images of labeled axons (A) (scale bar, 20 μ m) and quantifications (B). Values represent mean \pm SEM ($n = 3$ for each group; * $p < 0.05$; two-way ANOVA).

conditions and associated with very low expression levels. Upon SNL injury, there is an enhanced binding of Tet3 to these regions, accompanied by demethylation and induced gene expression. How Tet3 is targeted to these specific regions and how its binding is enhanced upon injury remain to be determined. One recent study published during the revision of this paper profiled 5hmC from the whole adult mouse DRGs and found large-scale changes, including regions associated with RAGs (Loh et al., 2017). Interestingly, peripheral injury triggers differential 5hmC changes that are associated with distinct signaling pathways compared to injury of the central branch of DRG neurons, which does not result in axon regeneration. Because of tremendous cellular heterogeneity in the adult mouse nervous system, genome-wide methylation and hydroxymethylation

analysis of a particular neuronal type of limited quantity in vivo remains a technical challenge (Shin et al., 2014a). Here, we purified DRG neurons from adult mice and focused on a few candidate genes as a proof of principle. Future technological developments may enable analysis of DNA methylomes in very small populations of defined cell types and contribute to a more comprehensive understanding of 5hmC/5mC dynamics in the regulation of RAG expression in neurons.

Tet function and DNA demethylation have been shown to promote other cellular reprogramming processes, such as reprogramming of somatic cells into pluripotency, although expression of Tet proteins alone is not sufficient (Bagci and Fisher, 2013). Here, we show that DNA demethylation removes one of the major barriers for axon regeneration, but it is likely not sufficient to switch mature neurons from a dormant state to an active axonal growth state. Instead, DNA demethylation may coordinate with other epigenetic mechanisms (Trakhtenberg and Goldberg, 2012), such as histone acetylation, which has been shown to promote PNS axon regeneration (Cho et al., 2013; Finelli et al., 2013; Gaub et al., 2011; Puttagunta et al., 2014). Interestingly, enhancing histone acetylation using HDAC inhibitors is not sufficient to turn on the expression of ATF3 and Smad1 in adult DRGs (Finelli et al., 2013), two genes that we found to be regulated by Tet3 and TDG (Figures 3A and 4G). Future studies will address how different epigenetic mechanisms coordinate to reactivate the robust axonal growth state. Notably, Tet proteins are known to interact with multiple chromatin regulators to modulate gene expression (Chen et al., 2013; Deplus et al., 2013; Perera et al., 2015).

In summary, our study identifies DNA methylation as an intrinsic barrier for functional regeneration of mature mammalian neurons. Different from recent studies of cell identity reprogramming (Arlotta and Berninger, 2014), our finding of a critical role of an epigenetic DNA modification mechanism in reprogramming mature neurons to an axon regeneration-competent state, without altering cell identity, extends the classic concept of reprogramming and may have broad implications for regenerative medicine.

STAR★METHODS

Detailed methods are provided in the online version of this paper and include the following:

- KEY RESOURCES TABLE
- CONTACT FOR REAGENT AND RESOURCE SHARING
- EXPERIMENTAL MODEL AND SUBJECT DETAILS
 - Animals
- METHOD DETAILS
 - AAV constructs
 - DRG cultures and neurite outgrowth assay
 - Animal surgery
 - Behavioral analysis
 - In situ hybridization
 - Western blot analysis
 - Gene expression and methylation analyses
 - In vivo DRG axon regeneration assay
 - Immunohistology

- Neuronal nuclei isolation
- 5hmC dot blot analysis
- Bisulfite sequencing
- ChIP analysis
- Optic nerve injury and quantification
- QUANTIFICATION AND STATISTICAL ANALYSIS
- DATA AND SOFTWARE AVAILABILITY

SUPPLEMENTAL INFORMATION

Supplemental Information includes five figures and one table and can be found with this article online at <http://dx.doi.org/10.1016/j.neuron.2017.03.034>.

AUTHOR CONTRIBUTIONS

Y.-L.W. led the project and was involved in all aspects of the study. R.A. performed surgical procedures and data quantification for DRG studies. J.C. led bisulfite sequencing and molecular analyses. J.J. performed western blot analysis and along with C.Z. contributed to other data collection. C.W. and Z.H. performed RGC experiments. R.M. and A.H. contributed to behavioral experimental design and testing. S.-G.J. and G.P.P. provided Tet3 antibodies for ChIP analysis. A.B. contributed Tdg^{fl/fl} mice. X.D. contributed Pirt-GCaMP3 reporter mice. Y.L.W., H.S., and G.M. designed the project, analyzed the data, and wrote the paper. All authors helped prepare the manuscript.

ACKNOWLEDGMENTS

We thank Dr. Hongyan Zou, members of Ming and Song laboratories, and The Dr. Miriam and Sheldon G. Adelson Medical Research Foundation (AMRF) investigators for discussion, and Y. Cai and L. Liu for technical support. This work was supported by grants from AMRF (to G.M., Z.H., and A.H.) and from NIH (P01NS097206 to H.S., R35NS097370 to G.M., R01CA160965 to G.P.P., R01CA78412 to A.B., and P30CA06927 to Fox Chase Cancer Center).

Received: September 24, 2016

Revised: February 5, 2017

Accepted: March 23, 2017

Published: April 19, 2017

REFERENCES

- Arlotta, P., and Berninger, B. (2014). Brains in metamorphosis: reprogramming cell identity within the central nervous system. *Curr. Opin. Neurobiol.* *27*, 208–214.
- Bagci, H., and Fisher, A.G. (2013). DNA demethylation in pluripotency and reprogramming: the role of tet proteins and cell division. *Cell Stem Cell* *13*, 265–269.
- Befort, K., Karchewski, L., Lanoue, C., and Woolf, C.J. (2003). Selective up-regulation of the growth arrest DNA damage-inducible gene Gadd45 alpha in sensory and motor neurons after peripheral nerve injury. *Eur. J. Neurosci.* *18*, 911–922.
- Belin, S., Nawabi, H., Wang, C., Tang, S., Latremoliere, A., Warren, P., Schorle, H., Uncu, C., Woolf, C.J., He, Z., and Steen, J.A. (2015). Injury-induced decline of intrinsic regenerative ability revealed by quantitative proteomics. *Neuron* *86*, 1000–1014.
- Bellacosa, A., and Drohat, A.C. (2015). Role of base excision repair in maintaining the genetic and epigenetic integrity of CpG sites. *DNA Repair (Amst.)* *32*, 33–42.
- Bonaguidi, M.A., Wheeler, M.A., Shapiro, J.S., Stadel, R.P., Sun, G.J., Ming, G.L., and Song, H. (2011). In vivo clonal analysis reveals self-renewing and multipotent adult neural stem cell characteristics. *Cell* *145*, 1142–1155.
- Chen, Q., Chen, Y., Bian, C., Fujiki, R., and Yu, X. (2013). TET2 promotes histone O-GlcNAcylation during gene transcription. *Nature* *493*, 561–564.
- Cho, Y., and Cavalli, V. (2014). HDAC signaling in neuronal development and axon regeneration. *Curr. Opin. Neurobiol.* *27*, 118–126.
- Cho, Y., Sloutsky, R., Naegle, K.M., and Cavalli, V. (2013). Injury-induced HDAC5 nuclear export is essential for axon regeneration. *Cell* *155*, 894–908.
- Cortellino, S., Xu, J., Sannai, M., Moore, R., Caretti, E., Cigliano, A., Le Coz, M., Devarajan, K., Wessels, A., Soprano, D., et al. (2011). Thymine DNA glycosylase is essential for active DNA demethylation by linked deamination-base excision repair. *Cell* *146*, 67–79.
- Costigan, M., Befort, K., Karchewski, L., Griffin, R.S., D'Urso, D., Allchorne, A., Sitariski, J., Mannion, J.W., Pratt, R.E., and Woolf, C.J. (2002). Replicate high-density rat genome oligonucleotide microarrays reveal hundreds of regulated genes in the dorsal root ganglion after peripheral nerve injury. *BMC Neurosci.* *3*, 16.
- Delree, P., LePrince, P., Schoenen, J., and Moonen, G. (1989). Purification and culture of adult rat dorsal root ganglia neurons. *J. Neurosci. Res.* *23*, 198–206.
- Deplus, R., Delatte, B., Schwinn, M.K., Defrance, M., Méndez, J., Murphy, N., Dawson, M.A., Volkmar, M., Putmans, P., Calonne, E., et al. (2013). TET2 and TET3 regulate GlcNAcylation and H3K4 methylation through OGT and SET1/COMPASS. *EMBO J.* *32*, 645–655.
- Di Maio, A., Skuba, A., Himes, B.T., Bhagat, S.L., Hyun, J.K., Tessler, A., Bishop, D., and Son, Y.J. (2011). In vivo imaging of dorsal root regeneration: rapid immobilization and presynaptic differentiation at the CNS/PNS border. *J. Neurosci.* *31*, 4569–4582.
- Duan, X., Chang, J.H., Ge, S., Faulkner, R.L., Kim, J.Y., Kitabatake, Y., Liu, X.B., Yang, C.H., Jordan, J.D., Ma, D.K., et al. (2007). Disrupted-In-Schizophrenia 1 regulates integration of newly generated neurons in the adult brain. *Cell* *130*, 1146–1158.
- Fagoie, N.D., Attwell, C.L., Kouwenhoven, D., Verhaagen, J., and Mason, M.R. (2015). Overexpression of ATF3 or the combination of ATF3, c-Jun, STAT3 and Smad1 promotes regeneration of the central axon branch of sensory neurons but without synergistic effects. *Hum. Mol. Genet.* *24*, 6788–6800.
- Feng, J., Shao, N., Szulwach, K.E., Vialou, V., Huynh, J., Zhong, C., Le, T., Ferguson, D., Cahill, M.E., Li, Y., et al. (2015). Role of Tet1 and 5-hydroxymethylcytosine in cocaine action. *Nat. Neurosci.* *18*, 536–544.
- Finelli, M.J., Wong, J.K., and Zou, H. (2013). Epigenetic regulation of sensory axon regeneration after spinal cord injury. *J. Neurosci.* *33*, 19664–19676.
- Gaub, P., Joshi, Y., Wuttke, A., Naumann, U., Schnichels, S., Heiduschka, P., and Di Giovanni, S. (2011). The histone acetyltransferase p300 promotes intrinsic axonal regeneration. *Brain* *134*, 2134–2148.
- Goldberg, J.L., Klassen, M.P., Hua, Y., and Barres, B.A. (2002). Amacrine-signaled loss of intrinsic axon growth ability by retinal ganglion cells. *Science* *296*, 1860–1864.
- Gräff, J., Kim, D., Dobbin, M.M., and Tsai, L.H. (2011). Epigenetic regulation of gene expression in physiological and pathological brain processes. *Physiol. Rev.* *91*, 603–649.
- Guo, J.U., Ma, D.K., Mo, H., Ball, M.P., Jang, M.H., Bonaguidi, M.A., Balazer, J.A., Eaves, H.L., Xie, B., Ford, E., et al. (2011a). Neuronal activity modifies the DNA methylation landscape in the adult brain. *Nat. Neurosci.* *14*, 1345–1351.
- Guo, J.U., Su, Y., Zhong, C., Ming, G.L., and Song, H. (2011b). Emerging roles of TET proteins and 5-hydroxymethylcytosines in active DNA demethylation and beyond. *Cell Cycle* *10*, 2662–2668.
- Guo, J.U., Su, Y., Zhong, C., Ming, G.L., and Song, H. (2011c). Hydroxylation of 5-methylcytosine by TET1 promotes active DNA demethylation in the adult brain. *Cell* *145*, 423–434.
- Guo, J.U., Szulwach, K.E., Su, Y., Li, Y., Yao, B., Xu, Z., Shin, J.H., Xie, B., Gao, Y., Ming, G.L., et al. (2014). Genome-wide antagonism between 5-hydroxymethylcytosine and DNA methylation in the adult mouse brain. *Front. Biol. (Beijing)* *9*, 66–74.
- Hammarlund, M., and Jin, Y. (2014). Axon regeneration in *C. elegans*. *Curr. Opin. Neurobiol.* *27*, 199–207.
- He, Z., and Jin, Y. (2016). Intrinsic control of axon regeneration. *Neuron* *90*, 437–451.

- He, Z., and Koprivica, V. (2004). The Nogo signaling pathway for regeneration block. *Annu. Rev. Neurosci.* 27, 341–368.
- He, Y.F., Li, B.Z., Li, Z., Liu, P., Wang, Y., Tang, Q., Ding, J., Jia, Y., Chen, Z., Li, L., et al. (2011). Tet-mediated formation of 5-carboxylcytosine and its excision by TDG in mammalian DNA. *Science* 333, 1303–1307.
- Iskandar, B.J., Rizk, E., Meier, B., Hariharan, N., Bottiglieri, T., Finnell, R.H., Jarrard, D.F., Banerjee, R.V., Skene, J.H., Nelson, A., et al. (2010). Folate regulation of axonal regeneration in the rodent central nervous system through DNA methylation. *J. Clin. Invest.* 120, 1603–1616.
- Ito, S., Shen, L., Dai, Q., Wu, S.C., Collins, L.B., Swenberg, J.A., He, C., and Zhang, Y. (2011). Tet proteins can convert 5-methylcytosine to 5-formylcytosine and 5-carboxylcytosine. *Science* 333, 1300–1303.
- Iurlaro, M., Ficiz, G., Oxley, D., Raiber, E.A., Bachman, M., Booth, M.J., Andrews, S., Balasubramanian, S., and Reik, W. (2013). A screen for hydroxymethylcytosine and formylcytosine binding proteins suggests functions in transcription and chromatin regulation. *Genome Biol.* 14, R119.
- Jaenisch, R., and Bird, A. (2003). Epigenetic regulation of gene expression: how the genome integrates intrinsic and environmental signals. *Nat. Genet.* 33 (Suppl.), 245–254.
- Jang, M.H., Bonaguidi, M.A., Kitabatake, Y., Sun, J., Song, J., Kang, E., Jun, H., Zhong, C., Su, Y., Guo, J.U., et al. (2013). Secreted frizzled-related protein 3 regulates activity-dependent adult hippocampal neurogenesis. *Cell Stem Cell* 12, 215–223.
- Jin, S.G., Zhang, Z.M., Dunwell, T.L., Harter, M.R., Wu, X., Johnson, J., Li, Z., Liu, J., Szabó, P.E., Lu, Q., et al. (2016). Tet3 reads 5-carboxylcytosine through its CXXC domain and is a potential guardian against neurodegeneration. *Cell Rep.* 14, 493–505.
- Kaas, G.A., Zhong, C., Eason, D.E., Ross, D.L., Vachhani, R.V., Ming, G.L., King, J.R., Song, H., and Sweatt, J.D. (2013). TET1 controls CNS 5-methylcytosine hydroxylation, active DNA demethylation, gene transcription, and memory formation. *Neuron* 79, 1086–1093.
- Kim, Y.S., Anderson, M., Park, K., Zheng, Q., Agarwal, A., Gong, C., Sajjilafu, Young, L., He, S., LaVinka, P.C., et al. (2016). Coupled activation of primary sensory neurons contributes to chronic pain. *Neuron* 91, 1085–1096.
- Kozlenkov, A., Roussos, P., Timashpolsky, A., Barbu, M., Rudchenko, S., Bibikova, M., Klotzle, B., Byne, W., Lyddon, R., Di Narzo, A.F., et al. (2014). Differences in DNA methylation between human neuronal and glial cells are concentrated in enhancers and non-CpG sites. *Nucleic Acids Res.* 42, 109–127.
- Lister, R., Mukamel, E.A., Nery, J.R., Urich, M., Puddifoot, C.A., Johnson, N.D., Lucero, J., Huang, Y., Dwork, A.J., Schultz, M.D., et al. (2013). Global epigenomic reconfiguration during mammalian brain development. *Science* 341, 1237905.
- Liu, K., Lu, Y., Lee, J.K., Samara, R., Willenberg, R., Sears-Kraxberger, I., Tedeschi, A., Park, K.K., Jin, D., Cai, B., et al. (2010). PTEN deletion enhances the regenerative ability of adult corticospinal neurons. *Nat. Neurosci.* 13, 1075–1081.
- Liu, K., Tedeschi, A., Park, K.K., and He, Z. (2011). Neuronal intrinsic mechanisms of axon regeneration. *Annu. Rev. Neurosci.* 34, 131–152.
- Loh, Y.E., Koemeter-Cox, A., Finelli, M.J., Shen, L., Friedel, R.H., and Zou, H. (2017). Comprehensive mapping of 5-hydroxymethylcytosine epigenetic dynamics in axon regeneration. *Epigenetics* 12, 77–92.
- Ma, D.K., Jang, M.H., Guo, J.U., Kitabatake, Y., Chang, M.L., Pow-Anpongkul, N., Flavell, R.A., Lu, B., Ming, G.L., and Song, H. (2009). Neuronal activity-induced Gadd45b promotes epigenetic DNA demethylation and adult neurogenesis. *Science* 323, 1074–1077.
- Ma, D.K., Marchetto, M.C., Guo, J.U., Ming, G.L., Gage, F.H., and Song, H. (2010). Epigenetic choreographers of neurogenesis in the adult mammalian brain. *Nat. Neurosci.* 13, 1338–1344.
- Mellén, M., Ayata, P., Dewell, S., Kriacionis, S., and Heintz, N. (2012). MeCP2 binds to 5hmC enriched within active genes and accessible chromatin in the nervous system. *Cell* 151, 1417–1430.
- Moore, D.L., and Goldberg, J.L. (2011). Multiple transcription factor families regulate axon growth and regeneration. *Dev. Neurobiol.* 71, 1186–1211.
- Park, K.K., Liu, K., Hu, Y., Smith, P.D., Wang, C., Cai, B., Xu, B., Connolly, L., Kramvis, I., Sahin, M., and He, Z. (2008). Promoting axon regeneration in the adult CNS by modulation of the PTEN/mTOR pathway. *Science* 322, 963–966.
- Perera, A., Eisen, D., Wagner, M., Laube, S.K., Künzel, A.F., Koch, S., Steinbacher, J., Schulze, E., Splith, V., Mittermeier, N., et al. (2015). TET3 is recruited by REST for context-specific hydroxymethylation and induction of gene expression. *Cell Rep.* 11, 283–294.
- Puttagunta, R., Tedeschi, A., Sória, M.G., Hervera, A., Lindner, R., Rathore, K.I., Gaub, P., Joshi, Y., Nguyen, T., Schmandke, A., et al. (2014). PCAF-dependent epigenetic changes promote axonal regeneration in the central nervous system. *Nat. Commun.* 5, 3527.
- Rishal, I., and Fainzilber, M. (2014). Axon-soma communication in neuronal injury. *Nat. Rev. Neurosci.* 15, 32–42.
- Rossi, F., Gianola, S., and Corvetto, L. (2007). Regulation of intrinsic neuronal properties for axon growth and regeneration. *Prog. Neurobiol.* 81, 1–28.
- Rudenko, A., Dawlaty, M.M., Seo, J., Cheng, A.W., Meng, J., Le, T., Faull, K.F., Jaenisch, R., and Tsai, L.H. (2013). Tet1 is critical for neuronal activity-regulated gene expression and memory extinction. *Neuron* 79, 1109–1122.
- Seiffers, R., Mills, C.D., and Woolf, C.J. (2007). ATF3 increases the intrinsic growth state of DRG neurons to enhance peripheral nerve regeneration. *J. Neurosci.* 27, 7911–7920.
- Shin, J.E., Cho, Y., Beirowski, B., Milbrandt, J., Cavalli, V., and DiAntonio, A. (2012). Dual leucine zipper kinase is required for retrograde injury signaling and axonal regeneration. *Neuron* 74, 1015–1022.
- Shin, J., Ming, G.L., and Song, H. (2014a). Decoding neural transcriptomes and epigenomes via high-throughput sequencing. *Nat. Neurosci.* 17, 1463–1475.
- Shin, J., Ming, G.L., and Song, H. (2014b). DNA modifications in the mammalian brain. *Philos. Trans. R. Soc. Lond. B Biol. Sci.* 369, <http://dx.doi.org/10.1098/rstb.2013.0512>.
- Shin, J.E., Geisler, S., and DiAntonio, A. (2014c). Dynamic regulation of SCG10 in regenerating axons after injury. *Exp. Neurol.* 252, 1–11.
- Silver, J., Schwab, M.E., and Popovich, P.G. (2014). Central nervous system regenerative failure: role of oligodendrocytes, astrocytes, and microglia. *Cold Spring Harb. Perspect. Biol.* 7, a020602.
- Smith, D.S., and Skene, J.H. (1997). A transcription-dependent switch controls competence of adult neurons for distinct modes of axon growth. *J. Neurosci.* 17, 646–658.
- Song, J., Zhong, C., Bonaguidi, M.A., Sun, G.J., Hsu, D., Gu, Y., Meletis, K., Huang, Z.J., Ge, S., Enikolopov, G., et al. (2012). Neuronal circuitry mechanism regulating adult quiescent neural stem-cell fate decision. *Nature* 489, 150–154.
- Spruijt, C.G., Gnerlich, F., Smits, A.H., Pfaffeneder, T., Jansen, P.W., Bauer, C., Münzel, M., Wagner, M., Müller, M., Khan, F., et al. (2013). Dynamic readers for 5-(hydroxy)methylcytosine and its oxidized derivatives. *Cell* 152, 1146–1159.
- Tahiliani, M., Koh, K.P., Shen, Y., Pastor, W.A., Bandukwala, H., Brudno, Y., Agarwal, S., Iyer, L.M., Liu, D.R., Aravind, L., and Rao, A. (2009). Conversion of 5-methylcytosine to 5-hydroxymethylcytosine in mammalian DNA by MLL partner TET1. *Science* 324, 930–935.
- Tedeschi, A., and Bradke, F. (2017). Spatial and temporal arrangement of neuronal intrinsic and extrinsic mechanisms controlling axon regeneration. *Curr. Opin. Neurobiol.* 42, 118–127.
- Thakur, M., Crow, M., Richards, N., Davey, G.I., Levine, E., Kelleher, J.H., Agle, C.C., Denk, F., Harridge, S.D., and McMahon, S.B. (2014). Defining the nociceptor transcriptome. *Front. Mol. Neurosci.* 7, 87.
- Trakhtenberg, E.F., and Goldberg, J.L. (2012). Epigenetic regulation of axon and dendrite growth. *Front. Mol. Neurosci.* 5, 24.

- Weng, Y.L., Joseph, J., An, R., Song, H., and Ming, G.L. (2016). Epigenetic regulation of axonal regenerative capacity. *Epigenomics* 8, 1429–1442.
- Williams, K., Christensen, J., Pedersen, M.T., Johansen, J.V., Cloos, P.A., Rappsilber, J., and Helin, K. (2011). TET1 and hydroxymethylcytosine in transcription and DNA methylation fidelity. *Nature* 473, 343–348.
- Wong, J.K., and Zou, H. (2014). Reshaping the chromatin landscape after spinal cord injury. *Front. Biol. (Beijing)* 9, 356–366.
- Wright, M.C., Mi, R., Connor, E., Reed, N., Vyas, A., Alspalter, M., Coppola, G., Geschwind, D.H., Brushart, T.M., and Höke, A. (2014). Novel roles for osteopontin and clusterin in peripheral motor and sensory axon regeneration. *J. Neurosci.* 34, 1689–1700.
- Wu, H., and Zhang, Y. (2014). Reversing DNA methylation: mechanisms, genomics, and biological functions. *Cell* 156, 45–68.
- Yao, B., Christian, K.M., He, C., Jin, P., Ming, G.L., and Song, H. (2016). Epigenetic mechanisms in neurogenesis. *Nat. Rev. Neurosci.* 17, 537–549.
- Yu, H., Su, Y., Shin, J., Zhong, C., Guo, J.U., Weng, Y.L., Gao, F., Geschwind, D.H., Coppola, G., Ming, G.L., and Song, H. (2015). Tet3 regulates synaptic transmission and homeostatic plasticity via DNA oxidation and repair. *Nat. Neurosci.* 18, 836–843.
- Zhou, F.Q., and Snider, W.D. (2006). Intracellular control of developmental and regenerative axon growth. *Philos. Trans. R. Soc. Lond. B Biol. Sci.* 361, 1575–1592.

Golgi-Resident $G\alpha_o$ Promotes Protrusive Membrane Dynamics

Gonzalo P. Solis,^{1,3,*} Oleksii Bilousov,^{1,3} Alexey Koval,¹ Anne-Marie Luchtenborg,¹ Chen Lin,¹ and Vladimir L. Katanaev^{1,2,4,*}

¹Department of Pharmacology and Toxicology, University of Lausanne, CH-1011 Lausanne, Switzerland

²School of Biomedicine, Far Eastern Federal University, Vladivostok 690950, Russian Federation

³These authors contributed equally

⁴Lead Contact

*Correspondence: gonzalo.solis@unil.ch (G.P.S.), vladimir.katanaev@unil.ch (V.L.K.)

<http://dx.doi.org/10.1016/j.cell.2017.07.015>

SUMMARY

To form protrusions like neurites, cells must coordinate their induction and growth. The first requires cytoskeletal rearrangements at the plasma membrane (PM), the second requires directed material delivery from cell's insides. We find that the $G\alpha_o$ -subunit of heterotrimeric G proteins localizes dually to PM and Golgi across phyla and cell types. The PM pool of $G\alpha_o$ induces, and the Golgi pool feeds, the growing protrusions by stimulated trafficking. Golgi-residing KDELR binds and activates monomeric $G\alpha_o$, atypically for G protein-coupled receptors that normally act on heterotrimeric G proteins. Through multidimensional screenings identifying > 250 $G\alpha_o$ interactors, we pinpoint several basic cellular activities, including vesicular trafficking, as being regulated by $G\alpha_o$. We further find small Golgi-residing GTPases Rab1 and Rab3 as direct effectors of $G\alpha_o$. This KDELR \rightarrow $G\alpha_o$ \rightarrow Rab1/3 signaling axis is conserved from insects to mammals and controls material delivery from Golgi to PM in various cells and tissues.

INTRODUCTION

G protein-coupled receptors (GPCRs) form the biggest receptor family in animals. Main intracellular GPCR effectors are heterotrimeric G proteins composed of α , β , and γ subunits, of which the α -subunit binds guanine nucleotides. Four main subgroups of $G\alpha$ -subunits exist: $G\alpha_s$, $G\alpha_q$, $G\alpha_i/o$, and $G\alpha_{12/13}$ (Milligan and Kostenis, 2006). When bound to guanosine diphosphate (GDP), heterotrimeric G protein is competent to interact with the cognate GPCR. The activated receptor acts as a guanine nucleotide exchange factor (GEF), catalyzing exchange of GDP for GTP on the $G\alpha$. This triggers dissociation of the G protein into $G\alpha$ -GTP and the $\beta\gamma$ -heterodimer, which can bind and activate downstream transducer proteins. When GTP on $G\alpha$ is hydrolyzed, the inactive $G\alpha\beta\gamma$ heterotrimer re-associates for a new cycle of activation. Alternatively, the $G\alpha$ -subunit can be reloaded with GTP and continue its signaling activity (Lin et al., 2014).

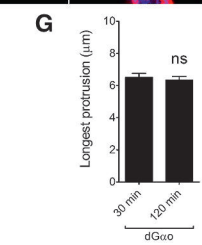
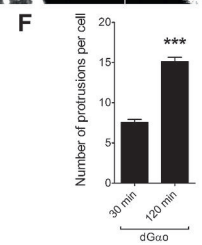
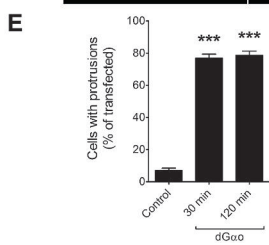
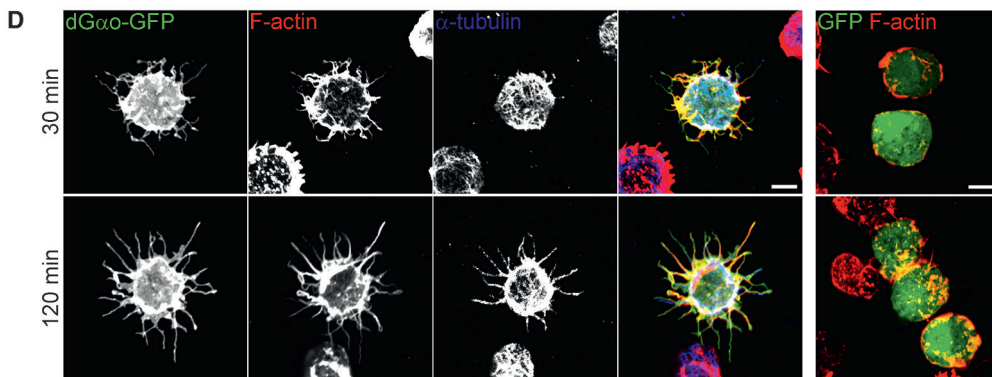
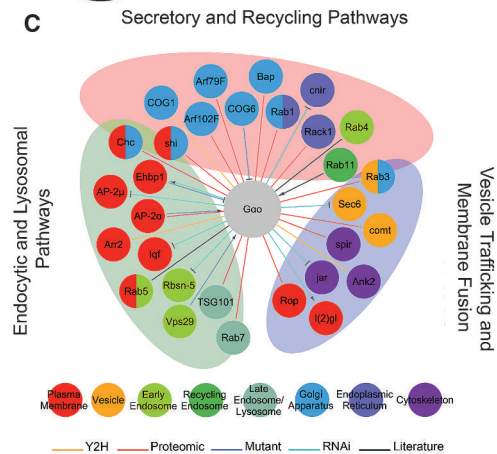
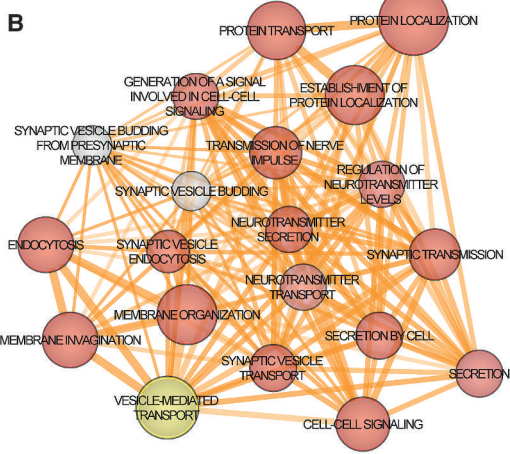
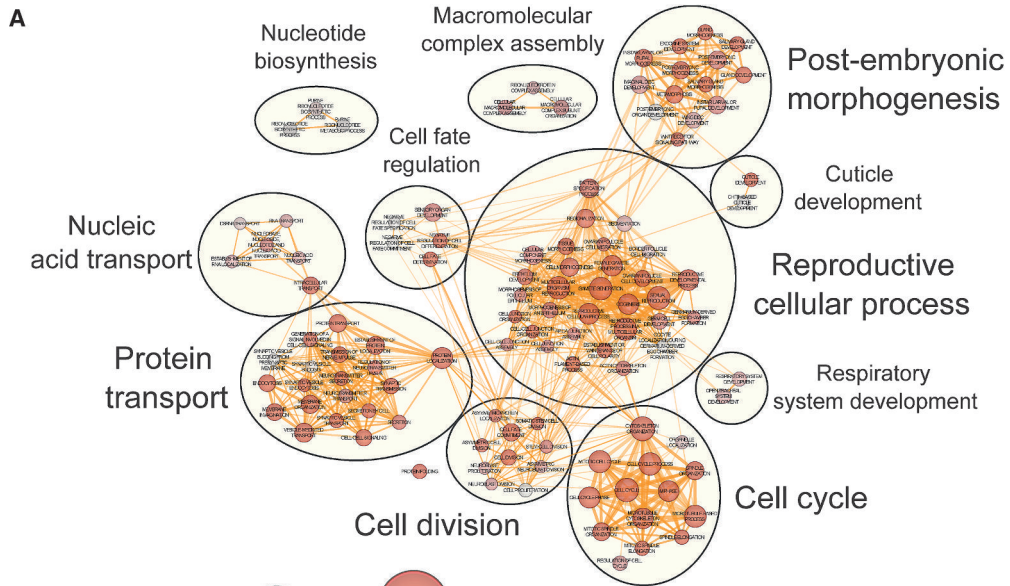
As $G\alpha$ -subunits provide the main specificity in GPCR-initiated signaling cascades (Milligan and Kostenis, 2006), identification of the $G\alpha$ targets is crucial to understand this type of signaling. $G\alpha_o$ was among the first α -subunits discovered and is the major $G\alpha$ -subunit of the nervous system across the animal kingdom (Sternweis and Robishaw, 1984; Wolfgang et al., 1990), controlling both development and adult physiology of the brain (Bromberg et al., 2008). $G\alpha_o$ is also expressed in other tissues and is a transducer of the developmentally and medically important Wnt signaling pathway (Egger-Adam and Katanaev, 2008; Koval et al., 2011).

Despite this importance, the list of known molecular targets of $G\alpha_o$ has been remarkably short. To uncover $G\alpha_o$ interactors, we performed several whole genome/proteome screenings resulting in > 250 candidate targets, most of which are not previously known to be regulated by $G\alpha$ proteins. These $G\alpha_o$ targets can be clustered into functional modules, identifying several basic cellular activities, conserved from insects to humans, as being under regulation of $G\alpha_o$ -mediated GPCR signaling. We focus on vesicular trafficking as one of these functional modules and show that $G\alpha_o$ controls multiple steps within it. From *Drosophila* epithelia to mammalian neuronal cells, $G\alpha_o$ controls outgrowth formation through coordinated activities from the plasma membrane (PM) and the Golgi apparatus, the latter involving the KDELR receptor and small GTPases Rab1 and Rab3.

RESULTS

Massive Screenings Identify Numerous $G\alpha_o$ Partners

With only a few $G\alpha_o$ effectors previously known, we performed several screenings to massively identify $G\alpha_o$ partners. Our primary screenings were: yeast two-hybrid (1), proteomic (2) and genetic suppressor-enhancer screens in *Drosophila* using $G\alpha_o$ overexpression (3), and RNAi-mediated downregulation (4). In a complementary manner, we expected to cover the complete $G\alpha_o$ interactome with these screenings. We then complemented these screens with an extensive scrutiny of the literature data (5) and bioinformatics analysis of the resulting network and translation of this network into proteins orthologous between *Drosophila* and humans. This type of interactome identification has not been performed for any $G\alpha$ protein and produced an impressive list of 254 proteins being candidate $G\alpha_o$ partners (Table S1; STAR Methods).



(legend on next page)

Next, we aimed at functional clusterization of the $G\alpha$ targets, performing the gene ontology enrichment analysis of the $G\alpha$ interactome. This analysis identifies several functional modules, such as cytoskeleton organization, cell division, cell adhesion, etc., within the $G\alpha$ interaction network (Figures 1A and S1A; Table S2). These modules may represent key cellular activities being directly controlled by $G\alpha$ -mediated GPCR signaling. As opposed to analysis of isolated individual targets, we decided to select a functional module from this network and to holistically investigate the role of $G\alpha$ in the regulation of this module. For this purpose, we selected the vesicular trafficking group of $G\alpha$ targets.

$G\alpha$ Induces Outgrowth Formation in Different Cellular Systems

Previously, we showed that *Drosophila* $G\alpha$ (d $G\alpha$) directly interacts with Rab5 to regulate the Wnt/Frizzled (Fz) signaling (Purvanov et al., 2010). The screenings now identified components of the vesicular trafficking machinery as partners of $G\alpha$ (Figures 1B and 1C; Table S2), suggesting that $G\alpha$ may function as a master regulator in vesicular trafficking.

To experimentally validate our hypothesis, we looked for a $G\alpha$ -mediated cellular program that may require vesicle-mediated transport. We chose the process of neurite formation, and more broadly, outgrowth formation, for this purpose. Indeed, $G\alpha$ expression in neuronal cells coincides with, and $G\alpha$ activity is required for, neuritogenesis (Frémion et al., 1999; Lee et al., 2006; Strittmatter et al., 1994; Wolfgang et al., 1990). The need for vesicle-mediated delivery of material to growing neurites is well-known, although $G\alpha$ has not previously been implicated in this vesicle delivery. $G\alpha$ is also required for the patterning and formation of *Drosophila* wing hairs—stable actin-rich outgrowths of wing epithelial cells (Katanaev et al., 2005).

Mouse neuroblastoma N2a cells rarely produce spontaneous neurites, which correlates with their low endogenous levels of $G\alpha$ (Figure S1B). As previously shown (Bromberg et al., 2008; Lüchtenborg et al., 2014), expression of $G\alpha$ in these cells induces a massive neurite outgrowth (Figures S1C and S1D) providing us with a necessary readout system.

We additionally used *Drosophila* S2 cells, which also have low endogenous $G\alpha$ levels (<http://flybase.org/reports/FBgn0001122.html>). Remarkably, we observed that d $G\alpha$ expression induced long protrusions, not typical for these cells (Figures 1D–1G). These protrusions are initially F-actin-positive, but with time become wider and additionally filled with microtubules (Figure 1D). Live imaging reveals the dynamic nature of these structures (Movie S1). $G\alpha$ -induced formation of protrusions

in S2 cells served as another, evolutionary distant, readout for the role of $G\alpha$ in trafficking.

$G\alpha$ Shows Dual Plasma Membrane and Golgi Localization

Before going further, we checked the subcellular localization of $G\alpha$ in our systems. In N2a cells transfected with human $G\alpha$, immunostainings showed expected PM localization and a strong perinuclear accumulation co-staining with the *trans*-Golgi marker GalT-GFP (Figure S1E). A functional C-terminal GFP-fusion of $G\alpha$ ($G\alpha$ -GFP) (Figures S1C and S1D) also stained PM and Golgi, the latter recognized by the *cis*-Golgi marker GM130 and a broader Golgi marker MannII-blue fluorescent protein (BFP) (Figure 2A). Golgi localization of $G\alpha$ was not affected by cycloheximide (up to 6 hr, not shown), and live imaging of $G\alpha$ -GFP revealed a rather static Golgi localization (Movie S2) as opposed to the more dynamic GalT-GFP marker (Movie S3), suggesting that $G\alpha$ does not merely stain Golgi on its way to PM after synthesis. Endogenous $G\alpha$ was also found dually at PM and Golgi in human neuroblastoma BE(2)C cells (Figure 2B) and in primary mouse cortical neurons (Figure S1F).

A Golgi localization of mammalian $G\alpha$, with unclear biological relevance, has been seen previously (Akgoz et al., 2004), while such localization has not been described for d $G\alpha$ or any insect $G\alpha$ -subunit. In *Drosophila*, Golgi stacks spread all over cytoplasm (Kondylis and Rabouille, 2009), and d $G\alpha$ -GFP in S2 cells localized at PM and at *cis*- and *trans*-Golgi stacks, identified, respectively, with the GMAP-210 and GalT-mRFP (Figure 2C). Upon heterologous expression in N2a cells, d $G\alpha$ -GFP also localized at PM and Golgi (Figure S1G).

As a *Drosophila* tissue with endogenous d $G\alpha$, pupal wings expressing dArf79F-GFP as a *cis*-Golgi marker (Shao et al., 2010) revealed d $G\alpha$ localized at PM and at compartments overlapping with this marker (Figure 2D). Some dArf79F-negative d $G\alpha$ clusters may represent *medial*- and *trans*-Golgi stacks, although we cannot exclude additional intracellular compartments. The immunostaining specificity was confirmed by RNAi knockdown (k/d) of d $G\alpha$ in pupal wings (Figure S1H).

Cumulatively, our findings in different cellular and organism readouts show a dual localization of $G\alpha$ to the PM and Golgi compartments.

$G\alpha$ Regulates Vesicular Trafficking at Golgi

To test for the role of the Golgi-localizing $G\alpha$, we first roughly approached the function of the Golgi apparatus in $G\alpha$ -induced neuritogenesis using brefeldin A (BFA). As expected (Nakamura et al., 1995), BFA induced diffuse GM130 staining

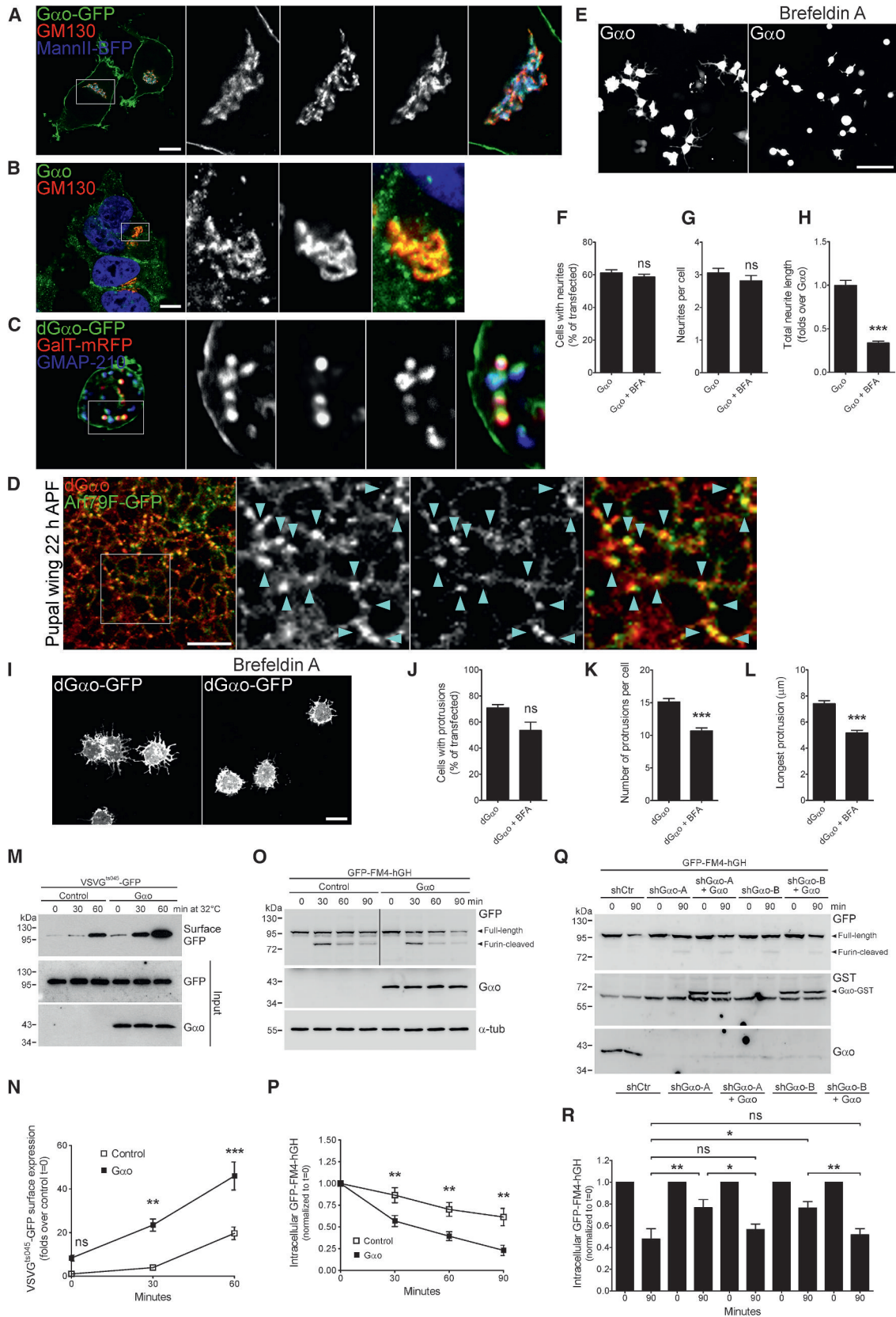
Figure 1. Bioinformatics Analysis of the $G\alpha$ Interactome

(A and B) Enrichment map of over-represented GO terms clustered in functional modules (A) built from $G\alpha$ partners. Zoom-in of the “Protein transport” module from (A) with the term “Vesicle-mediated transport” shown in green (B).

(C) $G\alpha$ partners of the term “Vesicle-mediated transport” grouped by function. Color codes for nodes and edges indicate subcellular localization and screening method, respectively.

(D–G) *Drosophila* S2 cells expressing d $G\alpha$ -GFP or GFP were allowed to spread for 30 (top) or 120 min (bottom) to form protrusions. Rhodamine-phalloidin and anti- α -tubulin stained F-actin and microtubules, respectively (D). Note that protrusions are initially F-actin-positive (30 min), but with time become wide and filled with microtubules (120 min). Quantification of parameters related to protrusion formation (E–G). Data represent mean \pm SEM. ns, not significant; *** $p \leq 0.001$. Scale bars, 5 μ m.

See also Figure S1, Tables S1 and S2, and Movie S1.



(legend on next page)

in *G α* -transfected N2a cells; loss of *G α* -GFP from the perinuclear region was also seen leaving the PM pool intact (Figure S1I), while total *G α* levels did not change (Figure S1J). We found that BFA-treated *G α* -expressing cells still formed neurites, with the percentage of cells with neurites and neurite number not significantly affected (Figures 2E–2G). However, these neurites were much shorter and thinner than in the control cells (Figures 2E and 2H).

Similarly, BFA treatment in *Drosophila* S2 cells had no effect on d*G α* protein levels (Figure S1K), but significantly reduced the length of protrusions (Figures 2I and 2L), confirming that Golgi functions are also required for protrusion elongation in S2 cells. However, BFA additionally reduced the average number of protrusions per cell (Figures 2I–2K), which may be due to instability of these structures.

These results indicate that Golgi is required for membrane trafficking needed during elongation of *G α* -induced protrusions. To test this directly, we quantified the PM-directed transport using GFP-fusion of the thermosensitive vesicular stomatitis virus glycoprotein (VSVG^{ts045}-GFP). This construct is retained in endoplasmic reticulum (ER) at 42°C, being released at 32°C for its transport to PM through Golgi (Presley et al., 1997). Analyzing kinetics of surface accumulation of this construct at 32°C, we found strong acceleration of PM delivery of VSVG^{ts045}-GFP upon co-expression of *G α* (Figures 2M and 2N).

To provide an independent meter of the effect of *G α* on the Golgi-emanating trafficking, we employed the reverse dimerization (RD) system, whereby the GFP-FM4-hGH fusion protein aggregates in ER until addition of the D/D solubilizer drug, permitting then the secretory trafficking (Gordon et al., 2010). We found that expression of *G α* in N2a cells strongly speeds up secretory protein trafficking of this construct (Figures 2O and 2P). Further, we show with two independent small hairpin RNAs (shRNAs) (Figures S2A and S2B) that k/d of endogenous *G α* from BE(2)C cells significantly slows down the secretory trafficking effect rescued by re-expression of *G α* (Figures 2Q and 2R). It can be seen from Figures 2M–2R that the speed of secretory trafficking is reduced ~2-fold upon k/d of *G α* in BE(2)C cells and increased > 2-fold upon expression of *G α* in N2a cells.

Collectively, these data suggest that Golgi *G α* regulates the PM-directed transport. Our data also indicate that the two pools of *G α* may function cooperatively in the outgrowths: the PM pool of *G α* providing the initial inductor signal for the outgrowth formation, and the Golgi pool maintaining and elongating the outgrowth through stimulating material delivery. In order to separate the PM and Golgi functions of *G α* , we generated a Golgi-only form, go*G α* (STAR Methods). In N2a cells, go*G α* shows a prominent Golgi but essentially no PM localization (Figure 3A) and robust interaction with Golgi partners of *G α* (Figure S2C, see below). Fully supporting our expectations, go*G α* fails to induce any neurite outgrowths (Figures S1C and S1D). At the same time, go*G α* parallels wild-type (WT) *G α* in the speeding up of material delivery from Golgi in the RD assay (Figures 3B and 3C).

***G α* Physically and Functionally Interacts with Small GTPases at Mammalian Golgi**

How does the Golgi pool of *G α* activate cargo delivery to PM? We hypothesized that this is achieved through direct interaction with *G α* targets of the vesicular trafficking module (Figure 1C; Table S2). The following mammalian orthologs of the d*G α* targets were chosen for physical interaction analysis: small GTPases of the Rab (Rab1a, Rab3a, Rab4a, Rab5a, Rab7a, and Rab11a) and Arf (Arf1–Arf6) families, dynamin-1 and -2, and clathrin, all crucial components of the secretory and/or endocytic pathways. GFP-fusions of these proteins were expressed in N2a cells together with *G α* -GST (that displayed correct dual localization) (Figure S2D) for the pull-down analysis; empty plasmid or GST-fusion of the Golgi-resident KDEL receptor (KDELRL) (Figure S2D) (Townsend et al., 1993) were used as controls. Pull-downs showed robust binding of *G α* -GST to Rab1a, Rab3a, Rab4a and Rab5a; Rab7a and Rab11a where only weakly co-precipitated (Figures 3D, S2E, and S2F). From the Arf family, *G α* -GST strongly interacted with all Golgi-associated Arfs (Arf1–Arf5) but not with the endocytic Arf6 (Figures 3D, S2E, and S2G). In contrast, no direct interactions were detected in this system for clathrin and dynamins (Figure S2H).

We next analyzed co-localization, expressing *G α* -mRFP with the GFP-fusions of the target proteins. Perinuclear *G α* strongly

Figure 2. Evolutionary Conserved Localization of *G α* at Golgi

(A–C) Golgi localization of *G α* -GFP determined in mouse N2a cells (A) by co-localization with Golgi markers GM130 and MannII-BFP. Human BE(2)C cells (B) showed endogenous *G α* co-localizing with GM130 at Golgi. In *Drosophila* S2 cells (C), d*G α* -GFP labeled Golgi stacks marked by GalT-mRFP and GMAP-210. Color-channels are listed vertically top-to-bottom and selected areas are magnified with the channels displayed horizontally in the same order left-to-right. Scale bars, 10 μ m (A and B); 5 μ m (C).

(D) Immunostaining of endogenous d*G α* in *Drosophila* pupal wings expressing the *cis*-Golgi marker Arf79F-GFP at 22 hr after puparium formation (APF). A selected region is magnified; d*G α* /Arf79F-positive clusters indicated by arrowheads. Scale bar, 50 μ m.

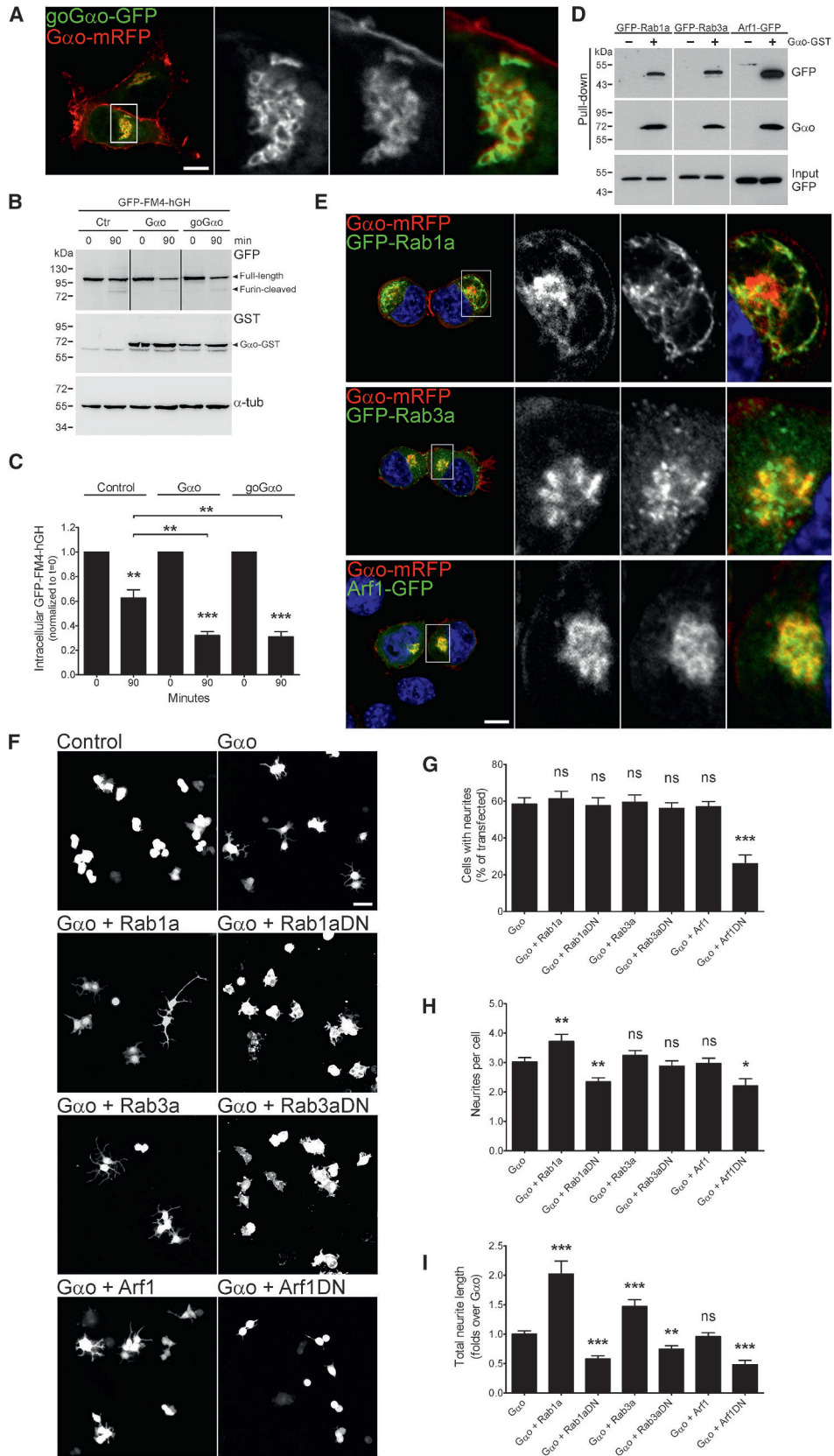
(E–L) Development of protrusions in N2a (E–H) and S2 cells (I–L) induced by *G α* in the absence or presence of BFA. In N2a cells, BFA-treatment affected only neurite length (E–H), whereas both protrusion number and length were reduced in S2 cells (I–L). Quantification of parameters linked to neurite and protrusion formation (F–H and J–L). Scale bar, 50 μ m (E); 10 μ m (I).

(M and N) *G α* speeds up trafficking to PM as measured with the VSVG^{ts045}-GFP assay in N2a cells (M). Surface biotinylation determined PM levels of VSVG^{ts045}-GFP at different time points at 32°C. Biotinylated and input samples were tested with Abs against GFP and *G α* . Quantification (N).

(O–R) Reverse dimerization assay in N2a (O and P) and BE(2)C (Q and R) cells. D/D solubilizer induces reduction of the full-length GFP-FM4-hGH and appearance and decrease of a furin-cleaved product (O and Q). *G α* overexpression strongly sped up secretory trafficking in N2a cells (O and P), and its downregulation significantly slowed it down in BE(2)C cells (Q and R). *G α* re-expression in knockdown BE(2)C cells rescued GFP-FM4-hGH secretion (Q and R). Cell extracts were tested with Abs against GFP, *G α* , α -tubulin (α -tub) and/or GST. Vertical line indicates that the two sides of the same membrane are shown with different exposition times for better visualization (O). Arrowheads point to relevant bands (O and Q). Quantification of the effect of *G α* overexpression (P) and its downregulation and re-expression (R).

Data represent mean \pm SEM. ns, not significant; * $p \leq 0.01$, ** $p \leq 0.005$, *** $p \leq 0.001$.

See also Figures S1 and S2, and Movies S2 and S3.



(legend on next page)

co-localized with the Golgi-associated Rab1a and Arf1-5 and to a lesser extent with Rab3a (Figures 3E and S3A). A limited co-localization was observed between perinuclear $G\alpha$ and Rab11a, clathrin and dynamins, and even less with the endocytic Rab4a, Rab5a, and Rab7a (Figures S3B and S3C). Together, these results identify the small GTPases Rab1a, Rab3a, and Arf1–Arf5 as potential players in the $G\alpha$ functions at Golgi.

Next, we analyzed cooperation of $G\alpha$ with these partners in neurite outgrowth, using WT and dominant-negative (DN) versions of Rab1a, Rab3a, and Arf1. While Rab1a, Rab3a, or Arf1 alone did not induce any neurite formation nor affected the length of the few spontaneous N2a cell neurites (Figures S3D–S3F), WT versions of Rab1a and Rab3a strongly potentiated, and their DN forms strongly suppressed the length of $G\alpha$ -induced neurites in N2a cells (Figures 3F and 3I). At the same time, the proportion of neurite-forming cells and the neurites-per-cell numbers were not influenced by WT and DN forms of Rab3a and modestly affected by the forms of Rab1a (Figures 3F–3H), confirming the interaction between $G\alpha$ and these GTPases is important for elongation but not induction of protrusions. In contrast to Rabs, Arf1 WT showed no functional interaction with $G\alpha$, while Arf1DN reduced all $G\alpha$ -dependent responses (Figures 3F–3I) through a yet unclarified reduction of $G\alpha$ protein levels not seen in other co-transfections (Figures S3G–S3I). Arf1DN also induced a predicted BFA-like phenotype (Dascher and Balch, 1994): loss of the Golgi marker GM130 and of the perinuclear $G\alpha$ (Figures S4A and S4B). Conversely, the DN versions of Rab1a and Rab3a had no obvious effect on $G\alpha$ localization (Figure S4B).

Together, these data show that physical and functional interactions of $G\alpha$ with Rab1a and Rab3a at Golgi are required for neurite elongation in N2a cells.

$G\alpha$ Functionally Interacts with Small GTPases at *Drosophila* Golgi

To support the above conclusion in an independent setting, we performed a similar set of experiments in *Drosophila* S2 cells. Upon co-transfection of mRFP-fusion constructs of dRab1, dRab3, and dArf79F with d $G\alpha$ -GFP, all three small GTPases co-localized with d $G\alpha$ at Golgi stacks stained by anti-GMAP-210 (Figures S4C and S4D). While expression of the GTPases alone did not induce protrusions (Figures S4E and S4F), dRab1 and dRab3 potentiated the number and length of d $G\alpha$ -induced outgrowths (Figures 4A–4D) without changing the d $G\alpha$ -GFP expression levels (Figures S4G and S4H). In contrast, dRab1DN and dRab3DN suppressed d $G\alpha$ -induced protrusions (Figures

4A–4D). To continue the similarity with the mammalian system, the dArf79FDN mutant caused an ~50% drop in d $G\alpha$ protein levels (Figures S4G and S4H) resulting in reduction in all parameters related to the formation of protrusions (Figures 4A–4D); it also was unique in disassembling Golgi stacks (Figure S5A).

Using live imaging, we found that the dynamics of d $G\alpha$ -induced protrusions in S2 cells was strongly suppressed by dRab1DN and strongly enhanced by dRab1WT (Movies S1, S4, and S5). These data show that the function of $G\alpha$ as a key player in the Golgi-controlled elongation of outgrowths is conserved from insects to mammals.

$G\alpha$ Genetically Interacts with Small GTPases in Developing *Drosophila* Tissues

We next aimed at testing the role of $G\alpha$ in regulation of vesicular trafficking through Golgi-residing small GTPases *in vivo*, using two well-characterized phenotypes induced by d $G\alpha$: planar cell polarity (PCP) and wing hair formation defects in developing insect's wings (Katanaev et al., 2005) and neuromuscular junction (NMJ) phenotypes in larvae (Lüchtenborg et al., 2014). Both phenotypes are linked to aberrant signaling by Fz receptors, which are GPCRs largely dependent upon $G\alpha$ for proper signal transduction (Egger-Adam and Katanaev, 2008; Koval et al., 2011). We hypothesized that these developmental processes may require not only the PM-associated activity of $G\alpha$ as a GPCR transducer but also its Golgi function as a regulator of vesicular trafficking.

In pupal wings, each epithelial cell produces a stable outgrowth called trichome or hair. Aberrant Fz and d $G\alpha$ activity results in the multiple wing hair (mwh) phenotype, when some cells form two or more hairs instead of one (Katanaev et al., 2005). Remarkably, co-overexpression of d $G\alpha$ with dRab3 and especially dRab1 produced a marked, up to 15-fold, enhancement of the d $G\alpha$ -induced mwh phenotype, whereas co-expression of dArf79F showed no enhancement (Figures 4E and 4F). Because the sole overexpression of each dRab produced no effect (Figures 4E and 4F), this result illustrates that d $G\alpha$ synergistically interacts with dRab1 and dRab3 in this *in vivo* setting.

Drosophila NMJ is a glutamatergic synapse made by several distinct circular structures—the synaptic boutons—at the axon terminus. Boutons can be visualized with the postsynaptic CD8-GFP-Sh and the presynaptic anti-HRP staining. In larval NMJs, loss or RNAi-mediated k/d of d $G\alpha$ leads to strong reduction in the number of boutons and to morphological abnormalities seen as elongated structures with defective overlap of

Figure 3. Functional Interaction of $G\alpha$ with Key Small GTPases

(A) In N2a cells, a Golgi-only form of $G\alpha$ (go $G\alpha$ -GFP) is mostly absent from PM as seen by co-expression of $G\alpha$ -mRFP. Scale bar, 10 μ m.
 (B and C) Reverse dimerization assay in N2a cells. D/D solubilizer induces reduction of the full-length GFP-FM4-hGH and appearance of a furin-cleaved product (B). go $G\alpha$ sped up secretory trafficking as efficiently as WT $G\alpha$ did (C). Cell extracts were tested with Abs against GFP, GST and α -tubulin (α -tub). Vertical lines indicate different exposition times for each membrane part for better visualization (B).
 (D) Pull-downs from N2a cells transfected with $G\alpha$ -GST and GFP-fusions of the small GTPases Rab1a, Rab3a, and Arf1.
 (E) Co-localization of $G\alpha$ -mRFP with GFP-tagged Rab1a, Rab3a, and Arf1 in N2a cells. Boxed areas are magnified (right). Scale bar, 10 μ m.
 (F–I) Neurite formation in N2a cells co-expressing $G\alpha$ -GFP with GFP-fusions of WT or DN forms of Rab1a, Rab3a, and Arf1 (F). Quantification of neurite-associated parameters (G–I). Scale bar, 20 μ m.
 Data represent mean \pm SEM. ns, not significant; * $p \leq 0.01$, ** $p \leq 0.005$, *** $p \leq 0.001$.
 See also Figures S2, S3, and S4 and Table S2.

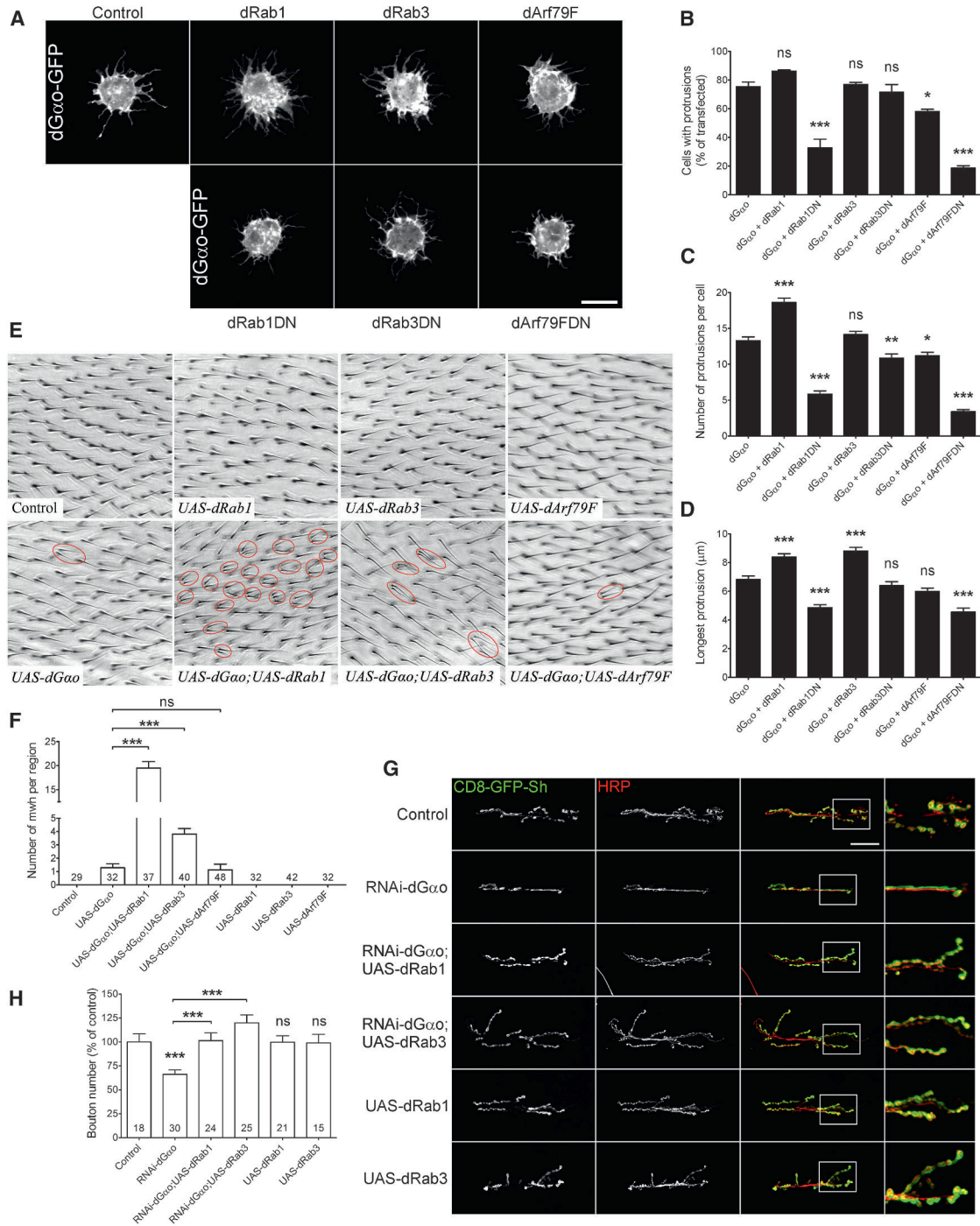


Figure 4. Gαo Interacts with Small GTPases in *Drosophila*

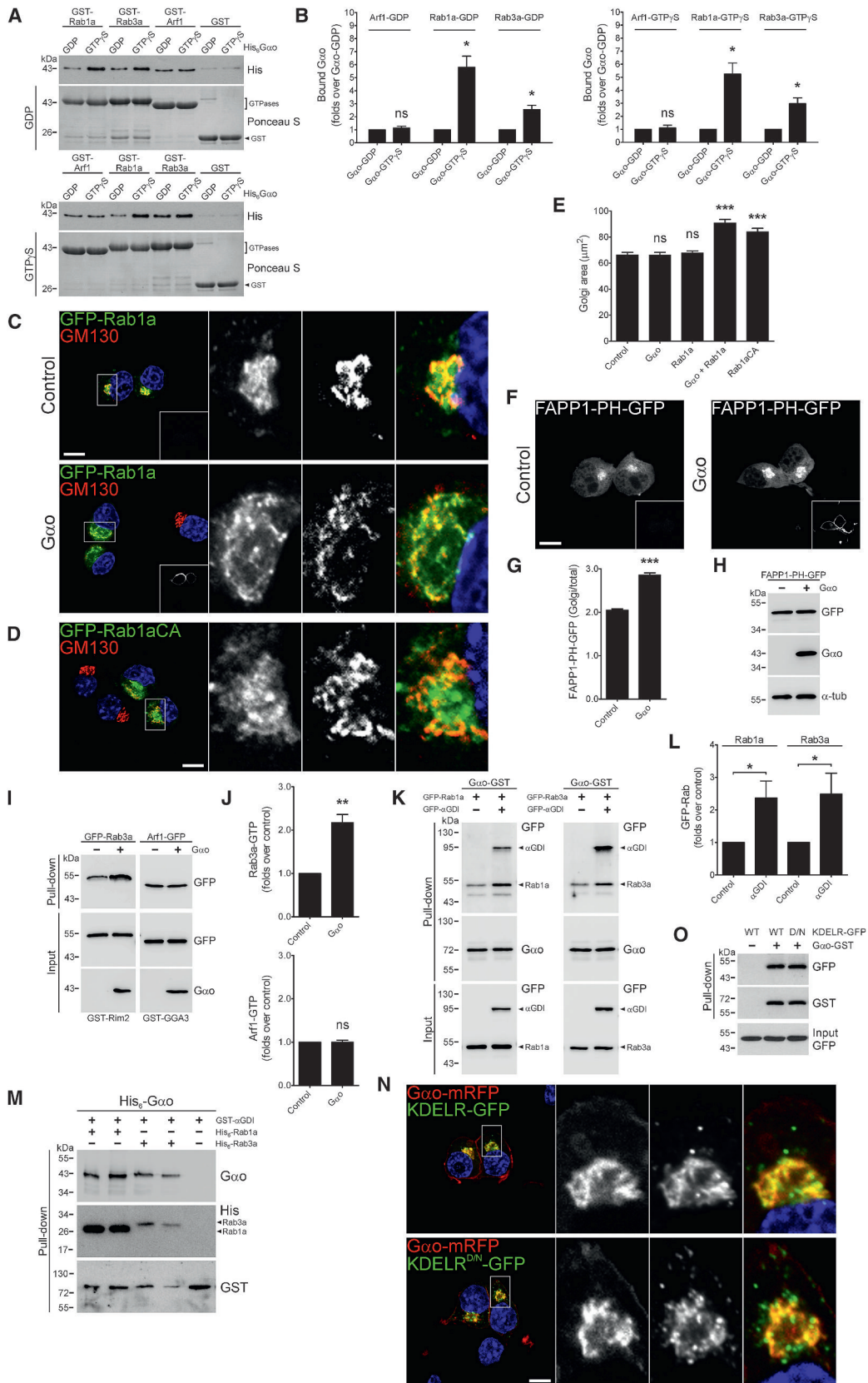
(A–D) Protrusions in S2 cells co-expressing dGαo-GFP with GFP-fusions of WT or DN forms of dRab1, dRab3, and dArf79F (A). Quantification of protrusion linked parameters (B–D). Scale bar, 5 μm.

(E and F) In *Drosophila* wings, the mwh phenotype induced by dGαo overexpression (red ovals) is boosted by dRab1 and dRab3 but not dArf79F (E). Quantification (F).

(G and H) The NMJ phenotypes induced by knockdown of dGαo in *Drosophila* larvae are suppressed by the overexpression of dRab1 and dRab3 overexpression (G). Note that the sole overexpression of dRab1 and dRab3 produced no phenotype compared to control (G). Synaptic boutons are visualized by CD8-GFP-Sh and anti-HRP staining. Boxed regions are zoomed-in (right). Quantification of synaptic bouton numbers (H). Scale bar, 50 μm.

Data represent mean ± SEM. Numbers in columns represent sample sizes. ns, not significant; *p ≤ 0.01, **p ≤ 0.005, ***p ≤ 0.001.

See also Figures S4 and S5 and Movies S1, S4, and S5.



(legend on next page)

pre- and postsynaptic markers (Figures 4G and 4H) (Lüchtenborg et al., 2014). We speculated that motoneuron-specific overexpression of dRab1 or dRab3 may revert this phenotype, provided that these Rabs act downstream of dG α o in NMJ formation. Indeed, we found that the dG α o k/d phenotype (both the number of boutons and the NMJ morphology) was fully rescued by overexpression of dRab1 or dRab3, while these overexpressions on the wild-type background produced no effects (Figures 4G and 4H). As the k/d effect of the dG α o-targeting RNAi cannot be down-titrated by overexpression of an unrelated protein (Lüchtenborg et al., 2014), these data demonstrate the in vivo functional interaction of dG α o with dRab1 and dRab3 during NMJ development.

The findings in this section provide evidence for the genetic interactions of G α o with Rab1 and Rab3 in vivo, in two different tissues, supporting our cellular observations.

G α o Activates Small GTPases at Golgi

Experiments described above show that G α o physically and functionally interacts with Golgi-residing small GTPases. Next, we bacterially produced GST-tagged Rab1a, Rab3a, and Arf1, as well as previously characterized His₆-tagged G α o (Lin et al., 2014) and preloaded these G proteins with GDP or GTP γ S mimicking their inactive and active conformations. Subsequent pull-downs confirmed that G α o interactions with Rab1a, Rab3a, and Arf1 are direct (Figure 5A). Importantly, while the nucleotide state of the small GTPases did not affect the interaction with G α o, G α o-GTP γ S bound Rab1a and Rab3a by folds more efficiently than G α o-GDP did (Figures 5A and 5B). In contrast, binding to Arf1 was not influenced by the nucleotide state of G α o (Figures 5A and 5B). These data might suggest that Rab1a and Rab3a are effectors of activated G α o at the Golgi apparatus.

Thus, we analyzed if G α o regulates Rab1a and Rab3a activities. Morphologically, co-expression of G α o-mRFP and GFP-Rab1a in N2a cells induced a striking enlargement of the perinuclear region positive for both proteins—the phenotype not seen for G α o co-expressions with other targets (Figure 3F). Similarly, in *Drosophila* S2 cells, co-expression of dG α o-GFP with mRFP-

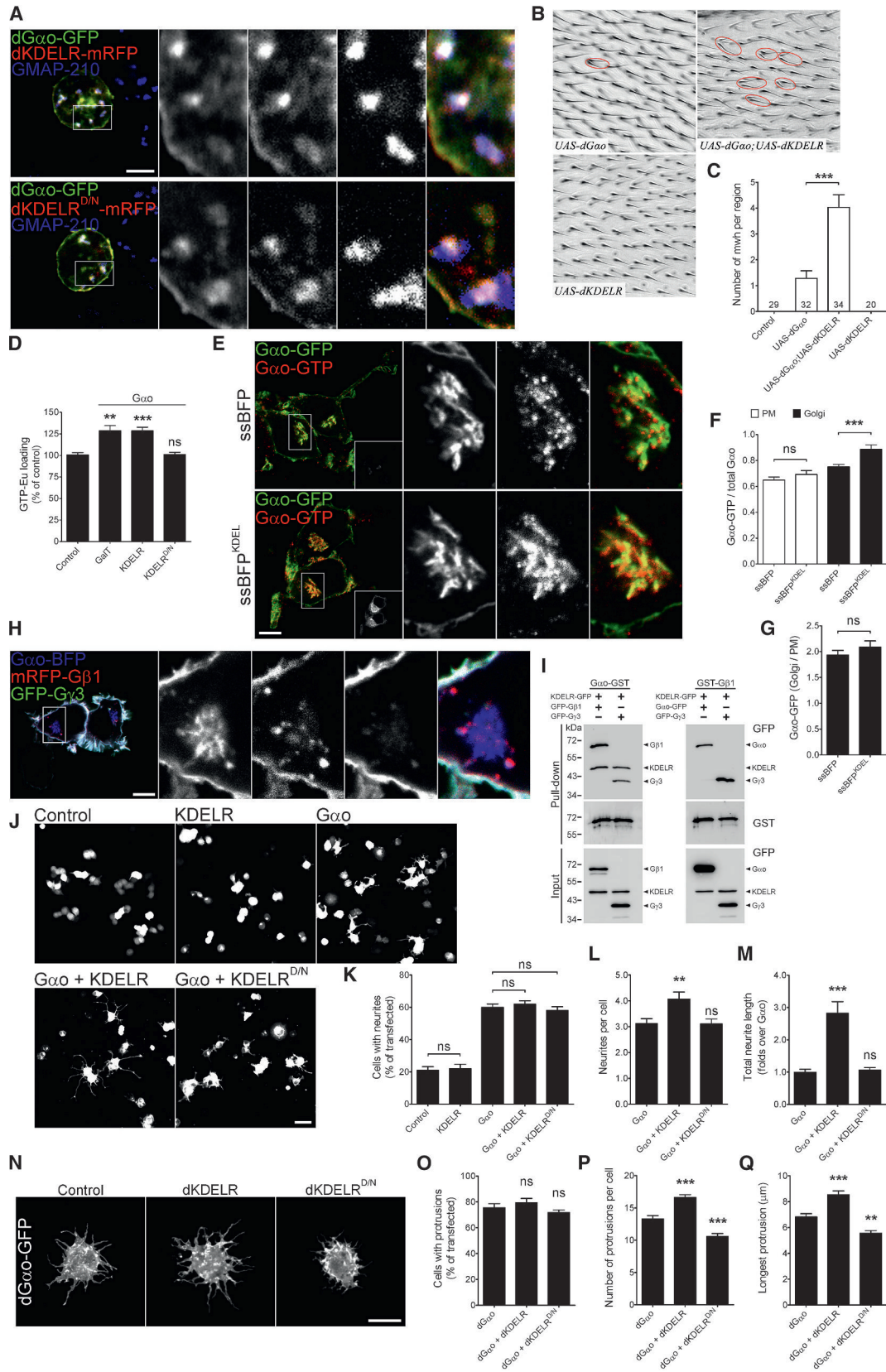
dRab1 induced clustering and tubulation of the Golgi stacks, also not seen in other experimental conditions (Figures S4C and S4D). As Rab1 has been previously associated with Golgi enlargement (Romero et al., 2013), we hypothesized that co-expression of G α o stimulates Rab1a that in turn increases the Golgi size, in a manner conserved from insect to mammalian cells.

To address this, we measured the Golgi area marked by GM130 in N2a cells co-expressing non-tagged G α o and GFP-Rab1a. While overexpression of G α o or Rab1a alone had no effect, their co-expression significantly increased the Golgi size (Figures 5C and 5E). Proving that Rab1a activation is the cause, we found a similar enlargement of the Golgi area induced by the constitutive active Q70L mutant of Rab1a (Figures 5D and 5E), but not by other mutant forms of Rab1a or G α o (Figure S5B). Co-expression with Rab1b also enlarged Golgi (Figure S5C), suggesting that G α o activation of Rab1 is not isoform-specific.

To further assess activation of Rab1 by G α o, we used a FAPP1-PH-GFP construct, commonly served to evaluate phosphatidylinositol 4-phosphate (PI4P) levels in Golgi membranes (Balla et al., 2005). Because Rab1 activation increases PI4P production, FAPP1-PH-GFP recruitment to Golgi indirectly monitors the activity of endogenous Rab1 (Dumaresq-Doiron et al., 2010). G α o overexpression in N2a cells significantly increased Golgi accumulation of FAPP1-PH-GFP (Figures 5F and 5G) without any changes in its protein levels (Figure 5H). As FAPP1-PH can also interact with Arf1-GTP (Balla et al., 2005), we separately employed a GST fusion of the Arf1 effector GGA3 (Dell'Angelica et al., 2000). G α o overexpression did not increase the amount of Arf1-GTP pulled down from N2a cell extracts by GST-GGA3 (Figures 5I and 5J). Thus, G α o can activate endogenous Rab1, but not Arf1, at Golgi. Similarly, pull-down of Rab3a-GTP by its effector Rim2 was used as a probe to monitor Rab3 activation (Fukuda, 2004), revealing that G α o overexpression increased 2-fold the amount of activated Rab3a (Figures 5I and 5J). We further found that G α o overexpression increased Golgi accumulation (Figures S5D and S5E) but not protein levels of GFP-Rim2 (Figure S5F) in N2a cells. Because Rab3a also localizes to regions other than Golgi (Figure 3F), these data suggest that G α o

Figure 5. G α o Activates Rab1 and Rab3

(A and B) G α o directly interacts with Rab1a, Rab3a, and Arf1. Recombinant His₆-tagged G α o is pulled down by GST-fusions of the small GTPases but not GST (A). GDP-loaded (top) and GTP γ S-loaded (bottom) conformations of Rab1 and Rab3a bound more efficiently GTP γ S-loaded G α o. Proteins were detected by anti-His-tag and Ponceau S. Quantification (B).
(C–E) Golgi enlargement in N2a cells by co-expression of G α o and GFP-Rab1a (C). Immunostainings against G α o (squares at right bottom corners of GFP-Rab1a panels) and GM130 confirmed co-expression and marked Golgi, respectively. Golgi expansion induced by a CA mutant of Rab1a (GFP-Rab1aCA; D). Selected regions are magnified to the right. Quantification of Golgi area (E).
(F–H) G α o enhanced the Golgi accumulation of FAPP1-PH-GFP in N2a cells (F). G α o co-expression confirmed as in (C). Mean fluorescence intensity ratios of FAPP1-PH-GFP at the Golgi versus total cell (G). Expression levels seen with Abs against GFP, G α o, and α -tubulin (H).
(I and J) G α o activates Rab3a but not Arf1 in N2a cells. Recombinant GST-Rim2 and GST-CCA3 were used to pull down activated GFP-Rab3a and Arf1-GFP, respectively (I). Abs against GFP and G α o used for detection. Quantification of Rab3a and Arf1 pulled-down (J).
(K and L) Pull-downs from N2a cells transfected with G α o-GST and GFP-fusions of Rab1a, Rab3a, and α GDI. Abs against GFP and G α o were used for detection (K). Quantification of Rab1a and Rab3a pulled down in the presence or absence of α GDI (L).
(M) Representative western blots for the G α o-Rab1a/Rab3a- α GDI complex formation in vitro. Purified GST- α GDI and His₆-tagged Rab1a or Rab3a were pre-assembled and immobilized on glutathione beads (in duplicate) to assess the interaction with His₆-G α o. GST- α GDI alone was used as control.
(N) Co-localization of G α o-mRFP with KDELR-GFP (top) and KDELR^{D/N} (bottom) in N2a cells. Boxed regions are magnified. Scale bar, 10 μ m.
(O) Pull-down assay from N2a cells transfected with G α o-GST and KDELR-GFP or KDELR^{D/N}-GFP. Abs against GFP and G α o used for detection. Data represent mean \pm SEM. ns, not significant; *p \leq 0.01, **p \leq 0.005, ***p \leq 0.001. Scale bars, 10 μ m.
See also Figures S5 and S6.



(legend on next page)

can activate endogenous Rab3 at Golgi, which results in recruitment of GFP-Rim2 to this compartment.

Overall, these results speak for Rab1 and Rab3 being direct binding partners of $G\alpha$. Further, $G\alpha$ can activate these small GTPases *in vivo*, resulting in enhanced Golgi-derived vesicular transport, necessary for the stabilization and elongation of membrane protrusions.

$G\alpha$ Interacts with the α GDI-Complexed Rab1/3 at Golgi

We hypothesized that $G\alpha$ might act as a GDI displacement factor, “handing over” Rabs from GDI to a bona fide GEF localized to the Golgi. To test this, we co-overexpressed Rab- α GDI—efficient GDI for both Rab1 and Rab3 (Yang et al., 1994)—together with $G\alpha$ and GFP-Rab1a/3a. Surprisingly, we found α GDI to promote $G\alpha$ -Rab1a/3a interactions (Figures 5K and 5L). $G\alpha$ also pulled down α GDI without co-expression of any Rab (Figure S5G); this interaction is likely mediated by endogenous Rabs as recombinant $G\alpha$ and α GDI did not directly interact (Figure 5M). In order to test if $G\alpha$ is able to directly interact with Rab/ α GDI complexes, we purified Rab1a and Rab3a using the baculovirus expression system preserving post-translational prenylation of Rabs, crucial for their interaction with GDIs (Maltese et al., 1996). As expected, prenylated Rab1a/Rab3a were also able to interact with $G\alpha$ (Figure S5H) but are not activated by $G\alpha$ *in vitro* (Figures S5I and S5J). Notably, we also succeeded in reconstitution of the $G\alpha$ -Rab1/3- α GDI complexes *in vitro* (Figure 5M). Cumulatively, these data indicate that multimeric $G\alpha$ -Rab1/3- α GDI complexes may exist at Golgi.

Stimulation of KDELR Activates $\beta\gamma$ -free $G\alpha$ at Golgi

We next investigated how $G\alpha$ activation at Golgi is organized, considering two possibilities: translocation of active $G\alpha$ from PM to Golgi post-activation by GPCRs versus the independent activation of $G\alpha$ at Golgi. It was suggested that $G\beta\gamma$ heterodimers, but not $G\alpha$ -subunits, could translocate from PM to Golgi after GPCR activation (Akgoz et al., 2004). Despite poor expression (Figures S6A and S6B), the $G\alpha^{\text{Gly92}}$ -GFP construct used in those previous experiments revealed the dual PM and Golgi

localization similar to our GFP-tagged $G\alpha$ construct (Figure S6C). We then applied 3 different means of $G\alpha$ activation at PM: co-transfection with muscarinic acetylcholine receptor 2 used in previous translocation studies (Akgoz et al., 2004) or with neuronal cannabinoid receptor type-1, followed by stimulation with acetylcholine or HU-210, respectively. Alternatively, we used the Gi/o-activating peptide mastoparan (Higashijima et al., 1988). In agreement with prior work (Akgoz et al., 2004), none of these treatments increased the perinuclear fluorescence of $G\alpha$ -GFP or $G\alpha^{\text{Gly92}}$ -GFP (Figures S6D–S6I), confirming that $G\alpha$ is not translocated from PM to Golgi upon activation.

Thus, $G\alpha$ is a resident of Golgi and must be activated at this compartment. A GPCR-like activity of KDELR has been implicated in activation of the Golgi pool of $G\alpha_q$ and $G\alpha_s$, which in turn regulate anterograde and retrograde trafficking, respectively (Cancino et al., 2014; Giannotta et al., 2012). KDELR is abundantly localized to Golgi, where it is constantly activated by the C-terminal KDEL sequence of chaperones delivering cargo from ER. A dominant-negative D193N mutant (KDELR^{D/N}) can bind the KDEL peptide but does not recycle to ER and cannot activate $G\alpha_q/G\alpha_s$ (Cancino et al., 2014; Giannotta et al., 2012; Townsley et al., 1993).

We found that KDELR-GFP co-localized with $G\alpha$ -mRFP at Golgi (Figure 5N) and was efficiently pulled down by $G\alpha$ -GST (Figure 5O) from N2a cells. Similarly, d $G\alpha$ and dKDELR co-localize at Golgi stacks in *Drosophila* S2 cells (Figure 6A). We generated a transgenic *Drosophila* line for *in vivo* overexpression of dKDELR (Figure S6J). Co-expression with dKDELR strongly enhanced the d $G\alpha$ -induced mwh phenotype in *Drosophila* wings, while the single overexpression of dKDELR produced no PCP phenotype (Figures 6B and 6C), demonstrating that d $G\alpha$ synergistically interacts with dKDELR *in vivo*. Together, these data show that $G\alpha$ and KDELR physically and functionally interact in an evolutionary conserved manner.

To test whether KDELR may possess a GEF activity toward $G\alpha$, we employed the GTP-Eu loading assay in saponin-permeabilized HeLa cells (Koval and Katanaev, 2011). We found that expression of $G\alpha$ renders them responsive to the external stimulation with a KDEL-containing synthetic peptide (Figure 6D).

Figure 6. Evolutionary Conserved Interaction of $G\alpha$ and KDELR

(A) Golgi co-localization of d $G\alpha$ -GFP with dKDELR-mRFP (top) and dKDELR^{D/N}-mRFP (bottom) in S2 cells stained against GMAP-210. Selected areas magnified to the right. Scale bar, 5 μ m.
 (B and C) d $G\alpha$ interacts *in vivo* with dKDELR seen by the enhancement of the mwh phenotype in *Drosophila* wings (red ovals; B). Quantification of mwh numbers (C).
 (D) Quantification of the GTP-Eu loading in saponin-permeabilized HeLa cells mock-transfected (control) or co-expressing $G\alpha$ with GFP-fusions of the Golgi marker GalT, KDELR, or KDELR^{D/N}.
 (E–G) Stimulation of KDELR activates $G\alpha$ in N2a cells (E). ssBFP^{KDEL} but not control ssBFP stimulates endogenous KDELR. Activated $G\alpha$ is detected by Abs against $G\alpha$ -GTP. Marked regions are zoomed-in. Mean fluorescence intensity ratios of active versus total $G\alpha$ calculated at the PM and Golgi (F) and of total $G\alpha$ -GFP at the Golgi versus PM (G). Scale bar, 10 μ m.
 (H) In N2a cells, $G\alpha$ -BFP strongly co-localizes with mRFP-G β 1 and GFP-G γ 3 at PM but not at Golgi. Marked region is magnified. Scale bar, 10 μ m.
 (I) Pull-downs from N2a cells transfected with $G\alpha$ -GST (left) or GST-G β 1 (right) and different combinations of KDELR-GFP, GFP-G β 1, GFP-G γ 3, and $G\alpha$ -GFP. Abs against GFP and GST used for detection.
 (J–M) Neurite outgrowth in N2a cells co-expressing $G\alpha$ -GFP with KDELR- or KDELR^{D/N}-GFP (J). Quantification of neurite linked parameters (K–M). Scale bar, 20 μ m.
 (N–Q) Development of protrusions in S2 cells co-expressing d $G\alpha$ -GFP with dKDELR- or dKDELR^{D/N}-mRFP (N). Quantification of protrusion related parameters (O–Q). Scale bar, 5 μ m.
 Data represent mean \pm SEM. Numbers in columns represent sample sizes. ns, not significant; **p \leq 0.005, ***p \leq 0.001. See also Figures S4, S6, and S7.

Co-expression of the D/N, but not WT KDELRL, blocked the KDEL-peptide-mediated activation of $G\alpha_o$ (Figure 6D).

We next tested where KDELRL activates $G\alpha_o$, using an antibody specific for the GTP-bound form of $G\alpha_o$ (Figures S6K and S6L). We generated a secretable BFP construct carrying a C-terminal KDEL signal (ssBFP^{KDEL}) that acts as a long-lasting KDELRL ligand (Figures S6M–S6O) (Pulvirenti et al., 2008). N2a cells were co-transfected with $G\alpha_o$ -GFP and ssBFP^{KDEL} or a control (ssBFP). The anti- $G\alpha_o$ -GTP staining and GFP-fluorescence were used to estimate the GTP-loading of $G\alpha_o$ relative to its total protein level at PM versus Golgi. We found that ssBFP^{KDEL} significantly increased the $G\alpha_o$ -GTP/ $G\alpha_o$ -total ratio at Golgi but not PM without changing the $G\alpha_o$ Golgi/PM distribution (Figures 6E–6G), proving that stimulation of endogenous KDELRL induced activation of $G\alpha_o$ at Golgi. Furthermore, KDELRL overexpression (known to induce its self-stimulation) (Hsu et al., 1992) also activated the Golgi $G\alpha_o$ (Figures S7A and S7B).

Although GPCRs act on heterotrimeric $G\alpha\beta\gamma$ proteins, we found no Golgi localization of the ubiquitous $G\beta_1$ -subunit (endogenous nor overexpressed) in $G\alpha_o$ -expressing N2a cells (Figure S7C). Even the triple co-expression of $G\alpha_o$, $G\beta_1$, and the neuronal $G\gamma_3$ (the complex previously reported to exist in Golgi) (Ajith Karunaratne et al., 2012) revealed essentially no localization of $G\beta\gamma$ to the Golgi enriched in $G\alpha_o$ in N2a cells (Figure 6H). We next performed pull-downs using GST- $G\alpha_o$ or GST- $G\beta_1$ from cells expressing GFP-fusions of KDELRL, $G\gamma_3$, and $G\beta_1$ or $G\alpha_o$. As expected, $G\alpha_o$ -GST efficiently precipitated not only KDELRL-GFP but also GFP- $G\beta_1$ and GFP- $G\gamma_3$ (Figure 6I). On the other hand, GST- $G\beta_1$ effectively pulled down $G\alpha_o$ and $G\gamma_3$ whereas binding with KDELRL was totally absent (Figure 6I). Together, these experiments suggest that uniquely for GPCRs, KDELRL interacts with and activates $\beta\gamma$ -free $G\alpha_o$ rather than a heterotrimeric $G\alpha_o\beta\gamma$ complex.

Next, we analyzed if the KDELRL \rightarrow $G\alpha_o$ activation influences neuritogenesis. We co-transfected N2a cells with both proteins and quantified the neurite outgrowth. We additionally used KDELRL^{D/N}, which did not affect $G\alpha_o$ localization (Figure 5N) and interacted as efficiently as the WT with $G\alpha_o$ -GST (Figure 5O). The sole expression of KDELRL did not induce neurite outgrowth, and co-expression of $G\alpha_o$ with the WT or D/N mutant of KDELRL did not change the percentage of cells forming neurites (Figures 6J and 6K). Yet, co-expression of WT KDELRL increased 3-fold the total neurite length accompanied by mild augmentation in neurite numbers (Figures 6J–6M) without varying $G\alpha_o$ protein levels (Figures S7D and S7E). Conversely, co-expression with KDELRL^{D/N} did not affect neurite number and length (Figures 6J–6M), implying that this mutant is unable to potentiate $G\alpha_o$ functions.

Similarly, dKDELRL co-expression increased the length and number of d $G\alpha_o$ -induced protrusions in *Drosophila* S2 cells (Figures 6N–6Q), whereas the sole expression of dKDELRL had no effect (Figures S4E and S4F). On the other hand, dKDELRL^{D/N} reduced both the length and number of protrusions induced by d $G\alpha_o$ (Figures 6N–6Q), without impact on d $G\alpha_o$ localization and expression (Figures 6A, S4G, and S4H). Regarding the KDELRL^{D/N} mutant, we provide evidence in three different cell types, in two of which it behaves dominant negatively (HeLa and S2) (Figures 6D and 6N–6Q) and in one, just negatively (N2a) (Figures 6J–6M). We suspect that the negative activity of

this form of KDELRL becomes dominant depending on the cell type and/or relative expression levels.

Thus, KDELRL emerges as an evolutionary conserved activator of the $\beta\gamma$ -free Golgi pool of $G\alpha_o$ required for the elongation of cellular protrusions.

KDELRL Acts on a Multiprotein Complex Containing $G\alpha_o$ and α GDI-Rab Complexes

As $G\alpha_o$ interacts with the α GDI-Rab1a/Rab3a pair, we wondered whether this pair might be present at the KDELRL- $G\alpha_o$ complexes instead of $G\beta\gamma$. Indeed, we found that the pull-down of α GDI (and by inference of α GDI-Rab complexes) is increased by several folds upon KDELRL overexpression (Figures 7A and 7B), although KDELRL does not interact with α GDI (Figure S5G) nor Rabs (Figure S2E) in the absence of $G\alpha_o$. Thus, we infer formation of multi-subunit assemblies containing KDELRL, $G\alpha_o$, α GDI, and Rabs at Golgi.

Next, we tested the reaction of these assemblies to KDELRL activation. We showed above that it results in the nucleotide exchange on $G\alpha_o$, as seen for other GPCRs. To continue this parallel, we find that KDELRL activation with ssBFP^{KDEL} dissociates $G\alpha_o$ from the receptor (Figures 7C and 7D). In further resemblance to the heterotrimeric G protein activation by GPCRs whereas the $G\beta\gamma$ dissociates from $G\alpha$, we find that the interaction of $G\alpha_o$ with α GDI (Figures 7A and 7B) and Rab1a/Rab3a (Figures 7E–7H) is strongly diminished upon KDELRL activation.

$G\alpha_o$ does not act as a GEF for Rab1a/Rab3a (Figures S5I and S5J). Further, nucleotide exchange on the small G proteins is not a prerequisite for the KDELRL-induced dissociation of Rab1a/Rab3a from $G\alpha_o$, as the Rab1aDN and Rab3aDN mutant forms incapable of GTP-loading are also dissociated from $G\alpha_o$ upon KDELRL activation (Figures 7E–7H). These findings imply an involvement of a bona fide Rab GEF localized to Golgi in the final step of Rab activation upon the release of Rabs from $G\alpha_o$. The interaction between $G\alpha_o$ and Rabs, dissociated by KDELRL activation, is a prerequisite for this final step.

To test if KDELRL activation indeed results in Golgi Rab activation, we took the BE(2)C cells naturally expressing $G\alpha_o$, stimulated endogenous KDELRL by expression of ssBFP^{KDEL}, and monitored Rab1 activation by the Golgi enrichment of FAPP1-PH-GFP (Figures 5F–5H). We indeed found that KDELRL stimulation leads to activation of Rab1 on Golgi (Figures 7I and 7J). This phenomenon is critically $G\alpha_o$ -dependent, as removal of $G\alpha_o$ by shRNA completely blocks activation of Rab1 by KDLER, and re-expression of $G\alpha_o$ rescues this block (Figures 7I and 7J).

Our work discovers a mechanism of KDELRL-induced activation of $G\alpha_o$ and Rab GTPases at Golgi needed to speed up material delivery to the growing cellular protrusions. The overall sequence of events starting from activation of KDELRL by the arrival of the KDEL-containing chaperones accompanying the ER-delivered cargos and leading, in the $G\alpha_o$ -dependent manner, to activation of Rabs, is schematized in Figure 7K and is further detailed in the Discussion.

DISCUSSION

Intracellular signaling pathways currently emerge more as dynamic networks of protein interactions rather than linear cascades

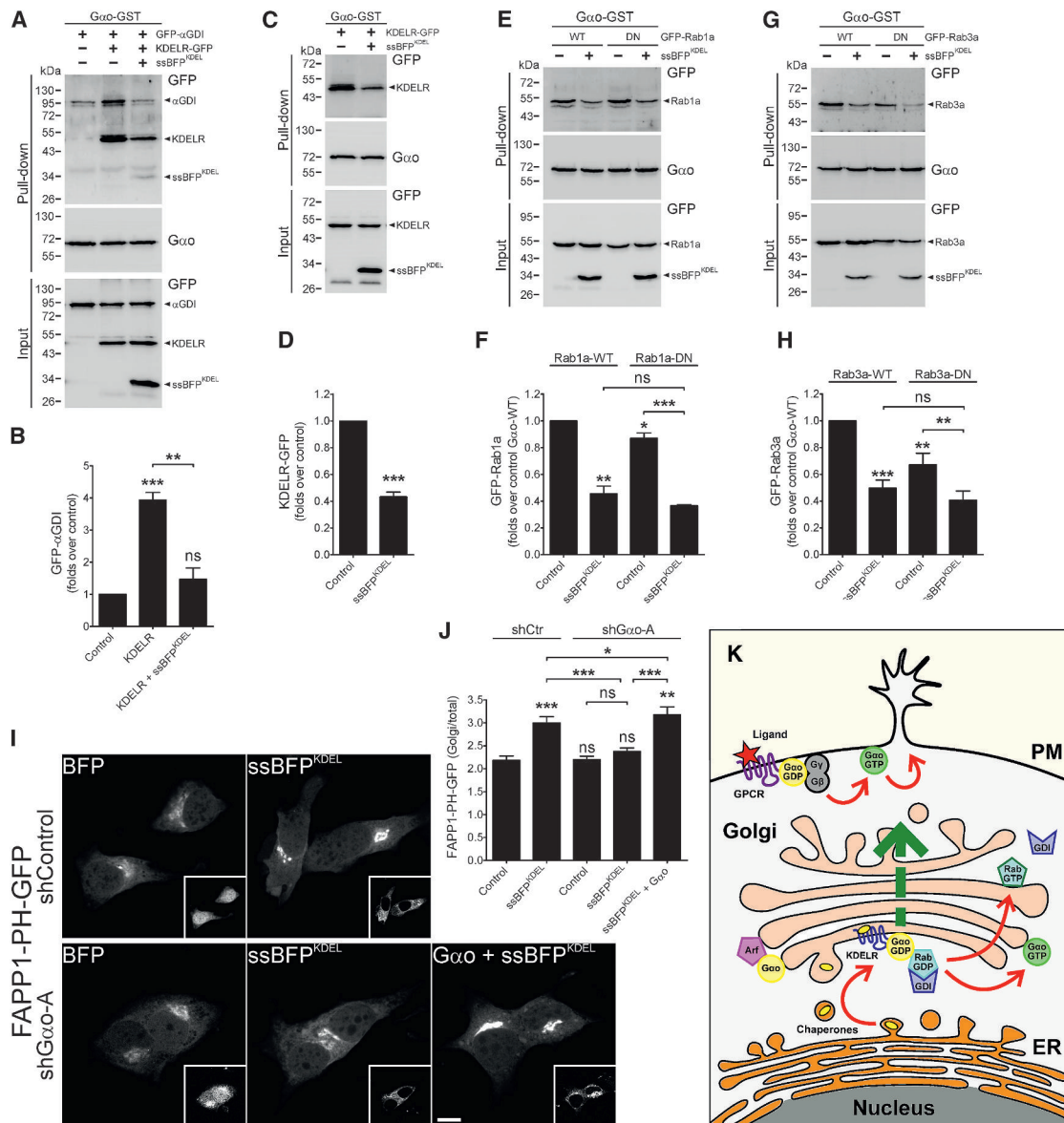


Figure 7. $G\alpha o$ Links KDEL R Signaling to Rab GTPases

(A and B) Pull-downs from N2a cells transfected with $G\alpha o$ -GST and combinations of GFP- α GDI, KDEL R-GFP and ssBFP^{KDEL}. Abs against GFP and $G\alpha o$ used for detection (A). Quantification of α GDI pulled down (B). (C and D) Effect of the co-expression of ssBFP^{KDEL} on $G\alpha o$ -GST pull-down of KDEL R-GFP in N2a cells. Abs against GFP and $G\alpha o$ used for detection (C). Quantification of KDEL R pulled down (D). (E–H) Pull-downs from N2a cells co-expressing $G\alpha o$ -GST and combinations of ssBFP^{KDEL}, GFP-Rab1a WT or DN (E), and GFP-Rab3a WT or DN (G). Abs against GFP and $G\alpha o$ used for detection (E and G). Quantification of Rab1a (F) and Rab3a (H) pulled down by $G\alpha o$. (I and J) $G\alpha o$ downregulation affects Golgi accumulation of FAPP1-PH-GFP in BE(2)C cells (I). Stimulation of endogenous KDEL R by ssBFP^{KDEL} but not ssBFP (squares at right bottom corners) increased Golgi recruitment of FAPP1-PH-GFP in control (shControl) cells, but not in $G\alpha o$ -depleted (sh $G\alpha o$ -A) cells. Re-expression of $G\alpha o$ (not shown) rescued this phenotype. Mean fluorescence intensity ratios of FAPP1-PH-GFP at the Golgi versus total cell (J). Scale bar, 10 μ m. (K) Model of $G\alpha o$ cooperative functions at the PM and Golgi apparatus required for protrusion outgrowth. Data represent mean \pm SEM. ns, not significant; * $p \leq 0.01$, ** $p \leq 0.005$, *** $p \leq 0.001$.

of activation/inactivation reactions. In this regard, thorough elucidation of the interaction targets of heterotrimeric G proteins—the immediate transducers of GPCRs—is of crucial importance to advance the understanding of this type of signal transduction. It

is especially true for $G\alpha o$. Being the most abundant G protein in the nervous system and controlling multiple evolutionary conserved developmental, physiologic, and pathologic programs, it has been remarkably shy in revealing its signaling

partners. Here, we disclose results of our multiple overlapping screens, identifying > 250 interaction partners of $G\alpha$. Each of the screens performed has its inherent advantages and limitations (Beltrao et al., 2012), and by complementation, we expect to have reached a near complete coverage of the $G\alpha$ interactome—an endeavor rarely performed for a signaling protein. Cherry-picking of individual proteins from this network resulted in detailed descriptions of mechanisms of $G\alpha$ -controlled regulation of Wnt/Fz signaling, synapse formation, PCP, asymmetric cell divisions, endocytic regulation, etc. (Egger-Adam and Katanaev, 2010; Kopein and Katanaev, 2009; Lin and Katanaev, 2013; Lin et al., 2014; Luchtenborg et al., 2014; Purvanov et al., 2010), validating the interactome findings.

As opposed to characterizations of selected individual $G\alpha$ partners, we now aimed at identifying functional modules within the interactome. For this, we performed bioinformatics analysis clustering the individual components by their functions. This resulted in appearance of several major cellular activities, which now emerge to be regulated by $G\alpha$ -dependent GPCR signaling. We selected one of them, vesicular trafficking, for detailed investigation. Many important components of this cellular function, both endocytic and exocytic, are found among $G\alpha$ targets. We previously characterized interaction of $G\alpha$ and the endocytic master regulator Rab5, important for GPCR internalization and signaling (Purvanov et al., 2010). Now, we focus more on the exocytic function of $G\alpha$. In various cell types (neuronal, epithelial, mesenchymal) of different animal groups (insect and mammalian) we now find a dual localization of $G\alpha$ to Golgi and PM, and we find the coordinated action of the two pools in exocytosis and formation of various types of cellular protrusions. We further uncover the evolutionary conserved KDEL → $G\alpha$ → Rab1/Rab3 pathway at Golgi, required for stimulated material delivery to PM and the growing protrusions.

KDEL is a Golgi-residing GPCR-like receptor, activated by the cargo delivery from ER and regulating both anterograde and retrograde trafficking from Golgi (Cancino et al., 2014; Giannotta et al., 2012; Townsley et al., 1993). Here, we show that from *Drosophila* to mammals, KDEL binds $G\alpha$ and activates it, potentiating $G\alpha$ -induced cellular responses. Intriguingly, we show that it is the $\beta\gamma$ -free form of $G\alpha$, which is the binding and activation partner of KDEL—in a sharp contrast to the action of typical PM-localized GPCRs that act on heterotrimeric $G\alpha\beta\gamma$ complexes. We further find that KDEL and $G\alpha$ form a multi-subunit complex, additionally containing Rab1/Rab3 GTPases and α GDI. Activation of KDEL results in the nucleotide exchange on $G\alpha$ and its dissociation from KDEL. Although recombinant Rabs interact stronger with the GTP-loaded $G\alpha$ in vitro in absence of α GDI, in cells we find that activation of $G\alpha$ leads to dissociation of the Rab1/Rab3- α GDI complexes, ultimately resulting in activation of the small GTPases and stimulated anterograde material delivery, necessary for the growth and stabilization of cellular protrusions. Activation of KDEL is known to induce formation of multicomponent aggregates recruiting a number of additional proteins (Majoul et al., 2001); recruitment of Rab-GEFs to these complexes to mediate ultimate activation of Rab1/Rab3 is also conceivable but will require further investigation. Importantly, the Golgi pool of $G\alpha$ plays key

roles in these processes, as the anterograde transport as well as KDEL-mediated Rab1 activation are inhibited upon depletion of $G\alpha$.

Based on the data presented here, a model emerges whereas specific $G\alpha$ pools at PM and Golgi play different but cooperative roles during neuritogenesis and protrusion formation in general. At PM, $G\alpha$ initiates neurite formation regulating actin and microtubule cytoskeletons (Bromberg et al., 2008; Luchtenborg et al., 2014) in response to activation by specific GPCRs. At Golgi, the atypical GPCR KDEL induces activation of $\beta\gamma$ -free $G\alpha$, which subsequently activates Rab1 and Rab3, and the combined action of these proteins potentiates the PM-directed trafficking required for elongation and stability of membrane protrusions (Figure 7K). Being conserved from *Drosophila* to mammals, this molecular mechanism is of basic importance for the understanding of G protein functions in development, physiology, and disease.

STAR★METHODS

Detailed methods are provided in the online version of this paper and include the following:

- KEY RESOURCES TABLE
- CONTACT FOR REAGENT AND RESOURCE SHARING
- EXPERIMENTAL MODEL AND SUBJECT DETAILS
 - *Drosophila* Stocks
 - Cell lines and culture conditions
- METHOD DETAILS
 - Screens
 - Bioinformatics analysis
 - Permanently-transfected BE(2) cells
 - Plasmids and molecular cloning
 - Immunofluorescence and microscopy
 - Neurite outgrowth assay
 - Protrusion formation assay in S2 cells
 - Biochemical analyses
 - GST-based pull-down
 - Pull-down of GTP-loaded Rab3a and Arf1
 - In vitro binding assay
 - Baculovirus protein expression and analysis
 - VSVG transport assay
 - Reverse dimerization assay
 - Quantification of Golgi area
 - Golgi accumulation of FAPP1-PH-GFP and GFP-Rim2
 - Europium-labeled GTP assay
 - Activation of $G\alpha$ by KDEL
 - RT-PCR
 - Live imaging
 - Analysis of *Drosophila* tissues
- QUANTIFICATION AND STATISTICAL ANALYSIS
- DATA AND SOFTWARE AVAILABILITY

SUPPLEMENTAL INFORMATION

Supplemental Information includes seven figures, three tables, and five movies and can be found with this article online at <http://dx.doi.org/10.1016/j.cell.2017.07.015>.

AUTHOR CONTRIBUTIONS

G.P.S., O.B., A.-M.L., C.L., and A.K. performed experiments. G.P.S. and V.L.K. designed the work and wrote the paper.

ACKNOWLEDGMENTS

We thank Alina Titova, Anke Ruedel, Birgit Gogol, Nadine Woessner, and Diane Egger-Adam for technical help in genetic screens, Pablo Serrano de Toro and Anne-Lise Maury Fraering for technical assistance, Valerie Franzen in cloning small GTPase mutants, Dmitry Ivankov and Natalya Bogatyreva for discussions on bioinformatics analysis, and Andrew Tomlinson for comments on the manuscript. This work was funded by Deutsche Forschungsgemeinschaft (SFB-TR11) and the Swiss National Science Foundation (31003A_138350 and 31003A_156762) to V.L.K.

Received: May 12, 2016

Revised: May 30, 2017

Accepted: July 13, 2017

Published: August 10, 2017; corrected online: August 24, 2017

REFERENCES

- Ajith Karunaratne, W.K., O'Neill, P.R., Martinez-Espinosa, P.L., Kalyanaraman, V., and Gautam, N. (2012). All G protein $\beta\gamma$ complexes are capable of translocation on receptor activation. *Biochem. Biophys. Res. Commun.* **421**, 605–611.
- Akgoz, M., Kalyanaraman, V., and Gautam, N. (2004). Receptor-mediated reversible translocation of the G protein betagamma complex from the plasma membrane to the Golgi complex. *J. Biol. Chem.* **279**, 51541–51544.
- Balla, A., Tuymetova, G., Tsiomenko, A., Várnai, P., and Balla, T. (2005). A plasma membrane pool of phosphatidylinositol 4-phosphate is generated by phosphatidylinositol 4-kinase type-III alpha: studies with the PH domains of the oxysterol binding protein and FAPP1. *Mol. Biol. Cell* **16**, 1282–1295.
- Beemiller, P., Hoppe, A.D., and Swanson, J.A. (2006). A phosphatidylinositol-3-kinase-dependent signal transition regulates ARF1 and ARF6 during Fc γ receptor-mediated phagocytosis. *PLoS Biol.* **4**, e162.
- Beltrao, P., Ryan, C., and Krogan, N.J. (2012). Comparative interaction networks: bridging genotype to phenotype. *Adv. Exp. Med. Biol.* **751**, 139–156.
- Bilousov, O., Koval, A., Keshelava, A., and Katanaev, V.L. (2014). Identification of novel elements of the *Drosophila* blisterome sheds light on potential pathological mechanisms of several human diseases. *PLoS ONE* **9**, e101133.
- Bromberg, K.D., Iyengar, R., and He, J.C. (2008). Regulation of neurite outgrowth by G(i/o) signaling pathways. *Front. Biosci.* **13**, 4544–4557.
- Cancino, J., Capalbo, A., Di Campli, A., Giannotta, M., Rizzo, R., Jung, J.E., Di Martino, R., Persico, M., Heinklein, P., Sallese, M., and Luini, A. (2014). Control systems of membrane transport at the interface between the endoplasmic reticulum and the Golgi. *Dev. Cell* **30**, 280–294.
- Choudhury, A., Dominguez, M., Puri, V., Sharma, D.K., Narita, K., Wheatley, C.L., Marks, D.L., and Pagano, R.E. (2002). Rab proteins mediate Golgi transport of caveola-internalized glycosphingolipids and correct lipid trafficking in Niemann-Pick C cells. *J. Clin. Invest.* **109**, 1541–1550.
- Chun, J., Shapovalova, Z., Dejgaard, S.Y., Presley, J.F., and Melançon, P. (2008). Characterization of class I and II ADP-ribosylation factors (Arfs) in live cells: GDP-bound class II Arfs associate with the ER-Golgi intermediate compartment independently of GBF1. *Mol. Biol. Cell* **19**, 3488–3500.
- Dascher, C., and Balch, W.E. (1994). Dominant inhibitory mutants of ARF1 block endoplasmic reticulum to Golgi transport and trigger disassembly of the Golgi apparatus. *J. Biol. Chem.* **269**, 1437–1448.
- Dell'Angelica, E.C., Puertollano, R., Mullins, C., Aguilar, R.C., Vargas, J.D., Hartnell, L.M., and Bonifacino, J.S. (2000). GGA: a family of ADP ribosylation factor-binding proteins related to adaptors and associated with the Golgi complex. *J. Cell Biol.* **149**, 81–94.
- Dumaresq-Doiron, K., Savard, M.F., Akam, S., Costantino, S., and Lefrançois, S. (2010). The phosphatidylinositol 4-kinase PI4KIIIalpha is required for the recruitment of GBF1 to Golgi membranes. *J. Cell Sci.* **123**, 2273–2280.
- Dupré, D.J., Robitaille, M., Ethier, N., Villeneuve, L.R., Mamarbachi, A.M., and Hébert, T.E. (2006). Seven transmembrane receptor core signaling complexes are assembled prior to plasma membrane trafficking. *J. Biol. Chem.* **281**, 34561–34573.
- Egger-Adam, D., and Katanaev, V.L. (2008). Trimeric G protein-dependent signaling by Frizzled receptors in animal development. *Front. Biosci.* **13**, 4740–4755.
- Egger-Adam, D., and Katanaev, V.L. (2010). The trimeric G protein Go inflicts a double impact on axin in the Wnt/frizzled signaling pathway. *Dev. Dyn.* **239**, 168–183.
- Frémion, F., Astier, M., Zaffran, S., Guillén, A., Homburger, V., and Sémériva, M. (1999). The heterotrimeric protein Go is required for the formation of heart epithelium in *Drosophila*. *J. Cell Biol.* **145**, 1063–1076.
- Fukuda, M. (2004). Alternative splicing in the first α -helical region of the Rab-binding domain of Rim regulates Rab3A binding activity: is Rim a Rab3 effector protein during evolution? *Genes Cells* **9**, 831–842.
- Giannotta, M., Ruggiero, C., Grossi, M., Cancino, J., Capitani, M., Pulvirenti, T., Consoli, G.M., Geraci, C., Fanelli, F., Luini, A., and Sallese, M. (2012). The KDEL receptor couples to G α q/11 to activate Src kinases and regulate transport through the Golgi. *EMBO J.* **31**, 2869–2881.
- Goedhart, J., von Stetten, D., Noirclerc-Savoye, M., Lelimosin, M., Joosen, L., Hink, M.A., van Weeren, L., Gadella, T.W., Jr., and Royant, A. (2012). Structure-guided evolution of cyan fluorescent proteins towards a quantum yield of 93%. *Nat. Commun.* **3**, 751.
- Gordon, D.E., Bond, L.M., Sahlender, D.A., and Peden, A.A. (2010). A targeted siRNA screen to identify SNAREs required for constitutive secretion in mammalian cells. *Traffic* **11**, 1191–1204.
- Higashijima, T., Uzu, S., Nakajima, T., and Ross, E.M. (1988). Mastoparan, a peptide toxin from wasp venom, mimics receptors by activating GTP-binding regulatory proteins (G proteins). *J. Biol. Chem.* **263**, 6491–6494.
- Hsu, V.W., Shah, N., and Klausner, R.D. (1992). A brefeldin A-like phenotype is induced by the overexpression of a human ERD-2-like protein, ELP-1. *Cell* **69**, 625–635.
- Katanaev, V.L., Ponzelli, R., Sémériva, M., and Tomlinson, A. (2005). Trimeric G protein-dependent frizzled signaling in *Drosophila*. *Cell* **120**, 111–122.
- Kondylis, V., and Rabouille, C. (2009). The Golgi apparatus: lessons from *Drosophila*. *FEBS Lett.* **583**, 3827–3838.
- Kopein, D., and Katanaev, V.L. (2009). *Drosophila* GoLoco-protein Pins is a target of Galph(o)-mediated G protein-coupled receptor signaling. *Mol. Biol. Cell* **20**, 3865–3877.
- Koval, A., and Katanaev, V.L. (2011). Wnt3a stimulation elicits G-protein-coupled receptor properties of mammalian Frizzled proteins. *Biochem. J.* **433**, 435–440.
- Koval, A., Purvanov, V., Egger-Adam, D., and Katanaev, V.L. (2011). Yellow submarine of the Wnt/Frizzled signaling: submerging from the G protein harbor to the targets. *Biochem. Pharmacol.* **82**, 1311–1319.
- Lee, E., and De Camilli, P. (2002). Dynamin at actin tails. *Proc. Natl. Acad. Sci. USA* **99**, 161–166.
- Lee, M.S., Jun, D.H., Hwang, C.I., Park, S.S., Kang, J.J., Park, H.S., Kim, J., Kim, J.H., Seo, J.S., and Park, W.Y. (2006). Selection of neural differentiation-specific genes by comparing profiles of random differentiation. *Stem Cells* **24**, 1946–1955.
- Lin, C., and Katanaev, V.L. (2013). Kermit interacts with G α , Vang, and motor proteins in *Drosophila* planar cell polarity. *PLoS ONE* **8**, e76885.
- Lin, C., Koval, A., Tishchenko, S., Gabdulkhakov, A., Tin, U., Solis, G.P., and Katanaev, V.L. (2014). Double suppression of the G α protein activity by RGS proteins. *Mol. Cell* **53**, 663–671.
- Lüchtenborg, A.M., Solis, G.P., Egger-Adam, D., Koval, A., Lin, C., Blanchard, M.G., Kellenberger, S., and Katanaev, V.L. (2014). Heterotrimeric Go protein

- links Wnt-Frizzled signaling with ankyrins to regulate the neuronal microtubule cytoskeleton. *Development* 141, 3399–3409.
- Majoul, I., Straub, M., Hell, S.W., Duden, R., and Söling, H.D. (2001). KDEL-cargo regulates interactions between proteins involved in COPI vesicle traffic: measurements in living cells using FRET. *Dev. Cell* 1, 139–153.
- Maltese, W.A., Wilson, A.L., and Erdman, R.A. (1996). Prenylation-dependent interaction of Rab proteins with GDP dissociation inhibitors. *Biochem. Soc. Trans.* 24, 703–708.
- Milligan, G., and Kostenis, E. (2006). Heterotrimeric G-proteins: a short history. *Br. J. Pharmacol.* 147(Suppl 1), S46–S55.
- Nakamura, N., Rabouille, C., Watson, R., Nilsson, T., Hui, N., Slusarewicz, P., Kreis, T.E., and Warren, G. (1995). Characterization of a cis-Golgi matrix protein, GM130. *J. Cell Biol.* 131, 1715–1726.
- Presley, J.F., Cole, N.B., Schroer, T.A., Hirschberg, K., Zaal, K.J., and Lippincott-Schwartz, J. (1997). ER-to-Golgi transport visualized in living cells. *Nature* 389, 81–85.
- Pulvirenti, T., Giannotta, M., Capestrano, M., Capitani, M., Pisanu, A., Polishchuk, R.S., San Pietro, E., Beznoussenko, G.V., Mironov, A.A., Turacchio, G., et al. (2008). A traffic-activated Golgi-based signalling circuit coordinates the secretory pathway. *Nat. Cell Biol.* 10, 912–922.
- Purvanov, V., Koval, A., and Katanaev, V.L. (2010). A direct and functional interaction between Go and Rab5 during G protein-coupled receptor signaling. *Sci. Signal.* 3, ra65.
- Romero, N., Dumur, C.I., Martinez, H., Garcia, I.A., Monetta, P., Slavin, I., Sampieri, L., Koritschoner, N., Mironov, A.A., De Matteis, M.A., and Alvarez, C. (2013). Rab1b overexpression modifies Golgi size and gene expression in HeLa cells and modulates the thyrotrophin response in thyroid cells in culture. *Mol. Biol. Cell* 24, 617–632.
- Shao, W., Wu, J., Chen, J., Lee, D.M., Tishkina, A., and Harris, T.J. (2010). A modifier screen for Bazooka/PAR-3 interacting genes in the Drosophila embryo epithelium. *PLoS ONE* 5, e9938.
- Solis, G.P., Schrock, Y., Hülsbusch, N., Wiechers, M., Plattner, H., and Stuermer, C.A. (2012). Reggies/flotillins regulate E-cadherin-mediated cell contact formation by affecting EGFR trafficking. *Mol. Biol. Cell* 23, 1812–1825.
- Sternweis, P.C., and Robishaw, J.D. (1984). Isolation of two proteins with high affinity for guanine nucleotides from membranes of bovine brain. *J. Biol. Chem.* 259, 13806–13813.
- Strittmatter, S.M., Fishman, M.C., and Zhu, X.P. (1994). Activated mutants of the alpha subunit of G(o) promote an increased number of neurites per cell. *J. Neurosci.* 14, 2327–2338.
- Subach, O.M., Cranfill, P.J., Davidson, M.W., and Verkhusa, V.V. (2011). An enhanced monomeric blue fluorescent protein with the high chemical stability of the chromophore. *PLoS ONE* 6, e28674.
- Thaler, C., Koushik, S.V., Blank, P.S., and Vogel, S.S. (2005). Quantitative multiphoton spectral imaging and its use for measuring resonance energy transfer. *Biophys. J.* 89, 2736–2749.
- Townsley, F.M., Wilson, D.W., and Pelham, H.R. (1993). Mutational analysis of the human KDEL receptor: distinct structural requirements for Golgi retention, ligand binding and retrograde transport. *EMBO J.* 12, 2821–2829.
- Wolfgang, W.J., Quan, F., Goldsmith, P., Unson, C., Spiegel, A., and Forte, M. (1990). Immunolocalization of G protein alpha-subunits in the Drosophila CNS. *J. Neurosci.* 10, 1014–1024.
- Yang, C., Slepnev, V.I., and Goud, B. (1994). Rab proteins form in vivo complexes with two isoforms of the GDP-dissociation inhibitor protein (GDI). *J. Biol. Chem.* 269, 31891–31899.

RNA Docking and Local Translation Regulate Site-Specific Axon Remodeling In Vivo

Hovy Ho-Wai Wong,¹ Julie Qiaojin Lin,^{1,3} Florian Ströhl,^{2,3} Cláudio Gouveia Roque,¹ Jean-Michel Cioni,¹ Roberta Cagnetta,¹ Benita Turner-Bridger,¹ Romain F. Laine,² William A. Harris,¹ Clemens F. Kaminski,² and Christine E. Holt^{1,4,*}

¹Department of Physiology, Development and Neuroscience, University of Cambridge, Cambridge CB2 3DY, UK

²Department of Chemical Engineering and Biotechnology, University of Cambridge, Cambridge CB3 0AS, UK

³These authors contributed equally

⁴Lead Contact

*Correspondence: ceh33@cam.ac.uk

<http://dx.doi.org/10.1016/j.neuron.2017.07.016>

SUMMARY

Nascent proteins can be positioned rapidly at precise subcellular locations by local protein synthesis (LPS) to facilitate localized growth responses. Axon arbor architecture, a major determinant of synaptic connectivity, is shaped by localized growth responses, but it is unknown whether LPS influences these responses in vivo. Using high-resolution live imaging, we examined the spatiotemporal dynamics of RNA and LPS in retinal axons during arborization in vivo. Endogenous RNA tracking reveals that RNA granules dock at sites of branch emergence and invade stabilized branches. Live translation reporter analysis reveals that de novo β -actin hotspots colocalize with docked RNA granules at the bases and tips of new branches. Inhibition of axonal β -actin mRNA translation disrupts arbor dynamics primarily by reducing new branch emergence and leads to impoverished terminal arbors. The results demonstrate a requirement for LPS in building arbor complexity and suggest a key role for pre-synaptic LPS in assembling neural circuits.

INTRODUCTION

CNS axons typically form highly branched terminal arbors in their synaptic target area. The branching complexity of an arbor defines the number and extent of post-synaptic partners a neuron can have and is a critical determinant of neural circuit assembly (Alsina et al., 2001; Meyer and Smith, 2006; Ruthazer et al., 2006). Previous studies have shown that retinal axon arbors are built in vivo through a highly dynamic process of branch extension, retraction, and stabilization (O'Rourke et al., 1994; Witte et al., 1996). Arbor size and dynamics are influenced by extrinsic stimuli, such as brain-derived neurotrophic factor (BDNF) and Netrin-1 (Cohen-Cory and Fraser, 1995; Manitt et al., 2009), and intrinsic factors, such as RNA-binding proteins (RBPs) (Hörnberg et al., 2013; Kalous et al., 2014). Branching is

fundamental to functioning neural circuits, yet, although well described in dendrites (Dong et al., 2015), relatively little is known about the molecular mechanisms underlying axonal terminal branching in vivo.

Many guidance cues that trigger local protein synthesis (LPS) in axons, such as Netrin-1, BDNF, Semaphorin 3A, and Slit2 (Campbell and Holt, 2001; Piper et al., 2006), are also axon branch regulators (Kalil and Dent, 2014), suggesting a link between LPS and axonal branching. Indeed, recent evidence shows that knock-down of specific RBPs—Vg1RBP and Hermes—reduces retinal axon terminal arborization in *Xenopus* (Hörnberg et al., 2013; Kalous et al., 2014). Conversely, downregulation of the RBP fragile X mental retardation protein (FMRP), a negative translation regulator, increases axonal branching in *Drosophila* (Pan et al., 2004) and zebrafish (Tucker et al., 2006) neurons, indicating that precise RBP-regulated mRNA translation is required for appropriate branching. These studies disrupted gene function across all neuronal compartments (soma, dendrites, and axons), however, leaving open the question of whether axonally localized LPS has a role in branching.

Culture studies have uncovered an association between axonal branching and LPS. For example, newly synthesized green fluorescent protein (GFP) puncta localize to the base of collateral spikes in cultured retinal axons (Brittis et al., 2002), and the translational machinery localizes to branch points in cultured dorsal root ganglion (DRG) neurons (Spillane et al., 2012). Moreover, axonally synthesized regulators of the actin-nucleating Arp2/3 complex are involved in nerve growth factor (NGF)-induced collateral branching (Spillane et al., 2012) and targeting β -actin mRNA to axons supports collateral branching in an injury-conditioned paradigm (Donnelly et al., 2013). Consistent with these findings, mRNAs encoding proteins associated with branching are actively translated in arborizing mouse retinal ganglion cell (RGC) axon terminals in vivo (Shigeoka et al., 2016). These findings suggest that LPS may provide a critical link between extrinsic (branch-regulating) signals and branching, but the precise spatiotemporal dynamics of mRNA and LPS and their roles in axonal branching in vivo have not been examined.

In this study, we investigated the spatiotemporal dynamics of RNA movements, LPS, and axon terminal arborization in vivo. We developed a method to visualize *endogenous* RNA granules for prolonged periods (>1 hr) in single axons in the *Xenopus*

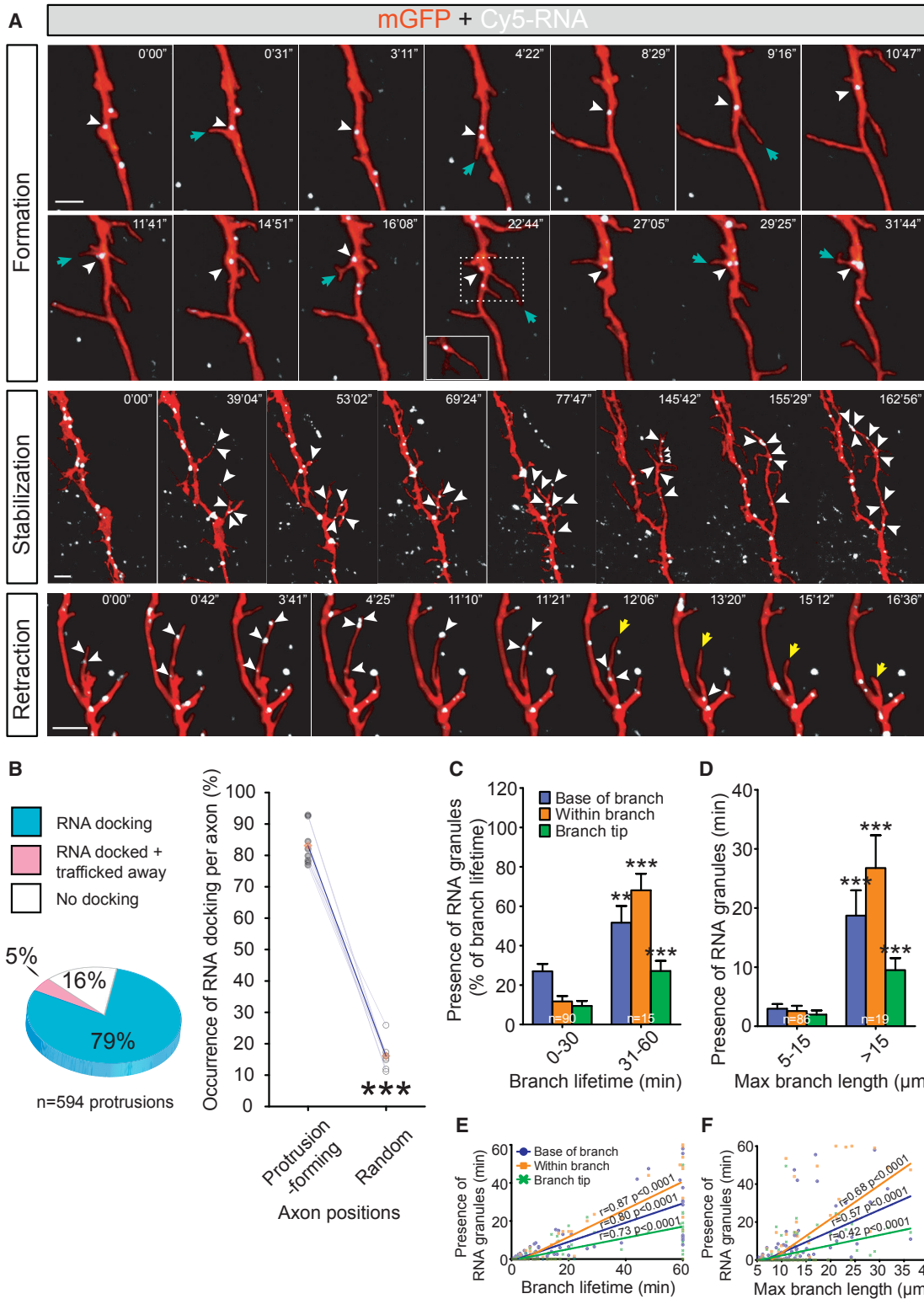


Figure 1. Dynamics of Endogenous RNA Granules Correlate with Distinct Aspects of Axon Branching In Vivo

(A) RNA granule (white arrowheads) docking in RGC axons during branching. Top: a single RNA granule docks at multiple branch point sites before the formation of protrusions (cyan arrows). The single z plane inset demonstrates localization of the RNA granule at the base of the protrusion. Middle: multiple RNA granules move into branches and to branch tips during protrusion stabilization. Bottom: branch retraction (yellow arrow) occurs shortly after RNA granules exit the branch.

(legend continued on next page)

visual system and performed live imaging to simultaneously capture arbor dynamics and RNA trafficking in vivo. Our results reveal a close relationship between arbor dynamics and RNA trafficking and show that RNA docking predicts sites of branch emergence. Live visualization of β -actin synthesis reveals the rapid accumulation of nascent β -actin in discrete “hotspots” in branches and at branch points. Functional experiments show that LPS is required for proper axon arbor formation in vivo. Knockdown of local β -actin synthesis causes a marked reduction in the emergence of new branches and results in impoverished axon terminal arbors. Collectively, the findings provide evidence of a pivotal role of LPS in determining axon arbor architecture in vivo.

RESULTS

Labeling Endogenous RNA for Live Imaging in Axons In Vivo

To label endogenous RNA, we delivered labeled uridine-5'-triphosphate (UTP) analogs, Cy5-UTP or biotin-UTP, intracellularly by eye electroporation or blastomere injection in *Xenopus* embryos. UTP analogs become incorporated into RNA during its synthesis and can then be monitored by live fluorescence imaging in putative ribonucleoproteins (RNPs) in retinal axons in vitro (Piper et al., 2015). The UTP analog was confirmed to be incorporated exclusively into RNA (including mRNA and rRNA) using qRT-PCR and bioanalyzer analysis of streptavidin/biotin-UTP pull-down following biotin-UTP blastomere injection and was not detected in genomic or mitochondrial DNA (Figures S1A–S1K). The method therefore provides an unbiased approach to label and track endogenous RNAs.

Next, we examined the general characteristics of endogenous RNA motility in RGC axon terminals in the tectum in vivo. Cy5-UTP was delivered into developing RGCs along with a membrane-targeted GFP (mGFP) reporter by targeted eye electroporation at stage 28, the beginning of RGC axonogenesis. Cy5-RNA and GFP-labeled axons were imaged in the optic tectum with time-lapse microscopy (10–20 frames/min for >1 hr) during the early phase of arborization and map formation (stages 41–43). Cy5-RNA appeared as punctate granules, often highly mobile, indicative of RNPs. We refer to these as “RNA granules.” Motile RNA granules were observed in the majority of GFP-labeled retinal axon terminals with an average density of 2.6 ± 0.29 granules/ $10 \mu\text{m}$ (Movies S1 and S2). During an average 1 min period, 59.2% of the RNA granules were mobile and moved in anterograde ($25.6\% \pm 3.4\%$) or retrograde ($27.7\% \pm 3.4\%$) directions or bi-directionally ($5.9\% \pm 2.0\%$), while $40.8\% \pm 3.9\%$ remained stationary (Figure S1L). An analysis of granule speed along the main axon shaft (excluding

branches) showed an average anterograde speed of $10.0 \pm 0.7 \mu\text{m}/\text{min}$ and retrograde speed of $11.4 \pm 1.3 \mu\text{m}/\text{min}$ (Figures S1M and S1N).

RNA Granules Dock at Sites of New Branch Emergence

We next investigated whether distinct aspects of branching, such as branch emergence and stabilization, are associated with the spatial and temporal positioning of RNA granules. New “branches” first appear as filopodial protrusions of less than $5 \mu\text{m}$ in length that emerge from the main axon shaft. Many of these are short lived, but some elongate to $>5 \mu\text{m}$ and persist. We refer to these longer structures as “branches” to distinguish them from the shorter filopodial protrusions. Motile RNA granules were often observed to pause briefly (>10 s), or “dock,” at sites of branch emergence in the axon shaft immediately preceding the appearance of a new protrusion. 84% of the filopodial protrusions exhibited docked RNA granules at their bases in the 10 s time window preceding their emergence. The docked RNA granules often persisted at the bases of filopodia during emergence, although in some cases (5%), the dwell time was transient (<10 s), and the granules moved away before the filopodia became visible (Figure 1B). Individual RNA granules occasionally exhibited repetitive docking at different sites along an axon where each dock site preceded the emergence of a new protrusion (Figure 1A; Movie S1), suggesting that specific RNA granules may be highly potent in their ability to initiate filopodial protrusions. Interestingly, while we rarely observed filopodial emergence, retraction, and re-emergence at the same sites, we often saw repeated cycles of partial retraction and extension (Movie S2) and instances of multiple filopodia emanating in different directions in 3D from the site of some docked RNA granules (green arrowheads from ~ 10 min onward in Movie S1).

To estimate what fraction of docking events lead to protrusion events, we generated 20 sets of time points and axon positions randomly for each axon ($n = 5$). The closest RNA granule to the randomized position was tracked across time to find the first instance of docking >10 s, and we then scored whether a protrusion emerges at this position within the 10 s of docking. We found that $22.0\% \pm 5.1\%$ of RNA granules displaying this docking motion were followed by protrusion emergence. To test the possibility that these correlations are meaningful and not simply coincidental, we compared how frequently RNA granules docked at random positions along the axons versus an equivalent number of *bone fide* protrusion sites. Even though some of the random positions fell indiscriminately on protrusion-forming sites, we found that RNA granules docked at just 16% of random sites, compared to 84% at protrusion sites. (Figure 1B), showing that the correlation between the site of branch initiation and RNA granule docking is not simply coincidental. Moreover, the

(B) Left: proportion of protrusions with RNA docking at the base for >10 s preceding protrusion formation. Right: occurrence of RNA docking in protrusion-forming or random positions in the same axons ($t_7 = 21.2$, $p < 0.0001$, paired t test). Red diamonds represent the averages.

(C) Time of RNA granules presence was longer in branches with longer lifetime (base of branch: $U = 369$, $p = 0.004$; within branch: $U = 137.5$, $p < 0.0001$; branch tip: $U = 225$, $p < 0.0001$).

(D) Time of RNA granules presence was longer in branches with longer maximal branch length (base of branch: $U = 240$, $p < 0.0001$; within branch: $U = 297$, $p < 0.0001$; branch tip: $U = 369$, $p < 0.0001$). Error bars represent SEM. ** $p < 0.01$, *** $p < 0.001$ (Mann-Whitney test for C and D).

(E and F) Pearson's correlation between time of RNA presence and lifetime of branch (E) or maximal branch length (F).

Scale bars, $5 \mu\text{m}$. See also Figures S1–S3.

temporal order in which these events occur (RNA docking followed by branch emergence) is consistent with a causal role of RNA granule docking in protrusion initiation.

RNA Dynamics Correlate Positively with Branch Stabilization

Previous work has shown that only a small subset of newly formed branches persist to form stabilized mature branches, while the majority are short lived and retract within 10 min (Witte et al., 1996). Therefore, we next asked whether branches with lifetimes > 30 min, which we define as “persistent,” exhibited any distinct RNA granule behavior. RNA granules were seen to invade persistent branches and often localized to their distal tips (>15 μm ; Figure 1A; Movie S2). By contrast, RNA granules were rarely observed making excursions into short-lived (<30 min) branches. Notably, RNA granules inside persistent branches often docked at sites from which a new protrusion or secondary branch emerged (arrowheads in Movie S2). The association between branch persistence and RNA invasion suggests a link between the two.

Occasionally, branches harboring RNA granules were seen to retract abruptly. Retrospective image analysis of these events showed, strikingly, that RNA granules were rapidly trafficked retrogradely out of the branch preceding retraction (yellow arrow in Figure 1A). Thus, branch formation, stabilization, and retraction appear to be closely coupled to the localization of RNA granules (Figure 1A; Movie S3).

To evaluate whether RNA localization correlates with branch lifetime and branch length, we categorized the branches into two groups on the basis of their lifetime—short lived (0–30 min) and persistent (31–60 min)—and length. The total time of the presence/absence of RNA granules at each of the three branch locations (base, tip, and intervening mid-region) was scored. RNA granules were present for significantly longer times in persistent branches compared with short-lived branches (Figure 1C). RNA granules were also present more of the time in longer branches (>15 μm) than in shorter branches (5–15 μm) (Figure 1D). In accordance with these results, we found that branch lifetime positively correlated with the duration of RNA localization at different branch positions (Figure 1E). In addition, the maximal branch length also correlated with the duration of RNA presence (Figure 1F). Thus, the spatial and temporal dynamics of RNA granules correlate with branch lifetime and length, consistent with the observation of increased RNA localization in stabilized branches.

Mitochondria Localize to Branch Points and Exhibit Parallel Behavior to RNA Granules

Mitochondria supply the energy for organelle trafficking and mRNA translation and have previously been shown to localize to branch points in axons *in vitro* (Couchet et al., 2013; Spillane et al., 2013). To visualize mitochondrial dynamics in axons *in vivo*, we introduced mitochondria-targeted GFP (mito-GFP) cDNA into RGCs by electroporation and conducted time-lapse imaging on axon arbors at stages 41–43. Mitochondria were commonly observed to accumulate at sites of axonal branch emergence (Figures S2A and S2B). They rarely entered transient branches but often moved into stabilized persistent branches (Figures

S2A and S2C–S2F). Inside the branch, they commonly remained motile moving back and forth along the length of the branch and stalled at sites of new (secondary) branch formation. Like RNA granules, mitochondria moved out of branches immediately preceding retraction (Figure S2A). Dual imaging confirmed that Cy5-UTP and mito-GFP label distinct structures (Figure S3; Movie S4) and revealed that motile RNA granules frequently visited and stopped on mitochondria, remaining juxtaposed for significant periods (>3 min), and exhibited synchronous movements indicative of close interactions. Overall, our data indicate that endogenous RNA and mitochondria dock at sites associated with axonal branching *in vivo*, and their dynamics suggest a coupling of energy supply to RNA regulation.

Translation Inhibition Disrupts Axonal Branching Dynamics *In Vivo*

RNA transport and localization is intimately linked to LPS in neuronal compartments (Aakalu et al., 2001; Cosker et al., 2016; Kim et al., 2013; Leung et al., 2006; Tatavarty et al., 2012; Wu et al., 2016). To test the functional role of LPS in axon branching *in vivo*, we first used a pharmacological approach on the exposed brain preparation. The intact larval brain was exposed by simple removal of the overlying skin epidermis and protein synthesis (PS) inhibitors (cycloheximide/CHX and anisomycin/ANI) were added to the medium. Following electroporation of fluorescent reporters in the eye optimized for single RGC labeling, the *in vivo* arborization dynamics of RGC axons were imaged in the optic tract and/or the optic tectum every 30 s over a period of 10 min (stages 41–43; Figure 2A). To confirm that the treatment effectively inhibited PS in live brains, we developed a puromycylation-based translation assay on whole-mount brains to obtain a quantitative measure of PS. Exposed brains were treated for 30 min with PS inhibitors, followed by puromycin (puro) treatment for 10 min and subsequent anti-puro immunocytochemistry in whole-mount brains. Puro mimics tRNA and, at the low concentration used, is incorporated into the C termini of polypeptide chains, releasing them from ribosomes. PS inhibitor treatment greatly reduced the puro-immuno signal, confirming the effectiveness of the PS inhibition (Figures 3B and 3C).

In the control condition, single axon arbors were highly dynamic, with an average of 50 filopodia and 8 branches added and removed in 10 min (Figure 2B; Movie S5). By contrast, in brains treated with PS inhibitors, the arbor dynamics were reduced by 40%–70% (Figures 2C–2F; Movie S5). A detailed analysis revealed that the balance of addition and retraction of protrusions was also affected. In the control condition, slightly more filopodia (52 versus 47) and branches (7.8 versus 5.3) were added than were retracted (Figure 2B). This bias leads to a small, but consistent, net increase in the number of protrusions. Interestingly, upon acute inhibition of PS, the number of protrusions being added or removed became indistinguishable, tipping the normal balance from a net increase to an equilibrium (Figures 2C and 2D). The observed deficits were not due to PS inhibition in the RGC soma as we removed the eye prior to drug treatment. Previously, it was shown that somaless RGC axons continue to navigate to the tectum and arborize in a grossly normal manner *in vivo* for up to 3 hr (Harris et al.,

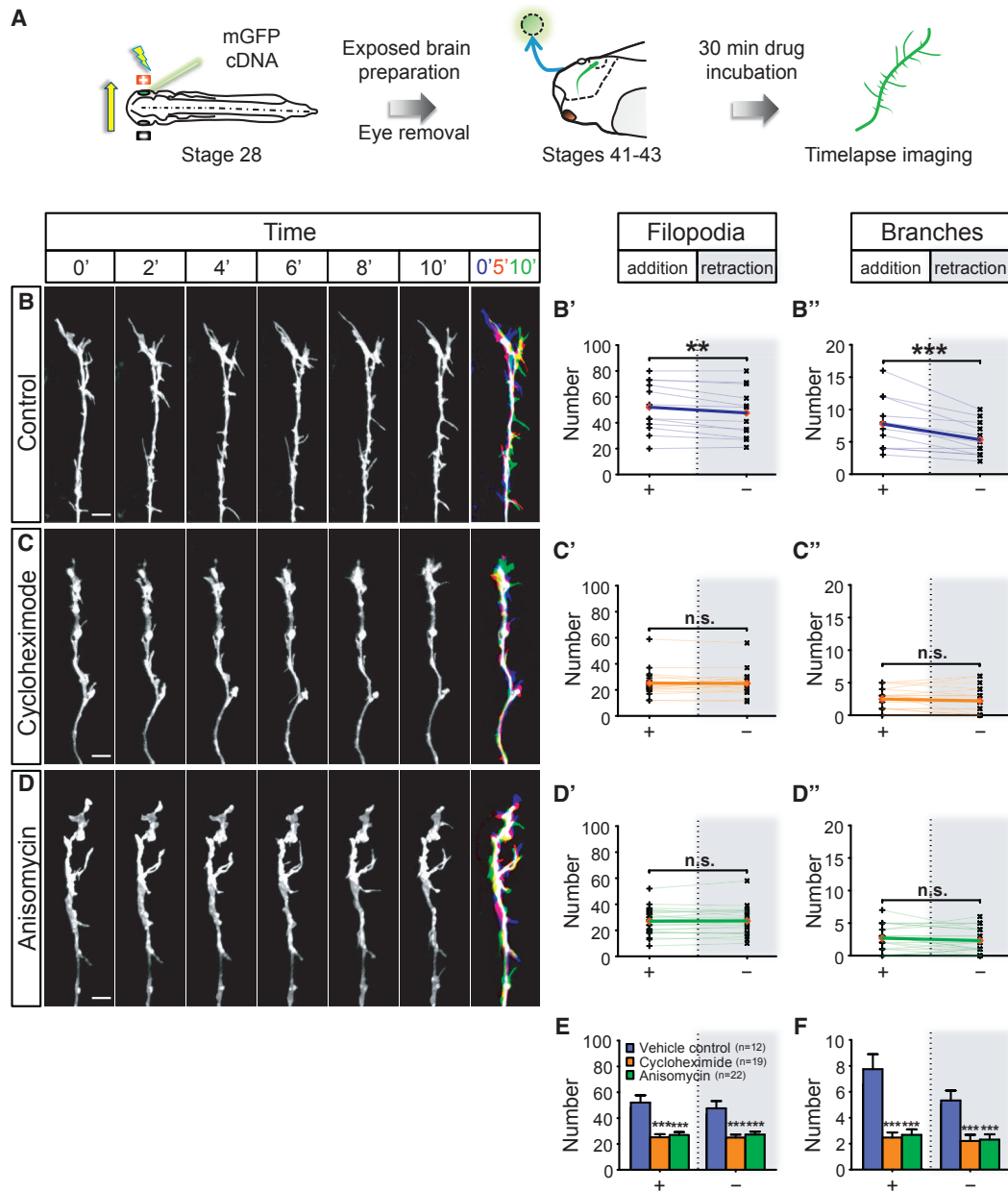


Figure 2. Acute Inhibition of Translation Disrupts Axonal Branching Dynamics In Vivo

(A) Live imaging experiment on branching dynamics of somalless RGC axons in the tectum in vivo. Electroporated eye was removed to eliminate somatic contribution.

(B–D) Axonal branching in control condition (B) and after incubation in translation inhibitors cycloheximide (C; CHX) and anisomycin (D; ANI). A merged overlay of three time points (0', 5', and 10' in blue, red, and green, respectively) is shown for each condition (far right). More protrusions were added than removed in control condition (filopodia: $t_{11} = 3.8$, $p = 0.003$; branches: $t_{11} = 4.6$, $p = 0.0008$) (B' and B''). No significant differences were observed in the number of protrusions that were added and removed in CHX condition (filopodia: $t_{18} = 0.2$, $p = 0.82$; branches: $t_{18} = 1.1$, $p = 0.29$) (C' and C''). No significant differences were observed in the number of protrusions that were added and removed in ANI condition (filopodia: $t_{21} = 0.5$, $p = 0.66$; branches: $t_{21} = 1.4$, $p = 0.18$) (D' and D'').

(E and F) The dynamics of filopodia (E; addition: $F_{2,50} = 18.7$, $p < 0.0001$; removal: $F_{2,50} = 13.0$, $p < 0.0001$) and branches (F; addition: $F_{2,50} = 20.2$, $p < 0.0001$; removal: $F_{2,50} = 9.5$, $p = 0.0003$) were inhibited by CHX or ANI treatment.

Error bars represent SEM. ** $p < 0.01$, *** $p < 0.001$ (paired t test for B–D) versus Control *** $p < 0.001$ (one-way ANOVA with Tukey multiple comparisons test for E and F). Red diamonds represent the averages (B–D). Scale bars, 5 μm . See also Figure S4.

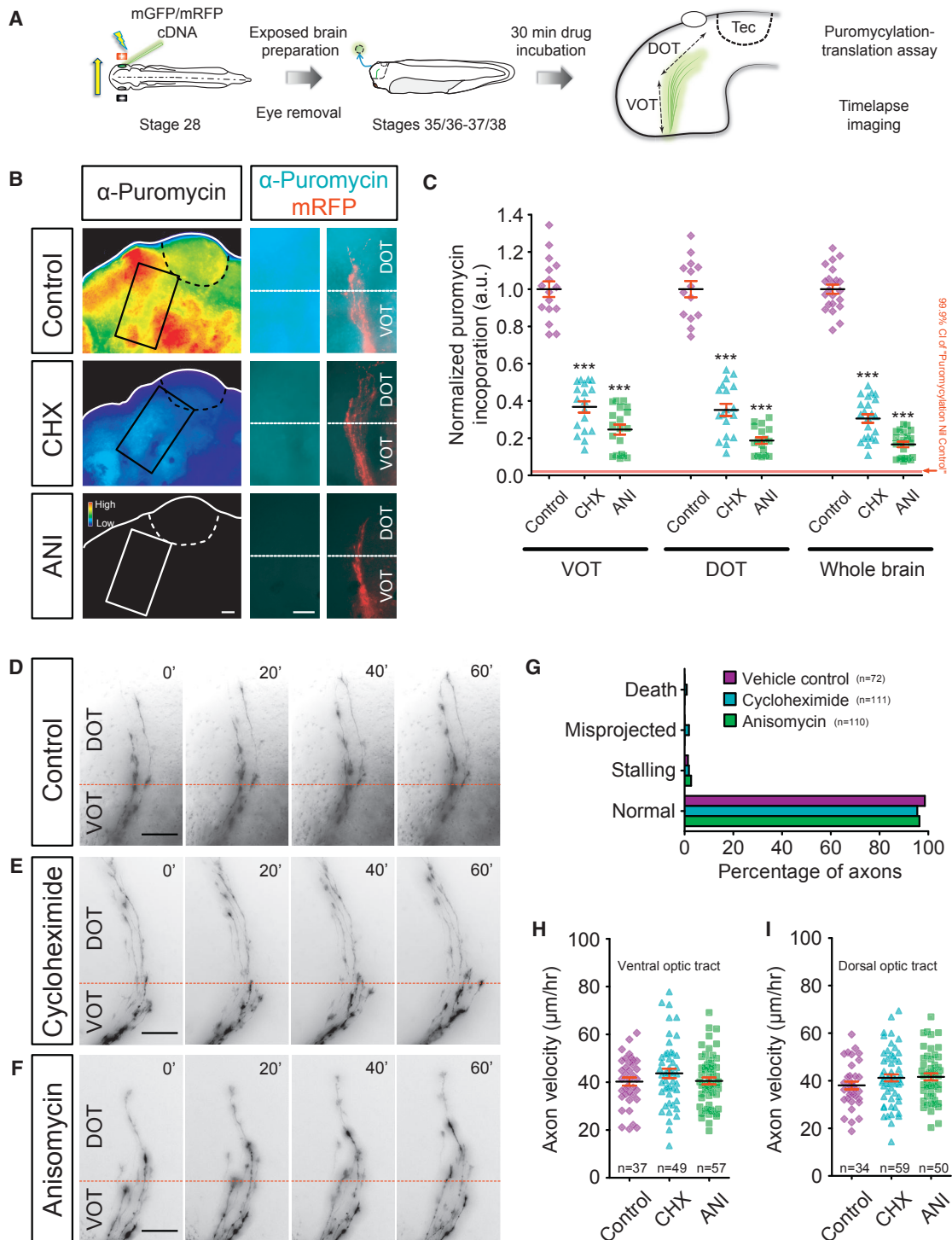


Figure 3. Axon Navigation in the Optic Tract Is Not Affected by Acute Inhibition of Translation

(A) Live imaging experiment on somaless RGC axon navigation in the optic tract *in vivo* and translation assay on whole brains. Electroporated eye was removed to eliminate somatic contribution.

(B) Anti-puromycin immunolabeling of whole-mount brains, shown as fluorescent intensity heatmaps, illustrates the incorporation of puromycin after 10 min, as readout of translation. Cycloheximide (CHX) and anisomycin (ANI) treatments greatly reduce puromycin immunolabeling.

(C) The incorporation of puromycin was reduced in the ventral optic tract (VOT) ($F_{3,67} = 204.6$, $p < 0.0001$), dorsal optic tract (DOT) ($F_{3,61} = 213.4$, $p < 0.0001$), and whole brain ($F_{3,80} = 501.9$, $p < 0.0001$) after CHX and ANI treatments.

(legend continued on next page)

1987). We extend these findings to show that within the time window of our experimental protocols (<1 hr), eye removal does not affect branching dynamics (Figure S4). These results are consistent with a possible role for LPS in axonal branching *in vivo*.

Embryos with eyes removed and treated with PS inhibitors for 30 min during the period of axon elongation in the optic tract (stages 35/36–37/38) did not exhibit abnormal pathfinding or stalling (Figure 3). Moreover, the speed of axon advance did not differ from control brains in either the ventral or the dorsal optic tract (Figures 3H and 3I). These findings indicate that acute PS inhibition does not cause gross defects in axon growth or navigation in the optic tract, whereas axonal branching is particularly sensitive to such treatment.

Knockdown of β -actin Synthesis Reduces Axon Arbor Complexity

β -actin mRNA localizes to axons (Bassell et al., 1998) and is locally translated *in vitro* in response to BDNF and Netrin-1 (Leung et al., 2006; Yao et al., 2006). These two cues are expressed in the optic tectum, and both act as key branch regulators of retinal axons in the tectum *in vivo* (Cohen-Cory and Fraser, 1995; Manitt et al., 2009). Furthermore, targeting of β -actin mRNA to injury-conditioned axons promotes branch formation *in vitro* (Donnelly et al., 2013), and the local remodeling of the actin network has been shown to regulate axonal branching *in vivo* (Chia et al., 2014). We thus focused on β -actin mRNA to further examine the role of LPS in the dynamics of axonal branching *in vivo*.

To block β -actin mRNA translation, a β -actin antisense morpholino (MO) was injected into the blastomeres fated to give rise to the CNS at the four-cell stage. This resulted in a 47% reduction in β -actin levels, in agreement with previous studies (Leung et al., 2006), and did not cause gross changes in embryogenesis (Figures S5A–S5E).

To target the β -actin knockdown to RGCs and to visualize the trajectories of single axons, we electroporated the β -actin MO together with a reporter mGFP plasmid into the eye at stage 28. At stage 45, when RGC axon arbors have reached maturity and become relatively stable, we imaged single arbors in the tectum and performed quantitative analysis. While highly complex arbors were seen in the control MO (Con MO) embryos, β -actin MO-axons exhibited much simpler arbors (Figure 4A). Quantitative branching analysis showed that the branch numbers decreased across different branch orders, leading to an overall drop of 56% (Figure 4B) and a 50% reduction of the total branch length (Figure 4C). The distribution of branches shifted toward lower branch orders in the β -actin MO condition compared to the Con MO condition, indicating that β -actin-depleted axons elaborate proportionally fewer high-order branches (Figure 4D). The axon complexity index (ACI) was used to assess the complexity of individual arbors (Figures 4E–4G), and arbors were classified as simple (ACI < 1.4) or complex

(ACI \geq 1.4). The results showed an average ACI of 1.83 for the Con MO condition that dropped dramatically to 1.38 in the β -actin MO condition. The majority of arbors (86%) in Con MO samples were in the complex category, compared to only 30% of those in the β -actin MO condition. Together, the data demonstrate that β -actin synthesis in RGCs is important for the elaboration of complex axon arbors *in vivo*.

β -actin Synthesis Promotes New Branch Emergence and Shifts Addition/Retraction Bias

The loss of arbor complexity could arise by a reduction in the emergence of new branches, a failure to stabilize new branches, or a combination of both. To understand the dynamic processes underlying axonal branching upon β -actin knockdown, we carried out live *in vivo* imaging following MO electroporation into the eye at stage 28 (Figure 4M). At stages 41–43, the dynamics of both filopodia and branches were significantly reduced after knocking down β -actin translation (Figures 4H and 4I; Movie S6). In the Con MO axons, there were, on average, 41 filopodia added and 35 retracted, while 21 filopodia were added and retracted in the β -actin MO axons (Figure 4K). For the branches, an average of 6.7 was added and 4.7 retracted in the control, compared to 1.3 and 1.5 for addition and retraction, respectively, in the β -actin MO condition (Figure 4L). Analogous to the trend observed with acute translation inhibition (Figure 2), the net increases in the control for both filopodia and branches were abolished in the β -actin knockdown (Figures 4H and 4I). To test the specificity of the β -actin MO, we electroporated an MO-insensitive β -actin construct into the eye along with the MO. The MO-insensitive β -actin was co-expressed with mGFP in a dual promoter construct to ensure that all observed GFP-positive axons also expressed the rescue construct. This rescued the branching deficits (Figures 4A–4M). Collectively, these results indicate that *de novo* synthesis of β -actin regulates axon branching dynamics in RGCs by promoting (1) the emergence of new branches and (2) a small bias in favor of branch stabilization over retraction.

Local β -actin mRNA Translation Is Autonomously Required in Axon Terminals for Branching

The above results point to a requirement for *de novo* β -actin synthesis for arborization but do not address whether the synthesis is localized to the axon because the translation-blocking MO was delivered into the cell somas in the eye. To confirm a local (axonal) effect, we delivered the MO directly into arborizing RGC axons in the tectum by electroporation at stages 41–43 (Figure 5E) and conducted live imaging immediately thereafter. In the Con MO condition, the arbors were dynamic with highly motile filopodia and branches, whereas the motility was severely reduced in the β -actin MO condition (Figures 5A–5D; Movie S7). In addition, we also recorded the expected biases in dynamics that resulted in net increases for both filopodia and branches

(D–F) Axon navigation through the VOT and DOT in control (D) and after incubation in translation inhibitors CHX (E) and ANI (F).

(G) Axon behaviors were unaffected in axons after CHX or ANI incubation (death: $p = 0.44$; misprojected: $p = 0.19$; stalling: $p = 0.80$; normal: $p = 0.47$, chi-square test).

(H and I) Axon elongation velocities were unaffected by CHX or ANI incubation (H, VOT: $F_{2,140} = 1.3$, $p = 0.29$; I, DOT: $F_{2,140} = 1.3$, $p = 0.27$).

Error bars represent SEM versus Control *** $p < 0.001$ (one-way ANOVA with Tukey multiple comparison's test for C, H, and I). Scale bars, 50 μ m.

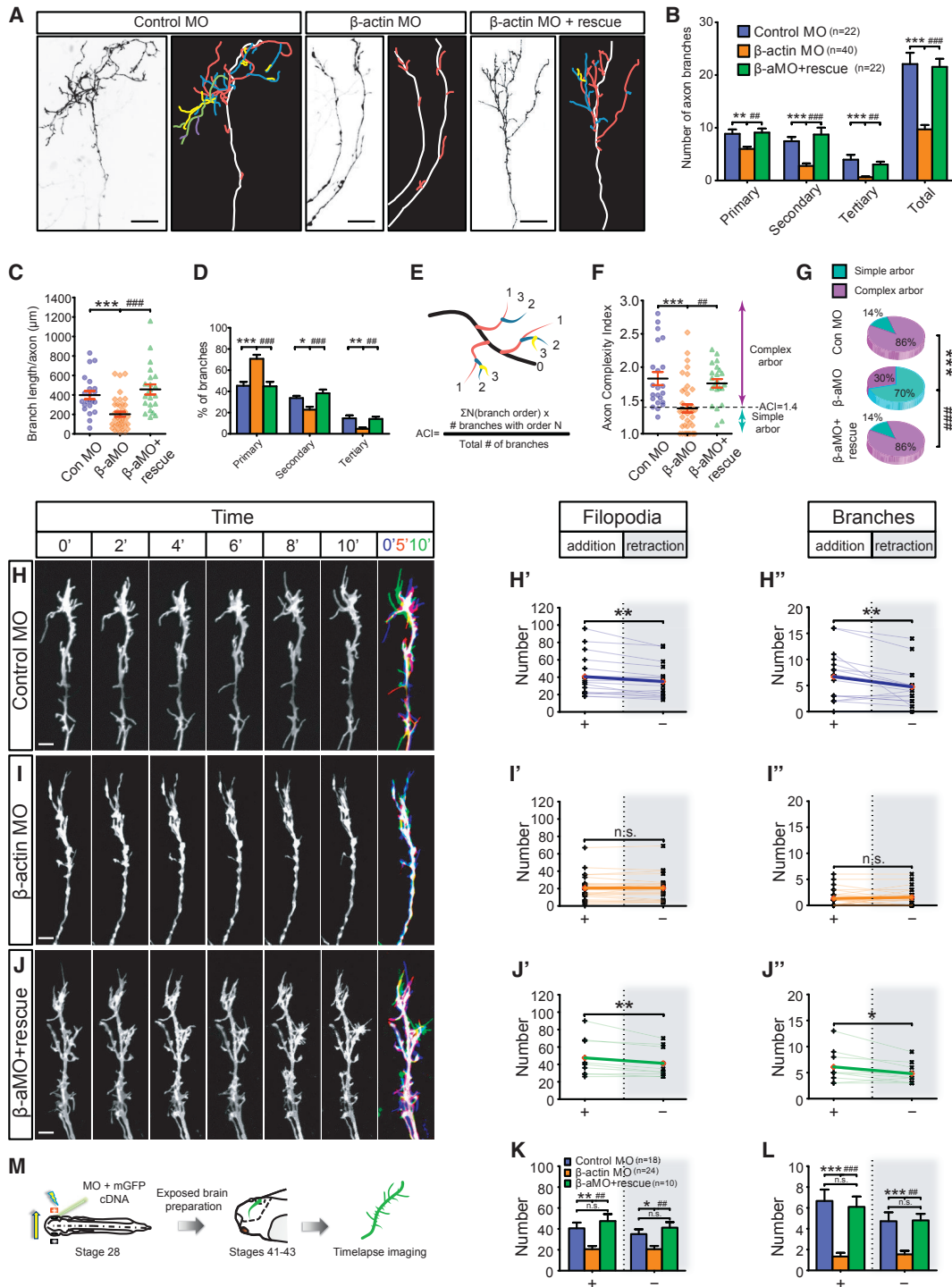


Figure 4. Knockdown of β -actin Reduces Axon Branching Dynamics and Arbor Complexity In Vivo

(A) Lateral view of single RGC axons in the tectum. Line drawings are shown with the branch order color coded: white, axon shaft; branches: red, primary; blue, secondary; yellow, tertiary; purple, quaternary.

(B) Reduction in number of branches in β -actin morphants (primary: $F_{2,81} = 8.9$, $p = 0.0003$; secondary: $F_{2,81} = 17.6$, $p < 0.0001$; tertiary: $F_{2,81} = 13.0$, $p < 0.0001$; total: $F_{2,81} = 29.3$, $p < 0.0001$).

(C) Branch length decreased in the β -actin MO (β -aMO) condition ($F_{2,81} = 14.69$, $p < 0.0001$).

(D) The proportion of branches in the β -aMO condition shifts toward lower branch orders (primary: $F_{2,81} = 2.1$, $p < 0.0001$; secondary: $F_{2,81} = 4.7$, $p = 0.0006$; tertiary: $F_{2,81} = 4.2$, $p = 0.0002$).

(legend continued on next page)

in the Con MO condition (Figure 5A). Similar to the global inhibition of β -actin translation in RGCs (Figure 4I), the local inhibition of β -actin translation abolished the net increases (Figure 5B). The defects in branching dynamics were partially rescued by locally co-electroporating the β -actin MO with a MO-insensitive β -actin mRNA (Figure S4). Because the electroporation protocol delivers the β -actin MO into surrounding tectal cells, as well as the RGC axons, it is possible that the axon branching defects arose due to non-autonomous effects. To eliminate this, we delivered the MO into the tectum *before* the arrival of RGC axons (stages 35/36–37/38) and subsequently visualized the branching dynamics of axons after tectal entry at stages 41–43 (Figure 5J). We found no difference in the branching dynamics between the Con MO and β -actin MO conditions (Figures 5F–5I), indicating that β -actin translation in tectal cells is not required for RGC axonal branching, at least in the short term. Thus, the data demonstrate that local β -actin synthesis promotes axonal branching in RGC axons *in vivo*.

In contrast to the severe effect on arborization, the trajectories of β -actin MO axons in the optic tract did not exhibit any major guidance defects or abnormal extension rates (Figures S5 and S6; Movie S8), indicating that axon pathfinding is not sensitive to the level of β -actin translation knockdown achieved.

De Novo β -actin Synthesis Visualized by FRAP in Axon Terminals *In Vivo*

We next sought to visualize newly synthesized β -actin during branching in axon terminals in the tectum *in vivo*. Fluorescence recovery after photobleaching (FRAP) of GFP has been used *in vitro* to demonstrate the local synthesis of proteins (Aakalu et al., 2001; Job and Eberwine, 2001). We expressed a fast-folding fluorescent β -actin translation reporter, Venus- β -actin (Figure 6A), and mRFP (general cell marker) in RGCs via targeted eye electroporation and conducted *in vivo* FRAP on RGC axons in the tectum (Figure 6B). The eye was removed to prevent diffusion of soma-derived, Venus-tagged proteins into the axons. Axon terminals expressing the Venus control showed a minimal amount of signal recovery (4.8%) 10 min post-photobleaching. By contrast, Venus- β -actin expressing axons exhibited rapid fluorescence recovery reaching 18.6% in just 5 min. Cycloheximide suppressed the recovery of Venus- β -actin (Figures 6C and 6D; Movie S9). These data demonstrate that Venus- β -actin is rapidly and locally synthesized in axon terminals in the tectum.

Surprisingly, when the same 10 min FRAP experiment was carried out on Venus- β -actin-expressing growth cones in the optic tract, no signal recovery was observed (Figure S7). This result

indicates that β -actin mRNA translation is relatively low in axon tips while navigating in the optic tract, consistent with our results showing that β -actin knockdown does not affect optic tract pathfinding. This contrasts with axon tips once they reach the optic tectum, where β -actin synthesis is significantly upregulated, consistent with a functional role in arborization.

Focal β -actin Translation Promotes the Formation of β -actin Microdomains in Axonal Branches *In Vivo*

De novo synthesis of β -actin could occur uniformly along the entire axon and/or branch providing a continuous supply of new actin monomers for branching axons. Alternatively, it could take place in focal hotspots, potentially providing new nucleation sites for actin polymerization. To investigate the spatial distribution of newly synthesized β -actin, we used FRAP with high-resolution time-lapse microscopy to map the subcellular location of newly synthesized β -actin in arborizing axons *in vivo* (Figure 7A).

Venus- β -actin showed a markedly different subcellular localization to the control Venus reporter. The control Venus reporter exhibited low intensity and fairly ubiquitous levels of signal recovery as expected for free diffusion, whereas the Venus- β -actin exhibited more concentrated spots of high intensity that we refer to as LPS hotspots (Figures 7B and 7C; Movie S10). The post-FRAP hotspots commonly appeared within 30 s and intensified over time, suggesting that the newly synthesized Venus- β -actin is retained focally at the site of translation, where it can potentially participate in nucleating F-actin polymerization. Moreover, consistent with the RNA granule docking behaviors observed during branching (Figure 1), these nascent protein hotspots were found at the branch points, within branches, and at branch tips (Figure 7C), which may reflect a role in elongating branches. A single branch can exhibit multiple hotspots, as shown in the kymograph (Figure 7C), where four distinct hotspots can be seen forming in different locations along the same branch with different kinetics. The remarkably rapid detection of the FRAP Venus- β -actin signal (10–20 s) was likely aided by the high sensitivity of the microscope custom built for single-molecule fluorescence and the exogenous nature of expression. The result indicates the existence of spatially and temporally distinct translation microdomains and suggests that locally synthesized β -actin may fuel different aspects of branch remodeling.

To perform an unbiased quantitative analysis of the hotspots, we measured the variation in the fluorescence signal, which is predicted to increase with the presence of hotspots. The standard deviation (SD) of fluorescence values was used to generate

(E) Formulation of axon complexity index (ACI).

(F) The ACI was reduced in the β -aMO condition ($F_{2,81} = 12.0$, $p < 0.0001$).

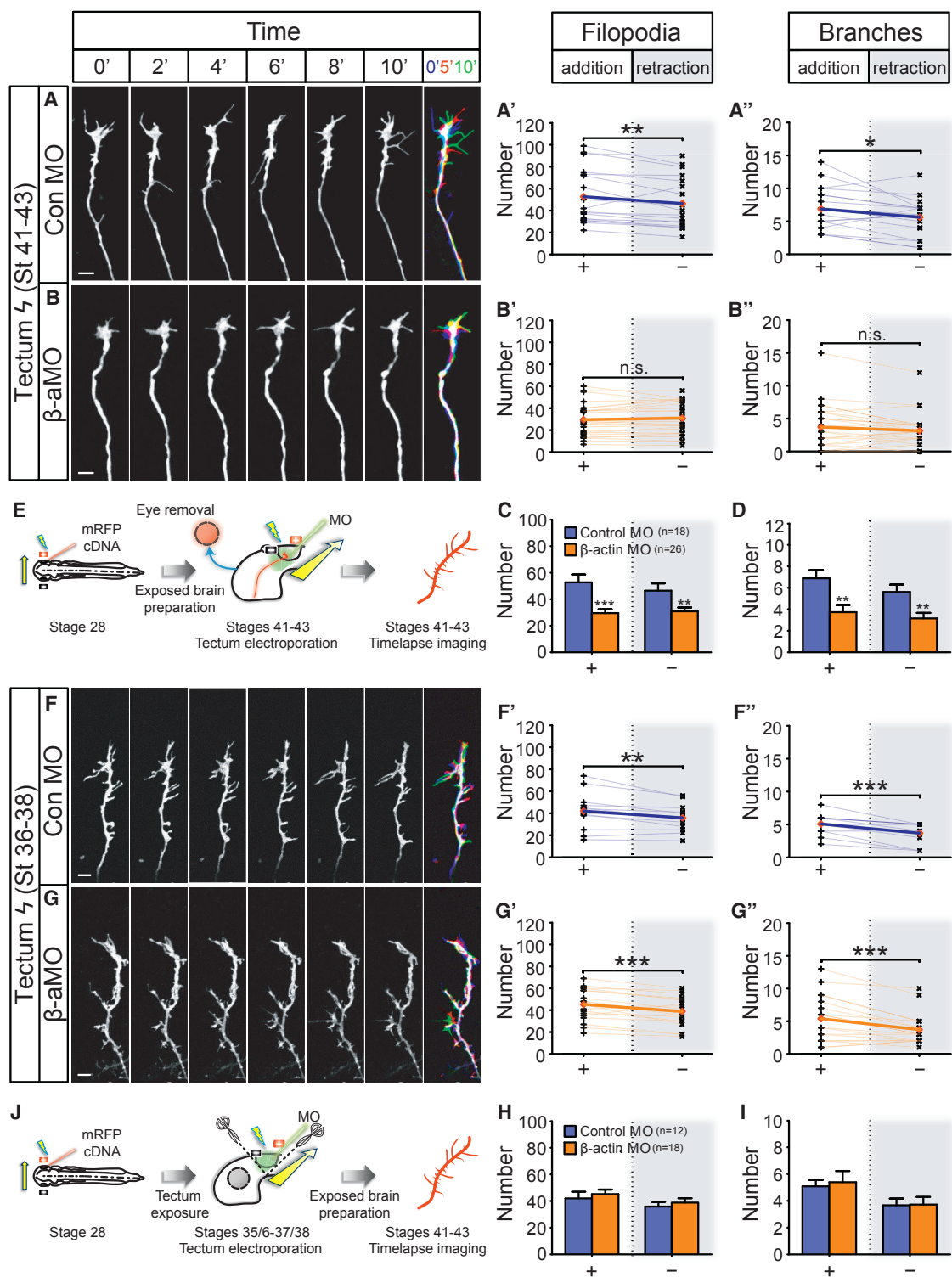
(G) The percentage of complex arbor (ACI ≥ 1.4) was reduced in β -aMO condition (*** $p < 0.0001$, **** $p < 0.0001$, Fisher's exact test).

(H–J) Axon branching in Con MO- (H) and β -aMO-positive (I) (+/- rescue construct; J) axons in the tectum. More protrusions were added than removed in control morphants (filopodia: $t_{17} = 3.9$, $p = 0.0011$; branches: $t_{17} = 3.2$, $p = 0.0049$) (H' and H''). No significant differences were observed in the number of protrusions that were added and removed in β -actin morphants (filopodia: $t_{23} = 0$, $p = 1$; branch: $t_{17} = 0.8$, $p = 0.42$) (I' and I''). More protrusions were added than removed in β -actin morphants that were rescued with β -aMO resistant construct (filopodia: $t_9 = 3.5$, $p = 0.007$; branches: $t_9 = 2.8$, $p = 0.022$) (J' and J'').

(K and L) The dynamics of filopodia (K; addition: $F_{2,49} = 9.3$, $p = 0.0004$; removal: $F_{2,49} = 6.6$, $p = 0.003$) and branches (L; addition: $F_{2,49} = 16.1$, $p < 0.0001$; removal: $F_{2,49} = 10.2$, $p = 0.0002$) were inhibited in β -actin morphants.

(M) Eye electroporation and live imaging of axonal branching.

Error bars represent SEM. * $p < 0.05$, ** $p < 0.01$, *** $p < 0.001$, **** $p < 0.0001$ (one-way ANOVA with Tukey multiple comparisons test for B–F, K, and L) and paired t test for H–J). Red diamonds represent the averages (H–J). Scale bars, 20 μm for (A) and 5 μm for (H–J). See also Figure S5.



(legend continued on next page)

a fluorescence variation index (FVI). The SD value of the fluorescence for the branches were internally normalized to the SD of the fluorescence for the axon shaft, where a ubiquitous recovery pattern would yield a $FVI \approx 1$ and the presence of hotspots would result in a $FVI > 1$ (Figure 7D). In agreement with our qualitative analysis, Venus- β -actin presented an increasingly larger FVI value, whereas the FVI remained largely the same for the Venus control (Figure 7E). Pre-treatment with cycloheximide abolished the rise of FVI for Venus- β -actin, confirming that this is PS dependent. Taken together, our data support a model whereby focally translated β -actin is retained in concentrated spots, where it may promote the local assembly of F-actin required for axonal branching.

Nascent β -actin Microdomains Form in Close Proximity to Docked RNA Granules In Vivo

To discover whether β -actin is synthesized at docked RNA granules, we carried out high-resolution FRAP experiments and recorded the recovery of Venus- β -actin signal simultaneously with Cy5-RNA localization in branching axons in vivo. Hotspots of β -actin recovery were found highly associated with docked RNA granules, beginning 10–20 s post-FRAP (Figures 8A and 8B; Movie S11). To quantify this relationship, we compiled each Cy5-RNA time series into a z stack and computed the median signal intensities as a representation of RNA dwell time at different positions in the axon. The resulting image was then used to calculate Pearson's correlation coefficient (R) with the Venus- β -actin cumulative recovery signal. We obtained a high R of 0.76 ± 0.04 (Figure 8C), supporting a strong association. To test for the significance of the observed association, we scrambled each image to create 1,000 random images and yielded an average R of 0.10 ± 0.02 . It is interesting to note that the Venus- β -actin hotspots frequently persisted for several minutes, suggesting that newly synthesized β -actin can be concentrated in microdomains.

DISCUSSION

We used live imaging to show that new axon branches commonly emerge at sites where RNA granules and mitochondria dock. We found that branch lifetime correlates positively with sustained RNA and mitochondrial invasion. Our functional analysis shows that PS is required for the elaboration of complex arbors and that local β -actin synthesis contributes to the addition and stabilization of new branches. Translation reporter experiments show that β -actin is focally synthesized and retained in concentrated microdomains at the bases and interiors of axonal

branches. Our findings are consistent with a model in which RNA localization and nascent β -actin help to direct branch emergence and expand arbor complexity in response to target post-synaptic cell contact.

Intracellular delivery of fluorescent UTP labels endogenous RNAs and has enabled us to perform tracking of the intra-axonal movements of RNA granules. These granules are highly fluorescent and photostable and can be followed for prolonged periods (>420 min). Because the fluorescent UTP is incorporated into RNA during transcription in vivo, the RNAs may associate with normal regulatory proteins inside the nucleus to form specific RNP complexes before export to the cytoplasm. The dynamic behavior of these granules therefore should provide an accurate reflection of their endogenous activities. The MS2 genetic system is a valuable alternative for labeling endogenous RNAs for live imaging (Beach et al., 1999; Bertrand et al., 1998) and has the advantage of being able to label specific RNAs. However, the multiple MS2 binding stem-loops in the RNA and the binding of multiple fluorescent proteins required for live tracking may hamper RNA-protein interactions and alter some aspects of motility and localization. Our finding that RNA granules frequently dock at sites immediately preceding filopodia emergence suggests that translation may occur at these sites and is supported by dual time-lapse imaging, showing a strong association between the positions of newly synthesized Venus- β -actin and docked RNA granules. Since our biochemical analysis showed that rRNA, similar to non-labeled RNA, makes up a large fraction of labeled RNA in larval brains, it is likely that the docked RNA granules represent accumulations of ribosomes as well as mRNAs. It is notable that the RNA docking behavior described here is similar to that reported for Vg1RBP (the major β -actin mRNA-binding protein) (Kalous et al., 2014), where GFP-Vg1RBP puncta dock at sites immediately preceding the emergence of filopodia from the axon shafts. Collectively, these data suggest that numerous translation-associated organelles and complexes (RNA granules, ribosomes, mitochondria, RBPs) co-dock at sites to promote branch emergence. In the future, it will be interesting to investigate the dynamics of multiple complexes simultaneously.

Our fast image-capture analysis enabled us to simultaneously track RNA, translation, and branching events and revealed the highly dynamic nature of developing axon arbors with multiple branches emerging and retracting over minutes. This is in broad agreement with previous studies using slower capture rates (Alsina et al., 2001; Cohen-Cory and Fraser, 1995; Harris et al., 1987; Hu et al., 2005; Meyer and Smith, 2006; O'Rourke et al., 1994; Ruthazer et al., 2006; Witte et al., 1996). We found a slight

(E) Local delivery of MO into RGC axons by tectum electroporation and imaged immediately thereafter. Electroporated eye was removed to eliminate somatic contribution.

(F and G) Time-lapse images of axonal branching in the tectum at stages 41–43 after local delivery of MO at stages 35/36–37/38. More protrusions were added than removed in Con MO condition (filopodia: $t_{11} = 3.4$, $p = 0.006$; branches: $t_{11} = 4.9$, $p = 0.0005$) (F' and F''). More protrusions were added than removed in β -aMO condition (addition: $t_{17} = 4.2$, $p = 0.0006$; removal: $t_{17} = 4.0$, $p = 0.0008$) (G' and G'').

(H and I) The dynamics of filopodia (H; addition: $t_{28} = 0.6$, $p = 0.58$; removal: $t_{28} = 0.6$, $p = 0.55$) and branches (I; addition: $t_{28} = 0.3$, $p = 0.78$; removal: $t_{28} = 0.07$, $p = 0.95$) were unaffected in β -aMO condition.

(J) Local delivery of MO into the tectum before tectal entry of RGC axons (stages 35/36–37/38) and live imaging of axonal branching after tectal entry of RGC axons (stages 41–43). Scissors and dashed line denote that only the skin overlying the tectal area was removed to minimize damage to the brain.

Error bars represent SEM. * $p < 0.01$, ** $p < 0.01$, *** $p < 0.001$ (paired t test for A, B, F, and G and unpaired t test for C, D, H, and I). Scale bars, 5 μ m. Red diamonds represent the averages (A, B, F, and G). See also Figures S4 and S6.

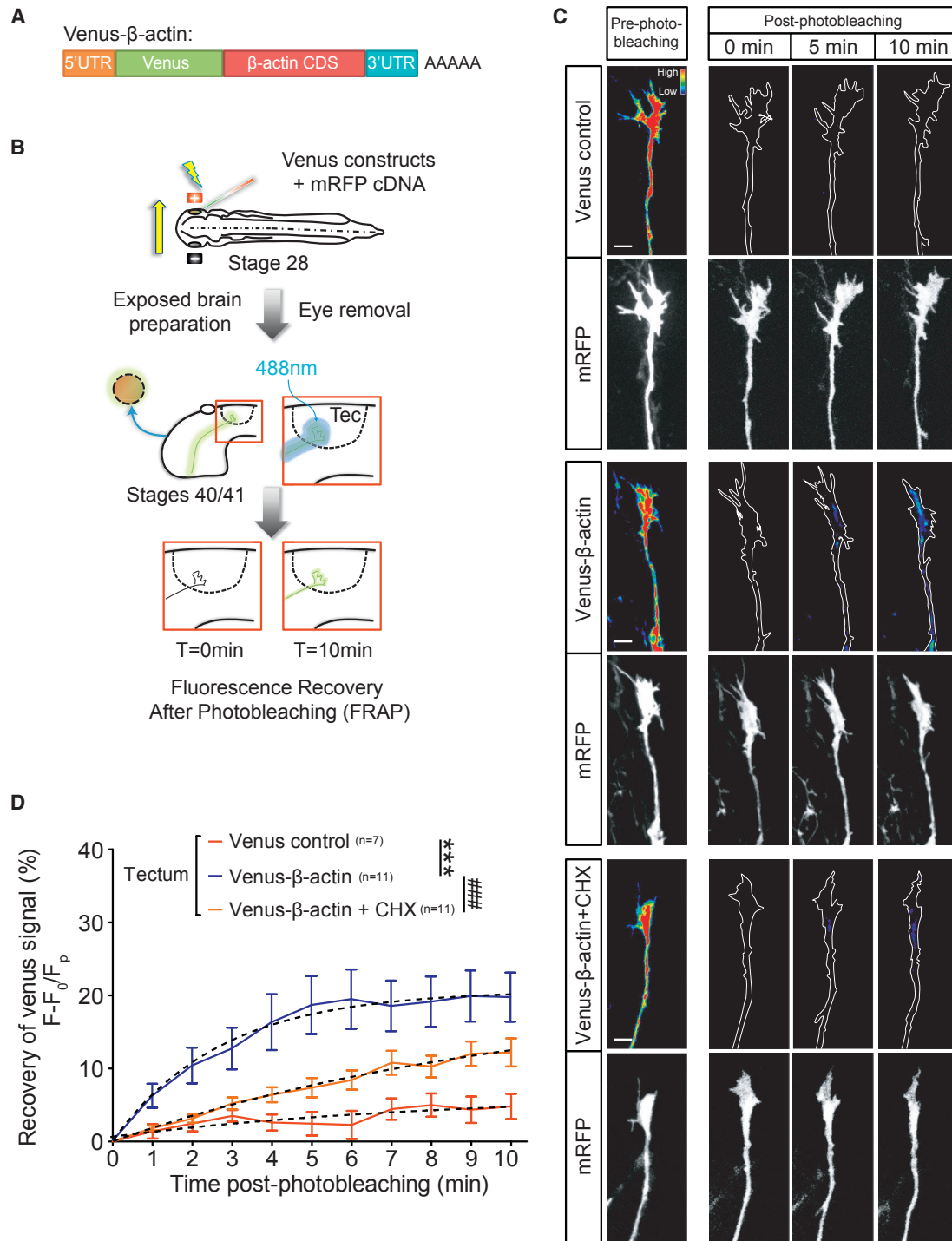


Figure 6. Visualization of De Novo β -actin Synthesis in Axon Terminals In Vivo

(A) Venus- β -actin construct as a reporter for β -actin translation.

(B) Fluorescence recovery after photobleaching experiment of Venus constructs in vivo. Electroporated eye was removed to eliminate somatic contribution. Tec, tectum.

(C) Fluorescence heatmaps illustrating that limited recovery was detected with the Venus control construct. In contrast, Venus- β -actin signal recovered soon after photobleaching and was inhibited by the translation inhibitor cycloheximide (CHX), indicating de novo synthesis of β -actin in RGC axon terminals in the tectum.

(D) FRAP over the course of 10 min. Dotted lines represent least-squares fits to a single-exponential function. (Venus control versus Venus- β -actin: $F_{3,191} = 36.0$, $p < 0.0001$; Venus- β -actin versus Venus- β -actin + CHX: $F_{3,236} = 21.8$, $p < 0.0001$; extra sum-of-squares F test). Error bars represent SEM. Scale bars, 5 μ m. See also Figure S7.

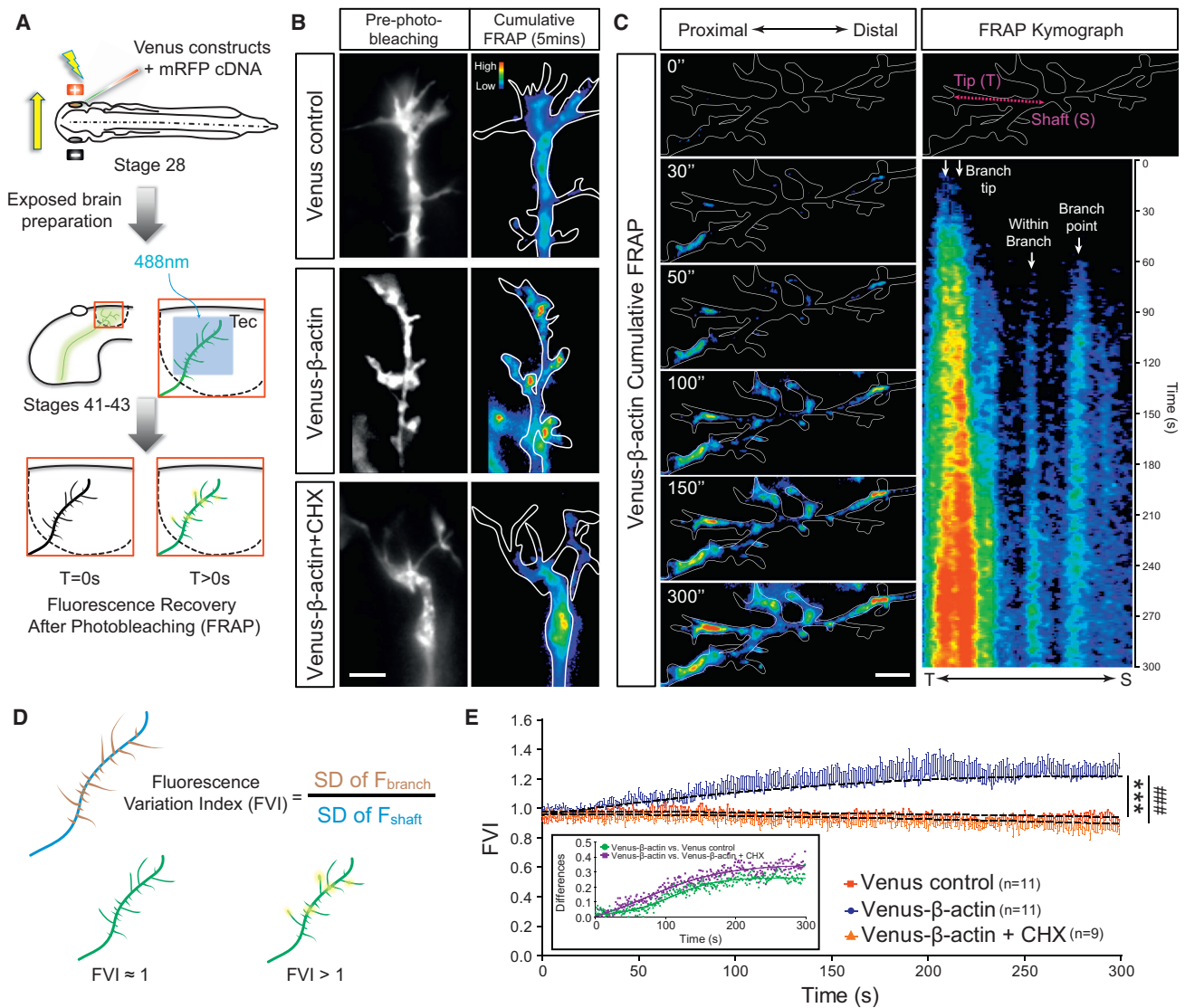


Figure 7. Focal hotspots of nascent β -actin at axonal branch points and within branches in vivo

(A) Fluorescence recovery after photobleaching experiment of Venus constructs in vivo.

(B) Fluorescence heatmaps illustrating a ubiquitous recovery pattern for the Venus control construct. In contrast, Venus- β -actin signal recovered in hotspots at branch points and within branches. The formation of these hotspots was inhibited by cycloheximide (CHX), indicating de novo synthesis and accumulation of β -actin in highly specific focal points in RGC axons.

(C) An example of multiple Venus- β -actin hotspots forming at different sub-compartments of a branch. Kymograph displays the 300 s FRAP from the branch tip to axon shaft as indicated by the magenta arrow. At least four distinct hotspots can be identified in this single branch.

(D) The fluorescence variation index (FVI) is defined by normalizing the standard deviation (SD) of fluorescence in branches (F_{branch}) to the SD of fluorescence in axon shaft (F_{shaft}).

(E) FVI after FRAP over the course of 5 min. Dotted lines represent least-squares fits to a quadratic function. (Venus control versus Venus- β -actin: $F_{3,6594} = 396$, $p < 0.0001$; Venus- β -actin versus Venus- β -actin + CHX: $F_{3,5994} = 466.7$, $p < 0.0001$). Inset displays the differences between the conditions. Error bars represent SEM. *** $p < 0.001$, #### $p < 0.001$ (extra sum-of-squares F test for E). Scale bars, 5 μm .

bias in favor of emergence over retraction, which leads to a progressive increase in arbor size and complexity. New branches emerging from the axon shaft typically appear at sites of transiently docked RNA granules and are often short lived, retracting within seconds, with the more stable branches invaded by RNA. Interestingly, the RNA docking sites closely resemble locations of presynaptic puncta, which are similarly correlated with branch

emergence and lifetime (Alsina et al., 2001; Hu et al., 2005; Meyer and Smith, 2006; Ruthazer et al., 2006). This suggests that translation and presynaptic components might coordinately control arbor remodeling and transmission. Many presynaptic proteins are axonally translated during arborization (Shigeoka et al., 2016), suggesting the possibility that the positioning of presynaptic proteins and puncta might be aided by RNA localization.

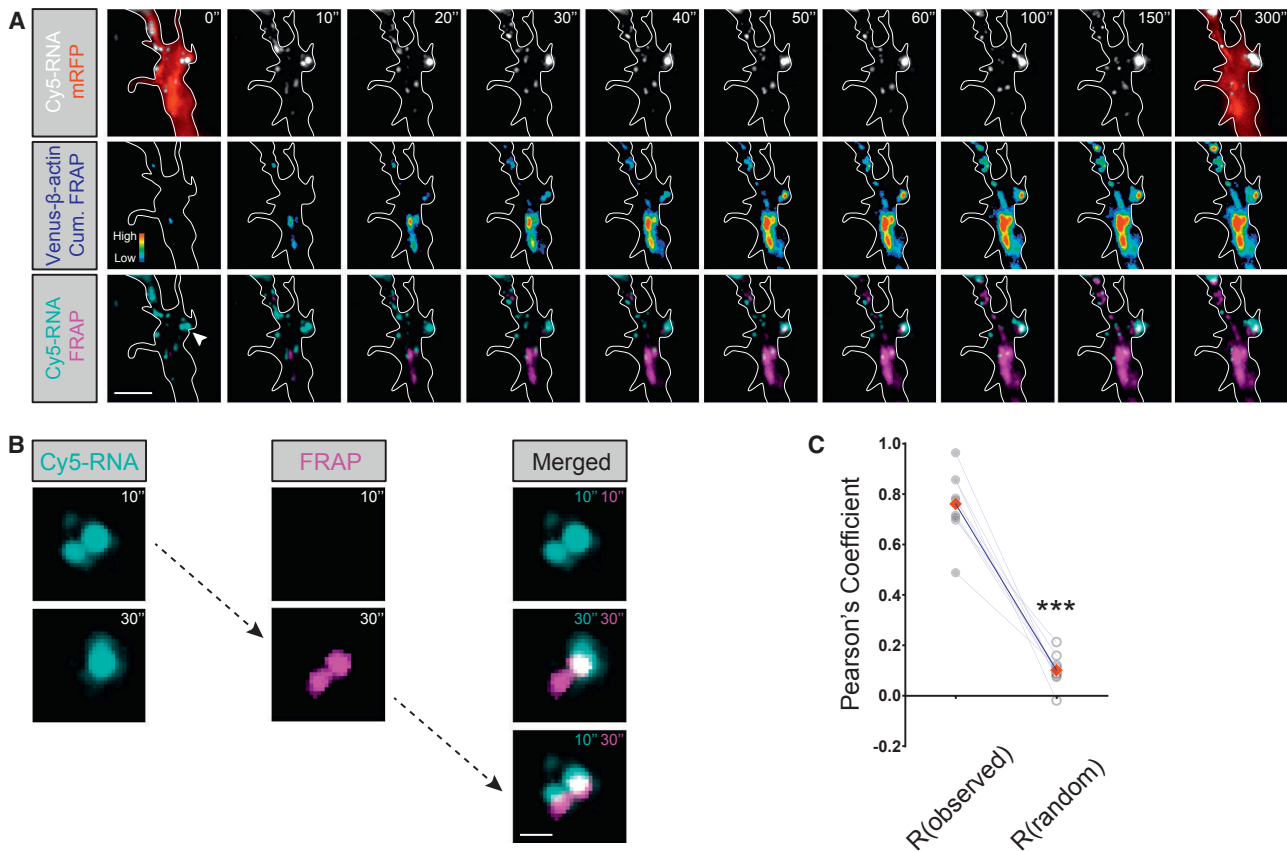


Figure 8. Nascent β -actin Microdomains Form in Close Proximity to Docked RNA Granules In Vivo

(A) Dual-channel simultaneous time-lapse images of Cy5-RNA and Venus- β -actin FRAP. The axon morphology was estimated by capturing a mRFP image before photobleaching and after time-lapse acquisition, which are overlaid on the Cy5-RNA images (gray scale, top) at time points 0" and 300", respectively. Axon outline of the mRFP image captured after time-lapse acquisition was used as an approximation for time points 10" to 300". Venus- β -actin signal recovery after photobleaching is illustrated by the fluorescence heatmaps (middle). The bottom row presents the overlays of Cy5-RNA (cyan) and Venus- β -actin FRAP (magenta).

(B) Enlarged images of area signified by the arrowhead in (A). The images of Cy5-RNA (cyan) and Venus- β -actin FRAP (magenta) are individually presented on the left and in the middle columns. Images on the right display image overlays. The FRAP signal positions at 30 s closely resemble the localization of RNA at 10 s.

(C) Cy5-RNA time series were compiled into z stacks and computed for the median signal intensities as a representation of RNA dwell time. The resulting images were then used to compute Pearson's correlation coefficient (R) with the Venus- β -actin cumulative recovery signal. The averages of R(observed) were significantly higher than averages of R(random) yielded from 1,000 random images scrambled from each original axon image ($t_8 = 11.55$, $p < 0.0001$, paired t test). Scale bars, 5 μ m for (A) and 1 μ m for (B).

Previous work has shown that LPS is required for growth cone turning in vitro in response to various factors, including Netrin-1 and BDNF (Campbell and Holt, 2001; Yao et al., 2006). Interestingly, Netrin-1 and BDNF are expressed in the tectum, but not in the optic tract, and are known to induce β -actin synthesis in retinal axons (Leung et al., 2006). In addition, the Netrin-1 receptor DCC, being bound to ribosomes, is directly linked to the translation machinery (Tcherkezian et al., 2010). Thus, it can be envisaged that on arrival in the tectum, contact with Netrin-1-bearing tectal dendrites triggers localized β -actin translation (via DCC activation) in retinal axons, which promotes branch emergence.

Defects in axon pathfinding were not detected in the current study after β -actin translation knockdown. This is consistent with the finding that Vg1RBP knockdown does not cause pathfinding defects but disrupts axon arborization (Kalous et al.,

2014). It is puzzling that β -actin translation knockdown affects growth cone turning in vitro, but not pathfinding in vivo. One possibility is that the growth-cone turning assay, which measures small shifts in the direction of axon growth over a 1 hr period, is not a faithful gauge of long-range axon pathfinding behavior in vivo. The limited behavioral responses possible in the reduced conditions of this in vitro assay system may, in fact, be more akin to an arborizing axon, although overt branching cannot occur because of the absence of appropriate cellular substrate and branch-inducing factors. The finding that RGC axonal growth cones can navigate accurately in optic tract despite reduced levels of β -actin mRNA translation is consistent with our observation of scant levels of new β -actin synthesis in the growth cones of navigating axons using a Venus- β -actin translation reporter. By contrast, the translation reporter revealed robust β -actin synthesis in the tips of axons that have entered the

tectum. Thus, our data indicate that growing retinal axons upregulate β -actin synthesis on entering the tectum, where it is required for branching. The results raise the interesting possibility that distinct aspects of axon development, such as axon pathfinding and branching, are differentially sensitive to local demands for de novo protein synthesis. Our results do not exclude the possibility that axon pathfinding requires some level of LPS. In commissural axons, although a requirement for LPS has not been demonstrated in pathfinding, a similar upregulation of EphA2 translation and Robo3.2 mRNA occurs after axons pass the midline of the spinal cord (Brittis et al., 2002; Colak et al., 2013). Moreover, >1,000 mRNAs were identified in the transcriptome of retinal axons elongating in the superior colliculus in embryonic day 17.5 (E17.5) mice (Shigeoka et al., 2016). LPS could aid short-range (within the target) pathfinding and promote the accuracy of connectivity. This is supported by the misrouting of retinal axons selectively in the optic tectum after the knock-down of specific microRNAs miR-124 (Baudet et al., 2011) or the axon-localizing miR-182 (Bellon et al., 2017), which modulate the translation of subsets of mRNA.

How might a small quantity of newly synthesized β -actin play a physiologically significant role in branch dynamics, promoting branch formation and stabilization, especially when there is a large pool of pre-existing actin? Locally synthesized β -actin has been estimated to constitute <1% of the actin in sympathetic neuron axons (Eng et al., 1999) and 7% of the actin needed for polymerization in migrating fibroblasts (Condeelis and Singer, 2005). Additionally, actin reportedly has a long half-life (2–3 days) (Antecol et al., 1986). In fibroblasts and growth cones, it has been proposed that microdomains of β -actin translation give rise to spatially confined pools of newly synthesized β -actin sufficiently concentrated to act as nucleation sites for the polymerization of new actin filaments that, in turn, bias the direction of migration (Katz et al., 2016; Kislauskis et al., 1997; Leung et al., 2006; Shestakova et al., 2001). Our experimental evidence showing the progressive accumulation of newly synthesized β -actin in microdomains over 5 min supports this idea. Moreover, since nascent β -actin lacks post-translational modifications, it may be a particularly potent driver of polymerization (Karakozova et al., 2006; Lin and Holt, 2007; Wang et al., 2001). Newly synthesized glutamate receptors and β -actin also accumulate in hotspots in dendrites in hippocampal neurons in vitro (Kim et al., 2013; Yoon et al., 2016). This contrasts with the more broadly distributed pattern of newly synthesized β -actin seen in axonal growth cones in culture (Ströhl et al., 2017), hinting at potential differences in terms of either nascent β -actin accumulation or the nature of translation (e.g., monosomal versus polysomal). The ability to extend a new branch based on LPS enables “on-site” and “on-demand” provision of the structural substrate needed for new branch formation and synaptogenesis in response to signals from target cell.

Impoverished neuronal arborization is a structural correlate of several neurodevelopmental disorders, such as autism and Down syndrome (Jan and Jan, 2010). However, previous studies have focused on dendrite rather than axon arborization and have not evaluated the contribution of *local* translation. Dysregulated translation, both too much or too little, can have profound effects on both axonal and dendritic branching and synapse formation

(Chihara et al., 2007; Jaworski et al., 2005; Santini et al., 2013). The demonstration here that axonal arborization is disrupted by a loss of β -actin translation implicates RNA localization and local translation broadly in wiring the nervous system and raises the possibility that axonal, as well as dendritic, arborization defects underlie some neurodevelopmental disorders.

STAR★METHODS

Detailed methods are provided in the online version of this paper and include the following:

- KEY RESOURCES TABLE
- CONTACT FOR REAGENT AND RESOURCE SHARING
- EXPERIMENTAL MODEL AND SUBJECT DETAILS
 - *Xenopus laevis* Embryos Maintenance
- METHOD DETAILS
 - DNA Constructs and Morpholino
 - Electroporation
 - In Vivo Imaging
 - Blastomere Injection
 - RNA Extraction
 - Biotin-RNA Pull-Down Assay (Low Stringency)
 - Biotin-RNA Pull-Down Assay (High Stringency)
 - RNA Analysis
 - RT-qPCR
 - Mitochondrial and Genomic DNA Extraction
 - Biotin-DNA Pull-Down Assay and DNA Analysis
 - Retinal Explant Culture and Imaging
 - Protein Synthesis Inhibitor Incubation
 - In Vivo Puromycin-Based Translation Assay
 - Western Blot
 - Dil Injection, Ventral and Lateral Imaging Preparations
 - In Vitro Transcription
 - In Vivo FRAP of β -actin Translation Reporter
- QUANTIFICATION AND STATISTICAL ANALYSIS
 - General Definition and Statistics
 - RNA, RT-qPCR, and DNA Analyses
 - RNA and Mitochondrial Dynamics
 - RNA and Mitochondria Colocalization Analysis
 - In Vivo Puromycin-Based Translation Assay
 - Western Blot Analysis
 - Axon Bundle Length and Width Analyses
 - Branching Dynamics
 - Axon Navigation
 - Axon Arbor Complexity Analysis
 - FRAP Analyses

SUPPLEMENTAL INFORMATION

Supplemental Information includes seven figures and eleven movies and can be found with this article online at <http://dx.doi.org/10.1016/j.neuron.2017.07.016>.

AUTHOR CONTRIBUTIONS

H.H.-W.W. and C.E.H. conceived the project and wrote the manuscript. H.H.-W.W. designed the experiments. H.H.-W.W. performed and analyzed experiments, except for those presented in Figures 7 and 8 (H.H.-W.W. and F.S.),

Figure S1F (H.H.-W.W. and C.G.R.), Figure S3F (J.-M.C.), and Figures S5J–S5M (J.Q.L.). R.C., B.T.-B., R.F.L., and C.F.K. provided research tools. W.A.H. and C.E.H. supervised the project.

ACKNOWLEDGMENTS

We thank M. Coleman for sharing the mito-GFP construct; A. Mele and J.K. Mooslehner for technical assistance; and X. Almeida, A. Bellon, and V. Urbančić for critical reading of the manuscript. This work was supported by Cambridge Trust, Croucher Foundation, Sir Edward Youde Memorial Fund (H.H.-W.W.), Gates Cambridge (J.Q.L.), Fundação para a Ciência e Tecnologia (C.M.R.), Wellcome Trust Senior Investigator Award (100329/Z/12/Z) (W.A.H.), EPSRC Grant (EP/H018301/1), MRC Grant (MR/K015850/1 and MR/K02292X/1), Wellcome Trust (089703/Z/09/Z) (C.F.K.), Wellcome Trust Programme Grant (085314/Z/08/Z), and ERC Advanced Grant (322817) (C.E.H.).

Received: January 29, 2017

Revised: June 9, 2017

Accepted: July 14, 2017

Published: August 3, 2017

REFERENCES

- Aakalu, G., Smith, W.B., Nguyen, N., Jiang, C., and Schuman, E.M. (2001). Dynamic visualization of local protein synthesis in hippocampal neurons. *Neuron* 30, 489–502.
- Alsina, B., Vu, T., and Cohen-Cory, S. (2001). Visualizing synapse formation in arborizing optic axons in vivo: dynamics and modulation by BDNF. *Nat. Neurosci.* 4, 1093–1101.
- Antecol, M.H., Darveau, A., Sonenberg, N., and Mukherjee, B.B. (1986). Altered biochemical properties of actin in normal skin fibroblasts from individuals predisposed to dominantly inherited cancers. *Cancer Res.* 46, 1867–1873.
- Bassell, G.J., Zhang, H., Byrd, A.L., Femino, A.M., Singer, R.H., Taneja, K.L., Lifshitz, L.M., Herman, I.M., and Kosik, K.S. (1998). Sorting of beta-actin mRNA and protein to neurites and growth cones in culture. *J. Neurosci.* 18, 251–265.
- Baudet, M.L., Zivraj, K.H., Abreu-Goodger, C., Muldal, A., Armisen, J., Blenkiron, C., Goldstein, L.D., Miska, E.A., and Holt, C.E. (2011). miR-124 acts through CoREST to control onset of Sema3A sensitivity in navigating retinal growth cones. *Nat. Neurosci.* 15, 29–38.
- Beach, D.L., Salmon, E.D., and Bloom, K. (1999). Localization and anchoring of mRNA in budding yeast. *Curr. Biol.* 9, 569–578.
- Bellon, A., Iyer, A., Bridi, S., Lee, F.C., Ovando-Vázquez, C., Corradi, E., Longhi, S., Roccozzio, M., Strohbuecker, S., Naik, S., et al. (2017). miR-182 regulates Slit2-mediated axon guidance by modulating the local translation of a specific mRNA. *Cell Rep.* 18, 1171–1186.
- Bertrand, E., Chartrand, P., Schaefer, M., Shenoy, S.M., Singer, R.H., and Long, R.M. (1998). Localization of ASH1 mRNA particles in living yeast. *Mol. Cell* 2, 437–445.
- Brittis, P.A., Lu, Q., and Flanagan, J.G. (2002). Axonal protein synthesis provides a mechanism for localized regulation at an intermediate target. *Cell* 110, 223–235.
- Campbell, D.S., and Holt, C.E. (2001). Chemotropic responses of retinal growth cones mediated by rapid local protein synthesis and degradation. *Neuron* 32, 1013–1026.
- Chia, P.H., Chen, B., Li, P., Rosen, M.K., and Shen, K. (2014). Local F-actin network links synapse formation and axon branching. *Cell* 156, 208–220.
- Chien, C.B., Rosenthal, D.E., Harris, W.A., and Holt, C.E. (1993). Navigational errors made by growth cones without filopodia in the embryonic *Xenopus* brain. *Neuron* 11, 237–251.
- Chihara, T., Luginbuhl, D., and Luo, L. (2007). Cytoplasmic and mitochondrial protein translation in axonal and dendritic terminal arborization. *Nat. Neurosci.* 10, 828–837.
- Cohen-Cory, S., and Fraser, S.E. (1995). Effects of brain-derived neurotrophic factor on optic axon branching and remodelling in vivo. *Nature* 378, 192–196.
- Colak, D., Ji, S.J., Porse, B.T., and Jaffrey, S.R. (2013). Regulation of axon guidance by compartmentalized nonsense-mediated mRNA decay. *Cell* 153, 1252–1265.
- Condeelis, J., and Singer, R.H. (2005). How and why does beta-actin mRNA target? *Biol. Cell* 97, 97–110.
- Cosker, K.E., Fenstermacher, S.J., Pazyra-Murphy, M.F., Elliott, H.L., and Segal, R.A. (2016). The RNA-binding protein SFPQ orchestrates an RNA regulon to promote axon viability. *Nat. Neurosci.* 19, 690–696.
- Courchet, J., Lewis, T.L., Jr., Lee, S., Courchet, V., Liou, D.Y., Aizawa, S., and Polleux, F. (2013). Terminal axon branching is regulated by the LKB1-NUAK1 kinase pathway via presynaptic mitochondrial capture. *Cell* 153, 1510–1525.
- Das, T., Payer, B., Cayouette, M., and Harris, W.A. (2003). In vivo time-lapse imaging of cell divisions during neurogenesis in the developing zebrafish retina. *Neuron* 37, 597–609.
- Dong, X., Shen, K., and Bülow, H.E. (2015). Intrinsic and extrinsic mechanisms of dendritic morphogenesis. *Annu. Rev. Physiol.* 77, 271–300.
- Donnelly, C.J., Park, M., Spillane, M., Yoo, S., Pacheco, A., Gomes, C., Vuppalanchi, D., McDonald, M., Kim, H.H., Merianda, T.T., et al. (2013). Axonally synthesized β -actin and GAP-43 proteins support distinct modes of axonal growth. *J. Neurosci.* 33, 3311–3322.
- Drinjakovic, J., Jung, H., Campbell, D.S., Strohlic, L., Dwivedy, A., and Holt, C.E. (2010). E3 ligase Nedd4 promotes axon branching by downregulating PTEN. *Neuron* 65, 341–357.
- Eng, H., Lund, K., and Campenot, R.B. (1999). Synthesis of beta-tubulin, actin, and other proteins in axons of sympathetic neurons in compartmented cultures. *J. Neurosci.* 19, 1–9.
- Falk, J., Drinjakovic, J., Leung, K.M., Dwivedy, A., Regan, A.G., Piper, M., and Holt, C.E. (2007). Electroporation of cDNA/Morpholinos to targeted areas of embryonic CNS in *Xenopus*. *BMC Dev. Biol.* 7, 107.
- Frangi, A.F., Niessen, W.J., Vincken, K.L., and Viergever, M.A. (1998). Multiscale vessel enhancement filtering. In *Medical Image Computing and Computer-Assisted Intervention—MICCAI'98*, W.M. Wells, A. Colchester, and S.L. Delp, eds. (Springer), pp. 130–137.
- Harris, W.A., Holt, C.E., and Bonhoeffer, F. (1987). Retinal axons with and without their somata, growing to and arborizing in the tectum of *Xenopus* embryos: a time-lapse video study of single fibres in vivo. *Development* 101, 123–133.
- Hörnberg, H., Wollerton-van Horck, F., Maurus, D., Zwart, M., Svoboda, H., Harris, W.A., and Holt, C.E. (2013). RNA-binding protein Hermes/RBPMS inversely affects synapse density and axon arbor formation in retinal ganglion cells in vivo. *J. Neurosci.* 33, 10384–10395.
- Hu, B., Nikolakopoulou, A.M., and Cohen-Cory, S. (2005). BDNF stabilizes synapses and maintains the structural complexity of optic axons in vivo. *Development* 132, 4285–4298.
- Jan, Y.N., and Jan, L.Y. (2010). Branching out: mechanisms of dendritic arborization. *Nat. Rev. Neurosci.* 11, 316–328.
- Jaworski, J., Spangler, S., Seeburg, D.P., Hoogenraad, C.C., and Sheng, M. (2005). Control of dendritic arborization by the phosphoinositide-3'-kinase-Akt-mammalian target of rapamycin pathway. *J. Neurosci.* 25, 11300–11312.
- Job, C., and Eberwine, J. (2001). Identification of sites for exponential translation in living dendrites. *Proc. Natl. Acad. Sci. USA* 98, 13037–13042.
- Kaili, K., and Dent, E.W. (2014). Branch management: mechanisms of axon branching in the developing vertebrate CNS. *Nat. Rev. Neurosci.* 15, 7–18.
- Kalous, A., Stake, J.I., Yisraeli, J.K., and Holt, C.E. (2014). RNA-binding protein Vg1RBP regulates terminal arbor formation but not long-range axon navigation in the developing visual system. *Dev. Neurobiol.* 74, 303–318.

- Karakozova, M., Kozak, M., Wong, C.C., Bailey, A.O., Yates, J.R., 3rd, Mogilner, A., Zebroski, H., and Kashina, A. (2006). Arginylation of beta-actin regulates actin cytoskeleton and cell motility. *Science* 313, 192–196.
- Katz, Z.B., English, B.P., Lionnet, T., Yoon, Y.J., Monnier, N., Ovryn, B., Bathe, M., and Singer, R.H. (2016). Mapping translation ‘hot-spots’ in live cells by tracking single molecules of mRNA and ribosomes. *eLife* 5, 5.
- Kim, T.K., Sul, J.Y., Helmfors, H., Langel, U., Kim, J., and Eberwine, J. (2013). Dendritic glutamate receptor mRNAs show contingent local hotspot-dependent translational dynamics. *Cell Rep.* 5, 114–125.
- Kislauskis, E.H., Zhu, X., and Singer, R.H. (1997). Beta-actin messenger RNA localization and protein synthesis augment cell motility. *J. Cell Biol.* 136, 1263–1270.
- Konopacki, F.A., Wong, H.H., Dwivedy, A., Bellon, A., Blower, M.D., and Holt, C.E. (2016). ESCRT-II controls retinal axon growth by regulating DCC receptor levels and local protein synthesis. *Open Biol.* 6, 150218.
- Leung, K.M., van Horck, F.P., Lin, A.C., Allison, R., Standart, N., and Holt, C.E. (2006). Asymmetrical beta-actin mRNA translation in growth cones mediates attractive turning to netrin-1. *Nat. Neurosci.* 9, 1247–1256.
- Lin, A.C., and Holt, C.E. (2007). Local translation and directional steering in axons. *EMBO J.* 26, 3729–3736.
- Longair, M.H., Baker, D.A., and Armstrong, J.D. (2011). Simple Neurite Tracer: open source software for reconstruction, visualization and analysis of neuronal processes. *Bioinformatics* 27, 2453–2454.
- Manitt, C., Nikolakopoulou, A.M., Almaro, D.R., Nguyen, S.A., and Cohen-Cory, S. (2009). Netrin participates in the development of retinotectal synaptic connectivity by modulating axon arborization and synapse formation in the developing brain. *J. Neurosci.* 29, 11065–11077.
- Marshak, S., Nikolakopoulou, A.M., Dirks, R., Martens, G.J., and Cohen-Cory, S. (2007). Cell-autonomous TrkB signaling in presynaptic retinal ganglion cells mediates axon arbor growth and synapse maturation during the establishment of retinotectal synaptic connectivity. *J. Neurosci.* 27, 2444–2456.
- Miura, K., Rueden, C., Hiner, M., Schindelin, J., and Rietdorf, J. (2014). ImageJ Plugin CorrectBleach V2.0.2 (Zenodo). <http://dx.doi.org/10.5281/zenodo.596358>.
- Meyer, M.P., and Smith, S.J. (2006). Evidence from in vivo imaging that synaptogenesis guides the growth and branching of axonal arbors by two distinct mechanisms. *J. Neurosci.* 26, 3604–3614.
- Nieuwkoop, P.D., and Faber, J. (1967). *Normal Table of Xenopus laevis (Daudin): A Systematical and Chronological Survey of the Development from the Fertilized Egg Till the End of Metamorphosis* (North-Holland Pub. Co.).
- O’Rourke, N.A., Cline, H.T., and Fraser, S.E. (1994). Rapid remodeling of retinal arbors in the tectum with and without blockade of synaptic transmission. *Neuron* 12, 921–934.
- Pan, L., Zhang, Y.Q., Woodruff, E., and Broadie, K. (2004). The Drosophila fragile X gene negatively regulates neuronal elaboration and synaptic differentiation. *Curr. Biol.* 14, 1863–1870.
- Piper, M., Anderson, R., Dwivedy, A., Weinl, C., van Horck, F., Leung, K.M., Cogill, E., and Holt, C. (2006). Signaling mechanisms underlying Slit2-induced collapse of Xenopus retinal growth cones. *Neuron* 49, 215–228.
- Piper, M., Lee, A.C., van Horck, F.P., McNeilly, H., Lu, T.B., Harris, W.A., and Holt, C.E. (2015). Differential requirement of F-actin and microtubule cytoskeleton in cue-induced local protein synthesis in axonal growth cones. *Neural Dev.* 10, 3.
- Poggi, L., Vitorino, M., Masai, I., and Harris, W.A. (2005). Influences on neural lineage and mode of division in the zebrafish retina in vivo. *J. Cell Biol.* 171, 991–999.
- Preibisch, S., Saalfeld, S., Schindelin, J., and Tomancak, P. (2010). Software for bead-based registration of selective plane illumination microscopy data. *Nat. Methods* 7, 418–419.
- Roque, C.G., Wong, H.H., Lin, J.Q., and Holt, C.E. (2016). Tumor protein Tctp regulates axon development in the embryonic visual system. *Development* 143, 1134–1148.
- Ruthazer, E.S., Li, J., and Cline, H.T. (2006). Stabilization of axon branch dynamics by synaptic maturation. *J. Neurosci.* 26, 3594–3603.
- Santini, E., Huynh, T.N., MacAskill, A.F., Carter, A.G., Pierre, P., Ruggero, D., Kaphzan, H., and Klann, E. (2013). Exaggerated translation causes synaptic and behavioural aberrations associated with autism. *Nature* 493, 411–415.
- Schindelin, J., Arganda-Carreras, I., Frise, E., Kaynig, V., Longair, M., Pietzsch, T., Preibisch, S., Rueden, C., Saalfeld, S., Schmid, B., et al. (2012). Fiji: an open-source platform for biological-image analysis. *Nat. Methods* 9, 676–682.
- Schmidt, E.K., Clavarino, G., Ceppi, M., and Pierre, P. (2009). SUnSET, a nonradioactive method to monitor protein synthesis. *Nat. Methods* 6, 275–277.
- Shestakova, E.A., Singer, R.H., and Condeelis, J. (2001). The physiological significance of beta-actin mRNA localization in determining cell polarity and directional motility. *Proc. Natl. Acad. Sci. USA* 98, 7045–7050.
- Shigeoka, T., Jung, H., Jung, J., Turner-Bridger, B., Ohk, J., Lin, J.Q., Amieux, P.S., and Holt, C.E. (2016). Dynamic axonal translation in developing and mature visual circuits. *Cell* 166, 181–192.
- Spillane, M., Ketschek, A., Donnelly, C.J., Pacheco, A., Twiss, J.L., and Gallo, G. (2012). Nerve growth factor-induced formation of axonal filopodia and collateral branches involves the intra-axonal synthesis of regulators of the actin-nucleating Arp2/3 complex. *J. Neurosci.* 32, 17671–17689.
- Spillane, M., Ketschek, A., Merianda, T.T., Twiss, J.L., and Gallo, G. (2013). Mitochondria coordinate sites of axon branching through localized intra-axonal protein synthesis. *Cell Rep.* 5, 1564–1575.
- Ströhl, F., Lin, J.Q., Laine, R.F., Wong, H.H., Urbančić, V., Cagnetta, R., Holt, C.E., and Kaminski, C.F. (2017). Single molecule translation imaging visualizes the dynamics of local β -actin synthesis in retinal axons. *Sci. Rep.* 7, 709.
- Tatavarty, V., Ifrim, M.F., Levin, M., Korza, G., Barbarese, E., Yu, J., and Carson, J.H. (2012). Single-molecule imaging of translational output from individual RNA granules in neurons. *Mol. Biol. Cell* 23, 918–929.
- Tcherkezian, J., Brittis, P.A., Thomas, F., Roux, P.P., and Flanagan, J.G. (2010). Transmembrane receptor DCC associates with protein synthesis machinery and regulates translation. *Cell* 141, 632–644.
- Tucker, B., Richards, R.I., and Lardelli, M. (2006). Contribution of mGluR and Fmr1 functional pathways to neurite morphogenesis, craniofacial development and fragile X syndrome. *Hum. Mol. Genet.* 15, 3446–3458.
- Wang, J., Boja, E.S., Tan, W., Tekle, E., Fales, H.M., English, S., Mieyal, J.J., and Chock, P.B. (2001). Reversible glutathionylation regulates actin polymerization in A431 cells. *J. Biol. Chem.* 276, 47763–47766.
- Witte, S., Stier, H., and Cline, H.T. (1996). In vivo observations of timecourse and distribution of morphological dynamics in Xenopus retinotectal axon arbors. *J. Neurobiol.* 31, 219–234.
- Wu, B., Eliscovich, C., Yoon, Y.J., and Singer, R.H. (2016). Translation dynamics of single mRNAs in live cells and neurons. *Science* 352, 1430–1435.
- Yao, J., Sasaki, Y., Wen, Z., Bassell, G.J., and Zheng, J.Q. (2006). An essential role for beta-actin mRNA localization and translation in Ca²⁺-dependent growth cone guidance. *Nat. Neurosci.* 9, 1265–1273.
- Yoon, Y.J., Wu, B., Buxbaum, A.R., Das, S., Tsai, A., English, B.P., Grimm, J.B., Lavis, L.D., and Singer, R.H. (2016). Glutamate-induced RNA localization and translation in neurons. *Proc. Natl. Acad. Sci. USA* 113, E6877–E6886.

Regulation of Cerebral Cortex Folding by Controlling Neuronal Migration via FLRT Adhesion Molecules

Daniel del Toro,^{1,4} Tobias Ruff,^{1,4} Erik Cederfjäll,¹ Ana Villalba,² Gönül Seyit-Bremer,¹ Víctor Borrell,² and Rüdiger Klein^{1,3,5,*}

¹Max Planck Institute of Neurobiology, Am Klopferspitz 18, 82152 Martinsried, Germany

²Instituto de Neurociencias, Consejo Superior de Investigaciones Científicas and Universidad Miguel Hernández, 03550 Sant Joan d'Alacant, Spain

³Munich Cluster for Systems Neurology (SyNergy), 80336 Munich, Germany

⁴These authors contributed equally

⁵Lead Contact

*Correspondence: rklein@neuro.mpg.de

<http://dx.doi.org/10.1016/j.cell.2017.04.012>

SUMMARY

The folding of the mammalian cerebral cortex into sulci and gyri is thought to be favored by the amplification of basal progenitor cells and their tangential migration. Here, we provide a molecular mechanism for the role of migration in this process by showing that changes in intercellular adhesion of migrating cortical neurons result in cortical folding. Mice with deletions of FLRT1 and FLRT3 adhesion molecules develop macroscopic sulci with preserved layered organization and radial glial morphology. Cortex folding in these mutants does not require progenitor cell amplification but is dependent on changes in neuron migration. Analyses and simulations suggest that sulcus formation in the absence of FLRT1/3 results from reduced intercellular adhesion, increased neuron migration, and clustering in the cortical plate. Notably, FLRT1/3 expression is low in the human cortex and in future sulcus areas of ferrets, suggesting that intercellular adhesion is a key regulator of cortical folding across species.

INTRODUCTION

The cerebral cortex is a central region in the brain that controls high-level cognitive functions (Geschwind and Rakic, 2013). During evolution, the cortex has undergone an enormous expansion that mostly accounts for the increase in brain size across mammalian species (Finlay and Darlington, 1995). Because the cerebral cortex is a laminar sheet of tissue, its expansion coincides with the formation of folds consisting of gyri and sulci. Based on cortical folding, mammals can be classified into gyrencephalic species (such as ferrets and most primates), which have folded brains, and lissencephalic species (such as mice), which have smooth-surfaced cortices.

Mechanistically, cortex folding is promoted by regional cortical growth together with tangential expansion (Borrell and Götz,

2014; Borrell and Reillo, 2012; Reillo et al., 2011). This model is based on the finding that one of the germinal zones of the cortex, the subventricular zone (SVZ), is subdivided into an inner (ISVZ) and outer (OSVZ) subventricular zone in gyrencephalic but not in lissencephalic species, (Reillo et al., 2011). The OSVZ is a proliferative region that contains transit-amplifying basal progenitors (BPs) that expands concomitant with the onset of cortical folding (Hansen et al., 2010; Lui et al., 2011). Recent observations have shown that local amplification of BPs can lead to gyrus formation in the smooth mouse cortex (Florio et al., 2015; Rash et al., 2013; Stahl et al., 2013; Wang et al., 2016), whereas a decrease of the BP pool reduces the gyrification index in the ferret (Reillo et al., 2011; Toda et al., 2016), indicating that expansion of BPs represents a key event to induce gyration of the mammalian brain. Interestingly, new findings have challenged this model regarding its predictive power on the gyration of the cortex. Recent studies have shown that increasing proliferation of BPs in the mouse SVZ per se increased the cortical thickness or surface but was not sufficient to cause gyrification (Nonaka-Kinoshita et al., 2013; Thomson et al., 2009; Wagenführ et al., 2015). Notably, the prevailing hypothesis proposes that it is the combination of BP amplification with divergent radial migration that contributes to the expansion of the cortex in radial and tangential axes and then its folding (Borrell and Reillo, 2012; Fernández et al., 2016; Lui et al., 2011; Reillo et al., 2011). According to this model, migrating neurons do not follow strictly parallel pathways but, instead, follow divergent trajectories, dispersing in the lateral axis, which leads to tangential cortical expansion and folding. Failure in neuronal migration causes severe abnormalities in cortical folding that result in human lissencephaly (Moon and Wynshaw-Boris, 2013). Moreover, recent findings directly support the radial divergence hypothesis by showing that, in the ferret cortex, migrating neurons do not follow strict radial pathways but, instead, follow more tortuous migration routes concomitant with the start of cortical folding (Gertz and Kriegstein, 2015). However, molecular mechanisms that affect neuronal migration and modulate this trajectory divergence, resulting in cortex folding, have not been found. Moreover, no mouse gene has yet been identified whose genomic or global modification (rather than acute and local) favors folding of the smooth mouse cortex.

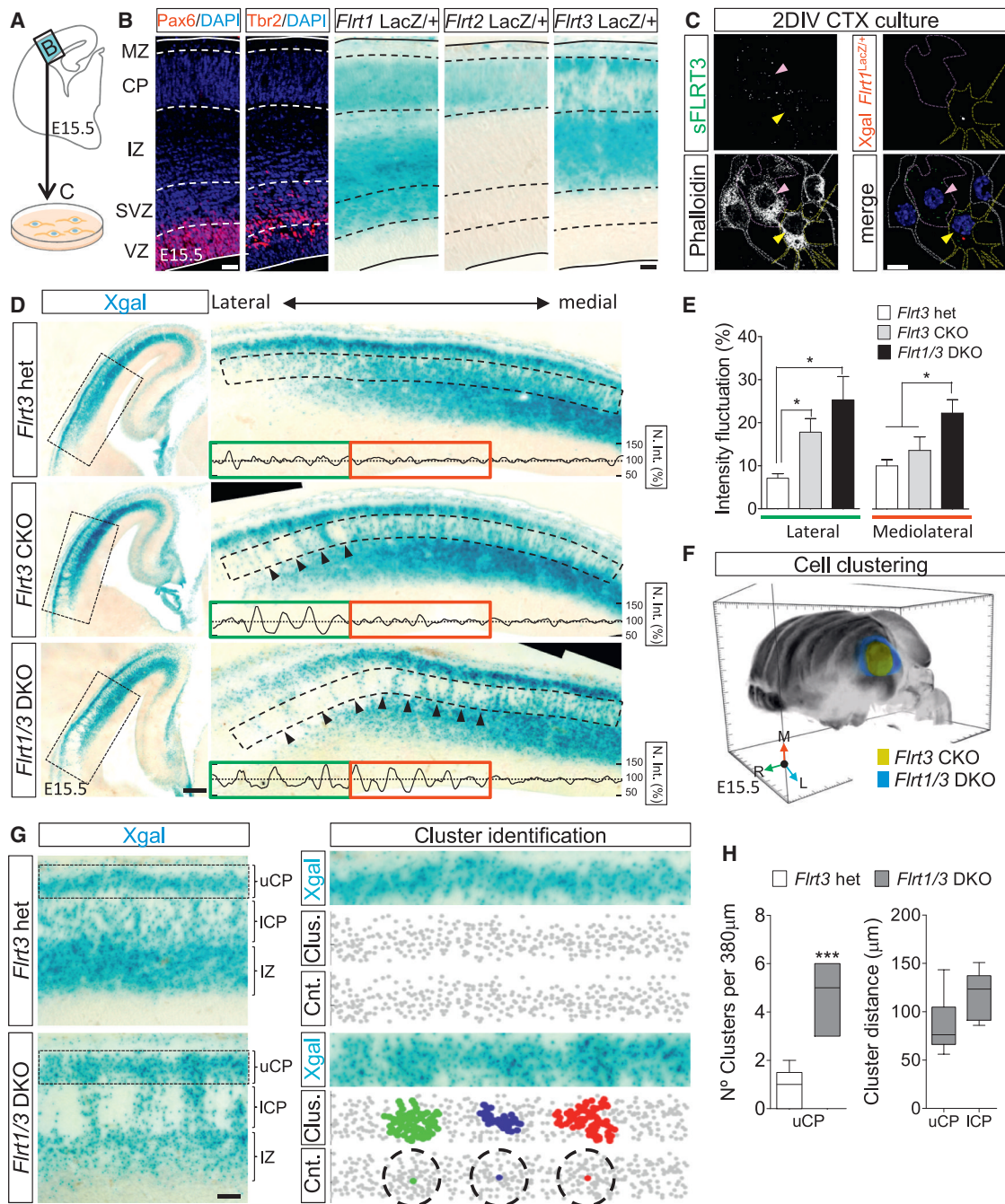


Figure 1. FLRT1 and FLRT3 Control Lateral Migration of Cortical Neurons

(A) Cortical region shown in (B) and source of cortical neurons shown in (C).
 (B) X-gal staining of FLRT1-3 expression on coronal sections of E15.5 cortex from *Flrt1-3^{lacZ/lx}* reporter lines. Cortical layers were identified by DAPI and immunostained for Pax6 and Tbr2.
 (C) *Flrt1^{lacZ/+}* cortical cultures at E15.5 (2 days in vitro), immunostained for FLRT3 (surface staining, green in merge), X-gal (for labeling *Flrt1+* cells, red in merge), and phalloidin. Yellow arrowheads/outlines indicate FLRT1/3 double-positive neurons. Magenta arrowheads/outlines show FLRT3 single-positive neurons. White outlines show FLRT3-negative neurons.
 (D) X-gal staining of coronal sections from E15.5 *Flrt3* heterozygous (*Flrt3^{ox/lacZ}*), *Flrt3* CKO and *Flrt1/3* DKO embryos. Areas in dashed rectangles are shown with higher magnification on the right. Normalized intensity plots are shown, obtained from the areas delineated with a dashed rectangle. Arrowheads indicate regions containing cell clusters, and green boxes highlight lateral and red boxes mediolateral portions of the cortex at intermediate-caudal levels.
 (E) Quantification of the intensity fluctuations in those portions of the neocortex; n = 3–5 mice/group, 2 sections/mouse; *p < 0.05, one-way ANOVA test with Tukey's post hoc analysis.

(legend continued on next page)

Previously, we have established that genetic ablation in mice of FLRT3, a member of the fibronectin leucine rich-repeat transmembrane protein (FLRT) family of cell adhesion molecules, leads to altered distribution of pyramidal neurons during cortical development, forming a repeated pattern of clusters along the tangential axis (Seiradake et al., 2014). FLRTs have the unique property of acting as adhesion molecules by homophilic and heterophilic binding to Latrophilin proteins and as repellents by binding to Unc5/Netrin receptors (Jackson et al., 2015, 2016; Yamagishi et al., 2011). Here we report that genetic ablation of FLRT1 and FLRT3 leads to the development of macroscopic cortical sulci during embryogenesis. Mechanistically, this process happens independent of progenitor cell amplification. Instead, we found that cortical neurons display reduced intercellular adhesion, faster neuronal migration, and clustering along the tangential axis, thereby leading to sulcus formation in the normally smooth mouse neocortex. Our results suggest that intercellular adhesion of migrating cortical neurons is a key factor underpinning folding of the cerebral cortex.

RESULTS

FLRT1 and FLRT3 Control the Lateral Dispersion of Pyramidal Neurons

Expression analysis of FLRTs in the developing cortex from embryonic day 13.5 (E13.5) to E17.5 (Figures 1A and 1B and Figures S1A–S1C and S1F) revealed a partial overlap between FLRT1 and FLRT3 in both the intermediate zone (IZ) and cortical plate (CP), whereas FLRT2 was confined to the CP. In cultures of dissociated cortical neurons from E15.5 embryos, approximately 30% were FLRT3-positive, and, among those, 35% co-expressed FLRT1 (Figure 1C). This finding was consistent with a molecular identity analysis from the E15.5 mouse cortex that also revealed strong enrichment of both FLRT1 and FLRT3 in migrating upper cortical neurons among other cell types (Figures S1D and S1G). To investigate whether FLRT1 plays a role in pyramidal neuron migration, possibly in a functionally redundant fashion with FLRT3, we generated double knockout mice lacking FLRT3 in developing neurons and progenitors and FLRT1 in all cells (*Flrt1*^{-/-}; *Flrt3*^{lox/lacZ}; *Nestin-Cre* mice; in short, *Flrt1/3* double knockout [DKO]) and compared them to the respective single mutants (*Flrt3*^{lox/lacZ}; *Nestin-Cre*; in short, *Flrt3* conditional knockout [CKO], and *Flrt1* knockout [KO] mice). In agreement with our previous work (Seiradake et al., 2014), we found that FLRT3-deficient (β -galactosidase [β -gal]⁺) neurons in *Flrt3* CKOs showed abnormal cell clustering in the lateral portion of the neocortex within the lower CP (Figures 1D and 1E; Figure S1I). Interestingly, this cell clustering effect was enhanced

in *Flrt1/3* DKO compared with *Flrt3* CKO mice, extending into medial and caudal regions of the cortex (Figures 1D–1F; Figure S1J; data not shown). To analyze the distribution of β -gal⁺ neurons, we calculated the normalized intensity profile of the X-gal staining in the lower half of the cortical plate (dashed region, Figure 1D), which revealed extended fluctuations in the density of *Flrt1/3* DKO neurons compared with *Flrt3* CKO and *Flrt3* heterozygous neurons (Figure 1E). To test whether the repeated pattern of cell clusters extended to the upper CP, we performed a distance-based clustering analysis, using as input the coordinates of X-gal-positive neurons populating the upper CP. We observed clustering of neurons in the upper CP of *Flrt1/3* DKO following a pattern of approximately 75- to 120- μ m intervals, in line with the pattern present in the lower CP (Figures 1G and 1H). This suggests that the altered localization and clustering of cells in the *Flrt1/3* DKO extended into the upper CP, where cells normally spread laterally to form cortical layers. Taken together, these results indicate partially redundant roles of FLRT1 and FLRT3 in controlling the tangential distribution of pyramidal neurons during cortical development.

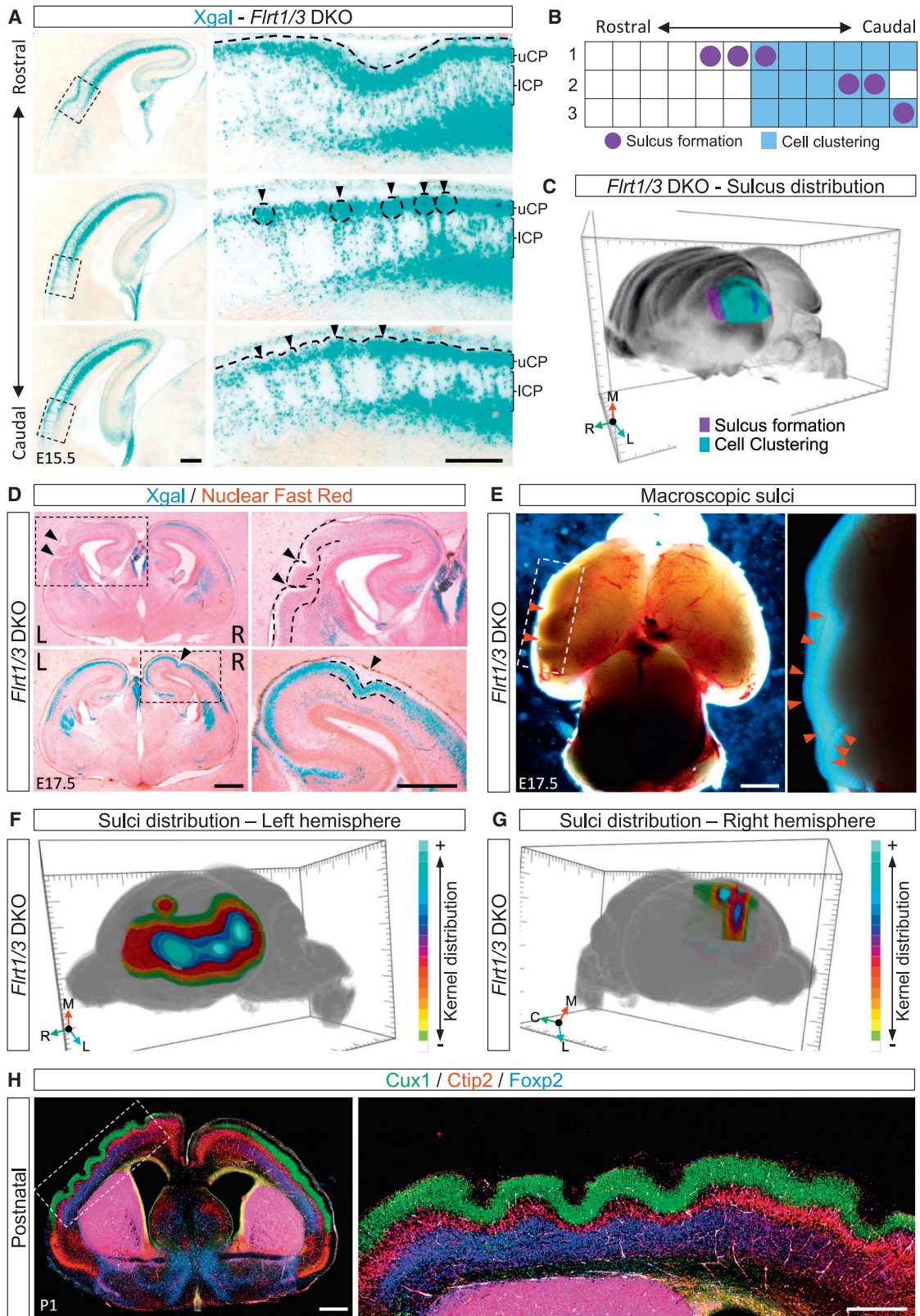
Flrt1/3 CKO Mice Develop Cortical Sulci

Upon further inspection of *Flrt1/3* DKO embryos, we found that, in 33% of the cases, the clustering of upper CP neurons at E15.5 correlated with the formation of an incipient sulcus in the otherwise smooth mouse neocortex (Figure 2A; Figures S2A and S2B). These cortical sulci developed on the lateral side of the cortex from intermediate to caudal levels where the repeated pattern of neuronal clusters was present in mutant embryos (Figures 2B and 2C), suggesting that these processes were causally linked. At later stages of cortical development (E17.5), cortical sulci were found in *Flrt1/3* DKO embryos, with a similar penetrance of 31% (Figure S2C). They showed considerable phenotypic variability between embryos, ranging from shallow to deep sulci that were easily visible in intact brains after removal of the meninges (Figures 2D and 2E).

Because cortical folding is not a random process but, rather, forms stereotyped patterns in gyrencephalic species (Borrell and Reillo, 2012), we determined the spatial distribution of sulci at E17.5. We used a kernel density estimator based on the location of sulci in coronal sections and plotted it onto a 3D mouse brain template. This analysis revealed that the left hemisphere had a higher probability of developing sulci and that they were mostly located between the perirhinal and postrhinal cortices of the mouse, close to the rhinal fissure (Beaudin et al., 2013; Figure 2F; Movie S1). In contrast, the right hemisphere developed sulci in rostro-medial cortical regions where clusters were not visible, suggesting that other mechanisms might also participate

(F) 3D mouse brain (template from the Allen Mouse Brain Atlas) with cortical areas displaying cell clustering in *Flrt3* CKO (green area) and *Flrt1/3* DKO (blue area) at E15.5.

(G) X-gal staining of coronal sections from E15.5 *Flrt3* heterozygous and *Flrt1/3* DKO embryos. Cell clusters in the upper CP were identified based on the position of individual X-gal⁺ neurons (areas in dashed rectangles are shown with higher magnification on the right) using a distance-based clustering method (a cluster was defined as a minimum of 25 cells spaced less than 20 μ m). Cluster identification is as follows. Neuron clusters in *Flrt1/3* DKO embryos are marked with different colors (red, green, and blue; "Clus"), and centroids of each cluster (cnt) are shown in the same color. Neurons that are not clustered are colored in gray. (H) Quantification of the number of clusters and the distance between them from the data shown in (G); n = 3–5 mice/group; ***p < 0.001, unpaired Student's t test. Whiskers in the box plot represent minimum and maximum. The data are presented as mean \pm SEM. Scale bars represent 150 μ m (B), 14 μ m (C), 300 μ m (D), and 50 μ m (G).



(legend on next page)

in this process (Figure 2G; Movie S1). The variability in sulcus location may have to do with the absence of gene expression microdomains. These structures play an important role in the generation of gyri/sulci at specific locations and are present in the developing cortex of gyrencephalic species such as the ferret but not in the lissencephalic mouse (de Juan Romero et al., 2015). Sulci were also found in postnatal stages of *Flrt1/3* DKO mice (penetrance, 24%) (Figure 2H; Figures S2D and S2E), indicating that these were not transient embryonic structures. The examination of single mutant brains revealed that *Flrt1* KO, but not *Flrt2* or *Flrt3* CKO, brains showed sulcus formation, albeit with lower penetrance (12%–16%; Figures S2C and S2D). In addition, *Flrt2/3* DKO brains rarely showed sulcus formation (1 in 13), suggesting that *Flrt1* plays a major role in the phenotype (Figures S2C and S2F). The morphologies of the sulci in *Flrt1* KO brains were comparable with those observed in *Flrt1/3* DKO brains (Figure S2G), suggesting that the underlying mechanisms were similar. These results indicate that FLRT1 and FLRT3 have partially redundant functions in the formation of a smooth neocortex.

Cortical Sulci Develop Independent of Cell Proliferation

As a first step toward understanding the mechanism involved in sulcus formation in *Flrt1/3* DKO brains, we analyzed cell proliferation in brain sections at different stages of cortical development by quantifying the numbers of apical (Pax6+) and basal (Tbr2+) progenitors (Englund et al., 2005). We also stained for the phosphorylated forms of vimentin (Pvim) and histone H3 (PH3) that label dividing radial glial (RG) and mitotic cells, respectively (Pilz et al., 2013). We did not find significant increases in mitotic and dividing RG cells in mutant embryos at different developmental stages and in different rostro-caudal regions, except for a small increase in intermediate cortical regions at E13.5 (Figures 3A–3C; Figures S3A–S3L). Moreover, the proportion of mitotic cells in basal versus apical germinal layers was unchanged in *Flrt1/3* mutant brains (Figure 3D; Figures S3D, S3H, and S3L), and the numbers of dividing basal RG cells were less than 5% in all experimental groups (data not shown). Quantification of total cell nuclei (stained with DAPI), Pax6+ and Tbr2+ progenitor cells, and short pulses of BrdU did not reveal significant increases in *Flrt1/3* mutant brains (Figure 3C; Figures S3C, S3G, S3K, and S3M–S3Q), suggesting that cortical sulci develop independent of changes in cell proliferation.

Next we explored alternative mechanisms underlying sulcus formation, such as alterations in the RG fiber scaffold, basement membrane formation, and Cajal-Retzius (CR) cell development. Tracing of individual RG fibers in *Flrt1/3* DKOs based on brain lipid-binding protein (BLBP) staining showed that RG processes located in sulcus areas reached the marginal zone (MZ), similar to control regions, even when sulci were very deep (Figure 3E; Figure S4A). The overall densities and lengths of RG processes in sulcus areas did not differ from adjacent regions (Figure S4B). The curvature index of RG processes was significantly higher in sulcus areas because of the convergence of fibers at sulcal pits (Figures 3E and 3F), similar to those reported in classic descriptions of gyrencephalic species such as ferrets and monkeys (Rakic, 1972; Smart and McSherry, 1986). Remarkably, the basal membrane was intact in seven of eight mutant brains (Figures S4C and S4D), suggesting that these sulci were not the result of neuronal ectopias as observed in cobblestone lissencephaly (Devisme et al., 2012). Because CR cells originating from the cortical hem (CH) express both FLRT1 and FLRT3 (Figures S4E–S4G), we also explored whether loss of FLRT1/3 affected CH-derived CR cell migration. We found that the distribution and density of CR cells in the MZ of sulcus areas in mutant brains appeared normal (Figure 3E), even in dramatic cases where the MZ followed the depth of the sulcus (Figure S4A). These results suggest that cortical sulci in *Flrt1/3* DKOs are not the result of alterations in RG scaffold, basal membrane formation, or CR cell development.

FLRT1/3-Deficient Pyramidal Neurons Reach Upper Cortical Layers Faster

Given the lack of strong alterations in progenitors and glial cells, we next asked whether sulcus formation correlated with changes in the migration and distribution of pyramidal neurons. Cortical layering seemed well preserved in sulcus areas of *Flrt1/3* DKO compared with controls (Figure 3G), but layer thickness was reduced, particularly in the lower CP (Figures S4H and S4I), similar to those reported in gyrencephalic species such as the ferret (Smart and McSherry, 1986). Notably, the proportion of Cux1+ neurons (Nieto et al., 2004) in the upper versus lower CP was significantly higher in sulci with respect to adjacent areas (Figures 3H and 3I). Similar results were obtained after bromodeoxyuridine (BrdU) pulse labeling of newborn pyramidal neurons at E14.5 and analyzing their distribution in the CP at E17.5

Figure 2. *Flrt1/3* CKO Mice Develop Cortical Sulci

(A) X-gal-stained serial coronal sections from the cortex of an E15.5 *Flrt1/3* DKO embryo. Areas in dashed rectangles are shown with higher magnification on the right. Dashed circles and arrowheads indicate prominent clustering of neurons in the upper CP, and horizontal dashed lines highlight incipient sulcus formation (top) and a wavy surface of the upper CP (bottom).

(B) Twelve sections, rostral to caudal, of three *Flrt1/3* DKO brains (rows 1–3) at E15.5 were analyzed for the presence of sulci (circles) or cell clustering (blue squares).

(C) 3D representation of the data shown in (B).

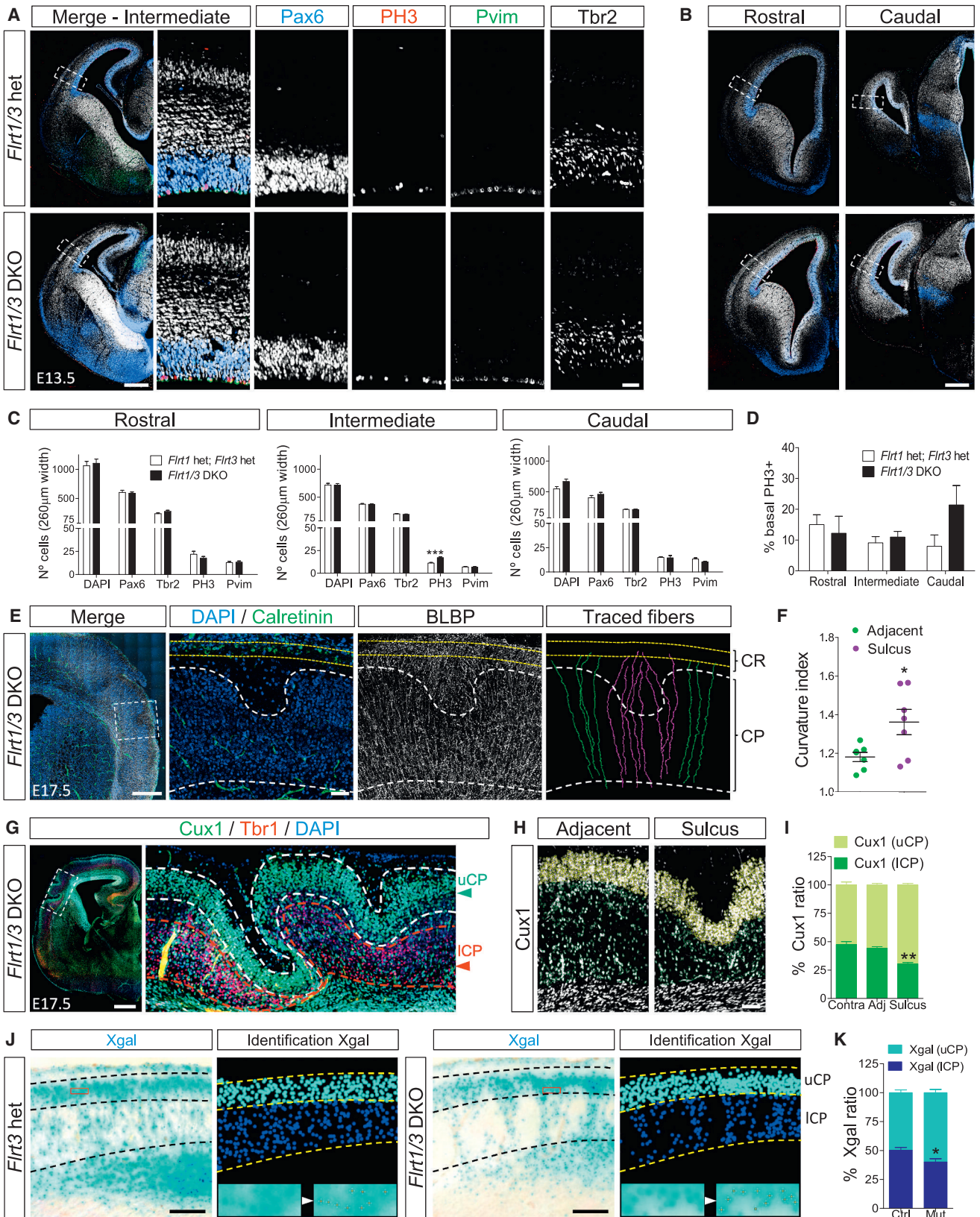
(D) Coronal sections from two E17.5 *Flrt1/3* DKO brains with different degrees of sulcus formation in the cortical plate (arrowheads). Sections were stained with X-gal and nuclear fast red. Areas in dashed rectangles are shown with higher magnification on the right.

(E) Macroscopic sulci in an E17.5 *Flrt1/3* DKO embryo. The area in the dashed rectangle is shown with higher magnification on the right, and sulci are indicated by arrowheads.

(F and G) Sulcus distribution in the left (F) and right (G) hemispheres of all E17.5 *Flrt1/3* DKO embryos. The color bar indicates a higher (blue colors) or lower (green-white) density of sulci.

(H) P1 FLRT1 KO brain section stained with Cux1, Ctip2, and Foxp2. Areas in dashed rectangles are shown with higher magnification on the right.

Scale bars represent 300 μ m (A), 500 μ m (D), 1 mm (E), and 2.4 mm and 0.4 mm (H).



(legend on next page)

(Figures S4J and S4K). These results suggested that either FLRT1/3-deficient pyramidal neurons migrated faster through the cortical plate, thereby causing sulcification, or that sulcification provided a shorter migration distance compared with non-sulcus areas, resulting in a higher proportion of cells in the upper CP. Given that only a portion of migrating neurons expressed FLRT proteins, we next analyzed the distribution of FLRT3-deficient (β -gal+) neurons and compared non-sulcus areas of *Flrt1/3* DKO with controls. We found that the proportion of cells in the upper CP was higher in *Flrt1/3* DKO (Figures 3J and 3K). These results suggest that FLRT1/3-deficient pyramidal neurons migrate faster through the cortical plate than FLRT1/3-expressing neurons.

Lack of FLRT1/3 Increases Migration Speed

To obtain direct evidence for changes in the migration speed of cortical neurons, we performed live imaging of embryonic cortices *ex vivo*. Control and *Flrt1/3* DKO brains were sliced and imaged 48 hr after electroporation with pCAG-CRE and the Cre reporter pCALNL-DsRed to visualize migrating cells. This approach (Cre electroporation into *Flrt1/3* DKO embryos) was chosen over Cre electroporation into *Flrt1^{-/-}Flrt3^{lox/lox}* brains because the latter approach did not reliably induce sulci compared with control brains, presumably because of the low abundance of electroporated cells (data not shown). A caveat of the former approach was that only a subset of Cre reporter-positive cells expressed FLRT proteins because these brains also contain many non-FLRT-expressing cells (Figure 4A; Figures S5A and S5B). Hence, a large proportion of Cre reporter-positive cells in *Flrt1/3* DKO brains were not directly affected by the *Flrt1/3* mutations, thereby potentially masking subtle defects. Individual Cre reporter-positive neurons entering the CP from the IZ were tracked and processed using a custom Python algorithm that allowed us to quantify migration parameters and to color-code portions of each track based on migration speed (Figure 4B). Overall, Cre+ cells in *Flrt1/3* DKO neurons displayed parallel and straight paths (Figure S5C), except in rare cases when migrating through a forming sulcus, where they displayed convergent paths (Figure S5D; Movie S2). Similar to controls,

Cre+ neurons exhibited the stereotypic RG-based locomotor pattern with high speeds ($>32 \mu\text{m/h}$) in the middle of the CP and decreasing speeds toward the upper CP (Kawauchi, 2015; Tabata and Nagata, 2016; Figure 4C). Given that Cre+ cells in *Flrt1/3* DKO neurons showed trends toward higher maximum speed and acceleration, we analyzed their speed profiles. These results revealed an increased proportion of high-speed segments ($>58 \mu\text{m/h}$) in *Flrt1/3* DKO compared with control brains (Figure 4D; Figures S4E and S4F). Plotting the relative frequencies of the maximum migration speeds revealed that the fraction of cells reaching $>70 \mu\text{m/h}$ was significantly increased in *Flrt1/3* DKO brains compared with controls (19% versus 12%) (Figure 4E). These results suggest that *Flrt1/3* mutant neurons reached higher speeds more often than control neurons.

To assess the morphologies of individual *Flrt1/3* mutant neurons, we sparsely labeled *Flrt1/3* DKO neurons in an otherwise control background by introducing Cre and a Cre reporter into *Flrt1^{-/-}Flrt3^{lox/lox}* brains using the Supernova system, which makes use of a leaky Tet promoter driving Cre expression in few cells (Mizuno et al., 2014; Figure 4F). The general complexity of mutant neurons populating the lower CP appeared similar to those observed in control sections, as assessed by Sholl analysis (data not shown). When categorizing the neurons according to increasing maturity into multipolar, unipolar and bipolar neurons, and “bipolar branched” morphologies (Figure 4F), we observed a significant shift toward immature morphologies in the upper CP of Cre-induced *Flrt1/3* mutant neurons compared with controls (Figure 4G). Thus, ablation of FLRT1/3 increases the abundance of immature neurons in the upper cortical plate.

Modeling Clustering and Speed Profiles of *Flrt1/3* DKO Neurons

So far our analysis suggested a model in which increased migration speeds of *Flrt1/3* mutant neurons and/or the formation of cell clusters in the CP could be causal to sulcus formation (Figure 5A). To test this hypothesis, we performed data-driven computational modeling of neurons migrating through the CP. We took the following points into consideration. Both FLRT3 gain- and loss-of-function experiments *in vivo* revealed a repeated pattern

Figure 3. Pyramidal Neuron Distribution, but Not Cell Proliferation, Is Changed in Sulcus Areas

(A and B) E13.5 cortices from intermediate (A) and rostral, caudal regions (B) of control and *Flrt1/3* DKO embryos were labeled for the neuronal progenitors Pax6 (blue) and Tbr2 (white), mitotic cells (PH3, red), and dividing RG cells (Pvim, green). Areas in dashed rectangles in (A) are shown with higher magnification on the right.

(C) Quantification of the data shown in (A) and (B) ($n = 3-4$ mice/group). *** $p < 0.001$, unpaired Student's t test.

(D) Proportion of basal mitotic cells (PH3) ($n = 3-4$ mice/group; no significant changes between groups, unpaired Student's t test).

(E) *Flrt1/3* DKO section immunostained for BLBP (white), calretinin (green), and DAPI (blue). The area in the dashed rectangle is shown with higher magnification on the right. White dashed lines delineate sulci, and yellow dashed lines show the margins of the MZ where calretinin+ CR cells are located. Single traced RG processes are colored in magenta (in the sulcus region) or green (adjacent areas).

(F) Quantification of the curvature index of traced fibers shown in (E). $n = 7$ adjacent fibers, $n = 8$ sulcus fibers. * $p < 0.05$, unpaired Student's t test.

(G) E17.5 *Flrt1/3* DKO cortex immunostained for upper (Cux1, green) and deeper-layer (Tbr1, red) neurons and DAPI (blue).

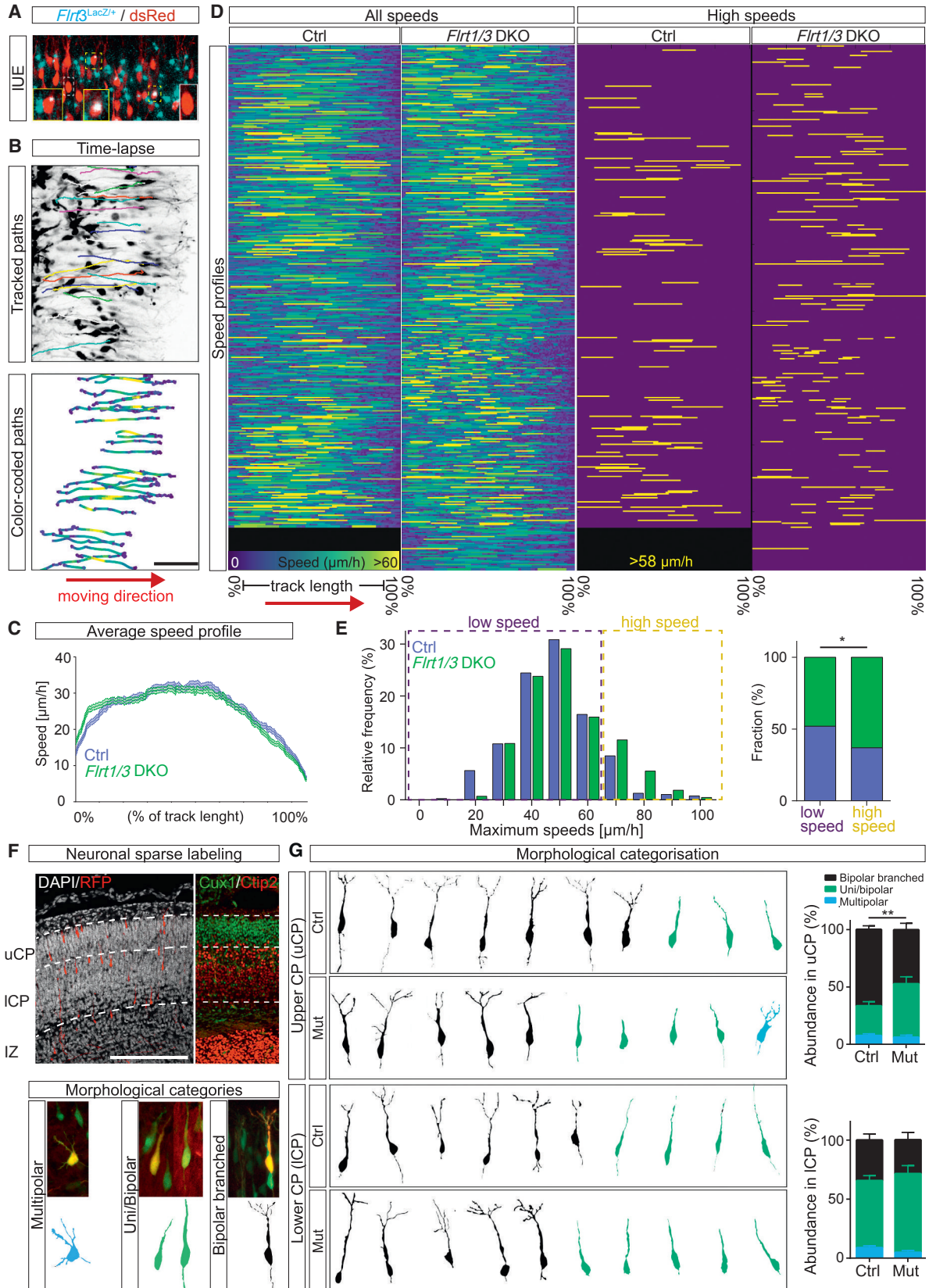
(H) Sulcus and adjacent region from an E17.5 *Flrt1/3* DKO section immunostained with Cux1 (white). Cux1+ cells in the upper CP are highlighted in light green, and Cux1+ cells still migrating in the lower CP are highlighted in dark green.

(I) Quantification of the data shown in (H) ($n = 12$ sections from a total of 5 mutant brains). ** $p < 0.01$, one-way ANOVA test with Tukey's post hoc analysis.

(J) X-gal staining of coronal sections from E15.5 *Flrt3* heterozygous and *Flrt1/3* DKO embryos. The CP was subdivided into upper and lower CP (Figure S11). The coordinates of X-gal precipitates (the red rectangle is shown with higher magnification on the right) were plotted as circles colored cyan (upper CP) and blue (lower CP).

(K) Quantification of the data shown in (J).

ICP, lower cortical plate (ICP). The data are represented as mean \pm SEM. Scale bars represent 400 and 150 μm (A), 400 μm (B), 600 and 100 μm (E), 500 μm (G), 90 μm (H), and 120 μm (J).



(legend on next page)

of cell clusters (Seiradake et al., 2014; Figure 1), which can be modeled as sine equations (Figure 5B). FLRTs act as cell adhesion molecules. This was shown for FLRT3 overexpression on cell clustering in vivo (Seiradake et al., 2014) and for FLRT-mediated cell aggregation in vitro (Figures S6A and S6B). The effects of *Flrt1/3* ablation on cell clustering in vivo are likely non-cell autonomous and may be the result of repulsive interactions with surrounding cells. Based on these considerations, we established two rules for the computational model: the sine equation modeled from gain-of-function experiments reflected the attraction forces of FLRT1/3+ neurons, and the sine equation from loss-of-function experiments represented the repulsion forces that FLRT1/3+ neurons are exposed to from surrounding cells. We distributed particles representing FLRT1/3-positive and -negative cells in a 2D grid, keeping equal distances and homogeneous distributions as observed in *Flrt1/3* heterozygous control sections. Particles representing FLRT1/3+ neurons showed attraction between them (first rule), whereas surrounding particles elicited repulsion toward them (second rule) (Figure 5C). To analyze the behavior of the particles during movement, particles were set to move along the z axis, and both speed and attraction-repulsion forces were random within a small range (ϵ) to mimic the fluctuations present in biological systems (Wilkinson, 2009). The attraction force was modulated by changing its amplitude and phase with respect to the repulsive force, which was kept constant under all conditions to reflect FLRT1/3 gain- and loss-of-function experiments (Figure S6C). Kernel distribution and minimum neighbor analysis of particles representing FLRT1/3+ neurons showed homogeneous distribution of particles when attraction and repulsion forces were balanced (Figures 5D and 5E). In contrast, particle clustering was observed when the attraction between particles was either high or low (Figures 5D and 5E; Figure S6D), which was consistent with the formation of neuronal clusters when FLRT1/3 were overexpressed or downregulated in vivo. Interestingly, the distribution of particles in the z axis was also influenced by attraction and repulsion forces. Under both high and balanced attraction conditions, the particles formed a smooth surface after moving along the z axis. Conversely, the low attraction paradigm resulted in a wavy surface because of an increased proportion of particles moving with high speed, reminiscent of the live imaging experiments with *Flrt1/3* DKO sections (Figures 5F and 5G).

Taken together, the low attraction paradigm of the computational model matched the experimental observations with *Flrt1/3* DKO mice rather well by generating particle clusters, increasing particle migration speed, and producing a wavy surface area.

FLRT Expression in Gyrencephalic Species

Given that FLRT1/3 ablation promoted sulcus formation in the normally smooth mouse neocortex, we set out to analyze endogenous FLRT1/3 expression in gyrencephalic species such as ferret and human. We hypothesized that FLRT1/3 expression levels may be generally low in gyrencephalic species to permit folding or relatively less abundant in sulcus than in gyrus areas. The ferret cortex is nearly lissencephalic at birth and undergoes complex and stereotyped postnatal folding (Reillo et al., 2011; Smart and McSherry, 1986). We analyzed ferret FLRT1/3 expression prior to morphological distinction of the prospective splenial gyrus and its adjacent lateral sulcus because previous studies have successfully identified genes involved in cortical folding in these regions (de Juan Romero et al., 2015; Figure S6E). In situ hybridization (ISH) for *Flrt1/3* revealed that both genes were mainly expressed in the CP, ISVZ, and OSVZ and, to a lesser extent, in the IZ at post-natal day 0 (P0) and P6 (Figures 6A and 6B; Figures S6F and S6G). Quantification of the expression levels revealed that both FLRT1 and FLRT3 were significantly less abundant in the cortical area that will form the lateral sulcus compared with the splenial gyrus (Figures 6C and 6D).

To study FLRT expression in human embryos, we used RNA sequencing (RNA-seq) data from three different sources. We first compared mouse FLRT1 and FLRT3 mRNA expression levels in E14 neocortex (subdivided into medial and lateral portions; (Wang et al., 2016) with RNA-seq data from human embryonic cortex at 12–19 post-conception weeks (pcw) (<http://www.brain-map.org>) normalized to the housekeeping gene GAPDH (Figures S6H and S6I). There were consistently higher levels in mouse cortex compared with a number of different cortical regions in human samples. Second, we analyzed mouse and human FLRT1 and FLRT3 normalized to GAPDH in different cortical layers (Fietz et al., 2012; Figures 6E and 6G). The abundance of mouse FLRT1 and FLRT3 mRNAs in the SVZ region ranged between 24%–49% of GAPDH, whereas the levels of human FLRT1 and FLRT3 ranged between 1%–3% of GAPDH (the human ISVZ

Figure 4. Faster Speed Profiles of *Flrt1/3* DKO Neurons

(A) *Flrt1/3* DKO embryos were electroporated at E13.5 with pCAG-Cre and the pCALNL-DsRed reporter plasmid (red staining; Figure S5). Yellow and white boxes indicate double dsRed/*Flrt3*+ and single dsRed+ cells, respectively.

(B) Time-lapse analysis of electroporated neurons migrating into the cortical plate in cultured E15.5 cerebral cortex slices. Migrating neurons were tracked (colored lines, top) and color-coded based on speeds in individual segments (bottom).

(C) Average speed profiles normalized to CP length of *Flrt1/3* DKO and littermate control embryos (from >400 tracked neurons).

(D) Color-coded speed profiles of >400 tracked neurons in controls and *Flrt1/3* DKO embryos normalized to total migration distance. Speeds higher than 58 $\mu\text{m}/\text{h}$ are highlighted in yellow on the right.

(E) Maximum speed frequency distribution of all tracked neurons in controls and *Flrt1/3* DKO embryos. Dashed rectangles indicate low (blue) and high (yellow) speed profiles, and their fraction is shown on the right. * $p < 0.05$, chi-square contingency analysis.

(F) Sparse cell labeling via electroporation at E13.5 of the Supernova vector system into either *Flrt1* $-/-$; *Flrt3**lx/lx* (mutant) or *Flrt1* $+/-$; *Flrt3**lx/+* (control) littermates. At E16.5, Cre+ neurons were imaged and categorized according to their degree of maturity into multipolar, uni/bipolar, or bipolar branched phenotypes (example images are shown). The upper third portion of the CP was designated as upper CP based on the staining of *Cux1* (top, green) and *Ctip2* (bottom, red) markers.

(G) Abundance of each category of neurons in the lower and upper CP of mutant and control brains (representative images are shown; >150 neurons/group, * $p < 0.05$, chi-square contingency analysis).

IUE, in utero electroporation. The data bars are represented as mean \pm SEM. Scale bars represent 50 μm (B) and 200 μm (F).

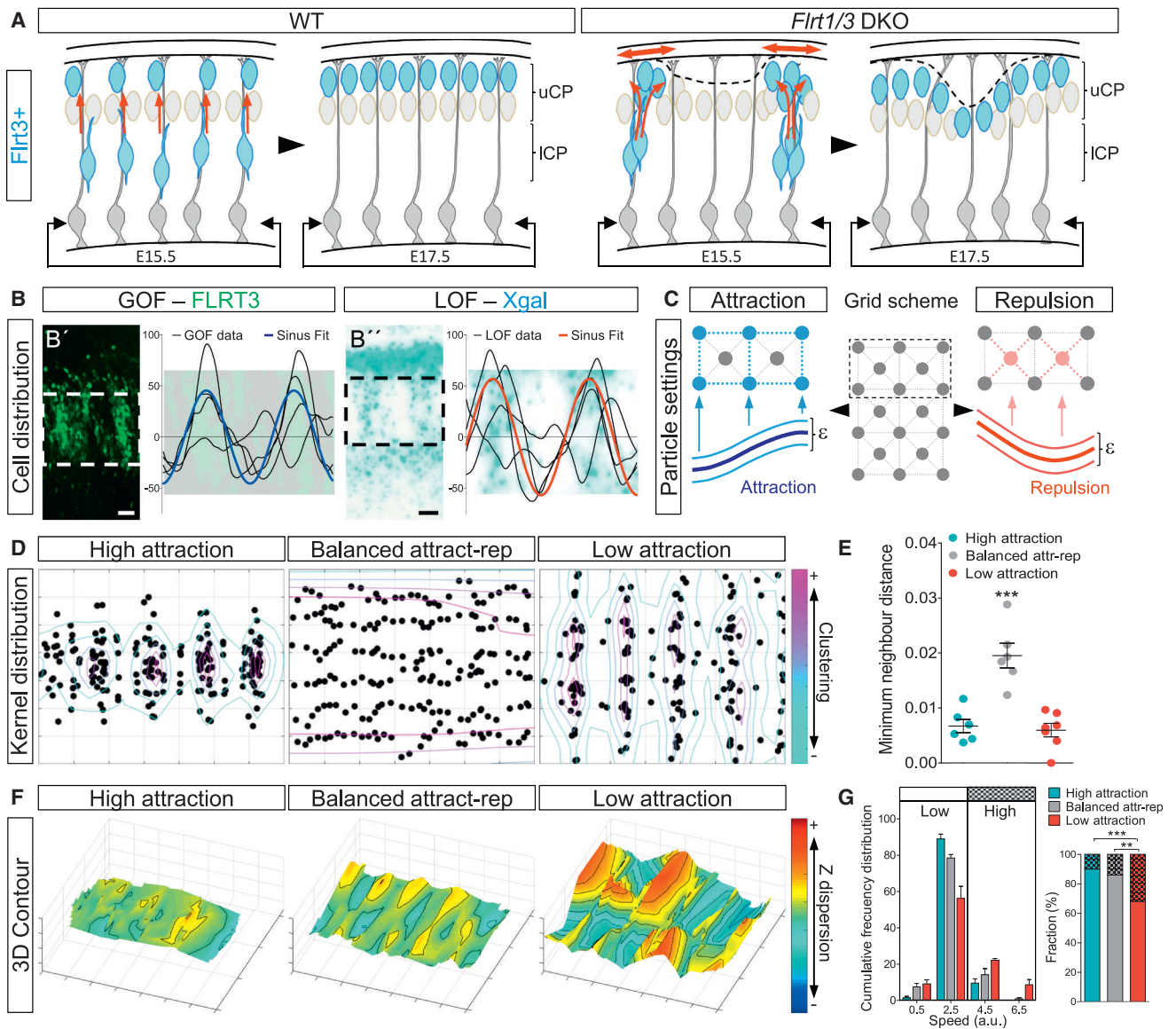


Figure 5. Computer Modeling Matches *Flrt1/3* DKO Experimental Observations

(A) Hypothetical model of sulcus formation in *Flrt1/3* DKO brains. In the wild-type (WT), *Flrt1/3*+ neurons show homogeneous distribution while migrating through the CP at E15.5 and form a uniform layer in the upper CP at E17.5. Loss of *FLRT1/3* induces cell clustering in the lower and upper CP, creating imbalanced tension forces, and loss of adhesion may increase tissue elasticity, ultimately leading to sulcus formation.

(B) *FLRT1/3* overexpression (GOF, B') or ablation (LOF, B'') alters the attraction-repulsion balance, resulting in the formation of neuronal cell clusters, which can be modeled as sinus equations. The graphs depict experimental data (black) and sinus fit (colored). The scale bar represents 40 μ m.

(C) Scheme illustrating how particles representing *FLRT1/3*-positive (blue) and -negative neurons (red) are arranged. Blue particles show attraction between them. Red particles repel blue particles. Both attraction and repulsion forces are based on the sinus equation modeled (B). ϵ represents noise added to the system.

(D) Distribution of particles representing *FLRT1/3*+ neurons after computer simulations with high, balanced, or low attraction forces. The colored lines indicate a higher (magenta) or lower (cyan) density of particles based on their kernel distribution.

(E) Minimum neighbor distance of particles shown in (D). $n = 10$ computer simulations comprising 480 particles. *** $p < 0.001$, one-way ANOVA test with Tukey's post hoc analysis.

(F) Distribution of particles on the z axis after computer simulations. Note that both high and balanced attraction conditions result in a uniform surface, whereas low attraction conditions produce a wavy surface after computer simulations.

(G) Frequency distribution of speed profiles of particles shown in (F). Rectangles indicate low (plain) and high (pattern) speed profiles, and their relative fractions are shown on the right. ** $p < 0.01$, *** $p < 0.001$, chi-square contingency analysis.

The data are represented as mean \pm SEM.

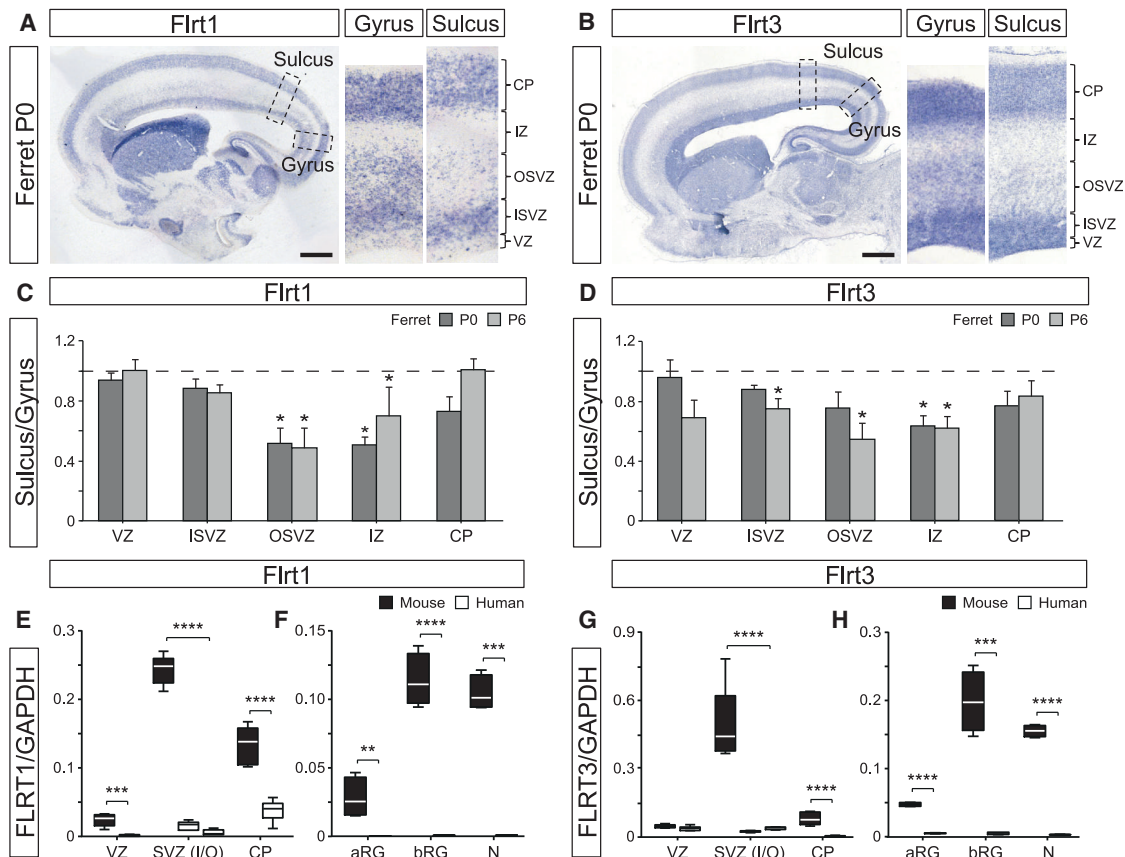


Figure 6. Low Endogenous Levels of FLRT1 and FLRT3 in a Future Sulcus Area of Ferret Cortex and in Specific Layers of Human Cortex (A and B) ISH for FLRT1 (A) and FLRT3 (B) in sagittal sections of ferret cortex at P0. Regions marked by dashed rectangles delineate a prospective lateral sulcus (Sulcus) and splenial gyrus (Gyrus) and are shown with higher magnification on the right. The scale bars represent 1 mm. (C and D) Intensity quantification of the images in (A) and (B) and Figures S6F and S6G, expressed as a ratio of sulcus/gyrus in different cortical layers at P0 and P6 ($n = 3$ separate ISH experiments for each group). * $p < 0.05$, unpaired Student's t test. (E–H) Comparison of FLRT1 and FLRT3 expression between mouse and human with sequencing data from Fietz et al. (2012) (GEO: GSE38805) and Florio et al. (2015) (GEO: GSE65000). FLRT1 and FLRT3 mRNAs are more abundant in mouse compared with human when comparing different germinal layers (E and G) and specific cell types, including apical radial glia cells (aRG), basal radial glial cells (bRG), and migrating neurons (F and H). FLRT sequencing data were normalized to housekeeping genes, including GAPDH (this figure) and PGK1 (Figures S6J–S6M). Whiskers in the boxplot represent minimum and maximum; unpaired Student's t test, ** $p < 0.01$, *** $p < 0.001$, **** $p < 0.0001$.

and OSVZ were combined). Relatively higher levels of mouse FLRT1 and FLRT3 were also seen in the CP. Higher levels of mouse FLRT1, but not FLRT3, were seen in the VZ. Normalizing FLRT1 and FLRT3 expression to another housekeeping gene (PGK1) gave similar results (Figures S6J and S6L). Third, we compared FLRT1/3 expression in apical and basal RG and migrating neurons in human and mouse (Florio et al., 2015; Figures 6F and 6H; Figures S6K and S6M). FLRT1 and FLRT3 expression in the mouse was highest in migrating neurons and basal RG cells, which are the mouse homologs of the outer RG cells found in gyrencephalic species (Borrell and Götz, 2014). Notably, FLRT1/3 levels in these cells were much higher in mouse than in human cortex. Given the high levels of FLRT1/3 in basal RG cells, we also asked whether the fraction of pvim-positive cells that display a basal radial glia-like morphology was altered in the FLRT1/3 DKO mice. This was not the case (Figures S6N and S6O), providing more evidence for lack of basal

radial glia involvement in the FLRT KO phenotype. Overall, these results revealed an inverse correlation between the presence of cortical folds/sulci and FLRT1/3 levels. Thus, the human neocortex expresses lower levels of FLRT1/3 compared with the mouse neocortex, and, in the ferret cortex, FLRT1/3 expression levels are less abundant in prospective sulcus than in gyrus areas.

DISCUSSION

In this study, we have identified FLRT1 and FLRT3 adhesion molecules as regulators of mammalian cortex folding. Genetic ablation of *Flrt1/3* in mice resulted in the formation of macroscopic cortical sulci that were maintained post-natally. These anatomical changes did not require progenitor cell amplification but, rather, correlated with changes in the behavior of migrating cortical neurons. Lack of FLRT1/3 reduced intercellular

adhesion, enhanced neuron clustering along the tangential axis, and mildly accelerated radial migration, resulting in a larger proportion of immature neurons reaching the upper cortical plate during late embryogenesis. These findings suggest that regulation of intercellular adhesion of migrating neurons is critical for sulcus formation in the cerebral cortex. Moreover, our expression analysis of FLRT1 and FLRT3 in gyrencephalic species revealed an inverse correlation between FLRT1/3 levels and sulcus formation, supporting a model by which increased abundance of FLRT1/3 levels during evolution led to the smoothing of an ancestral folded cortex. Therefore, *Flrt1/3* DKO mice are an interesting genetic model to study the cellular and molecular mechanisms of cortex folding induced by migrating neurons independent of progenitor amplification.

Mechanisms of FLRT1/3 Function

Flrt1/3 DKO mice are a unique genetic mouse model in which the cortex is folded without increases in neurogenic progenitor cells and basal radial glia. The lack of effects on neurogenic progenitor cells in *Flrt1/3* DKO is consistent with the lack of FLRT1/3 expression in apical or BPs (Figure 1; Figure S1; data not shown). Previous work in lissencephalic mice linked the expansion of the BP pool to gyrus formation (Florio et al., 2015; Ju et al., 2016; Rash et al., 2013; Stahl et al., 2013; Wang et al., 2016). In the gyrencephalic ferret, cortical regions with abundant BPs are more likely to develop into a gyrus than regions with fewer BPs (de Juan Romero et al., 2015; Reillo et al., 2011). Ectopic expansion of the BP pool in the ferret generates additional gyri (Masuda et al., 2015; Nonaka-Kinoshita et al., 2013), and its reduction has a stronger effect on cortical layering of gyri than sulci (Toda et al., 2016). The absence of BP pool expansion and of increases in neuron numbers in folded regions of *Flrt1/3* DKO mice suggests that the folds do not represent radial expansions and gyrus-like structures but, rather, furrows and sulcus-like structures.

FLRT1 and FLRT3 regulate the tangential distribution of cortical neurons. Lack of FLRT1/3 leads to transient neuron clustering in the embryonic cortical plate, and this process is spatially correlated with sulcus formation in early embryonic stages, suggesting that the two events are causally linked. Linking cortical folding to cell clustering and lowered intercellular adhesion may not be without precedent. Overexpression of the hominoid-specific gene *TBC1D3* in the mouse brain leads to cortical folding and increased generation of basal progenitors (Ju et al., 2016). *TBC1D3*-expressing cells show decreased levels of the adhesion protein N-cadherin and exhibit a clustered distribution reminiscent of cell clustering in *Flrt1/3* DKO brains. Although the authors of that study concentrated mainly on the link between cell proliferation and cortex folding, our computational model suggests that reduced intercellular adhesion and cell clustering may be a salient feature of *TBC1D3*-induced cortex folding.

The horizontal layers of the mammalian cortex are organized in cortical columns that contain closely related neurons. Clonal studies of cortical migration show that, in rodents, cortical neurons mostly migrate radially along a single parent RG fiber (Nocctor et al., 2001); however, in folded brains like those of the ferret or macaque, migrating neurons show increased cellular dynamics and exploratory behavior, including increased lateral

dispersion (Kornack and Rakic, 1995; Ware et al., 1999), but the mechanisms controlling this process are largely unknown. Our findings suggest that neuron clustering along the tangential axis in *Flrt1/3* DKO mice resembles the lateral dispersion observed in gyrencephalic species. This raises the interesting possibility that the underlying mechanisms may be similar. Neuron clustering in *Flrt1/3* DKO mice is likely the result of reduced intercellular adhesion, which alters the delicate balance of adhesion/repulsion required for cell migration (Cooper, 2013; Solecki, 2012). This conclusion is supported by our computational model, which shows that changes in the balance of adhesion/repulsion alter the distribution of cells from a uniform salt-and-pepper distribution to a clustered pattern. Hence, the increased lateral dispersion of cortical neurons in gyrencephalic brains may be the result of lowered intercellular adhesion.

The clustering mechanism alone is not likely to cause cortex folding because other mouse models with altered tangential neuron distribution do not show cortex folding (Dimidschstein et al., 2013; Torii et al., 2009). Our findings suggest that *Flrt1/3* DKO mice combine neuron clustering with increased migration speed and that this combination underlies sulcus formation. Similar to neuron clustering, increased migration speed may also be caused by reduced intercellular adhesion. This is suggested by our computational model, by previous mathematical models (DiMilla et al., 1991; Zaman et al., 2005), and by experimental studies (Lauro et al., 2006). A higher migration speed may increase the intercalation of neurons in local areas of the upper cortical plate (uCP), which, according to the radial intercalation hypothesis, increases tension and alters tissue elasticity, leading to sulcus formation (Striedter et al., 2015). We also find that the increased proportion of neurons reaching the upper CP of *Flrt1/3* DKO causes a shift toward more immature morphologies. Indeed, previous studies have shown that improper laminar position affects dendritic arborization of cortical neurons (Morgan-Smith et al., 2014). Whether this also contributes to sulcus formation will have to await further experimental analysis.

Evolutionary Considerations

The finding that lack of FLRT1/3 favors sulcus formation in the normally smooth mouse neocortex raised the question to what extent FLRT1/3 proteins are relevant for regulating cortical folding during evolution. Some studies suggest that the most recent common mammalian ancestor was gyrencephalic (Lewitus et al., 2014; O'Leary et al., 2013), and it was hypothesized that several transitions from gyrencephaly to lissencephaly occurred during mammalian evolution (Kelava et al., 2012; Lewitus et al., 2014). This conclusion is supported by the finding that the marmoset, despite being a lissencephalic species, retains neurogenic features characteristic of gyrencephalic neocortices (Kelava et al., 2012). Although these studies point out that lissencephaly has evolved from gyrencephaly, the mechanisms controlling this process are not known.

Our results suggest that FLRT1/3 expression levels might have participated in the transition from gyrencephaly to lissencephaly. In the wild-type mouse brain, high expression levels of FLRT1/3 promote adhesion between neurons, resulting in coordinated migration and little lateral dispersion, which favors the formation

of homogeneous and smooth cortical layers. Conversely, the absence of FLRT1/3 expression reduces adhesion between neurons, allowing them to acquire wide dynamic migratory profiles and a lateral distribution, which are features characteristic of neurons in the ferret at the onset of cortical folding (Gertz and Kriegstein, 2015). Interestingly, the gyrencephalic human neocortex expresses much lower levels of FLRT1/3 compared with the lissencephalic mouse neocortex, and regions in the ferret neocortex undergoing sulcus formation have lower levels of FLRT1/3 compared with regions developing into a gyrus. Notably, this markedly distinct expression pattern was mainly seen in the OSVZ, which is a key layer involved in cortical folding of gyrencephalic species (Borrell and Götz, 2014; Lui et al., 2011).

Our findings thus unraveled FLRT1/3 as key factors involved in the regulation of cortical migration and sulcus formation. Manipulations of their expression levels have a profound effect on the coordination of cortical migration and lateral dispersion of neurons, which, in turn, influences cortical folding. This scenario provides molecular and cellular insights into the evolution of neuronal migration from gyrencephalic to lissencephalic species.

STAR★METHODS

Detailed methods are provided in the online version of this paper and include the following:

- KEY RESOURCES TABLE
- CONTACT FOR REAGENT AND RESOURCE SHARING
- EXPERIMENTAL MODEL AND SUBJECT DETAILS
 - Mouse lines
 - Ferret
 - Primary cultures
- METHOD DETAILS
 - Immunohistochemistry and enzymatic staining
 - In utero electroporation assays
 - Time-lapse experiments
 - Nissl Staining
 - Cell morphology analysis
 - BrdU analysis
 - Computer modeling
 - in situ hybridization
 - RNaseq analysis
- QUANTIFICATION AND STATISTICAL ANALYSIS

SUPPLEMENTAL INFORMATION

Supplemental Information includes six figures and two movies and can be found with this article online at <http://dx.doi.org/10.1016/j.cell.2017.04.012>.

AUTHOR CONTRIBUTIONS

D.d.T. characterized the Flrt1/3 DKO phenotype, performed neuronal cultures/explants, and designed the computational model. T.R. characterized the Flrt1 KO and performed IUE and time-lapse and morphology analyses. E.C. performed bioinformatics analysis of RNA-seq data and analysis of the Flrt2/3 DKO. G.S.B. characterized FLRT1-3 expression and assisted with IF assays. A.V. performed ISH on ferret sections. R.K. and V.B. supervised experiments. D.d.T. and R.K. wrote the manuscript with input from all other authors.

ACKNOWLEDGMENTS

We thank M. Götz for her insightful comments during the course of this study, R. Portugués and A. Boehm for help with the computational model, S. Falk for help with setting up time-lapse experiments, R. Kasper for technical help with the time-lapse setup, A. Yeroslaviz and B. Habermann for help with gene expression analysis, T. Gaitanos for help with Cell Profiler, T. Iwasato for the Supernova system, and H. Kucukdereli and A. Kist for help with Python programming. T.R., a member of the graduate program IMPRS-LS, was funded by a Boehringer Ingelheim Ph.D. fellowship. E.C. was supported by a postdoctoral research fellowship from the Alexander von Humboldt Foundation, and A.V. was supported by a predoctoral Severo Ochoa contract with the Spanish Ministry of Economy and Competitiveness (MINECO, SVP-2014-068671). This work was funded by the Max Planck Society and the Deutsche Forschungsgemeinschaft (Synergy) (to R.K.) and by the European Research Council (CORTEXFOLDING, 309633) and MINECO (SAF2015-69168-R to V.B.).

Received: October 6, 2016

Revised: February 9, 2017

Accepted: April 7, 2017

Published: May 4, 2017

REFERENCES

- Bauduin, S.A., Singh, T., Agster, K.L., and Burwell, R.D. (2013). Borders and comparative cytoarchitecture of the perirhinal and postrhinal cortices in an F1 hybrid mouse. *Cereb. Cortex* 23, 460–476.
- Borrell, V., and Götz, M. (2014). Role of radial glial cells in cerebral cortex folding. *Curr. Opin. Neurobiol.* 27, 39–46.
- Borrell, V., and Reillo, I. (2012). Emerging roles of neural stem cells in cerebral cortex development and evolution. *Dev. Neurobiol.* 72, 955–971.
- Bribián, A., Nocentini, S., Llorens, F., Gil, V., Mire, E., Reginensi, D., Yoshida, Y., Mann, F., and del Río, J.A. (2014). Sema3E/PlexinD1 regulates the migration of hem-derived Cajal-Retzius cells in developing cerebral cortex. *Nat. Commun.* 5, 4265.
- Buchholz, J. (2009). MATLAB Particles 2.0.
- Cooper, J.A. (2013). Cell biology in neuroscience: mechanisms of cell migration in the nervous system. *J. Cell Biol.* 202, 725–734.
- de Juan Romero, C., Bruder, C., Tomasello, U., Sanz-Anquela, J.M., and Borrell, V. (2015). Discrete domains of gene expression in germinal layers distinguish the development of gyrencephaly. *EMBO J.* 34, 1859–1874.
- Devisme, L., Bouchet, C., Gonzalès, M., Alanio, E., Bazin, A., Bessières, B., Bigi, N., Blanchet, P., Bonneau, D., Bonnières, M., et al. (2012). Cobblestone lissencephaly: neuropathological subtypes and correlations with genes of dystroglycanopathies. *Brain* 135, 469–482.
- Dimidschstein, J., Passante, L., Dufour, A., van den Ameer, J., Tiberi, L., Hrechdakian, T., Adams, R., Klein, R., Lie, D.C., Jossin, Y., and Vanderhaeghen, P. (2013). Ephrin-B1 controls the columnar distribution of cortical pyramidal neurons by restricting their tangential migration. *Neuron* 79, 1123–1135.
- DiMilla, P.A., Barbee, K., and Lauffenburger, D.A. (1991). Mathematical model for the effects of adhesion and mechanics on cell migration speed. *Biophys. J.* 60, 15–37.
- Egea, J., Erlacher, C., Montanez, E., Burtscher, I., Yamagishi, S., Hess, M., Hampel, F., Sanchez, R., Rodriguez-Manzaneque, M.T., Bösl, M.R., et al. (2008). Genetic ablation of FLRT3 reveals a novel morphogenetic function for the anterior visceral endoderm in suppressing mesoderm differentiation. *Genes Dev.* 22, 3349–3362.
- Englund, C., Fink, A., Lau, C., Pham, D., Daza, R.A.M., Bulfone, A., Kowalczyk, T., and Hevner, R.F. (2005). Pax6, Tbr2, and Tbr1 are expressed sequentially by radial glia, intermediate progenitor cells, and postmitotic neurons in developing neocortex. *J. Neurosci.* 25, 247–251.
- Fernández, V., Llinares-Benadero, C., and Borrell, V. (2016). Cerebral cortex expansion and folding: what have we learned? *EMBO J.* 35, 1021–1044.

- Fietz, S.A., Lachmann, R., Brandl, H., Kircher, M., Samusik, N., Schröder, R., Lakshmanaperumal, N., Henry, I., Vogt, J., Riehn, A., et al. (2012). Transcriptomes of germinal zones of human and mouse fetal neocortex suggest a role of extracellular matrix in progenitor self-renewal. *Proc. Natl. Acad. Sci. USA* *109*, 11836–11841.
- Finlay, B.L., and Darlington, R.B. (1995). Linked regularities in the development and evolution of mammalian brains. *Science* *268*, 1578–1584.
- Florio, M., Albert, M., Taverna, E., Namba, T., Brandl, H., Lewitus, E., Haffner, C., Sykes, A., Wong, F.K., Peters, J., et al. (2015). Human-specific gene ARHGAP11B promotes basal progenitor amplification and neocortex expansion. *Science* *347*, 1465–1470.
- Gertz, C.C., and Kriegstein, A.R. (2015). Neuronal Migration Dynamics in the Developing Ferret Cortex. *J. Neurosci.* *35*, 14307–14315.
- Geschwind, D.H., and Rakic, P. (2013). Cortical evolution: judge the brain by its cover. *Neuron* *80*, 633–647.
- Gorski, J.A., Talley, T., Qiu, M., Puelles, L., Rubenstein, J.L., and Jones, K.R. (2002). Cortical excitatory neurons and glia, but not GABAergic neurons, are produced in the Emx1-expressing lineage. *J. Neurosci.* *22*, 6309–6314.
- Hansen, D.V., Lui, J.H., Parker, P.R.L., and Kriegstein, A.R. (2010). Neurogenic radial glia in the outer subventricular zone of human neocortex. *Nature* *464*, 554–561.
- Jackson, V.A., del Toro, D., Carrasquero, M., Roversi, P., Harlos, K., Klein, R., and Seiradake, E. (2015). Structural basis of latrophilin-FLRT interaction. *Structure* *23*, 774–781.
- Jackson, V.A., Mehmood, S., Chavent, M., Roversi, P., Carrasquero, M., Del Toro, D., Seyit-Bremer, G., Ranaivoson, F.M., Comoletti, D., Sansom, M.S.P., et al. (2016). Super-complexes of adhesion GPCRs and neural guidance receptors. *Nat. Commun.* *7*, 11184.
- Ju, X.-C., Hou, Q.-Q., Sheng, A.-L.S., Wu, K.-Y., Zhou, Y., Jin, Y., Wen, T., Yang, Z., Wang, X., and Luo, Z.-G. (2016). The hominoid-specific gene TBC1D3 promotes generation of basal neural progenitors and induces cortical folding in mice. *eLife* *5*, e18197.
- Kawauchi, T. (2015). Cellular insights into cerebral cortical development: focusing on the locomotion mode of neuronal migration. *Front. Cell. Neurosci.* *9*, 394.
- Kelava, I., Reillo, I., Murayama, A.Y., Kalinka, A.T., Stenzel, D., Tomancak, P., Matsuzaki, F., Lebrand, C., Sasaki, E., Schwamborn, J.C., et al. (2012). Abundant occurrence of basal radial glia in the subventricular zone of embryonic neocortex of a lissencephalic primate, the common marmoset *Callithrix jacchus*. *Cereb. Cortex* *22*, 469–481.
- Kornack, D.R., and Rakic, P. (1995). Radial and horizontal deployment of clonally related cells in the primate neocortex: relationship to distinct mitotic lineages. *Neuron* *15*, 311–321.
- Lauro, C., Catalano, M., Trettel, F., Mainiero, F., Ciotti, M.T., Eusebi, F., and Limatola, C. (2006). The chemokine CX3CL1 reduces migration and increases adhesion of neurons with mechanisms dependent on the beta1 integrin subunit. *J. Immunol.* *177*, 7599–7606.
- Lewitus, E., Kelava, I., Kalinka, A.T., Tomancak, P., and Huttner, W.B. (2014). An adaptive threshold in mammalian neocortical evolution. *PLoS Biol.* *12*, e1002000.
- Liao, Y., Smyth, G.K., and Shi, W. (2014). featureCounts: an efficient general purpose program for assigning sequence reads to genomic features. *Bioinformatics* *30*, 923–930.
- Love, M.I., Huber, W., and Anders, S. (2014). Moderated estimation of fold change and dispersion for RNA-seq data with DESeq2. *Genome Biol.* *15*, 550.
- Lui, J.H., Hansen, D.V., and Kriegstein, A.R. (2011). Development and evolution of the human neocortex. *Cell* *146*, 18–36.
- Masuda, K., Toda, T., Shinmyo, Y., Ebisu, H., Hoshiba, Y., Wakimoto, M., Ichikawa, Y., and Kawasaki, H. (2015). Pathophysiological analyses of cortical malformation using gyrencephalic mammals. *Sci. Rep.* *5*, 15370.
- Matsuda, T., and Cepko, C.L. (2007). Controlled expression of transgenes introduced by in vivo electroporation. *Proc. Natl. Acad. Sci. USA* *104*, 1027–1032.
- Mizuno, H., Luo, W., Tarusawa, E., Saito, Y.M., Sato, T., Yoshimura, Y., Itohara, S., and Iwasato, T. (2014). NMDAR-regulated dynamics of layer 4 neuronal dendrites during thalamocortical reorganization in neonates. *Neuron* *82*, 365–379.
- Moon, H.M., and Wynshaw-Boris, A. (2013). Cytoskeleton in action: lissencephaly, a neuronal migration disorder. *Wiley Interdiscip. Rev. Dev. Biol.* *2*, 229–245.
- Morgan-Smith, M., Wu, Y., Zhu, X., Pringle, J., and Snider, W.D. (2014). GSK-3 signaling in developing cortical neurons is essential for radial migration and dendritic orientation. *eLife* *3*, e02663.
- Nieto, M., Monuki, E.S., Tang, H., Imitola, J., Haubst, N., Khoury, S.J., Cunningham, J., Gotz, M., and Walsh, C.A. (2004). Expression of Cux-1 and Cux-2 in the subventricular zone and upper layers II-IV of the cerebral cortex. *J. Comp. Neurol.* *479*, 168–180.
- Noctor, S.C., Flint, A.C., Weissman, T.A., Dammerman, R.S., and Kriegstein, A.R. (2001). Neurons derived from radial glial cells establish radial units in neocortex. *Nature* *409*, 714–720.
- Nonaka-Kinoshita, M., Reillo, I., Artegiani, B., Martínez-Martínez, M.Á., Nelson, M., Borrell, V., and Calegari, F. (2013). Regulation of cerebral cortex size and folding by expansion of basal progenitors. *EMBO J.* *32*, 1817–1828.
- O’Leary, M.A., Bloch, J.I., Flynn, J.J., Gaudin, T.J., Giallombardo, A., Giannini, N.P., Goldberg, S.L., Kraatz, B.P., Luo, Z.-X., Meng, J., et al. (2013). The placental mammal ancestor and the post-K-Pg radiation of placentals. *Science* *339*, 662–667.
- Pilz, G.-A., Shitamukai, A., Reillo, I., Pacary, E., Schwausch, J., Stahl, R., Ninkovic, J., Snippert, H.J., Clevers, H., Godinho, L., et al. (2013). Amplification of progenitors in the mammalian telencephalon includes a new radial glial cell type. *Nat. Commun.* *4*, 2125.
- Rakic, P. (1972). Mode of cell migration to the superficial layers of fetal monkey neocortex. *J. Comp. Neurol.* *145*, 61–83.
- Rash, B.G., Tomasi, S., Lim, H.D., Suh, C.Y., and Vaccarino, F.M. (2013). Cortical gyrification induced by fibroblast growth factor 2 in the mouse brain. *J. Neurosci.* *33*, 10802–10814.
- Reillo, I., de Juan Romero, C., García-Cabezas, M.Á., and Borrell, V. (2011). A role for intermediate radial glia in the tangential expansion of the mammalian cerebral cortex. *Cereb. Cortex* *21*, 1674–1694.
- Schindelin, J., Arganda-Carreras, I., Frise, E., Kaynig, V., Longair, M., Pietzsch, T., Preibisch, S., Rueden, C., Saalfeld, S., Schmid, B., et al. (2012). Fiji: an open-source platform for biological-image analysis. *Nat. Methods* *9*, 676–682.
- Seiradake, E., del Toro, D., Nagel, D., Cop, F., Härtl, R., Ruff, T., Seyit-Bremer, G., Harlos, K., Border, E.C., Acker-Palmer, A., et al. (2014). FLRT structure: balancing repulsion and cell adhesion in cortical and vascular development. *Neuron* *84*, 370–385.
- Smart, I.H., and McSherry, G.M. (1986). Gyrus formation in the cerebral cortex of the ferret. II. Description of the internal histological changes. *J. Anat.* *147*, 27–43.
- Solecki, D.J. (2012). Sticky situations: recent advances in control of cell adhesion during neuronal migration. *Curr. Opin. Neurobiol.* *22*, 791–798.
- Stahl, R., Walcher, T., De Juan Romero, C., Pilz, G.A., Cappello, S., Irmier, M., Sanz-Aguela, J.M., Beckers, J., Blum, R., Borrell, V., and Götz, M. (2013). Trnp1 regulates expansion and folding of the mammalian cerebral cortex by control of radial glial fate. *Cell* *153*, 535–549.
- Striedter, G.F., Srinivasan, S., and Monuki, E.S. (2015). Cortical folding: when, where, how, and why? *Annu. Rev. Neurosci.* *38*, 291–307.
- Tabata, H., and Nagata, K. (2016). Decoding the molecular mechanisms of neuronal migration using in utero electroporation. *Med. Mol. Morphol.* *49*, 63–75.
- Thomson, R.E., Kind, P.C., Graham, N.A., Etherson, M.L., Kennedy, J., Fernandes, A.C., Marques, C.S., Hevner, R.F., and Iwata, T. (2009). Fgf receptor 3 activation promotes selective growth and expansion of occipitotemporal cortex. *Neural Dev.* *4*, 4.

- Toda, T., Shinmyo, Y., Dinh Duong, T.A., Masuda, K., and Kawasaki, H. (2016). An essential role of SVZ progenitors in cortical folding in gyrencephalic mammals. *Sci. Rep.* *6*, 29578.
- Torii, M., Hashimoto-Torii, K., Levitt, P., and Rakic, P. (2009). Integration of neuronal clones in the radial cortical columns by EphA and ephrin-A signalling. *Nature* *461*, 524–528.
- Trapnell, C., Roberts, A., Goff, L., Pertea, G., Kim, D., Kelley, D.R., Pimentel, H., Salzberg, S.L., Rinn, J.L., and Pachter, L. (2012). Differential gene and transcript expression analysis of RNA-seq experiments with TopHat and Cufflinks. *Nat. Protoc.* *7*, 562–578.
- Tronche, F., Kellendonk, C., Kretz, O., Gass, P., Anlag, K., Orban, P.C., Bock, R., Klein, R., and Schütz, G. (1999). Disruption of the glucocorticoid receptor gene in the nervous system results in reduced anxiety. *Nat. Genet.* *23*, 99–103.
- Wagenführ, L., Meyer, A.K., Braunschweig, L., Marrone, L., and Storch, A. (2015). Brain oxygen tension controls the expansion of outer subventricular zone-like basal progenitors in the developing mouse brain. *Development* *142*, 2904–2915.
- Wang, L., Hou, S., and Han, Y.-G. (2016). Corrigendum: Hedgehog signaling promotes basal progenitor expansion and the growth and folding of the neocortex. *Nat. Neurosci.* *19*, 1115.
- Ware, M.L., Tavazoie, S.F., Reid, C.B., and Walsh, C.A. (1999). Coexistence of widespread clones and large radial clones in early embryonic ferret cortex. *Cereb. Cortex* *9*, 636–645.
- Wilkinson, D.J. (2009). Stochastic modelling for quantitative description of heterogeneous biological systems. *Nat. Rev. Genet.* *10*, 122–133.
- Yamagishi, S., Hampel, F., Hata, K., Del Toro, D., Schwark, M., Kvachnina, E., Bastmeyer, M., Yamashita, T., Tarabykin, V., Klein, R., and Egea, J. (2011). FLRT2 and FLRT3 act as repulsive guidance cues for Unc5-positive neurons. *EMBO J.* *30*, 2920–2933.
- Zaman, M.H., Kamm, R.D., Matsudaira, P., and Lauffenburger, D.A. (2005). Computational model for cell migration in three-dimensional matrices. *Biophys. J.* *89*, 1389–1397.

Nucleolin-Mediated RNA Localization Regulates Neuron Growth and Cycling Cell Size

Rotem Ben-Tov Perry,^{1,7} Ida Rishal,^{1,7} Ella Doron-Mandel,^{1,7} Ashley L. Kalinski,² Katalin F. Medzihradzsky,³ Marco Terenzio,¹ Stefanie Alber,¹ Sandip Koley,¹ Albina Lin,¹ Meir Rozenbaum,¹ Dmitry Yudin,¹ Pabitra K. Sahoo,² Cynthia Gomes,² Vera Shinder,⁴ Wasim Geraisy,⁵ Eric A. Huebner,⁶ Clifford J. Woolf,⁶ Avraham Yaron,¹ Alma L. Burlingame,³ Jeffery L. Twiss,² and Mike Fainzilber^{1,*}

¹Department of Biomolecular Sciences, Weizmann Institute of Science, Rehovot 76100, Israel

²Department of Biological Sciences, University of South Carolina, Columbia, SC 29208, USA

³Mass Spectrometry Facility, Department of Pharmaceutical Chemistry, University of California, San Francisco, San Francisco, CA 94158, USA

⁴Department of Chemical Research Support, Weizmann Institute of Science, Rehovot 76100, Israel

⁵Tnuva, Bet Shean 11710, Israel

⁶F.M. Kirby Neurobiology Center, Boston Children's Hospital and Harvard Medical School, Boston, MA 02115, USA

⁷Co-first author

*Correspondence: mike.fainzilber@weizmann.ac.il

<http://dx.doi.org/10.1016/j.celrep.2016.07.005>

SUMMARY

How can cells sense their own size to coordinate biosynthesis and metabolism with their growth needs? We recently proposed a motor-dependent bidirectional transport mechanism for axon length and cell size sensing, but the nature of the motor-transported size signals remained elusive. Here, we show that motor-dependent mRNA localization regulates neuronal growth and cycling cell size. We found that the RNA-binding protein nucleolin is associated with importin β 1 mRNA in axons. Perturbation of nucleolin association with kinesins reduces its levels in axons, with a concomitant reduction in axonal importin β 1 mRNA and protein levels. Strikingly, subcellular sequestration of nucleolin or importin β 1 enhances axonal growth and causes a subcellular shift in protein synthesis. Similar findings were obtained in fibroblasts. Thus, subcellular mRNA localization regulates size and growth in both neurons and cycling cells.

INTRODUCTION

Cell size homeostasis is one of the most fundamental aspects of biology, with distinct size ranges for individual cell types (Ginzberg et al., 2015). Growing cells must match transcriptional and translational output to their size change needs, but the mechanisms underlying such coordination are largely unknown (Marguerat and Bähler, 2012). Neurons exhibit the greatest size differences of any class of cells, having process lengths ranging from a few microns in central interneurons to meters in large mammals. Embryonic neuron growth rates vary according to the distances they must travel at different stages of elongating growth in the embryo (Lallemend et al., 2012). Moreover, axonal

lengths impose a significant delay between transcription and biosynthesis in the cell body and delivery of the components necessary for growth and maintenance to the axon. How then can large cells such as neurons coordinate between their transcriptional and metabolic output to the growth and maintenance needs of differently sized axonal arbors?

Most studies of neuronal growth have focused on extrinsic influences, such as neurotrophic factors secreted by adjacent or target cells (Harrington and Ginty, 2013). Intrinsic regulation of neuronal growth has been reported in different neuronal subtypes (Albus et al., 2013), but the underlying mechanisms are largely unknown. The large dimensions of a growing neuron require active transport by molecular motors for transfer of signals between neurites and cell body. In previous work, we examined the possibility that molecular motor-based signaling might allow distance sensing between cell center and axon endings on a continuous basis, enabling regulation of axon growth rates. Computational modeling directed our attention to a bilateral mechanism with regulatory feedback (Rishal et al., 2012).

In this model, a cell body signal is anterogradely transported by kinesin motors to the neurite end, where it activates dynein-mediated retrograde transport of another cargo to the cell center. The retrograde signal then represses the original anterograde entity, thus periodically resetting the system and generating an oscillating retrograde signal, with frequencies that decrease as a function of increasing cell length. Simulations show that reductions in anterograde or retrograde signals in this model cause a slowing in the rate of frequency decrease with time in the system. If growth rates are correlated with retrograde signal frequency, this leads to the counter-intuitive prediction that reducing either anterograde or retrograde signals should lead to increased axon lengths in both cases. We confirmed this prediction for specific kinesins and for dynein heavy chain 1 in adult sensory neurons and in mouse embryonic fibroblasts (Rishal et al., 2012), demonstrating a role for microtubule-bound motors in cell size sensing and growth control. However, the nature of the motor-transported size signals remained unknown.

Here we identify RNA localization and localized protein translation as critical aspects of motor-dependent size sensing. We show that depletion of the nuclear import factor importin β 1 from axons by a 3' UTR knockout (KO) or by sequestration of nucleolin, an RNA-binding protein (RBP) involved in importin β 1 axonal localization, enhances neuronal outgrowth, concomitantly with a subcellular shift in protein synthesis. Similar perturbations affect the morphology and size of fibroblasts in culture. Thus, the subcellular localization of nucleolin-associated mRNAs regulates cell size and growth control mechanisms.

RESULTS

Increased Axonal Growth Rates in Sensory Neurons Lacking Axonal Importin β 1

To identify participants in motor-dependent cell length sensing, we screened a number of mouse mutants for increased axonal outgrowth of adult sensory neurons in culture. We crossed candidate mouse lines to Thy1/yellow fluorescent protein (YFP) mice (Feng et al., 2000) to allow live imaging of growing neurons. Calculation of ongoing growth rates from such experiments confirmed previous observations (Rishal et al., 2012) that the *Loa* point mutation in dynein heavy chain 1 (*Dync1h1*) induces a significantly higher axonal growth rate in heterozygous sensory neurons (Figures S1A and S1B). A similar result was observed for sensory neuron cultures from a mouse with a 3' UTR deletion in importin β 1. The importin β 1 3' UTR^{-/-} mouse revealed subcellular depletion of importin β 1 protein from sensory axons with no change in neuronal cell bodies (Perry et al., 2012). Strikingly, YFP-labeled importin β 1 3' UTR^{-/-} neurons revealed significantly higher axon growth rates than neurons from wild-type (WT) littermates (Figures 1A and 1B). Moreover, quantification of axon lengths in vivo during the normal elongating phase of development revealed ~35% more axon growth in the mutants than in WT littermates at embryonic day (E11.5) (Figures 1C and 1D). We further confirmed specific axonal reduction of importin β 1 in growing sensory axons from adult KO mice (Figures 1E–1G). These findings suggest that the subcellular localization of importin β 1 plays a role in setting neuronal growth rates both in vitro and in vivo.

Previous work had demonstrated local translation of importin β 1 in sensory axons upon nerve injury (Hanz et al., 2003; Yudin et al., 2008). To test whether importin β 1 also might be locally translated in the axons of actively growing neurons, we took advantage of the RiboTag transgenic mouse model (Sanz et al., 2009) to examine endogenous mRNA interaction with ribosomes. We crossed RiboTag and *Islet1-Cre* mice to generate HA-tagged ribosomes in sensory neurons, and we verified neuron-specific expression of the HA tag in dorsal root ganglia (DRG) cultures (Figure S1C). HA-tagged ribosomes were present in axons and axon tips of growing sensory neurons (Figures 1H and S1C). Axon and cell body extracts from compartmentalized cultures were subjected to HA immunoprecipitation followed by qPCR for ribosome-associated RNAs. Ribosome immunoprecipitation was confirmed by qPCR for 18S RNA (Figure 1I). Importin β 1 mRNA was found to be associated with ribosomes in both cell body and axonal compartments (Figure 1I), supporting its local translation in growing axons.

Locally translated importin β 1 is retrogradely transported from axon to soma by dynein in injured sensory neurons (Hanz et al., 2003; Perry et al., 2012). To determine whether importin β 1 also is associated with dynein in growing axons, we used in situ proximity ligation assay (PLA) (Söderberg et al., 2006) for direct visualization of the association of endogenous proteins within growing axons. Robust colocalization of importin β 1 and dynein was observed in growing axons (Figure 1J), with little or no background in single-antibody controls (Figure S1D). Association of importin β 1 and dynein also was confirmed by co-immunoprecipitation from axoplasm (Figure 1K). The influence of dynein depletion on the subcellular distribution of importin β 1 was further assessed by capillary electrophoresis immuno-quantification (Harris, 2015), showing reduced axonal and increased soma importin β 1 in *Loa* dynein mutant neurons (Figure S1E). The small interfering RNA (siRNA)-mediated knockdowns of *Kif5A* and *Kif5B* had a similar effect on importin β 1 mRNA levels in axons versus soma of compartmentalized neuron cultures (data not shown). In this context, it is noteworthy that siRNA knockdown of these two kinesins previously was shown to induce axon lengthening in sensory neuron cultures (Rishal et al., 2012).

Delineation of an Axon-Localizing Stem-Loop Motif in Importin β 1 3' UTR

Taken together, the above data show that importin β 1 is present in growing axons as mRNA in association with ribosomes and as protein in association with dynein and that its subcellular removal from axons enhances their growth. We therefore set out to identify the molecular determinants of axonal localization of importin β 1 mRNA. We used Mfold (Zuker, 2003) to predict secondary structures between 793 and 1,148 nt of the importin β 1 3' UTR, which we previously had shown harbors the axon-localizing element (Perry et al., 2012). Based on these predictions, we then generated a series of deletion mutants within this region as shown in Figure 2A, and we tested their capacity to localize a destabilized GFP reporter construct upon transfection of sensory neurons. Fluorescence recovery after photobleaching (FRAP) experiments with these constructs showed a loss of axon-localizing activity upon deletion of the motif between 916 and 994 nt in the 3' UTR (Figures 2B–2D, S2A, and S2B).

Secondary structure analyses for this region and adjacent segments identified a predicted stem-loop motif of 34 nt spanning positions 991–1,024 (Figure 2B). This motif is hereby designated as motif for axonal importin localization (MAIL). Fluorescence in situ hybridization (FISH) showed that deletion of MAIL removed axonal localization capacity of the importin β 1 3' UTR, while fusion of two MAIL sequences to the short 1–134 non-localizing variant of importin β 1 3' UTR (Perry et al., 2012) conveyed axon-localizing capacity (Figures 2E and S2C). U-G mutations in the loop region of MAIL were used to generate a mutant termed GMAIL (Figure 2B) that revealed reduced axon-localizing activity (Figures S2D and S2E). A combination of the GMAIL mutations with additional mutations in the stem region generated a stem-and-loop mutant completely devoid of localizing activity termed inactive MAIL (IMAIL; Figure 2B). FISH and FRAP assays with reporter

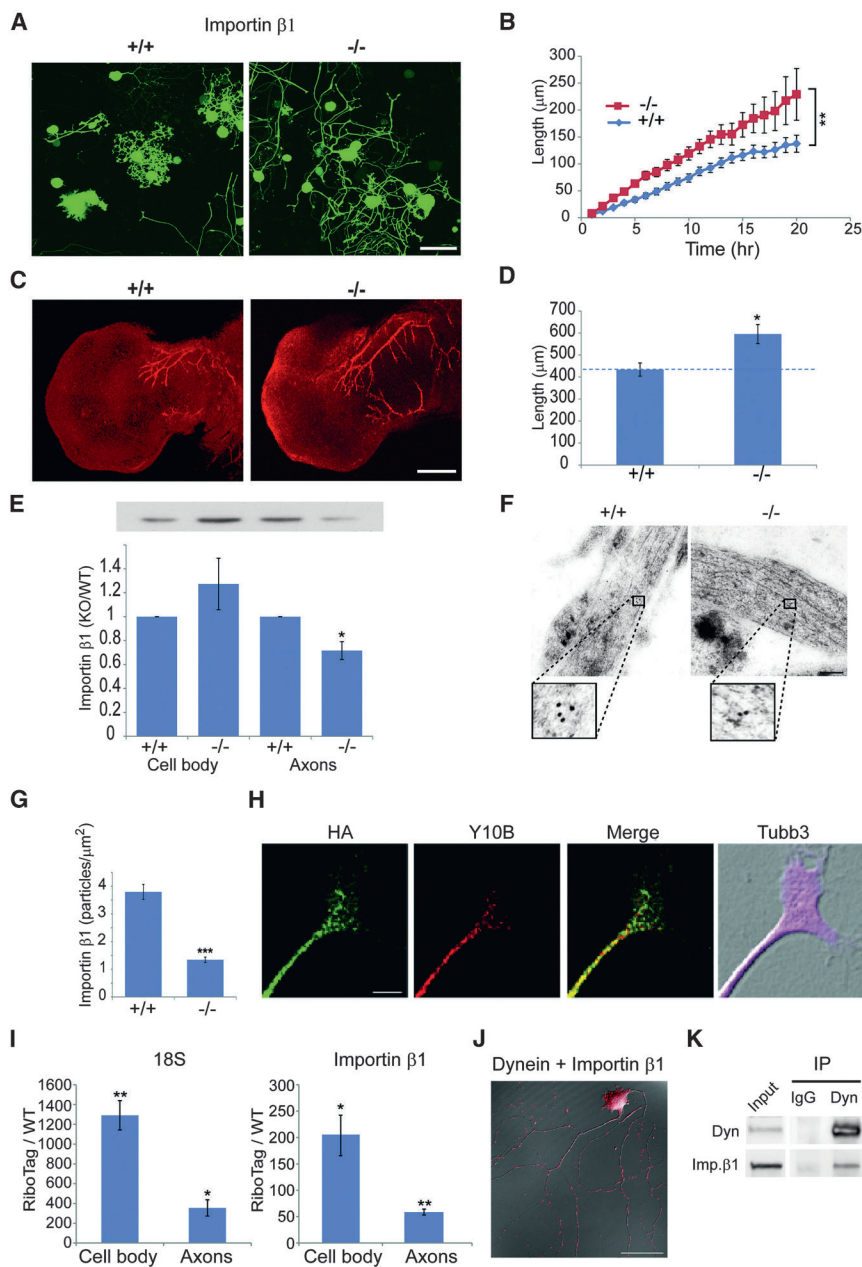


Figure 1. Increased Axonal Growth Rates in Importin β 1 Mutant Sensory Neurons

(A) Fluorescent images show cultured YFP-expressing DRG neurons from WT versus importin β 1 3' UTR-null mice at 48 hr in vitro. Scale bar, 100 μ m.

(B) Quantification of time-lapse imaging of YFP-expressing DRG neurons in culture. Images were taken every hour in a Fluoview FV10i incubator microscope. 3×3 montages of neighboring acquisition sites were analyzed using ImageJ. Longest neurite growth rates in these experiments were $6.9 \pm 0.6 \mu\text{m/hr}$ for WT versus $11.5 \pm 0.9 \mu\text{m/hr}$ for importin β 1 3' UTR^{-/-} mice. Mean \pm SEM; $n \geq 30$ cells per experimental group; * $p < 0.05$ for comparison of growth rates, one-way ANOVA.

(C) Whole-mount neurofilament staining in E11.5 limbs in WT and importin β 1 3' UTR^{-/-} mice is shown. Scale bar, 200 μ m.

(D) Quantification reveals significantly longer total neurite lengths at E11.5 in importin β 1 3' UTR^{-/-} embryos than in WT littermates ($n \geq 7$; * $p < 0.05$, Student's t test).

(E) Western blot quantifications for importin β 1 in axon versus cell body compartments of sensory neurons cultured for 48 hr in compartmentalized Boyden chambers. A representative blot with the same loading order is shown above the graph. WT versus importin β 1 3' UTR^{-/-} neurons are shown. Mean \pm SEM; $n = 3$; * $p < 0.05$, Student's t test.

(F) Electron micrographs show immunogold labeling for importin β 1 on ultrathin monolayer sections of cultured DRG neurons from WT and importin β 1 3' UTR^{-/-} mice. Scale bar, 200 nm; gold particle diameter, 10 nm.

(G) Quantification of immunogold labeling confirms reduced levels of importin β 1 protein in growing sensory axons of importin β 1 3' UTR^{-/-} mice. Mean \pm SEM; $n \geq 50$; *** $p < 0.001$, Student's t test.

(H) DRG neuron cultures from Islet-Cre RiboTag mice were immunostained for the tagged ribosome epitope (HA), ribosomal RNA (Y10B), and axonal tubulin (Tubb3). A representative axon tip is shown. Scale bar, 5 μ m. For additional images see Figure S1C.

(I) Quantification of ribosomal 18S RNA (left) and importin β 1 mRNA (right) in HA-RiboTag pull-downs from axonal and cell body compartments from Islet-Cre RiboTag DRG neurons cultured for 96 hr in compartmentalized Boyden chambers.

RNA levels are quantified as fold change of levels in control pull-downs from WT cultures. Mean \pm SEM; $n = 4$; * $p < 0.05$ and ** $p < 0.005$, Student's t test.

(J) Representative PLA images to identify importin β 1-dynein complexes in DRG neurons grown for 48 hr in culture. After 48 hr the neurons were fixed and stained for dynein and importin β 1, followed by the PLA probes. Scale bar, 50 μ m. See also Figures S1D and S1E.

(K) Co-immunoprecipitation (coIP) of importin β 1 with dynein from axoplasm. Immunoprecipitations were carried out with dynein IC74.1 intermediate-chain antibody versus non-immunized mouse IgG.

See also Figure S1.

constructs comparing MAIL with these mutated motifs confirmed specific MAIL-dependent axon localization in sensory neurons (Figures 2E, S2D, and S2E). Comparisons of importin β 1 sequence from a diversity of mammalian species revealed high conservation of the MAIL motif, especially in the loop region (Figure S2F).

Identification of Nucleolin as a Binding Protein for the Importin β 1 3' UTR MAIL Motif

We then sought to identify RBPs that interact with the MAIL motif. Pull-downs of bovine sciatic nerve axoplasm with biotinylated RNA motifs revealed clear differences in the interacting protein profile between MAIL and GMAIL (Figures 3A,

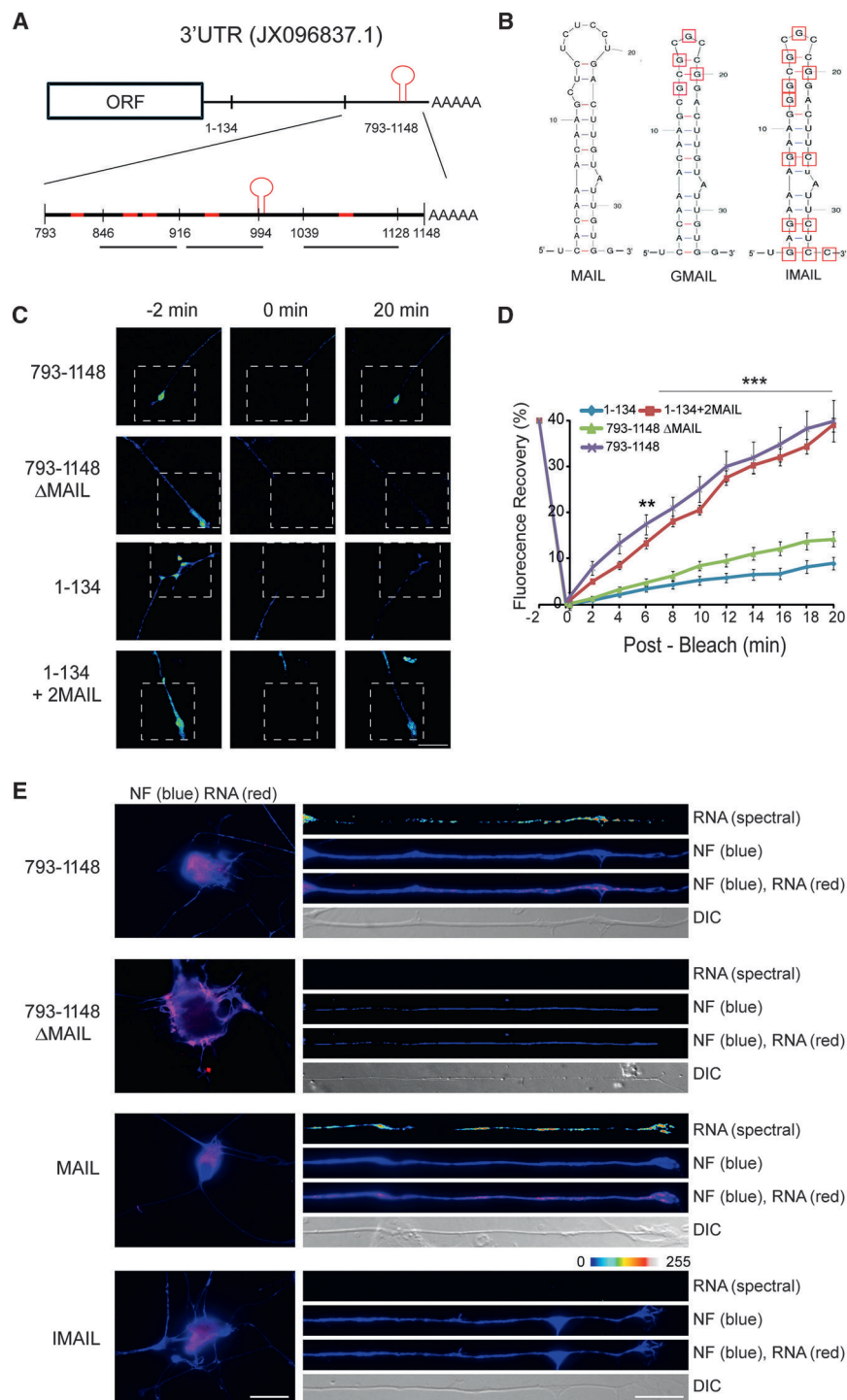


Figure 2. MAIL, A Localization Motif for Importin β 1 mRNA

(A) Schematic diagram of segments from the importin β 3' UTR (GenBank: JX096837.1) evaluated for axon-localizing activity. Regions predicted to contain stem-loop secondary structures are highlighted in red. The region between 1 and 134 nt encompasses the short form of importin β 3' UTR, which is restricted to the cell body. The motif for axonal importin localization (MAIL) is shown as a red stem-loop structure at 991–1,024 nt.

(B) Sequences and schematic structure predictions of the MAIL motif and two derived mutants, GMAIL, with four U-G mutations in the loop region as shown, and IMAIL, which carries the GMAIL mutations together with additional mutations in the stem region, are shown.

(C) Constructs containing deletions or fusions of the MAIL motif as indicated were fused with a destabilized myr-EGFP reporter and transfected to sensory neurons for FRAP analyses, with recovery monitored over 20 min. Representative images from time-lapse sequences before (–2 min) and after photobleaching (0 and 20 min) in the boxed region of interest are shown. For data from additional constructs, see Figure S2A. Scale bar, 25 μ m.

(D) Quantification of the FRAP analyses shown in (C). Average recoveries are shown (percentage of pre-bleach levels \pm SEM). Anisomycin-treated neurons were exposed to 50 μ M inhibitor prior to the imaging sequence. Time points with significant differences in axonal fluorescence compared to that observed in anisomycin-treated cultures are indicated (** $p < 0.01$ and *** $p < 0.001$, two-way ANOVA). For results with additional deletion constructs and anisomycin controls, see Figure S2B. (E) In situ hybridization on neurons transfected with the indicated constructs. Exposure-matched images show that only GFP mRNA with the MAIL element localizes into axons (right panel), while all reporter mRNAs are clearly expressed in corresponding cell body images (left panel). Scale bars, 25 μ m (cell body) and 10 μ m (axons). See also Figure S2C. See also Figure S2.

S3A, and S3B). Tryptic digest and mass spectrometric analyses identified the RBP nucleolin as a major MAIL-bound component (Figures S3A–S3C). Nucleolin is a multifunctional protein that contains four RNA-binding domains, and it is found in cells both within the nucleus and at the plasma membrane (Abdelmohsen and Gorospe, 2012); hence, it is well placed to play a role in signaling systems linking the cell center with its periphery.

We verified the nucleolin-MAIL interaction by pull-down of rat sciatic nerve axoplasm with RNA probes encoding MAIL, GMAIL, or the Zipcode motif of β -actin mRNA (Kim et al., 2015) (Figure 3B). A reverse pull-down by immunoprecipitation of axoplasm with anti-nucleolin antibody followed by RT-PCR for importin β or β -actin as a control likewise confirmed specific association of neuronal importin β transcript with nucleolin (Figure 3C). To test for a direct interaction of importin β mRNA with nucleolin, we incubated purified recombinant nucleolin with biotinylated MAIL, IMAIL, or β -actin Zipcode RNA motifs, before precipitating the complexes over immobilized streptavidin. Immunoblotting

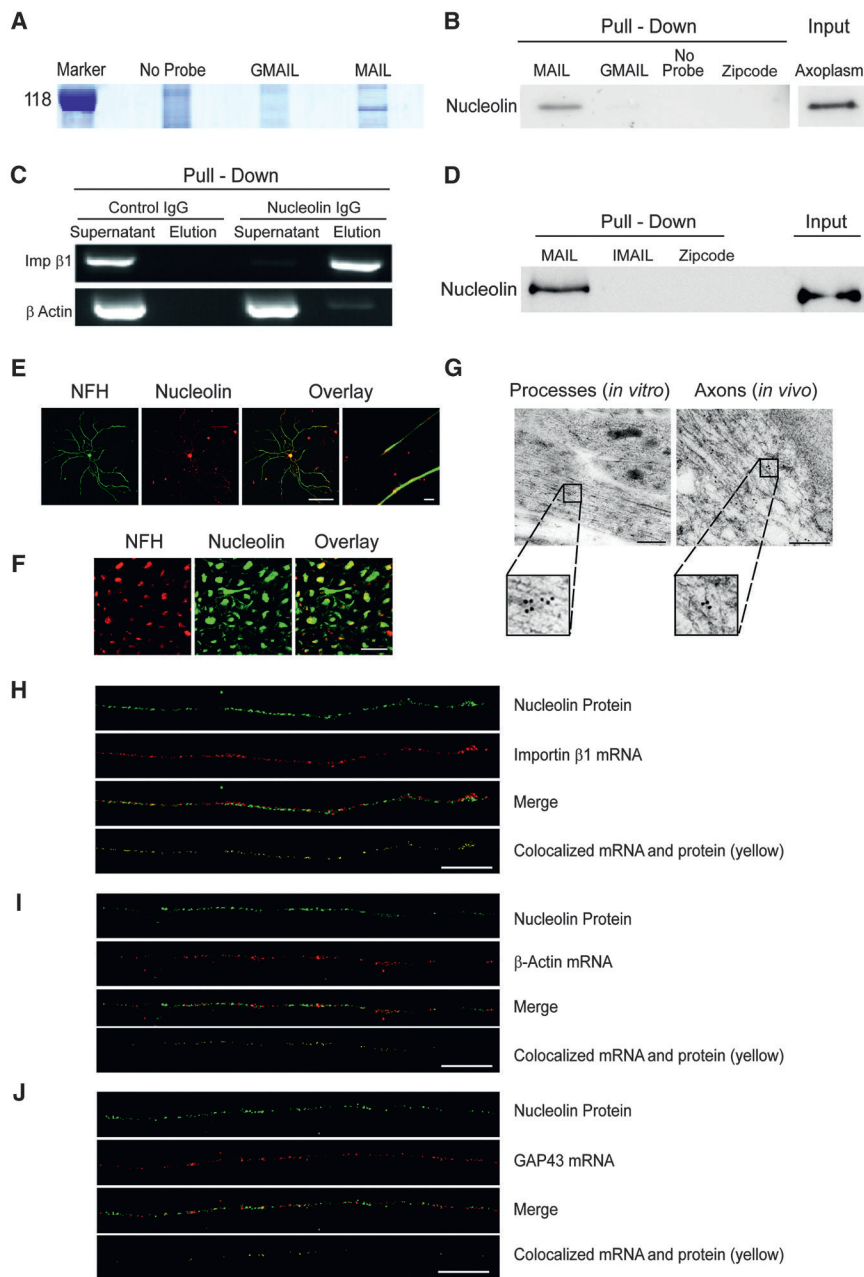


Figure 3. Axonal Nucleolin Interacts with the Importin β 1 MAIL Motif

(A) Bovine axoplasm (10 mg/lane) was precipitated on immobilized MAIL or GMAIL RNA motifs, and eluted proteins were separated by 10% SDS-PAGE. The gel region containing the major differential band is shown here and the complete gel is shown in Figure S3A. Mass spectrometry analyses identified nucleolin as the major unique MAIL-bound component (Figures S3A–S3C).

(B) Western blot of nucleolin precipitated from rat sciatic nerve axoplasm with MAIL, GMAIL, or β -actin Zipcode RNA motifs. Precipitates were separated on 10% SDS-PAGE, blotted onto nitrocellulose, and probed with antibody against nucleolin.

(C) Immunoprecipitation of 200 μ g rat sciatic nerve axoplasm samples with control IgG or anti-nucleolin antibodies followed by RT-PCR for importin β 1 or β -actin mRNAs.

(D) Western blot of recombinant nucleolin precipitated with MAIL, IMAIL, or β -actin Zipcode RNA motifs. Input was 1 μ g recombinant nucleolin per lane.

(E) Primary cultured rat sensory neurons immunostained with antibodies against nucleolin (red) and NFH (green), revealing nucleolin in both neuronal cell bodies and axons. Scale bar, 20 μ m; right overlay panel scale bar, 10 μ m.

(F) Sciatic nerve cross-sections immunostained with antibodies against nucleolin (red) and NFH (green), revealing nucleolin within sensory axons in vivo. Scale bar, 20 μ m.

(G) Electron micrographs showing immunogold labeling for nucleolin in axons on ultrathin monolayer sections of cultured mouse DRG neurons (left) or of sciatic nerve (right). Nucleolin is present in axons in vitro and in vivo. Scale bars, 200 nm; gold particle diameter, 10 nm.

(H) Colocalization of nucleolin protein (immunostaining, green) and importin β 1 mRNA (FISH, red) in sensory axons. Importin β 1 mRNA colocalized with nucleolin protein (yellow) is shown in a single optical plane (scale bar, 5 μ m). For cell body signal and scrambled probe control, see Figure S3D. Pearson's correlation coefficient for importin β 1 colocalization with nucleolin 0.37 ± 0.04 ($n = 29$) differs significantly from Pearson's for β -actin or GAP43 (see below) (p value for importin β 1 versus β -actin < 0.004 , p value for importin β 1 versus GAP43 < 0.0001 ; ANOVA with Bonferroni post hoc correction in both cases).

(I) Colocalization of nucleolin protein (immunostaining, green) and β -actin mRNA (FISH, red) in sensory axons. Colocalization is shown in yellow in a single optical plane (scale bar, 5 μ m). For cell body signal and scrambled probe control, see Figure S3D. Pearson's correlation coefficient for β -actin colocalization with nucleolin 0.19 ± 0.03 ($n = 20$).

(J) Colocalization of nucleolin protein (immunostaining, green) and GAP43 mRNA (FISH, red) in sensory axons. Colocalization is shown in yellow in a single optical plane (scale bar, 5 μ m). For cell body signal and scrambled probe control, see Figure S3D. Pearson's correlation coefficient for GAP43 colocalization with nucleolin 0.05 ± 0.01 ($n = 48$).

See also Figure S3.

confirmed a direct and specific interaction of nucleolin with the importin β 1 MAIL motif (Figure 3D).

We next asked if nucleolin localizes to sensory axons. Immunofluorescence revealed nucleolin in both cell bodies and axons of proprioceptive sensory neurons in culture (Figure 3E) and in

axons of myelinated sensory neurons in vivo (Figure 3F). Both these observations were confirmed by electron microscopy (EM) immunogold labeling (Figure 3G). Immunostaining for nucleolin protein concomitantly with FISH for importin β 1 mRNA revealed extensive axonal colocalization (Figures 3H

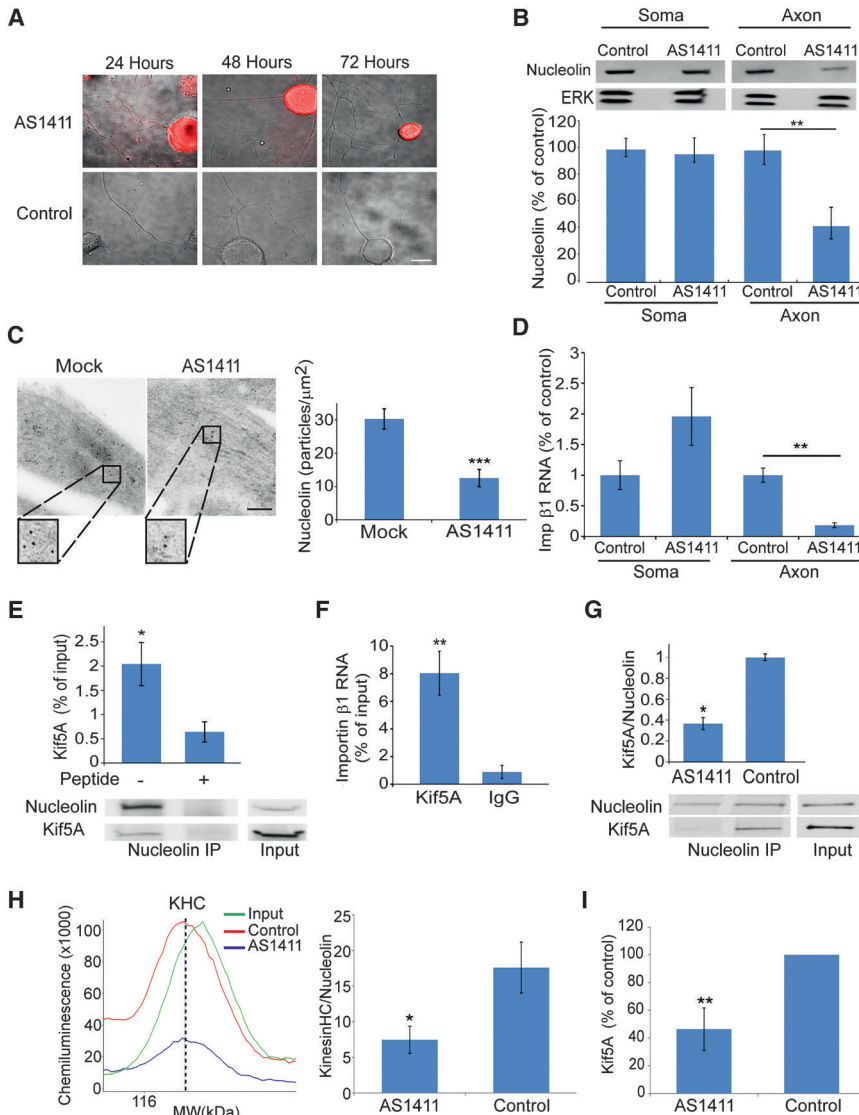


Figure 4. Depletion of Axonal Nucleolin Reduces Importin β 1 Transcript in Sensory Axons

(A) Cy3-labeled AS1411 and control aptamers were added to sensory neuron cultures to a final concentration of 20 μ M. Neurons were fixed at the indicated time points. Scale bar, 10 μ m. See also Figures S4A and S4B.

(B) Western blots for nucleolin on axon versus cell body extracts from sensory neurons in compartmentalized Boyden chambers treated with AS1411 or control aptamers for 48 hr before transfer to aptamer-free medium for another 24 hr. Quantifications of blots are shown below. Mean \pm SEM; n = 4; **p < 0.01, Student's t test.

(C) Electron micrographs of cultured DRG neuron processes show immunogold labeling for nucleolin after AS1411 treatment. Scale bar, 200 nm; gold particle, 10 nm. Mean \pm SEM; n \geq 25; ***p < 0.001, Student's t test.

(D) Quantification of relative importin β 1 transcript levels by qPCR on cell bodies and axons of cells treated with AS1411 or control DNAs. β -actin served as an internal control and did not change. Mean \pm SEM; n = 3; **p < 0.01, Student's t test.

(E) ColP of Kif5A with nucleolin from sciatic nerve axoplasm. The control immunoprecipitation is in the presence of a blocking peptide for the nucleolin antibody. A supporting experiment is shown in Figure S4C. Quantification of the Kif5A-nucleolin colP is shown above. Mean \pm SEM; n = 5; *p < 0.05, paired Student's t test.

(F) Importin β 1 transcript levels co-precipitated with Kif5A. Mean \pm SEM; n = 5; **p < 0.01, ratio-paired Student's t test.

(G) Quantification of Kif5A on fluorescent Li-COR western blots of nucleolin immunoprecipitations from sciatic nerve axoplasm, after pre-incubation with AS1411 or control aptamer. Representative blots are shown below the graph. Mean \pm SEM; n = 3; *p < 0.05, paired Student's t test. Similar results were obtained from neuronal cultures (Figure S4D).

(H) Automated capillary electrophoresis quantification of kinesin heavy-chain (KHC) immunoreactivity co-precipitated with nucleolin from sciatic

nerve axoplasm, after pre-incubation with AS1411 or control aptamer. Representative traces of the KHC immunoreactive peaks are shown on the left and quantifications are shown on the right. Mean \pm SEM; n = 3; *p < 0.05, paired Student's t test.

(I) Quantification of Kif5A protein pulled down by a MAIL RNA probe from sciatic nerve axoplasm pre-incubated with AS1411 or control DNA. Protein levels were quantified by automated capillary electrophoresis. Data are shown as percentage from control. Mean \pm SEM; n = 9; **p < 0.01, paired Student's t test. See also Figure S4.

and S3D), as compared to similar analyses for β -actin (Figures 3I and S3D) or GAP43 mRNAs (Figures 3J and S3D). Pearson's coefficient calculations showed significantly more colocalization of axonal importin β 1 mRNA with nucleolin than either β -actin or GAP43 mRNAs with nucleolin (Figures 3H–3J). Thus, nucleolin is localized to the axons of sensory neurons both in vivo and in culture and is associated with importin β 1 mRNA in axons.

Restriction of Nucleolin to Neuronal Cell Bodies Enhances Axon Growth

We then examined the effects of a nucleolin-targeting aptamer on proprioceptive neurons. The AS1411 aptamer is a quadru-

plex-forming oligodeoxynucleotide that internalizes to cells and binds nucleolin with high affinity and specificity (Bates et al., 2009). AS1411 induces death of a variety of tumor cells and has undergone evaluation in clinical trials for leukemia and breast cancer (Berger et al., 2015). Fluorescently labeled AS1411 was internalized at both axons and cell bodies of proprioceptive neurons in culture, but over time in culture the aptamer was concentrated in cell bodies only, leaving the axons clear (Figures 4A and S4A). AS1411 treatment caused a decrease in nucleolin levels in axons without affecting cell body levels (Figure 4B). Similar findings were obtained by quantification of aptamer fluorescence in cell bodies versus axons (Figures S4A and S4B) and by

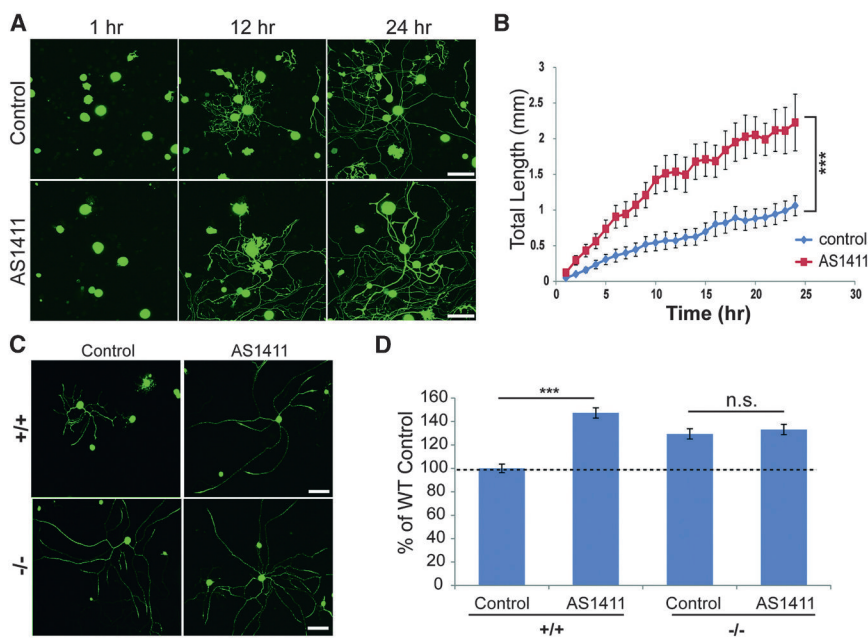


Figure 5. AS1411 Enhances Sensory Axon Growth Rates in WT, but Not in Importin β 1 3' UTR^{-/-} Neurons

(A) Cultured DRG neurons from adult YFP/WT mice were treated with 10 μ M control or AS1411 aptamer for 48 hr, and then they were replated in fresh medium without aptamer and allowed to re-grow. Representative images at three time points following replating are shown. Scale bar, 100 μ m. (B) Quantification of total neurite outgrowth of sensory neurons in culture from the experiment described in (A). Total neurite growth rates in these experiments were 45.7 \pm 11.2 μ m/hr for control versus 90.1 \pm 16.1 μ m/hr for AS1411 treatment. Mean \pm SEM; n \geq 60 cells per experimental group; ***p < 0.001 for comparison of growth rates, one-way ANOVA.

(C) Representative images of cultured WT or importin β 1 3' UTR^{-/-} sensory neurons treated with 10 μ M control or AS1411 aptamer for 48 hr and then replated and cultured for an additional 24 hr in fresh medium without aptamer. Neurons were finally fixed, immunostained for NFH (green), and imaged. Scale bar, 200 μ m.

(D) Quantification of total neurite outgrowth in the experiment described in (C) reveals a significant increase in axon growth in WT neurons pretreated with AS1411, but not in importin β 1 3' UTR^{-/-} neurons. Mean \pm SEM; n \geq 300 cells per experimental group; ***p < 0.001, Student's t test. See also Figure S5.

immunogold labeling on EM sections of aptamer-treated sensory neurons (Figure 4C). AS1411 treatment also significantly reduced importin β 1 mRNA in axons, concomitantly with an apparent increase in neuronal cell bodies (Figure 4D).

We surmised that AS1411-induced sequestration of nucleolin and associated importin β 1 transcript from axons might be due to perturbation of transport of the RBP complex from the cell soma. We therefore examined whether nucleolin interacts with kinesin motors, and we observed specific co-immunoprecipitation of nucleolin with the kinesin Kif5A (Figure 4E). This interaction was further confirmed by co-precipitation of kinesin heavy chain with nucleolin (Figure S4C). Importin β 1 transcript also co-precipitated with Kif5A (Figure 4F), indicating that kinesins transport nucleolin and associated mRNAs into sensory axons. Strikingly, pre-incubation with the AS1411 aptamer significantly reduced co-precipitation of Kif5A or of kinesin heavy chains with nucleolin from axoplasm (Figures 4G and 4H) or from neuronal cultures (Figure S4D). Moreover, Kif5A pull-down from axoplasm by a MAIL RNA probe was significantly reduced after pre-incubation with the AS1411 aptamer (Figure 4I). Hence, AS1411-induced restriction of nucleolin and its mRNA cargo to the neuronal soma is most likely due to the perturbation of nucleolin association with kinesins, thereby preventing transport of the complex from soma to axon.

To evaluate the effects of nucleolin restriction to the soma on axon outgrowth, we pretreated proprioceptive sensory neurons with AS1411 or control aptamer for 48 hr in culture, and then we replated them in fresh medium without aptamer. Under these conditions, AS1411 significantly enhanced total axonal outgrowth (Figures 5A and 5B) without any observable effect

on cell viability. To test whether such effects also could be observed in other neuronal subtypes, we treated cultures of nociceptor neurons in the same manner. As shown in Figure S5, nociceptor neurons pretreated with AS1411 also exhibited significantly more axon growth than cultures pretreated with control aptamer. Finally, we examined whether these aptamer effects were mediated by importin β 1 mislocalization. Axon growth after AS1411 pretreatment was increased in WT proprioceptive neurons to levels similar to those seen in importin β 1 3' UTR^{-/-} neurons not exposed to the aptamer. Moreover, AS1411 had no growth-promoting effect on 3' UTR^{-/-} neurons as compared to control aptamer (Figures 5C and 5D). These experiments were quantified at 24 hr after replating of the neurons, and, since it is possible to monitor continuing growth over 96 hr in culture, the lack of effect of AS1411 on 3' UTR^{-/-} neurons is not due to saturation of their growth capacity. Taken together, these results indicate that nucleolin restriction to neuronal cell bodies enhances neurite outgrowth by a mechanism dependent on the axonal localization of importin β 1 mRNA.

Perturbation of Nucleolin Affects Size in Non-neuronal Cells

The above data suggest that nucleolin-dependent importin β 1 mRNA transport regulates neuronal growth. Since nucleolin is widely expressed in different cell types, we wished to test whether such a mechanism also might function in non-neuronal cells, using 3T3 fibroblasts as a model. We first asked whether importin β 1 and nucleolin interact with molecular motors in 3T3 cells. As shown in Figure 6A, importin β 1 readily co-precipitated with dynein from 3T3 cell lysate and likewise nucleolin with Kif5B.

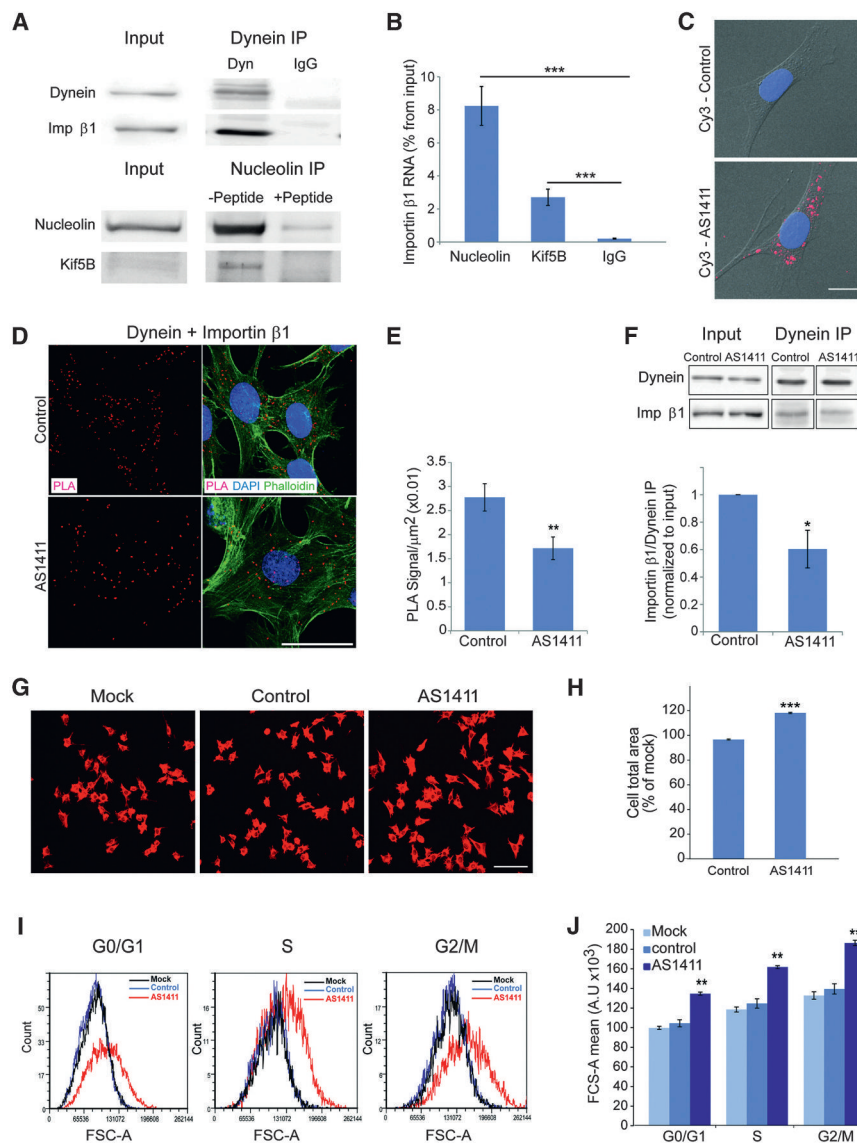


Figure 6. AS1411 Treatment Increases 3T3 Fibroblast Cell Size

(A) Western blots showing coIP of importin β 1 with dynein heavy chain 1 and nucleolin with Kif5B from confluent 3T3 cell cultures. Control immunoprecipitations were with non-immune IgG for the dynein immunoprecipitation and with blocking peptide for the precipitating antibody in the nucleolin immunoprecipitation.

(B) Quantification of relative importin β 1 transcript levels after pull-down for Kif5A or nucleolin is shown. Mean \pm SEM; $n = 4$; *** $p < 0.001$, ratio-paired Student's t test.

(C) Representative images for uptake of AS1411-Cy3 into 3T3 cells are shown. Blue, DAPI; red, AS1411. Scale bar, 10 μ m.

(D) Representative PLA images of importin β 1-dynein complexes in 3T3 cells incubated for 48 hr with AS1411 or control aptamers. After 48 hr the cells were fixed and stained with phalloidin-Cy3 and for dynein and importin β 1, followed by the PLA probes. Scale bar, 50 μ m.

(E) Quantification of the assay shown in (D). PLA signal per cell body area was quantified using CellProfiler software, revealing a significant reduction in signal density in 3T3 cells incubated with the AS1411 aptamer. Mean \pm SEM; $n = 3$; ** $p < 0.01$, Student's t test.

(F) Representative western blots of importin β 1 co-precipitated with dynein from 3T3 cells after 48 hr in culture in the presence of AS1411 or control aptamers. The quantification below shows a significant decrease in coIP of importin β 1 with dynein after AS1411 treatment. Mean \pm SEM; $n = 3$; * $p < 0.05$, paired Student's t test.

(G) 3T3 cells were incubated with 10 μ M AS1411 or control aptamer for 48 hr, after which 20,000 cells were replated for another 24 hr in fresh medium without aptamer before fixing and staining with rhodamine-phalloidin. Representative images are shown. Scale bar, 100 μ m. See also Figure S6 for higher magnification images of nuclear morphology. (H) Quantification of 3T3 cell area from the experiment described in (G) reveals a significant increase upon AS1411 treatment. Mean \pm SEM; $n > 1,000$; *** $p < 0.001$, Student's t test. The experiment was replicated on three independent cultures.

(I) 3T3 cell size at different stages of the cell cycle after 48 hr incubation with AS1411 or control aptamers at 10 μ M, followed by harvesting and incubation with 10 μ g/ml Hoechst 33342 and 5 μ g/ml propidium iodide for live cell cycle analyses by FACS. 30,000 events were collected per sample. AS1411 treatment causes a marked increase in cell size, as shown by the right shift in population distribution in comparison to mock and control at all stages of the cell cycle.

(J) Quantification of the FACS described in (I) for three independent experiments reveals a significant increase of cell size upon AS1411 treatment in all cell cycle phases. Mean \pm SEM; $n = 3$; ** $p < 0.01$, Student's t test. See also Figure S6.

Moreover, importin β 1 mRNA was co-precipitated with both nucleolin and Kif5B (Figure 6B). These data indicate that importin β 1 mRNA is transported by a nucleolin-kinesin complex in 3T3 cells and that importin β 1 protein is transported by dynein, similar to the findings in neurons. We therefore set out to test the effects of the AS1411 aptamer in 3T3 cells. Since AS1411 can induce death in various types of cycling cells, we first determined the effects of different concentrations of aptamer on 3T3 cell survival and size (Figures S6A and S6B). Exposure to 10 μ M AS1411 for 48 hr induced efficient uptake into 3T3 cells (Figure 6C), with concomitant increase in cell area without affecting

cell survival (Figures S6A and S6B). Nuclear area and shape were not perturbed (Figures S6C–S6E). This application regimen was therefore used in all subsequent experiments.

If translation of nucleolin-transported importin β 1 mRNA in the distal region of the cytoplasm is indeed the source of retrogradely transported importin β 1 protein, one would expect to observe reduced levels of importin β 1 interacting with dynein in AS1411-treated cells. Indeed, AS1411-treated cells revealed reduced association of importin β 1 with dynein by PLA analyses (Figures 6D and 6E) and co-immunoprecipitation (Figure 6F). Furthermore, we observed a decrease in MAIL motif

association with kinesin heavy-chain complexes upon AS1411 treatment (Figure S6F), in a manner similar to that previously observed in axoplasm. MAIL-associated nucleolin levels were not changed following AS1411 treatment (data not shown), indicating that, in 3T3 cells similar to neurons, AS1411 reduces the association of nucleolin and its cargo mRNAs with kinesins, therefore reducing their transport to the cell periphery.

We then tested the effects of aptamer treatment on the size of the cells. AS1411 caused a significant increase in cell body area compared to cells exposed to control aptamer (Figures 6G and 6H). To discriminate between overall size increase versus enhanced cell spreading on the substrate, we assessed 3T3 cell size by fluorescence-activated cell sorting (FACS). In this case, cells were exposed to AS1411 or control aptamer for 48 hr, and then they were harvested and labeled with Hoechst and propidium iodide dyes for live cell cycle analysis by flow cytometry. This analysis showed that AS1411 causes a significant increase in cell size at all stages of the cell cycle (Figures 6I and 6J). The latter result suggests that AS1411's effect on cell size is due to a general change in cell metabolism and physiology and not by a single change in a cell cycle checkpoint. Thus, motor-dependent nucleolin-mediated RNA transport regulates size in both cycling fibroblasts and post-mitotic neurons.

Nucleolin and Importin Localization Regulates Cellular Protein Synthesis

To obtain further insights on how nucleolin might modulate cell size, we examined the effect of its localization on mRNA translation rates. We quantified overall protein synthesis levels by puromycin incorporation (Schmidt et al., 2009), and we observed a significant and marked overall increase in protein synthesis levels in AS1411-treated neurons (Figures S7A and S7B). A less prominent but still significant increase in protein synthesis levels also was observed in importin β 3' UTR^{-/-} neurons as compared to WT (Figures S7C and S7D). We then examined the effect of nucleolin or importin β 1 sequestration on subcellular levels of protein synthesis at axon tips by puromycin labeling and immunostaining. AS1411 treatment reduced protein synthesis levels at axon tips of cultured neurons (Figures 7A, 7B, S7E, and S7F). A similar reduction in axon tip protein synthesis was observed in importin β 1 3' UTR^{-/-} neurons as compared to WT, and AS1411 treatment did not have any further effect in the 3' UTR^{-/-} neurons (Figures 7A and 7B). These results suggest that nucleolin sequestration by the AS1411 aptamer and importin β 1 mislocalization in the 3' UTR^{-/-} both impact on protein synthesis at axon tips. To examine whether a similar effect is found in cycling cells, we visualized puromycin incorporation in the cytoplasm of aptamer-treated 3T3 fibroblasts (Figure 7C). Quantification of puromycin incorporation levels in peripheral versus total cytoplasm revealed a reduction in the peripheral region of AS1411-treated fibroblast cells as compared to mock or control aptamer-treated cells (Figure 7D). Taken together, these findings show that AS1411 treatment or importin β 1 3' UTR KO causes a subcellular shift in protein synthesis, concomitantly with their effects on axon length or fibroblast cell size.

DISCUSSION

Cell size homeostasis is a ubiquitous feature of biological systems, but a comprehensive answer to the question of how cellular dimensions are encoded or sensed by molecular networks is still lacking (Ginzberg et al., 2015). We recently proposed that growing neurons might sense their axon lengths by bidirectional signaling via molecular motors (Rishal et al., 2012). Experimental testing of model predictions supported a role of kinesin and dynein motors in such a mechanism (Rishal et al., 2012), and others have implicated myosin and kinesin motors in size and growth control in neurons (van Diepen et al., 2009; Watt et al., 2015). However, the nature of the signals involved in motor-dependent size sensing remained elusive. In this paper, we provide evidence that nucleolin-mediated RNA localization affects cell growth and size in both neurons and cycling cells, suggesting that subcellular RNA localization is a key mechanism for cell size regulation (Figure 7E).

The initial observation implicating importin β 1 in size regulation was increased growth of importin β 1 3' UTR^{-/-} sensory axons, analogous to the results we had reported previously from dynein-mutant mice (Rishal et al., 2012). The identification of nucleolin as an RBP for importin β 1 mRNA, and the length and size effects observed upon perturbation of nucleolin with AS1411, shed additional light on the mechanism proposed by Rishal et al. (2012). Sequestration of importin β 1 by direct targeting of its 3' UTR or by perturbation of nucleolin localization with a specific aptamer induces changes in growth rates and cell size. In essence these findings suggest that local translation of nucleolin cargo mRNAs provides the positive feedback arm of the proposed mechanism and that the retrograde signals are dependent on de-novo-translated proteins trafficked by dynein and importins. RNA localization and local protein translation are ubiquitous features of all eukaryotic cells, and they play critical roles in defining localized proteome specialization (Jung et al., 2014). Previous work had shown that local translation enables communication between distal axonal sites and the nucleus upon injury (Perry et al., 2012), and our current findings expand the scope of such mechanisms to size regulation in growing cells.

Nucleolin seems well suited for a pivotal role in size regulation by nucleus-periphery communication, since it shuttles among nucleus, cytosol, and the cell surface (Hovanessian et al., 2010) and it has a broad phylogenetic distribution, including yeast, plant, and animal cells (Riordan et al., 2011; Abdelmohsen and Gorospe, 2012). Nucleolin contains four RNA-binding domains that may interact with diverse target RNAs via a number of short RNA motifs (Abdelmohsen et al., 2011; Ginisty et al., 2001; Ishimaru et al., 2010; Riordan et al., 2011). None of these motifs is similar in sequence to the importin β 1 MAIL element, but, since functional localization motifs in RNA are structure and not sequence based (Andreassi and Riccio, 2009), this is not surprising. A comprehensive characterization of the nucleolin cargo RNA ensemble may reveal additional components of the size-sensing mechanism.

We found that the nucleolin-specific AS1411 aptamer (Bates et al., 2009) attenuates nucleolin association with kinesin motors, thereby enabling its sequestration from distal regions of the cell without affecting overall expression levels of the protein. This is

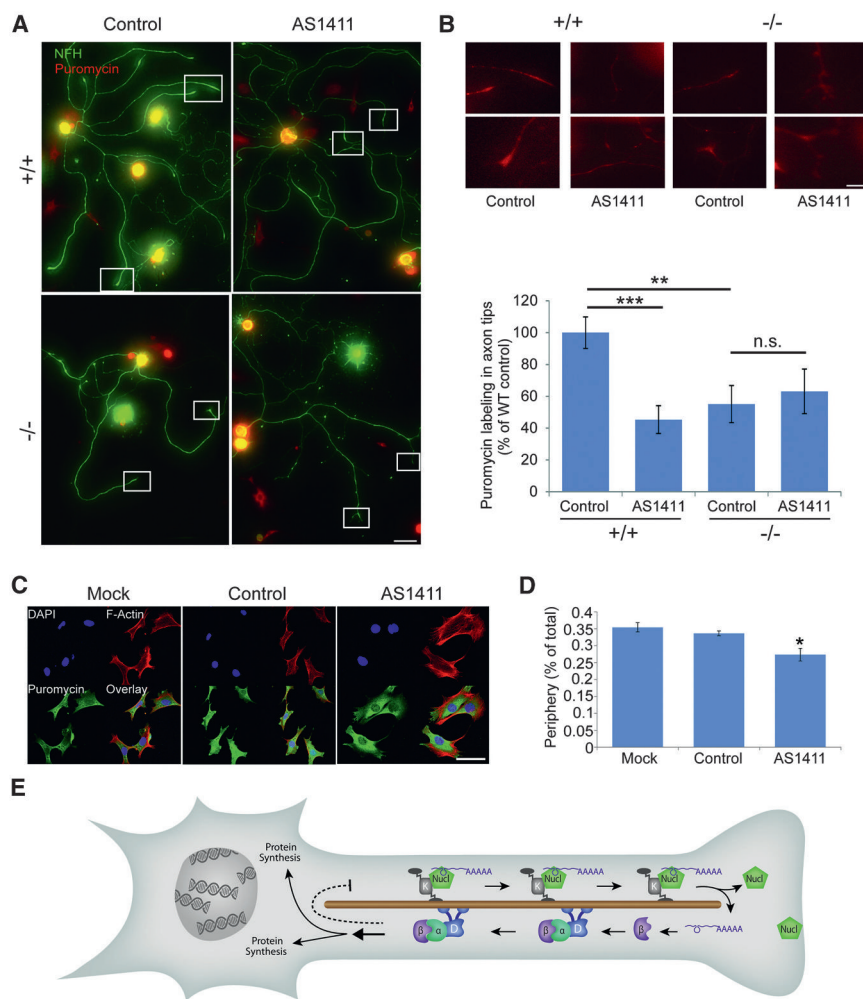


Figure 7. Nucleolin and Importin $\beta 1$ Localization Regulate Protein Synthesis

(A) The translational activity of DRG neurons in culture was assessed by puromycin incorporation. Cultures were grown in the presence of AS1411 or control aptamer for 48 hr, and then they were replated and cultured for an additional 24 hr in fresh medium without aptamer. Neurons were then pulsed with 5 mM puromycin for 10 min at 37°C or preincubated with 40 mM anisomycin for 30 min followed by the 5 mM puromycin pulse, and then they were fixed. Fixed cultures were immunostained for NfH (green) and α -puromycin (red). Scale bar, 100 μ m. For anisomycin control, see Figures S7E and S7F.

(B) Representative high-sensitivity zoom images of the boxed regions in (A) reveal protein synthesis in axon tips. Scale bar, 20 μ m. Quantification reveals a significant decrease in protein synthesis in axon tips of AS1411-treated WT neurons, as well as in importin $\beta 1$ 3' UTR^{-/-} neurons. Axon tip synthesis was quantified as ratios of cell body values and then normalized to WT control. Mean \pm SEM; $n \geq 80$ cells from three independent cultures; ** $p < 0.01$ and *** $p < 0.001$, Student's *t* test.

(C) Representative images of cultured 3T3 cells treated with 10 μ M control or AS1411 aptamer for 48 hr and then replated and cultured for an additional 24 hr in fresh medium without aptamer. The cells subsequently were incubated with puromycin with or without anisomycin as described above, and then they were fixed and stained for F-Actin, DAPI, and α -puromycin. Scale bar, 50 μ m. (D) Quantification of puromycin labeling in the cytoplasm of 3T3 cells from the experiment described in (C) reveals a significant decrease in protein synthesis at the cell periphery in AS1411-treated cells. Mean \pm SEM; $n \geq 200$ cells from five independent cultures; * $p < 0.05$, one-way ANOVA with Bonferroni post hoc test.

(E) Schematic model of the mechanism proposed in this study. Nucleolin binds importin $\beta 1$ and likely

other mRNAs, and the complex is transported by a kinesin motor to the axon in a neuron or the cell cortex in cycling cells. Upon arrival at the end of the microtubules, the complex is disassembled, with nucleolin likely docking to the plasma membrane. Local translation of the cargo RNAs generates proteins that are retrogradely transported with dynein to influence protein synthesis in the soma. The dashed line indicates a negative feedback loop postulated in the original model (Rishal et al., 2012), the details of which are still unknown. See also Figure S7.

consistent with a previous study that demonstrated continuous and rapid turnover of cell surface nucleolin in parallel with stability of the nuclear pool (Hovanessian et al., 2010). Interestingly, calcium is required for nucleolin internalization (Hovanessian et al., 2010) and also for importin $\beta 1$ local translation (Yudin et al., 2008), suggesting that nucleolin-membrane interactions might trigger RNA cargo dissociation and local translation. Perturbation of this process by nucleolin sequestration causes a size increase in both neurons and fibroblasts. These findings raise the intriguing possibility that sequestration of critical components of the pathway, for example, as done here by AS1411 treatment, might open new avenues for accelerating axonal growth. In essence such treatments would cause the size-sensing mechanism to sense a shorter axon than is actually present, inducing the cell to generate the metabolic output required to sustain rapid growth.

The increased growth observed in importin $\beta 1$ 3' UTR^{-/-} neurons or upon sequestration of nucleolin from axons or in 3T3 cells is correlated with subcellular changes in protein synthesis. Interestingly, recent work in bacteria and in yeast implicates differential protein synthesis rates in cell size control (Basan et al., 2015; Schmoller et al., 2015). The latter study suggests that size control arises from differences in the size dependence of synthesis of a cell cycle activator versus a cell cycle inhibitor, but it does not show how different protein synthesis pathways can differ in their size sensitivity (Schmoller and Skotheim, 2015). Our findings show that nucleolin and importin $\beta 1$ perturbation can affect both levels and localization of protein synthesis. The latter finding is especially striking since it provides a plausible transport-regulated mechanism for size-sensitive protein synthesis at cellular extremities, with concomitant size-insensitive synthesis in the cell center. The motor-dependent RNA localization

mechanisms delineated in this study provide a mechanism for size sensing that may work via regulation of the subcellular localization of protein synthesis in large cells. Importin β 1 may act to link critical regulators to the system, since importin-dynein complexes have been shown to transport transcription factors and other regulatory molecules. These and other questions regarding the proposed mechanism remain open for future work.

To summarize, our findings implicate microtubule motors, mRNA localization, and local translation in the regulation of cell size homeostasis. We propose that feedback monitoring of microtubule cytoskeleton length by transport of locally translated mRNAs enables neuron length and cell size sensing.

EXPERIMENTAL PROCEDURES

Animals, Preparations, and Cultures

All rat and mouse strains used were bred and maintained at the Veterinary Resources Department of the Weizmann Institute. DRG neuron culture preparations were as previously described (Rishal et al., 2010). The study was conducted in accordance with the guidelines of the Weizmann and University of South Carolina (USC) Institutional Animal Care and Use Committees (IACUCs).

Capillary Electrophoresis Immuno-quantification

Automated capillary electrophoresis immuno-quantification runs were conducted on a Wes instrument (ProteinSimple) as described (Harris, 2015). Analyses were performed on 15 s or 30 s image exposures.

DRG Neuron Cultures and Growth Rate Analyses

DRG neurons from the indicated conditions and genotypes were imaged periodically in continuous culture in a Fluoview (FV10i, Olympus) automated confocal laser-scanning microscope with built-in incubator chamber or in an ImageXpress Micro (Molecular Devices) automated microscopy system.

The 20 μ M AS1411 or control DNAs were added to rat DRG culture media for 48 hr. Cells were replated to tissue culture inserts for 24 hr before isolation of RNA or protein. Adult YFP/WT mice were treated with control or AS1411 aptamer for 48 hr and then replated and imaged for 24 hr as described above. Cultured DRG neurons from WT or importin β 1 3' UTR KO mice were fixed 24 hr after replating and stained with anti-NFH for process length determination. Neuronal morphology was quantified using WIS-Neuromath (Rishal et al., 2013) or MetaXpress (Molecular Devices).

EM

Samples were prepared for EM as previously described (Rishal et al., 2012). Quantitative analysis was performed using a Fiji macro script written in house.

Fibroblast Cell Imaging and FACS Analysis

AS1411 DNA or control DNA (10 μ M) was added to the culture media of 3T3 cells. After 48 hr the cells were replated for another 24 hr without the aptamer for imaging or for live cell cycle analysis by flow cytometry.

FISH

Antisense oligonucleotide probes for importin β 1 were designed using Oligo 6 software and checked for homology and specificity by BLAST. cRNA probes for GFP reporter mRNA were as previously described (Vuppalanchi et al., 2010). Hybridization to DRG neuronal cultures was as previously described (Willis et al., 2007). For colocalization of RNA and protein, fluorescently labeled Stellaris RNA probes were used (BiosearchTech) as previously described (Spillane et al., 2013).

FRAP

Dissociated DRG cultures were transfected with importin β 1 3' UTR axonal and cell body variants using Amaxa nucleofection. Terminal axons were subjected to FRAP sequence at 37°C with 488 nm laser line of Leica TCS/SP2 confocal microscope as described with minor modifications (Yudin et al., 2008). Prior to bleaching, neurons were imaged every 30 s for 2 min at 15% laser power. For

photobleaching, the region of interest (ROI) was exposed to 75% laser power every 1.6 s for 40 frames. Recovery was monitored every 60 s over 20 min at 15% laser power. To test for translation dependence, cultures were pretreated with 50 μ M anisomycin for 30 min before the photobleaching sequence. FRAP quantification and statistical tests are detailed in the Supplemental Experimental Procedures.

Pull-downs and Mass Spectrometry

Axoplasm from rat or mouse sciatic nerve was extracted as previously described (Rishal et al., 2010), and RBP pull-downs were carried out as described (Doron-Mandel et al., 2016). Bovine axoplasm was extracted by the same procedure, using sciatic nerve dissected on site from fresh bovine carcasses within 20 min of slaughter at the Tnuva Slaughterhouse. Streptavidin magnetic beads were washed several times with different concentrations of NaCl, and they were then incubated with 100 μ M of the different RNA probes or DNA probes, except for the no-probe sample that was incubated with water. All samples were incubated for 1 hr at 4°C. After washing the resin, 0.5 mg rat axoplasm extract or 10 mg bovine axoplasm extract was applied to the no-probe resin for 30 min to deplete unspecific proteins, and then the unbound fraction was added to the specific probe resin for another 30 min. After intensive washing, bound material was eluted from the resin using SDS sample buffer. The samples from the bovine axoplasm pull-down were loaded into 10% SDS-PAGE gels, followed by Colloidal Blue staining, in-gel digest, and mass spectrometry (see the Supplemental Experimental Procedures).

Protein Synthesis Assays by Puromycin Incorporation

Overall protein synthesis levels were quantified by puromycin incorporation as previously described (Schmidt et al., 2009). Subcellular visualization of protein synthesis in situ was by puromycin immunostaining as described (David et al., 2012).

qPCR

The qPCR was performed using Taqman primer kits for β -actin (normalization control) and importin β 1 or perfecta SYBR green (Quanta Biosciences) and gene-specific primers for importin β 1 and 18S.

Statistical Methods

Data represent mean \pm SEM, unless otherwise noted. Groupwise analyses were conducted by one- or two-way ANOVA with Bonferroni post hoc test. Pairwise analyses were conducted by two-tailed Student's *t* tests (unpaired, unless otherwise noted; see figure legends). Statistical analyses were conducted using GraphPad Prism, Synergy Kaleidagraph, or Microsoft Excel. Significance was considered as *p* values < 0.05.

SUPPLEMENTAL INFORMATION

Supplemental Information includes Supplemental Experimental Procedures and seven figures and can be found with this article online at <http://dx.doi.org/10.1016/j.celrep.2016.07.005>.

AUTHOR CONTRIBUTIONS

M.F., R.B.-T.P., I.R., and E.D.-M. designed the study. R.B.-T.P., I.R., E.D.-M., A.L.K., M.T., S.A., S.K., A.L., M.R., D.Y., P.K.S., C.G., and E.A.H. performed experiments and data analyses. K.F.M. carried out mass spectrometry analyses. V.S. performed EM. W.G. supervised bovine dissections and sample preparation. M.F., J.L.T., A.L.B., A.Y., and C.J.W. supervised research. M.F., R.B.-T.P., I.R., and E.D.-M. wrote the initial manuscript draft. All authors revised the manuscript and approved the final version.

ACKNOWLEDGMENTS

We thank Nitzan Korem for excellent technical assistance; Ofra Golani and Rinat Nevo for expert advice on image analyses; Shifra Ben-Dor for expert assistance with bioinformatics; Hanna Vega for graphics; and Dalia Gordon, Elizabeth M.C. Fisher, and Giampietro Schiavo for helpful comments on earlier

drafts of this manuscript. This work was supported by funding from the European Research Council (Neurogrowth, M.F.), the Dr. Miriam and Sheldon G. Adelson Medical Research Foundation (M.F., J.L.T., C.J.W., and A.L.B.), the Israel Science Foundation (1284/13, M.F.), the Minerva Foundation (M.F.), the USA-Israel Binational Science Foundation (2011329, M.F. and J.L.T.), the U.S. Army Medical Research Program (W81XWH-13-1-0308, J.L.T. and M.F.), and the NIH (National Institute of General Medical Sciences [NIGMS] 8P41GM103481, A.L.B.; National Institute of Neurological Disorders and Stroke [NINDS] 5R01NS041596, J.L.T.). M.F. is the incumbent of the Chaya Professorial Chair in Molecular Neuroscience at the Weizmann Institute of Science. J.L.T. is the incumbent of the SmartState Chair in Childhood Neurotherapeutics at the University of South Carolina. A.Y. is the incumbent of the Jack & Simon Djanogly Professorial Chair in Biochemistry at the Weizmann Institute of Science.

Received: June 23, 2014

Revised: January 23, 2016

Accepted: July 4, 2016

Published: July 28, 2016

REFERENCES

- Abdelmohsen, K., and Gorospe, M. (2012). RNA-binding protein nucleolin in disease. *RNA Biol.* 9, 799–808.
- Abdelmohsen, K., Tominaga, K., Lee, E.K., Srikantan, S., Kang, M.J., Kim, M.M., Selimyan, R., Martindale, J.L., Yang, X., Carrier, F., et al. (2011). Enhanced translation by Nucleolin via G-rich elements in coding and non-coding regions of target mRNAs. *Nucleic Acids Res.* 39, 8513–8530.
- Albus, C.A., Rishal, I., and Fainzilber, M. (2013). Cell length sensing for neuronal growth control. *Trends Cell Biol.* 23, 305–310.
- Andreassi, C., and Riccio, A. (2009). To localize or not to localize: mRNA fate is in 3'UTR ends. *Trends Cell Biol.* 19, 465–474.
- Basan, M., Zhu, M., Dai, X., Warren, M., Sévin, D., Wang, Y.P., and Hwa, T. (2015). Inflating bacterial cells by increased protein synthesis. *Mol. Syst. Biol.* 11, 836.
- Bates, P.J., Laber, D.A., Miller, D.M., Thomas, S.D., and Trent, J.O. (2009). Discovery and development of the G-rich oligonucleotide AS1411 as a novel treatment for cancer. *Exp. Mol. Pathol.* 86, 151–164.
- Berger, C.M., Gaume, X., and Bouvet, P. (2015). The roles of nucleolin subcellular localization in cancer. *Biochimie* 113, 78–85.
- David, A., Dolan, B.P., Hickman, H.D., Knowlton, J.J., Clavarino, G., Pierre, P., Bennink, J.R., and Yewdell, J.W. (2012). Nuclear translation visualized by ribosome-bound nascent chain puromylation. *J. Cell Biol.* 197, 45–57.
- Doron-Mandel, E., Alber, S., Oses, J.A., Medzihradzky, K.F., Burlingame, A.L., Fainzilber, M., Twiss, J.L., and Lee, S.J. (2016). Isolation and analyses of axonal ribonucleoprotein complexes. *Methods Cell Biol.* 137, 467–486.
- Feng, G., Mellor, R.H., Bernstein, M., Keller-Peck, C., Nguyen, Q.T., Wallace, M., Nerbonne, J.M., Lichtman, J.W., and Sanes, J.R. (2000). Imaging neuronal subsets in transgenic mice expressing multiple spectral variants of GFP. *Neuron* 28, 41–51.
- Ginisty, H., Amalric, F., and Bouvet, P. (2001). Two different combinations of RNA-binding domains determine the RNA binding specificity of nucleolin. *J. Biol. Chem.* 276, 14338–14343.
- Ginzberg, M.B., Kafri, R., and Kirschner, M. (2015). Cell biology. On being the right (cell) size. *Science* 348, 1245075.
- Hanz, S., Perlson, E., Willis, D., Zheng, J.Q., Massarwa, R., Huerta, J.J., Koltzenburg, M., Kohler, M., van-Minnen, J., Twiss, J.L., and Fainzilber, M. (2003). Axoplasmic importins enable retrograde injury signaling in lesioned nerve. *Neuron* 40, 1095–1104.
- Harrington, A.W., and Ginty, D.D. (2013). Long-distance retrograde neurotrophic factor signalling in neurons. *Nat. Rev. Neurosci.* 14, 177–187.
- Harris, V.M. (2015). Protein detection by Simple Western™ analysis. *Methods Mol. Biol.* 1312, 465–468.
- Hovanessian, A.G., Soundaramourty, C., El Khoury, D., Nondier, I., Svab, J., and Krust, B. (2010). Surface expressed nucleolin is constantly induced in tumor cells to mediate calcium-dependent ligand internalization. *PLoS ONE* 5, e15787.
- Ishimaru, D., Zuraw, L., Ramalingam, S., Sengupta, T.K., Bandyopadhyay, S., Reuben, A., Fernandes, D.J., and Spicer, E.K. (2010). Mechanism of regulation of bcl-2 mRNA by nucleolin and A+U-rich element-binding factor 1 (AUF1). *J. Biol. Chem.* 285, 27182–27191.
- Jung, H., Gkogkas, C.G., Sonenberg, N., and Holt, C.E. (2014). Remote control of gene function by local translation. *Cell* 157, 26–40.
- Kim, H.H., Lee, S.J., Gardiner, A.S., Perrone-Bizzozero, N.I., and Yoo, S. (2015). Different motif requirements for the localization zipcode element of β -actin mRNA binding by HuD and ZBP1. *Nucleic Acids Res.* 43, 7432–7446.
- Lallemend, F., Sterzenbach, U., Hadjab-Lallemend, S., Aquino, J.B., Castelo-Branco, G., Sinha, I., Villaescusa, J.C., Levanon, D., Wang, Y., Franck, M.C., et al. (2012). Positional differences of axon growth rates between sensory neurons encoded by Runx3. *EMBO J.* 31, 3718–3729.
- Marguerat, S., and Bähler, J. (2012). Coordinating genome expression with cell size. *Trends Genet.* 28, 560–565.
- Perry, R.B., Doron-Mandel, E., Iavnilovitch, E., Rishal, I., Dagan, S.Y., Tsoory, M., Coppola, G., McDonald, M.K., Gomes, C., Geschwind, D.H., et al. (2012). Subcellular knockout of importin β 1 perturbs axonal retrograde signaling. *Neuron* 75, 294–305.
- Riordan, D.P., Herschlag, D., and Brown, P.O. (2011). Identification of RNA recognition elements in the *Saccharomyces cerevisiae* transcriptome. *Nucleic Acids Res.* 39, 1501–1509.
- Rishal, I., Michalevski, I., Rozenbaum, M., Shinder, V., Medzihradzky, K.F., Burlingame, A.L., and Fainzilber, M. (2010). Axoplasm isolation from peripheral nerve. *Dev. Neurobiol.* 70, 126–133.
- Rishal, I., Kam, N., Perry, R.B., Shinder, V., Fisher, E.M., Schiavo, G., and Fainzilber, M. (2012). A motor-driven mechanism for cell-length sensing. *Cell Rep.* 1, 608–616.
- Rishal, I., Golani, O., Rajman, M., Costa, B., Ben-Yaakov, K., Schoenmann, Z., Yaron, A., Basri, R., Fainzilber, M., and Galun, M. (2013). WIS-NeuroMath enables versatile high throughput analyses of neuronal processes. *Dev. Neurobiol.* 73, 247–256.
- Sanz, E., Yang, L., Su, T., Morris, D.R., McKnight, G.S., and Amieux, P.S. (2009). Cell-type-specific isolation of ribosome-associated mRNA from complex tissues. *Proc. Natl. Acad. Sci. USA* 106, 13939–13944.
- Schmidt, E.K., Clavarino, G., Ceppi, M., and Pierre, P. (2009). SUnSET, a nonradioactive method to monitor protein synthesis. *Nat. Methods* 6, 275–277.
- Schmoller, K.M., and Skotheim, J.M. (2015). The biosynthetic basis of cell size control. *Trends Cell Biol.* 25, 793–802.
- Schmoller, K.M., Turner, J.J., Köivomägi, M., and Skotheim, J.M. (2015). Dilution of the cell cycle inhibitor Whi5 controls budding-yeast cell size. *Nature* 526, 268–272.
- Söderberg, O., Gullberg, M., Jarvius, M., Ridderstråle, K., Leuchowius, K.J., Jarvius, J., Wester, K., Hydbring, P., Bahram, F., Larsson, L.G., and Landegren, U. (2006). Direct observation of individual endogenous protein complexes in situ by proximity ligation. *Nat. Methods* 3, 995–1000.
- Spillane, M., Ketschek, A., Merianda, T.T., Twiss, J.L., and Gallo, G. (2013). Mitochondria coordinate sites of axon branching through localized intra-axonal protein synthesis. *Cell Rep.* 5, 1564–1575.
- van Diepen, M.T., Parsons, M., Downes, C.P., Leslie, N.R., Hindges, R., and Eickholt, B.J. (2009). MyosinV controls PTEN function and neuronal cell size. *Nat. Cell Biol.* 11, 1191–1196.
- Vuppalaanchi, D., Coleman, J., Yoo, S., Merianda, T.T., Yadhati, A.G., Hossain, J., Blesch, A., Willis, D.E., and Twiss, J.L. (2010). Conserved 3'-untranslated region sequences direct subcellular localization of chaperone protein mRNAs in neurons. *J. Biol. Chem.* 285, 18025–18038.

- Watt, D., Dixit, R., and Cavalli, V. (2015). JIP3 activates kinesin-1 motility to promote axon elongation. *J. Biol. Chem.* *290*, 15512–15525.
- Willis, D.E., van Niekerk, E.A., Sasaki, Y., Mesngon, M., Merianda, T.T., Williams, G.G., Kendall, M., Smith, D.S., Bassell, G.J., and Twiss, J.L. (2007). Extracellular stimuli specifically regulate localized levels of individual neuronal mRNAs. *J. Cell Biol.* *178*, 965–980.
- Yudin, D., Hanz, S., Yoo, S., Iavnilovitch, E., Willis, D., Gradus, T., Vuppalaanchi, D., Segal-Ruder, Y., Ben-Yaakov, K., Hieda, M., et al. (2008). Localized regulation of axonal RanGTPase controls retrograde injury signaling in peripheral nerve. *Neuron* *59*, 241–252.
- Zuker, M. (2003). Mfold web server for nucleic acid folding and hybridization prediction. *Nucleic Acids Res.* *31*, 3406–3415.

Human iPSC-Derived Cerebral Organoids Model Cellular Features of Lissencephaly and Reveal Prolonged Mitosis of Outer Radial Glia

Marina Bershteyn,^{1,2,6,*} Tomasz J. Nowakowski,^{1,3} Alex A. Pollen,^{1,3} Elizabeth Di Lullo,^{1,3} Aishwarya Nene,⁴ Anthony Wynshaw-Boris,^{2,5,*} and Arnold R. Kriegstein^{1,3,7,*}

¹Eli and Edythe Broad Center of Regeneration Medicine and Stem Cell Research, University of California, San Francisco, San Francisco, CA 94143, USA

²Institute for Human Genetics, University of California, San Francisco, San Francisco, CA 94143, USA

³Department of Neurology, University of California, San Francisco, San Francisco, CA 94143, USA

⁴California Institute of Technology, Pasadena, CA 91125, USA

⁵Department of Genetics and Genome Sciences, Case Western Reserve University, Cleveland, OH 44106, USA

⁶Present address: Neurona Therapeutics, South San Francisco, CA 94080, USA

⁷Lead Contact

*Correspondence: mbershteyn@gmail.com (M.B.), ajw168@case.edu (A.W.-B.), kriegsteina@stemcell.ucsf.edu (A.R.K.)

<http://dx.doi.org/10.1016/j.stem.2016.12.007>

SUMMARY

Classical lissencephaly is a genetic neurological disorder associated with mental retardation and intractable epilepsy, and Miller-Dieker syndrome (MDS) is the most severe form of the disease. In this study, to investigate the effects of MDS on human progenitor subtypes that control neuronal output and influence brain topology, we analyzed cerebral organoids derived from control and MDS-induced pluripotent stem cells (iPSCs) using time-lapse imaging, immunostaining, and single-cell RNA sequencing. We saw a cell migration defect that was rescued when we corrected the MDS causative chromosomal deletion and severe apoptosis of the founder neuroepithelial stem cells, accompanied by increased horizontal cell divisions. We also identified a mitotic defect in outer radial glia, a progenitor subtype that is largely absent from lissencephalic rodents but critical for human neocortical expansion. Our study, therefore, deepens our understanding of MDS cellular pathogenesis and highlights the broad utility of cerebral organoids for modeling human neurodevelopmental disorders.

INTRODUCTION

The human cerebral cortex develops from a pseudostratified layer of neuroepithelial stem cells (NESCs) into a functionally complex, six-layered structure with a folded (gyrencephalic) surface. The molecular underpinnings of brain size and topology are encoded by the genome and distinguish us from species with a small and smooth (lissencephalic) brain surface, such as mice. Although brain folding in the human does not begin until the end of the second trimester (after gestation week [GW] 23) (Chi et al., 1977; Martin et al., 1988; Hansen

et al., 1993; Armstrong et al., 1995), many of the key cellular events that influence this process, including expansion of the progenitor population and neuronal migration, occur starting around GW4 (Lui et al., 2011; Sidman and Rakic, 1973; Stiles and Jernigan 2010). Genetic and infectious diseases that disrupt these processes underlie a number of cortical malformations and cause mental retardation, mortality, and morbidity (Guerrini and Dobyns 2014; Hu et al., 2014). Despite the prevalence and societal burden of cortical malformations, our understanding of how disease-linked mutations disrupt brain development is still limited.

Miller-Dieker syndrome (MDS) is a severe cortical malformation characterized by nearly absent cortical folding (lissencephaly) often associated with reduced brain size (microcephaly), craniofacial dysmorphisms, mental retardation, and intractable epilepsy (Dobyns et al., 1983, 1991; Nagamani et al., 2009). MDS is caused by large heterozygous deletions of human band 17p13.3, harboring dozens of genes, including *PAFAH1B1* (LIS1 protein) and *YWHAE* (14-3-3 ϵ protein) (Dobyns et al., 1983; Reiner et al., 1993; Hattori et al., 1994; Chong et al., 1997; Cardoso et al., 2003). Smaller deletions or mutations in *PAFAH1B1* are the major cause of isolated lissencephaly sequence (ILS), which exhibits less severe degrees of lissencephaly (Ledbetter et al., 1992; Lo Nigro et al., 1997; Pilz et al., 1998; Barkovich et al., 1991; Cardoso et al., 2003). Insight into lissencephaly pathogenesis is largely derived from mouse models and limited analyses of postmortem human brains. Reduction in LIS1 levels in *Pafah1b1* mutant mice leads to defects in neuronal migration (Hirotsumi et al., 1998; Smith et al., 2000), consistent with the disrupted cortical layering and neuron dispersion seen in the postmortem MDS brain (Sheen et al., 2006b; Saito et al., 2011). LIS1 is an atypical microtubule-associated protein that regulates microtubule dynamics and nuclear-centrosomal coupling during neuronal migration (Faulkner et al., 2000; Gambello et al., 2003; Shu et al., 2004; Tanaka et al., 2004; Youn et al., 2009). Collectively, these studies led to the prevailing model that lissencephaly is due to defective neuronal migration (Kato and Dobyns, 2003). However, the mouse brain is naturally lissencephalic,

suggesting that certain aspects of cortical development may not be adequately assessed in mice.

Recent work has uncovered critical cellular and molecular differences between cortical development in humans and mice, further underscoring the need to develop human model systems. In the developing human cortex, the outer subventricular zone (OSVZ) is greatly expanded (Smart et al., 2002; Lukaszewicz et al., 2005). OSVZ progenitors, which include transit-amplifying intermediate progenitor (IP) cells and outer or basal radial glia (oRG/bRG) (Hansen et al., 2010; Fietz et al., 2010; Betizeau et al., 2013), have been proposed to contribute to the majority of upper-layer neurogenesis (Smart et al., 2002; Lukaszewicz et al., 2005). Although IP cells are conserved between humans and mice, oRG cells are largely absent from the developing cortices of lissencephalic rodents (Shitamukai et al., 2011; Wang et al., 2011), which may explain why the phenotypes in *Pafah1b1*^{+/-} mice are substantially milder than in human patients with heterozygous *PAFAH1B1* mutations. Multiple lines of evidence suggest that the high abundance and proliferative capacity of oRG cells are critical for the vast developmental and evolutionary increase in cortical size (Stahl et al., 2013; Reillo et al., 2011).

To bridge the gap between mouse models and human disease, patient-derived induced pluripotent stem cells (iPSCs) (Takahashi et al., 2007; Yu et al., 2007; Park et al., 2008) represent a promising approach to study disease pathogenesis in a relevant genetic and cellular context. Human iPSCs provide a renewable source of neuronal progenitors and neurons, can be genetically and pharmacologically manipulated, and can recapitulate key cellular processes of in vivo brain development (Eiraku et al., 2008; Gaspard et al., 2008). Studies have shown that oRG-like cortical cells can be produced from human, but not mouse, iPSCs (Shi et al., 2012; Kadoshima et al., 2013; Lancaster et al., 2013; Qian et al., 2016), highlighting the advantage of the species-specific cellular model systems. However, the extent to which in vitro-derived oRG cells recapitulate the functional properties and molecular identity of primary oRG cells has not been determined. Here we implement a 3D cerebral organoid culture method (Kadoshima et al., 2013) to analyze the effect of MDS lissencephaly mutations on distinct biological processes and cell types corresponding to the first trimester of cortical development. Using a multifaceted approach integrating histology, live cell imaging, and single-cell transcriptomics, we uncover cell type-specific defects in lissencephaly spanning the stages of neuroepithelial cell expansion, neuronal migration, and the mitotic properties of oRG progenitors, providing deeper insight into human cortical development and lissencephaly.

RESULTS

Increased Apoptosis of NESCs in MDS Cortical Organoids

To study MDS pathogenesis, we generated iPSCs from three MDS individuals (Figures 1A–1C) using non-integrating episomal reprogramming vectors (Okita et al., 2011; Bershteyn et al., 2014). From each individual, we chose two independent iPSC clones with confirmed pluripotency, normal karyotype, and stable maintenance of the 17p13.3 deletion for subsequent studies (Bershteyn et al., 2014, and data not shown). To assess the effect

of MDS on NESCs, we implemented a published suspension culture method whereby equal numbers of dissociated iPSCs are quickly re-aggregated in serum-free cortical differentiation medium (Kadoshima et al., 2013). Initially and on day 3, there were no significant differences in the size of wild-type (WT) and MDS aggregates (Figures S1A and S1C). However, by 2.5 weeks of suspension culture (day 18 ± 1), the MDS organoids were significantly smaller (Figure 1D; Figures S1B–S1D). We observed that 25% of MDS organoids (n = 3 individuals, 2 iPSC clones each) were very small (less than 0.5 mm in circumference; Figure 1D) and invariably disintegrated before they could be analyzed. Of note, organoids derived from both of the MDS4 clones exhibited particularly poor growth in suspension and were therefore omitted from most of the subsequent assays.

The larger organoids were fixed and sectioned after 5 weeks of differentiation for further characterization. At this time point, the organoids consisted of NESCs organized into multiple pseudo-stratified VZ-like progenitor regions expressing SOX2 (Figures 1E). Cortical patterning was verified by co-expression of the dorsal telencephalon progenitor marker PAX6 (Georgala et al., 2011) in the VZ-like regions, which were surrounded by doublecortin (DCX)-positive neurons also expressing the deep-layer subcortical projection neuron marker CTIP2 (Molyneaux et al., 2005; Leone et al., 2008; Figure S2). Consistent with reduced organoid size, we found markedly increased apoptosis in the MDS cortical VZ-like regions, whereas the marker of proliferation was not significantly altered (Figures 1F–1H). Interestingly, although acute removal of *Pafah1b1* in the mouse telencephalon at embryonic day (E) 8–E8.5 leads to NESC apoptosis, genetic *Pafah1b1* heterozygosity does not exhibit a strong phenotype in the mouse neuroepithelium (Hirotsumi et al., 1998; Yingling et al., 2008). Our results suggest that the human genetic model may be more sensitive in recapitulating lissencephaly severity and highlight an early defect in the founder population of neuroepithelial stem cells independent of neurogenesis or neuronal migration.

Increased Incidence of Horizontal Cleavage Angles in MDS Neuroepithelium at 5 Weeks

NESCs undergo interkinetic nuclear migration (INM) coordinately with the cell cycle and expand through symmetrical divisions with vertically oriented cleavage planes (60°–90° relative to the ventricular surface) at the apical VZ surface (Götz and Huttner, 2005). These cell-intrinsic properties, including apical-basal polarity, dynamic behavior, and precise regulation of mitotic spindle orientation, are recapitulated in vitro in cortical organoids (Movie S1; Kadoshima et al., 2013). We consistently found that both WT and MDS SOX1 and SOX2 NESC nuclei were distributed throughout the apical-basal VZ axis in a pseudo-stratified fashion, with mitotic cells expressing phospho-Vimentin and phospho-Histone H3 (Figures 2A and 2B), located at the apical surface. Other apical determinants, including α protein kinase C (α PKC), N-Cadherin, and Pericentrin, which marks the centrosomes, were generally localized at the apical surface in both genotypes (Figures 2A–2C). Notably, we sometimes observed a less organized cellular structure and a discontinuous VZ surface in MDS organoids (Figure 2B, right).

LIS1 and ASPM (a microcephaly causative gene) were shown to regulate mitotic spindle orientation in the developing mouse

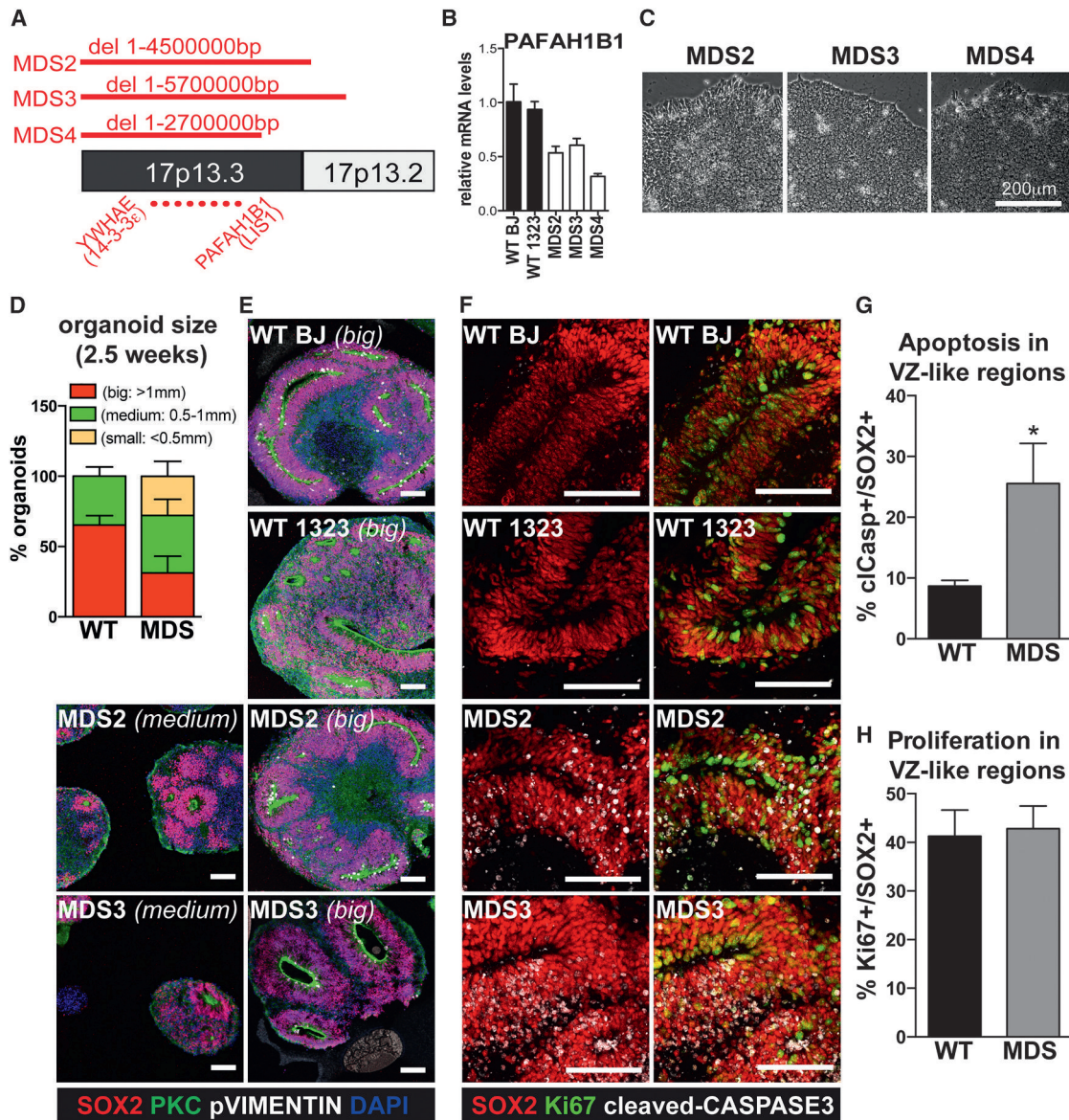


Figure 1. Apoptosis of NESCs in MDS Organoids

(A) Schematic and coordinates of the deletions (red lines) on chromosome 17 in MDS cells used in this study. The *YWHAE* and *PAFAH1B1* genes delineate the minimal critical deletion that causes MDS.

(B) Quantitative real-time PCR analysis of *PAFAH1B1* expression in the WT and MDS fibroblasts that were used to make iPSCs. Average values \pm SD for each individual are shown.

(C) Representative images of MDS iPSCs grown on Matrigel. Scale bar, 200 μ m.

(D) Analysis of organoid sizes at 2.5 weeks of differentiation, representing an average \pm SEM from WT ($n = 4$ independent iPSC clones) and MDS ($n = 6$ iPSC clones) (also see the table in STAR Methods).

(E) Representative images of organoid sections after 5 weeks of differentiation. Scale bar, 100 μ m.

(F) Representative images of organoid sections in 5-week organoids immunostained with the apoptotic marker cleaved CASPASE-3 (CASP3) and the proliferation marker Ki67. Scale bar, 100 μ m.

(G and H) Percent of SOX2⁺ cells in VZ-like regions expressing cleaved CASP3 (G) and Ki67 (H). Average values \pm SEM for WT ($n = 3$) and MDS ($n = 3$) are plotted (also see the table in STAR Methods). Statistical analysis was done using a *t* test ($p = 0.04$).

See also Figures S1 and S2 and Table S2.

forebrain, with loss of function leading to increased horizontal divisions associated with premature neurogenesis (Fish et al., 2006; Yingling et al., 2008; Pawlisch et al., 2008; Pramparo et al., 2010; Xie et al., 2013). To determine whether a similar

defect is present in human lissencephaly, we analyzed mitotic cells in VZ-like regions of week 5 cortical organoids using time-lapse imaging (Figure 2C) and immunostaining (Figure 2D). In WT organoids, the majority of cleavage planes in the VZ were

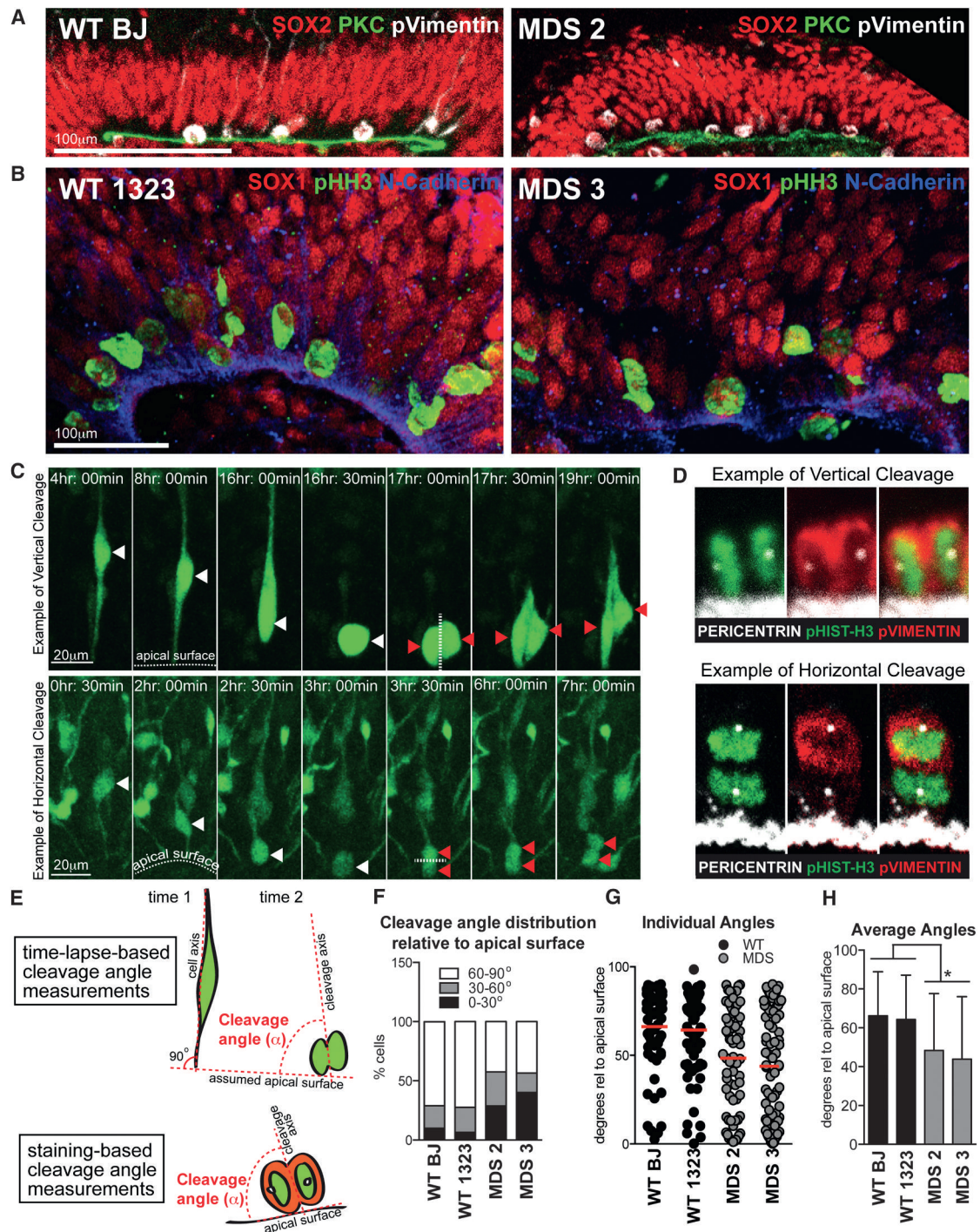


Figure 2. Increased Incidence of Horizontal Cleavage Angles in MDS VZ-like Regions at 5 Weeks

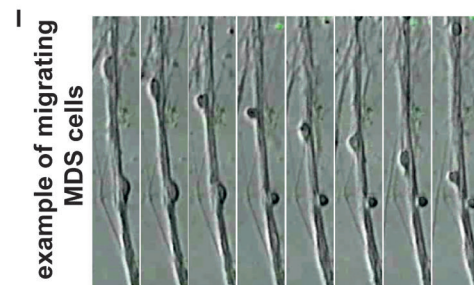
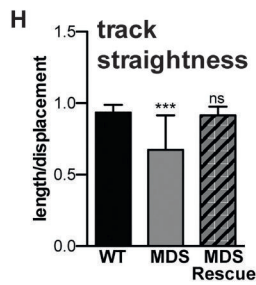
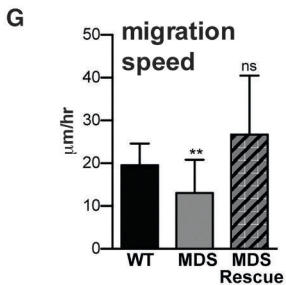
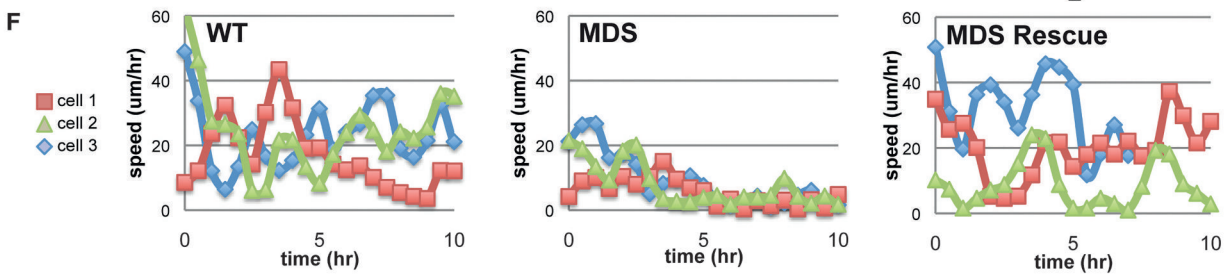
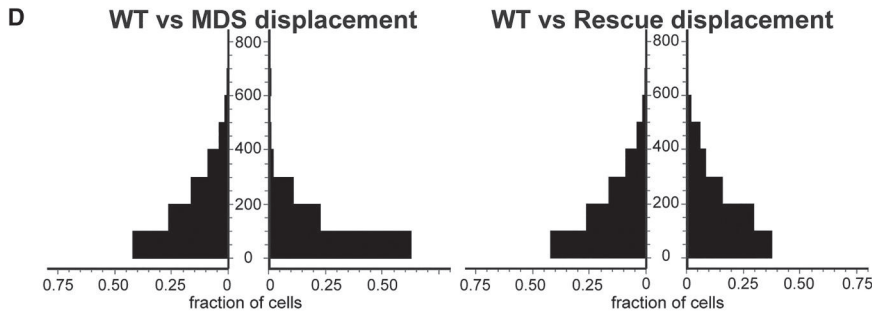
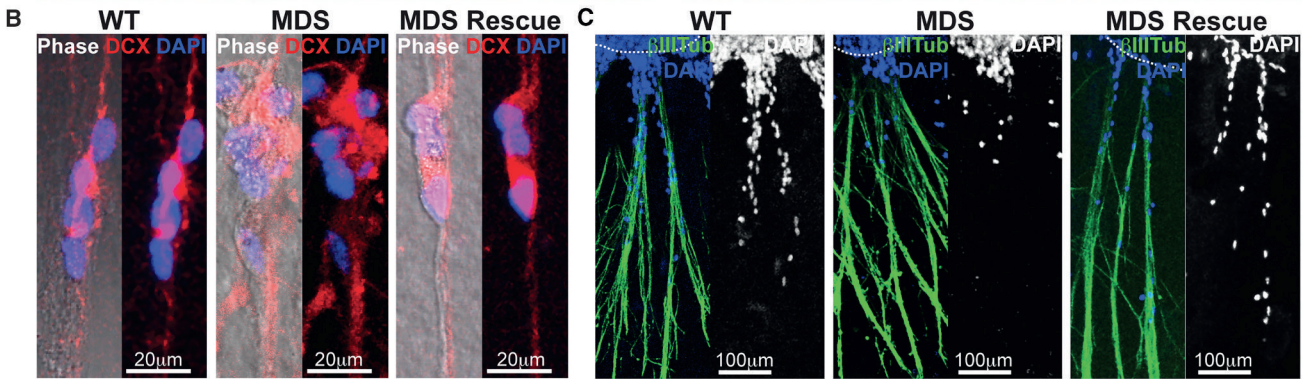
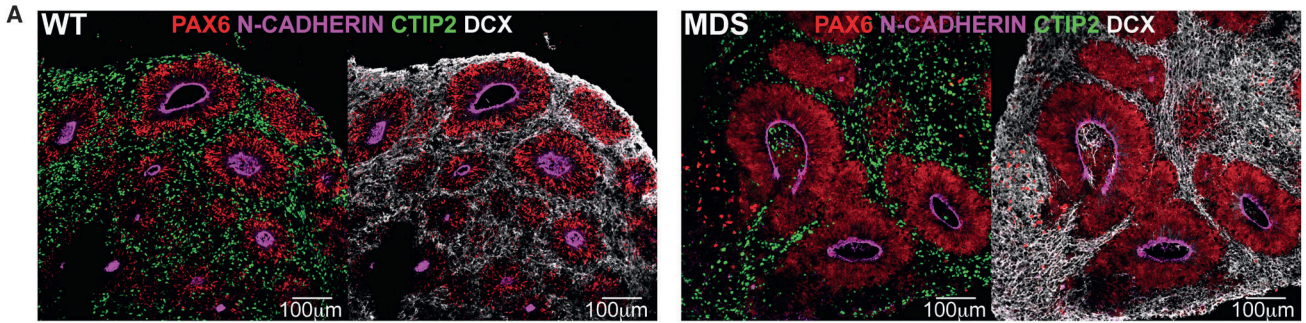
(A and B) Representative images of VZ-like regions in WT (left column) and MDS (right column). Scale bar, 100 μ m.

(C) Frames from time-lapse imaging showing examples of vertical (top) and horizontal (bottom) divisions. Scale bar, 20 μ m. White arrowheads mark the parent cell, and red arrowheads mark the progeny. The apical surface and the axis of the cleavage plane are demarcated with dotted white lines.

(D) Examples of vertical and horizontal divisions observed in VZ-like regions of fixed organoids. Anaphase mitoses were identified by chromosomal position and morphology; only anaphase cells were considered for analysis of the cleavage angle.

(E) Schematic of how cleavage angles were measured from time-lapse and immunostaining data.

(F–H) Quantification of cleavage angle data. Collectively, 70–92 dividing cells were analyzed from WT (n = 2) and MDS (n = 2) individuals. The red line in (G) represents the mean cleavage angle. Average cleavage angles \pm SD for each individual are shown (H). Statistical analysis was done using a t test ($p = 0.0158$). See also Movies S1 and S2 and Table S2.



(legend on next page)

perpendicular to the apical surface, with an average angle of $\sim 65^\circ$ (Figures 2E–2H). In contrast, dividing cells in the VZ regions of MDS organoids displayed more frequent horizontal cleavage planes and a significantly reduced average cleavage angle of $\sim 46^\circ$ (Figures 2E–2H; Movie S2). Collectively, our analyses suggest that expansion of the founder NESCs is greatly diminished in MDS because of increased apoptosis and decreased vertical divisions.

Defective Neuronal Migration in MDS Organoids at 5 Weeks

Defective radial migration of cortical neurons is a well-established developmental phenotype in lissencephaly (Hirotsune et al., 1998; Gambello et al., 2003; Youn et al., 2009; Toyo-oka et al., 2003; Sheen et al., 2006b; Saito et al., 2011). However, direct visualization and analysis of radial migration of human lissencephalic neurons have not been achieved. Thus, we sought to develop functional assays to analyze radial migration using the human organoid model system. Early-born subcortical projection neurons expressing CTIP2 and DCX were present by 5 weeks of differentiation (Figures S2 and 3A). Within a day of attachment to a Matrigel-coated surface, numerous processes began extending from the organoids. These processes were marked by expression of the neuronal proteins DCX and TUJ1 as well as the radial glia proteins BLBP and NESTIN (Figure S3), suggesting that they belong to bundles of neurites and radial glia fibers. The abundance and lengths of processes were comparable between WT and MDS organoids (Figure 3C; Figures S3A and S4D). Over the next 48 hr, DCX-positive neurons were observed migrating out of the organoids along these processes (Figures 3B and 3C; Figures S3 and S4D; Movie S3), akin to radial migration. We measured the displacement of neurons on fibers from the edge of the organoid 3 days after attachment to Matrigel. Migration of WT neurons was very robust, with more than 55% of migrating cells reaching 100–800 μm from the edge of the organoids (Figures 3C–3E; Figure S2A). In contrast, fewer MDS neurons migrated out of the organoids despite abundant processes, and the majority (65%) of migrating neurons were within 100 μm of the edge (Figures 3C–3E).

In addition to endpoint analyses, we tracked migrating neurons in real time using live imaging starting 1 day after organoid attachment for up to 48 hr. WT neurons migrated in a characteristic saltatory fashion (Figure 3F) with an average speed of 20 $\mu\text{m}/\text{hr}$ (Figure 3G; Movie S3), comparable with what has been recorded during radial neuronal migration in ferret cortical

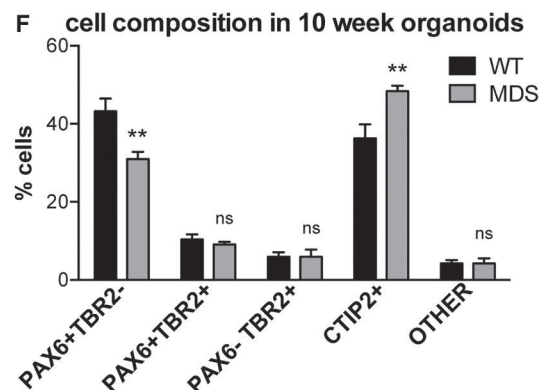
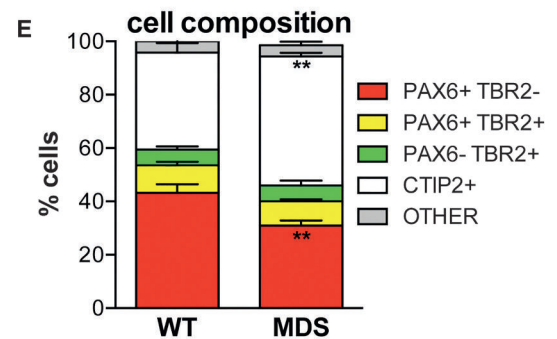
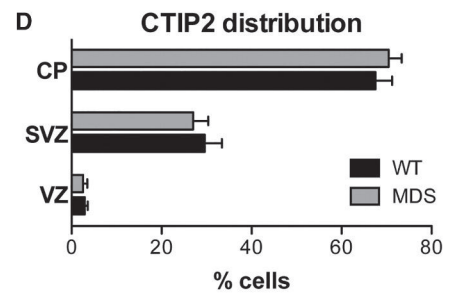
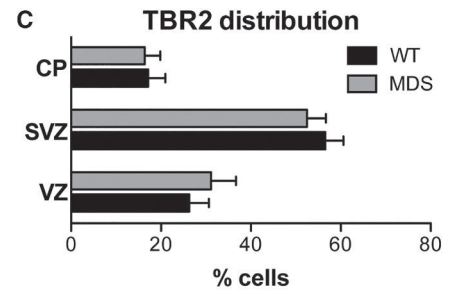
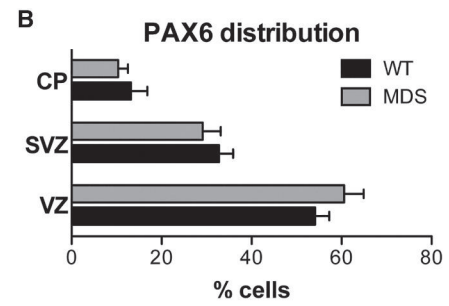
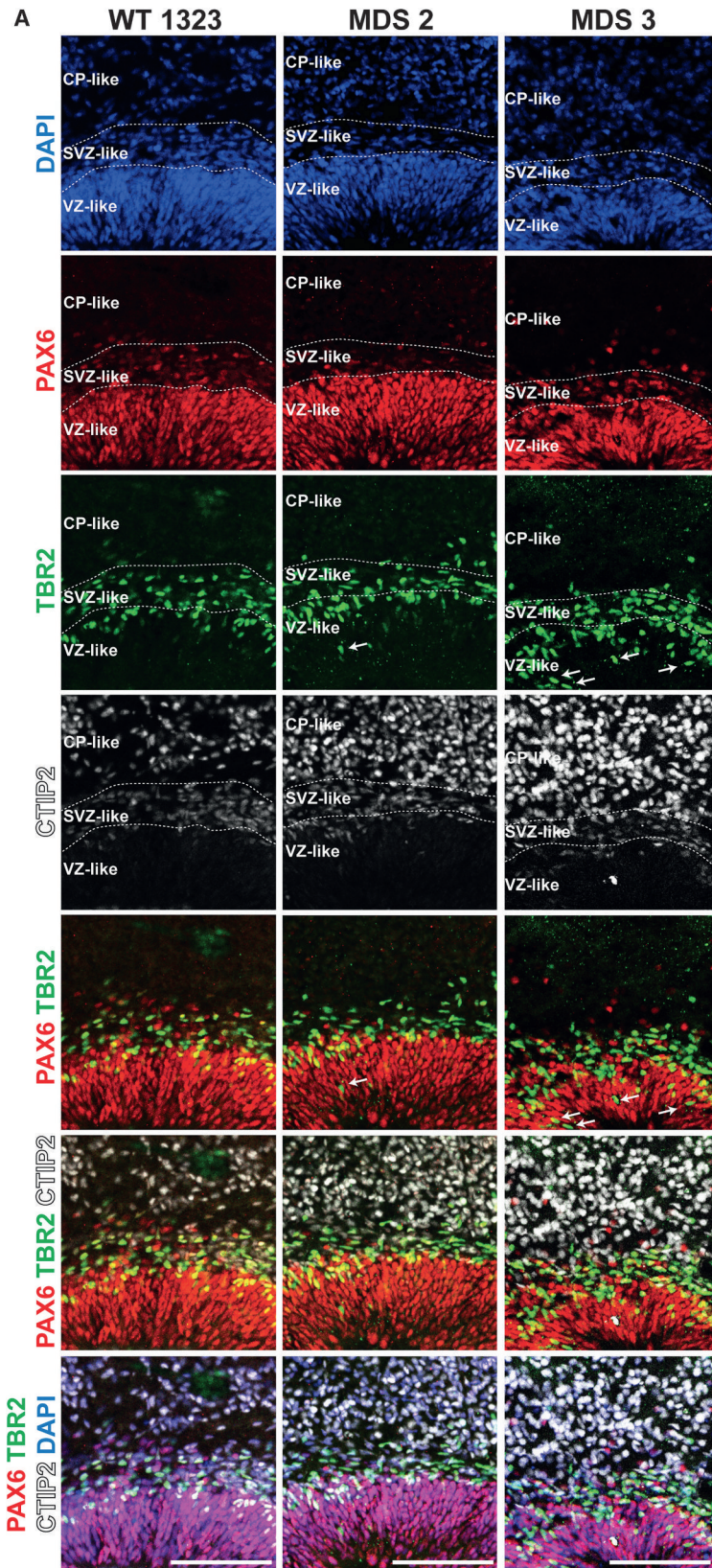
explants (Gertz and Kriegstein, 2015). In addition, WT neurons nearly always migrated away from the organoid along the processes. As a result, the calculated total length of the migratory track divided by the net displacement, or track straightness, was close to 1 for WT neurons (Figure 3H). In contrast, many of the MDS neurons initiated, but did not maintain, saltatory migration on processes, spending much of the time tumbling in place or not moving (Figures 3F and 3G; Movie S4), which significantly reduced the average migration speed (13 $\mu\text{m}/\text{hr}$, $p = 0.0004$) and track straightness (Figures 3G–3I). In addition, migrating MDS neurons had less elongated nuclei than WT neurons (Movie S4), consistent with reduced tension during nucleokinesis (Tanaka et al., 2004).

LIS1 and 14-3-3 ϵ proteins are part of a complex with cytoplasmic dynein that regulates neuronal migration (Toyo-oka et al., 2003). The corresponding genes, *PAFAH1B1* and *YWHAE*, are several megabases apart on locus 17p13.3 (Figure 1A) and would be challenging to rescue in MDS. However, we previously reported a reprogramming-induced rescue of an MDS case in which the 5.7-Mbp deletion affecting locus 17p13.3 was in a ring chromosome (Bershteyn et al., 2014). Upon reprogramming fibroblasts from this individual (MDS1), the ring was lost and replaced by a second copy of the wild-type chromosome 17 through compensatory uniparental isodisomy. As a consequence, the whole deletion was rescued in MDS1 iPSCs, and we showed that LIS1 and 14-3-3 ϵ proteins were restored to WT levels (Bershteyn et al., 2014). Remarkably, when we performed endpoint and live imaging-based migration assays with organoids from these iPSCs, we observed that MDS1 neurons were indistinguishable from the WT, completely rescuing neuronal displacement, migration speed, and track straightness (Figures 3C–3H; Movie S4).

Finally, to find out whether migration defects in MDS neurons are cell-autonomous, we developed a new assay using coculture of organoids with human cortical tissue explants. Specifically, week 5 organoids were infected with a non-replicating, adeno-associated virus expressing td-Tomato fluorescent protein under the control of the CAG promoter (AAV1-cag-Tomato), which preferentially labels neurons (Figures S4A–S4D). About 60% of cells labeled with this virus expressed the neuronal marker CTIP2, and about 25% of the labeled cells expressed the progenitor marker SOX1, in both WT and MDS organoids (Figures S4B and S4C). Separately, slices of human cortical tissue (GW18.5) were infected with a cytomegalovirus (CMV)-GFP adenovirus and then placed tightly against the organoids to allow

Figure 3. Defective Neuronal Migration in MDS Is Rescued by Compensatory Duplication of Wild-Type Chromosome 17

- (A) Representative images of WT and MDS cortical organoids after 5 weeks of differentiation. Scale bar, 100 μm .
 (B and C) Immunostaining of cells migrating on processes with DCX (B) and TUJ1 (C) 3 days after intact organoids were attached to Matrigel. Some of the processes seen in phase are not marked by DCX (B), suggesting that these may be radial glia fibers (see also Figure S3).
 (D) Quantification of cell displacement along the processes on day 3. Shown on the y axis is distance from the edge of the organoid (micrometers), and shown on the x axis is the fraction of total migrating cells at the corresponding distance bin from WT (left side) and MDS or MDS rescue (right side) organoids. Migration assays were performed with WT ($n = 3$), MDS ($n = 3$), and MDS rescue ($n = 1$) individuals. Data from the third MDS individual are not represented in this quantification because there were very few (almost no) migrating cells (data not shown).
 (E) Summary of cell distribution across 200- μm bins of displacement.
 (F) Representative tracks of speed over time for three different WT, MDS, and MDS rescue cells.
 (G and H) Migration speed (G) and track straightness (H). Average \pm SD is plotted.
 (I) Frames from time-lapse imaging of an MDS sample, showing two cells migrating on processes. The top cell exhibits a saltatory migration pattern of rounding up, followed by leading process extension, whereas the bottom cell rounds up but fails to continue migration.
 See also Figures S3 and S4, Movies S3 and S4, and Table S2.



(legend on next page)

attachment of the differentially labeled tissues. The human cortical tissue thus provided a physiological substrate for migration of iPSC-derived neurons (Figure S4E). After 4 days of co-culture, Tomato-expressing cells from the organoids were found throughout the cortical tissue explants, and their position relative to the ventricular and pial surfaces was quantified. Fifty percent of the WT iPSC-derived neurons that migrated had reached the pial surface after 4 days (Figure S4G). In contrast, only about 10% of the MDS iPSC-derived neurons that migrated had reached the pial surface on the cortical tissue explants (Figure S4G), suggesting that MDS migration defects are cell-autonomous. Collectively, we established two novel *in vitro* migration assays that are sensitive to defects associated with human lissencephaly and can be used *in vitro* to study multiple dynamic aspects of neuronal migration. Moreover, we demonstrated that this major developmental phenotype in MDS is functionally rescued through the duplication of the wild-type homolog of chromosome 17, confirming that the migration defects were due to the heterozygous deletion.

Normal Lamination with Increased Abundance of Deep-Layer Neurons in MDS Organoids at 10 Weeks

Although the long-term consequence of increased horizontal divisions is expected to be a reduction in total neuronal output through depletion of the progenitor pool (Pawlisz et al., 2008), the short-term consequence might be the opposite; i.e., overproduction of neurons. To examine this, we analyzed the distribution of progenitor cells and neurons in 10-week cortical organoids. At this time point, staining with the RG marker PAX6, the IP cell marker TBR2/EOMES (eomesodermin) (Hevner et al., 2006), and the deep-layer cortical neuron marker CTIP2 revealed three distinct regions resembling the developing VZ, SVZ, and cortical plate (CP). The boundaries between these regions could be consistently demarcated in WT and MDS organoids based on cell density, cell orientation, and expression of the three transcription factors. Thus, the VZ was defined based on dense vertical columns of PAX6-positive RG cells (Figure 4A). The SVZ was defined based on less dense, horizontally oriented cells, many of which expressed TBR2 (Figure 4A). Immediately superficial to the TBR2 boundary was the rudimentary CP, with strong expression of CTIP2 (Figure 4A). These well-organized structures were found close to the surface in every cortical organoid (typically one to five per organoid), with neurons always found on the outside, superficial to the progenitors.

We analyzed the distribution of the PAX6-, TBR2-, and CTIP2-expressing cell populations in at least 12 organoids from WT ($n = 3$) and MDS ($n = 2$) individuals generated in multiple independent differentiations. The distribution of PAX6, TBR2, and CTIP2

was not significantly different between the two genotypes, with the majority of PAX6⁺ cells (~60%) found in the VZ, the majority of TBR2⁺ cells (~55%) in the SVZ, and the majority of CTIP2⁺ cells (~70%) in the CP, as expected (Figures 4B–4D), indicating that the general laminar distribution of cell types is preserved. However, in MDS organoids, particularly in the more severe MDS3 case, there was a notable increase in the abundance of IP cells located in the apical portions of the VZ (arrows in Figure 4A). In addition, analysis of relative cell proportions in the organized cortical regions revealed a slight but significant decrease in PAX6⁺/TBR2⁻ RG cells with a complementary increase in CTIP2⁺ neurons in MDS (Figures 4A, 4E, and 4F). These findings are consistent with the increase in horizontal divisions we observed at earlier time points in MDS organoids and indicate an overproduction of deep-layer neurons. Moreover, these data indicate that migration defects are not likely to be a secondary consequence of neuronal deficiency because no such deficiency was observed up to this point.

Histological and Molecular Evidence of oRG-like Cell Production in WT and MDS Organoids after 10 Weeks

By 10 weeks, close to 30% of PAX6-positive cells within organized structures were located in the SVZ-like regions (Figures 4A and 4B) and expressed other canonical radial glia genes such as SOX2 and SOX1 (Figure 5A and data not shown). We sought to determine whether some of these cells might be oRGs. In contrast to the ventricular or apical radial glia (vRG/aRG), which extend bipolar processes and attach to the ventricular surface (Florio and Huttner, 2014), oRG cells reside in the SVZ and are typically unipolar, extending a single basal process toward the pial surface (Hansen et al., 2010; Fietz et al., 2010). After 10–15 weeks of culture, the outer edge of the organoids contained many radially oriented cells with unipolar processes pointing away from the center of the organoids (white arrows in Figures 5B; Figure S5A). Many of these unipolar cells expressed the radial glia marker SOX2 (Figure 5C; Figure S5A), consistent with oRG identity. Within the same regions, IP-like cells with characteristic multipolar morphologies and expression of TBR2/EOMES could be clearly distinguished from oRG-like cells (blue arrow in Figure S5A).

A recent study used transcriptome-wide profiling of single cells to show that stem cell-derived cerebral organoids can recapitulate many of the molecular pathways that control normal human cortical neurogenesis (Camp et al., 2015). We reasoned that a subset of radial glia derived *in vitro* may adopt the molecular profile of oRG cells. Therefore, we analyzed single-cell gene expression from WT and MDS organoids after 5, 10, and 15 weeks of differentiation. We identified a group of 95 cortical

Figure 4. Increased Abundance of CTIP2-Positive Neurons in MDS Organoids at 10 Weeks

(A) Representative images of WT (1323), MDS2, and MDS3 cortical organoids. Scale bar, 100 μ m. The inferred VZ-, SVZ-, and CP-like regions are delineated based on the combination of DAPI, PAX6, TBR2, and CTIP2 staining patterns. White arrows in the MDS TBR2 and PAX6/TBR2 panels point to IP cells located in the apical portions of the VZ.

(B–F) Analysis of marker distribution across the VZ/SVZ/CP (B–D) and cell composition (E and F) within the organized regions in WT (12 total organoids from 3 individuals, 4 iPSC clones) and MDS (13 organoids from 2 individuals, 3 iPSC clones) organoids. The average value \pm SEM is plotted after collapsing technical replicates from each clone (WT, $n = 4$; MDS, $n = 3$). Two-way ANOVA followed by Bonferroni's adjustment for multiple comparisons was performed to determine statistical significance. For cell distribution (B and C), the only significant source of variation was region. For cell composition, there was a significant difference between WT and MDS in the proportion of PAX6⁺TBR2⁻ cells and CTIP2⁺ cells.

See also Table S2.

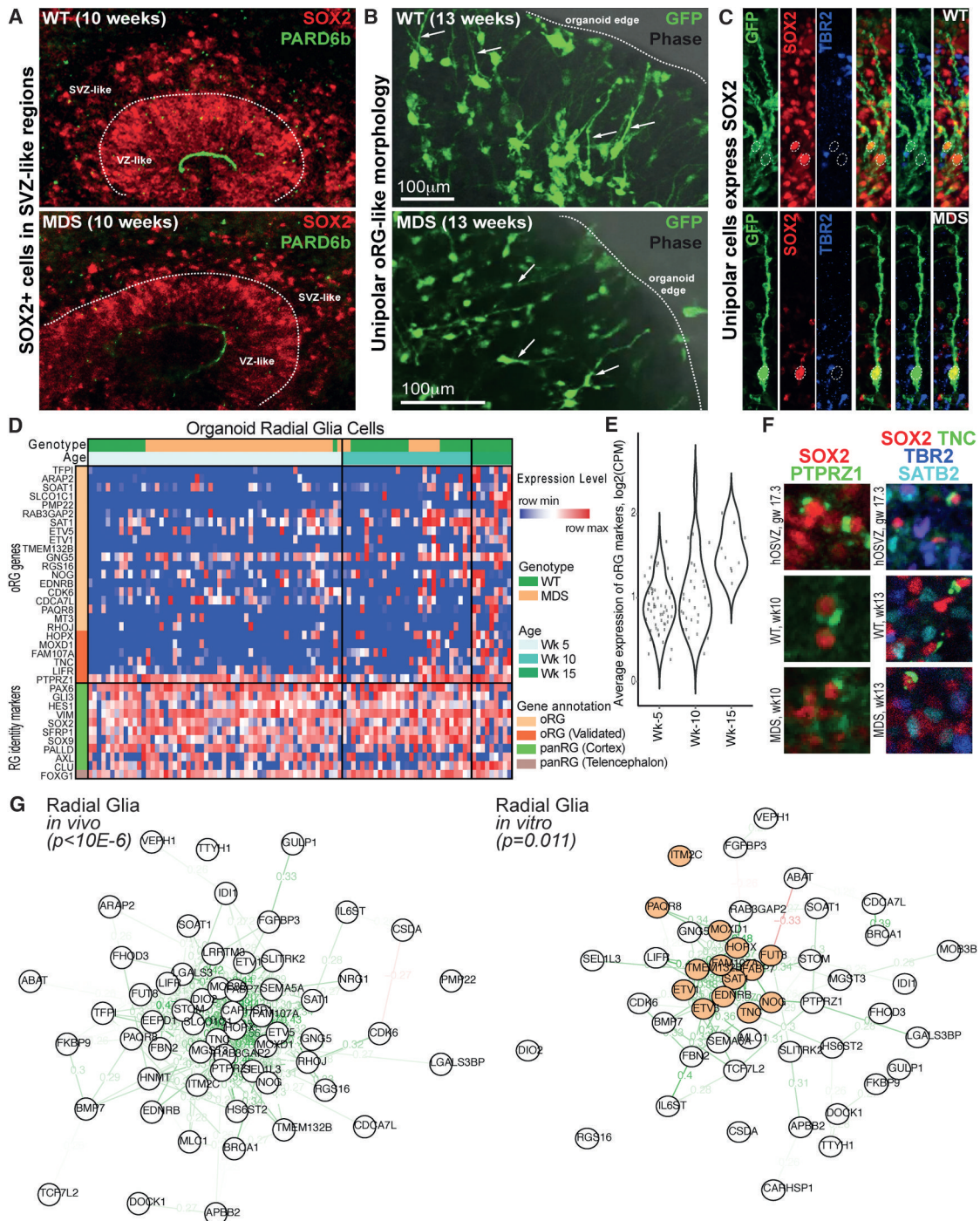


Figure 5. Production of oRG Cells in Organoids after 10 Weeks

(A) Representative images of WT and MDS progenitor zones in 10-week organoids.

(B) GFP labeling with adenovirus reveals unipolar morphology and radial orientation of cells close to the edge of the organoids. Scale bar, 100 μ m.

(C) Immunostaining confirms radial glia fate of unipolar cells that express SOX2 and not the IP cell marker TBR2.

(D) Heatmap showing relative gene expression levels across 95 single radial glia cells captured from cerebral organoid samples ($n = 5$ individuals from both WT and MDS). Genes represent canonical markers of radial glia (green bar) and forebrain identity (brown bar) as well as genes correlated with oRG identity (light and dark orange; the dark shade highlights genes validated *in vivo*) (Pollen et al., 2015). The expression of oRG-correlated genes increases with age of the organoid (also see Figure S5).

(E) Violin plots representing distribution of the average expression of oRG marker genes across single cells captured from cerebral organoids at each stage of differentiation.

(legend continued on next page)

radial glia-like cells (Figure 5D) out of all the in vitro-derived cells (Figure S6A; see STAR Methods for clustering methods). Among these radial glia-like cells, we found that the oRG gene expression signature (Pollen et al., 2015) emerged at week 10 and became stronger at week 15 (Figure 5E; Figures S6B and S6C), consistent with observations from histology. We confirmed the expression of a few oRG markers in a subset of organoid radial glia that showed consistent subcellular localization to human tissue (Figure 5F). In addition, the expression of many of the predicted and validated oRG markers is well correlated across radial glia-like cells from organoids, indicating that these genes are also co-expressed in the in vitro system (Figure 5G). Together, these data establish the presence of oRG-like cells that share features of tissue-level distribution, morphology, and molecular identity with oRG cells found in the developing human cortex.

oRG Cell-Specific Cytokinesis Delay in Human Lissencephaly

The ability to recapitulate human oRG production and 3D organization in vitro enabled us to analyze the effect of lissencephaly mutations on this class of progenitors. Toward that end, we performed time-lapse imaging following infection of 10-week organoids with CMV-GFP adenovirus, which labels all dividing progenitors including vRG, IP, and oRG cells. The morphology, spatial organization, and mitotic behavior of GFP-labeled progenitors were consistent with properties observed in vivo. IP-like cells had a larger cell body with multiple short processes (blue arrows in Figure 6A and Figure S5A), and they divided in place without much movement (Figure S5B). vRG cells were typically bipolar, with apical processes coalescing at a common VZ-like surface, and their nuclei underwent apically oriented INM prior to division at the apical surface (arrowheads in Figures 6A, 1 and 2, and 6D). In contrast, oRG cells had a single long basal process and a very short apical process, were located above the ventricular-like zone (stars in Figure 6A, 1, and Figure S5C), and underwent a rapid mitotic somal translocation (MST) in the direction of the basal process prior to division (Figure 6G; Movie S5).

To examine whether MDS mutations affect the behavior of vRG and oRG cells, we measured multiple dynamic properties. For both vRG and oRG cells, we measured the *time* from when the dividing cell was rounded up to when the two daughters first appeared and the *angle* of the cleavage plane relative to the basal fiber (Figures 6B and 6C). In addition, we measured MST *distance* for oRG cells (Figure 6C). We found that WT oRG and vRG cells divided within 50 min from the time that the cell rounded up (Figures 6D, 6F, 6G, and 6J; Movie S5). Surprisingly, MDS oRG cells tended to translocate farther during MST (Figure 6K) but then remained in mitosis for prolonged periods (up to several hours) prior to cytokinesis (Figures 6H and 6J; Figure S5C; Movie S5). The delay in cell division appeared to be

specific to MDS oRG cells because a similar defect was not observed in vRG or IP cell divisions from the same imaging sessions (Figures 6E and 6F; Figure S5B). Of note, this behavior mimicked a phenotype previously observed in primary oRG cells treated with a microtubule-depolymerizing agent, nocodazole (Ostrem et al., 2014). We also compared the division cleavage angle relative to the basal process in dividing vRG and oRG cells between WT and MDS groups using live imaging. This analysis confirmed in vivo observations that vRG divisions become less tightly controlled with developmental maturation and that the majority of oRG divisions occur perpendicular to the basal process (Figures 6L and 6M; LaMonica et al., 2013). There were no significant differences between the two genotypes in terms of division cleavage angles (Figures 6K and 6L). Collectively, our findings implicate MDS-deleted genes in the regulation of oRG cell division and point to a possible involvement of oRG cells in the pathogenesis of human lissencephaly.

DISCUSSION

By implementing a patient iPSC-derived 3D model of early corticogenesis, we were able to delineate cell type- and cell stage-specific defects in human lissencephaly caused by deletions of the distal tip of chromosome 17. Ultimately, these defects need to be linked with the corresponding genetic regulators for a deeper understanding of lissencephaly pathogenesis and human cortical development. Although *Pafah1b1* (LIS1) and *YWHAE* (14-3-3 ϵ) mutations have been modeled in the rodent (Hirotsune et al., 1998; Toyo-oka et al., 2003; Gambello et al., 2003; Youn et al., 2009), there has been a lack of laboratory models that recapitulate the complete genetic defects of MDS. Thus, the roles of most of the deleted genes in brain development or MDS pathogenesis have not been examined. Here we provide a platform and establish functional assays that will enable validation of additional gene candidates in distinct cell types and cellular processes and will lead to identification of novel regulators of cortical development and malformation.

Several of the conserved developmental phenotypes implicated in lissencephaly by mouse models, including dysregulation of the NESc mitotic spindle (Faulkner et al., 2000; Yingling et al., 2008; Pawlisz et al., 2008; Pramparo et al., 2010; Xie et al., 2013; Moon et al., 2014) and neuronal migration defects (Hirotsune et al., 1998; Gambello et al., 2003; Youn et al., 2009; Toyo-oka et al., 2003) are recapitulated here. Deficiencies in neural progenitor cell viability in human MDS were previously implicated by Sheen et al. (2006a) based on the analysis of post-mortem samples but without distinguishing which progenitor subclasses were affected. Here, by following in vitro differentiation from patient-derived iPSCs, we were able to recapitulate developmental lineage progression from NESc to vRG to IP and oRG with spatial and temporal resolution that could not have been achieved with previous methods. Our analyses

(F) Validation of oRG marker (PTPRZ1 and tenascin C [TNC]) co-expression with the radial glia marker SOX2 in 10-week organoids. Note the similarity in the staining pattern between human OSVZ (GW17.3) and iPSC-derived organoids.

(G) Network maps representing Pearson's correlation between oRG marker genes across single cells in primary human brain tissue (Pollen et al., 2015) (left) and across cells captured from cerebral organoids (right). Correlations greater than 0.25 are highlighted with a pale green line, and correlations greater than 0.5 are highlighted with a dark green line. Genes that are most highly correlated across in vitro cells out of the oRG marker genes are highlighted in orange.

See also Figures S5 and S6, Tables S1 and S2, and dbGaP: phs000989.v3.p1.

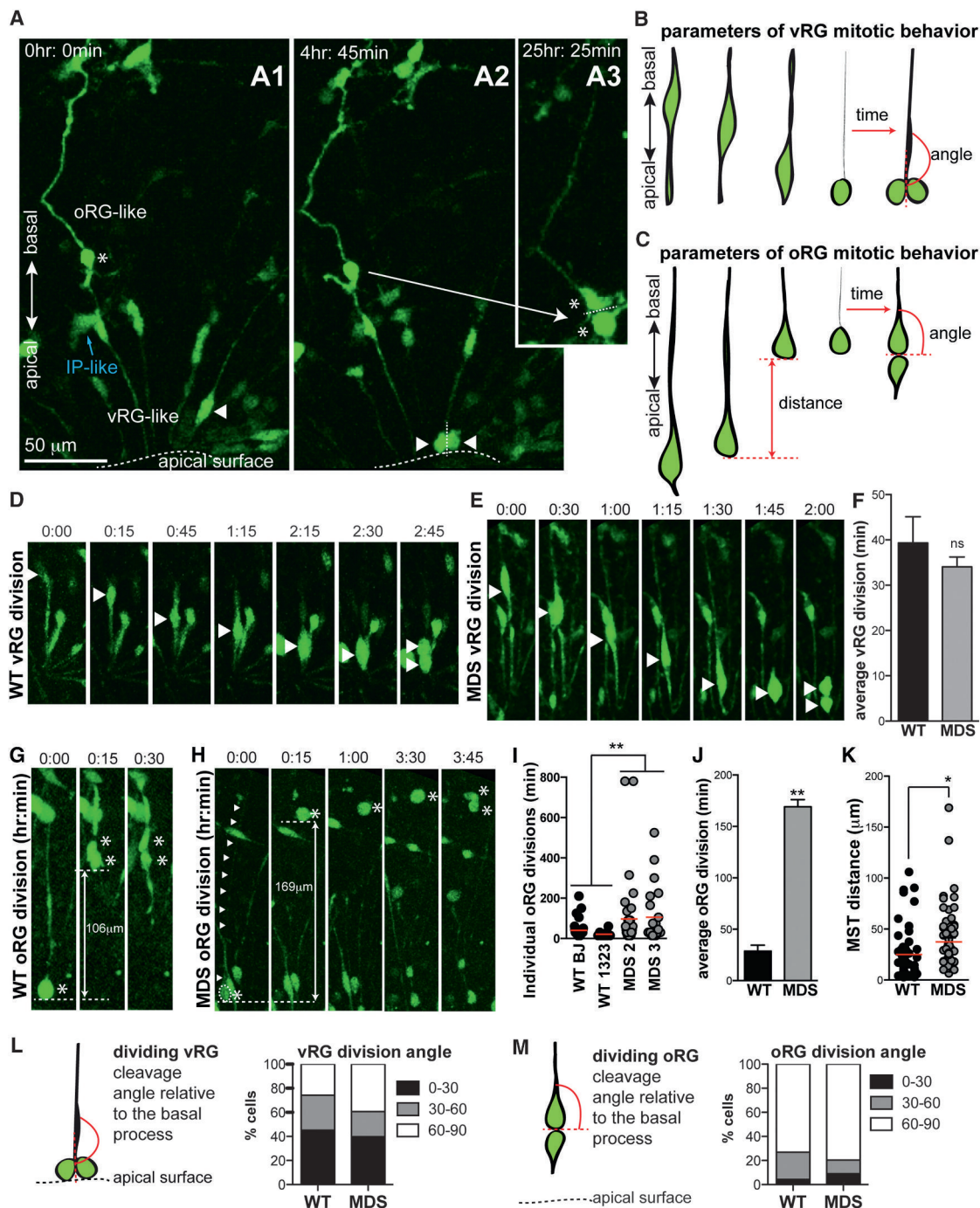


Figure 6. Prolonged Mitosis in MDS oRG, but Not vRG, Cells at 10 Weeks

(A) Frames from time-lapse imaging showing representative examples of distinct vRG and oRG cell morphology, orientation, and dividing properties in the same imaging field. The oRG-like cell is marked with a white star. Note the long basal process and its superficial location relative to the bipolar vRG-like cells (example: white arrowhead). The indicated bipolar vRG-like cell from A1 moves apically and divides in A2 with a cleavage angle parallel to its basal process. In contrast, the indicated oRG-like cell undergoes an MST in the basal direction (data not shown) and divides in A3 with a cleavage angle perpendicular to its basal process. Scale bar, 50 μ m.

(B) Schematic of parameters used to analyze vRG mitotic behavior: time from cell rounding to the first appearance of two daughters and angle of cleavage relative to the cell body axis just prior to basal process retraction.

(C) Schematic of parameters used to analyze oRG mitotic behavior: MST distance, time from cell rounding to the first appearance of two daughters, and angle of cleavage relative to the basal process.

(D and E) Frames from time-lapse imaging showing representative examples of WT (D) and MDS (E) vRG-like divisions.

(F) Quantification of vRG divisions.

(legend continued on next page)

suggest that founder NESCs and oRG cells are particularly vulnerable in MDS, whereas vRG and IP cells seem to be less affected.

Outer RG progenitors are thought to support the developmental and evolutionary expansion of the human neocortex because of their tremendous proliferative potential (Lukaszewicz et al., 2005; Hansen et al., 2010; Fietz et al., 2010; Pollen et al., 2015). In addition, oRG cells have been proposed to promote cortical folding by producing large numbers of neurons and by providing divergent tracks for increased tangential dispersion of migrating neurons along their basal fibers (Lui et al., 2011; Fietz and Huttner, 2011; Hevner and Haydar, 2012; Florio and Huttner, 2014; Taverna et al., 2014; Borrell and Götz, 2014; Nowakowski et al., 2016a). Our studies identified specific mitotic defects in oRG cells from a severe form of lissencephaly, providing another link between this cell type and human neocortical gyration.

Prolonged mitosis of mouse cortical radial glia in a *Magoh*^{+/-} model of microcephaly was recently shown to induce preferential production of neurons rather than progenitors as well as increased incidence of apoptotic progeny (Pilaz et al., 2016). Mitotic delay through pharmacological means also altered cell fate, producing more apoptotic progeny or leading to ectopic neuronal differentiation. Similarly to Pilaz et al. (2016), we observed examples of apoptotic oRG-like cells (data not shown); however, the technical challenges of prolonged time-lapse imaging of organoid slices precluded us from direct visualization of progeny fate. Interestingly, *Magoh* functions upstream of *Pafah1b1*, with loss of function leading to decreased LIS1 protein levels during neurogenesis (Silver et al., 2010). This connection suggests a possible mechanistic basis for the convergence of microcephaly and lissencephaly phenotypes in MDS.

The genetic factors that regulate oRG behavior have been difficult to study because of the scarcity of these cells in mice. Here we find that cerebral organoids generate oRG-like cells with matching properties defined in vivo, including position, morphology, mitotic behavior, and molecular identity. In addition, we show that the DNA sequence in the MDS deletion interval is necessary for normal MST behavior. MDS oRG cells exhibited increased MST distance, similar to the effect of nocodazole (Ostrem et al., 2014), which interferes with microtubule cytoskeleton polymerization. Among the deleted genes, *PAFAH1B1* is known to control microtubule dynamics during mitosis (Yingling et al., 2008; Moon et al., 2014), pointing to a possible oRG-specific regulatory mechanism that may be LIS1-dependent. However, LIS1 haploinsufficiency alone cannot account for the severity of MDS because mutations or smaller deletions affecting only *Pafah1b1* have less severe outcomes and are not associated with human microcephaly (Ledbetter et al., 1992; Lo Nigro et al., 1997; Pilz et al., 1998; Barkovich et al., 1991; Cardoso et al., 2003). Therefore, additional genes in the MDS-deleted locus are likely involved in

the regulation of oRG cell division. Future studies can examine the role of specific candidate genes in this interval using the organoid model system, which recapitulates key features of oRG biology.

Finally, the involvement of oRG cells in the pathophysiology of MDS suggests a link between this radial glial subtype and the development of lissencephaly. In addition to genetic causes, cortical abnormalities, including lissencephaly and microcephaly, may also result from infectious diseases, including cytomegalovirus (CMV) and West Nile virus (Lanari et al., 2012; Teissier et al., 2014; O'Leary et al., 2006). Recently, Zika virus has been declared a public health emergency of international concern (Heymann et al., 2016) because of a strong correlation with increased incidence of microcephaly, which has been reported to involve lissencephaly (Oliveira Melo et al., 2016; Schuler-Faccini et al., 2016; Mlakar et al., 2016). These infectious diseases may preferentially affect the same cell types and developmental process that are vulnerable in genetic forms of microcephaly and lissencephaly. The Zika virus can infect human cortical neural progenitors, leading to cell death and cell cycle dysregulation (Tang et al., 2016; Qian et al., 2016) and has been shown to infect human skin cells through the phosphatidyserine receptor AXL (Hamel et al., 2015). We have found that radial glia cells show very high expression of the candidate Zika virus entry factor AXL (Nowakowski et al., 2016b), and the current study highlights how stalled mitosis of oRG cells may relate to lissencephaly. Collectively, these observations support the hypothesis that oRG dysfunction may be a feature of cortical malformations associated with lissencephaly.

STAR★METHODS

Detailed methods are provided in the online version of this paper and include the following:

- KEY RESOURCES TABLE
- CONTACT FOR REAGENT AND RESOURCE SHARING
- EXPERIMENTAL MODEL AND SUBJECT DETAILS
 - hiPSC derivation and culture methods
- METHOD DETAILS
 - Cerebral organoid generation and culture
 - Quantitative PCR (qPCR)
 - Organoid slice culture, viral infection and time-lapse imaging
 - Neuronal migration assays
 - Immunocytochemistry
 - Single Cell RNA-Sequencing
 - Outlier removal and enrichment for cortical lineage cells
 - Identification of radial glia-like cells and analysis of heterogeneity

(G and H) Frames from time-lapse imaging showing representative examples of WT (G) and MDS (H) oRG-like divisions.

(I and J) Quantification of oRG division time showing individual events (I) and average values for each genotype (J) ($p = 0.0028$).

(K) Quantification of oRG MST distance ($p = 0.05$).

(L and M) Schematic and quantification of vRG (L) and oRG (M) cleavage angle relative to the basal process.

Average values \pm SEM are plotted in (F) and (J). Statistical analysis was done using a t test (WT, $n = 3$; MDS, $n = 2$). For all phenotypes, 20–50 cells were analyzed from each individual. See also Figure S5, Movie S5, and Table S2.

- QUANTIFICATION AND STATISTICAL ANALYSIS
- DATA AND SOFTWARE AVAILABILITY
 - Data Resources

SUPPLEMENTAL INFORMATION

Supplemental Information includes six figures, two tables, and five movies and can be found with this article online at <http://dx.doi.org/10.1016/j.stem.2016.12.007>.

AUTHOR CONTRIBUTIONS

M.B. conceived the project with guidance from A.W.B. and A.R.K. All experiments were designed and performed by M.B. with help from E.D.L. and A.N. Single-cell capture was performed by M.B. and T.J.N. RNA sequencing data analysis was performed by T.J.N. and A.A.P. M.B. prepared the figures and wrote the manuscript with input from all authors.

ACKNOWLEDGMENTS

The authors are grateful to Joseph Loturco, Catherine Priest, Haim Belinson, Carmen Sandoval Espinosa, and members of the A.R.K. and A.W.B. labs for helpful feedback on the manuscript. We thank Melanie Bedolli, Lillian Adame, and Yingying Wang for technical support. M.B. was supported by a postdoctoral fellowship from the California Institute for Regenerative Medicine, CIRM (Grant TG2-01153), and a K99 career development award from the National Institute for Neurological Disorders and Stroke (Grant 5K99NS088572). This research was funded by NIH Grants NS075998 and MH105989 and CIRM Award GCIR-06673 (to A.R.K.).

Received: July 8, 2016

Revised: October 16, 2016

Accepted: December 16, 2016

Published: January 19, 2017

REFERENCES

- Armstrong, E., Schleicher, A., Omran, H., Curtis, M., and Zilles, K. (1995). The ontogeny of human gyrification. *Cereb. Cortex* **5**, 56–63.
- Barkovich, A.J., Koch, T.K., and Carrol, C.L. (1991). The spectrum of lissencephaly: report of ten patients analyzed by magnetic resonance imaging. *Ann. Neurol.* **30**, 139–146.
- Bershteyn, M., Hayashi, Y., Desachy, G., Hsiao, E.C., Sami, S., Tsang, K.M., Weiss, L.A., Kriegstein, A.R., Yamanaka, S., and Wynshaw-Boris, A. (2014). Cell-autonomous correction of ring chromosomes in human induced pluripotent stem cells. *Nature* **507**, 99–103.
- Betizeau, M., Cortay, V., Patti, D., Pfister, S., Gautier, E., Bellemin-Ménard, A., Afanassieff, M., Huissoud, C., Douglas, R.J., Kennedy, H., and Dehay, C. (2013). Precursor diversity and complexity of lineage relationships in the outer subventricular zone of the primate. *Neuron* **80**, 442–457.
- Borrell, V., and Götz, M. (2014). Role of radial glial cells in cerebral cortex folding. *Curr. Opin. Neurobiol.* **27**, 39–46.
- Camp, J.G., Badsha, F., Florio, M., Kanton, S., Gerber, T., Wilsch-Bräuninger, M., Lewitus, E., Sykes, A., Hevers, W., Lancaster, M., et al. (2015). Human cerebral organoids recapitulate gene expression programs of fetal neocortex development. *Proc. Natl. Acad. Sci. USA* **112**, 15672–15677.
- Cardoso, C., Leventer, R.J., Ward, H.L., Toyo-Oka, K., Chung, J., Gross, A., Martin, C.L., Allanson, J., Pilz, D.T., Olney, A.H., et al. (2003). Refinement of a 400-kb critical region allows genotypic differentiation between isolated lissencephaly, Miller-Dieker syndrome, and other phenotypes secondary to deletions of 17p13.3. *Am. J. Hum. Genet.* **72**, 918–930.
- Chi, J.G., Dooling, E.C., and Gilles, F.H. (1977). Gyral development of the human brain. *Ann. Neurol.* **1**, 86–93.
- Chong, S.S., Pack, S.D., Roschke, A.V., Tanigami, A., Carrozzo, R., Smith, A.C.M., Dobyns, W.B., and Ledbetter, D.H. (1997). A revision of the lissencephaly and Miller-Dieker syndrome critical regions in chromosome 17p13.3. *Hum. Mol. Genet.* **6**, 147–155.
- Dobyns, W.B., Stratton, R.F., Parke, J.T., Greenberg, F., Nussbaum, R.L., and Ledbetter, D.H. (1983). Miller-Dieker syndrome: Lissencephaly and monosomy 17p. *J. Pedod.* **102**, 552–558.
- Dobyns, W.B., Curry, C.J.R., Hoyme, H.E., Turlington, L., and Ledbetter, D.H. (1991). Clinical and molecular diagnosis of Miller-Dieker syndrome. *Am. J. Hum. Genet.* **48**, 584–594.
- Eiraku, M., Watanabe, K., Matsuo-Takasaki, M., Kawada, M., Yonemura, S., Matsumura, M., Wataya, T., Nishiyama, A., Muguruma, K., and Sasai, Y. (2008). Self-organized formation of polarized cortical tissues from ESCs and its active manipulation by extrinsic signals. *Cell Stem Cell* **3**, 519–532.
- Faulkner, N.E., Dujardin, D.L., Tai, C.Y., Vaughan, K.T., O'Connell, C.B., Wang, Y., and Vallee, R.B. (2000). A role for the lissencephaly gene LIS1 in mitosis and cytoplasmic dynein function. *Nat. Cell Biol.* **2**, 784–791.
- Fietz, S.A., and Huttner, W.B. (2011). Cortical progenitor expansion, self-renewal and neurogenesis—a polarized perspective. *Curr. Opin. Neurobiol.* **21**, 23–35.
- Fietz, S.A., Kelava, I., Vogt, J., Wilsch-Bräuninger, M., Stenzel, D., Fish, J.L., Corbeil, D., Riehn, A., Distler, W., Nitsch, R., and Huttner, W.B. (2010). OSVZ progenitors of human and ferret neocortex are epithelial-like and expand by integrin signaling. *Nat. Neurosci.* **13**, 690–699.
- Fish, J.L., Kosodo, Y., Enard, W., Pääbo, S., and Huttner, W.B. (2006). Aspm specifically maintains symmetric proliferative divisions of neuroepithelial cells. *Proc. Natl. Acad. Sci. USA* **103**, 10438–10443.
- Florio, M., and Huttner, W.B. (2014). Neural progenitors, neurogenesis and the evolution of the neocortex. *Development* **141**, 2182–2194.
- Gambello, M.J., Darling, D.L., Yingling, J., Tanaka, T., Gleeson, J.G., and Wynshaw-Boris, A. (2003). Multiple dose-dependent effects of Lis1 on cerebral cortical development. *J. Neurosci.* **23**, 1719–1729.
- Gaspard, N., Bouschet, T., Hourez, R., Dimidschstein, J., Naeije, G., van den Aemele, J., Espuny-Camacho, I., Herpoel, A., Passante, L., Schiffmann, S.N., et al. (2008). An intrinsic mechanism of corticogenesis from embryonic stem cells. *Nature* **455**, 351–357.
- Georgala, P.A., Carr, C.B., and Price, D.J. (2011). The role of Pax6 in forebrain development. *Dev. Neurobiol.* **71**, 690–709.
- Gertz, C.C., and Kriegstein, A.R. (2015). Neuronal Migration Dynamics in the Developing Ferret Cortex. *J. Neurosci.* **35**, 14307–14315.
- Götz, M., and Huttner, W.B. (2005). The cell biology of neurogenesis. *Nat. Rev. Mol. Cell Biol.* **6**, 777–788.
- Guerrini, R., and Dobyns, W.B. (2014). Malformations of cortical development: clinical features and genetic causes. *Lancet Neurol.* **13**, 710–726.
- Hamel, R., Dejamac, O., Wichit, S., Ekchariyawat, P., Neyret, A., Luplertlop, N., Perera-Lecoin, M., Surasombatpattana, P., Talignani, L., Thomas, F., et al. (2015). Biology of Zika Virus Infection in Human Skin Cells. *J. Virol.* **89**, 8880–8896.
- Hansen, P.E., Ballesteros, M.C., Soila, K., Garcia, L., and Howard, J.M. (1993). MR imaging of the developing human brain. Part 1. Prenatal development. *Radiographics* **13**, 21–36.
- Hansen, D.V., Lui, J.H., Parker, P.R., and Kriegstein, A.R. (2010). Neurogenic radial glia in the outer subventricular zone of human neocortex. *Nature* **464**, 554–561.
- Hattori, M., Adachi, H., Tsujimoto, M., Arai, H., and Inoue, K. (1994). Miller-Dieker lissencephaly gene encodes a subunit of brain platelet-activating factor acetylhydrolase [corrected]. *Nature* **370**, 216–218.
- Hevner, R.F., and Haydar, T.F. (2012). The (not necessarily) convoluted role of basal radial glia in cortical neurogenesis. *Cereb. Cortex* **22**, 465–468.
- Hevner, R.F., Hodge, R.D., Daza, R.A., and Englund, C. (2006). Transcription factors in glutamatergic neurogenesis: conserved programs in neocortex, cerebellum, and adult hippocampus. *Neurosci. Res.* **55**, 223–233.
- Heymann, D.L., Hodgson, A., Sall, A.A., Freedman, D.O., Staples, J.E., Althabe, F., Baruah, K., Mahmud, G., Kandun, N., Vasconcelos, P.F.C., et al.

- (2016). Zika virus and microcephaly: why is this situation a PHEIC? *Lancet* 387, 719–721.
- Hirotsune, S., Fleck, M.W., Gambello, M.J., Bix, G.J., Chen, A., Clark, G.D., Ledbetter, D.H., McBain, C.J., and Wynshaw-Boris, A. (1998). Graded reduction of Pafah1b1 (Lis1) activity results in neuronal migration defects and early embryonic lethality. *Nat. Genet.* 19, 333–339.
- Hu, W.F., Chahrouh, M.H., and Walsh, C.A. (2014). The diverse genetic landscape of neurodevelopmental disorders. *Annu. Rev. Genomics Hum. Genet.* 15, 195–213.
- Kadoshima, T., Sakaguchi, H., Nakano, T., Soen, M., Ando, S., Eiraku, M., and Sasai, Y. (2013). Self-organization of axial polarity, inside-out layer pattern, and species-specific progenitor dynamics in human ES cell-derived neocortex. *Proc. Natl. Acad. Sci. USA* 110, 20284–20289.
- Kato, M., and Dobyns, W.B. (2003). Lissencephaly and the molecular basis of neuronal migration. *Hum. Mol. Genet.* 12, R89–R96.
- Kreitzer, F.R., Salomonis, N., Sheehan, A., Huang, M., Park, J.S., Spindler, M.J., Lizarraga, P., Weiss, W.A., So, P.L., and Conklin, B.R. (2013). A robust method to derive functional neural crest cells from human pluripotent stem cells. *Am. J. Stem Cells* 2, 119–131.
- LaMonica, B.E., Lui, J.H., Hansen, D.V., and Kriegstein, A.R. (2013). Mitotic spindle orientation predicts outer radial glial cell generation in human neocortex. *Nat. Commun.* 4, 1665.
- Lanari, M., Capretti, M.G., Lazzarotto, T., Gabrielli, L., Rizzollo, S., Mostert, M., and Manzoni, P. (2012). Neuroimaging in CMV congenital infected neonates: how and when. *Early Hum. Dev.* 88 (Suppl 2), S3–S5.
- Lancaster, M.A., Renner, M., Martin, C.-A., Wenzel, D., Bicknell, L.S., Hurles, M.E., Homfray, T., Penninger, J.M., Jackson, A.P., and Knoblich, J.A. (2013). Cerebral organoids model human brain development and microcephaly. *Nature* 501, 373–379.
- Ledbetter, S.A., Kuwano, A., Dobyns, W.B., and Ledbetter, D.H. (1992). Microdeletions of chromosome 17p13 as a cause of isolated lissencephaly. *Am. J. Hum. Genet.* 50, 182–189.
- Leone, D.P., Srinivasan, K., Chen, B., Alcamo, E., and McConnell, S.K. (2008). The determination of projection neuron identity in the developing cerebral cortex. *Curr. Opin. Neurobiol.* 18, 28–35.
- Lo Nigro, C., Chong, C.S., Smith, A.C., Dobyns, W.B., Carrozzo, R., and Ledbetter, D.H. (1997). Point mutations and an intragenic deletion in LIS1, the lissencephaly causative gene in isolated lissencephaly sequence and Miller-Dieker syndrome. *Hum. Mol. Genet.* 6, 157–164.
- Lui, J.H., Hansen, D.V., and Kriegstein, A.R. (2011). Development and evolution of the human neocortex. *Cell* 146, 18–36.
- Lukaszewicz, A., Savatier, P., Cortay, V., Giroud, P., Huissoud, C., Berland, M., Kennedy, H., and Dehay, C. (2005). G1 phase regulation, area-specific cell cycle control, and cytoarchitectonics in the primate cortex. *Neuron* 47, 353–364.
- Martin, E., Kikinis, R., Zuerrer, M., Boesch, C., Briner, J., Kewitz, G., and Kaelin, P. (1988). Developmental stages of human brain: an MR study. *J. Comput. Assist. Tomogr.* 12, 917–922.
- Mlakar, J., Korva, M., Tul, N., Popović, M., Poljšak-Prijatelj, M., Mraz, J., Kolenc, M., Resman Rus, K., Vesnaver Vipotnik, T., Fabjan Vodusek, V., et al. (2016). Zika Virus Associated with Microcephaly. *N. Engl. J. Med.* 374, 951–958.
- Molyneaux, B.J., Arlotta, P., Hirata, T., Hibi, M., and Macklis, J.D. (2005). Fezl is required for the birth and specification of corticospinal motor neurons. *Neuron* 47, 817–831.
- Moon, H.M., Youn, Y.H., Pemble, H., Yingling, J., Wittmann, T., and Wynshaw-Boris, A. (2014). LIS1 controls mitosis and mitotic spindle organization via the LIS1-NDEL1-dynein complex. *Hum. Mol. Genet.* 23, 449–466.
- Nagamani, S.C., Zhang, F., Shchelochkov, O.A., Bi, W., Ou, Z., Scaglia, F., Probst, F.J., Shinawi, M., Eng, C., Hunter, J.V., et al. (2009). Microdeletions including YWHAE in the Miller-Dieker syndrome region on chromosome 17p13.3 result in facial dysmorphisms, growth restriction, and cognitive impairment. *J. Med. Genet.* 46, 825–833.
- Nowakowski, T.J., Pollen, A.A., Sandoval-Espinosa, C., and Kriegstein, A.R. (2016a). Transformation of the Radial Glia Scaffold Demarcates Two Stages of Human Cerebral Cortex Development. *Neuron* 91, 1219–1227.
- Nowakowski, T.J., Pollen, A.A., Di Lullo, E., Sandoval-Espinosa, C., Bershteyn, M., and Kriegstein, A.R. (2016b). Expression Analysis Highlights AXL as a Candidate Zika Virus Entry Receptor in Neural Stem Cells. *Cell Stem Cell* 18, 591–596.
- Okita, K., Matsumura, Y., Sato, Y., Okada, A., Morizane, A., Okamoto, S., Hong, H., Nakagawa, M., Tanabe, K., Tezuka, K., et al. (2011). A more efficient method to generate integration-free human iPS cells. *Nat. Methods* 8, 409–412.
- O’Leary, D.R., Kuhn, S., Kniss, K.L., Hinckley, A.F., Rasmussen, S.A., Pape, W.J., Kightlinger, L.K., Beecham, B.D., Miller, T.K., Neitzel, D.F., et al. (2006). Birth outcomes following West Nile Virus infection of pregnant women in the United States: 2003–2004. *Pediatrics* 117, e537–e545.
- Oliveira Melo, A.S., Malinge, G., Ximenes, R., Szejnfeld, P.O., Alves Sampaio, S., and Bispo de Filippis, A.M. (2016). Zika virus intrauterine infection causes fetal brain abnormality and microcephaly: tip of the iceberg? *Ultrasound Obstet. Gynecol.* 47, 6–7.
- Ostrem, B.E., Lui, J.H., Gertz, C.C., and Kriegstein, A.R. (2014). Control of outer radial glial stem cell mitosis in the human brain. *Cell Rep.* 8, 656–664.
- Park, I.H., Zhao, R., West, J.A., Yabuuchi, A., Huo, H., Ince, T.A., Lerou, P.H., Lensch, M.W., and Daley, G.Q. (2008). Reprogramming of human somatic cells to pluripotency with defined factors. *Nature* 451, 141–146.
- Pawlisz, A.S., Mutch, C., Wynshaw-Boris, A., Chenn, A., Walsh, C.A., and Feng, Y. (2008). Lis1-Nde1-dependent neuronal fate control determines cerebral cortical size and lamination. *Hum. Mol. Genet.* 17, 2441–2455.
- Pilaz, L.J., McMahon, J.J., Miller, E.E., Lennox, A.L., Suzuki, A., Salmon, E., and Silver, D.L. (2016). Prolonged Mitosis of Neural Progenitors Alters Cell Fate in the Developing Brain. *Neuron* 89, 83–99.
- Pilz, D.T., Macha, M.E., Precht, K.S., Smith, A.C., Dobyns, W.B., and Ledbetter, D.H. (1998). Fluorescence in situ hybridization analysis with LIS1 specific probes reveals a high deletion mutation rate in isolated lissencephaly sequence. *Genet. Med.* 1, 29–33.
- Pollen, A.A., Nowakowski, T.J., Chen, J., Retallack, H., Sandoval-Espinosa, C., Nicholas, C.R., Shuga, J., Liu, S.J., Oldham, M.C., Diaz, A., et al. (2015). Molecular identity of human outer radial glia during cortical development. *Cell* 163, 55–67.
- Pramparo, T., Youn, Y.H., Yingling, J., Hirotsune, S., and Wynshaw-Boris, A. (2010). Novel embryonic neuronal migration and proliferation defects in Dcx mutant mice are exacerbated by Lis1 reduction. *J. Neurosci.* 30, 3002–3012.
- Qian, X., Nguyen, H.N., Song, M.M., Hadiono, C., Ogden, S.C., Hammack, C., Yao, B., Hamersky, G.R., Jacob, F., Zhong, C., et al. (2016). Brain-Region-Specific Organoids Using Mini-bioreactors for Modeling ZIKV Exposure. *Cell* 165, 1238–1254.
- Reillo, I., de Juan Romero, C., Garcia-Cabezas, M.Á., and Borrell, V. (2011). A role for intermediate radial glia in the tangential expansion of the mammalian cerebral cortex. *Cereb. Cortex* 21, 1674–1694.
- Reiner, O., Carrozzo, R., Shen, Y., Wehnert, M., Faustinella, F., Dobyns, W.B., Caskey, C.T., and Ledbetter, D.H. (1993). Isolation of a Miller-Dieker lissencephaly gene containing G protein beta-subunit-like repeats. *Nature* 364, 717–721.
- Saito, T., Hanai, S., Takashima, S., Nakagawa, E., Okazaki, S., Inoue, T., Miyata, R., Hoshino, K., Akashi, T., Sasaki, M., et al. (2011). Neocortical layer formation of human developing brains and lissencephalies: consideration of layer-specific marker expression. *Cereb. Cortex* 21, 588–596.
- Schuler-Faccini, L., Ribeiro, E.M., Feitosa, I.M., Horovitz, D.D., Cavalcanti, D.P., Pessoa, A., Doriqui, M.J., Neri, J.L., Neto, J.M., Wanderley, H.Y., et al.; Brazilian Medical Genetics Society–Zika Embryopathy Task Force (2016). Possible Association Between Zika Virus Infection and Microcephaly – Brazil, 2015. *MMWR Morb. Mortal. Wkly. Rep.* 65, 59–62.
- Sheen, V.L., Ferland, R.J., Harney, M., Hill, R.S., Neal, J., Banham, A.H., Brown, P., Chenn, A., Corbo, J., Hecht, J., et al. (2006a). Impaired proliferation

- and migration in human Miller-Dieker neural precursors. *Ann. Neurol.* **60**, 137–144.
- Sheen, V.L., Ferland, R.J., Neal, J., Harney, M., Hill, R.S., Banham, A., Brown, P., Chenn, A., Corbo, J., Hecht, J., et al. (2006b). Neocortical neuronal arrangement in Miller Dieker syndrome. *Acta Neuropathol.* **111**, 489–496.
- Shi, Y., Kirwan, P., Smith, J., Robinson, H.P.C., and Livesey, F.J. (2012). Human cerebral cortex development from pluripotent stem cells to functional excitatory synapses. *Nat. Neurosci.* **15**, 477–486, S1.
- Shitamukai, A., Konno, D., and Matsuzaki, F. (2011). Oblique radial glial divisions in the developing mouse neocortex induce self-renewing progenitors outside the germinal zone that resemble primate outer subventricular zone progenitors. *J. Neurosci.* **31**, 3683–3695.
- Shu, T., Ayala, R., Nguyen, M.D., Xie, Z., Gleeson, J.G., and Tsai, L.H. (2004). Ndel1 operates in a common pathway with LIS1 and cytoplasmic dynein to regulate cortical neuronal positioning. *Neuron* **44**, 263–277.
- Sidman, R.L., and Rakic, P. (1973). Neuronal migration, with special reference to developing human brain: a review. *Brain Res.* **62**, 1–35.
- Silver, D.L., Watkins-Chow, D.E., Schreck, K.C., Pierfelice, T.J., Larson, D.M., Burnetti, A.J., Liaw, H.J., Myung, K., Walsh, C.A., Gaiano, N., and Pavan, W.J. (2010). The exon junction complex component Magoh controls brain size by regulating neural stem cell division. *Nat. Neurosci.* **13**, 551–558.
- Smart, I.H., Dehay, C., Giroud, P., Berland, M., and Kennedy, H. (2002). Unique morphological features of the proliferative zones and postmitotic compartments of the neural epithelium giving rise to striate and extrastriate cortex in the monkey. *Cereb. Cortex* **12**, 37–53.
- Smith, D.S., Niethammer, M., Ayala, R., Zhou, Y., Gambello, M.J., Wynshaw-Boris, A., and Tsai, L.H. (2000). Regulation of cytoplasmic dynein behaviour and microtubule organization by mammalian Lis1. *Nat. Cell Biol.* **2**, 767–775.
- Stahl, R., Walcher, T., De Juan Romero, C., Pilz, G.A., Cappello, S., Irmner, M., Sanz-Aguela, J.M., Beckers, J., Blum, R., Borrell, V., and Götz, M. (2013). Trnp1 regulates expansion and folding of the mammalian cerebral cortex by control of radial glial fate. *Cell* **153**, 535–549.
- Stiles, J., and Jernigan, T.L. (2010). The basics of brain development. *Neuropsychol. Rev.* **20**, 327–348.
- Takahashi, K., Tanabe, K., Ohnuki, M., Narita, M., Ichisaka, T., Tomoda, K., and Yamanaka, S. (2007). Induction of pluripotent stem cells from adult human fibroblasts by defined factors. *Cell* **131**, 861–872.
- Tanaka, T., Serneo, F.F., Higgins, C., Gambello, M.J., Wynshaw-Boris, A., and Gleeson, J.G. (2004). Lis1 and doublecortin function with dynein to mediate coupling of the nucleus to the centrosome in neuronal migration. *J. Cell Biol.* **165**, 709–721.
- Tang, H., Hammack, C., Ogden, S.C., Wen, Z., Qian, X., Li, Y., Yao, B., Shin, J., Zhang, F., Lee, E.M., et al. (2016). Zika Virus Infects Human Cortical Neural Progenitors and Attenuates Their Growth. *Cell Stem Cell* **18**, 587–590.
- Taverna, E., Götz, M., and Huttner, W.B. (2014). The cell biology of neurogenesis: toward an understanding of the development and evolution of the neocortex. *Annu. Rev. Cell Dev. Biol.* **30**, 465–502.
- Teissier, N., Fallet-Bianco, C., Delezoide, A.L., Laquerrière, A., Marcorelles, P., Khung-Savatovsky, S., Nardelli, J., Cipriani, S., Csaba, Z., Picone, O., et al. (2014). Cytomegalovirus-induced brain malformations in fetuses. *J. Neuropathol. Exp. Neurol.* **73**, 143–158.
- Toyo-oka, K., Shionoya, A., Gambello, M.J., Cardoso, C., Leventer, R., Ward, H.L., Ayala, R., Tsai, L.H., Dobyns, W., Ledbetter, D., et al. (2003). 14-3-3epsilon is important for neuronal migration by binding to NUDEL: a molecular explanation for Miller-Dieker syndrome. *Nat. Genet.* **34**, 274–285.
- Wang, X., Tsai, J.W., LaMonica, B., and Kriegstein, A.R. (2011). A new subtype of progenitor cell in the mouse embryonic neocortex. *Nat. Neurosci.* **14**, 555–561.
- Xie, Y., Jüschke, C., Esk, C., Hirotsune, S., and Knoblich, J.A. (2013). The phosphatase PP4c controls spindle orientation to maintain proliferative symmetric divisions in the developing neocortex. *Neuron* **79**, 254–265.
- Yingling, J., Youn, Y.H., Darling, D., Toyo-Oka, K., Pramparo, T., Hirotsune, S., and Wynshaw-Boris, A. (2008). Neuroepithelial stem cell proliferation requires LIS1 for precise spindle orientation and symmetric division. *Cell* **132**, 474–486.
- Youn, Y.H., Pramparo, T., Hirotsune, S., and Wynshaw-Boris, A. (2009). Distinct dose-dependent cortical neuronal migration and neurite extension defects in Lis1 and Ndel1 mutant mice. *J. Neurosci.* **29**, 15520–15530.
- Yu, J., Vodyanik, M.A., Smuga-Otto, K., Antosiewicz-Bourget, J., Frane, J.L., Tian, S., Nie, J., Jonsdottir, G.A., Ruotti, V., Stewart, R., et al. (2007). Induced pluripotent stem cell lines derived from human somatic cells. *Science* **318**, 1917–1920.

Retrogradely Transported TrkA Endosomes Signal Locally within Dendrites to Maintain Sympathetic Neuron Synapses

Kathryn M. Lehigh,^{1,2} Katherine M. West,¹ and David D. Ginty^{1,3,*}

¹Department of Neurobiology, Howard Hughes Medical Institute, Harvard Medical School, 220 Longwood Avenue, Boston, MA 02115, USA

²Neuroscience Training Program, Department of Neuroscience, The Johns Hopkins University School of Medicine, Baltimore, MD 21205, USA

³Lead Contact

*Correspondence: david_ginty@hms.harvard.edu

<http://dx.doi.org/10.1016/j.celrep.2017.03.028>

SUMMARY

Sympathetic neurons require NGF from their target fields for survival, axonal target innervation, dendritic growth and formation, and maintenance of synaptic inputs from preganglionic neurons. Target-derived NGF signals are propagated retrogradely, from distal axons to somata of sympathetic neurons via TrkA signaling endosomes. We report that a subset of TrkA endosomes that are transported from distal axons to cell bodies translocate into dendrites, where they are signaling competent and move bidirectionally, in close proximity to synaptic protein clusters. Using a strategy for spatially confined inhibition of TrkA kinase activity, we found that distal-axon-derived TrkA signaling endosomes are necessary within sympathetic neuron dendrites for maintenance of synapses. Thus, TrkA signaling endosomes have unique functions in different cellular compartments. Moreover, target-derived NGF mediates circuit formation and synapse maintenance through TrkA endosome signaling within dendrites to promote aggregation of postsynaptic protein complexes.

INTRODUCTION

Development of nervous system connectivity involves the orchestration of several events: axons are guided to their targets, axons and dendrites elaborate and form synaptic connections, and excess or improper synaptic connections are pruned (Jiang and Nardelli, 2016). A useful model system for studying the development of neural connectivity has been the sympathetic nervous system (SNS) because it is easily accessible and has well-defined anatomy: preganglionic sympathetic neurons are located in the intermediolateral region of the spinal cord; their axons exit the spinal cord via ventral roots and project to sympathetic ganglia, where they form synapses upon dendrites of postganglionic sympathetic neurons. As the SNS is a major

regulator of body homeostasis, disruption of SNS circuits causes several human pathological conditions. For example, Horner's syndrome, a disorder affecting the rostral-most ganglion of the sympathetic chain, the superior cervical ganglion (SCG), is caused by an interruption of SCG connectivity. Consequently, Horner's syndrome patients exhibit miosis, ptosis, and anhidrosis (Fields and Barker, 1992). Investigations of how SNS synapses are formed and maintained will reveal mechanisms that underlie SNS disorders such as Horner's syndrome.

Nerve growth factor (NGF), the prototypical neurotrophin, is essential for development and maintenance of sympathetic neurons. Seminal work by Levi-Montalcini and Booker, (1960) showed that NGF mediates survival of sympathetic neurons, whereas later work demonstrated that NGF also controls sympathetic neuron target field innervation, dendrite elaboration, and formation and maintenance of synapses with preganglionic partners (Glebova and Ginty, 2004; Njå and Purves, 1978; Ruit et al., 1990; Ruit and Snider, 1991; Sharma et al., 2010). How NGF derived from sympathetic neuron target fields promotes and maintains synaptic connections between preganglionic and postganglionic sympathetic neurons remains to be determined.

Considerable evidence supports a model in which NGF/TrkA signaling endosomes mediate long-range retrograde signaling to promote sympathetic neuron survival. NGF is produced in sympathetic target tissues throughout development and adulthood (Heumann et al., 1984; Sofroniew et al., 2001), where it binds to its receptor, the tyrosine kinase TrkA, initiating endocytosis of the ligand and receptor complex at distal axons followed by retrograde transport of NGF/TrkA endosomes to cell bodies (Riccio et al., 1997; Tsui-Pierchala and Ginty, 1999; Watson et al., 1999). Application of NGF to distal axons of neurons grown in compartmentalized cultures supports cell survival (Campenot, 1977) as well as TrkA signaling within cell bodies (Riccio et al., 1997; Senger and Campenot, 1997; Tsui-Pierchala and Ginty, 1999; Watson et al., 1999), which in turn is required for activation of NGF/TrkA signaling effectors that promote survival (Kuruvilla et al., 2000; Riccio et al., 1997; Ye et al., 2003). Furthermore, disruption of TrkA signaling and downstream effectors in cell bodies of sympathetic neurons following NGF application to distal axons results in cell death (Kuruvilla et al., 2000, 2004; Ye et al., 2003). Together, these findings support a model in which

signals emanating from distal-axon-derived NGF/TrkA endosomes within cell bodies are required for survival of sympathetic neurons. Interestingly, NGF acting exclusively on distal axons of cultured sympathetic neurons can also support the formation of clusters of postsynaptic density (PSD) proteins on dendrites (Sharma et al., 2010). Under these conditions, inhibition of TrkA signaling within the somatodendritic compartment of cultured neurons leads to loss of PSD clusters. These observations raise the intriguing possibility that TrkA endosomes may traffic from distal axons, where they are formed, into the cell soma and then into dendrites where they signal locally, within dendrites, to promote formation and maintenance of synapses between preganglionic and postganglionic sympathetic neurons.

Here, we report that TrkA endosomes originating in sympathetic neuron distal axons are transported retrogradely into dendrites as signaling-competent entities that move in a unique, bidirectional manner, as compared to TrkA endosomes in axons, and in close proximity to PSD clusters. We also find signaling-competent TrkA endosomes within sympathetic neuron dendrites *in vivo*, adjacent to synapses, at both early and late stages of dendrite development and synapse formation. Importantly, we show that TrkA kinase activity within the SCG is essential for the maintenance of synapses between preganglionic and postganglionic sympathetic neurons *in vivo*. Moreover, distal-axon-derived TrkA signaling endosomes function within dendrites, not cell bodies, for maintenance of dendritic PSD clusters *in vitro*. Thus, target-derived NGF supports synapse formation and maintenance through local TrkA endosome signaling within sympathetic neuron dendrites.

RESULTS

Live-Cell Imaging of TrkA Endosomes Reveals Unique Dynamics in Different Cellular Compartments

The observation that distal-axon-derived TrkA endosomes are transported from the soma into the dendrites of sympathetic neurons (Sharma et al., 2010) suggests novel TrkA signaling functions within that cellular compartment. To gain insight into TrkA endosome function in dendrites, we first sought to characterize TrkA endosome dynamics within dendrites and their location, with respect to dendritic PSDs. To monitor TrkA endosome dynamics, we developed a live-cell imaging paradigm that enables visualization of TrkA endosomes in real time, thus providing a means to compare their movement in axons, cell bodies, and dendrites. This live-cell imaging paradigm involves culturing dissociated postganglionic sympathetic neurons obtained from the *TrkA^{Flag}* mouse line, which expresses Flag epitope-tagged TrkA protein from the endogenous *TrkA* locus (Sharma et al., 2010), in microfluidic chambers (Taylor et al., 2010). Addition of an anti-Flag primary and fluorescent secondary antibody conjugate, followed by application of NGF, to the distal-axon compartment, allows for real-time visualization of newly internalized TrkA endosomes as they are retrogradely trafficked from distal axons into cell bodies and dendrites (Figure 1A; Movies S1, S2, S3, S4, and S5). Importantly, fluorescent puncta were not observed in control wild-type neurons, indicating that the Flag and fluorescent secondary antibody combination specifically recognizes Flag-TrkA in *TrkA^{Flag}* neurons (Figure 1B).

Using this live-cell TrkA imaging assay, we found that TrkA endosomes move in a saltatory manner retrogradely through axons (Figures 1C and 1E; Movie S1) with highly variable rates, averaging $1.22 \pm 0.23 \mu\text{m/s}$ (Figures 2A, S1B, and S1C), which is similar to the rate of retrograde axonal transport of its ligand, NGF (Cui et al., 2007; Hendry et al., 1974). TrkA endosomes in axons move exclusively in a retrograde manner, from distal axons to cell bodies (Figure 2C; Movies S1, S3, and S4). This is expected because trafficking of NGF-containing endosomes in axons is dependent on the retrograde motor protein dynein (Heerssen et al., 2004). We noted that TrkA endosomes in the same axon frequently paused at similar or identical locations (Movies S1, S3, and S4). Faster endosomes more quickly traversed the length of the axon, whereas slower endosomes typically exhibited frequent pauses or became stationary for the duration of the recording (Figures 1E and S1C; Movie S1).

We observed that TrkA endosomes retrogradely trafficked from distal axons first arrive in cell bodies between 15 and 30 min following NGF application to distal axons (data not shown). Upon arrival in the soma, labeled endosomes slow down or halt, resulting in their accumulation within cell bodies (Movies S2, S3, S4, and S5). We photobleached accumulated endosomes within the soma to monitor movement of endosomes that were newly transported from the axon into the soma, and this revealed that TrkA endosomes within the soma move at an average rate of $0.14 \pm 0.02 \mu\text{m/s}$ (Figure 2A). Many somatic endosomes were localized to a perinuclear region where they did not exhibit appreciable movement (Figure S1A).

Peripherally located somatic endosomes were often observed moving from cell body to dendrites after minor pauses (Movie S3). We determined that $4.2\% \pm 0.3\%$ of TrkA endosomes in the somatodendritic compartment 3 hr after NGF application to distal axons were in dendrites. Thus, we next used the live-cell TrkA endosome assay to monitor TrkA endosome movement within dendrites (day *in vitro* [DIV] 14–16) that were identified via post hoc MAP2 immunocytochemistry (ICC) (Figure 1G). We observed that distal-axon-derived TrkA endosomes within dendrites move in a bidirectional manner (Figures 1D and 1F; Movies S4 and S5), representing a fundamental difference from the manner in which TrkA endosomes travel within axons (Figure 2C; Movie S5). Although dendritic TrkA endosomes are capable of moving at rates that are comparable to those in axons (Figure S1B), their unique dynamics (i.e., frequent direction changes and oscillatory movements) result in an overall lower average rate of movement (Figure 2A) and a lower net displacement as a function of time compared to endosomes in axons (Figure 2B). This distinction is readily appreciated upon visualization of dendritic TrkA endosome dynamics in real time as they tend to hover around small regions of dendrite, in contrast to the much longer distances covered by TrkA endosomes in axons (Figures 1E and 1F; Movies S4 and S5). Furthermore, we observed a substantial subset (~20%) of distal-axon-derived Flag-TrkA endosomes within dendrites that remain stationary (Figure 1F; Movies S4 and S5). However, this is not the fate of the majority of dendritic TrkA endosomes, which maintain mobility (Figure 2D) and may even return to the soma (Movie S5). These experiments show that the dynamics of movement of distal-axon-derived TrkA endosomes differ markedly within cellular compartments.

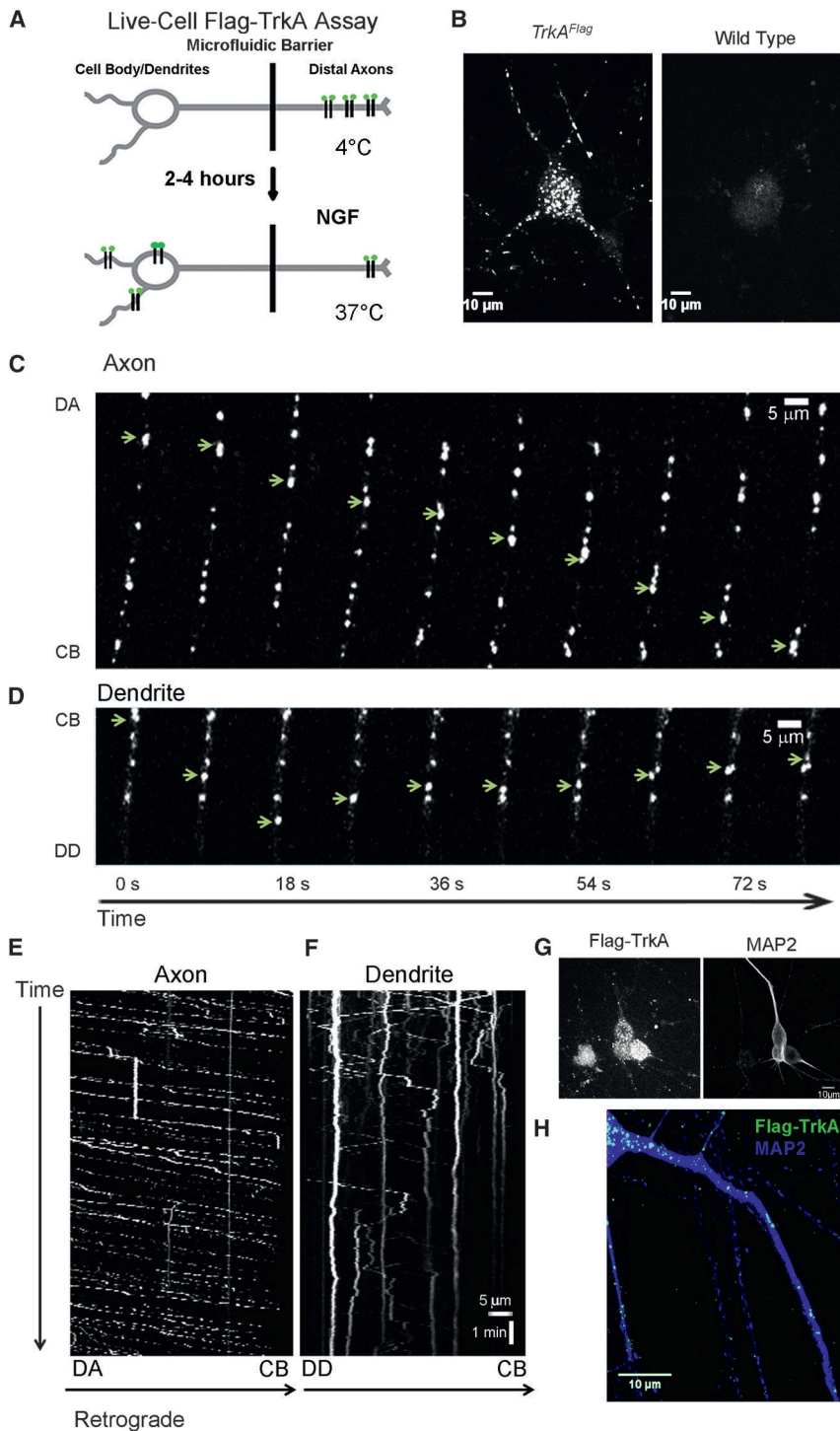


Figure 1. Live-Cell Imaging Reveals Distinct Trafficking Dynamics of Distal-Axon-Derived TrkA Endosomes in Different Neuronal Compartments

(A) Schematic of the live-cell Flag-TrkA endosome visualization assay to assess movement of TrkA endosomes in axons, soma, and dendrites of sympathetic neurons.

(B) Live-cell images of TrkA endosomes in *TrkA^{Flag}* neurons (left) and wild-type neurons (right).

(C) Individual Flag-TrkA endosomes in axons tracked in real time moving retrogradely from distal axons (DA) toward the cell body (CB).

(D) Individual Flag-TrkA endosomes in dendrites tracked in real time moving toward the distal dendrite (DD), some switching directions and moving toward the CB. In (C) and (D), each image represents a frame acquired every 3.0 s. Arrows denote one endosome over time.

(E) Kymograph of Flag-TrkA endosome movement in axons from time-lapse images acquired every 2.3 s.

(F) Kymograph of Flag-TrkA endosome movement in dendrites from same video in (E). In (E) and (F), spatial and temporal scale are the same.

(G) Live-cell Flag-TrkA endosomes align with post hoc IHC for MAP2, a dendritic marker.

(H) Retrogradely trafficked TrkA endosomes are found throughout the MAP2⁺ dendritic arbor of sympathetic neurons. See also Figure S1.

that traffic into dendrites are signaling competent. TrkA kinase activation results in autophosphorylation of specific TrkA tyrosine (Y) residues, including Y490 and Y785. Once phosphorylated, these TrkA phosphotyrosine motifs recruit adaptor and effector complexes to the membrane to promote downstream NGF/TrkA signaling pathways, including the Ras/ERK, PI3 kinase, and PLC- γ pathways (Barford et al., 2016). Therefore, we used antibodies directed against the phosphorylated forms of TrkA Y490 and Y785 (Huang et al., 2015) to assess the extent to which TrkA endosomes in dendrites are signaling competent.

First, specificity of the TrkA Y490 and Y785 antibodies in this paradigm was tested using a chemical-genetic strategy with compartmentalized cultures of sympathetic neurons from *TrkA^{F592A}* mice. *TrkA^{F592A}* mice harbor a single phenylalanine-to-alanine amino acid substitution

in the TrkA protein kinase domain, which allows TrkA^{F592A}, but not wild-type TrkA, catalytic activity to be selectively blocked by the membrane-permeable small molecule 1NMPP1 (Chen et al., 2005), thereby providing a means of selective inhibition of TrkA autophosphorylation and signaling. Indeed, we observed nearly complete loss of P-TrkA (Y490) and P-TrkA (Y785)

Distal-Axon-Derived TrkA Endosomes in Dendrites Are Signaling Competent and Located Near PSDs

The current view of NGF signal transduction is that TrkA endosomes carry critical retrograde signals from the periphery to cell bodies of sympathetic neurons (Barford et al., 2016; Harrington et al., 2011). Therefore, we asked whether TrkA endosomes

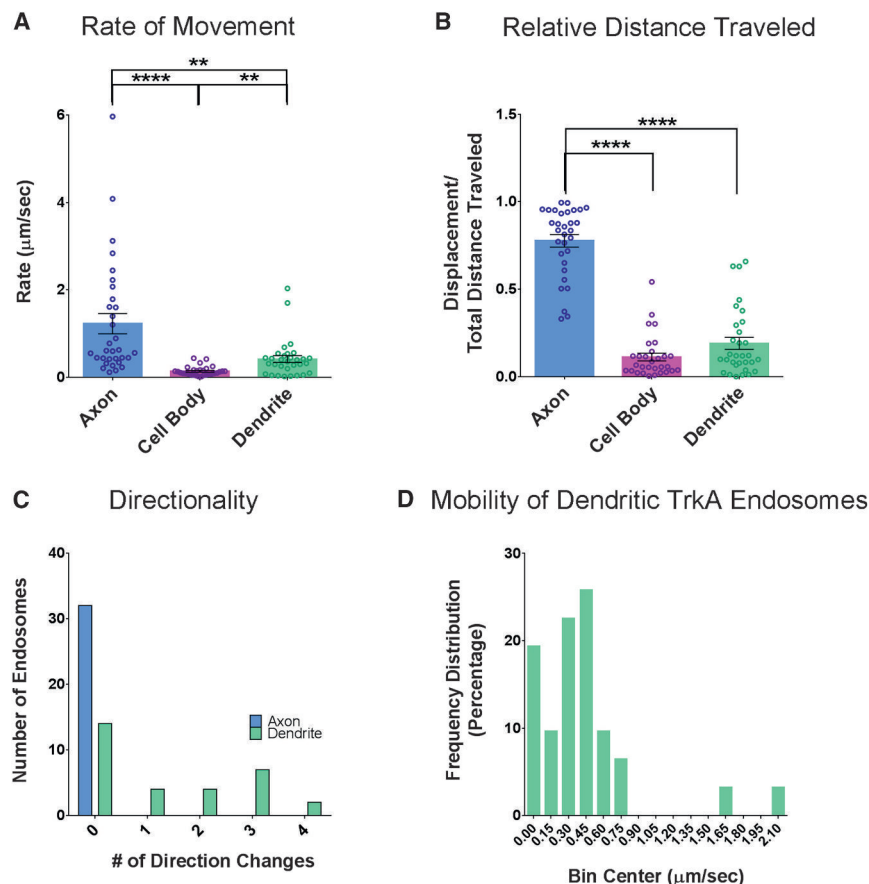


Figure 2. Comparison of TrkA Endosome Movement Dynamics within Different Cellular Compartments

(A) The average rate of movement of Flag-TrkA endosomes tracked in axons, cell bodies, and dendrites, including stationary endosomes. Kruskal-Wallis test, $p < 0.0001$, $F_{(2,90)} = 41.00$; post hoc Dunn's multiple-comparison test: for axon versus cell body (CB), $****p < 0.0001$; for axon versus dendrite, $**p < 0.001$; for CB versus dendrite, $**p < 0.001$.

(B) Quantification of relative distance traveled by endosomes in each cellular compartment (displacement over total net movement). Kruskal-Wallis test, $p < 0.0001$, $F_{(2,89)} = 57.72$; post hoc Dunn's multiple-comparison test: for axon versus CB, $****p < 0.0001$; for axon versus dendrite, $****p < 0.0001$. (A and B) $n(\text{axon}) = 32$, $n(\text{CB}) = 30$, $n(\text{dendrite}) = 31$.

(C) Histogram denoting the number of times an individual endosome changes its direction.

(D) Frequency distribution of the rate (micrometers per second) of TrkA endosomes within dendrites. The first bin is categorized as stationary. Bin size is $0.15 \mu\text{m/s}$. See also Figure S1.

Graphs are data presented as the mean, with error bars representing \pm SEM.

TrkA endosomes and dendritic synapses, we determined the extent to which dendritic TrkA endosomes derived from distal axons are localized in close proximity to PSDs. Following NGF application solely

immunoreactivity in *TrkA*^{F592A} neurons treated with 1NMPP1 but no change in the number of P-TrkA puncta in 1NMPP1-treated wild-type neurons (Figures 3A and S2A–S2D). We conclude that the antibodies directed against the phosphorylated forms of TrkA Y490 and Y785 specifically label these phospho-TrkA motifs in our ICC experiments.

Next, we used these specific phospho-TrkA antibodies to ask whether distal-axon-derived TrkA endosomes in dendrites are signaling competent by performing P-TrkA staining on compartmentalized *TrkA*^{Flag} neurons after NGF application to distal axons. Following a 2- to 4-hr incubation period to allow accumulation of retrogradely transported Flag-TrkA endosomes and P-TrkA puncta within dendrites, $\sim 34\%$ of Flag-TrkA endosomes in dendrites were found to be P-TrkA (Y785) positive and $\sim 15\%$ were P-TrkA (Y490) positive (Figures 3B–3D) at this time point. Flag-TrkA endosomes that are not P-TrkA (Y785) or P-TrkA (Y490) positive may represent TrkA endosomes returning to the cell body or endosomes on the pathway to lysosomal degradation (Hu et al., 2015). Conversely, P-TrkA endosomes that are not Flag-TrkA positive likely represent NGF-activated TrkA not bound by Flag antibody during the pulse application of Flag antibody to distal axons.

The presence of signaling-competent TrkA endosomes in dendrites lends support to the idea that distal-axon-derived TrkA endosomes within dendrites contribute to synapse formation and/or maintenance. To explore the relationship between

to distal axons of sympathetic neurons, Flag-TrkA endosomes were often observed adjacent to membrane-associated guanylate kinase (MAGUK)-positive PSDs throughout the dendritic arbor (Figure 3E). In the same experimental paradigm, double-labeling ICC experiments revealed a non-random, close spatial relationship, with some co-localization, between P-TrkA (Y785) signaling-competent endosomes and PSDs labeled with both MAGUK (Figures 3F–3H) and Homer1 (Figure S2E). A nearest-neighbor analysis comparing the spatial relationship between the different puncta types showed that the proximity of signaling-competent TrkA endosomes (P-TrkA [Y785] puncta) to MAGUK puncta is considerably closer than what would be expected by chance alone (Figures 3G, 3H, S2F, and S2G). This intimate spatial relationship between TrkA endosomes and PSDs within dendrites suggests that distal-axon-derived TrkA signaling endosomes are poised to promote or maintain PSD component clustering or function.

Distal-Axon-Derived Endosomes Are Signaling Competent in Dendrites of Postganglionic Neurons in Sympathetic Ganglia In Vivo

We next sought to determine whether distal-axon-derived TrkA endosomes are trafficked into sympathetic neuron dendrites in vivo. To this end, we analyzed endosomes derived from sympathetic neuron axonal terminals innervating the eye, a major target of the SCG. Injection of fluorescently conjugated

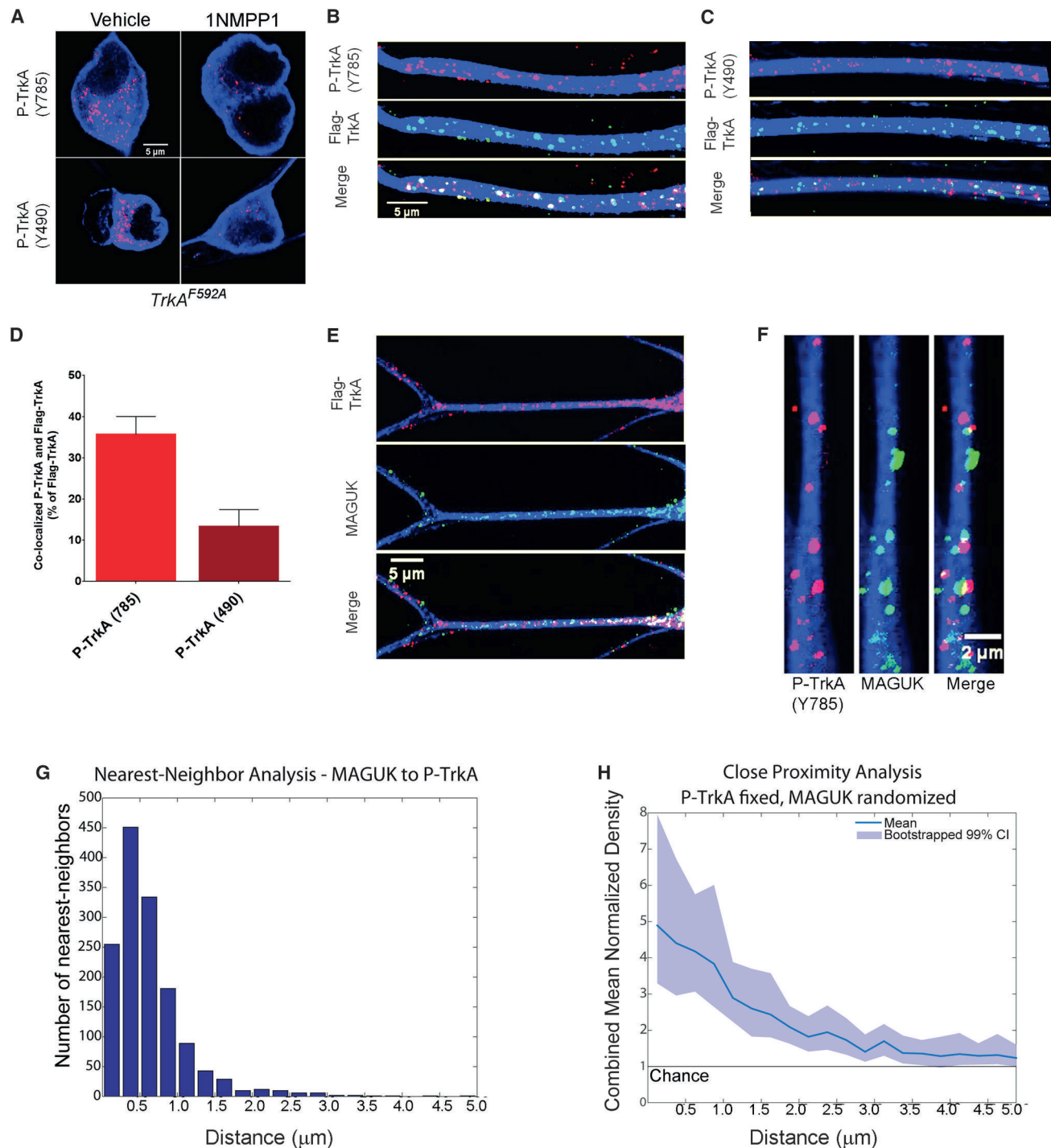


Figure 3. Distal-Axon-Derived TrkA Endosomes in Dendrites Are Signaling Competent and Localized in Close Proximity to PSDs

(A) Images of *TrkA^{F592A}* cell bodies immunostained for P-TrkA (Y785) puncta in both vehicle (top left) and 1NMPP1 (top right) conditions, as well as cell bodies immunostained for P-TrkA (Y490) puncta in both vehicle (bottom left) and 1NMPP1 (bottom right) conditions, showing specificity of P-TrkA antibodies.

(B–H) Panels represent data 3–6 hr after NGF application to the distal-axon compartment. (B and C) Images illustrating co-localization of retrograde Flag-TrkA endosomes and P-TrkA (Y785) (B) and Y490 (C) in dendrites. (C) is same scale as (B). (D) Quantification of co-localization between retrogradely trafficked Flag-TrkA endosomes and P-TrkA (Y785) and P-TrkA (Y490) ($n = 3$). (E) Images of distal-axon-derived Flag-TrkA endosomes (top) in close proximity to the PSD protein MAGUK (middle) in dendrites of sympathetic neurons. (F) High-magnification image of P-TrkA puncta (left) within dendrites in close proximity to MAGUK puncta

(legend continued on next page)

wheat germ agglutinin (WGA) into the anterior chamber of the eye resulted in its uptake into endosomes at sympathetic neuron distal axons and retrograde transport within sympathetic neuron axons, into cell bodies of the SCG, and ultimately into SCG sympathetic neuron dendrites (Figures 4A–4D). WGA-containing endosomes were confined to the ganglion ipsilateral to the injected anterior chamber, and not present in the contralateral ganglion (Figure 4B). Because sympathetic neurons project exclusively to ipsilateral targets, this finding indicates that uptake and transport occurs from the target region via sympathetic neuron axons (Figure 4C) and not via leak into the circulatory system, which would be expected to result in direct uptake at the soma of both ipsilateral and contralateral ganglia. The appearance of WGA vesicles in both soma and dendrites of neurons in the ipsilateral ganglion occurred within 16 hr postinjection (Figure 4D), consistent with the previously described timing of retrograde transport of NGF from distal target innervating axonal terminals to SCG cell bodies (Hendry et al., 1974). To ask whether TrkA^{Flag} receptors endocytosed at the distal axon were transported into dendrites, we performed the WGA eye injection assay on adult *TrkA^{Flag}* mice and indeed observed that endosomes with retrogradely transported WGA protein co-localized with Flag-TrkA-labeled puncta in neuronal dendrites (Figures 4E and 4G). We confirmed that Flag staining in SCG tissue is specific to *TrkA^{Flag}* mice, observing no labeled puncta in wild-type animals (Figure 4H). These observations support the idea that TrkA endosomes are trafficked retrogradely from sympathetic axon terminals into SCG dendrites in vivo.

We next asked whether target-derived TrkA endosomes observed in vivo are signaling competent by combining the WGA eye injection retrograde tracing assay with P-TrkA (Y785) immunohistochemistry (IHC). Indeed, as the in vitro findings suggested, co-localization between WGA-positive vesicles and P-TrkA-positive puncta was observed (Figures 4F and 4G). The number of WGA vesicles transported into dendrites was not significantly different for Flag-TrkA or P-TrkA experiments (Figure S3C). Moreover, the specificity of the P-TrkA antibody in these in vivo experiments was confirmed using chemical-genetic *TrkA^{F592A}* mice (Figures 4I, S3A, and S3B). Thus, TrkA endosomes found in dendrites of sympathetic neurons are derived from distal axons and signaling competent.

Signaling-Competent Endosomes Are Found within Dendrites and in Close Proximity to SCG Neuron Synapses throughout Development

If retrogradely transported NGF-TrkA endosomes signal locally within dendrites to promote formation and maintenance of synaptic connectivity, then we would expect to find signaling-competent endosomes within dendrites of sympathetic neurons not only throughout the period of robust synapse development but later as well. Utilizing *TH^{2a-CreER}; R26^{-LSL-YFP}* (Ai3) mice

(Abraira et al., 2017) and postnatal tamoxifen injection to achieve sparse genetic labeling of sympathetic neurons and their dendrites within the SCG (Figures S4A and S4B), we observed the presence of P-TrkA (Y785) puncta associated with sympathetic neuron dendrites at all examined postnatal ages: postnatal day 7 (P7), P14, P21, and P42–P56 (Figure 5A). We note that both the number of P-TrkA (Y785) puncta (Figure 5B) and the number of synapses (immunohistochemically defined as Homer1-VACHT double-positive puncta) within dendrites increase between developmental (P14) and young adult (P42–P56) ages (Figures 5C and S4C). These findings suggest that TrkA signals are propagated within dendrites during the most robust stages of dendritic growth (Voyvodic, 1987) and synapse formation (Smolen and Raisman, 1980) as well as during periods of final synapse formation (Smolen and Raisman, 1980), maturation, and maintenance (Heath et al., 1992).

We next asked whether there is a close relationship between TrkA signaling endosomes and synaptic proteins in vivo. Indeed, we found that P-TrkA (Y785) puncta within sympathetic neuron dendrites are in close proximity to presynaptic cholinergic terminals of preganglionic sympathetic neurons as measured by VACHT labeling (Figure 5A). Interestingly, the percentage of P-TrkA endosomes that were within 1 μ m of a VACHT punctum increased from ~30% at early developmental stages (P7–P14) to ~45% at later stages (P21–P56). A similar increase was observed with presynaptic and postsynaptic proteins; the percentage of Homer1 puncta located within 1 μ m of a VACHT punctum increased from ~50% to ~80% during this period (Figures 5D and 5E). Together, these findings suggest that distal-axon-derived TrkA endosomes are trafficked into dendrites both in vitro and in vivo, where they are signaling competent and located in close proximity to nascent synapses.

Inhibition of TrkA Kinase Activity Selectively within the SCG Decreases Synapse Number and Function

Our findings, together with previous observations (Sharma et al., 2010), support a model in which dendritic TrkA endosomes function within the somatodendritic compartment, and possibly within dendrites themselves, to promote synapse formation and maintenance. To test this model, we asked whether inhibiting TrkA kinase activity selectively within the ganglion, but not in distal axons, would alter the number of dendritic synapses found at P21, an age at which postganglionic sympathetic neuron dendrites are elaborate with an abundance of mature synapses, yet new synapses continue to develop (Figure 5C) (Smolen and Raisman, 1980; Voyvodic, 1987). As previously demonstrated, TrkA kinase activity can be specifically and efficiently inhibited in *TrkA^{F592A}* mice by administering 1NMPP1, and the extent and localization of TrkA inhibition can be monitored by IHC using the specific P-TrkA (Y785) antibody (Figures 3A and 4I). To restrict inhibition of TrkA signaling to the somatodendritic

(middle). (G) Histogram of nearest-neighbor analysis of nearest MAGUK puncta to P-TrkA (Y785) puncta. (H) Population-level analysis comparing the proximity of P-TrkA (Y785) and MAGUK puncta to that expected by chance, represented on the y axis as 1. Transparent band shows 99% confidence intervals determined by bootstrapping. (G and H) n = 22 dendrites, 4 chambers, 2 independent experiments. (A–F) MAP2 ICC is in blue. See also Figure S2. Graphs are data presented as the mean, with errors bars representing \pm SEM.

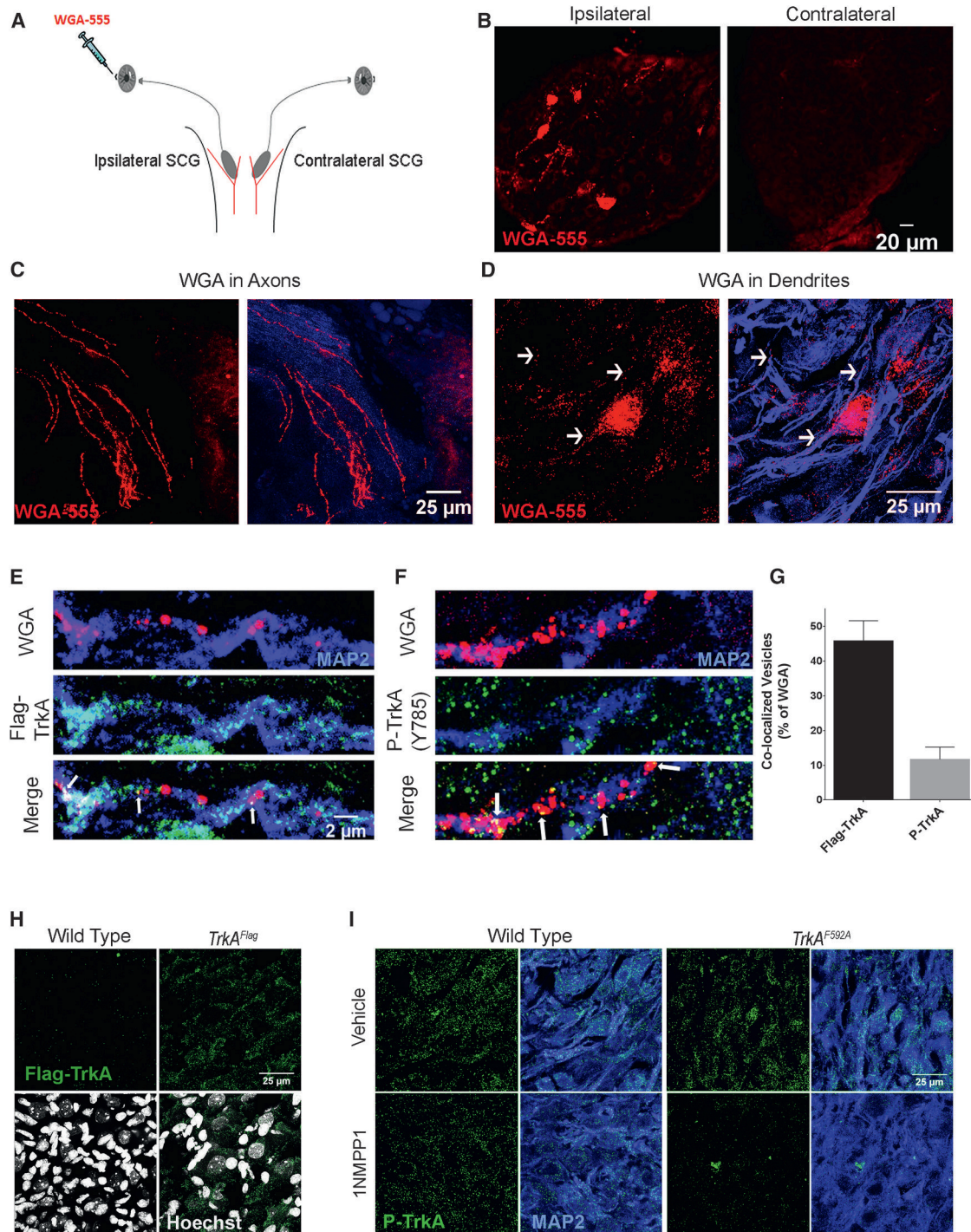


Figure 4. Distal-Axon-Derived, Signaling-Competent TrkA Endosomes Are Localized within Sympathetic Neuron Dendrites In Vivo

(A) Schematic of the assay used to track retrograde vesicle transport from the ipsilateral sympathetic target field to postganglionic neuron CBs and dendrites. WGA-555 injected into the anterior chamber of the eye is endocytosed by sympathetic neuron distal axons and transported retrogradely to the CBs and dendrites of sympathetic neurons residing in the SCG, located where the carotid artery branches into internal and external branches (red).

(B) Specific WGA-555 labeling of neurons in the ipsilateral ganglion (left) but not the contralateral (right).

(C) WGA-555 vesicles in sympathetic axons.

(D) WGA-555 vesicles in MAP2⁺ dendrites.

(E) Retrogradely trafficked WGA vesicles are co-localized with Flag-TrkA puncta in dendrites 16 hr postinjection.

(F) Retrogradely trafficked WGA vesicles are co-localized with P-TrkA puncta in dendrites 16 hr postinjection. (E) is same scale as (F).

(legend continued on next page)

compartment of SCG neurons we developed a procedure in which 1NMPP1 incorporated into poly-lactic-co-glycolic-acid (PLGA) microspheres is injected directly into the SCG (Figure 6A). PLGA microspheres are a biodegradable drug delivery vehicle that release incorporated molecules as they undergo hydrolysis in aqueous environments (Makadia and Siegel, 2011) and are thus ideal for sustained and local 1NMPP1 release. To ensure specificity of the approach, we performed a series of control experiments: First, we confirmed that PLGA-1NMPP1 microspheres effectively inhibit TrkA signaling in cultured sympathetic neurons obtained from *TrkA*^{F592A} mice but not wild-type mice (Figures S6E and S6I). Second, successful spatial inhibition of TrkA kinase activity and minimal effects from drug diffusion were confirmed in experiments that showed a dramatic loss of P-TrkA (Y785) puncta in neurons only within the injected ganglia, not in neurons of contralateral ganglia, of *TrkA*^{F592A} mice (Figure 6B), and no obvious differences in P-TrkA (Y785) levels in tyrosine hydroxylase (TH)-positive axons innervating the ipsilateral iris (Figure 6D). Third, we confirmed pharmacogenetic specificity of the approach by observing no inhibition of P-TrkA signaling in wild-type mice injected with PLGA-1NMPP1 microspheres or in *TrkA*^{F592A} mice injected with control microspheres (Figures 6C and S5A). Thus, 1NMPP1-loaded PLGA microspheres injected into the SCG enables specific inhibition of TrkA kinase activity exclusively within proximal axons, cell bodies, and dendrites of sympathetic neurons of the injected ganglion and not within distal axons or neighboring tissues.

Remarkably, inhibition of somatodendritic TrkA kinase activity for only 6–8 hr resulted in a marked reduction in the number of postsynaptic Homer1 puncta and presynaptic VAcHT puncta in injected ganglia as compared to uninjected, contralateral ganglia (Figures 6E, 6F, and 6G). Importantly, this reduction was observed only in *TrkA*^{F592A} mice, not in wild-type mice, injected with 1NMPP1-loaded microspheres (Figures 6E, 6F, 6G, and S5B). We next asked whether the decrease in SCG synapses following TrkA kinase inhibition in the somatodendritic compartment in vivo was associated with a corresponding functional disruption of SNS function. For this, we examined the eye region of treated animals because interruption of SNS circuitry results in ptosis, or eyelid droop, a symptom observed in patients with Horner's syndrome (Fields and Barker, 1992). Strikingly, ptosis was observed in the ipsilateral, but not contralateral eye of *TrkA*^{F592A} animals injected with 1NMPP1-loaded PLGA microspheres. This phenotype was not observed in mice injected with control microspheres or in wild-type mice receiving PLGA-1NMPP1 microspheres (Figures 6H, 6I, and S5I). These experiments demonstrate that local TrkA endosome signaling, within the somatodendritic compartment of sympathetic neurons, is necessary for the proper number of synaptic complexes associated with dendrites as well as for SNS function in vivo.

Local TrkA Kinase Activity within Dendrites Is Required for PSD Maintenance

Our findings revealed a requirement of retrograde NGF-TrkA signaling within cell bodies, dendrites, or both, for synapse maintenance in vivo. The presence of signaling-competent TrkA endosomes in dendrites and their close proximity to synapses in vivo and PSDs in vitro support the notion that TrkA endosome signaling within dendrites themselves promotes synapse maintenance. To distinguish between a requirement for TrkA endosome signaling in cell bodies or dendrites for synapse maintenance, we devised an experiment in which the effect of TrkA kinase activity inhibition solely within dendrites can be assessed. We adapted the use of 1NMPP1-loaded PLGA microspheres for in vitro microfluidic, compartmentalized sympathetic neuron experiments. To first test their efficacy, a large number of 1NMPP1-PLGA microspheres were applied exclusively to the somatodendritic compartment of cultured *TrkA*^{F592A} sympathetic neurons, thereby attaining sustained TrkA kinase inhibition within this compartment while simultaneously applying NGF solely to the distal-axon compartment. PLGA-1NMPP1 microspheres, but not control PLGA microspheres, eliminated P-TrkA (Y785) puncta observed in cell bodies and dendrites of *TrkA*^{F592A} sympathetic neurons (Figures S6E and S6G). Importantly, P-TrkA immunoreactivity, and thus TrkA signaling, was observed at normal levels in distal axons, indicating the spatial specificity of this approach (Figure S6D).

To achieve selective inhibition within dendritic locales, a limiting number of biotinylated PLGA-1NMPP1 microspheres was applied to the somatodendritic compartment of neurons grown on streptavidin-coated coverslips, thus anchoring the microspheres and ensuring release of 1NMPP1 in the same locations for the duration of the experiment (Figures 7A and 7B). Biotinylation did not alter the effectiveness of 1NMPP1-PLGA microspheres on TrkA^{F592A} kinase inhibition (Figure S6F). After 6–8 hr of biotinylated PLGA-1NMPP1 microsphere application, we measured the distance between the center of manually identified microspheres and fluorescent puncta above a specified intensity within dendrites. These experiments revealed a greater than 2-fold increase in the distance between the locations of PLGA-1NMPP1 microspheres and P-TrkA puncta compared to that of control PLGA microspheres and P-TrkA puncta (Figures 7C and 7E), indicating effective, local inhibition of TrkA kinase activities within small regions of dendrites. Importantly, the number of P-TrkA puncta within neuronal cell bodies in control and PLGA-1NMPP1 microsphere conditions was not significantly different (Figures 7D and 7G). We also ensured that these results were not skewed by a difference in the distance between the microspheres and dendrites in the control and drug conditions (Figures 7F and 7I).

Having shown that PLGA-1NMPP1 microspheres could be used as a platform of sustained, focal 1NMPP1 release to create

(G) Quantification of (E) and (F); n = 3 animals.

(H) 5- μ m sections of SCG tissue immunostained for Flag-TrkA and labeled with Hoechst (bottom), showing specific Flag puncta, not in wild-type (left) but only in *TrkA*^{Flag} (right) animals.

(I) 3- μ m sections of SCG tissue immunostained for P-TrkA (Y785) and MAP2 of both WT (left) and *TrkA*^{F592A} (right) animals treated with intraperitoneal (IP) injections of either vehicle (top) or 1NMPP1 (bottom). There is specific reduction of P-TrkA puncta in 1NMPP1-treated *TrkA*^{F592A} but not control animals. See also Figure S3.

Graphs are data presented as the mean, with errors bars representing \pm SEM.

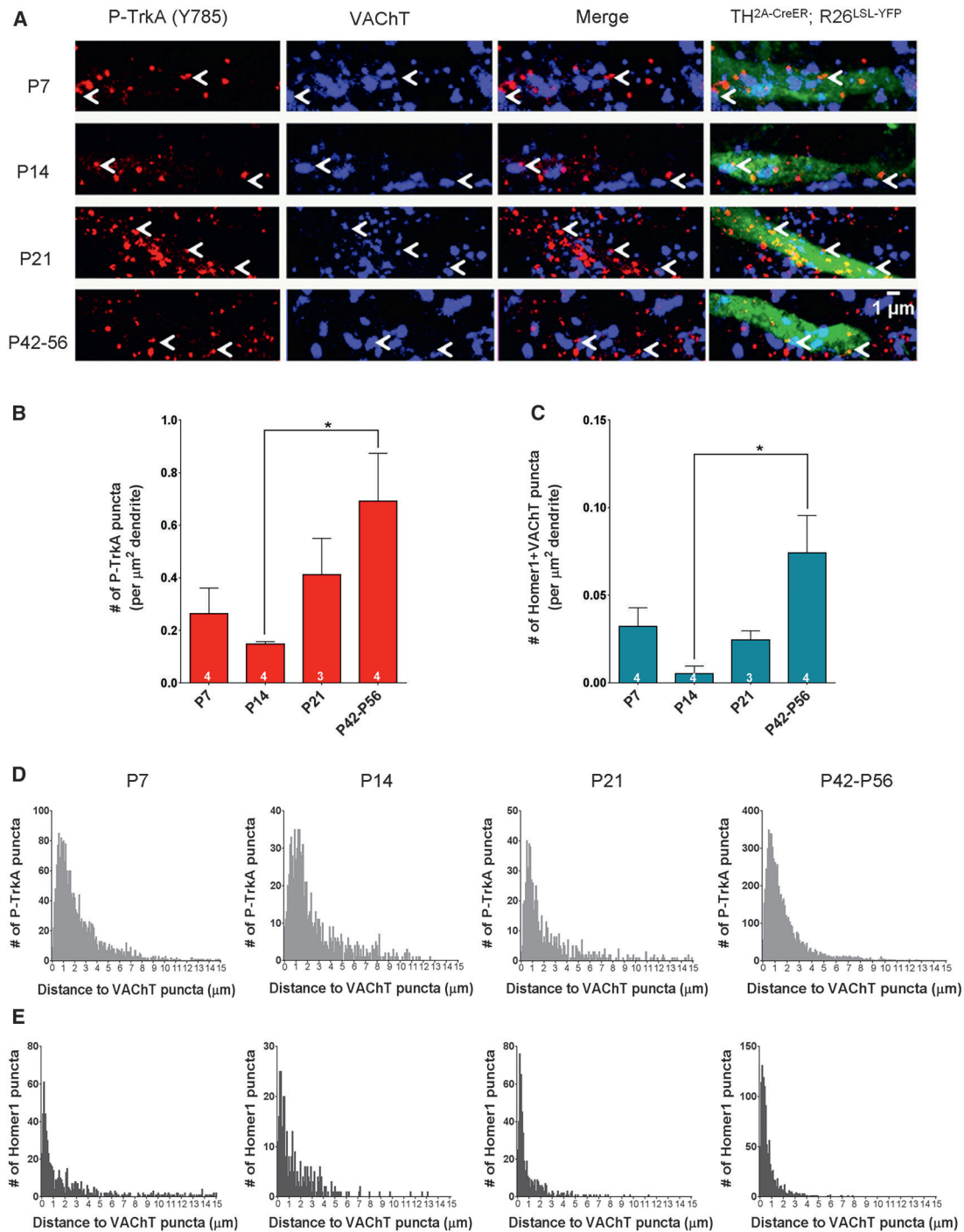


Figure 5. TrkA Signaling Endosomes Are Found in Dendrites and in Close Proximity to Synapses throughout Development In Vivo

(A) Dendrites of $TH^{2A-CreER};R26^{LSL-YFP}$ (Ai3) sparsely labeled cells in the SCG at developmental time points P7, P14, P21, and P42–P56 immunostained for P-TrkA (Y785) (left) and VAcHT (left middle). Arrowheads denote P-TrkA (Y785) puncta found in dendrites close to VAcHT puncta.

(B) Quantification of the number of P-TrkA puncta per square micrometer of labeled dendrite. One-way ANOVA, $F_{(3,11)} = 3.845$, $p < 0.05$; post hoc Tukey's multiple-comparison test: $*p < 0.05$.

(C) Quantification of the number of co-localized Homer1 and VAcHT puncta per square micrometer of labeled dendrite. One-way ANOVA, $F_{(3,11)} = 5.147$, $p < 0.05$; post hoc Tukey's multiple-comparison test: $*p < 0.05$.

(D) Histograms of the distance between P-TrkA puncta and the nearest VAcHT punctum within labeled dendrites.

(E) Histograms of the distance between Homer1 puncta and their nearest VAcHT punctum within labeled dendrites. (D and E) Bin size is $0.1 \mu\text{m}$. See also Figure S4. Graphs are data presented as the mean, with errors bars representing \pm SEM.

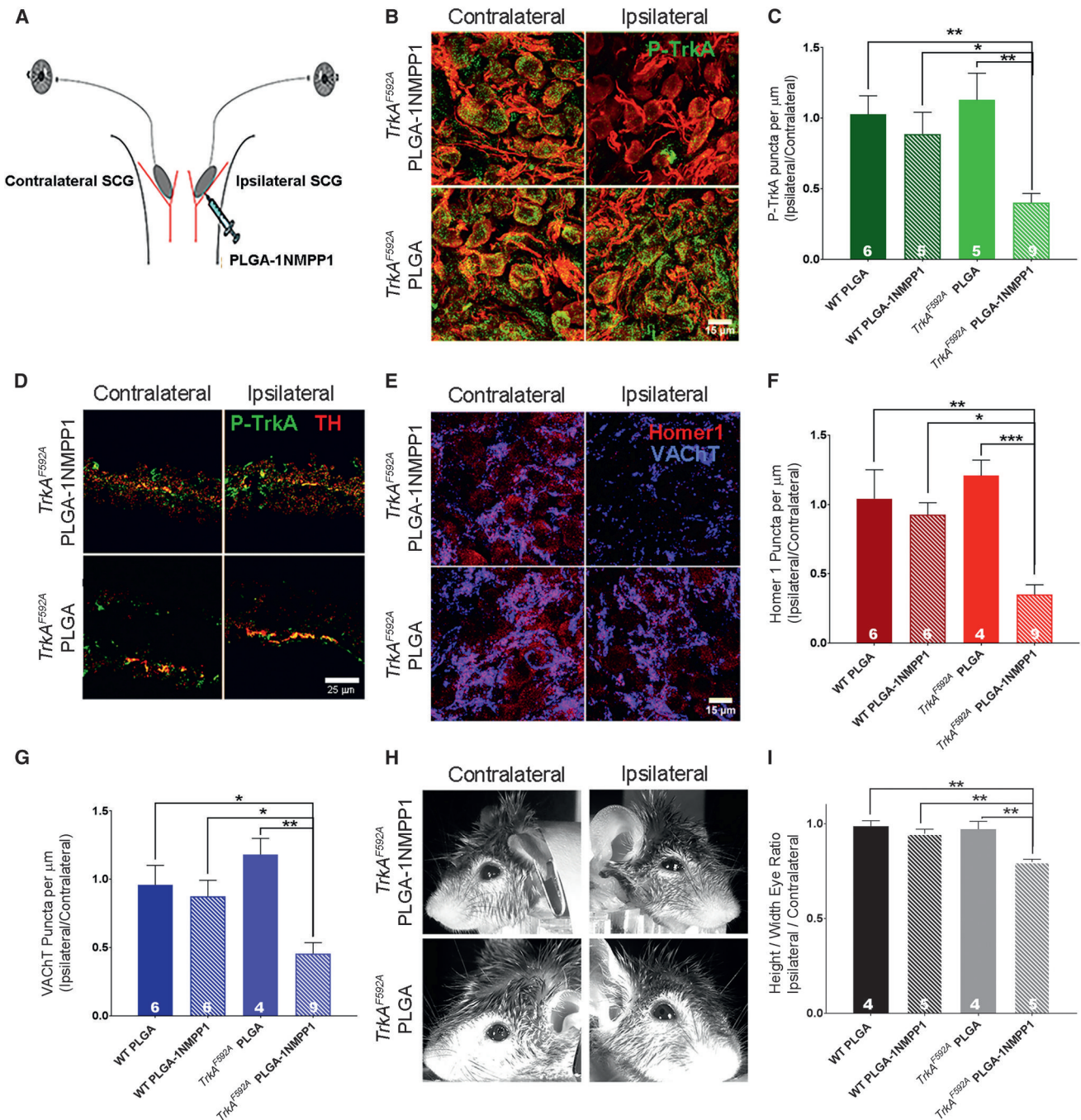


Figure 6. Somatodendritic TrkA Kinase Inhibition Results in Decreased Synaptic Puncta in the SCG

(A) Schematic of the assay used to inhibit TrkA signaling in the somatodendritic compartment of postganglionic neurons in vivo: injection of 1NMPP1-loaded PLGA microspheres into one (ipsilateral) SCG of *TrkA^{F592A}* mice. All analyses were performed 6–8 hr after injection.

(B) Reduction of P-TrkA puncta in the injected ganglion (right), but not the contralateral ganglion (left) of *TrkA^{F592A}* mice. No changes of P-TrkA level was observed in *TrkA^{F592A}* mice injected with control PLGA microspheres.

(C) Quantification of number of ipsilateral P-TrkA puncta compared to number of contralateral P-TrkA puncta in PLGA microsphere or PLGA-1NMPP1 microsphere-injected *TrkA^{F592A}* and wild-type (WT) mice. One-way ANOVA, $F_{(3,21)} = 8.091$, $p < 0.001$; post hoc Tukey's multiple-comparison test: $*p < 0.05$.

(D) Similar level of P-TrkA (Y785) staining in TH⁺ sympathetic axons innervating the iris was observed in both contralateral (left) and ipsilateral (right) target fields in *TrkA^{F592A}* mice injected with either PLGA microspheres or PLGA-1NMPP1 microspheres.

(E) Reduction of VAcHT and Homer1 puncta in the ipsilateral ganglion (right), but not the contralateral ganglion (left) of *TrkA^{F592A}* mice.

(legend continued on next page)

small pockets of local TrkA kinase inhibition, we next asked whether TrkA kinase signaling in dendrites, the soma, or both, is required to maintain PSD clusters. If P-TrkA signaling is necessary within dendrites to maintain PSDs, we would expect to find a decrease of MAGUK clusters in areas of TrkA kinase inhibition. Indeed, we found a significant increase in the distance from 1NMPP1 microspheres to the nearest MAGUK puncta within dendrites, compared to dendrites of neurons exposed to control microspheres (Figures 7C and 7H). Taken together, these findings indicate that distal-axon-derived TrkA endosome signaling within dendrites is necessary for maintenance of PSD clusters.

DISCUSSION

How synaptic connections are formed and maintained is a central question in neuroscience. Here, a live-cell imaging assay was used to reveal that TrkA endosome trafficking in sympathetic neuron axons, cell bodies, and dendrites is remarkably distinct with respect to kinetics of movement and directionality. Moreover, signaling-competent TrkA endosomes are often found within close proximity to synapses of sympathetic neuron dendrites *in vitro* as well as sympathetic neuron dendrites *in vivo*, throughout development. A chemical-genetic approach to locally inhibit TrkA kinase activity within the SCG *in vivo* was used to reveal the necessity of somatodendritic TrkA signaling for maintenance of both postsynaptic and presynaptic structures. The loss of somatodendritic TrkA signaling and synapses leads to ptosis, indicative of a deficit in SNS function. Importantly, spatially restricted chemical-genetic inhibition of TrkA signaling within dendrites *in vitro* showed that TrkA endosome signaling within sympathetic neuron dendrites supports the maintenance of PSD clusters. Together, our findings show that peripheral target fields govern synaptic connectivity between preganglionic and postganglionic sympathetic neurons through distal-axon-derived TrkA endosomes that traffic the entire length of postganglionic sympathetic neurons to signal locally, within their dendrites, to promote and maintain synapses (Figure S7).

TrkA Endosome Dynamics Reflect Function

We observed that TrkA endosomes in axons, cell bodies, and dendrites move in a markedly different manner. In agreement with quantum dot-NGF tracking studies in sensory neurons (Cui et al., 2007), we found that TrkA endosomes within sympathetic neuron axons move solely retrogradely and in a saltatory manner with highly variable rates and intermittent pauses. Within axons, NGF endosomes are actively transported along uniformly oriented microtubules (Maday et al., 2014) by the motor protein dynein (Heerssen et al., 2004). In contrast to movement dy-

namics observed in axons, we found bidirectional movement of distal-axon-derived TrkA endosomes within dendrites. Presuming the motor protein dynein underlies dendritic endosome trafficking, the bidirectionality of TrkA endosomes within dendrites may be explained by the mixed polarity of microtubules within that cellular compartment (Baas et al., 1991; Yau et al., 2016). Thus, we speculate that the distinct movement dynamics of TrkA endosomes within different cellular compartments reflects differences in cytoskeletal organization and dynein-microtubule interactions. Also, in contrast to axonal endosomal movement, TrkA endosomes in dendrites exhibit frequent oscillatory pauses in relatively small areas of the dendrite. Examination of mitochondrial motility has revealed similar findings; mitochondria in dendrites have a smaller excursion length than those in axons, which may be reflective of higher metabolic demands within dendrites (Li et al., 2004; Overly et al., 1996). It is likely that TrkA endosome dynamics also reflect functional requirements within different regions of the cell; the unidirectional and processive movement of TrkA endosomes in axons may reflect the necessity of retrograde transport to cell bodies to support somatic signaling, gene expression, and survival, whereas the movement of TrkA endosomes in dendrites may reflect their function in that compartment for promoting and maintaining clustering of PSD proteins at synapses.

An interesting observation is that a substantial number of dendritically localized TrkA endosomes (~25%) are stationary. These endosomes may be targeted for degradation, and, consistent with this, stationary mitochondria in neuronal processes are thought to be targeted for proteasomal degradation upon disengagement from motor complexes (Wang et al., 2011). Alternatively, stationary TrkA puncta in dendrites may reflect receptors that have been re-inserted or anchored to the plasma membrane (K.M.L. and D.D.G., unpublished data); some of these are phospho-TrkA positive, which suggests they could act as signaling platforms to recruit PSD proteins. Further work addressing how the signaling state of TrkA endosomes affects their metabolism and dynamics may clarify this issue and provide insight into how TrkA endosome movement within dendrites corresponds to function. Noting that the maintenance of retrograde transport of NGF-containing endosomes in axons is independent of TrkA kinase activity (Ye et al., 2003), it will be interesting in the future to determine whether non-phosphorylated TrkA endosomes in dendrites are halted or return to the soma, and whether re-phosphorylation results in active movement or targeted transportation to dendrites. The present work indicates that endosomes of the same origin move differently depending on their cellular location, which likely reflects distinct states of TrkA activity and distinct functions within different regions of the neuron.

(F and G) Quantification of number of ipsilateral SCG Homer1 (F) and VACHT (G) puncta compared to the number of contralateral SCG Homer1 (F) and VACHT (G) puncta in either PLGA microsphere or PLGA-1NMPP1 microsphere-injected *TrkA^{F592A}* and WT mice. Homer1: one-way ANOVA, $F_{(3,21)} = 10.06$, $p < 0.0005$; post hoc Tukey's multiple-comparison test: * $p < 0.05$. VACHT: one-way ANOVA, $F_{(3,21)} = 10.06$, $p < 0.005$, post hoc Tukey's multiple-comparison test: * $p < 0.05$. (H) Representative images of ptosis in ipsilateral eyes compared to contralateral of PLGA microsphere or PLGA-1NMPP1 microsphere-injected *TrkA^{F592A}* mice. (I) Quantification of ptosis (ratio of height over width of the eye) comparing the ipsilateral eye to the contralateral eye. One-way ANOVA, $F_{(3,14)} = 10.64$, $p < 0.001$; post hoc Tukey's multiple-comparison test: * $p < 0.05$. See also Figure S5. Graphs are data presented as the mean, with errors bars representing \pm SEM.

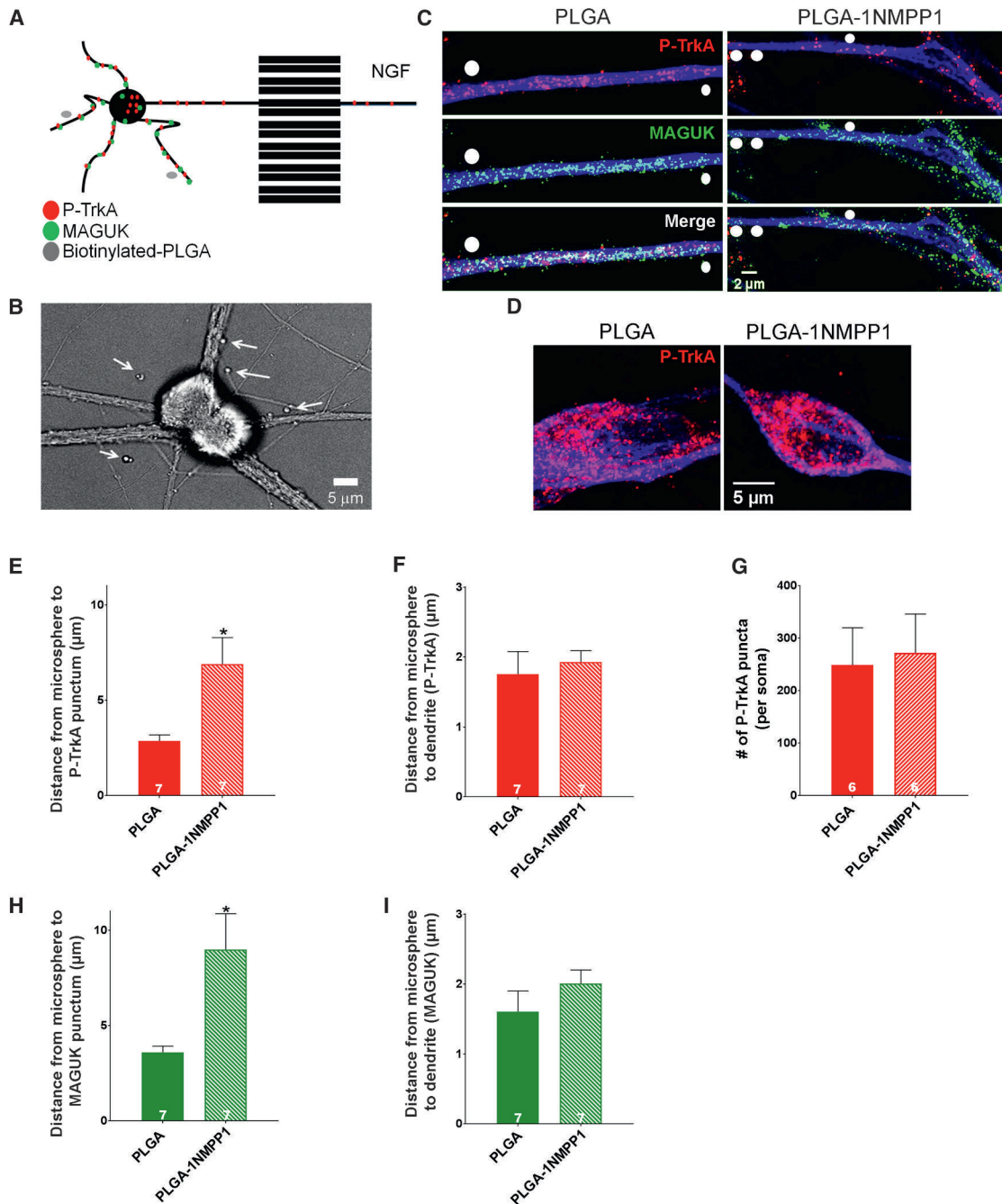


Figure 7. Distal-Axon-Derived TrkA Signals Locally, within Dendrites, to Maintain PSDs in Sympathetic Neurons

(A) Biotinylated-PLGA-1NMPP1 microspheres were applied to the somatodendritic compartment of DIV 14 compartmentalized *TrkA*^{F592A} sympathetic neurons on coverslips precoated with streptavidin while NGF was applied to distal axons to achieve localized TrkA kinase inhibition pockets adjacent to dendrites.

(B) Bright-field image of SCG neurons. Arrows denote PLGA-1NMPP1 microspheres.

(C) P-TrkA and MAGUK puncta in dendrites of neurons treated with PLGA (left) or PLGA-1NMPP1 (right) microspheres. White circles are drawn over microspheres.

(D) P-TrkA puncta in soma of neurons treated with PLGA (left) or PLGA-1NMPP1 (right) microspheres, quantified in (G).

(E and H) Quantification of the distance between PLGA or PLGA-1NMPP1 microspheres and the nearest P-TrkA (D) or MAGUK (G) punctum; Welch's t test, * $p < 0.05$.

(F and I) Quantification of the distance between each PLGA microspheres and dendrite mask per experiment. See also Figure S6.

Graphs are data presented as the mean, with errors bars representing \pm SEM.

Long-Distance Endosome Transport and Signaling in Dendrites May Provide a General Mechanism of Circuit Regulation

Our findings reveal a mechanism of neural circuit modification: target fields supply NGF to distal axons, initiating the formation of TrkA endosomes that are trafficked from axons into the cell body, and a subset move into dendrites where they signal locally to promote formation and maintenance of PSD clusters. NGF/TrkA signaling promotes PSD clustering in sympathetic neurons in a manner that is both independent of transcription (Sharma et al., 2010) and remarkably rapid (within 3 hr); however, the precise signals emanating from TrkA endosomes to support PSD formation remain to be elucidated. We observed that TrkA endosomes in dendrites are likely to signal through multiple downstream effector pathways; dendritic TrkA endosomes contain phosphorylated TrkA tyrosine residues 785 and 490, which associate with distinct sets of effectors and thus diversify the nature of the signal emanating from dendritic TrkA endosomes. It is noteworthy that our *in vivo* experiments that analyzed retrogradely trafficked WGA vesicles point to the presence of non-TrkA-positive distal-axon-derived vesicles. We speculate that these may contain additional signals that instruct sympathetic neuron development, dendritic growth, and synaptic connectivity. Members of the bone morphogenetic protein (BMP) family are candidates for these processes, as they appear to contribute to sympathetic neuron dendrite length and complexity during developmental and adult periods (Majdazari et al., 2013). Thus, in addition to NGF, local signaling by other target-derived cues within dendrites may provide a general mechanism by which target fields instruct dendrite and synapse development and maintenance throughout the nervous system.

Local TrkA Signaling, within Dendrites, Is Necessary for Synapse Maintenance and Function

Building on research implicating target-derived NGF in sympathetic neuron axon growth and target field innervation, survival, and synapse formation, the present work reveals a mechanism by which peripheral target fields regulate synaptic connectivity within the SNS. We found that the number of P-TrkA puncta within dendrites is correlated with the number of synapses during development. Moreover, using a spatially restricted and specific TrkA inhibition paradigm, we found that TrkA signaling within the SCG is essential for both presynaptic and postsynaptic specializations. In addition, blocking TrkA signaling within the SCG, thereby disrupting synapses, has readily apparent consequences—ptosis, a hallmark symptom of the SNS disorder Horner's syndrome. Remarkably, both the decrease in synapse number and the ptosis phenotype resulting from TrkA inhibition within the ganglion were observed within 6–8 hr, emphasizing the importance of continual TrkA signaling in the somatodendritic compartment for SNS circuit function. These findings indicate that NGF-TrkA signaling is required *in vivo*, in the SCG itself, for proper functioning of postganglionic sympathetic neurons. This, together with the *in vitro* findings indicating a requirement of TrkA signaling within dendrites for PSD maintenance, supports a model whereby target field regulation of TrkA signaling within dendrites controls synapse development and maintenance,

and possibly plasticity, thereby ensuring the proper function of SNS circuits.

This type of synaptic regulation controlled by target fields of sympathetic neurons may be at play in other neural circuits. Cholinergic neurons of the basal forebrain, for example, rely on target-derived NGF signaling for maintenance of their biochemical and anatomical phenotype (Cuello et al., 2010; Parikh et al., 2013), and knockdown of TrkA expression results in Alzheimer's disease (AD)-like symptoms in aged mice (Parikh et al., 2013; Sanchez-Ortiz et al., 2012). Investigating synapses that form upon forebrain cholinergic neurons may yield insight into the role retrograde NGF-TrkA signaling plays in preserving cholinergic neuron circuit function. As cholinergic neuron dysfunction in the CNS is implicated in aging disorders such as AD as well as developmental disorders such as Down syndrome (Schliebs and Arendt, 2011), how synapses of cholinergic forebrain neurons are formed and maintained by target fields may prove an important area of future research. Furthermore, many autism spectrum disorder and schizophrenia etiologies involve disruption of synapses, and more specifically, aberrant PSD proteins within developing circuits (de Bartolomeis et al., 2014). Thus, an exciting direction will be to determine the role of local dendritic signaling, orchestrated by trophic cues derived from target fields, in synapse development and maintenance within CNS circuits under both normal and disease states.

EXPERIMENTAL PROCEDURES

Animal Studies

Mice were handled and housed in accordance with Harvard Medical School and Johns Hopkins University Institutional Animal Care and Use Committee (IACUC) guidelines.

Compartmentalized Sympathetic Neuron Experiments

Dissociated SCG neurons were prepared (Wickramasinghe et al., 2008; Ye et al., 2003) and grown in microfluidic chambers as described (Park et al., 2006). The fixed-cell Flag-TrkA transport assay was performed as described previously (Sharma et al., 2010). The live-cell Flag-TrkA trafficking imaging assay used the Flag antibody (either M1 [1 μ g/mL] or FlagM1-FAB [6 μ g/mL]) incubated with 2 μ g/mL Alexa Fluor secondary antibody, diluted in DMEM, for 1 hr at room temperature on a shaker, prior to application to distal axons and imaging. Imaging was done using a Yokogawa spinning-disk microscope (Zeiss) or the Harvard Neurodiscovery Center Enhanced Neuroimaging Core Andor Revolution Spinning-Disk Microscope, using fast piezo Z sectioning (Prior piezo stage with 250- μ m travel; Z250). Trafficking analysis was done by manual tracking of individual endosomes using either IMARIS spot tracking or an ImageJ TTrackJ plugin (Meijering et al., 2012).

Eye Injections

Eye injections for retrograde-labeling experiments were done using male mice (P21) anesthetized via continuous inhalation of isoflurane (1%–3%) from a precision vaporizer for the 10-min duration of the surgery. Sixteen hours following surgery, animals were euthanized, SCGs were removed, and standard IHC procedures were followed.

1NMPP1 PLGA Microsphere Experiments

Control (Phosphorex; PLGA 50:50, 5- μ m diameter) and 1NMPP1-loaded microspheres (Phosphorex; PLGA 50:50, 11.5% 1NMPP1 loading, 3- μ m diameter) were biotinylated, and applied to cell body and dendrite compartments of sympathetic neurons grown on coverslips plated with streptavidin. After 1 hr, cultures were washed with DMEM to remove unbound microspheres. NGF was then applied to distal axons, and cultures were incubated at 37°C for the duration of the experiment (6–8 hr). Cultures were then fixed

and used for ICC using standard procedures. For in vivo SCG injections of PLGA-1NMPP1 microspheres, a Hamilton syringe was used to inject 1–5 μ L of 0.5-mg microspheres diluted in 10 mL of 0.9% saline: either control (Phosphorex; PLGA 50:50, 5- μ m diameter) or 1NMPP1-loaded PLGA microspheres (Phosphorex; PLGA 50:50, 11.5% 1NMPP1 loading, 3- μ m diameter) were injected. Six to 8 hr following surgery, animals were sacrificed, and SCGs were removed and processed for IHC.

Statistical Analysis

Statistical analysis was done using GraphPad Prism 6 software. Comparisons between two groups were done using Student's *t* test, unless otherwise reported. Non-significant *p* values are not reported. Data are presented as mean \pm SEM, and numbers per group are represented in bars or legends of each panel.

SUPPLEMENTAL INFORMATION

Supplemental Information includes Supplemental Experimental Procedures, seven figures, and five movies and can be found with this article online at <http://dx.doi.org/10.1016/j.celrep.2017.03.028>.

AUTHOR CONTRIBUTIONS

K.M.L. and D.D.G. conceived the study. K.M.L. developed the Flag-TrkA live-cell imaging assay and the use of 1NMPP1-loaded microspheres for both SCG injection assay and local dendritic inhibition assay and performed all experiments and analysis with assistance from K.M.W. for genotyping, tissue preparation, IHC, and image analysis. K.M.L. and D.D.G. wrote the paper with editing by K.M.W.

ACKNOWLEDGMENTS

We thank Clinton Cave, Chenghua Gu, Tracy Huang, David Paul, and members of the D.D.G. laboratory for discussion and comments on the manuscript. We thank Amanda Zimmerman (HMS) for use of *TH^{2A-CreER}* mouse line. We thank Mollie Meffert (JHMI) for use of the Yokogawa spinning-disk confocal microscope, Michele Pucak of the JHMI Multiphoton Imaging Core, Lai Ding and Daniel Tom of the Harvard NeuroDiscovery Center, and Michelle Ocana of the HMS Neurobiology Imaging Facility for microscope training and advice on imaging and analysis. We thank Hunter Elliott of the Harvard IDAC Core for image analysis advice and the close proximity script. We thank William Colgan (HMS) and Daniel Tom for creating ImageJ macros for puncta analysis and microsphere analysis, respectively. We thank the Harvard Research Instrumentation Core for equipment. We thank Huy Vo of the Johns Hopkins BME Machine Shop for microfluidic device advice and fabrication. This work was supported by NIH Grant NS097344 (D.D.G.) and an IES Brain Research Foundation Fellowship (K.M.W.). D.D.G. is an Investigator of the Howard Hughes Medical Institute.

Received: October 3, 2016

Revised: February 10, 2017

Accepted: March 7, 2017

Published: April 4, 2017

REFERENCES

Abraira, V.E., Kuehn, E.D., Chirila, A.M., Springel, M.W., Toliver, A.A., Zimmerman, A.L., Orefice, L.L., Boyle, K.A., Bai, L., Song, B.J., et al. (2017). The cellular and synaptic architecture of the mechanosensory dorsal horn. *Cell* 168, 295–310.e19.

Baas, P.W., Slaughter, T., Brown, A., and Black, M.M. (1991). Microtubule dynamics in axons and dendrites. *J. Neurosci. Res.* 30, 134–153.

Barford, K., Deppmann, C., and Winckler, B. (2016). The neurotrophin receptor signaling endosome: where trafficking meets signaling. *Dev. Neurobiol.* Published online February 24, 2017. <http://dx.doi.org/10.1002/dneu.22427>.

Campenot, R.B. (1977). Local control of neurite development by nerve growth factor. *Proc. Natl. Acad. Sci. USA* 74, 4516–4519.

Chen, X., Ye, H., Kuruvilla, R., Ramanan, N., Scangos, K.W., Zhang, C., Johnson, N.M., England, P.M., Shokat, K.M., and Ginty, D.D. (2005). A chemical-genetic approach to studying neurotrophin signaling. *Neuron* 46, 13–21.

Cuello, A.C., Bruno, M.A., Allard, S., Leon, W., and Iulita, M.F. (2010). Cholinergic involvement in Alzheimer's disease. A link with NGF maturation and degradation. *J. Mol. Neurosci.* 40, 230–235.

Cui, B., Wu, C., Chen, L., Ramirez, A., Bearer, E.L., Li, W.P., Mobley, W.C., and Chu, S. (2007). One at a time, live tracking of NGF axonal transport using quantum dots. *Proc. Natl. Acad. Sci. USA* 104, 13666–13671.

de Bartolomeis, A., Latte, G., Tomasetti, C., and Iasevoli, F. (2014). Glutamatergic postsynaptic density protein dysfunctions in synaptic plasticity and dendritic spines morphology: relevance to schizophrenia and other behavioral disorders pathophysiology, and implications for novel therapeutic approaches. *Mol. Neurobiol.* 49, 484–511.

Fields, C.R., and Barker, F.M., 2nd. (1992). Review of Horner's syndrome and a case report. *Optom. Vis. Sci.* 69, 481–485.

Glebova, N.O., and Ginty, D.D. (2004). Heterogeneous requirement of NGF for sympathetic target innervation in vivo. *J. Neurosci.* 24, 743–751.

Harrington, A.W., St Hillaire, C., Zweifel, L.S., Glebova, N.O., Philippidou, P., Haleboua, S., and Ginty, D.D. (2011). Recruitment of actin modifiers to TrkA endosomes governs retrograde NGF signaling and survival. *Cell* 146, 421–434.

Heath, J.W., Glenfield, P.J., and Rostas, J.A. (1992). Structural maturation of synapses in the rat superior cervical ganglion continues beyond four weeks of age. *Neurosci. Lett.* 142, 17–21.

Heerssen, H.M., Pazyra, M.F., and Segal, R.A. (2004). Dynein motors transport activated Trks to promote survival of target-dependent neurons. *Nat. Neurosci.* 7, 596–604.

Hendry, I.A., Stöckel, K., Thoenen, H., and Iversen, L.L. (1974). The retrograde axonal transport of nerve growth factor. *Brain Res.* 68, 103–121.

Heumann, R., Korsching, S., Scott, J., and Thoenen, H. (1984). Relationship between levels of nerve growth factor (NGF) and its messenger RNA in sympathetic ganglia and peripheral target tissues. *EMBO J.* 3, 3183–3189.

Hu, Y.B., Dammer, E.B., Ren, R.J., and Wang, G. (2015). The endosomal-lysosomal system: from acidification and cargo sorting to neurodegeneration. *Transl. Neurodegener.* 4, 18.

Huang, S., O'Donovan, K.J., Turner, E.E., Zhong, J., and Ginty, D.D. (2015). Extrinsic and intrinsic signals converge on the Runx1/CBF β transcription factor for nonpeptidergic nociceptor maturation. *eLife* 4, e10874.

Jiang, X., and Nardelli, J. (2016). Cellular and molecular introduction to brain development. *Neurobiol. Dis.* 92 (Pt A), 3–17.

Kuruvilla, R., Ye, H., and Ginty, D.D. (2000). Spatially and functionally distinct roles of the PI3-K effector pathway during NGF signaling in sympathetic neurons. *Neuron* 27, 499–512.

Kuruvilla, R., Zweifel, L.S., Glebova, N.O., Lonze, B.E., Valdez, G., Ye, H., and Ginty, D.D. (2004). A neurotrophin signaling cascade coordinates sympathetic neuron development through differential control of TrkA trafficking and retrograde signaling. *Cell* 118, 243–255.

Levi-Montalcini, R., and Booker, B. (1960). Destruction of the sympathetic ganglia in mammals by an antiserum to a nerve-growth protein. *Proc. Natl. Acad. Sci. USA* 46, 384–391.

Li, Z., Okamoto, K., Hayashi, Y., and Sheng, M. (2004). The importance of dendritic mitochondria in the morphogenesis and plasticity of spines and synapses. *Cell* 119, 873–887.

Maday, S., Twelvetrees, A.E., Moughamian, A.J., and Holzbaur, E.L. (2014). Axonal transport: cargo-specific mechanisms of motility and regulation. *Neuron* 84, 292–309.

Majdazari, A., Stubbusch, J., Müller, C.M., Hennchen, M., Weber, M., Deng, C.X., Mishina, Y., Schütz, G., Deller, T., and Rohrer, H. (2013). Dendrite complexity of sympathetic neurons is controlled during postnatal development by BMP signaling. *J. Neurosci.* 33, 15132–15144.

- Makadia, H.K., and Siegel, S.J. (2011). Poly lactic-co-glycolic acid (PLGA) as biodegradable controlled drug delivery carrier. *Polymers (Basel)* *3*, 1377–1397.
- Meijering, E., Dzyubachyk, O., and Smal, I. (2012). Methods for cell and particle tracking. *Methods Enzymol.* *504*, 183–200.
- Njå, A., and Purves, D. (1978). The effects of nerve growth factor and its anti-serum on synapses in the superior cervical ganglion of the guinea-pig. *J. Physiol.* *277*, 53–75.
- Overly, C.C., Rieff, H.I., and Hollenbeck, P.J. (1996). Organelle motility and metabolism in axons vs dendrites of cultured hippocampal neurons. *J. Cell Sci.* *109*, 971–980.
- Parikh, V., Howe, W.M., Welchko, R.M., Naughton, S.X., D'Amore, D.E., Han, D.H., Deo, M., Turner, D.L., and Sarter, M. (2013). Diminished trkA receptor signaling reveals cholinergic-attentional vulnerability of aging. *Eur. J. Neurosci.* *37*, 278–293.
- Park, J.W., Vahidi, B., Taylor, A.M., Rhee, S.W., and Jeon, N.L. (2006). Microfluidic culture platform for neuroscience research. *Nat. Protoc.* *1*, 2128–2136.
- Riccio, A., Pierchala, B.A., Ciarallo, C.L., and Ginty, D.D. (1997). An NGF-TrkA-mediated retrograde signal to transcription factor CREB in sympathetic neurons. *Science* *277*, 1097–1100.
- Ruit, K.G., and Snider, W.D. (1991). Administration or deprivation of nerve growth factor during development permanently alters neuronal geometry. *J. Comp. Neurol.* *314*, 106–113.
- Ruit, K.G., Osborne, P.A., Schmidt, R.E., Johnson, E.M., Jr., and Snider, W.D. (1990). Nerve growth factor regulates sympathetic ganglion cell morphology and survival in the adult mouse. *J. Neurosci.* *10*, 2412–2419.
- Sanchez-Ortiz, E., Yui, D., Song, D., Li, Y., Rubenstein, J.L., Reichardt, L.F., and Parada, L.F. (2012). TrkA gene ablation in basal forebrain results in dysfunction of the cholinergic circuitry. *J. Neurosci.* *32*, 4065–4079.
- Schliebs, R., and Arendt, T. (2011). The cholinergic system in aging and neuronal degeneration. *Behav. Brain Res.* *221*, 555–563.
- Senger, D.L., and Campenot, R.B. (1997). Rapid retrograde tyrosine phosphorylation of trkA and other proteins in rat sympathetic neurons in compartmented cultures. *J. Cell Biol.* *138*, 411–421.
- Sharma, N., Deppmann, C.D., Harrington, A.W., St Hillaire, C., Chen, Z.Y., Lee, F.S., and Ginty, D.D. (2010). Long-distance control of synapse assembly by target-derived NGF. *Neuron* *67*, 422–434.
- Smolen, A., and Raisman, G. (1980). Synapse formation in the rat superior cervical ganglion during normal development and after neonatal deafferentation. *Brain Res.* *181*, 315–323.
- Sofroniew, M.V., Howe, C.L., and Mobley, W.C. (2001). Nerve growth factor signaling, neuroprotection, and neural repair. *Annu. Rev. Neurosci.* *24*, 1217–1281.
- Taylor, A.M., Dieterich, D.C., Ito, H.T., Kim, S.A., and Schuman, E.M. (2010). Microfluidic local perfusion chambers for the visualization and manipulation of synapses. *Neuron* *66*, 57–68.
- Tsui-Pierchala, B.A., and Ginty, D.D. (1999). Characterization of an NGF-P-TrkA retrograde-signaling complex and age-dependent regulation of TrkA phosphorylation in sympathetic neurons. *J. Neurosci.* *19*, 8207–8218.
- Voyvodic, J.T. (1987). Development and regulation of dendrites in the rat superior cervical ganglion. *J. Neurosci.* *7*, 904–912.
- Wang, X., Winter, D., Ashrafi, G., Schlehe, J., Wong, Y.L., Selkoe, D., Rice, S., Steen, J., LaVoie, M.J., and Schwarz, T.L. (2011). PINK1 and Parkin target Miro for phosphorylation and degradation to arrest mitochondrial motility. *Cell* *147*, 893–906.
- Watson, F.L., Heerssen, H.M., Moheban, D.B., Lin, M.Z., Sauvageot, C.M., Bhattacharyya, A., Pomeroy, S.L., and Segal, R.A. (1999). Rapid nuclear responses to target-derived neurotrophins require retrograde transport of ligand-receptor complex. *J. Neurosci.* *19*, 7889–7900.
- Wickramasinghe, S.R., Alvania, R.S., Ramanan, N., Wood, J.N., Mandai, K., and Ginty, D.D. (2008). Serum response factor mediates NGF-dependent target innervation by embryonic DRG sensory neurons. *Neuron* *58*, 532–545.
- Yau, K.W., Schätzle, P., Tortosa, E., Pagès, S., Holtmaat, A., Kapitein, L.C., and Hoogenraad, C.C. (2016). Dendrites in vitro and in vivo contain microtubules of opposite polarity and axon formation correlates with uniform plus-end-out microtubule orientation. *J. Neurosci.* *36*, 1071–1085.
- Ye, H., Kuruvilla, R., Zweifel, L.S., and Ginty, D.D. (2003). Evidence in support of signaling endosome-based retrograde survival of sympathetic neurons. *Neuron* *39*, 57–68.

Ligl1 Connects Cell Polarity with Cell-Cell Adhesion in Embryonic Neural Stem Cells

Yves Jossin,^{1,5,7,*} Minhui Lee,^{2,3,7} Olga Klezovitch,^{2,7} Elif Kon,⁵ Alexia Cossard,⁵ Wen-Hui Lien,^{2,3,6} Tania E. Fernandez,² Jonathan A. Cooper,^{1,3} and Valera Vasioukhin^{2,3,4,8,*}

¹Division of Basic Sciences

²Division of Human Biology

Fred Hutchinson Cancer Research Center, Seattle, WA 98109, USA

³Molecular and Cellular Biology Program

⁴Department of Pathology, Institute for Stem Cell and Regenerative Medicine

University of Washington, Seattle, WA 98195, USA

⁵Mammalian Development & Cell Biology Unit, Institute of Neuroscience, Université Catholique de Louvain, 1200 Brussels, Belgium

⁶Present address: de Duve Institute, Université Catholique de Louvain, 1200 Brussels, Belgium

⁷These authors contributed equally

⁸Lead Contact

*Correspondence: yves.jossin@uclouvain.be (Y.J.), vvasiouk@fhcrc.org (V.V.)

<http://dx.doi.org/10.1016/j.devcel.2017.05.002>

SUMMARY

Malformations of the cerebral cortex (MCCs) are devastating developmental disorders. We report here that mice with embryonic neural stem-cell-specific deletion of *Ligl1* (*Nestin-Cre/Ligl1^{fl/fl}*), a mammalian ortholog of the *Drosophila* cell polarity gene *lgl*, exhibit MCCs resembling severe periventricular heterotopia (PH). Immunohistochemical analyses and live cortical imaging of PH formation revealed that disruption of apical junctional complexes (AJCs) was responsible for PH in *Nestin-Cre/Ligl1^{fl/fl}* brains. While it is well known that cell polarity proteins govern the formation of AJCs, the exact mechanisms remain unclear. We show that LLGL1 directly binds to and promotes internalization of N-cadherin, and N-cadherin/LLGL1 interaction is inhibited by atypical protein kinase C-mediated phosphorylation of LLGL1, restricting the accumulation of AJCs to the basolateral-apical boundary. Disruption of the N-cadherin-LLGL1 interaction during cortical development *in vivo* is sufficient for PH. These findings reveal a mechanism responsible for the physical and functional connection between cell polarity and cell-cell adhesion machineries in mammalian cells.

INTRODUCTION

The cerebral cortex is a highly organized brain structure responsible for acquisition and processing of information. During normal cortical development, embryonic neural stem cells (ENSCs) localize to the ventricular surface and organize into a pseudostratified epithelium. These cells are highly polarized with their cell bodies close to the ventricle and their long cytoplasmic processes extending radially away from the ventricle to the pial surface of the cortex. ENSCs are connected by prom-

inent cell-cell adhesion structures called apical junctional complexes (AJCs) (Chenn et al., 1998). ENSCs divide asymmetrically in a stem-cell-like fashion to replenish themselves and to give rise to immature neurons, which are committed to differentiation. These daughter cells are guided by radial glia processes to migrate away from the ventricular zone and eventually differentiate to become neurons.

Abnormalities in this well-orchestrated process of cerebral cortical development lead to malformations of the cerebral cortex (MCCs), which are leading causes of drug-resistant epilepsies, intellectual disability, and other cognitive disorders (Mochida and Walsh, 2004). Primary cellular defects leading to MCCs range from disorders of cell proliferation and cell survival (genetic microcephaly syndromes) to defects in the integrity of the pial surface (cobblestone dysplasia) (Mochida and Walsh, 2004). A large proportion of MCCs, including classical lissencephaly, lissencephaly with cerebellar hypoplasia, X-linked lissencephaly with abnormal genitalia, subcortical band heterotopia (SBH), and periventricular heterotopia (PH), exhibit abnormal localization of cortical neurons (Francis et al., 2006; Mochida and Walsh, 2004). PH is characterized by ectopic deposition of neurons at the lateral ventricle, which is distinct from SBH displaying ectopic layer of neurons separated from the lateral ventricle by a layer of white matter.

While the dynamics and mechanisms of PH are not completely understood, it is believed that impaired migration from the ventricular zone, abnormal proliferation and differentiation, or disruption of the integrity of the neuroepithelium are responsible for this MCC (Lian and Sheen, 2015). Inactivating mutations in human Filamin A (*FLNA*), a large actin-binding protein, are responsible for X-linked bilateral PH in females suffering from epilepsy (Fox et al., 1998). *FLNA* is responsible for cross-linking cortical actin into a three-dimensional structure and connecting the actin cytoskeleton to the plasma membrane. Both functions are critical for changes in cell shape, cell adhesion, and migration (Feng and Walsh, 2004). A microcephaly-associated variant of PH is caused by mutations in *ARFGEF2* (Sheen et al., 2004). *ARFGEF2* is required for vesicle trafficking from the *trans*-Golgi network and is necessary for proper membrane delivery of E-cadherin/ β -catenin components

of the junctional complex in MDCK cells (Sheen et al., 2004). In addition, mutations in genes encoding the receptor-ligand cadherin pair DCHS1 and FAT4 result in abnormal ENSC accumulation, resulting in PH (Cappello et al., 2013).

To explore the role of cell polarity mechanisms in mammalian brain development, we examined the functional significance of the cell polarity protein Lethal giant larvae (Lgl). Lgl is an evolutionarily conserved WD40 domain-containing protein that plays a critical role in the maintenance of cell polarity downstream of the Par3/Par6/aPKC cell polarity complex and Disheveled, an essential mediator of Wnt signaling (Betschinger et al., 2003; Dollar et al., 2005). Studies in *Drosophila* revealed that Lgl regulates cell polarity by maintaining the identity of the basal and lateral membrane domain by counteracting the activity of the Par3/Par6/aPKC and Crumbs/Stardust-Patj protein complexes responsible for maintenance of the apical membrane domain (Tanentzapf and Tepass, 2003; Yamanaka et al., 2003). When activated by Cdc42, aPKC phosphorylates and inactivates Lgl at the apical side, while active nonphosphorylated Lgl at the basolateral side excludes Par6/Par3 from the cellular cortex (Betschinger et al., 2003, 2005; Plant et al., 2003).

Mammalian genomes contain two Lgl homologs, *Lgl1* and *Lgl2* (Sripathy et al., 2011; Vasioukhin, 2006). *Lgl1*^{-/-} mice display severe brain disorganization and hemorrhagic hydrocephalus leading to neonatal death (Klezovitch et al., 2004). To rescue hydrocephalus and analyze the role of *Lgl1* in the adult brain, we used a conditional knockout approach deleting *Lgl1* in ENSCs. The mutant mice show symptoms of epilepsy, and their brains display ectopic deposition of neurons at the ventricular surface, which resembles severe cases of PH. Analyses of *Lgl1* cKO brains reveal decreased size of the AJCs in ENSCs leading to focal disruption of neuroepithelium, formation of neuroepithelial rosettes, and internalization of ENSCs into the developing cortex. Internalized *Lgl1* cKO ENSCs produce neurons ectopically toward the ventricle as well as normally toward the cortical plate. Mechanistically, we demonstrate that Lgl1 directly binds to N-cadherin and this interaction is negatively regulated by atypical protein kinase C (aPKC)-mediated phosphorylation of Lgl1. We show that Lgl1 is necessary to stabilize N-cadherin in AJCs, which are required for structural integrity of the neuroepithelium. These findings link apical-basal cell polarity with properly localized formation of AJCs responsible for strong cell-cell adhesion between ENSCs.

RESULTS

Ablation of *Lgl1* in ENSCs Results in Severe Brain Malformation

To generate mice with a deletion of *Lgl1* in ENSCs at the beginning of neurogenesis, mice with a conditional *Lgl1* allele (*Lgl1*^{loxP/loxP}) (Klezovitch et al., 2004) were crossed with mice carrying a Nestin promoter-driven Cre recombinase (*Nestin-Cre*^{+/-}), which is expressed in CNS ENSCs starting at embryonic day 10.5 (E10.5) (Graus-Porta et al., 2001). Western blot analysis of total brain proteins revealed a gradual decrease in the levels of LLGL1 starting at day E12.5 of development (Figure 1A). Levels of ENSC marker Nestin were gradually increased, and the levels of differentiated neuronal marker neurofilament were modestly decreased in postnatal *Lgl1* cKO brains (Figures 1A and 1B).

At birth, CNS-specific *Lgl1* cKO mice were indistinguishable from their heterozygous and wild-type littermates. Although growth of mutant pups was delayed, their brains were approximately normal size (Figures 1C and 1D). *Lgl1* cKO adult mice exhibited sporadic seizures associated with falls and convulsions (Movies S1–S4). Histological analysis of *Lgl1* cKO brains revealed completely penetrant disorganization of cerebral cortices where an ectopic second layer of gray matter was formed between the white matter and the lateral ventricle (Figures 1E', 1F', 1G', 1I', and 1J', arrows). The hippocampus in the *Lgl1* cKO brains was also severely disorganized and only rudimentary in size with the CA1–CA3 fields being especially affected (Figures 1G' and 1H').

Periventricular Heterotopia in *Lgl1* cKO Brains

To identify the cells forming the ectopic layer of gray matter in the cerebral cortex of *Lgl1* cKO brains, we performed immunostainings with cell-type-specific markers, NeuroN, a marker of differentiated neurons, and GFAP, a marker of astrocytes. In 2-month-old wild-type mice, NeuroN+ cells were localized to the cortical plate above GFAP+ astrocytes, which lined the corpus callosum and the axonal tracts in the white matter (Figure 2A). A similar NeuroN+ cortical plate was located above GFAP+ astrocytes in *Lgl1* cKO brains, but the ectopic gray matter also contained predominantly NeuroN+ cells and few GFAP+ astrocytes (Figure 2A'). Thus, we conclude that the ectopic gray matter in *Lgl1* cKO brains is composed of differentiated neurons.

To determine the developmental origin of the ectopic neurons, we performed additional cell-type-specific stainings and bromodeoxyuridine (BrdU) birth-dating experiments. The *Lgl1* cKO cortical plate showed the normal features of cortical stratification, with early-born neurons, labeled with BrdU on day E13.5 and expressing TBR1 (layer VI) and CTIP2 (layer V), positioned below later-born neurons, labeled with BrdU on day E16.5 and expressing BRN1 (layers II–IV) and CUX1 (layers II–IV) (Figures 2B–2G' and S1A). However, the ectopically localized NeuroN+ neurons expressed BRN1 and CUX1, with only few cells expressing TBR1 and CTIP2, and were prominently labeled with BrdU on day E16.5 but less on E13.5, implying that the majority of these neurons were born during late neurogenesis (Figures 2C–2G' and S1B). Remarkably, new cell birth could still be detected in *Lgl1* cKO cortices at E18.5, when cortical neurogenesis was almost completed in wild-type brains (Figures 2H and 2H'). Overall, we conclude that the ectopic gray matter in *Lgl1* cKO brains is composed of neurons that are mostly born during late stages of neurogenesis and express appropriate stage-specific markers, while the layering of the primary cortical plate is not grossly altered. The MCC in *Lgl1* cKO brains is strikingly similar to MCC in human patients suffering from severe PH, which is characterized by the formation of ectopic nodules or a band of neurons along the lateral ventricle. Remarkably, sporadic seizures are one of the main symptoms of patients with PH (Lu and Sheen, 2005). We conclude that CNS-specific *Lgl1* cKO mice develop prominent MCC, which is consistent with PH.

Mislocalization of ENSCs prior to the Formation of a Second Cortical Neuronal Layer in *Lgl1* cKO Brains

To determine the cellular mechanisms responsible for cortical malformation in *Lgl1*^{-/-} brains, we analyzed mutant mice at

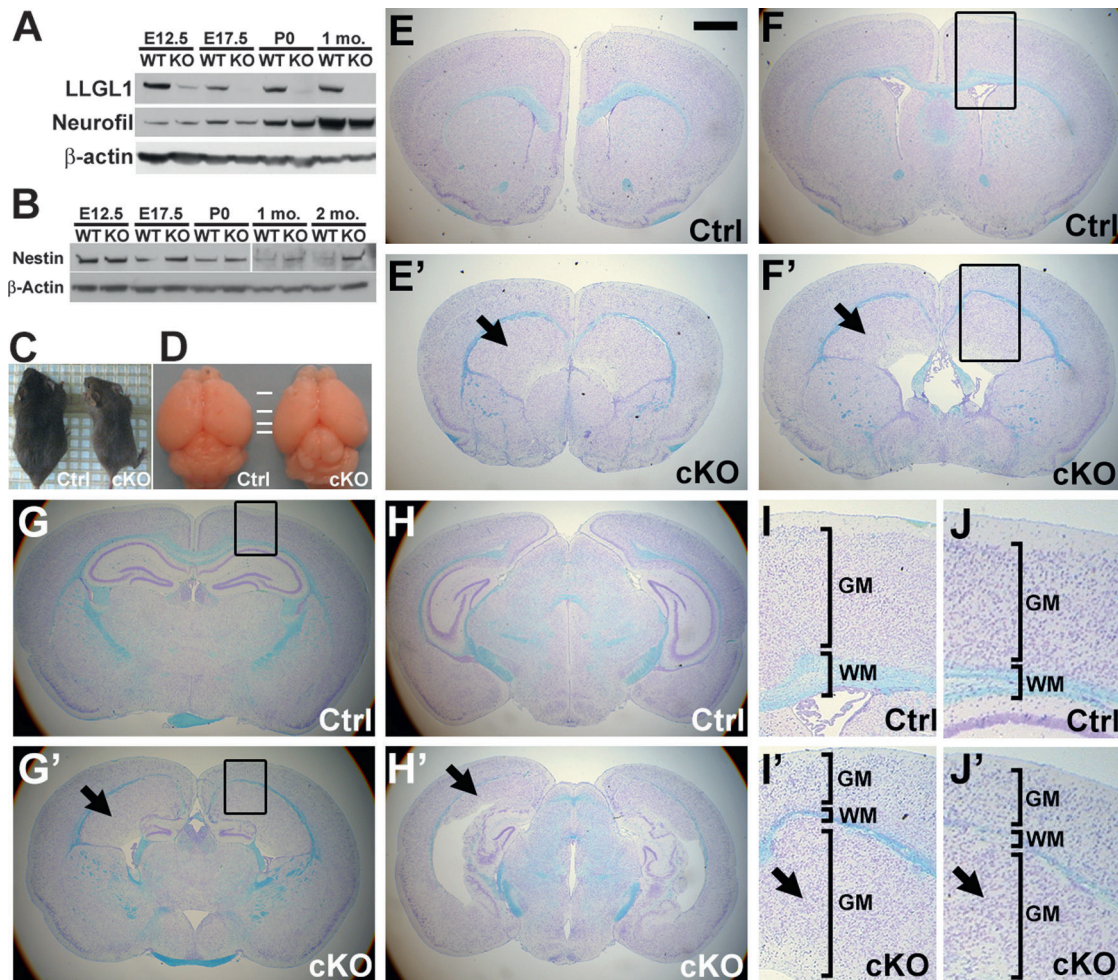


Figure 1. Severe Brain Malformation in *Lgl1*^{LoxP/LoxP}/*Nestin-Cre*^{+/-}, cKO *Lgl1*, Mice

(A and B) Western blot analysis of total protein extracts from E12.5, E17.5, P0, and 1 month-old (1 mo.) control (Ctrl) and cKO *Lgl1* (cKO) brains with anti-*Lgl1*, anti-Nestin, anti-Neurofilament, and anti- β -actin antibodies.

(C and D) General appearance and brains of 2-month-old control (Ctrl) and cKO *Lgl1* (cKO) mice.

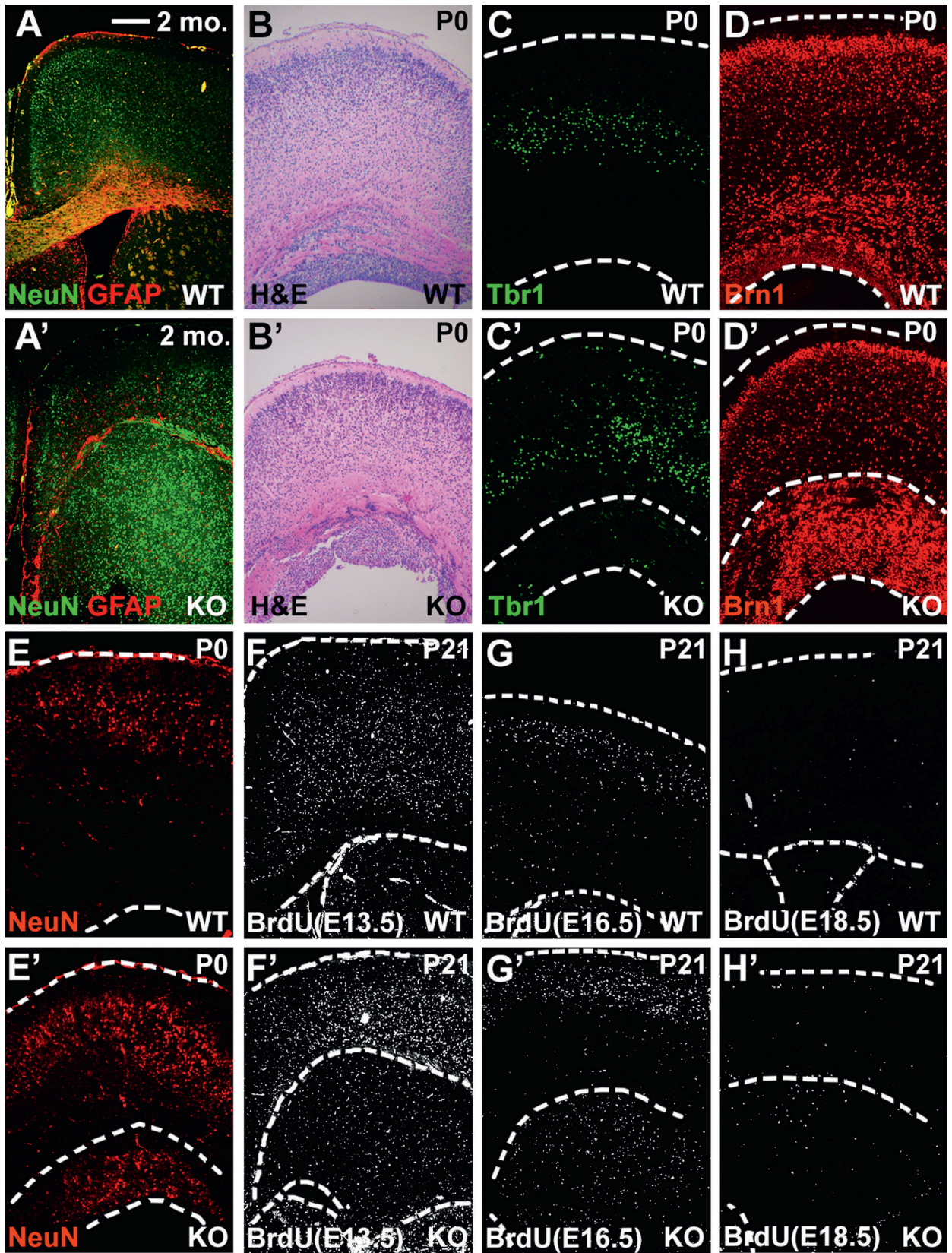
(E–J) Histologic appearance of brains from 2-month-old control (Ctrl) and cKO *Lgl1* (cKO) mice. Nissl staining of coronal sections at the levels of the lateral ventricles (E–F', I, and I') and hippocampus (G–H', J, and J'). Boxed areas in (F), (F'), (G), and (G') are shown at higher magnification in (I), (I'), (J), and (J'), respectively. GM indicates gray matter. WM indicates white matter. Arrows indicate ectopically formed layer of gray matter. Representative images from five Ctrl and six cKO *Lgl1* brains.

Bar in (E) represents 830 μ m in (E) and (E'), 930 μ m in (F) and (F'), 1 mm in (G) and (G'), 1.03 mm in (H) and (H'), 410 μ m in (I) and (I'), and 212 μ m in (J) and (J').

various times during embryonic development (Figure 3). During normal neurogenesis, self-renewing ENSCs (Nestin⁺/Pax6⁺/Tbr2⁻) localize at the surface of the lateral ventricles (Figures 3A and 3F). ENSCs are highly polarized cells with apical membrane domains facing the ventricle (Crb3⁺) and long glial processes (RC2⁺) pointing away from the ventricle toward the developing cortex (Figure 3E). Endogenous LLGL1 is prominently expressed and is localized to the lateral membrane domain and the cytoplasm of ENSCs (Figure S2). During neurogenesis, ENSCs divide asymmetrically to self-renew and to generate subventricular zone (SVZ) progenitors (Nestin⁻/Pax6⁻/Tbr2⁺), which are committed to differentiation. SVZ progenitors do not maintain AJCs and do not incorporate into the ventricular wall. These cells reside in a position basal to the ENSCs, somewhat removed from the ventricles (Figures 3F

and 3G, green). SVZ progenitors divide to generate post-mitotic, immature neurons, which use radial glial processes of neural progenitors to migrate toward the developing cortical plate, where they differentiate into neurons (β -Tubulin III⁺) (Figure 3B).

To analyze the dynamics of cortical malformation in *Lgl1*^{-/-} brains we first used immunostaining with anti-Nestin and anti- β -Tubulin III antibodies. While Nestin⁺ ENSCs were located normally at the edge of the ventricle in E12.5 *Lgl1* cKO brains, by E14.5 the ENSC layer was discontinuous, and small β -Tubulin III⁺ neuronal nodules formed at the ventricular surface (Figure 3A', white arrowhead). The total length of the neurogenic region was also noticeably increased in mutant brains, suggesting a significant increase in area of the neurogenic surface (Figure 3A'). By E17.5, the ENSC niche disintegrated into distinct foci surrounded by differentiating neurons (Figures 3B' and



(legend on next page)

3C', arrows). Nestin+ cells had largely disappeared from normal cortex after birth, but were still detected in mutant cortex until P5, forming a discontinuous layer in the middle of the developing cortex (Figure 3D', arrow). At the cellular level, wild-type ENSCs display their apical membrane domains facing the ventricle (Crb3+) and radial glial processes extending toward the cortical plate (Figure 3E). In contrast, *Lig1* cKO ENSCs that were mislocalized to the inside of the developing cortices contained apical membrane domains in the middle of Nestin+ cell masses and extended radial glial processes toward the ventricle as well as toward the developing cortical plate (Figures 3E and 3E'). Nestin+ cells in the middle of *Lig1* cKO cortices were composed of both ENSCs (Pax6+) and differentiating SVZ progenitors (Tbr2+) (Figures 3F–3G'). This organization and cell-type specificity of Nestin+ cells inside the *Lig1* cKO cortices suggested that ENSCs were internalized in E17.5 *Lig1* cKO brains.

Absence of LLGL1 Perturbs Cell Migration during Development

To visualize the formation of PH in *Lig1* cKO cortices, we used time-lapse video microscopy with organotypic embryonic brain slices. For this purpose, we first utilized an in utero electroporation procedure to introduce a plasmid encoding nuclear GFP into E12.5 ENSCs (Tabata and Nakajima, 2001). One day later, we isolated the brains and prepared cortical slices and genotyped the embryos. GFPs expressing slices from control and *Lig1* cKO cortices were identified and imaged for 12–16 hr. Imaging cortical slices from control embryos revealed interkinetic nuclear movements of ENSCs (Movie S5). During this process, ENSC nuclei move from a basal position to the apical surface where the cells divide mitotically, and afterward their nuclei again migrate basally away from the ventricular surface (Spear and Erickson, 2012) (Figure 4A and Movie S5). In contrast, in *Lig1* cKO cortical slices, ENSC nuclei did not migrate toward the apical surface and divided at a more basal position. In addition, daughter cells exhibited random movements with a tendency to move toward the apical surface (Figure 4A and Movie S5).

When ENSCs were electroporated in utero with GFP plasmid at E14.5 and then imaged 2 days later at E16.5, *Lig1* cKO ENSCs formed rosette-like structures (Figure 4B and Movie S6). These are likely the origin of the rosettes detected in fixed sections at E17.5 (Figure 3F').

Cortical electroporation is a highly invasive procedure which, while relatively well tolerated in normal cortices, may potentially accelerate disorganization in *Lig1* cKO brains. Therefore, we decided to label and image ENSCs using a less invasive technique. We labeled ENSCs by injecting membrane-permeable Cell Tracker Green into E13.5 brain ventricles. We then gener-

ated cortical slices and imaged them for 12–16 hr. While imaging of cells labeled with cell tracker dye provided less contrast than imaging of cells expressing nuclear GFP, this approach enabled us to commence imaging of cortices before *Lig1* cKO brains are overtly disorganized. Imaging cortical slices from control animals reveal ENSCs close to the ventricular surface at the beginning of the time lapse with cell bodies moving toward more basal position (Movie S7). In contrast, in *Lig1* cKO cortical slices, we observed focal disruption of the ventricular wall and prominent movement of cells into the ventricular space (Movie S7).

Disruption of Ventricular Wall Integrity Results in Internalization of ENSCs in *Lig1* cKO Brains

To reveal the mechanisms responsible for internalization of *Lig1* cKO ENSCs, we analyzed developing cortices at E14.5, before fragmentation and mislocalization of ENSC niches occurs. In wild-type brains, the ventricular surface is lined by the apical membrane domains of ENSCs. N-cadherin-based cell-cell adhesion structures called AJCs separate the apical and basolateral membrane domains of ENSCs. Reinforced by the actin cytoskeleton, AJCs connect ENSCs to each other at the surface of the ventricle to form a strong net that keeps ENSCs inside the cortex and prevents their emergence on the ventricular surface (Kadowaki et al., 2007). Interestingly, immunostaining for the AJC markers N-cadherin and α -catenin revealed focal disruption of AJCs in *Lig1* cKO ENSCs at E14.5, the time point immediately before the disruption of ENSC niches and mislocalization of ENSCs takes place (Figures 4C–4D' and S3). Short fragments of E14.5 *Lig1* cKO cortices displayed complete loss of AJCs (Figures 4D, 4D', and S3B–S3B'', arrowheads). Cells in these areas protruded into the ventricular space (Figures 4D' and S3B–S3B''), resembling focal protrusion and movement of ventricular zone cells into the ventricular space observed by live imaging (Movie S7). These protrusions were still populated by Nestin+ ENSCs (Figures S3E–S3G). Localized disruption of AJCs in *Lig1* cKO brain may be responsible for focal protrusion and expansion of nonpolarized cells on the ventricular surface in these cortical areas. As these nonpolarized cells continue to expand at the ventricular surface later in development, fragments of the neuroepithelium containing polarized ENSCs maintaining residual AJCs can become completely engulfed by their nonpolarized neighbors and internalized into the cortex. Indeed, later in development at E17.5, the apical membrane domains and AJCs localize to the center of rosettes in the middle of developing *Lig1* cKO cortices (Figures 4E, 4E', and S3C–S3D''). These findings are consistent with a model where focal disruption of AJCs in *Lig1* cKO cortices is responsible for protrusion of

Figure 2. Periventricular Heterotopia in cKO *Lig1* Brains

(A and A') Immunostaining of coronal cerebral cortical sections from 2-month-old (2 mo.) control (Ctrl) and cKO *Lig1* (cKO) brains with anti-NeuroN (NeuN) and anti-GFAP antibodies. Representative images from two Ctrl and three cKO *Lig1* brains.

(B–E') Stainings of coronal cortical sections from newborn (P0) control (Ctrl) and cKO *Lig1* (cKO) brains with H&E (B and B'), or with anti-Tbr1 (C and C'), anti-Brn1 (D and D'), and anti-NeuroN (NeuN, E and E') antibodies. Representative images from six Ctrl and four cKO *Lig1* brains.

(F–H) BrdU birth dating of cells in control (Ctrl) and cKO *Lig1* (cKO) cortices. BrdU was injected at E13.5 (F and F', four Ctrl and three cKO mice), E16.5 (G and G', five Ctrl and five cKO mice), E18.5 (H and H', three Ctrl and three cKO mice). Cells that incorporated BrdU at the time of injection were revealed by immunostaining with anti-BrdU antibodies 21 days after birth (P21). Dashed lines in (C)–(H) indicate boundaries of the cortex. The additional dashed line in the middle of the cortex in the KO panels indicates the location of the white matter separating the cerebral cortical plate and ectopic neuronal layer at the ventricular surface.

Bar in (A) represents 265 μ m in (A), (A'), and (F)–(H'), 125 μ m in (B) and (B'), and 105 μ m in (C)–(E'). See also Figure S1.

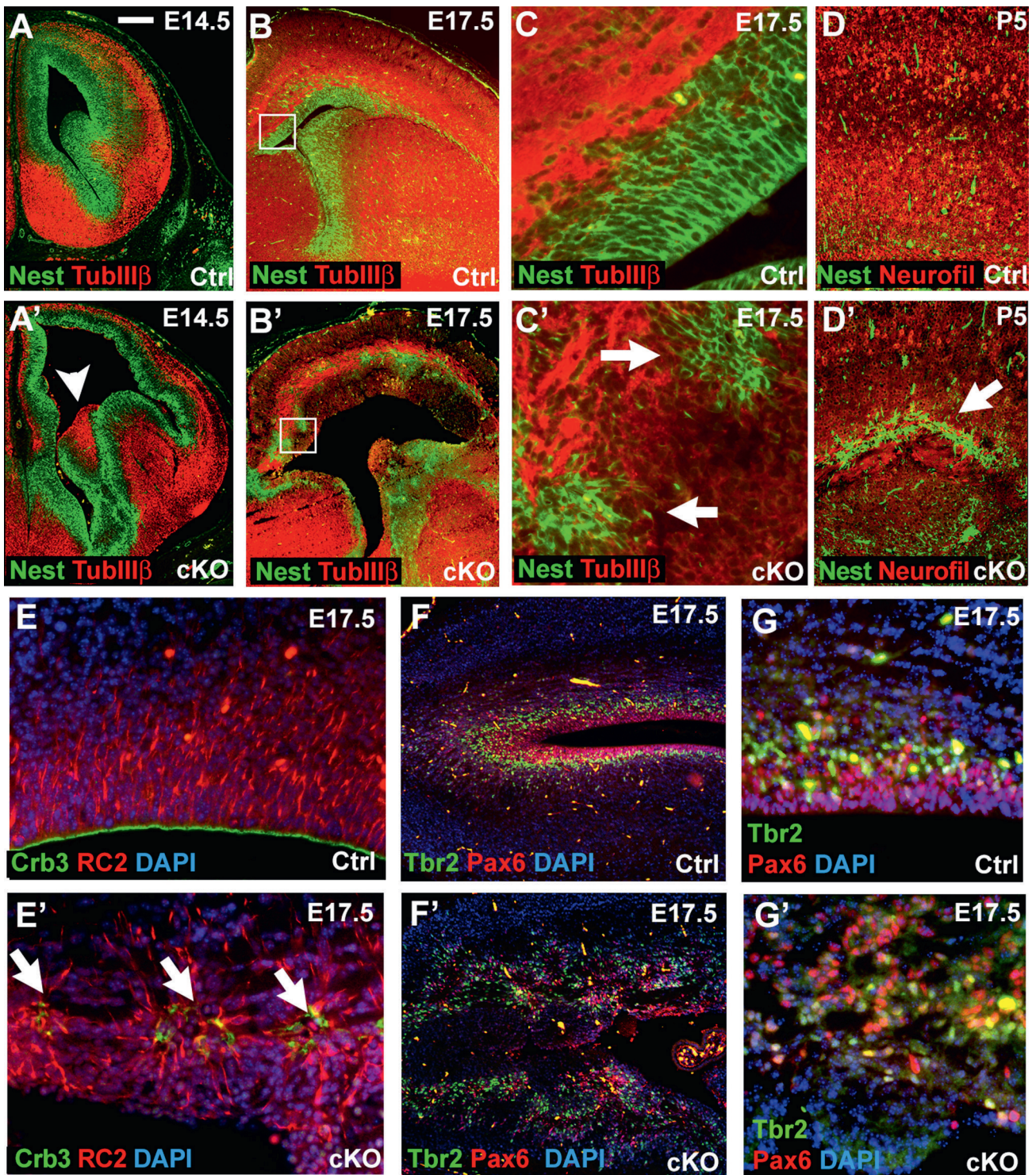


Figure 3. Dynamics of Periventricular Heterotopia in cKO *Lgl1* Brains

(A–C) Immunostainings of coronal brain sections at the level of the lateral ventricle from E14.5 (A and A') and E17.5 (B–C') control (Ctrl) and cKO *Lgl1* (cKO) brains with anti-Nestin (Nest, ENSC marker, green), anti- β -Tubulin III (TubIII β , early neuronal marker, red) antibodies. Boxed areas in (B) and (B') are shown at higher magnification in (C) and (C'), respectively. Representative images from three Ctrl and three cKO *Lgl1* brains. Arrows indicate misplaced ENSCs.

(D and D') Immunostainings of coronal brain sections at the level of the lateral ventricle from 5-day-old (P5) control (Ctrl) and cKO *Lgl1* (cKO) brains with anti-Nestin (green) and anti-Neurofilament (red) antibodies. Representative images from two Ctrl and three cKO *Lgl1* brains. Arrow indicates a layer of ENSCs in the middle of cKO cortex.

(legend continued on next page)

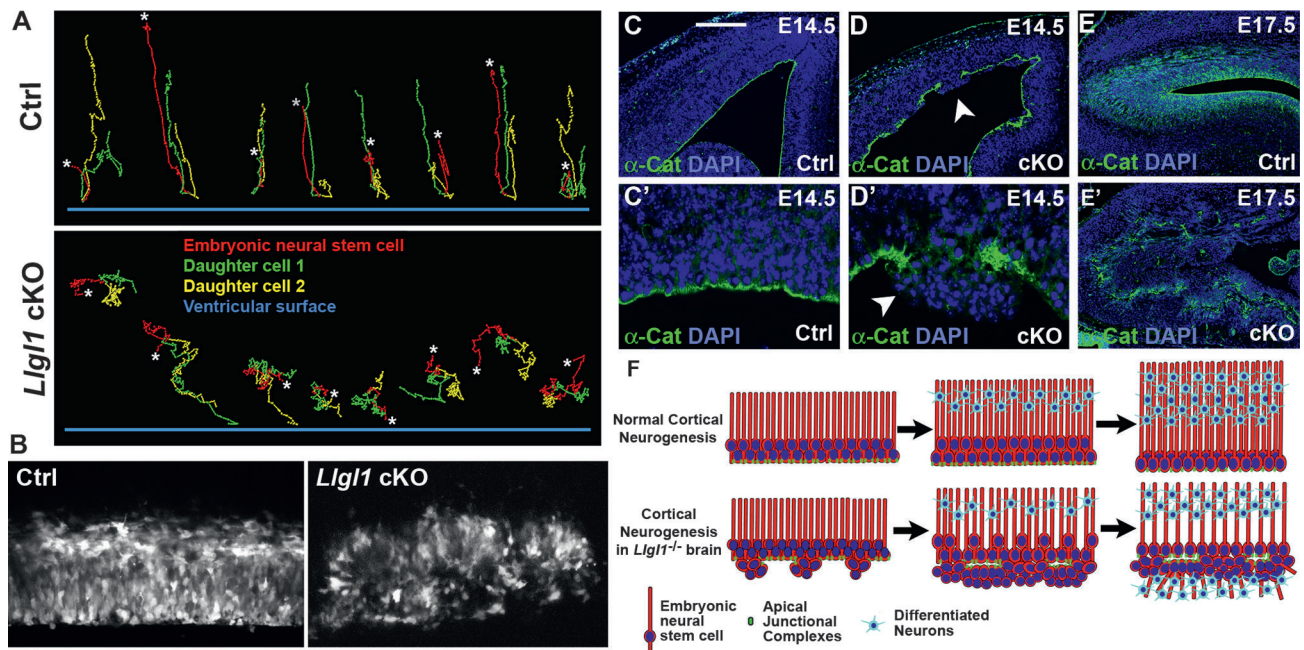


Figure 4. In Vivo Time-Lapse Imaging and Immunostaining Analyses Reveal Disruption of AJCs and Internalization of ENSCs in cKO *Lgl1* Brains

(A) Nuclear tracks of ENSCs and their daughters in the ventricular zone of control (Ctrl) and cKO *Lgl1* (cKO) brains from Movie S5. Brains were electroporated with NLS-GFP expressing vector at E12.5, and cortical slices were prepared and imaged at E13.5. $n = 2$ for Ctrl and $n = 2$ for cKO *Lgl1*. Note, in control cortices, nuclei of ENSCs (in red) move toward the ventricular surface (blue line) to divide. The two daughter cells (green and yellow) then move away from the ventricular surface. In contrast, cKO *Lgl1* ENSCs show random movements and divide at a distance from the ventricular surface. Asterisks show the initial position of tracked cells. (B) Neuroepithelial rosettes in cKO *Lgl1* (cKO) brains. Still image from Movie S6. Brains were electroporated with NLS-GFP expressing vector at E14.5, and cortical slices were prepared and imaged at E16.5. $n = 2$ for Ctrl and $n = 2$ for cKO *Lgl1*.

(C–E) Coronal brain sections from E14.5 and E17.5 control (Ctrl) and cKO *Lgl1* (cKO) brains were stained with anti- α -Catenin (α -Cat, AJC marker, green) antibodies. Note protrusion of cortical cells in the areas with disrupted AJCs in E14.5 cKO *Lgl1* brains (white arrowheads), and complete internalization of AJCs in E17.5 mutants. Representative images from three Ctrl and three cKO *Lgl1* brains.

(F) Model of PH formation in cKO *Lgl1* brains. ENSCs display focal loss of AJCs. Cortical cells protrude into the ventricle and expand on the apical membrane domains of polarized ENSCs. ENSCs are engulfed by nonpolarized neighbors and are misplaced inside the developing cortex. Misplaced ENSCs send neurons toward both the developing cortical plate and the ventricle, creating an ectopic neuronal layer at the ventricular surface.

Bar in (C) represents 210 μm in (C), (D), (E), and (E') and 70 μm in (C') and (D'). See also Figure S3.

ENSCs into the ventricular space, formation of neuroepithelial rosettes, and internalization of ENSCs (Figure 4F).

LLGL1 Is Necessary for the Maintenance of Prominent AJCs in ENSCs

Since immunostaining for markers of AJCs of ENSCs demonstrated focal loss of staining in E14.5 *Lgl1* cKO cortices (Figures 4D and 4D'), we analyzed AJCs using electron microscopy. As expected, electron-dense AJCs were found at the interface between apical and lateral membrane domains of ENSCs in control embryos (Figures 5A and 5A', arrows). AJCs were present in the regions containing polarized ENSCs in *Lgl1* cKO cortices (Figures 5B and 5B', arrowheads). However, these structures were absent from cells that protruded into the ventricle (Figures 5C and C'). Quantitation of the lengths of AJCs revealed significant

decrease in the size of AJCs in E14.5 *Lgl1* cKO ENSCs in the areas that maintained cell polarity (Figure 5D, *Lgl1* cKO P). These findings indicate overall decrease in size and focal loss of AJCs in E14.5 *Lgl1* cKO ENSCs, which is likely responsible for the focal loss of ventricular wall integrity and protrusion of cells into the ventricular space.

AJCs in ENSCs are made primarily by the adherens junctions containing N-cadherin (Chenn et al., 1998). In agreement with electron microscopy, high magnification confocal microscope analysis of N-cadherin staining revealed prominent disorganization of N-cadherin-containing AJCs in E14.5 *Lgl1* cKO cortices, even in the areas that maintained the integrity of the ventricular wall (Figure S4). Abnormal junctions may be the result from decreased levels of adherens junction proteins N-cadherin, α - and β -catenins, failure of cadherin-catenin protein complex

(E–G') Immunostainings of coronal brain sections from E17.5 control (Ctrl) and cKO *Lgl1* (cKO) brains with anti-RC2 (radial glial marker, red in E and E'), anti-Crumb3 (Crb3, apical membrane domain marker, green in E and E'), anti-Pax6 (VZ ENSC marker, red in F–G') and anti-Tbr2 (SVZ progenitor marker, green in F–G'). Representative images from three Ctrl and three cKO *Lgl1* brains. Arrows indicate neuroepithelial rosettes in cKO *Lgl1* brains. Bar in (A) represents 260 μm in (A) and (A'), 210 μm in (B) and (B'), 21 μm in (C) and (C'), 105 μm in (D) and (D'), 20 μm in (E), (E'), (G), and (G'), and 80 μm in (F) and (F'). See also Figure S2.

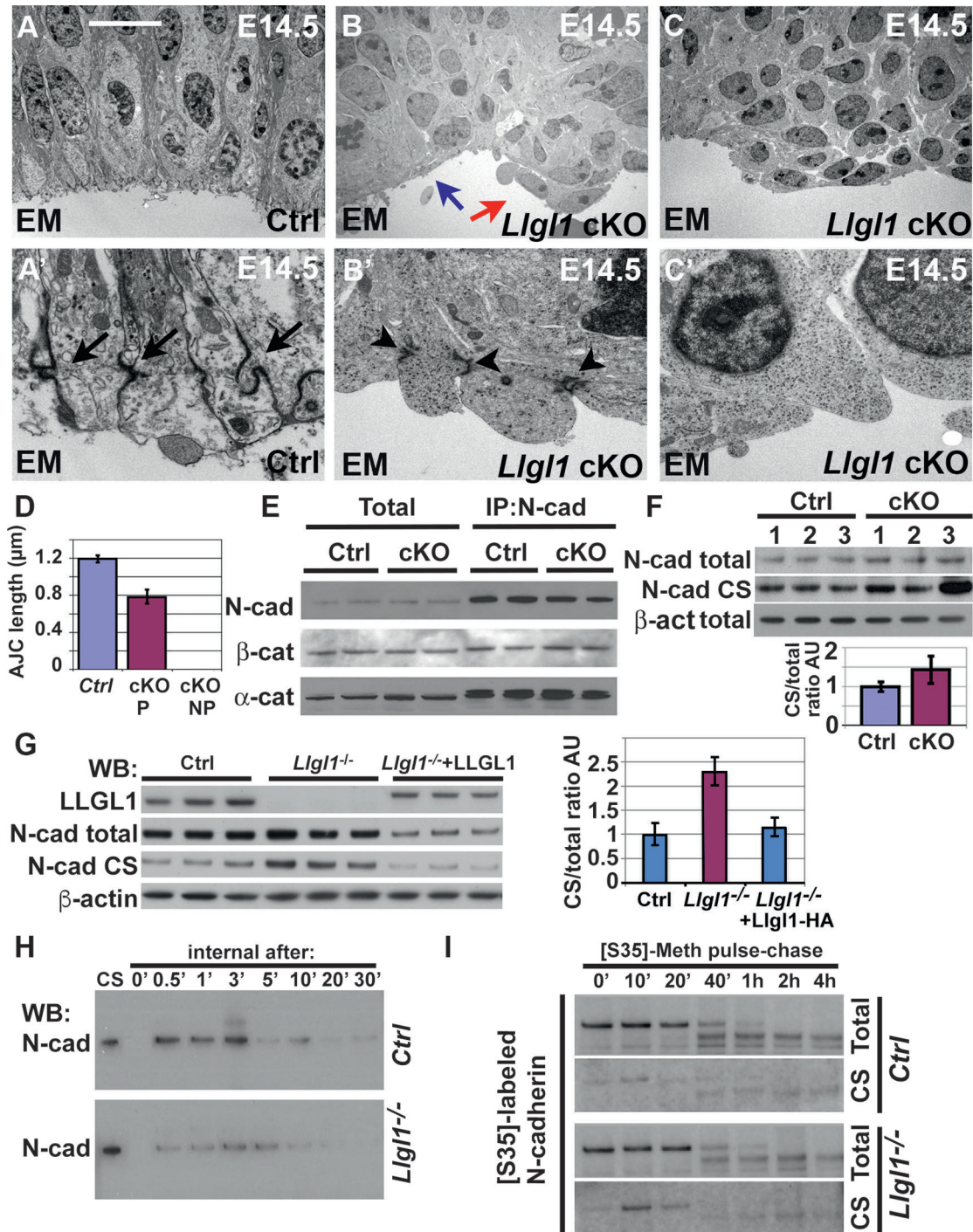


Figure 5. LLGL1 Is Necessary for the Maintenance of AJCs in ENSCs

(A–C') Electron microscopy analysis of cortical sections from E14.5 wild-type (WT) and *Lgl1* cKO (KO) embryos. Self-renewing WT VZ ENSCs display prominent AJCs (A, A'). Black arrows indicate AJCs. (B) shows the boundary between properly polarized adhesive ENSCs (blue arrow) and the cells protruding into the ventricle (red arrow). Polarized *Lgl1* cKO VZ ENSCs display small AJCs (black arrowheads in B'). Representative images from the analyses of three Ctrl and three *Lgl1* cKO brains. (C) and (C') show the area protruding into the ventricle ENSCs lacking AJCs. Bar in (A) represents 9 μm in (A)–(C) and 1.5 μm in (A')–(C').

(D) Quantitation of the lengths of AJCs in control (Ctrl) and polarized (P) and nonpolarized (NP) *Lgl1* cKO (cKO) ENSCs. Data from three Ctrl and three *Lgl1* cKO brains. $n = 102$ for Ctrl, $n = 71$ for *Lgl1* cKO. Graph shows mean values \pm SD.

(E) Normal cadherin/catenin complex formation in *Lgl1* cKO brains. Total protein lysates from E14.5 two Ctrl and two *Lgl1* cKO brains were immunoprecipitated with anti-N-cadherin antibodies and analyzed by western blotting with anti-N-cadherin, anti- β -catenin, and anti- α -catenin antibodies.

(legend continued on next page)

formation, failure of cadherin-catenin complex delivery and retention at the plasma membrane, or failure of clustering and stabilization of adhesion complexes by association with the actin cytoskeleton (Yap et al., 2015). We found no differences in the total levels of cadherin and catenin proteins or in the cadherin-catenin complex formation in E14.5 *Lig1* cKO ENSCs (Figure 5E). The levels of cell-surface N-cadherin were not decreased but increased in *Lig1* cKO ENSCs, and this phenotype was rescued by re-expression of LLGL1 (Figures 5F and 5G). Endocytosis experiments revealed prominent decrease in internalization of N-cadherin in *Lig1* cKO ENSCs (Figure 5H), while overall rates of N-cadherin protein synthesis and degradation were unchanged (Figure 5I). These data and the decrease in the length and focal disruption of AJCs in *Lig1* cKO ENSCs, which was observed by electron microscopy (Figures 5A–5D), suggest the defects in polarized clustering of cadherin-catenin proteins and their assembly into the AJCs in *Lig1*^{-/-} cells.

Physical Interaction between LLGL1 and N-Cadherin

To understand how LLGL1 regulates formation of AJCs, we decided to analyze whether LLGL1 physically interacts with cadherin-catenin proteins. Indeed, co-immunoprecipitation experiments revealed association between endogenous LLGL1 and N-cadherin in E14.5 brains (Figures 6A and 6B). In pull-down assays with purified β -catenin or cytoplasmic domain of N-cadherin, LLGL1 preferentially bound to N-cadherin (Figure 6C). LLGL1 function is negatively regulated by aPKC-mediated phosphorylation of five evolutionary conserved serines in the middle of the protein (Plant et al., 2003), which results in interaction between the N- and C-terminal domains of Lgl and release of cortical Lgl into the cytoplasm (Betschinger et al., 2005; Prehoda, 2009). To determine whether interaction between LLGL1 and N-cadherin is regulated by phosphorylation at aPKC target sites, we generated expression constructs encoding wild-type, phospho-mimicking 5SD and the unable to be phosphorylated 5SA mutant of LLGL1. Both the wild-type and 5SA mutant of LLGL1 interacted with the cytosolic fragment of N-cadherin (Figures 6D and S5A). In contrast, the 5SD mutant LLGL1 displayed weak binding to N-cadherin (Figure S5A). Co-expression of constitutively active aPKC decreased the binding between wild-type LLGL1 and N-cadherin, while interaction between the 5SA mutant LLGL1 and N-cadherin was not affected (Figure 6D). These data indicate that aPKC-mediated phosphorylation inhibits LLGL1-N-cadherin interaction.

To map the domains of LLGL1 and N-cadherin responsible for interaction, we generated and performed immunoprecipitation experiments with various truncated fragments of both LLGL1

and N-cadherin (Figures 6E–6H'). The fragments containing the C-terminal WD14 domain of LLGL1 and, to a lesser degree, the fragment containing the WD10 domain were responsible for interaction with N-cadherin (Figures 6E–6F'). Conversely, the β -catenin-binding region and the adjacent C-terminal portion of N-cadherin were necessary for interaction with LLGL1 (Figures 6G–6H'). Since we found an overlap between β -catenin and LLGL1-binding regions on N-cadherin, we analyzed whether binding of N-cadherin to LLGL1 and β -catenin is mutually exclusive. Co-immunoprecipitation experiments demonstrated that LLGL1, N-cadherin, and β -catenin form tripartite complex, and N-cadherin is necessary for interaction between LLGL1 and β -catenin (Figure S5B). To determine whether the LLGL1-N-cadherin interaction is direct, we performed pull-down experiments with proteins purified from bacteria. The C-terminal WD14 domain-containing fragment, but not the fragment containing aPKC phosphorylation sites of LLGL1 directly bound the cytoplasmic domain of N-cadherin, indicating that LLGL1-N-cadherin interaction is direct (Figure 6I). Finally, we found that C-terminal truncation deleting both N-cadherin-binding sites of LLGL1 (WD14 and WD10) was necessary to prevent interaction between LLGL1 and N-cadherin (Figure S5C).

Disruption of LLGL1-N-Cadherin Interaction in Developing Brain In Vivo Results in Periventricular Heterotopia

To determine the significance of the LLGL1-N-cadherin interaction, we decided to disrupt it using a dominant-negative approach. We hypothesized that overexpression of directly interacting with the N-cadherin C-terminal WD14 domain of LLGL1 would compete with full-length endogenous LLGL1 for binding to N-cadherin. Indeed, overexpression of a protein containing a triple repeat of the C-terminal WD14 domain of LLGL1 linked to GFP (3xLLGL1#9-GFP) significantly decreased, but did not completely abolish, the interaction between LLGL1 and N-cadherin (Figure 7A).

To determine the functional significance of interaction between LLGL1 and N-cadherin in developing brain in vivo, we decided to use the in utero electroporation technique, which is capable of delivering DNA expression constructs into E15.5 cortices (Saito, 2006). Since these experiments significantly differ from genetic inactivation of *Lig1* at E10.5 by *Nestin-Cre*, we first analyzed whether loss of endogenous *Lig1* in the framework of such an experiment would generate neuronal heterotopia resembling the cortical phenotype in *Lig1* cKO embryos. As expected, in utero electroporation of E15.5 cortices with plasmids expressing nontargeting shRNA did not result in the

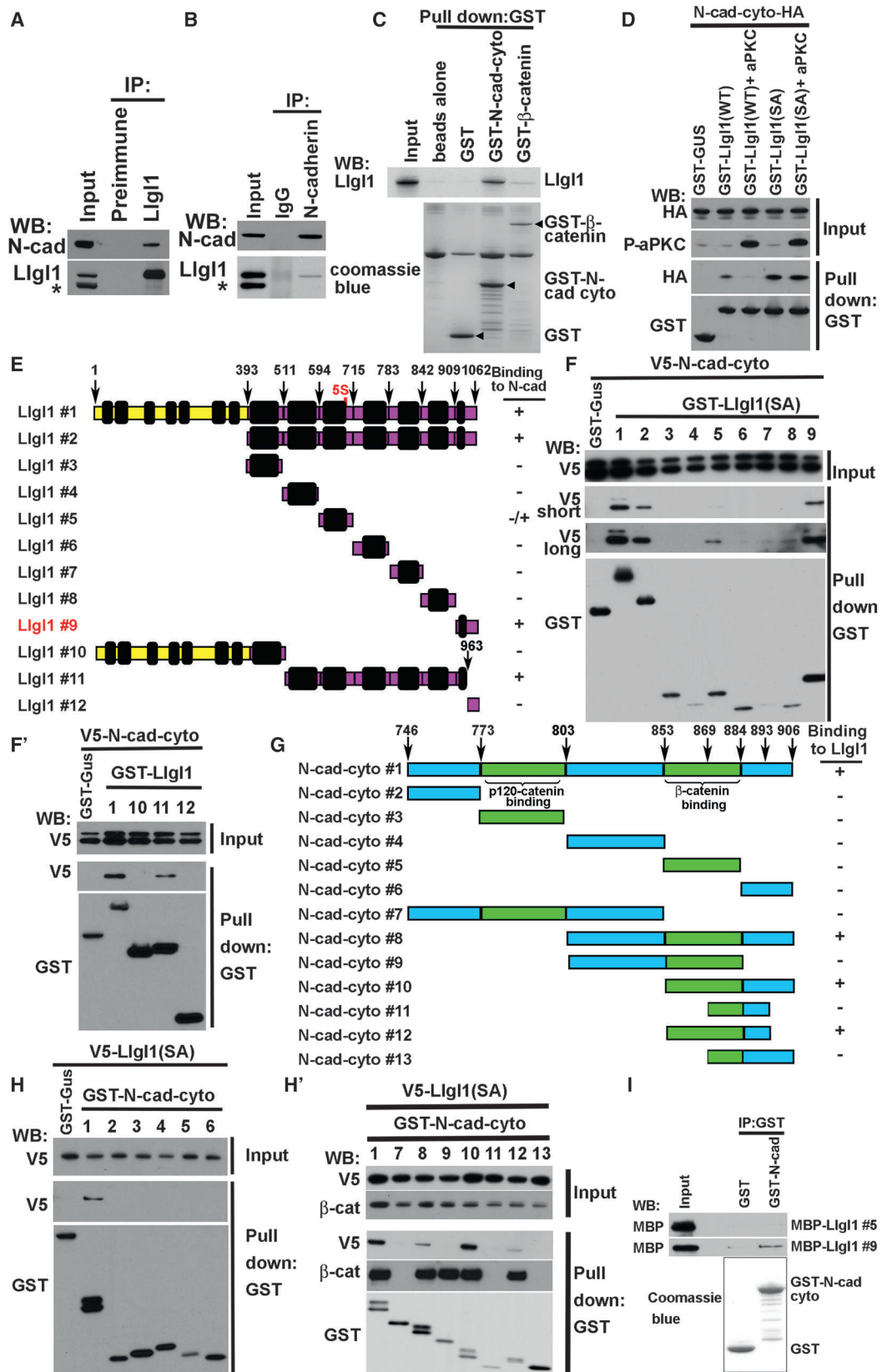
(F) Cell-surface (CS) levels of N-cadherin in E14.5 three control (Ctrl) and three *Lig1* cKO ENSCs. Cell-surface proteins on isolated ENSCs were biotinylated, precipitated with streptavidin-Sepharose and blotted with anti-N-cadherin antibodies. Quantitation of CS to total levels of N-cadherin. Graph shows mean values \pm SD. Ratio of surface to total levels of N-cadherin in control (Ctrl) cells is arbitrary adjusted to 1.

(G) Cell-surface (CS) levels of N-cadherin in three cultured control (Ctrl), three *Lig1*^{-/-}, and three rescued by re-expression of LLGL1 in *Lig1*^{-/-} cells (*Lig1*^{-/-} + LLGL1) ENSCs. Graph shows mean values \pm SD.

(H) Internalization of cell-surface N-cadherin in cultured control (Ctrl) and *Lig1*^{-/-} ENSCs. Cell-surface proteins were biotinylated, incubated at 37°C for the indicated number of minutes, stripped with reduced glutathione, precipitated with streptavidin-Sepharose, and blotted with anti-N-cadherin antibodies. CS total levels of cell-surface N-cadherin. Representative data from three independent experiments.

(I) Cell-surface delivery and retention of N-cadherin in cultured control (Ctrl) and *Lig1*^{-/-} ENSCs. Newly synthesized proteins were labeled by pulse of [S35]Met/Cys and chased for the indicated times. Proteins were immunoprecipitated with anti-N-cadherin antibodies, released from the beads (total new N-cadherin), and then re-precipitated by streptavidin-Sepharose (cell surface, CS, new N-cadherin). Representative data from three independent experiments.

See also Figure S4.



(legend on next page)

development of heterotopia (Figure 7B). In contrast, in utero electroporation of the plasmid expressing sh-Llg1 resulted in the development of focal neuronal heterotopia in all electroporated cortices (Figures 7B and S6 white arrow). This phenotype was rescued by simultaneous expression of full-length, but not C-terminally truncated, unable to bind to N-cadherin human LLGL1 (Figure 7B). Since aPKC-mediated phosphorylation decreases the binding between N-cadherin and LLGL1, we analyzed whether activation and plasma membrane targeting of aPKC can mimic the shLlg1 phenotype. While expression of activation loop constitutively active aPKC (CA-aPKC) or its binding partner Par3 alone did not cause heterotopia (data not shown), co-expression of CA-aPKC and Par3 resulted in the completely penetrant neuronal heterotopia phenotype (Figure 7C). Importantly, this phenotype was partially rescued (3 out of 5) by simultaneous expression of nonphosphorylatable 5SA LLGL1 (Figure 7C).

Since expression of 3xLLGL1#9-GFP weakens the interaction between LLGL1 and N-cadherin, we also analyzed the consequences of disruption of endogenous LLGL1-N-cadherin binding using in utero electroporation. Expression of 3xLLGL1#9-GFP protein resulted in the development of a partially penetrant neuronal heterotopia phenotype (4 out of 7 brains) (Figure 7C). Therefore, we concluded that direct interaction between LLGL1 and N-cadherin is necessary for stabilization of N-cadherin at the AJCs.

DISCUSSION

MCC is a constellation of devastating human brain disorders that account for a significant proportion of epilepsy and intellectual disability (Mochida and Walsh, 2004). The dynamics and molecular mechanisms that underlie human MCCs have remained poorly understood. Studies of human brain tissues from patients with MCC associated with PH have led to the general conclusion that ectopic deposition of neurons results from defects in neuronal migration (Mochida and Walsh, 2004) or loss of neuroepithelial integrity (Ferland et al., 2009). The integrity of the ventricular surface during development is maintained by the AJCs of ENSCs. Disruption of AJCs by genetic or shRNA-mediated

inactivation of RhoA, N-cadherin, α - or β -catenin results in profound defects in proliferation, differentiation, and delamination of ENSCs (Cappello et al., 2006, 2012; Junghans et al., 2005; Kadowaki et al., 2007; Katayama et al., 2011; Kim et al., 2010; Lien et al., 2006; Machon et al., 2003; Zechner et al., 2003). Loss of AJCs during neurogenesis in RhoA or α E-catenin mutants or in embryos with shRNA-mediated knock-down of Filamin A results in formation of ectopically positioned neuronal masses resembling PH (Cappello et al., 2012; Carabona et al., 2012; Schmid et al., 2014). *ARFGEF2*, a gene previously implicated in PH in human patients, may also be responsible for the maintenance of AJCs due to its involvement in the membrane delivery of N-cadherin/ β -catenin complexes, which is necessary for proper cell-cell adhesion (Sheen et al., 2004).

We found that deletion of *Lgl1* during cortical neurogenesis results in the development of PH. Presently, the phenotypes of humans with mutations in *LLGL1* are not known, and it is not clear if some patients with neuronal heterotopias have mutations in this gene. We analyzed the cellular mechanisms responsible for the formation of PH in *Lgl1* cKO mice using a variety of techniques, including live imaging of developing *Lgl1* cKO cortices. To our knowledge, this is the first imaging of PH formation in live cortical tissue. We found that LLGL1 is necessary for the maintenance of prominent AJCs in ENSCs and that ablation of *Lgl1* results in focal disruption of the integrity of the ventricular wall and internalization of ENSCs, which maintain residual cell polarity and AJCs. Internalized ENSCs form neuroepithelial rosette-like structures in the middle of the developing cortex and send out differentiating neurons to both normal cortical plate and the ventricular surface, effectively creating an ectopic layer of neurons at the ventricular surface of *Lgl1* cKO cortices.

LLGL1 is an apical-basal cell polarity protein; however, we found that maintenance of AJCs is the critical function of LLGL1 in mammalian brain. Cell polarity pathways may be intimately interconnected with cell-cell adhesion complexes. AJC represents the structure that physically separates the apical and basolateral membrane domains. Basolateral polarity complexes Lgl/Dlg/Scribble are required for AJC formation in epithelial cells (Bilder et al., 2003; Laprise et al., 2004; Qin et al., 2005;

Figure 6. Physical Interaction between N-Cadherin and Lgl1

(A and B) Co-immunoprecipitation between endogenous N-cadherin and Lgl1 in embryonic brains. Western blot (WB) analyses of total (Input) and immunoprecipitated using control preimmune, anti-Lgl1, or anti-N-cadherin antibodies proteins with anti-N-cadherin and anti-Lgl1 antibodies. Representative data from two independent experiments for (A) and three independent experiments for (B). Asterisks indicate nonspecific band.

(C) Western blot (WB) analysis and Coomassie staining of total (Input) and pulled down using beads alone, GST, GST-N-cadherin cytoplasmic domain (N-cad-cyto), and GST- β -catenin embryonic brain proteins. Representative data from two independent experiments.

(D) Western blot (WB) analyses of total (Input) and GST pull-down using control GST-GUS, GST-LLGL1 wild-type (LLGL1 WT), and GST-LLGL1 five SA mutant (LLGL1 SA) proteins extracted from HEK293 cells transfected with HA-tagged N-cadherin cytoplasmic domain (N-cad-cyto-HA) and constitutively active aPKC (aPKC) expression constructs. Representative data from three independent experiments.

(E) Diagram of LLGL1 fragment/deletion constructs used to identify N-cadherin binding domain. WD domains 1–14 are shown in black.

(F and F') C-terminal domain of LLGL1 binds to N-cadherin. Western blot (WB) analyses of proteins pulled down with glutathione Sepharose extracted from HEK293 cells expressing V5-tagged N-cadherin cytoplasmic domain (V5-N-cad cyto) and indicated GST-tagged fragments of LLGL1. V5-short and V5-long indicate shorter and longer exposure. Representative data from two independent experiments.

(G) Diagram showing N-cadherin cytoplasmic domain fragments/deletion constructs used to identify LLGL1 binding domain.

(H and H') Region containing amino acids 853–893 of murine N-cadherin binds to LLGL1, which is not phosphorylated by aPKC. Western blot (WB) analyses of proteins pulled down with glutathione Sepharose extracted from HEK293 cells expressing V5-tagged LLGL1(SA) mutant and indicated GST-tagged fragments of N-cadherin. Representative data from two independent experiments.

(I) Direct interaction between LLGL1 and N-cadherin. Western blot (WB) analysis and Coomassie staining of inputs and proteins pulled down with GST or GST-N-cadherin cytoplasmic domain (IP:GST) MBP-tagged LLGL1#5 and #9 (see E). Representative data from two independent experiments.

See also Figure S5.

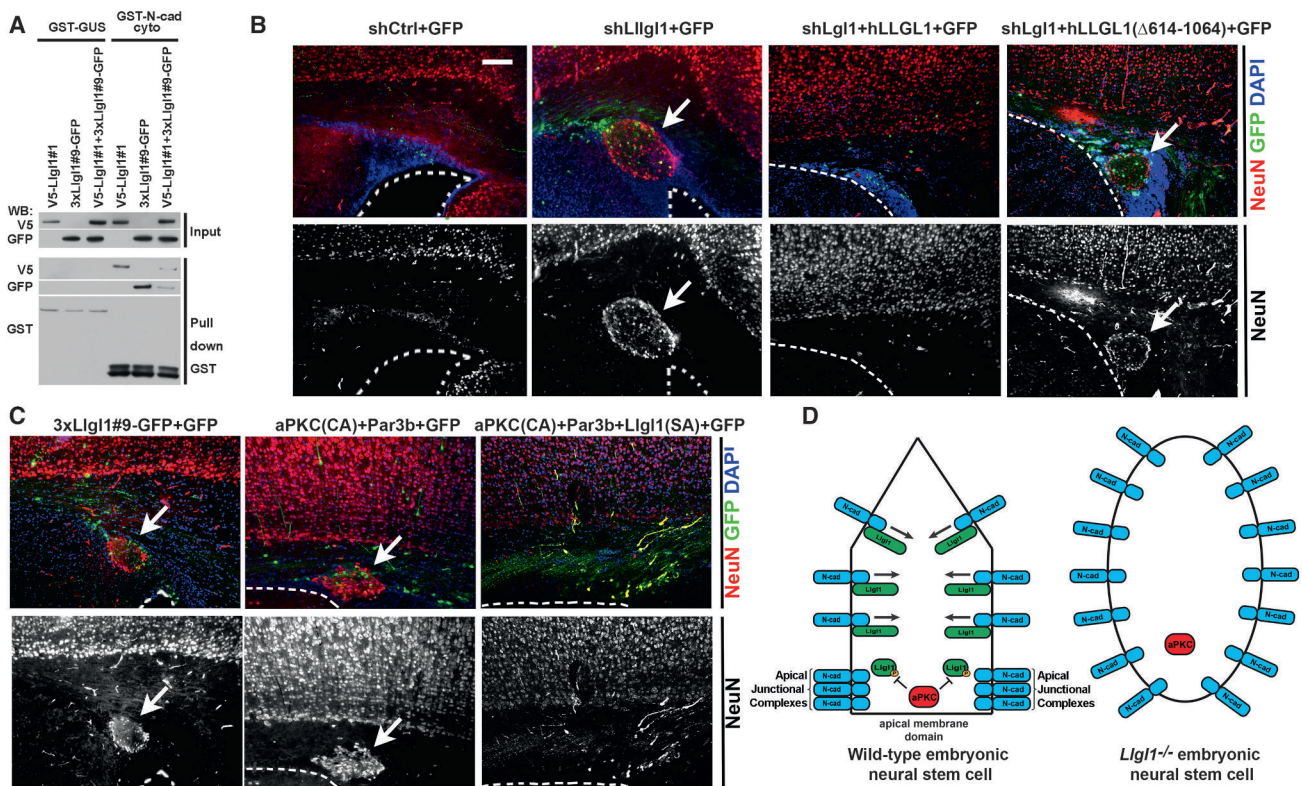


Figure 7. In Vivo Disruption of Interaction between LLGL1 and N-Cadherin during Brain Development Results in Formation of PH

(A) Multimerized LLGL1 fragment #9 weakens interaction between N-cadherin and LLGL1. Western blot (WB) analyses of total protein extracts (Input) or proteins pulled down with glutathione Sepharose extracted from HEK293 cells expressing a triple tandem repeat of LLGL1 #9 fused to GFP (3xLLgl1#9-GFP), full-length V5-tagged LLGL1(SA) mutant, negative control GST-GUS, and GST-N-cadherin cytoplasmic domain proteins. Representative data from two independent experiments.

(B and C) Expression of shLLgl1, membrane-targeted constitutively active aPKC or multimerized LLGL1 fragment #9 in the developing cerebral cortex results in neuronal heterotopia. Immunostainings of coronal brain sections (at the level of the lateral ventricle) from P7 wild-type pups that were electroporated in utero at E15.5 with GFP-encoding plasmid and negative control shRNA (shCtrl, 0 brains with heterotopia out of 6 electroporated brains), shLLgl1 (3 brains with heterotopia out of 3 electroporated brains), shLLgl1+human LLGL1 (0 brains with heterotopia out of 3 electroporated brains), shLLgl1+human LLGL1 Δ 614-1064 (3 brains with heterotopia out of 4 electroporated brains), aPKC+PAR3 (3 brains with heterotopia out of 3 electroporated brains), aPKC+Par3+SA-LLGL1 (3 complete rescues out of 5 electroporated brains), or triple tandem repeat of LLGL1 #9 fused to GFP (3xLLgl1#9-GFP, 4 brains with heterotopia out of 7 electroporated brains). Red-neuronal cell marker NeuroN (NeuN). Green-GFP. Blue-DAPI. Note GFP-positive ectopic neuronal nodules in cortices expressing shLLgl1, CA-aPKC+PAR3 and 3xLLgl1#9-GFP (arrows). White dotted lines indicate the position of the ventricular surface. Bar in (B) represents 105 μ m in (B) and (C).

(D) Hypothetical model of LLGL1 function in AJC maintenance. Nonphosphorylated by aPKC, LLGL1 binds to N-cadherin and promotes its internalization at the basolateral membrane domain. aPKC-mediated phosphorylation prevents LLGL1-N-cadherin interaction and promotes accumulation of N-cadherin at the interface between basolateral and apical membrane domains. See also Figure S6.

Tanentzapf and Tepass, 2003). We now demonstrate that mammalian LLGL1 is necessary for the maintenance of AJCs and that loss of adhesion is responsible for PH in *Llgl1* cKO brains. What is the mechanism responsible for LLGL1 function in AJC maintenance? We found that LLGL1 directly interacts with N-cadherin, and this binding is negatively regulated by aPKC-mediated phosphorylation. This interaction is important for LLGL1 function in brain development, because targeted disruption of this interaction in vivo is sufficient for neuronal heterotopia. We propose that the direct interaction of LLGL1 with N-cadherin contributes to the strengthening of AJCs and helps to maintain the integrity of the ventricular wall during embryonic brain development. Since interaction between LLGL1 and N-cadherin is disrupted by aPKC-mediated phosphorylation of LLGL1, and aPKC is concentrated at the AJCs of the ENSCs

(Manabe et al., 2002), LLGL1 would not be able to bind N-cadherin at this location. Thus, we propose the following hypothetical model of LLGL1 function (Figure 7D). Since LLGL1 is necessary for internalization of plasma membrane bound N-cadherin, it can differentially regulate N-cadherin internalization, promoting internalization at the lateral membrane domain but failing to do so at the AJCs, where aPKC phosphorylates LLGL1 and prevents LLGL1-N-cadherin interaction (Figure 7D). In this scenario, the local concentration of N-cadherin at the AJCs will increase, while the concentration of N-cadherin at the large lateral membrane domain will be kept at a minimum via LLGL1-mediated internalization. If this model is correct, aPKC should be essential for AJC formation, because without aPKC, LLGL1 would promote internalization of N-cadherin at the AJCs and, therefore, destabilize their integrity. Remarkably, in vivo deletion

of aPKC lambda in ENSCs results in a complete loss of AJCs, which is in an agreement with this prediction (Imai et al., 2006).

It has been reported previously that LLGL proteins physically interact with Myosin II and that aPKC-mediated phosphorylation disrupts this binding (Dahan et al., 2014; Strand et al., 1995). This functional interaction is important for microridge elongation in developing zebrafish epidermis (Raman et al., 2016). It is possible that LLGL1 links N-cadherin with myosin IIB, which can potentially facilitate clustering of cadherins into prominent AJC structures. Indeed, Myosin IIB is colocalized with AJCs, and it is critical for AJC maintenance (Ma et al., 2007; Smutny et al., 2010). We analyzed the possible role of LLGL1 in linking N-cadherin with myosin IIB; however, we found that overexpressed in HEK293 cells, LLGL1 and Myosin IIB compete for rather than facilitate each other in the interaction with N-cadherin (Figure S6B), indicating that this mechanism of LLGL1 function in AJC formation is not very likely. In addition to the direct interaction between LLGL1 and N-cadherin reported here, LLGL1 may potentially indirectly regulate AJCs via its role in the regulation of Par3-aPKC complexes, Rab-mediated endosomal trafficking, and/or its role in negative regulation of Notch signaling (Clark et al., 2012; Das et al., 1990; Klezovitch et al., 2004; Yamanaka et al., 2003). Additional research will be necessary to examine the mechanisms of LLGL1 in N-cadherin-mediated cell-cell adhesion.

STAR★METHODS

Detailed methods are provided in the online version of this paper and include the following:

- KEY RESOURCES TABLE
- CONTACT FOR REAGENT AND RESOURCE SHARING
- EXPERIMENTAL MODEL AND SUBJECT DETAILS
 - Mouse Strains and Genotyping
 - In Utero Electroporation of Developing Cerebral Cortices
 - Organotypic Slice Culture of Cerebral Cortices and Time-Lapse Confocal Microscopy
 - Labeling of Ventricular Zone Neurons with CMFDA Compound
 - Isolation, Culture and Nucleofection of Primary Murine ENSCs
 - Cell Lines
- METHOD DETAILS
 - Histology and Electron Microscopy
 - Immunofluorescence
 - Antibodies
 - Molecular Cloning
 - Immunoprecipitation and Western Blot Analysis
 - Cell-Surface Labeling, Internalization and Pulse-Chase Protein Expression Analyses
 - Statistical Analysis

SUPPLEMENTAL INFORMATION

Supplemental Information includes six figures, one table, and seven movies and can be found with this article online at <http://dx.doi.org/10.1016/j.devcel.2017.05.002>.

AUTHOR CONTRIBUTIONS

Conceptualization, Y.J., M.L., and V.V.; Methodology, Y.J., J.A.C., and V.V.; Investigation, Y.J., M.L., O.K., W.-H.L., E.K., A.C., and T.E.F.; Writing – Original Draft, Y.J., J.A.C., and V.V.; Writing – Review & Editing, all authors; Funding Acquisition, Y.J., M.L., J.A.C., and V.V.; Supervision, Y.J., J.A.C., and V.V.

ACKNOWLEDGMENTS

This work was partially supported by the FHCRC bridge funds, NIH grants CA131047, NS080194, CA179914, and 5T32HD007183, and FNRS grants J.0129.15 and J.0179.16. Y.J. is supported by the Belgian National Funds for Scientific Research (FNRS).

Received: June 22, 2016

Revised: April 11, 2017

Accepted: May 1, 2017

Published: May 25, 2017

REFERENCES

- Betschinger, J., Mechtler, K., and Knoblich, J.A. (2003). The Par complex directs asymmetric cell division by phosphorylating the cytoskeletal protein Lgl. *Nature* 422, 326–330.
- Betschinger, J., Eisenhaber, F., and Knoblich, J.A. (2005). Phosphorylation-induced autoinhibition regulates the cytoskeletal protein lethal (2) giant larvae. *Curr. Biol.* 15, 276–282.
- Bilder, D., Schober, M., and Perrimon, N. (2003). Integrated activity of PDZ protein complexes regulates epithelial polarity. *Nat. Cell Biol.* 5, 53–58.
- Bonifacino, J.S. (1998). *Current Protocols in Cell Biology* (John Wiley).
- Cappello, S., Attardo, A., Wu, X., Iwasato, T., Itoharu, S., Wilsch-Brauninger, M., Eilken, H.M., Rieger, M.A., Schroeder, T.T., Huttner, W.B., et al. (2006). The Rho-GTPase cdc42 regulates neural progenitor fate at the apical surface. *Nat. Neurosci.* 9, 1099–1107.
- Cappello, S., Bohringer, C.R., Bergami, M., Conzelmann, K.K., Ghanem, A., Tomassy, G.S., Arlotta, P., Mainardi, M., Allegra, M., Caleo, M., et al. (2012). A radial glia-specific role of RhoA in double cortex formation. *Neuron* 73, 911–924.
- Cappello, S., Gray, M.J., Badouel, C., Lange, S., Einsiedler, M., Srouf, M., Chitayat, D., Hamdan, F.F., Jenkins, Z.A., Morgan, T., et al. (2013). Mutations in genes encoding the cadherin receptor-ligand pair DCHS1 and FAT4 disrupt cerebral cortical development. *Nat. Genet.* 45, 1300–1308.
- Carabalona, A., Beguin, S., Pallesi-Pocachard, E., Buhler, E., Pellegrino, C., Arnaud, K., Hubert, P., Oualha, M., Siffroi, J.P., Khantane, S., et al. (2012). A glial origin for periventricular nodular heterotopia caused by impaired expression of Filamin-A. *Hum. Mol. Genet.* 21, 1004–1017.
- Chenn, A., Zhang, Y.A., Chang, B.T., and McConnell, S.K. (1998). Intrinsic polarity of mammalian neuroepithelial cells. *Mol. Cell Neurosci.* 11, 183–193.
- Chou, M.M., Hou, W., Johnson, J., Graham, L.K., Lee, M.H., Chen, C.S., Newton, A.C., Schaffhausen, B.S., and Toker, A. (1998). Regulation of protein kinase C zeta by PI 3-kinase and PDK-1. *Curr. Biol.* 8, 1069–1077.
- Clark, B.S., Cui, S., Miesfeld, J.B., Klezovitch, O., Vasioukhin, V., and Link, B.A. (2012). Loss of Lgl1 in retinal neuroepithelia reveals links between apical domain size, Notch activity and neurogenesis. *Development* 139, 1599–1610.
- Dahan, I., Petrov, D., Cohen-Kfir, E., and Ravid, S. (2014). The tumor suppressor Lgl1 forms discrete complexes with NMII-A and Par6alpha-aPKCzeta that are affected by Lgl1 phosphorylation. *J. Cell Sci.* 127, 295–304.
- Das, B.S., Thurnham, D.I., Patnaik, J.K., Das, D.B., Satpathy, R., and Bose, T.K. (1990). Increased plasma lipid peroxidation in riboflavin-deficient, malaria-infected children. *Am. J. Clin. Nutr.* 51, 859–863.
- Dollar, G.L., Weber, U., Mlodzik, M., and Sokol, S.Y. (2005). Regulation of lethal giant larvae by Dishevelled. *Nature* 437, 1376–1380.
- Feng, Y., and Walsh, C.A. (2004). The many faces of filamin: a versatile molecular scaffold for cell motility and signalling. *Nat. Cell Biol.* 6, 1034–1038.

- Ferland, R.J., Batiz, L.F., Neal, J., Lian, G., Bundock, E., Lu, J., Hsiao, Y.C., Diamond, R., Mei, D., Banham, A.H., et al. (2009). Disruption of neural progenitors along the ventricular and subventricular zones in periventricular heterotopia. *Hum. Mol. Genet.* *18*, 497–516.
- Fox, J.W., Lamperti, E.D., Eksioğlu, Y.Z., Hong, S.E., Feng, Y., Graham, D.A., Scheffer, I.E., Dobyns, W.B., Hirsch, B.A., Radtke, R.A., et al. (1998). Mutations in filamin 1 prevent migration of cerebral cortical neurons in human periventricular heterotopia. *Neuron* *21*, 1315–1325.
- Francis, F., Meyer, G., Fallet-Bianco, C., Moreno, S., Kappeler, C., Socorro, A.C., Tuy, F.P., Beldjord, C., and Chelly, J. (2006). Human disorders of cortical development: from past to present. *Eur. J. Neurosci.* *23*, 877–893.
- Graus-Porta, D., Blaess, S., Senften, M., Littlewood-Evans, A., Damsky, C., Huang, Z., Orban, P., Klein, R., Schittny, J.C., and Müller, U. (2001). Beta1-class integrins regulate the development of laminae and folia in the cerebral and cerebellar cortex. *Neuron* *31*, 367–379.
- Harlow, E., and Lane, D. (1999). *Using Antibodies: A Laboratory Manual* (Cold Spring Harbor Laboratory Press).
- Imai, F., Hirai, S., Akimoto, K., Koyama, H., Miyata, T., Ogawa, M., Noguchi, S., Sasaoka, T., Noda, T., and Ohno, S. (2006). Inactivation of aPKC λ results in the loss of adherens junctions in neuroepithelial cells without affecting neurogenesis in mouse neocortex. *Development* *133*, 1735–1744.
- Joberty, G., Petersen, C., Gao, L., and Macara, I.G. (2000). The cell-polarity protein Par6 links Par3 and atypical protein kinase C to Cdc42. *Nat. Cell Biol.* *2*, 531–539.
- Johansson, C.B., Momma, S., Clarke, D.L., Risling, M., Lendahl, U., and Frisen, J. (1999). Identification of a neural stem cell in the adult mammalian central nervous system. *Cell* *96*, 25–34.
- Jossin, Y., and Cooper, J.A. (2011). Reelin, Rap1 and N-cadherin orient the migration of multipolar neurons in the developing neocortex. *Nat. Neurosci.* *14*, 697–703.
- Jossin, Y., and Goffinet, A.M. (2007). Reelin signals through phosphatidylinositol 3-kinase and Akt to control cortical development and through mTor to regulate dendritic growth. *Mol. Cell Biol.* *27*, 7113–7124.
- Jossin, Y., Ogawa, M., Metin, C., Tissir, F., and Goffinet, A.M. (2003). Inhibition of SRC family kinases and non-classical protein kinases C induce a reeler-like malformation of cortical plate development. *J. Neurosci.* *23*, 9953–9959.
- Junghans, D., Hack, I., Frotscher, M., Taylor, V., and Kemler, R. (2005). Beta-catenin-mediated cell-adhesion is vital for embryonic forebrain development. *Dev. Dyn.* *233*, 528–539.
- Kadowaki, M., Nakamura, S., Machon, O., Krauss, S., Radice, G.L., and Takeichi, M. (2007). N-cadherin mediates cortical organization in the mouse brain. *Dev. Biol.* *304*, 22–33.
- Katayama, K., Melendez, J., Baumann, J.M., Leslie, J.R., Chauhan, B.K., Nemkul, N., Lang, R.A., Kuan, C.Y., Zheng, Y., and Yoshida, Y. (2011). Loss of RhoA in neural progenitor cells causes the disruption of adherens junctions and hyperproliferation. *Proc. Natl. Acad. Sci. USA* *108*, 7607–7612.
- Kim, S., Lehtinen, M.K., Sessa, A., Zappaterra, M.W., Cho, S.H., Gonzalez, D., Boggan, B., Austin, C.A., Wijnholds, J., Gambello, M.J., et al. (2010). The apical complex couples cell fate and cell survival to cerebral cortical development. *Neuron* *66*, 69–84.
- Klezovitch, O., Fernandez, T.E., Tapscott, S.J., and Vasioukhin, V. (2004). Loss of cell polarity causes severe brain dysplasia in Lgl1 knockout mice. *Genes Dev.* *18*, 559–571.
- Laprise, P., Viel, A., and Rivard, N. (2004). Human homolog of disc-large is required for adherens junction assembly and differentiation of human intestinal epithelial cells. *J. Biol. Chem.* *279*, 10157–10166.
- Lian, G., and Sheen, V.L. (2015). Cytoskeletal proteins in cortical development and disease: actin associated proteins in periventricular heterotopia. *Front. Cell. Neurosci.* *9*, 99.
- Lien, W.H., Klezovitch, O., Fernandez, T.E., Delrow, J., and Vasioukhin, V. (2006). alphaE-catenin controls cerebral cortical size by regulating the hedgehog signaling pathway. *Science* *311*, 1609–1612.
- Lien, W.H., Gelfand, V.I., and Vasioukhin, V. (2008). Alpha-E-catenin binds to dynactin and regulates dynactin-mediated intracellular traffic. *J. Cell Biol.* *183*, 989–997.
- Lu, J., and Sheen, V. (2005). Periventricular heterotopia. *Epilepsy Behav.* *7*, 143–149.
- Ma, X., Bao, J., and Adelstein, R.S. (2007). Loss of cell adhesion causes hydrocephalus in nonmuscle myosin II-B-ablated and mutated mice. *Mol. Biol. Cell* *18*, 2305–2312.
- Machon, O., van den Bout, C.J., Backman, M., Kemler, R., and Krauss, S. (2003). Role of beta-catenin in the developing cortical and hippocampal neuroepithelium. *Neuroscience* *122*, 129–143.
- Manabe, N., Hirai, S., Imai, F., Nakanishi, H., Takai, Y., and Ohno, S. (2002). Association of ASIP/mPAR-3 with adherens junctions of mouse neuroepithelial cells. *Dev. Dyn.* *225*, 61–69.
- Matsuda, T., and Cepko, C.L. (2004). Electroporation and RNA interference in the rodent retina in vivo and in vitro. *Proc. Natl. Acad. Sci. USA* *101*, 16–22.
- Mochida, G.H., and Walsh, C.A. (2004). Genetic basis of developmental malformations of the cerebral cortex. *Arch. Neurol.* *61*, 637–640.
- Plant, P.J., Fawcett, J.P., Lin, D.C., Holdorf, A.D., Binns, K., Kulkarni, S., and Pawson, T. (2003). A polarity complex of mPar-6 and atypical PKC binds, phosphorylates and regulates mammalian Lgl. *Nat. Cell Biol.* *5*, 301–308.
- Prehoda, K.E. (2009). Polarization of *Drosophila* neuroblasts during asymmetric division. *Cold Spring Harb. Perspect. Biol.* *1*, a001388.
- Qin, Y., Capaldo, C., Gumbiner, B.M., and Macara, I.G. (2005). The mammalian Scribble polarity protein regulates epithelial cell adhesion and migration through E-cadherin. *J. Cell Biol.* *171*, 1061–1071.
- Raman, R., Damle, I., Rote, R., Banerjee, S., Dingare, C., and Sonawane, M. (2016). aPKC regulates apical localization of Lgl to restrict elongation of micro-ridges in developing zebrafish epidermis. *Nat. Commun.* *7*, 11643.
- Saito, T. (2006). In vivo electroporation in the embryonic mouse central nervous system. *Nat. Protoc.* *1*, 1552–1558.
- Schmid, M.T., Weinandy, F., Wilsch-Brauninger, M., Huttner, W.B., Cappello, S., and Gotz, M. (2014). The role of alpha-E-catenin in cerebral cortex development: radial glia specific effect on neuronal migration. *Front. Cell. Neurosci.* *8*, 215.
- Sheen, V.L., Ganesh, V.S., Topcu, M., Sebire, G., Bodell, A., Hill, R.S., Grant, P.E., Shugart, Y.Y., Imitola, J., Khoury, S.J., et al. (2004). Mutations in ARFGEF2 implicate vesicle trafficking in neural progenitor proliferation and migration in the human cerebral cortex. *Nat. Genet.* *36*, 69–76.
- Smutny, M., Cox, H.L., Leerberg, J.M., Kovacs, E.M., Conti, M.A., Ferguson, C., Hamilton, N.A., Parton, R.G., Adelstein, R.S., and Yap, A.S. (2010). Myosin II isoforms identify distinct functional modules that support integrity of the epithelial zonula adherens. *Nat. Cell Biol.* *12*, 696–702.
- Spear, P.C., and Erickson, C.A. (2012). Interkinetic nuclear migration: a mysterious process in search of a function. *Dev. Growth Differ.* *54*, 306–316.
- Sripathy, S., Lee, M., and Vasioukhin, V. (2011). Mammalian Lgl2 is necessary for proper branching morphogenesis during placental development. *Mol. Cell Biol.* *31*, 2920–2933.
- Strand, D., Unger, S., Corvi, R., Hartenstein, K., Schenkel, H., Kalmes, A., Merdes, G., Neumann, B., Krieg-Schneider, F., Coy, J.F., et al. (1995). A human homologue of the *Drosophila* tumour suppressor gene *l(2)gl* maps to 17p11.2-12 and codes for a cytoskeletal protein that associates with non-muscle myosin II heavy chain. *Oncogene* *11*, 291–301.
- Tabata, H., and Nakajima, K. (2001). Efficient in utero gene transfer system to the developing mouse brain using electroporation: visualization of neuronal migration in the developing cortex. *Neuroscience* *103*, 865–872.
- Tanentzapf, G., and Tepass, U. (2003). Interactions between the crumbs, lethal giant larvae and bazooka pathways in epithelial polarization. *Nat. Cell Biol.* *5*, 46–52.
- Teng, J., Rai, T., Tanaka, Y., Takei, Y., Nakata, T., Hirasawa, M., Kulkarni, A.B., and Hirokawa, N. (2005). The KIF3 motor transports N-cadherin and organizes the developing neuroepithelium. *Nat. Cell Biol.* *7*, 474–482.

- Tronche, F., Kellendonk, C., Kretz, O., Gass, P., Anlag, K., Orban, P.C., Bock, R., Klein, R., and Schutz, G. (1999). Disruption of the glucocorticoid receptor gene in the nervous system results in reduced anxiety. *Nat. Genet.* **23**, 99–103.
- Vasioukhin, V. (2006). Lethal giant puzzle of Lgl. *Dev. Neurosci.* **28**, 13–24.
- Wei, Q., and Adelstein, R.S. (2000). Conditional expression of a truncated fragment of nonmuscle myosin II-A alters cell shape but not cytokinesis in HeLa cells. *Mol. Biol. Cell* **11**, 3617–3627.
- Yamanaka, T., Horikoshi, Y., Sugiyama, Y., Ishiyama, C., Suzuki, A., Hirose, T., Iwamatsu, A., Shinohara, A., and Ohno, S. (2003). Mammalian Lgl forms a protein complex with PAR-6 and aPKC independently of PAR-3 to regulate epithelial cell polarity. *Curr. Biol.* **13**, 734–743.
- Yap, A.S., Gomez, G.A., and Parton, R.G. (2015). Adherens junctions revisited: organizing cadherins as nanoassemblies. *Dev. Cell* **35**, 12–20.
- Zechner, D., Fujita, Y., Hulsken, J., Muller, T., Walther, I., Taketo, M.M., Crenshaw, E.B., 3rd, Birchmeier, W., and Birchmeier, C. (2003). beta-Catenin signals regulate cell growth and the balance between progenitor cell expansion and differentiation in the nervous system. *Dev. Biol.* **258**, 406–418.

Synaptic Vesicle Endocytosis Occurs on Multiple Timescales and Is Mediated by Formin-Dependent Actin Assembly

Tolga Soykan,¹ Natalie Kaempf,¹ Takeshi Sakaba,⁴ Dennis Vollweiler,¹ Felix Goerdeler,^{1,2} Dmytro Puchkov,¹ Natalia L. Kononenko,^{1,3,5} and Volker Haucke^{1,2,3,6,*}

¹Leibniz-Institut für Molekulare Pharmakologie (FMP), 13125 Berlin, Germany

²Freie Universität Berlin, Faculty of Biology, Chemistry and Pharmacy, 14195 Berlin, Germany

³NeuroCure Cluster of Excellence, Charité Universitätsmedizin Berlin, 10117 Berlin, Germany

⁴Doshisha University, Graduate School of Brain Science, Kyoto 610-0394, Japan

⁵CECAD Research Center, University of Cologne, 50931 Cologne, Germany

⁶Lead Contact

*Correspondence: haucke@fmp-berlin.de

<http://dx.doi.org/10.1016/j.neuron.2017.02.011>

SUMMARY

Neurotransmission is based on the exocytic fusion of synaptic vesicles (SVs) followed by endocytic membrane retrieval and the reformation of SVs. Recent data suggest that at physiological temperature SVs are internalized via clathrin-independent ultrafast endocytosis (UFE) within hundreds of milliseconds, while other studies have postulated a key role for clathrin-mediated endocytosis (CME) of SV proteins on a timescale of seconds to tens of seconds. Here we demonstrate using cultured hippocampal neurons as a model that at physiological temperature SV endocytosis occurs on several timescales from less than a second to several seconds, yet, is largely independent of clathrin. Clathrin-independent endocytosis (CIE) of SV membranes is mediated by actin-nucleating formins such as mDia1, which are required for the formation of presynaptic endosome-like vacuoles from which SVs reform. Our results resolve previous discrepancies in the field and suggest that SV membranes are predominantly retrieved via CIE mediated by formin-dependent actin assembly.

INTRODUCTION

Neuronal communication depends on the regulated release of neurotransmitters from synaptic vesicles (SVs) by calcium-triggered exocytic fusion at specialized presynaptic release sites within active zones (AZs) (Dittman and Ryan, 2009; Haucke et al., 2011; Kononenko and Haucke, 2015; Rizzoli, 2014; Saheki and De Camilli, 2012). To prevent expansion of the presynaptic plasma membrane and to sustain neurotransmission, SV endocytosis is followed by compensatory endocytic membrane retrieval and the reformation of SVs. In spite of more than 40 years of research, the mechanisms involved in SV endocytosis and reformation remain controversial (Aravanis et al., 2003; Cheung and

Cousin, 2012; Dittman and Ryan, 2009; Granseth et al., 2006; Kononenko and Haucke, 2015; Saheki and De Camilli, 2012; Watanabe et al., 2014; and below).

Electron microscopy (EM) analysis of stimulated frog neuromuscular junctions (Heuser and Reese, 1973) and subsequent work on mammalian synapses has suggested that SV membranes are recycled by clathrin-mediated endocytosis (CME) from the plasma membrane (Dittman and Ryan, 2009; Granseth et al., 2006; Kim and Ryan, 2009; Saheki and De Camilli, 2012), a pathway that crucially depends on clathrin and its major adaptor protein 2 (AP-2) and occurs on a timescale of tens of seconds, at least in non-neuronal cells (Dittman and Ryan, 2009). Using the same preparation, but a different stimulation paradigm, Ceccarelli et al. (Ceccarelli et al., 1972) proposed an alternative clathrin-independent rapid mode of SV recycling by kiss-and-run exo-/endocytosis of SVs involving a transient fusion pore. While kiss-and-run exocytosis clearly has been observed in neuroendocrine cells (Albillos et al., 1997; Zhao et al., 2016), its role in primary neurons is debated. Recent data from invertebrate (Watanabe et al., 2013a) and hippocampal synapses (Watanabe et al., 2013b, 2014) using high-pressure freezing EM paired with optogenetic stimulation suggest that SVs are recycled extremely rapidly via clathrin-independent ultrafast endocytosis (UFE) within hundreds of milliseconds. UFE is followed by clathrin-dependent SV reformation from internal endosome-like vacuolar structures (Watanabe et al., 2014). As UFE seems to depend on physiological temperature, the authors have argued that some of the discrepancies in the field (e.g., regarding the time course of endocytosis; Eguchi et al., 2012; Granseth et al., 2006; Jockusch et al., 2005; Watanabe et al., 2013b; Wu et al., 2014a) may be related to temperature artifacts due to experimentation at room temperature (Watanabe et al., 2014).

These discrepant views on the mechanism and speed of SV endocytosis may, at least in part, relate to the caveats inherent to the experimental approaches used to study SV exo-/endocytosis. PHluorins and related pH sensors report on pH changes that occur as a consequence of SV fusion and post-endocytic reacidification. These assays offer a kinetic resolution that is limited by the rate of SV reacidification (approximately 3–4 s; Atluri and Ryan, 2006) and, thus, is blind to fast modes of SV

recycling such as UFE. Conversely, imaging approaches, such as high-pressure freezing EM (Watanabe et al., 2013b, 2014) or electrophysiological capacitance measurements at large synapses (Delvendahl et al., 2016; Eguchi et al., 2012; Hosoi et al., 2009; Wu et al., 2014a) are incapable of monitoring the endocytic fate of SV proteins inserted into the plasma membrane in response to stimulation (Kavalali and Jorgensen, 2014; Kononenko and Haucke, 2015).

Here we combine optical imaging of pHluorin probes, capacitance measurements, and ultrastructural analysis by EM to show that SV endocytosis in hippocampal neurons occurs on multiple timescales from less than a second to several seconds at physiological temperature, yet, is largely independent of clathrin and its major adaptor AP-2. Clathrin-independent endocytosis (CIE) of SV membranes is mediated by formins such as mDia1, an evolutionary conserved family of actin-nucleating proteins (Goode and Eck, 2007; Levayer et al., 2011; Prosser et al., 2011) present within axons (Ganguly et al., 2015) and pre-synaptic nerve terminals (Wagh et al., 2015). Our results resolve previous discrepancies in the field and suggest that SVs are predominantly reformed from endosome-like vacuoles generated via formin-mediated CIE of SV membranes.

RESULTS

SV Proteins Are Endocytosed on Multiple Timescales from Less Than a Second to Several Seconds at Physiological Temperature

Previous measurements of the rate of SV endocytosis in hippocampal neurons using chimeric reporters between SV proteins and a pH-sensitive pHluorin variant of GFP have yielded endocytic time constants between 6–7 and 50 s, depending on the duration and strength of the stimulus (Armbruster et al., 2013; Ferguson et al., 2007; Granseth et al., 2006; Kim and Ryan, 2009; Saheki and De Camilli, 2012; Wienisch and Klingauf, 2006). These values are several orders of magnitude slower than UFE of SVs in optogenetically stimulated neurons expressing channelrhodopsin reported to occur within 50 to 500 ms (Watanabe et al., 2013a, 2013b, 2014). The direct cause of the decline in the pHluorin signal after exocytosis is the reacidification of the endocytosed vesicles by the proton ATPase, which occurs with a time constant of about 3–4 s (Atluri and Ryan, 2006). It is therefore possible that previous experiments using pHluorin reporters might have missed UFE due to the limits imposed by the rate of reacidification. Moreover, most optical recordings of SV endocytosis in hippocampal neurons have been carried out at or slightly above room temperature, conditions under which UFE has been reported to cease operation (Watanabe et al., 2014). Given these caveats it appears that the kinetics of SV endocytosis in hippocampal neurons deserve to be revisited.

To measure the true rate of SV endocytosis in hippocampal neurons at physiological temperature we used an approach that was independent of pH changes inside the retrieved SV. This method takes advantage of the fact that newly exocytosed pHluorin-tagged SV proteins can be quenched instantaneously by extracellular application of a low pH buffer to the medium using fast perfusion (Merrifield et al., 2005). Concurrent blocking of vesicle reacidification post-endocytosis by folimycin, a selective

inhibitor of the proton ATPase (Granseth et al., 2006) allowed us to quantitatively determine the endocytosis of SV proteins as a fraction of the amount of exocytosed SV proteins at defined time intervals (*t*) after the end of the stimulation (Figure 1A and STAR Methods). We stimulated hippocampal neurons expressing synaptotagmin 1-pHluorin with 200 action potentials (APs) applied at 40 Hz at physiological temperature (37°C) and determined the fraction of synaptotagmin 1-pHluorin retrieval 1 s after the end of the stimulation train. If all SV proteins were retrieved ultrafast, we would expect synaptotagmin 1-pHluorin endocytosis to be complete within 1 s at physiological temperature (Watanabe et al., 2014). We observed that only a minor fraction of about 20% of all synaptotagmin 1-pHluorin molecules had undergone endocytosis at this time point (Figures 1C and 1D). Similar results were seen, if synaptotagmin 1-pHluorin was replaced by synaptophysin-pHluorin as a probe for SV endocytosis. In this case a fraction of about 30% of all exocytosed synaptophysin-pHluorin molecules were retrieved within 1 s post-stimulation for 5 s at 40 Hz (Figures S1A and S1E). Application of dynasore, an inhibitor of dynamin (Macia et al., 2006) and possibly other GTPases (Park et al., 2013), largely blocked the formation of this acid-resistant pool, suggesting that our assay indeed measures SV endocytosis (Figures S1C and S1D). When the experiment was repeated at 25°C, a temperature when UFE ceases to operate according to Watanabe et al. (2014), the acid-resistant fraction decreased to about 10%–12% of all exocytosed synaptotagmin 1-pHluorin molecules (Figures 1B and 1D).

Although UFE after optogenetic stimulation has been proposed to be the predominant pathway of SV retrieval up to 100 APs (Watanabe et al., 2014), it is nonetheless possible that the capacity of the pathway is limited. To investigate this possibility, we measured the fraction of retrieved acid-resistant SV proteins using different stimulation paradigms and pHluorin reporters. The fraction of endocytosed synaptotagmin 1-pHluorin within 1 s post-stimulation remained at about 20%, if neurons were stimulated with a milder AP train for 5 s at 10 Hz and dropped to roughly 15% following brief high-frequency stimulation for 1 s at 40 Hz (Figure 1E). Probing the kinetics of SV protein internalization at physiological temperature independent of reacidification in response to stimulation with 50 APs at 10 Hz was best fit with a single exponential with a time constant of 25.5 s (Figure S1B). Stimulation of synaptophysin-pHluorin-expressing neurons with only 10 APs in the presence of 4 mM extracellular calcium (as in Watanabe et al., 2013b, 2014) likewise resulted in the rapid retrieval of about 18% of all exocytosed molecules (Figures 1F and 1H). Interestingly, the fraction of rapidly endocytosed SV proteins rose to almost 50%, if neurons were stimulated at physiological temperature with 2 APs at 4 Hz (Figure 1H), suggesting that UFE is a fast pathway for SV protein endocytosis whose capacity is limited to stimulation with single or few APs (as in Watanabe et al., 2013a, 2013b), at least in hippocampal synapses. Consistent with this hypothesis, we found that the kinetics of SV protein internalization in response to stimulation with either 10 APs at 10 Hz or 2 APs at 4 Hz yielded fast and slow time constants of about 0.7 s and 26 s or 12 s, respectively, when fit by a double exponential decay curve (Figure 1I).

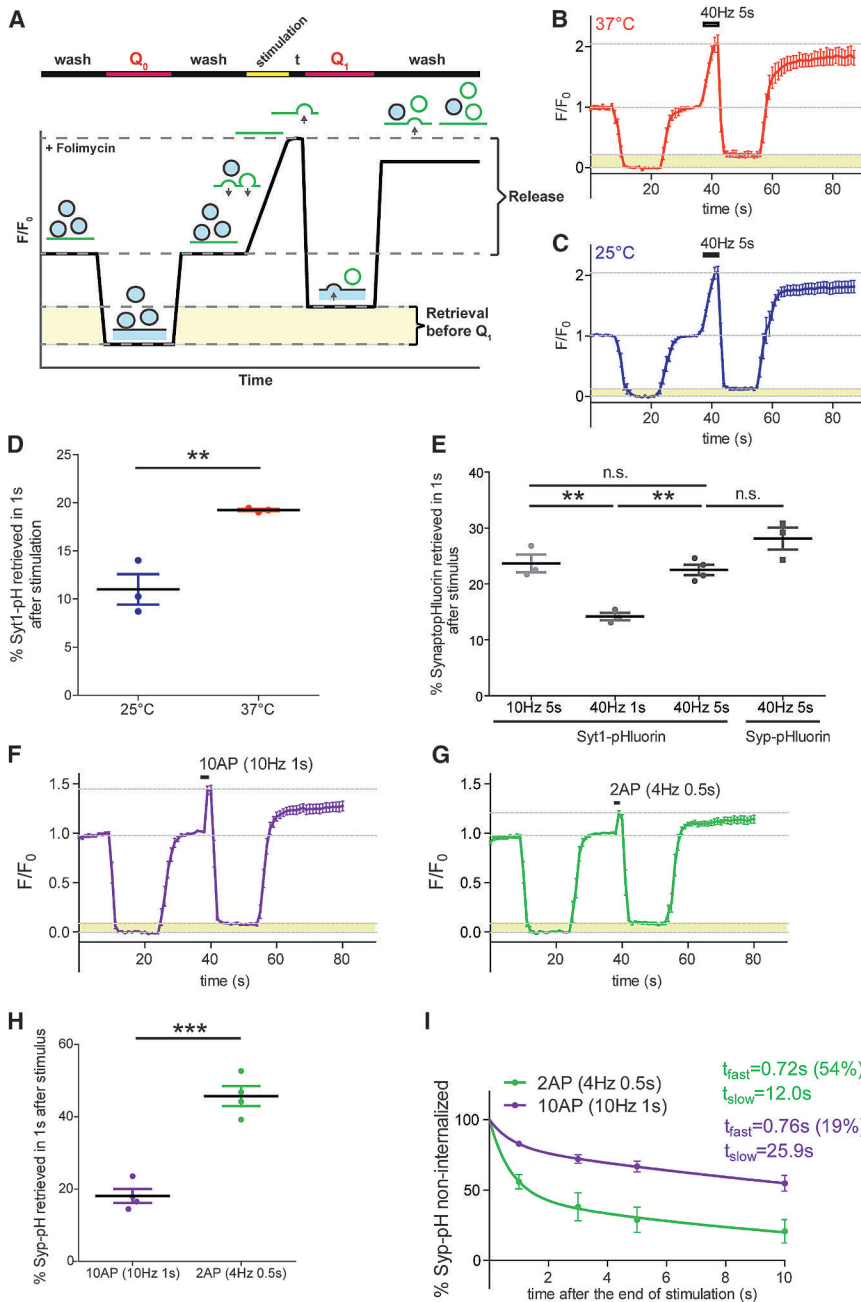


Figure 1. SV Proteins Are Endocytosed on Multiple Timescales Ranging from Less Than a Second to Several Seconds at Physiological Temperature

(A) Scheme for pHluorin experiment coupled to external acid pulse. Synaptotagmin-1-pHluorin-expressing cultured neurons are subjected to a brief phase of external acidic buffer 15 s before (Q_0) and t number of seconds after (Q_1) a train of stimulation, in the presence of folimycin. The relative amounts of synaptotagmin-1-pHluorin released (the steep rise in fluorescence upon stimulation) and retrieved within the t seconds after stimulation (already internalized proteins not affected by surface quenching, shaded in yellow) is derived from the normalized fluorescence values as indicated. Representative SVs and presynaptic plasma membrane are depicted for each step of the protocol. Blue shade represents acidic pH, black and green outlines represent quenched and unquenched fluorescence of pHluorin, respectively.

(B and C) The acid quench protocol reveals the fraction of SV proteins retrieved immediately after stimulation. The average traces for synaptotagmin-1-pHluorin-expressing neurons exposed to external acidic buffer 15 s before and 1 s after a 40 Hz 5 s stimulation at 37°C (B) and 25°C (C). The fractions corresponding to fast retrieval of pHluorin are shaded in yellow. Traces represent the mean \pm SEM of $n = 15$ (25°C) and 13 (37°C) neurons measured in $N = 3$ independent experiments.

(D) SV protein endocytosis is temperature dependent. Decreased levels of synaptotagmin-1-pHluorin retrieval in 1 s after 40 Hz 5 s stimulation at 25°C ($11.0\% \pm 1.6\%$), as compared to 37°C ($19.2\% \pm 0.1\%$, $p < 0.01$). Data shown represent the mean \pm SEM of $N = 3$ independent experiments, $n = 13$ and 15 neurons in total for 37°C and 25°C.

(E) Percentage of synaptotagmin-1-pHluorin retrieved in 1 s after 10 Hz 5 s ($23.7\% \pm 1.6\%$), 40 Hz 1 s ($14.2\% \pm 0.7\%$), and 40 Hz 5 s ($22.5\% \pm 0.9\%$) and synaptophysin-pHluorin retrieved in 1 s after 40 Hz 5 s ($28.1\% \pm 2.0\%$) stimulation. Data shown represent the mean \pm SEM of $N = 3$ or 4 independent experiments, $n = 7, 10, 10,$ and 12 neurons measured in total. Significance evaluated using one-way ANOVA.

(F and G) The average traces for synaptophysin-pHluorin-expressing neurons exposed to external acidic buffer 15 s before and 1 s after a 10 Hz 1 s (F) and 4 Hz 0.5 s (G) stimulation in the presence of folimycin and 4 mM extracellular calcium. The

fractions corresponding fast retrieval of synaptophysin-pHluorin are shaded in yellow. Traces represent the mean \pm SEM of $n = 15$ (2 AP) and 19 (10 AP) neurons measured in $N = 4$ independent experiments.

(H) Percentage of synaptophysin-pHluorin retrieved in 1 s after 10 Hz 1 s ($18.1\% \pm 1.9\%$) and 4 Hz 0.5 s ($45.7\% \pm 2.8\%$, $p < 0.001$). Data shown represent the mean \pm SEM of $N = 4$ experiments, $n = 15$ and 19 neurons measured for 2 AP and 10 AP, respectively.

(I) The time course of synaptophysin-pHluorin retrieval after 10 Hz 1 s and 4 Hz 0.5 s stimulation measured by applying an acid pulse at 1, 3, 5, and 10 s after the end of the stimulation. The data points were fit with biexponential decay curves, yielding two time constants $\tau_{fast} = 0.76$ s (19%) and $\tau_{slow} = 25.9$ s for 10 AP and $\tau_{fast} = 0.72$ s (54%) and $\tau_{slow} = 12.0$ s for 2 AP stimulation. Please note that the determination of τ_{fast} is associated with some imprecision as the assay is “blind” to endocytosis that occurs during the stimulation.

Statistically significant estimates of data shown were obtained from N independent experiments. See also Figure S1.

These results demonstrate that the majority of SV proteins under most stimulation conditions tested is not internalized with ultrafast, i.e., subsecond, kinetics in response to electrical stim-

ulation, although we observe a minor fraction of SV proteins to be endocytosed within less than a second, likely corresponding to (ultra-) fast SV endocytosis seen at hippocampal (Watanabe

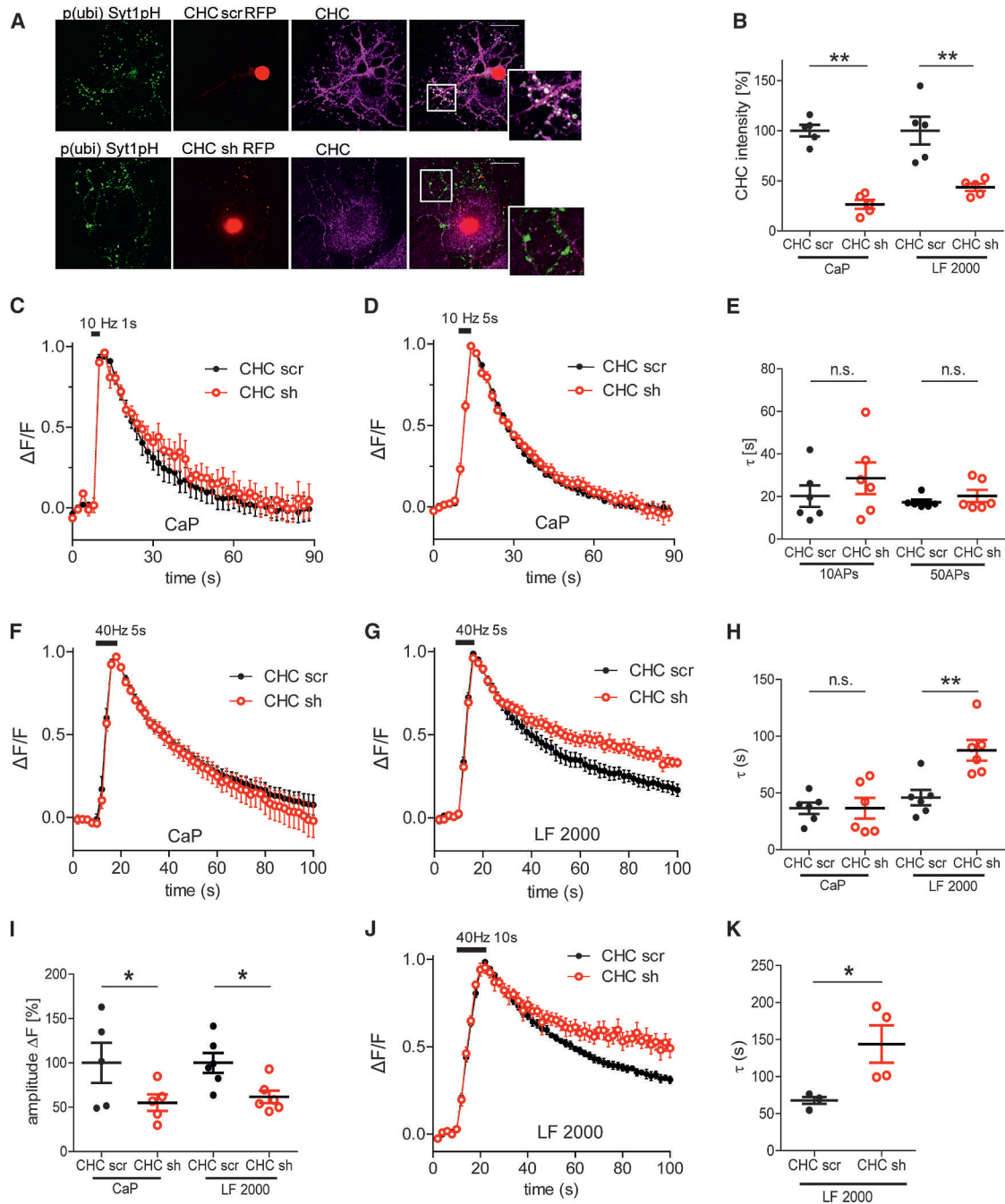


Figure 2. Endocytosis of SV Proteins Is Largely Independent of Clathrin and AP-2 and, Thus, of CME in Hippocampal Neurons

(A) Primary hippocampal neurons from WT mice transfected with ubiquitin-promoter controlled synaptotagmin 1-pHluorin (green) and scrambled or CHC shRNA (red) using calcium-phosphate or lipofectamine were immunostained with CHC antibodies (magenta). Scale bar, 20 μm .

(B) Levels of clathrin (CHC) quantified from (A). Transfection with CHC shRNA leads to depletion of CHC down to 26.6% \pm 4.5% ($p < 0.01$) in calcium-phosphate (CaP) and 43.5% \pm 3.6% ($p < 0.05$) in lipofectamine-transfected (LF 2000) neurons. Data shown represent the mean \pm SEM of $N = 5$ with $n = 135$ and $n = 118$ neurons in total for lipofectamine-transfected scrambled shRNA and CHC shRNA and $N = 5$ with $n = 84$ and $n = 86$ neurons in total for calcium-transfected scrambled shRNA and CHC shRNA.

(C–E) Depletion of clathrin does not affect endocytic retrieval during mild stimulation. Average normalized traces for calcium-phosphate transfected neurons coexpressing synaptophysin-pHluorin and scrambled shRNA or clathrin (CHC) shRNA in response to 10 APs with 10 Hz, 1 s stimulation in 4 mM extracellular calcium (C) and 50 APs (10 Hz, 5 s), (D). (E) Endocytic decay constant of calcium-phosphate-transfected neurons coexpressing synaptophysin-pHluorin and scrambled shRNA (20.2 \pm 5.0 s) or clathrin (CHC) shRNA (28.6 \pm 7.4 s) at 10 APs and neurons coexpressing synaptophysin-pHluorin and scrambled shRNA (17.3 \pm 1.2 s) or clathrin (CHC) shRNA (20.2 \pm 2.9 s) at 50 APs. Data shown represent the mean \pm SEM of $N = 6$ independent experiments with $n = 26$ and $n = 17$

(legend continued on next page)

et al., 2013b, 2014) and cerebellar mossy fiber synapses (Delvendahl et al., 2016). While UFE may be an important pathway of SV endocytosis in neurons stimulated with single or few APs, the majority of SV proteins appears to be internalized on a timescale of 10–30 s following AP train stimulation at physiological temperature, consistent with prior data from conventional pHluorin-based kinetic measurements (Ferguson et al., 2007; Granseth et al., 2006; Kavalali and Jorgensen, 2014; Kim and Ryan, 2009; Kononenko et al., 2014; Wienisch and Klingauf, 2006). Thus, SV endocytosis depending on stimulation occurs on multiple timescales from less than a second to several seconds.

Endocytosis of SV Proteins in Cultured Hippocampal Neurons Is Largely Independent of Clathrin and AP-2

Endocytosis of SV proteins on a timescale of seconds is compatible with their internalization via clathrin/AP-2-mediated endocytosis (CME). Conflicting data regarding the role of CME in SV endocytosis have been reported (Delvendahl et al., 2016; Granseth et al., 2006; Kasprovicz et al., 2008; Kononenko et al., 2014; Nicholson-Fish et al., 2015; Watanabe et al., 2013b, 2014; Wu et al., 2014b). While we (Kononenko et al., 2014) and others (Delvendahl et al., 2016; Kasprovicz et al., 2008; Kim and Ryan, 2009; Watanabe et al., 2014; Wu et al., 2014b) have recently shown that the kinetics of endocytic retrieval of SV proteins are largely unaffected by lentiviral knockdown (KD) of clathrin or genetic knockout (KO) of its essential adaptor AP-2, other reports (Granseth et al., 2006; Nicholson-Fish et al., 2015) have suggested an essential role for clathrin in SV endocytosis in hippocampal neurons. One possible explanation for these discrepant results is the possibility that depletion of clathrin or KO of AP-2 alone may be insufficient to completely eliminate all CME in neurons. We therefore investigated the function of CME in SV endocytosis by KD of clathrin in neurons from tamoxifen-inducible conditional AP-2 KO mice. As expected tamoxifen induction of the AP-2(μ) KO resulted in the near complete elimination of the AP-2 complex (<17% of WT levels, further depletion over time below this level caused extensive neuronal death) measured by its α -subunit (Figures S2A and S2B; Kononenko et al., 2014). Transfection of AP-2 KO or wild-type neurons

from littermate controls with shRNA directed against clathrin heavy chain efficiently depleted clathrin levels to about 35% of that seen in controls (Figure S2C), in good agreement with previous data (Granseth et al., 2006; Kononenko et al., 2014; Nicholson-Fish et al., 2015; Watanabe et al., 2014; Wu et al., 2014b). Thus, the efficacy of CME in AP-2 KO neurons depleted of clathrin is expected to be reduced to about 7% ($0.17 \times 0.35 \times 100$) of control neurons. Consistently, we found CME of transferrin in primary neurons lacking AP-2 or both AP-2 and clathrin together to be blocked completely (Figure S2D). To assess the effects of CME blockade on the kinetics of SV protein endocytosis synaptotagmin 1-pHluorin-expressing hippocampal neurons from WT or AP-2(μ) KO mice depleted of clathrin or expressing non-targeting control shRNA were stimulated with 50 APs applied at 10 Hz at physiological temperature. Strikingly, synaptotagmin 1-pHluorin exo-/endocytosis proceeded with unaltered kinetics following 50 AP stimulation, irrespective of the depletion of clathrin and/or AP-2 (Figures S2E and S2F). Similar results were seen if neurons were stimulated with 200 APs applied at 40 Hz (data not shown).

A second possibility why effects of clathrin depletion on the kinetics of SV endocytosis may have been missed is the use of different stimulation paradigms in different studies. To test this control or clathrin-depleted neurons expressing pHluorin-tagged synaptophysin or synaptotagmin 1 were stimulated with comparably mild stimuli of 10 or 50 APs at 10 Hz or challenged with a high-frequency train of 200 APs at 40 Hz. SV endocytosis proceeded with similar kinetics in control and clathrin-depleted neurons under all conditions (Figures 2C–2F and 2H), confirming that clathrin is not essential for the speed of SV endocytosis, although clathrin/AP-2 play an important role in SV reformation (Kononenko et al., 2014; Watanabe et al., 2014) and possibly in SV protein sorting.

As other investigators have observed delayed kinetics of pHluorin endocytosis and/or reacidification (Granseth et al., 2006; Nicholson-Fish et al., 2015), we tested whether differences in the experimental protocol might be responsible for the discrepant results. We noticed that these prior studies had used a lipofectamine-based protocol for transfection. We therefore directly compared the effects of clathrin KD on SV

neurons in total for scrambled shRNA and CHC shRNA for 10 APs stimulation and N = 6 independent experiments with n = 40 and n = 26 neurons in total for scrambled shRNA and CHC shRNA for 50 APs.

(F–H) Depletion of clathrin affects the time course of endocytosis in lipofectamine-transfected neurons. Average normalized traces for calcium-phosphate-transfected (F) and lipofectamine-transfected (G) neurons coexpressing synaptotagmin 1-pHluorin and scrambled shRNA or clathrin (CHC) shRNA in response to strong stimulation with 200 APs (40 Hz, 5 s). (H) Endocytic decay constant of calcium-phosphate-transfected neurons coexpressing synaptotagmin 1-pHluorin and scrambled shRNA (36.6 ± 5.0 s) or clathrin (CHC) shRNA (36.6 ± 9.1 s) and lipofectamine-transfected neurons coexpressing synaptotagmin 1-pHluorin and scrambled shRNA (45.9 ± 6.7 s) or clathrin (CHC) shRNA (87.6 ± 9.2 s, $p < 0.01$) in response to 200 APs (40 Hz, 5 s).

(I) Depletion of clathrin leads to reduced peak amplitude of synaptotagmin 1-pHluorin, independent of the method of transfection. Relative peak amplitude of synaptotagmin 1-pHluorin in calcium phosphate-transfected neurons expressing scrambled shRNA ($100\% \pm 22.5\%$) or clathrin (CHC) shRNA ($57.1\% \pm 9.1\%$, $p < 0.05$) and lipofectamine-transfected neurons expressing scrambled shRNA ($100\% \pm 11.2\%$) or CHC shRNA ($61.7\% \pm 7.1\%$, $p < 0.05$) in response to 200 APs (40 Hz, 5 s).

(F–I) Data shown represent the mean \pm SEM of N = 6 with n = 49 and n = 30 neurons in total for lipofectamine-transfected scrambled shRNA and CHC shRNA and N = 6 with n = 38 and n = 37 neurons in total for calcium-transfected scrambled shRNA and CHC shRNA.

(J) Average normalized traces for lipofectamine-transfected neurons coexpressing synaptotagmin 1-pHluorin and scrambled shRNA or clathrin (CHC) shRNA in response to strong stimulation with 400 APs (40 Hz, 10 s) as in Nicholson-Fish et al. (2015).

(K) Endocytic decay constant of lipofectamine-transfected neurons coexpressing synaptotagmin 1-pHluorin and scrambled shRNA (67.8 ± 4.6 s) or CHC shRNA (143.9 ± 25.3 s, $p < 0.05$) in response to 40 Hz 10 s stimulation. Data shown represent the mean \pm SEM of N = 4 independent experiments with n = 33 and n = 14 neurons in total for scrambled shRNA and CHC shRNA.

Statistically significant estimates of data shown were obtained from N independent experiments. See also Figure S2.

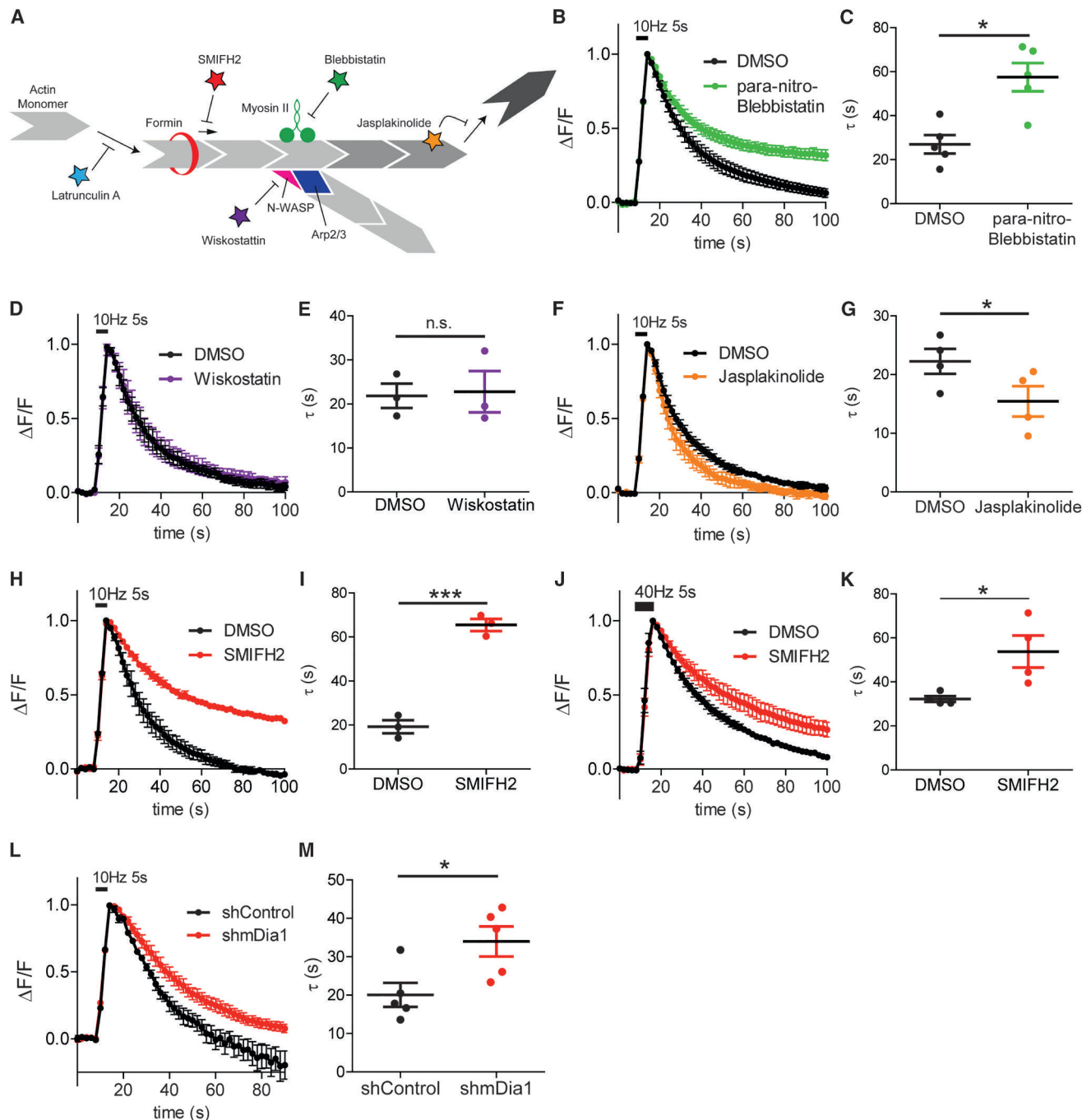


Figure 3. SV Endocytosis Is Driven by Formin-Mediated Actin Assembly and Myosin II Activity in Hippocampal Neurons

(A) Schematic illustrating the mode of action of the actin modulating drugs used in the study. Latrunculin A binds to actin monomers and prevents their incorporation into existing actin filaments. SMIFH2 inhibits formins and blocks linear actin polymerization. Wiskostatin inhibits N-WASP and blocks branched actin nucleation. Blebbistatin inhibits the ATPase activity of Myosin II. Jasplakinolide stabilizes actin filaments by preventing polymer disassembly.

(B) Averaged normalized traces for neurons expressing synaptophysin-pHluorin in response to 10 Hz 5 s stimulation, treated with 0.1% DMSO or 20 μ M para-nitroblebbistatin.

(C) $\tau_{\text{DMSO}} = 27.0 \pm 4.2$ s, $\tau_{\text{para-nitro-Blebbistatin}} = 57.5 \pm 6.5$ s, $p < 0.05$. Data shown represent the mean \pm SEM of $N = 5$ independent experiments, $n = 61$ and 49 neurons in total for DMSO and para-nitroblebbistatin.

(D) Averaged normalized traces for neurons expressing synaptophysin-pHluorin in response to 10 Hz 5 s stimulation, treated with 0.1% DMSO or 10 μ M Wiskostatin.

(E) $\tau_{\text{DMSO}} = 21.9 \pm 2.8$ s, $\tau_{\text{Wiskostatin}} = 22.8 \pm 4.7$ s, $p = 0.71$. Data shown represent the mean \pm SEM of $N = 3$ independent experiments, $n = 28$ and 27 neurons in total for DMSO and Wiskostatin.

(legend continued on next page)

endocytosis in neurons transfected using calcium-phosphate or Lipofectamine 2000. Strikingly, KD of clathrin by lipofectamine-based transfection reproduced the previously reported delay in synaptotagmin 1-pHluorin endocytosis and/or reacidification in response to stimulation with 200 or 400 APs (Figures 2G, 2J, 2H, and 2K). By contrast, the endocytic response of calcium-phosphate-transfected neurons was indistinguishable from controls (Figures 2F and 2H), akin to AP-2 KO neurons or lentivirally transduced clathrin KD assayed under different stimulation paradigms (Kononenko et al., 2014). The difference between calcium-phosphate- and lipofectamine-based transfection was not the result of the differential efficacy of clathrin depletion. Calcium phosphate (Figures 2A and 2B) or lentiviral transduction (compare Kononenko et al., 2014; Wu et al., 2014b) were at least equally efficient if not superior to lipofectamine with respect to reducing clathrin expression. Consistent with that, clathrin KD by either method resulted in a significant reduction in the amount of exocytosis elicited by electrical stimulation (Figures 2I, S2G, and S2H), as reported before (Kononenko et al., 2014; Watanabe et al., 2014). These data argue that the previously reported dependence of SV endocytosis on clathrin (Granseth et al., 2006; Nicholson-Fish et al., 2015) in cultured hippocampal neurons may have resulted from the use of lipofectamine as a transfection agent. One possibility is that lipofectamine directly or indirectly affects the rate of reacidification, e.g., by adversely affecting the mitochondrial membrane potential and therefore neuronal ATP levels, resulting in delayed quenching of pHluorin-tagged SV proteins present in large endosome-like vacuoles (ELVs) accumulated in the absence of clathrin (Kononenko et al., 2014; Watanabe et al., 2014). Consistent with this possibility, we found lipofectamine-transfected neurons to suffer from reduced mitochondrial activity (Figures S2I and S2J).

Collectively, our data show that endocytosis of SV proteins in hippocampal neurons in culture can occur in the near absence of CME, similar to what has been observed at the *Drosophila* neuromuscular junction (Heerssen et al., 2008; Kasprowitz et al., 2008), photoreceptor terminals (Fuchs et al., 2014), and at cochlear inner hair cells in vivo (Jung et al., 2015). Of note these results are consistent with a key function for clathrin/AP-2 and other adaptors in SV protein sorting from the neuronal surface (Dittman and Ryan, 2009; Kononenko et al., 2013; Kononenko and Haucke, 2015; Koo et al., 2015). These data do not

rule out the possibility that CME plays a more prominent role in SV endocytosis at other synapses (e.g., reticulospinal synapses of the lamprey [Evergren et al., 2004], which operate at low temperature), as suggested by acute peptide-based perturbation experiments (Evergren et al., 2004; Hosoi et al., 2009; Watanabe et al., 2010).

CIE of SVs Involves Formin-Mediated Actin Assembly

As SV endocytosis in response to AP trains neither occurred predominantly via UFE nor required clathrin/AP-2, we hypothesized that SV membranes might be internalized by a form of clathrin-independent endocytosis (CIE). Previous genetic, biochemical, and morphological data have established a key function for dynamin in SV endocytosis (Dittman and Ryan, 2009; Ferguson et al., 2007; Raimondi et al., 2011; Rizzoli, 2014; Saheki and De Camilli, 2012; Takei et al., 1996). Lack or inhibition of dynamin or dynamin-binding SH3 domain proteins such as endophilin (Gad et al., 2000; Milosevic et al., 2011; Ringstad et al., 1999) is accompanied by the accumulation of filamentous actin at stalled endocytic intermediates in neurons and in non-neuronal cells, suggesting a close interplay between dynamin and the actomyosin cytoskeleton. We first probed a potential role of the actomyosin cytoskeleton in SV endocytosis by applying para-nitroblebbistatin, a variant of the non-muscle myosin II inhibitor blebbistatin (Figure 3A) that is photostable and, thus, non-cytotoxic (Képiró et al., 2014). We stimulated synaptophysin-pHluorin-expressing hippocampal neurons that were either mock treated or treated with para-nitroblebbistatin with 50 APs at 10 Hz. Inhibition of myosin II activity by para-nitroblebbistatin caused a significant delay in SV endocytosis resulting in a more than 2-fold increase in the time constant for endocytosis and reacidification (Figures 3B and 3C). These results are consistent with previous morphological observations in blebbistatin-treated neurons and in myosin II KO mice (Chandrasekar et al., 2013; Yue and Xu, 2014) as well as with the reported role of myosin II in endocytic membrane fission (Flores et al., 2014).

To further dissect the function of actomyosin, we explored the role of actin nucleation that underlies F-actin assembly and, therefore, actomyosin function. The formation of branched actin networks is mediated by neural Wiskott-Aldrich-syndrome protein (N-WASP) and the Arp2/3 complex, while linear actin filaments are nucleated by formins, a large family of myosin-associated

(F) Averaged normalized traces for neurons expressing synaptophysin-pHluorin in response to 10 Hz 5 s stimulation, treated with 0.5% DMSO or 5 μ M Jasplakinolide.

(G) $\tau_{\text{DMSO}} = 22.3 \pm 2.1$ s, $\tau_{\text{Jasplakinolide}} = 15.5 \pm 2.6$ s, $p < 0.05$. Data shown represent the mean \pm SEM of N = 3 independent experiments, n = 30 and 26 neurons in total for DMSO and Jasplakinolide.

(H) Averaged normalized traces for neurons expressing synaptophysin-pHluorin in response to 10 Hz 5 s stimulation, treated with 0.1% DMSO or 30 μ M SMIFH2.

(I) $\tau_{\text{DMSO}} = 19.2 \pm 3.0$ s, $\tau_{\text{SMIFH2}} = 65.5 \pm 2.8$ s, $p < 0.001$. Data shown represent the mean \pm SEM of N = 3 independent experiments, n = 22 and 18 neurons in total for DMSO and SMIFH2.

(J) Averaged normalized traces for neurons expressing synaptotagmin 1-pHluorin in response to 40 Hz 5 s stimulation, treated with 0.1% DMSO or 30 μ M SMIFH2.

(K) $\tau_{\text{DMSO}} = 32.3 \pm 1.4$ s, $\tau_{\text{SMIFH2}} = 58.3 \pm 9.6$ s, $p < 0.05$. Data shown represent the mean \pm SEM of N = 4 independent experiments, n = 34 and 26 neurons in total for DMSO and SMIFH2.

(L) Averaged normalized traces for neurons coexpressing synaptophysin-pHluorin and shRNA plasmid targeting mDia1 (shmDia1) or a non-target shRNA (shControl) in response to 10 Hz 5 s stimulation.

(M) $\tau_{\text{shControl}} = 20.1 \pm 3.1$ s, $\tau_{\text{shmDia1}} = 34.0 \pm 3.9$ s, $p < 0.05$. Data shown represent the mean \pm SEM of N = 5 independent experiments, n = 32 and 45 neurons in total for shControl and shmDia1.

Statistically significant estimates of data shown were obtained from N independent experiments. See also Figure S3.

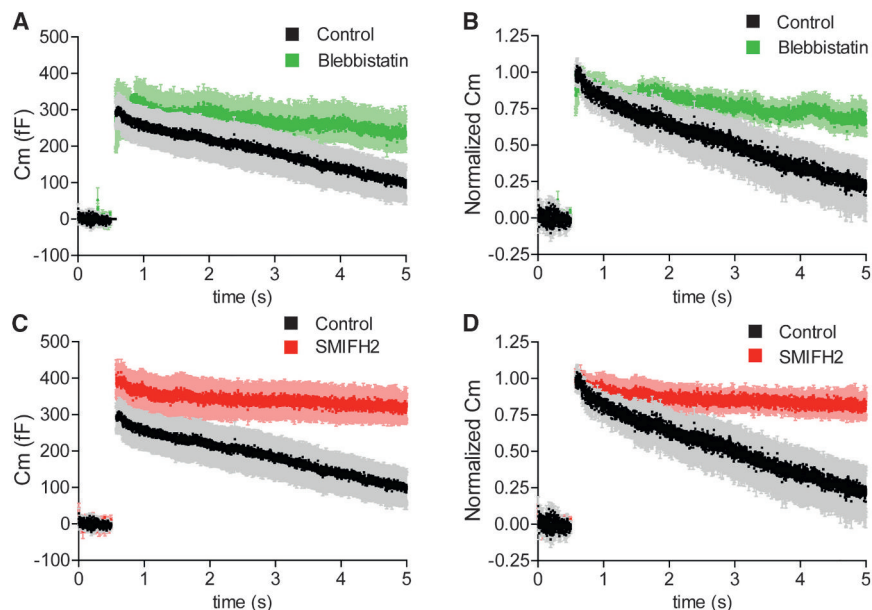


Figure 4. Formin and Myosin II Are Required for SV Endocytosis at the Calyx of Held

(A–D) The calyx of Held terminals (P8–P12) were patch clamped and depolarized from -80 mV to 0 mV for 50 ms to deplete the RRP of synaptic vesicles. Application of blebbistatin and SMIFH2 leads to slower capacitance decays (absolute in A and C and normalized in B and D). Traces represent the mean \pm SEM of $n = 9$, 8 , and 7 calyces measured for control, blebbistatin, and SMIFH2, respectively. See also Figure S4.

To test whether the function of formins in SV endocytosis is restricted to hippocampal synapses, we turned to the calyx of Held, a giant synapse in the auditory brain stem that can respond to firing rates up to several hundred Hz and, thus, is expected to capitalize on a particularly effective machinery for SV recycling. Calyx of Held terminals (postnatal days 8–

12 [P8–P12]) were patch clamped to measure capacitance responses at near physiological temperature (32°C – 34°C) (Renden and von Gersdorff, 2007). The terminal was depolarized from -80 mV to 0 mV for 50 ms to deplete the readily releasable pool of SVs and capacitance changes as well as Ca^{2+} currents (Figure S4) were recorded in the presence or absence of the myosin II inhibitor blebbistatin or the formin inhibitor SMIFH2. Stimulation induced similar exocytic capacitance increases in control, blebbistatin-, or SMIFH2-treated preparations (Figures 4A and 4C). In controls, the exocytic capacitance jump was followed by endocytic decay on a timescale of several seconds. By contrast, SV membrane endocytosis was strongly reduced in blebbistatin-treated and nearly eliminated in SMIFH2-treated calyces (Figures 4B and 4D). As SMIFH2 (Figure S4B) but not blebbistatin (Figure S4A) application also led to increased calcium influx into the calyx, we analyzed whether the adverse effect of SMIFH2 on the kinetics of SV endocytosis might be indirectly caused by elevated intracellular calcium levels. However, mimicking increased intracellular calcium by elevating its extracellular concentration (Figure S4C) had no effect on the kinetics of SV membrane internalization in the calyx (Figure S4D). Hence, endocytosis of SV membranes requires formin-mediated actin assembly at the calyx of Held, akin to what is observed in hippocampal neurons in culture.

Our collective data identify a critical function of formin-mediated actin assembly in the endocytosis of SV membranes.

To corroborate these results from pharmacological perturbation of formin-mediated actin assembly by an independent approach, we used an shRNA-based strategy to deplete hippocampal neurons of distinct formin isoforms. shRNA-mediated knockdown of the diaphanous-related formin mDia1 (Figures S3C and S3D), a formin isoform present in neurons including synapses (Figures S3E–S3G) and previously implicated in endocytic pathways in non-neuronal cells (Gasman et al., 2003; Levayer et al., 2011), slowed the kinetics of SV endocytosis similar to formin inhibition by SMIFH2 (Figures 3L and 3M). These data indicate that mDia1, and, possibly, other formin family members mediate F-actin assembly to regulate SV endocytosis.

Formins Are Required for the Formation of Endosome-like Vacuoles from which SVs Reform

Given the functional importance of formin-mediated actin assembly in SV endocytosis, we explored the consequences of inhibition of formin function in SV endocytosis at the ultrastructural level. Mock- or SMIFH2 inhibitor-treated hippocampal neurons were kept either at rest or stimulated with 200 APs at 40 Hz, fixed 20 s afterward, and analyzed by thin-section electron microscopy (Figure 5A). Stimulation with 200 APs elicited the

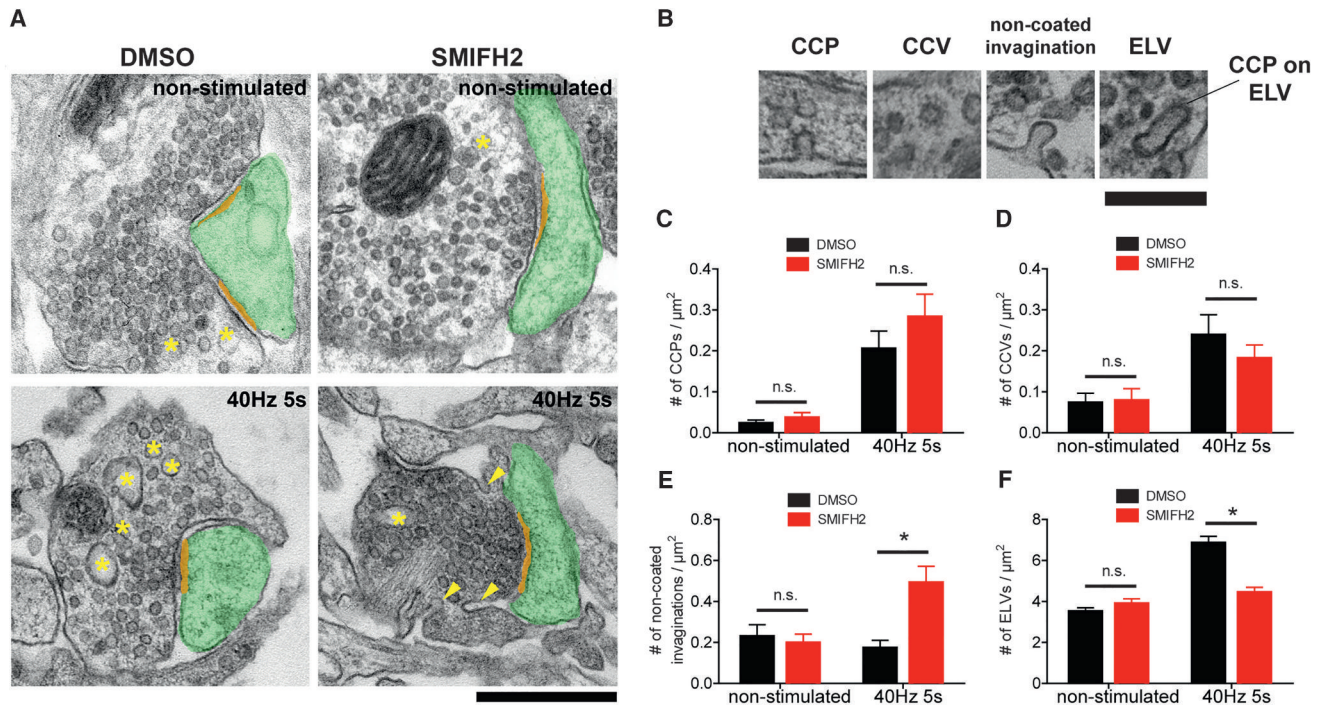


Figure 5. Formins Are Required for Formation of Endosome-like Vacuoles

(A) Electron micrographs of endocytic intermediates at hippocampal synapses treated with DMSO or SMIFH2 and non-stimulated or stimulated with 200 APs (40 Hz 5 s) and chemically fixed 20 s afterward. Endosome-like vacuoles (ELVs) and non-coated invaginations are marked with * and arrowheads, respectively. Postsynaptic compartment and the postsynaptic density are highlighted in yellow and orange, respectively. Scale bar, 500 nm.

(B) Example images of clathrin-coated vesicles (CCV), clathrin-coated pits (CCP), non-coated invaginations, and ELVs. Scale bar, 250 nm.

(C–F) Formin inhibition leads to reduced ELV formation and the accumulation of non-coated presynaptic plasma membrane invaginations in stimulated boutons.

(C) Average number of CCPs per μm^2 in non-stimulated (DMSO: 0.02 ± 0.01 , SMIFH2: 0.03 ± 0.01) and stimulated (DMSO: 0.20 ± 0.05 , SMIFH2: 0.28 ± 0.06) boutons.

(D) Average number of CCVs per μm^2 in non-stimulated (DMSO: 0.07 ± 0.03 , SMIFH2: 0.08 ± 0.03) and stimulated (DMSO: 0.24 ± 0.05 , SMIFH2: 0.18 ± 0.04) boutons.

(E) Average number of non-coated invaginations per μm^2 in non-stimulated (DMSO: 0.22 ± 0.06 , SMIFH2: 0.19 ± 0.05) and stimulated (DMSO: 0.17 ± 0.04 , SMIFH2: 0.49 ± 0.09 , $p < 0.05$) boutons.

(F) Average number of ELVs per μm^2 in non-stimulated (DMSO: 3.46 ± 0.23 , SMIFH2: 3.84 ± 0.28) and stimulated (DMSO: 6.81 ± 0.37 , SMIFH2: 4.39 ± 0.30 , $p < 0.05$) boutons.

Data shown represent the mean \pm SEM of $N = 4$ independent experiments, $n > 200$ boutons analyzed per condition.

formation of internal endosome-like vacuoles (ELVs) that apparently had undergone fission from the plasma membrane. Stimulated neurons also displayed an increased number of clathrin-coated pits (CCPs) formed at both the plasma membrane (Figure 5B, CCP) and at ELVs (Figure 5B, ELV) and of clathrin-coated vesicles (CCVs). These were much lower in number compared to ELVs (compare Figures 5C, 5D, and 5F) and may reflect intermediates en route to SV reformation. Moreover, synapses contained plasma membrane invaginations devoid of a morphologically discernible coat (non-coated invaginations) irrespective of whether neurons had been stimulated (Figures 5B–5F). Inhibition of formin-mediated actin assembly by application of SMIFH2 reduced the number of ELVs to those seen in non-stimulated control neurons (Figure 5E), while a concomitant large elevation in the number of non-coated plasma membrane invaginations was observed (Figure 5F), suggesting a precursor-product relationship between these structures. In extreme

cases, these invaginations adopted the shape of long tubular extensions of the plasma membrane that apparently had failed to undergo membrane fission (Figure 5A, lower right). By contrast, formin inhibition had no effect on the number or morphology of clathrin-coated intermediates (Figures 5C and 5D). These ultrastructural observations suggest that formin-mediated actin assembly is required for the formation of ELVs, likely by facilitating fission (Flores et al., 2014) of non-coated membrane invaginations that may mediate CIE of SV proteins from the neuronal surface.

DISCUSSION

We show here by combined optical imaging of pHluorin probes, capacitance measurements, and ultrastructural analysis that SV endocytosis occurs on multiple timescales that range from less than one second to several seconds at physiological

temperature. Moreover, we corroborate that in hippocampal neurons the kinetics of SV endocytosis are largely independent of clathrin and AP-2, consistent with data from a variety of systems (Fuchs et al., 2014; Heerssen et al., 2008; Jung et al., 2015; Kasprovicz et al., 2008; Kim and Ryan, 2009; Kononenko et al., 2014; Watanabe et al., 2013a, 2014). Instead, we find that mammalian neurons including hippocampal neurons in culture and globular bushy cells that form calyx of Held synapses capitalize on clathrin-independent endocytosis (CIE) via formin-dependent actin assembly, likely in conjunction with myosin II, to internalize SV membranes into synaptic ELVs from which SVs reform. Our data provide a possible explanation for at least some of the previous discrepant results regarding the time course and mechanism of SV endocytosis and recycling. Using an acid quench protocol (Merrifield et al., 2005) to probe the rate of endocytosis independent of reacidification, we show that in response to AP trains the majority of SV proteins is internalized over many seconds, while a minor fraction of SV proteins (10%–30%) appears to be endocytosed rapidly at physiological temperature. Interestingly, we observe that about half of all SV proteins exocytosed in response to 2 AP stimuli are endocytosed with ultrafast kinetics: we estimate a τ_{fast} of 0.7 s, although the true time constant might be somewhat slower as the assay is “blind” to endocytosis that occurs during the stimulation. Irrespective of these considerations, our results suggest that UFE has a low capacity that may be limited to single or few APs (as in Watanabe et al., 2013a, 2013b; Delvendahl et al., 2016), at least in hippocampal synapses. Whether UFE represents a kinetic component of CIE or is a mechanistically distinct pathway remains to be determined.

Moreover, we demonstrate that previous data based on pHluorin imaging suggesting an essential role for clathrin in SV endocytosis may be explained at least in part by adverse effects of lipofectamine, e.g., due to impaired reacidification as a consequence of reduced mitochondrial function. Delayed pHluorin quenching in clathrin-depleted neurons transfected with lipofectamine, thus, likely reflects the accumulation of enlarged ELVs (Heerssen et al., 2008; Kasprovicz et al., 2008; Kononenko et al., 2014; Watanabe et al., 2014), which exhibit delayed acidification due to their decreased surface-to-volume ratio compared to small vesicles. The time course and mechanism of SV endocytosis determined here closely matches observations in a variety of other systems. Capacitance measurements at the calyx of Held (Eguchi et al., 2012; Okamoto et al., 2016; Wu et al., 2014a), ribbon synapses of retinal bipolar cells (Llobet et al., 2011), and inner hair cells (Beutner et al., 2001), and of cerebellar mossy fiber synapses (Delvendahl et al., 2016) have revealed time constants for endocytosis that range from less than one second up to tens of seconds (Okamoto et al., 2016), depending on stimulation. We observe a slowing of SV endocytosis with increasing stimulus strength at physiological temperature (e.g., about 0.7 and 12 s for 2 APs, 0.7 and 26 s for 10 APs at 10 Hz, >30 s for 200 APs at 40 Hz) in agreement with prior data (Armbruster et al., 2013), although the precise τ values vary depending on the experimental conditions (e.g., extracellular calcium) and the pHluorin reporter used (e.g., we observe a tendency for faster kinetics of synaptophysin compared to synaptotagmin 1 internalization in conventional

pHluorin [compare Figures 2E and S2F] and in acid quench [Figure 1E] assays). The latter may reflect distinct rates and/or efficiencies of SV protein sorting at the cell surface (Kaempfer et al., 2015; Kononenko et al., 2013; Zhang et al., 2015) among other possibilities.

We show that the kinetics of SV endocytosis are largely independent of clathrin and AP-2, and, thus, of classical CME, at least in hippocampal neurons in culture. CIE of SV membranes has been observed at inner hair cell synapses from conditional AP-2 KO mice (Jung et al., 2015), cerebellar mossy fiber synapses (at least for low to moderate stimuli; Delvendahl et al., 2016), and in retinal bipolar neurons (Llobet et al., 2011). Moreover, our data are in good agreement with the observed formation of non-coated endocytic intermediates within 4–30 s in microwave-fixed electrically stimulated hippocampal neurons (Schikorski, 2014) and in photoreceptors (Fuchs et al., 2014). Finally, CIE of SVs is consistent with the surprisingly mild phenotypes of genetic KO of clathrin (Sato et al., 2009), AP-2 (Gu et al., 2008; Kononenko et al., 2014), AP180 (Koo et al., 2015), or stonin 2 (Kononenko et al., 2013) on the kinetics of SV retrieval in different organisms and systems. We favor a model according to which clathrin-associated endocytic adaptors (e.g., AP-2, AP180, or stonin 2) serve to concentrate SV proteins at endocytic sites on the neuronal surface to ensure their sorting into endocytic carriers formed largely by CIE. As these endocytic carriers pinch off from the plasma membrane by formin-mediated actin assembly and dynamin activity, clathrin coats assemble to facilitate the reformation of SVs from ELVs (Figure 6). Consistent with this model, ELVs accumulate following sustained or acute inactivation of clathrin or AP-2 (Heerssen et al., 2008; Jung et al., 2015; Kasprovicz et al., 2008; Kononenko et al., 2014; Watanabe et al., 2014), resulting in depression of exocytic neurotransmitter release (compare Figure 2I; Jung et al., 2015; Kononenko et al., 2014; Watanabe et al., 2014). This may relate to the fact that at least in non-neuronal cells clathrin coat assembly is a slow process with a lifetime of 60–90 s (McMahon and Boucrot, 2011). Depending on the rate of membrane fission by formin/F-actin and dynamin that may conceivably be controlled by neuronal activity (Armbruster et al., 2013; Ferguson et al., 2007; Wu et al., 2014a), clathrin coat assembly occurs either on the plasma membrane (e.g., under conditions of sustained low-frequency stimulation [Kononenko et al., 2014]) or on ELVs post-fission akin to the clathrin-coated structures observed on lysed nerve terminal preparations *in vitro* (Takei et al., 1996). It is, therefore, possible that at synapses, where the rate of fission is low (e.g., reticulospinal synapses of the lamprey [Evergren et al., 2004], which operate at low temperature), CME may play a more important role in regulating the kinetics of SV endocytosis (Evergren et al., 2004; Hosoi et al., 2009; Watanabe et al., 2010). Future studies using tools (e.g., genetic models) that specifically target CME but not CIE are needed to address this possibility.

Our own data together with prior results favor a model in which the internalization step of SV endocytosis is driven by formin/mDia1-mediated assembly of actin (Ganguly et al., 2015), which has recently been shown to be required for SV endocytosis (Wu et al., 2016). Linear actin filaments anchored to the membrane by formin/mDia1 provide a substrate for membrane fission by dynamin (Armbruster et al., 2013; Ferguson et al., 2007;

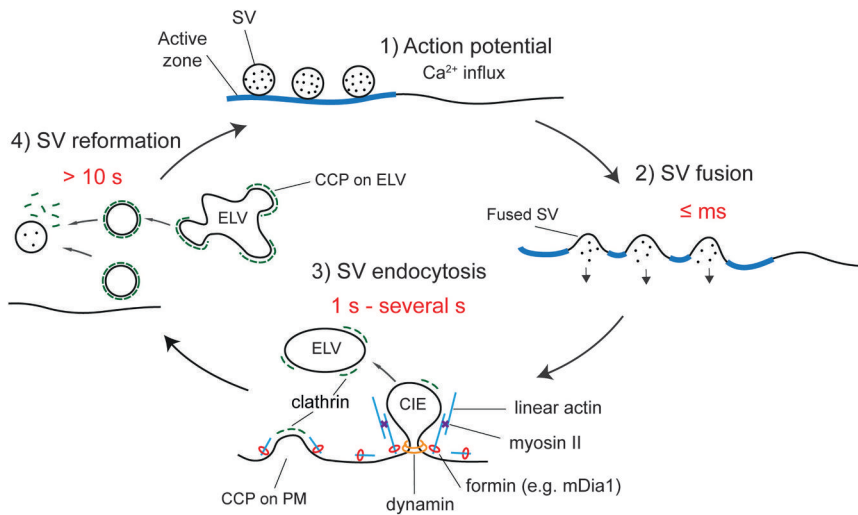


Figure 6. A Model for the Mechanism of SV Endocytosis

A schematic summarizing clathrin-independent endocytosis (CIE) of synaptic vesicles (SVs). Exocytic fusion of SVs is followed by actomyosin-driven membrane invagination, regulated by membrane-associated formins such as mDia1, independent of clathrin and adaptors. The invaginated membrane undergoes fission by the combined forces of dynamin and myosin II motors to form an endosome-like vacuole (ELV). This process starts rapidly (i.e., less than 1 s) after a brief stimulus, but depending on the number of fused SVs may take up to several seconds to complete. Concurrently, adaptor proteins and clathrin accumulate on invaginating membranes and ELVs to cluster SV proteins and generate clathrin-coated vesicles (CCVs), which will subsequently lose their coat to reform SVs.

Raimondi et al., 2011) and endophilin (Boucrot et al., 2015; Llobet et al., 2011; Milosevic et al., 2011) that act in conjunction with myosin II motors (Chandrasekar et al., 2013; Flores et al., 2014; Yue and Xu, 2014) to catalyze membrane fission. This pathway bears similarity to CIE in yeast, which requires the assembly of linear actin filaments by the formin Bni1 but not N-WASP/Arp2/3-dependent branched actin networks (Prosser et al., 2011). In this model, dynamin and formin/mDia1-based actomyosin filaments cooperate to facilitate membrane internalization (as seen for CIE of Shiga toxin [Renard et al., 2015]) and, thereby, restore membrane tension, which likely is required for the maintenance of exocytic fusion competence. SV reformation by clathrin-dependent and possibly other budding events (Wu et al., 2014b) can occur with a kinetic delay as synapses capitalize on a large reserve SV pool (Denker et al., 2011). Such a two-step mechanism (Figure 6) may be of fundamental importance for synapse function as it enables neurons to plastically control exo-/endocytic SV membrane dynamics in order to be able to respond to a wide range of stimuli (single APs to hundreds of Hz) at different types of synapses. How this pathway is kinetically controlled and how such control relates to synaptic activity will be an important subject of future studies.

STAR★METHODS

Detailed methods are provided in the online version of this paper and include the following:

- KEY RESOURCES TABLE
- CONTACT FOR REAGENT AND RESOURCE SHARING
- EXPERIMENTAL MODEL AND SUBJECT DETAILS
- METHOD DETAILS
 - Preparation of neuronal cell cultures, tamoxifen treatment, transfection
 - Generation and Use of Plasmids
 - Immunocytochemistry analysis of cultured neurons
 - Live imaging of SV endocytosis by probing resistance to acid quenching
 - Electron microscopy

- Capacitance Recordings at the calyx of Held
- Experimental Design
- QUANTIFICATION AND STATISTICAL ANALYSIS

SUPPLEMENTAL INFORMATION

Supplemental Information includes four figures and can be found with this article online at <http://dx.doi.org/10.1016/j.neuron.2017.02.011>.

AUTHOR CONTRIBUTIONS

Conceptualization: T. Soykan, N.L.K., and V.H.; Investigation: T. Soykan, N.K., D.P., N.L.K., D.V., F.G., and T. Sakaba; Writing: T. Soykan and V.H.; Funding Acquisition: V.H. and T. Sakaba.

ACKNOWLEDGMENTS

We thank Sabine Hahn, Delia Löwe, Silke Zillmann, Svea Hohensee and Martina Ringling for expert technical assistance. Supported by grants from the German Research Foundation (SFB958/A01 and Reinhart-Koselleck Award/ HA2686/13-1 to V.H.), the NeuroCure Cluster of Excellence (Exc-257, V.H. and N.L.K.), Japan Society for the Promotion of Science (KAKENHI grant 15H04261 and Core-to-Core Program, A. Advanced Research Networks to T. Sakaba).

Received: July 8, 2016

Revised: December 12, 2016

Accepted: January 23, 2017

Published: February 22, 2017

REFERENCES

- Albillos, A., Dernick, G., Horstmann, H., Almers, W., Alvarez de Toledo, G., and Lindau, M. (1997). The exocytotic event in chromaffin cells revealed by patch amperometry. *Nature* 389, 509–512.
- Aravanis, A.M., Pyle, J.L., and Tsien, R.W. (2003). Single synaptic vesicles fusing transiently and successively without loss of identity. *Nature* 423, 643–647.
- Armbruster, M., Messa, M., Ferguson, S.M., De Camilli, P., and Ryan, T.A. (2013). Dynamin phosphorylation controls optimization of endocytosis for brief action potential bursts. *eLife* 2, e00845.
- Atluri, P.P., and Ryan, T.A. (2006). The kinetics of synaptic vesicle reacidification at hippocampal nerve terminals. *J. Neurosci.* 26, 2313–2320.

- Beutner, D., Voets, T., Neher, E., and Moser, T. (2001). Calcium dependence of exocytosis and endocytosis at the cochlear inner hair cell afferent synapse. *Neuron* 29, 681–690.
- Bleckert, A., Photowala, H., and Alford, S. (2012). Dual pools of actin at presynaptic terminals. *J. Neurophysiol.* 107, 3479–3492.
- Boucrot, E., Ferreira, A.P., Almeida-Souza, L., Debard, S., Vallis, Y., Howard, G., Bertot, L., Sauvonnet, N., and McMahon, H.T. (2015). Endophilin marks and controls a clathrin-independent endocytic pathway. *Nature* 517, 460–465.
- Ceccarelli, B., Hurlbut, W.P., and Mauro, A. (1972). Depletion of vesicles from frog neuromuscular junctions by prolonged tetanic stimulation. *J. Cell Biol.* 54, 30–38.
- Chandrasekar, I., Huettner, J.E., Turney, S.G., and Bridgman, P.C. (2013). Myosin II regulates activity dependent compensatory endocytosis at central synapses. *J. Neurosci.* 33, 16131–16145.
- Cheung, G., and Cousin, M.A. (2012). Adaptor protein complexes 1 and 3 are essential for generation of synaptic vesicles from activity-dependent bulk endosomes. *J. Neurosci.* 32, 6014–6023.
- Delvendahl, I., Vyleta, N.P., von Gersdorff, H., and Hallermann, S. (2016). Fast, Temperature-Sensitive and Clathrin-Independent Endocytosis at Central Synapses. *Neuron* 90, 492–498.
- Denker, A., Bethani, I., Kröhnert, K., Körber, C., Horstmann, H., Wilhelm, B.G., Barysch, S.V., Kuner, T., Neher, E., and Rizzoli, S.O. (2011). A small pool of vesicles maintains synaptic activity in vivo. *Proc. Natl. Acad. Sci. USA* 108, 17177–17182.
- Dittman, J., and Ryan, T.A. (2009). Molecular circuitry of endocytosis at nerve terminals. *Annu. Rev. Cell Dev. Biol.* 25, 133–160.
- Eguchi, K., Nakanishi, S., Takagi, H., Taoufiq, Z., and Takahashi, T. (2012). Maturation of a PKG-dependent retrograde mechanism for exoendocytic coupling of synaptic vesicles. *Neuron* 74, 517–529.
- Evergren, E., Marcucci, M., Tomilin, N., Löw, P., Slepnev, V., Andersson, F., Gad, H., Brodin, L., De Camilli, P., and Shupliakov, O. (2004). Amphiphysin is a component of clathrin coats formed during synaptic vesicle recycling at the lamprey giant synapse. *Traffic* 5, 514–528.
- Ferguson, S.M., Brasnjo, G., Hayashi, M., Wölfel, M., Collesi, C., Giovedi, S., Raimondi, A., Gong, L.W., Ariel, P., Paradise, S., et al. (2007). A selective activity-dependent requirement for dynamin 1 in synaptic vesicle endocytosis. *Science* 316, 570–574.
- Flores, J.A., Balseiro-Gomez, S., Cabeza, J.M., Acosta, J., Ramirez-Ponce, P., and Ales, E. (2014). A new role for myosin II in vesicle fission. *PLoS ONE* 9, e100757.
- Fuchs, M., Brandstätter, J.H., and Regus-Leidig, H. (2014). Evidence for a Clathrin-independent mode of endocytosis at a continuously active sensory synapse. *Front. Cell. Neurosci.* 8, 60.
- Gad, H., Ringstad, N., Löw, P., Kjaerulf, O., Gustafsson, J., Wenk, M., Di Paolo, G., Nemoto, Y., Crun, J., Ellisman, M.H., et al. (2000). Fission and uncoating of synaptic clathrin-coated vesicles are perturbed by disruption of interactions with the SH3 domain of endophilin. *Neuron* 27, 301–312.
- Ganguly, A., Tang, Y., Wang, L., Ladit, K., Loi, J., Dargent, B., Leterrier, C., and Roy, S. (2015). A dynamic formin-dependent deep F-actin network in axons. *J. Cell Biol.* 210, 401–417.
- Gasman, S., Kalaidzidis, Y., and Zerial, M. (2003). RhoD regulates endosome dynamics through Diaphanous-related Formin and Src tyrosine kinase. *Nat. Cell Biol.* 5, 195–204.
- Goode, B.L., and Eck, M.J. (2007). Mechanism and function of formins in the control of actin assembly. *Annu. Rev. Biochem.* 76, 593–627.
- Granseth, B., Odermatt, B., Royle, S.J., and Lagnado, L. (2006). Clathrin-mediated endocytosis is the dominant mechanism of vesicle retrieval at hippocampal synapses. *Neuron* 51, 773–786.
- Gu, M., Schuske, K., Watanabe, S., Liu, Q., Baum, P., Garriga, G., and Jorgensen, E.M. (2008). Mu2 adaptor facilitates but is not essential for synaptic vesicle recycling in *Caenorhabditis elegans*. *J. Cell Biol.* 183, 881–892.
- Haucke, V., Neher, E., and Sigrist, S.J. (2011). Protein scaffolds in the coupling of synaptic exocytosis and endocytosis. *Nat. Rev. Neurosci.* 12, 127–138.
- Heerssen, H., Fetter, R.D., and Davis, G.W. (2008). Clathrin dependence of synaptic-vesicle formation at the *Drosophila* neuromuscular junction. *Curr. Biol.* 18, 401–409.
- Heuser, J.E., and Reese, T.S. (1973). Evidence for recycling of synaptic vesicle membrane during transmitter release at the frog neuromuscular junction. *J. Cell Biol.* 57, 315–344.
- Higashida, C., Suetsugu, S., Tsuji, T., Monypenny, J., Narumiya, S., and Watanabe, N. (2008). G-actin regulates rapid induction of actin nucleation by mDia1 to restore cellular actin polymers. *J. Cell Sci.* 121, 3403–3412.
- Hosoi, N., Holt, M., and Sakaba, T. (2009). Calcium dependence of exo- and endocytotic coupling at a glutamatergic synapse. *Neuron* 63, 216–229.
- Jockusch, W.J., Praefcke, G.J., McMahon, H.T., and Lagnado, L. (2005). Clathrin-dependent and clathrin-independent retrieval of synaptic vesicles in retinal bipolar cells. *Neuron* 46, 869–878.
- Jung, S., Maritzen, T., Wichmann, C., Jing, Z., Neef, A., Revelo, N.H., Al-Moyed, H., Meese, S., Wojcik, S.M., Panou, I., et al. (2015). Disruption of adaptor protein 2 μ (AP-2 μ) in cochlear hair cells impairs vesicle reloading of synaptic release sites and hearing. *EMBO J.* 34, 2686–2702.
- Kaempf, N., Kochlamazashvili, G., Puchkov, D., Maritzen, T., Bajjalieh, S.M., Kononenko, N.L., and Haucke, V. (2015). Overlapping functions of stonin 2 and SV2 in sorting of the calcium sensor synaptotagmin 1 to synaptic vesicles. *Proc. Natl. Acad. Sci. USA* 112, 7297–7302.
- Kasprowicz, J., Kuenen, S., Miskiewicz, K., Habets, R.L., Smits, L., and Verstreken, P. (2008). Inactivation of clathrin heavy chain inhibits synaptic recycling but allows bulk membrane uptake. *J. Cell Biol.* 182, 1007–1016.
- Kavalali, E.T., and Jorgensen, E.M. (2014). Visualizing presynaptic function. *Nat. Neurosci.* 17, 10–16.
- Képiró, M., Várkuti, B.H., Végner, L., Vörös, G., Hegyi, G., Varga, M., and Málnási-Csizmadia, A. (2014). para-Nitroblebbistatin, the non-cytotoxic and photostable myosin II inhibitor. *Angew. Chem. Int. Ed. Engl.* 53, 8211–8215.
- Kim, S.H., and Ryan, T.A. (2009). Synaptic vesicle recycling at CNS synapses without AP-2. *J. Neurosci.* 29, 3865–3874.
- Kononenko, N.L., and Haucke, V. (2015). Molecular mechanisms of presynaptic membrane retrieval and synaptic vesicle reformation. *Neuron* 85, 484–496.
- Kononenko, N.L., Diril, M.K., Puchkov, D., Kintscher, M., Koo, S.J., Pfuhl, G., Winter, Y., Wienisch, M., Klingauf, J., Breustedt, J., et al. (2013). Compromised fidelity of endocytic synaptic vesicle protein sorting in the absence of stonin 2. *Proc. Natl. Acad. Sci. USA* 110, E526–E535.
- Kononenko, N.L., Puchkov, D., Classen, G.A., Walter, A.M., Pechstein, A., Sawade, L., Kaempf, N., Trimbuch, T., Lorenz, D., Rosenmund, C., et al. (2014). Clathrin/AP-2 mediate synaptic vesicle reformation from endosome-like vacuoles but are not essential for membrane retrieval at central synapses. *Neuron* 82, 981–988.
- Koo, S.J., Kochlamazashvili, G., Rost, B., Puchkov, D., Gimber, N., Lehmann, M., Tadeus, G., Schmoranz, J., Rosenmund, C., Haucke, V., and Maritzen, T. (2015). Vesicular Synaptobrevin/VAMP2 Levels Guarded by AP180 Control Efficient Neurotransmission. *Neuron* 88, 330–344.
- Levayer, R., Pelissier-Monier, A., and Lecuit, T. (2011). Spatial regulation of Dia and Myosin-II by RhoGEF2 controls initiation of E-cadherin endocytosis during epithelial morphogenesis. *Nat. Cell Biol.* 13, 529–540.
- Lobet, A., Gallop, J.L., Burden, J.J., Camdere, G., Chandra, P., Vallis, Y., Hopkins, C.R., Lagnado, L., and McMahon, H.T. (2011). Endophilin drives the fast mode of vesicle retrieval in a ribbon synapse. *J. Neurosci.* 31, 8512–8519.
- Macia, E., Ehrlich, M., Massol, R., Boucrot, E., Brunner, C., and Kirchhausen, T. (2006). Dynasore, a cell-permeable inhibitor of dynamin. *Dev. Cell* 10, 839–850.
- McMahon, H.T., and Boucrot, E. (2011). Molecular mechanism and physiological functions of clathrin-mediated endocytosis. *Nat. Rev. Mol. Cell Biol.* 12, 517–533.

- Merrifield, C.J., Perrais, D., and Zenisek, D. (2005). Coupling between clathrin-coated-pit invagination, cortactin recruitment, and membrane scission observed in live cells. *Cell* 121, 593–606.
- Milosevic, I., Giovedi, S., Lou, X., Raimondi, A., Collesi, C., Shen, H., Paradise, S., O'Toole, E., Ferguson, S., Cremona, O., and De Camilli, P. (2011). Recruitment of endophilin to clathrin-coated pit necks is required for efficient vesicle uncoating after fission. *Neuron* 72, 587–601.
- Nicholson-Fish, J.C., Kokotos, A.C., Gillingwater, T.H., Smillie, K.J., and Cousin, M.A. (2015). VAMP4 Is an Essential Cargo Molecule for Activity-Dependent Bulk Endocytosis. *Neuron* 88, 973–984.
- Okamoto, Y., Lipstein, N., Hua, Y., Lin, K.H., Brose, N., Sakaba, T., and Midorikawa, M. (2016). Distinct modes of endocytotic presynaptic membrane and protein uptake at the calyx of Held terminal of rats and mice. *eLife* 5, 5.
- Park, R.J., Shen, H., Liu, L., Liu, X., Ferguson, S.M., and De Camilli, P. (2013). Dynamin triple knockout cells reveal off target effects of commonly used dynamin inhibitors. *J. Cell Sci.* 126, 5305–5312.
- Prosser, D.C., Drivas, T.G., Maldonado-Báez, L., and Wendland, B. (2011). Existence of a novel clathrin-independent endocytic pathway in yeast that depends on Rho1 and formin. *J. Cell Biol.* 195, 657–671.
- Raimondi, A., Ferguson, S.M., Lou, X., Armbruster, M., Paradise, S., Giovedi, S., Messa, M., Kono, N., Takasaki, J., Cappello, V., et al. (2011). Overlapping role of dynamin isoforms in synaptic vesicle endocytosis. *Neuron* 70, 1100–1114.
- Renard, H.F., Simunovic, M., Lemièrre, J., Boucrot, E., Garcia-Castillo, M.D., Arumugam, S., Chambon, V., Lamaze, C., Wunder, C., Kenworthy, A.K., et al. (2015). Endophilin-A2 functions in membrane scission in clathrin-independent endocytosis. *Nature* 517, 493–496.
- Renden, R., and von Gersdorff, H. (2007). Synaptic vesicle endocytosis at a CNS nerve terminal: faster kinetics at physiological temperatures and increased endocytotic capacity during maturation. *J. Neurophysiol.* 98, 3349–3359.
- Ringstad, N., Gad, H., Löw, P., Di Paolo, G., Brodin, L., Shupliakov, O., and De Camilli, P. (1999). Endophilin/SH3p4 is required for the transition from early to late stages in clathrin-mediated synaptic vesicle endocytosis. *Neuron* 24, 143–154.
- Rizzoli, S.O. (2014). Synaptic vesicle recycling: steps and principles. *EMBO J.* 33, 788–822.
- Saheki, Y., and De Camilli, P. (2012). Synaptic vesicle endocytosis. *Cold Spring Harb. Perspect. Biol.* 4, a005645.
- Sankaranarayanan, S., Atluri, P.P., and Ryan, T.A. (2003). Actin has a molecular scaffolding, not propulsive, role in presynaptic function. *Nat. Neurosci.* 6, 127–135.
- Sato, K., Ernstrom, G.G., Watanabe, S., Weimer, R.M., Chen, C.H., Sato, M., Siddiqui, A., Jorgensen, E.M., and Grant, B.D. (2009). Differential requirements for clathrin in receptor-mediated endocytosis and maintenance of synaptic vesicle pools. *Proc. Natl. Acad. Sci. USA* 106, 1139–1144.
- Schikorski, T. (2014). Readily releasable vesicles recycle at the active zone of hippocampal synapses. *Proc. Natl. Acad. Sci. USA* 111, 5415–5420.
- Schneggenburger, R., Meyer, A.C., and Neher, E. (1999). Released fraction and total size of a pool of immediately available transmitter quanta at a calyx synapse. *Neuron* 23, 399–409.
- Takei, K., Mundigl, O., Daniell, L., and De Camilli, P. (1996). The synaptic vesicle cycle: a single vesicle budding step involving clathrin and dynamin. *J. Cell Biol.* 133, 1237–1250.
- Wagh, D., Terry-Lorenzo, R., Waites, C.L., Leal-Ortiz, S.A., Maas, C., Reimer, R.J., and Garner, C.C. (2015). Piccolo directs activity dependent F-actin assembly from presynaptic active zones via Daam1. *PLoS ONE* 10, e0120093.
- Watanabe, H., Yamashita, T., Saitoh, N., Kiyonaka, S., Iwamatsu, A., Campbell, K.P., Mori, Y., and Takahashi, T. (2010). Involvement of Ca²⁺ channel synprint site in synaptic vesicle endocytosis. *J. Neurosci.* 30, 655–660.
- Watanabe, S., Liu, Q., Davis, M.W., Hollopeter, G., Thomas, N., Jorgensen, N.B., and Jorgensen, E.M. (2013a). Ultrafast endocytosis at *Caenorhabditis elegans* neuromuscular junctions. *eLife* 2, e00723.
- Watanabe, S., Rost, B.R., Camacho-Pérez, M., Davis, M.W., Söhl-Kielczynski, B., Rosenmund, C., and Jorgensen, E.M. (2013b). Ultrafast endocytosis at mouse hippocampal synapses. *Nature* 504, 242–247.
- Watanabe, S., Trimbuch, T., Camacho-Pérez, M., Rost, B.R., Brokowski, B., Söhl-Kielczynski, B., Felies, A., Davis, M.W., Rosenmund, C., and Jorgensen, E.M. (2014). Clathrin regenerates synaptic vesicles from endosomes. *Nature* 515, 228–233.
- Wienisch, M., and Klingauf, J. (2006). Vesicular proteins exocytosed and subsequently retrieved by compensatory endocytosis are nonidentical. *Nat. Neurosci.* 9, 1019–1027.
- Wu, X.S., Zhang, Z., Zhao, W.D., Wang, D., Luo, F., and Wu, L.G. (2014a). Calcineurin is universally involved in vesicle endocytosis at neuronal and non-neuronal secretory cells. *Cell Rep.* 7, 982–988.
- Wu, Y., O'Toole, E.T., Girard, M., Ritter, B., Messa, M., Liu, X., McPherson, P.S., Ferguson, S.M., and De Camilli, P. (2014b). A dynamin 1-, dynamin 3- and clathrin-independent pathway of synaptic vesicle recycling mediated by bulk endocytosis. *eLife* 3, e01621.
- Wu, X.S., Lee, S.H., Sheng, J., Zhang, Z., Zhao, W.D., Wang, D., Jin, Y., Charnay, P., Ervasti, J.M., and Wu, L.G. (2016). Actin is crucial for all kinetically distinguishable forms of endocytosis at synapses. *Neuron* 92, 1020–1035.
- Yue, H.Y., and Xu, J. (2014). Myosin light chain kinase accelerates vesicle endocytosis at the calyx of Held synapse. *J. Neurosci.* 34, 295–304.
- Zhang, N., Gordon, S.L., Fritsch, M.J., Esoof, N., Campbell, D.G., Gourlay, R., Velupillai, S., Macartney, T., Pegg, M., van Aalten, D.M., et al. (2015). Phosphorylation of synaptic vesicle protein 2A at Thr84 by casein kinase 1 family kinases controls the specific retrieval of synaptotagmin-1. *J. Neurosci.* 35, 2492–2507.
- Zhao, W.D., Hamid, E., Shin, W., Wen, P.J., Krystofiak, E.S., Villarreal, S.A., Chiang, H.C., Kachar, B., and Wu, L.G. (2016). Hemi-fused structure mediates and controls fusion and fission in live cells. *Nature* 534, 548–552.



OUR NETWORK IS YOUR NETWORK

With Cell Press Webinars, our network is your network!

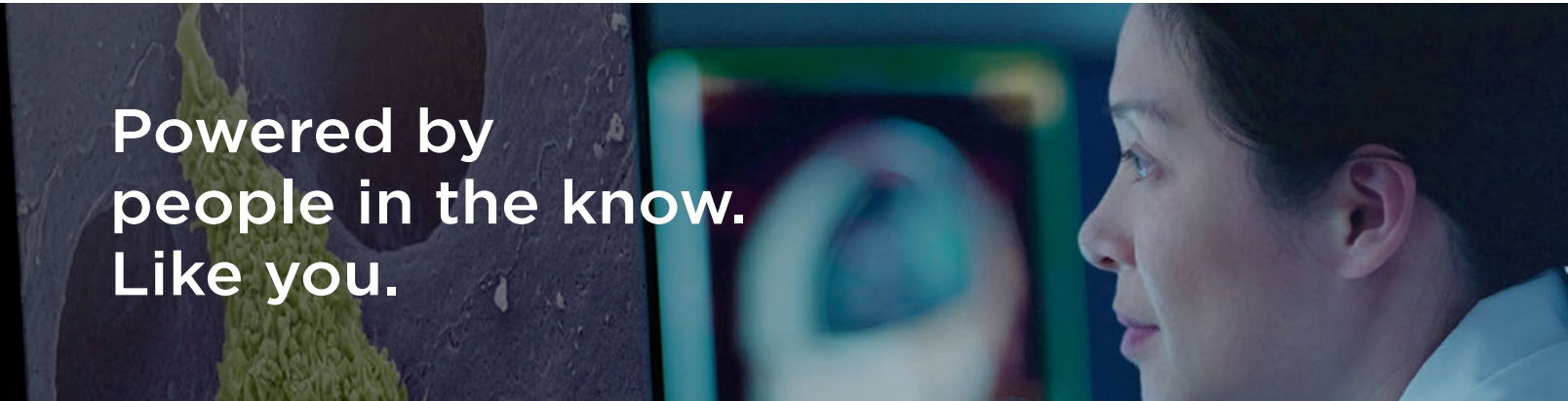
Cell Press Webinars give you access to hot topics in emerging research and the application of new technology.

Watch essential, need-to-know webcasts via live streaming or on demand from the comfort and convenience of your office, lab, or home.

Need-to-know topics, editorially curated

World-class presenters, experts in their field

Moderated by Cell Press editors



Powered by
people in the know.
Like you.

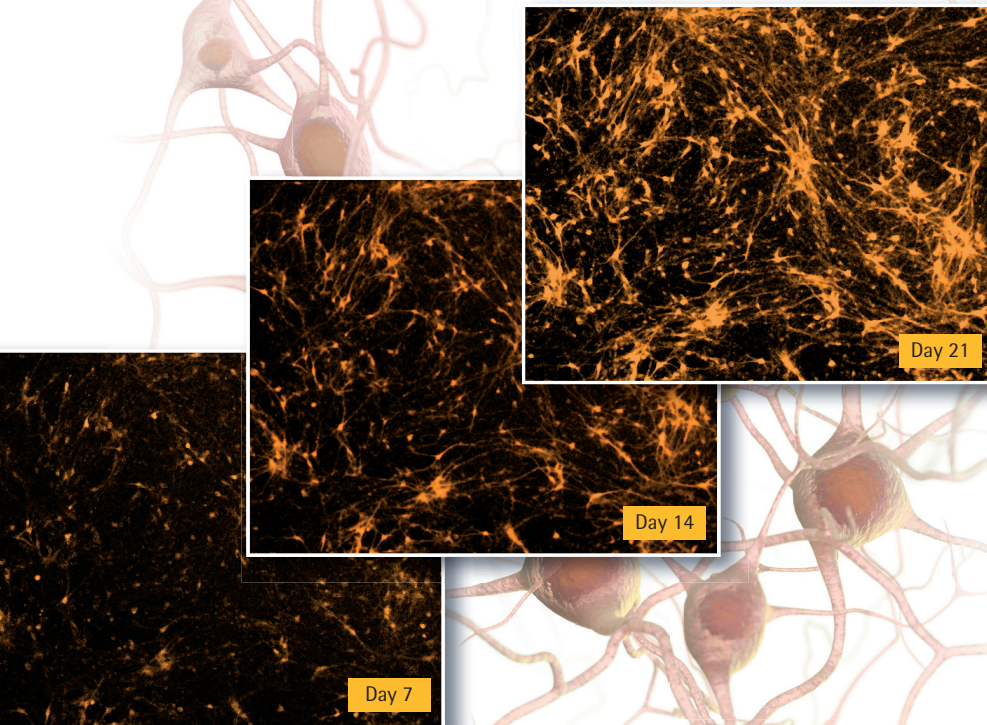
Tap into our network today!
Visit www.cell.com/webinars

CellPress
Webinars



sartorius

Monitor and analyze hiPSC-derived neurons



Human induced pluripotent stem cell-derived neurons provide a new approach aimed at modeling neurological diseases and are critical for the characterization and evaluation of these novel model systems.

Reveal the dynamic nature of hiPSC-derived neurons in mono or co-culture conditions using the IncuCyte® S3 System for real-time, long-term quantitative analysis.

Essenbio.com/neuroscience

- Optimize culture conditions for (hiPSC)-derived neurons.
- Visualize and quantify neurite dynamics using phase (monoculture) or fluorescent (co-culture) IncuCyte® NeuroTrack software.
- Monitor neuronal cell health (e.g. apoptosis) and validate mechanisms.



turning science **into solutions**

IncuCyte®
by SARTORIUS